THE CHEMICAL EVOLUTION OF STAR-FORMING GALAXIES

A DISSERTATION SUBMITTED TO THE GRADUATE DIVISION OF THE UNIVERSITY OF HAWAI'I AT MĀNOA IN PARTIAL FULFILLMENT OF THE REQUIREMENTS FOR THE DEGREE OF

DOCTOR OF PHILOSOPHY

IN

ASTRONOMY

AUGUST 2014

By
H. Jabran Zahid

Dissertation Committee:

Lisa Kewley, Chairperson
Rolf Kudritzki
Fabio Bresolin
Mike Dopita
Dave Sanders
Kim Binsted

The truth about the world, he said, is that anything is possible. Had you not seen it all from birth and thereby bled it of its strangeness it would appear to you for what it is, a hat trick in a medicine show, a fevered dream, a trance bepopulate with chimeras having neither analogue nor precedent, an itinerant carnival, a migratory tentshow whose ultimate destination after many a pitch in many a mudded field is unspeakable and calamitous beyond reckoning.

The universe is no narrow thing and the order within it is not constrained by any latitude in its conception to repeat what exists in one part in any other part. Even in this world more things exist without our knowledge than with it and the order in creation which you see is that which you have put there, like a string in a maze, so that you shall not lose your way. For existence has its own order and that no man's mind can compass, that mind itself being but a fact among others.

- Cormac McCarthy, *Blood Meridian, or the Evening Redness in the West*

Acknowledgements

I am indebted to all the collaborators I have had the pleasure of working with. Without their contributions, much of the work presented in this dissertation would not be possible. In alphabetical order these people are: Fabio Bresolin, Alison Coil, Emanuele Daddi, Romeel Davé, Gabriel Dima, Mike Dopita, Dawn Erb, Dan Fabricant, Margaret Geller, Lars Hernquist, Ho Seong Hwang, Daichi Kashino, Rolf-Peter Kudritzki, Mike Kurtz, Lisa Kewley, Christian Maier, Dave Sanders, John Silverman, Paul Torrey, Mark Vogelsberger and Robert Yates. The support of my family was very important for providing the motivation required to finish this dissertation. I also would like to thank my wonderful and beautiful wife Megan Taddonio for sticking by my side while I completed this dissertation. Finally, I would like to thank my friends for helping me stay "balanced" over the last six.

Abstract

The gas-phase oxygen abundance, i.e. metallicity, of a galaxy is set by the interplay between star formation and gas flows. Metals are dispersed into the interstellar medium by stellar winds and supernovae. Metals accumulate in the interstellar medium of star-forming galaxies and provide a record of star-formation. However, inflows of unenriched gas into galaxies and metal-rich outflows of gas from galaxies can both reduce the metallicity. Thus, measurements of the metallicity across cosmic time provide important constraints for understanding the cycling of gas through galaxies as they build their stellar mass and evolve. I have measured the chemical evolution of galaxies over the last 10 billion years of cosmic time. These measurements provide a coherent picture of how galaxies enrich as they build their stellar mass. Using these measurements, I have conducted the first census of oxygen in star-forming galaxies. The oxygen census reveals that over their lifetime, star-forming galaxies expel a substantial fraction of the oxygen they produce in outflows. The mass of oxygen missing from galaxies provides one of the most robust empirical constraints for the total mass lost via outflows in galaxies. I show that the amount of mass loss currently implemented in theoretical models is 1-2 orders of magnitude larger than the empirical estimates for mass loss from the oxygen census. The discrepancy between empirical and theoretical constraints for the amount of mass loss has important implications for our understanding of galaxy evolution. I conclude with a model that suggests that the chemical evolution of star-forming galaxies is very simple. The metallicity of star-forming galaxies for $z \sim 1.5$ only depends on the stellar-to-gas mass ratio. The relation between metallicity and stellar-to-gas mass ratio is an universal relation followed by all galaxies as they evolve.

Table of Contents

List of Tables

List of Figures

Chapter 1

Introduction

This dissertation represents six years of hard work. It is comprised of nine first-author publications which focus on measuring and modeling the chemical evolution of star-forming galaxies. Chapters 2 - 5 are observational studies which present measurements of the chemical evolution of star-forming galaxies across cosmic time. Chapters 6 - 9 are mostly phenomenological investigations of the physical processes governing the chemical evolution of star-forming galaxies. They are phenomenological in the sense that they combine empirical constraints within a theoretical framework in order to develop a semi-empirical model of galactic chemical evolution. Chapter 10 is a synthesis of the observations and phenomenological models which provides us with a fundamentally new, simple and elegant model for understanding galactic chemical evolution: the so-called universal metallicity relation.

Seven of the chapters of this dissertation are published articles which have been accepted by reputable journals only after a standard scientific peer review process. The other two chapters (Chapters 4 and 10) are currently under review and should be accepted shortly. With the exception of a few minor editions, the articles are included in their entirety. Each chapter therefore is self-contained and can be read individually. However, in this chapter I will provide a comprehensive introduction of the dissertation in order to provide context and scope for the work presented herein. Those reading this dissertation in its entirety are

free to skip the introductory section of each subsequent chapter and in many cases the data and methods sections as these sections may be redundant.

1.1 The Metallicities and Star Formation Rates of Galaxies

Gas flows and star formation govern the evolution of galaxies. A key diagnostic of gas flows and star formation in galaxies is the amount of heavy elements relative to hydrogen in the interstellar medium (ISM). Heavy elements are produced by massive stars and are dispersed into the ISM by stellar mass loss processes. Therefore, the ISM metal content is closely linked to the stellar mass of a galaxy. The heavy element abundance is measured relative to hydrogen and therefore also depends on the gas content of galaxies. The rate at which stars form is also regulated by the gas content. Understanding the relation between stellar mass, metallicity and star formation rate (SFR) of galaxies and its evolution is fundamental for developing a comprehensive theory of galaxy evolution.

1.1.1 The Mass-Metallicity Relation

Oxygen is the most abundant heavy element formed in the Universe. Therefore, the abundance of oxygen can be used as a proxy for the production of all heavy elements. The gas-phase oxygen abundance is correlated to the stellar mass in star-forming galaxies. This relation is known as the mass-metallicity (MZ) relation. The MZ relation was first observed in a small sample of nearby galaxies by Lequeux et al. (1979). They measured that galaxy metallicity increases with stellar mass. Subsequently, Tremonti et al. (2004) measure the MZ relation of $\sim 50,000$ star-forming galaxies in the Sloan Digital Sky Survey (SDSS). They find a tight MZ relation ($\sim$0.1 dex scatter) extending over three orders of magnitude in stellar mass.

Several independent approaches suggest that the MZ relation extends down to very low stellar masses. From the examination of $\sim$ 27 nearby dwarf irregular galaxies, Lee et al. (2006) argue that the MZ relation extends down to $\sim 10^6 M_{\odot}$. Berg et al. (2012) reach similar conclusions from examination of 42 low luminosity galaxies in the local volume.

Based on a substantially larger sample, in Zahid et al. (2012a) I show that the scatter in metallicities increases at lower stellar masses and the distribution appears to follow the observed MZ relation for galaxies with stellar masses $\gtrsim 10^9 M_\odot$. Finally, from stacking analysis, Andrews & Martini (2013) show that the MZ relation is continuous down to $10^7 M_\odot$.

The MZ relation is a relation between the gas-phase oxygen abundances and the stellar masses of galaxies. A similar relation is observed between the mean or mass-weighted stellar oxygen abundance and stellar mass of galaxies. Since stars form from gas that is enriched by previous generations of star-formation, this is to be expected. Gallazzi et al. (2005) show that average stellar metallicities determined from integrated spectra of a large sample of SDSS galaxies are correlated to the host galaxy stellar masses. A relation between stellar mass and stellar metallicity is also seen when metallicities are determined from individual stars (Kudritzki et al. 2008, 2012; Kirby et al. 2013; Hosek et al. 2014). Stellar abundance analyses are not limited to just oxygen and a large number of elements now show a correlation with stellar mass (e.g. Conroy et al. 2013). All these studies support the conclusion that more massive systems are more chemically evolved.

The MZ relation is one of the primary observations for measuring the chemical evolution of galaxies. Savaglio et al. (2005) first showed the MZ relation for galaxies outside the local Universe. Many subsequent studies have shown the MZ relation is observed for galaxies out to $z \sim 3$ (Erb et al. 2006; Maier et al. 2005, 2006; Cowie & Barger 2008; Maiolino et al. 2008; Mannucci et al. 2009; Zahid et al. 2011; Yabe et al. 2012; Zahid et al. 2012b, 2013a,b; Yabe et al. 2014) and perhaps beyond (Laskar et al. 2011; Møller et al. 2013). Observations of the MZ relation reveal that the metallicities of galaxies increase with time. Kewley & Ellison (2008) show that various abundance diagnostics are not consistent. Therefore, quantifying the evolution of the MZ relation requires a consistent methodology.

1.1.2 The Mass-SFR Relation

Recent observations indicate that stellar mass growth of most star-forming galaxies is dominated by secular evolution over the last ∼10 billion years. A strong correlation between stellar mass and SFR is observed out to at least $z \sim 2.5$ (Noeske et al. 2007b; Salim et al. 2007; Elbaz et al. 2007; Daddi et al. 2007; Pannella et al. 2009; Whitaker et al. 2012; Reddy et al. 2012) and is found to be independent of environment (Peng et al. 2010; Wijesinghe et al. 2012; Koyama et al. 2013). The small scatter (~ 0.25 dex) of the stellar mass - SFR relation is independent of redshift suggesting that secular processes such as cosmological gas accretion dominate over mergers in building up the stellar mass of galaxies since at least $z \sim 2-3$. The observed stellar mass-SFR (MS) relation places strong constraints on the star formation histories of galaxies (Noeske et al. 2007a; Conroy & Wechsler 2009; Leitner 2012; Zahid et al. 2012b). The observed MS relation at several epochs implies that the majority of local star-forming galaxies are best characterized by continuous star formation histories. The observations demand that the majority of local star-forming galaxies maintain SFRs that do not vary significantly from their mean SFRs over most of their lifetime (Noeske et al. 2007b).

1.1.3 Second Parameter Dependencies of the MZ relation

The scatter observed in the MZ relation is correlated with other physical properties. These correlations provide clues to the origin of the MZ relation. Ellison et al. (2008) first showed that the MZ relation depends on specific SFR and galaxy size. At a fixed stellar mass, galaxies with high specific SFRs or large half-light radii have systematically lower gas-phase metallicities than galaxies with low specific SFRs or small radii.

Several studies have built on the results of Ellison et al. (2008). A relation between stellar mass, metallicity and star formation rate (SFR) is observed in local (Mannucci et al. 2010; Lara-López et al. 2010; Yates et al. 2012; Andrews & Martini 2013) and high redshift galaxies (Zahid et al. 2013b; Yabe et al. 2014; Troncoso et al. 2014). At stellar masses $\lesssim 10^{10.5} M_{\odot}$, galaxies with high SFRs typically have lower metallicities and vice versa.

Mannucci et al. (2010) derive a relation between stellar mass, metallicity and SFR that minimizes the scatter of metallicity in the local galaxy population. They argue that the minimum scatter relation between stellar mass, metallicity and SFR that they derive is independent of redshift. They refer to this minimum scatter relation as the fundamental metallicity relation (FMR). For the FMR, the higher SFRs observed in high redshift galaxies account for their lower metallicities. However, the redshift independence of the relation between stellar mass, metallicity and SFR remains tentative (Niino 2012; Pérez-Montero et al. 2013; Sánchez et al. 2013; Zahid et al. 2013b; Ly et al. 2014).

Both the SFR and metallicity are dependent on the gas content and the anti-correlation between metallicity and SFR is likely the result of variations in gas content (Hughes et al. 2012; Lara-López et al. 2013; Bothwell et al. 2013). Recently, Bothwell et al. (2013) present observations suggesting that the FMR derived by Mannucci et al. (2010) is the result of a relation between stellar mass, metallicity and gas content. At a fixed stellar mass, galaxies with higher gas fractions will exhibit elevated SFRs and lower metallicity. In the Bothwell et al. interpretation, the SFR acts as a proxy for gas content in the FMR proposed by Mannucci et al. (2010). Bothwell et al. (2013) are not able to investigate the redshift dependence of the relation between stellar mass, metallicity and gas content due to lack of measurements of atomic gas in galaxies outside the local Universe.

1.2 Outflows in Star-Forming Galaxies

Galaxy scale winds are fundamental to galaxy evolution. The observed baryon content of galaxies is substantially below the cosmic baryon fraction (Papastergis et al. 2012). To account for this deficit, galaxy formation theories require mechanisms to reduce the efficiency with which galaxies grow (e.g., Springel & Hernquist 2003). Consequently, strong feedback which is capable of launching galactic scale outflows is central to semi-analytic and hydrodynamical galaxy formation models (e.g., Somerville & Primack 1999; Springel & Hernquist 2003; Schaye et al. 2010; Davé et al. 2011; Vogelsberger et al. 2013, plus

many others). In simulations, energy and/or momentum injected by massive stars or active galactic nuclei is capable of driving gas out of galaxies. Although these outflows are primarily required to regulate the growth of galaxies, they also drive metals out of the ISM. Outflows reduce the metal content in galaxies and contribute to the enrichment of the circumgalactic and intergalactic medium (e.g. Springel & Hernquist 2003; Oppenheimer & Davé 2006; Davé et al. 2011).

1.2.1 Physical Properties of Outflows

Despite the need for outflows to regulate the growth of galaxies, the physical properties of galactic scale winds are poorly determined observationally. The lack of understanding is partly due to the complex multi-phase structure of the gas, which can only be characterized in detail with observations over a broad range of wavelengths (Veilleux et al. 2005). While absorption line studies permit direct measurements of outflow velocities (e.g. Heckman et al. 2000; Rupke et al. 2005; Weiner et al. 2009; Chen et al. 2010; Erb et al. 2012; Martin et al. 2012; Rubin et al. 2013), estimates of the magnitude of mass loss in winds are much more difficult to obtain. Moreover, the metallicity of the wind material is constrained by only a few observations (e.g., Martin et al. 2002).

In the absence of a complete understanding of the character of outflows, theories employ wind prescriptions that are tuned to reproduce the observed properties of the galaxy population (e.g., the galaxy stellar mass function). This is typically achieved by assuming that a constant amount of energy or momentum is injected per unit star formation and that the wind speed scales in proportion to the galaxy escape velocity (Martin 2005). However, in detail, the normalization and scaling of outflows vary significantly between implementations. For example, the galaxy stellar mass functions derived by Davé et al. (2011) and Puchwein & Springel (2013) both provide satisfactory fits to the stellar mass function of local galaxies; this is in spite of mass loading factors that have normalization offsets of an order of magnitude for low stellar mass (i.e. $M_* \sim 10^9 M_\odot$) systems. The uncertainties in our understanding of the physical properties of galactic winds are further

complicated by numerical approximations that vary substantially from one simulation code to another (e.g Kereš et al. 2012; Sijacki et al. 2012; Torrey et al. 2013; Nelson et al. 2013; Vogelsberger et al. 2013, 2014).

1.2.2 Effect of Outflows on Metallicity

Gas outflows deplete the heavy element content of galaxies. Typically it is assumed that the wind material has the same metallicity as the ambient ISM. However, the actual wind metallicity relative to the ISM may be greater if it is primarily comprised of supernova ejecta or substantially depressed if a sufficient amount of metal-poor gas is entrained as the wind propagates out of the galaxy. The total amount of metals ejected from the ISM will be proportional to the magnitude and metallicity of the outflowing gas, modulo the amount of metals ejected and subsequently reaccreted. In the absence of direct measurements characterizing these physical processes, we must rely on empirical constraints for the total metal loss in the local galaxy population to infer the properties of outflows and reaccretion.

1.2.3 Dust Driven Outflows

Recent theoretical considerations suggest that momentum, unlike energy which can be radiated away, may be the primary driver of large scale gas flows (Murray et al. 2005). Dust plays a crucial role since radiation couples to dust over a large and continuous range of wavelengths (Draine 2003) and provides a convenient mechanism for momentum transfer between the radiation field and the gas (e.g. Murray et al. 2005).

Dust is a fundamental constituent of the ISM of galaxies. Dust forms from material recycled back to the ISM through stellar winds or supernovae. The AGB phase of intermediate mass stars ($1 \lesssim M_{\odot} \lesssim 8$) and massive stars ($\gtrsim 8M_{\odot}$) which end their lives as Type II supernovae (SNe) are considered the dominant source of stellar dust production in star-forming galaxies while dust in the ISM may also form *in situ* from accretion of enriched gas processed by stars (Dwek 1998). Dust forms from metals and a strong correlation between gas-phase oxygen abundance and dust content is observed in local (Heckman et al.

1998; Boissier et al. 2004; Asari et al. 2007; Garn & Best 2010; Xiao et al. 2012; Zahid et al. 2012b) and high redshifts galaxies (Reddy et al. 2010; Domínguez et al. 2013).

Dust is composed of heavy elements and therefore the chemical and dust properties of galaxies should evolve consistently. For less massive galaxies, Lara-López et al. (2010) and Mannucci et al. (2010) find that metallicity is *anti*-correlated to SFR at a fixed stellar mass. Like Mannucci et al. (2010) and Lara-López et al. (2010), Yates et al. (2012) find a similar relation for low mass galaxies. However, they show that for massive galaxies the metallicity and SFR are *positively* correlated at a fixed stellar mass. Thus, there is a "twist" in the relation between stellar mass, metallicity and SFR. Not surprisingly, in these same galaxies, a similar twist is observed in the relation between stellar mass, dust extinction and SFR (Zahid et al. 2013c).

The potential importance of radiation pressure acting on dust in the context of galactic mass loss is well recognized. Chiao & Wickramasinghe (1972) suggest that under the influence of radiation pressure, dust may escape galaxies along magnetic field lines. Ferrara (1993) posits that dusty diffuse clouds embedded in a anisotropic radiation field will feel a net acceleration due to radiation pressure. Davies et al. (1998) argue that driven by an imbalance between radiation and gravitational forces, disk galaxies may expel a large fraction (90%) of dust produced over $\sim$ 1Gyr timescales. Dynamical coupling of dust and gas through collisions or coulomb interactions could provide a mechanism for transferring momentum from the radiation field to the gas (Draine 2004). Using cosmological simulations, Aguirre et al. (2001) show that the IGM could be enriched by the expulsion of dust and gas driven by radiation pressure. Several models incorporating dust driven winds have recently been considered in the literature (Zu et al. 2011; Sharma et al. 2011; Sharma & Nath 2012; Chattopadhyay et al. 2012; Wise et al. 2012).

1.3 The Origin of the Mass-Metallicity Relation and the Chemical Evolution of Star-Forming Galaxies

Uncovering the origin of the MZ relation is crucial for understanding gas flows and star formation in galaxies. It is clear that the MZ relation depends on gas flows and star formation. Still, despite numerous studies of the MZ relation over the last few decades, the physical origin of the MZ relation remains uncertain. The MZ relation could possibly be the result of metal-rich outflows (Larson 1974), inefficient star formation in less massive galaxies (Brooks et al. 2007; Finlator & Davé 2008; Calura et al. 2009), metal-poor inflows (Dalcanton et al. 2004), variations in the initial mass function (IMF; Köppen et al. 2007) or some combination of these physical processes.

1.4 The Content of this Dissertation

Measurements of the MZ relation ranging out to $z \sim 1.5$ are presented in Chapters 2 - 5. These measurements show that the the shape of the MZ relation evolves with time. The MZ relation of the most massive galaxies flattens as the Universe evolves (Zahid et al. 2013a). This flattening is a result of an empirical upper limit in galaxy metallicity. The most massive galaxies, even at high redshifts, evolve chemically to this upper metallicity limit (Zahid et al. 2013a,b). The stellar mass where the MZ relation flattens is ~ 0.7 dex lower now than at $z \sim 0.8$ (Zahid et al. 2013a).

The well defined MS and MZ relations observed over cosmological time provide purely empirical constraints for continuous stellar mass growth and chemical enrichment of galaxies as they evolve (see Zahid et al. 2012b). A major step forward for understanding the origin of the MZ relation is the empirical constraints for the magnitude of oxygen mass loss that I derive from the oxygen census. This is presented in Chapter 6. The oxygen census shows that the mass of oxygen expelled from galaxies is (nearly) directly proportional to the stellar mass of the galaxy. This means that outflows act with uniform efficiency in terms of oxygen ejection, though in practice this does not necessarily imply that outflows act with uniform

efficiency in terms of gas ejection. In Chapter 7, these empirical constraints are combined with theoretical models of galaxy formation to provide a robust parameterization of the metal mass loss as a function of dark matter halo mass.

Dust appears to be similarly distributed to metals in local-star forming galaxies. Yates et al. (2012) show a twist in the relation between stellar mass, metallicity and SFR. A similar twist in seen in the relation between stellar mass, dust extinction and SFR. These observations are presented in Chapter 8. Dust is formed from metals and we argue for a common physical origin for both relations. I attempt to understand trends in the metal and dust distribution of local galaxies in the context of this empirical framework. In Chapter 9 I present a model where trends in the metal and dust distribution are naturally explained as a consequence of star-formation and large scale galactic gas flows. The magnitude of mass loss in these dust driven outflows is consistent with the magnitude of oxygen loss inferred from the oxygen census.

The empirical constraints for oxygen mass loss allow me to derive analytical solutions for models of chemical evolution. These models can be compared directly to observations allowing me to interpret the parameters I fit to the MZ relation I measure for $z \lesssim 1.5$. On the basis of this interpretation, I conclude that galaxies follow a simple relation between metallicity and stellar-to-gas mass ratio. This relation is independent of redshift. On the basis of numerical modeling, I argue that the relation between metallicity and stellar-to-gas mass is a universal relation that is followed by all galaxies as they evolve. I present the universal metallicity relation in Chapter 10. In Chapter 11 I present the conclusions of this dissertation and future directions for investigation.

References

Aguirre, A., Hernquist, L., Katz, N., Gardner, J., & Weinberg, D. 2001, ApJ, 556, L11

Andrews, B. H., & Martini, P. 2013, ApJ, 765, 140

Asari, N. V., Cid Fernandes, R., Stasińska, G., Torres-Papaqui, J. P., Mateus, A., Sodré, L., Schoenell, W., & Gomes, J. M. 2007, MNRAS, 381, 263

Berg, D. A., et al. 2012, ApJ, 754, 98

Boissier, S., Boselli, A., Buat, V., Donas, J., & Milliard, B. 2004, A&A, 424, 465

Bothwell, M. S., Maiolino, R., Kennicutt, R., Cresci, G., Mannucci, F., Marconi, A., & Cicone, C. 2013, MNRAS, 433, 1425

Brooks, A. M., Governato, F., Booth, C. M., Willman, B., Gardner, J. P., Wadsley, J., Stinson, G., & Quinn, T. 2007, ApJ, 655, L17

Calura, F., Pipino, A., Chiappini, C., Matteucci, F., & Maiolino, R. 2009, A&A, 504, 373

Chattopadhyay, I., Sharma, M., Nath, B. B., & Ryu, D. 2012, MNRAS, 423, 2153

Chen, Y.-M., Tremonti, C. A., Heckman, T. M., Kauffmann, G., Weiner, B. J., Brinchmann, J., & Wang, J. 2010, AJ, 140, 445

Chiao, R. Y., & Wickramasinghe, N. C. 1972, MNRAS, 159, 361

Conroy, C., Graves, G., & van Dokkum, P. 2013, ArXiv e-prints

Conroy, C., & Wechsler, R. H. 2009, ApJ, 696, 620

Cowie, L. L., & Barger, A. J. 2008, ApJ, 686, 72

Daddi, E., et al. 2007, ApJ, 670, 156

Dalcanton, J. J., Yoachim, P., & Bernstein, R. A. 2004, ApJ, 608, 189

Davé, R., Oppenheimer, B. D., & Finlator, K. 2011, ArXiv e-prints

Davies, J. I., Alton, P., Bianchi, S., & Trewhella, M. 1998, MNRAS, 300, 1006

Domínguez, A., et al. 2013, ApJ, 763, 145

Draine, B. T. 2003, ARA&A, 41, 241

—. 2004, Astrophysics of Dust in Cold Clouds (Springer), 213

Dwek, E. 1998, ApJ, 501, 643

Elbaz, D., et al. 2007, A&A, 468, 33

Ellison, S. L., Patton, D. R., Simard, L., & McConnachie, A. W. 2008, ApJ, 672, L107

Erb, D. K., Quider, A. M., Henry, A. L., & Martin, C. L. 2012, ApJ, 759, 26

Erb, D. K., Shapley, A. E., Pettini, M., Steidel, C. C., Reddy, N. A., & Adelberger, K. L. 2006, ApJ, 644, 813

Ferrara, A. 1993, ApJ, 407, 157

Finlator, K., & Davé, R. 2008, MNRAS, 385, 2181

Gallazzi, A., Charlot, S., Brinchmann, J., White, S. D. M., & Tremonti, C. A. 2005, MNRAS, 362, 41

Garn, T., & Best, P. N. 2010, MNRAS, 409, 421

Heckman, T. M., Lehnert, M. D., Strickland, D. K., & Armus, L. 2000, ApJS, 129, 493

Heckman, T. M., Robert, C., Leitherer, C., Garnett, D. R., & van der Rydt, F. 1998, ApJ, 503, 646

Hosek, Jr., M. W., et al. 2014, ArXiv e-prints

Hughes, T. M., Cortese, L., Boselli, A., Gavazzi, G., & Davies, J. I. 2012, ArXiv e-prints

Kereš, D., Vogelsberger, M., Sijacki, D., Springel, V., & Hernquist, L. 2012, MNRAS, 425, 2027

Kewley, L. J., & Ellison, S. L. 2008, ApJ, 681, 1183

Kirby, E. N., Cohen, J. G., Guhathakurta, P., Cheng, L., Bullock, J. S., & Gallazzi, A. 2013, ApJ, 779, 102

Köppen, J., Weidner, C., & Kroupa, P. 2007, MNRAS, 375, 673

Koyama, Y., et al. 2013, MNRAS

Kudritzki, R.-P., Urbaneja, M. A., Bresolin, F., Przybilla, N., Gieren, W., & Pietrzyński, G. 2008, ApJ, 681, 269

Kudritzki, R.-P., Urbaneja, M. A., Gazak, Z., Bresolin, F., Przybilla, N., Gieren, W., & Pietrzyński, G. 2012, ApJ, 747, 15

Lara-López, M. A., et al. 2010, A&A, 521, L53+

—. 2013, MNRAS, 433, L35

Larson, R. B. 1974, MNRAS, 169, 229

Laskar, T., Berger, E., & Chary, R.-R. 2011, ApJ, 739, 1

Lee, H., Skillman, E. D., Cannon, J. M., Jackson, D. C., Gehrz, R. D., Polomski, E. F., & Woodward, C. E. 2006, ApJ, 647, 970

Leitner, S. N. 2012, ApJ, 745, 149

Lequeux, J., Peimbert, M., Rayo, J. F., Serrano, A., & Torres-Peimbert, S. 1979, A&A, 80, 155

Ly, C., Malkan, M. A., Nagao, T., Kashikawa, N., Shimasaku, K., & Hayashi, M. 2014, ApJ, 780, 122

Maier, C., Lilly, S. J., Carollo, C. M., Meisenheimer, K., Hippelein, H., & Stockton, A. 2006, ApJ, 639, 858

Maier, C., Lilly, S. J., Carollo, C. M., Stockton, A., & Brodwin, M. 2005, ApJ, 634, 849

Maiolino, R., et al. 2008, A&A, 488, 463

Mannucci, F., Cresci, G., Maiolino, R., Marconi, A., & Gnerucci, A. 2010, MNRAS, 408, 2115

Mannucci, F., et al. 2009, MNRAS, 398, 1915

Martin, C. L. 2005, ApJ, 621, 227

Martin, C. L., Kobulnicky, H. A., & Heckman, T. M. 2002, ApJ, 574, 663

Martin, C. L., Shapley, A. E., Coil, A. L., Kornei, K. A., Bundy, K., Weiner, B. J., Noeske, K. G., & Schiminovich, D. 2012, ApJ, 760, 127

Møller, P., Fynbo, J. P. U., Ledoux, C., & Nilsson, K. K. 2013, MNRAS, 430, 2680

Murray, N., Quataert, E., & Thompson, T. A. 2005, ApJ, 618, 569

Nelson, D., Vogelsberger, M., Genel, S., Sijacki, D., Kereš, D., Springel, V., & Hernquist, L. 2013, MNRAS, 429, 3353

Niino, Y. 2012, ApJ, 761, 126

Noeske, K. G., et al. 2007a, ApJ, 660, L47

—. 2007b, ApJ, 660, L43

Oppenheimer, B. D., & Davé, R. 2006, MNRAS, 373, 1265

Pannella, M., et al. 2009, ApJ, 698, L116

Papastergis, E., Cattaneo, A., Huang, S., Giovanelli, R., & Haynes, M. P. 2012, ApJ, 759, 138

Peng, Y.-j., et al. 2010, ApJ, 721, 193

Pérez-Montero, E., et al. 2013, A&A, 549, A25

Puchwein, E., & Springel, V. 2013, MNRAS, 428, 2966

Reddy, N. A., Erb, D. K., Pettini, M., Steidel, C. C., & Shapley, A. E. 2010, ApJ, 712, 1070

Reddy, N. A., Pettini, M., Steidel, C. C., Shapley, A. E., Erb, D. K., & Law, D. R. 2012, ApJ, 754, 25

Rubin, K. H. R., Prochaska, J. X., Koo, D. C., Phillips, A. C., Martin, C. L., & Winstrom, L. O. 2013, ArXiv e-prints

Rupke, D. S., Veilleux, S., & Sanders, D. B. 2005, ApJS, 160, 115

Salim, S., et al. 2007, ApJS, 173, 267

Sánchez, S. F., et al. 2013, A&A, 554, A58

Savaglio, S., et al. 2005, ApJ, 635, 260

Schaye, J., et al. 2010, MNRAS, 402, 1536

Sharma, M., & Nath, B. B. 2012, ApJ, 750, 55

Sharma, M., Nath, B. B., & Shchekinov, Y. 2011, ApJ, 736, L27

Sijacki, D., Vogelsberger, M., Kereš, D., Springel, V., & Hernquist, L. 2012, MNRAS, 424, 2999

Somerville, R. S., & Primack, J. R. 1999, MNRAS, 310, 1087

Springel, V., & Hernquist, L. 2003, MNRAS, 339, 289

Torrey, P., Vogelsberger, M., Genel, S., Sijacki, D., Springel, V., & Hernquist, L. 2013, ArXiv e-prints

Tremonti, C. A., et al. 2004, ApJ, 613, 898

Troncoso, P., et al. 2014, A&A, 563, A58

Veilleux, S., Cecil, G., & Bland-Hawthorn, J. 2005, ARA&A, 43, 769

Vogelsberger, M., Genel, S., Sijacki, D., Torrey, P., Springel, V., & Hernquist, L. 2013, ArXiv e-prints

Vogelsberger, M., et al. 2014, Nature, 509, 177

Weiner, B. J., et al. 2009, ApJ, 692, 187

Whitaker, K. E., van Dokkum, P. G., Brammer, G., & Franx, M. 2012, ApJ, 754, L29

Wijesinghe, D. B., et al. 2012, MNRAS, 423, 3679

Wise, J. H., Abel, T., Turk, M. J., Norman, M. L., & Smith, B. D. 2012, MNRAS, 427, 311

Xiao, T., Wang, T., Wang, H., Zhou, H., Lu, H., & Dong, X. 2012, MNRAS, 421, 486

Yabe, K., et al. 2014, MNRAS, 437, 3647

—. 2012, PASJ, 64, 60

Yates, R. M., Kauffmann, G., & Guo, Q. 2012, MNRAS, 422, 215

Zahid, H. J., Bresolin, F., Kewley, L. J., Coil, A. L., & Davé, R. 2012a, ApJ, 750, 120

Zahid, H. J., Dima, G. I., Kewley, L. J., Erb, D. K., & Davé, R. 2012b, ApJ, 757, 54

Zahid, H. J., Geller, M. J., Kewley, L. J., Hwang, H. S., Fabricant, D. G., & Kurtz, M. J. 2013a, ApJ, 771, L19

Zahid, H. J., et al. 2013b, ArXiv e-prints

Zahid, H. J., Kewley, L. J., & Bresolin, F. 2011, ApJ, 730, 137

Zahid, H. J., Yates, R. M., Kewley, L. J., & Kudritzki, R. P. 2013c, ApJ, 763, 92

Zahid, J., Dima, G., Kudritzki, R., Kewley, L., Geller, M., & Hwang, H. S. 2014, ArXiv e-prints

Zu, Y., Weinberg, D. H., Davé, R., Fardal, M., Katz, N., Kereš, D., & Oppenheimer, B. D. 2011, MNRAS, 412, 1059

Chapter 2

The Mass-Metallicity and Luminosity-Metallicity Relations from DEEP2 at $z \sim 0.8$

Note: This chapter originally appeared as Zahid, H.J, Kewley, L.J, & Bresolin, F. 2011, ApJ 730, 137. This work was primarily based on publicly available data from the Deep Extragalactic Evolutionary Probe 2 (DEEP2) and Sloan Digital Sky Survey (SDSS) surveys. I am the primary author of this work.

Abstract

We present the mass-metallicity (MZ) and luminosity-metallicity (LZ) relations at $z \sim 0.8$ from ~ 1350 galaxies in the Deep Extragalactic Evolutionary Probe 2 (DEEP2) survey. We determine stellar masses by fitting the spectral energy distribution inferred from photometry with current stellar population synthesis models. This work raises the number of galaxies with metallicities at z$\sim$ 0.8 by more than an order of magnitude. We investigate the evolution in the MZ and LZ relations in comparison with local MZ and LZ relations determined in a consistent manner using $\sim 21,000$ galaxies in the Sloan Digital Sky Survey. We show that high stellar mass galaxies ($M \sim 10^{10.6} M_{\odot}$) at z$\sim$ 0.8 have attained the chemical enrichment seen in the local universe, while lower stellar mass galaxies ($M \sim 10^{9.2} M_{\odot}$) at z$\sim$ 0.8 have lower metallicities (Δlog(O/H) $\sim$ 0.15 dex) than galaxies at the same stellar mass in the local universe. We find that the LZ relation evolves in both metallicity and B-band luminosity between z$\sim$ 0.8 and $z \sim 0$, with the B-band luminosity

evolving as a function of stellar mass. We emphasize that the B-band luminosity should not be used as a proxy for stellar mass in chemical evolution studies of star-forming galaxies. Our study shows that both the metallicity evolution and the B-band luminosity evolution for emission-line galaxies between the epochs are a function of stellar mass, consistent with the cosmic downsizing scenario of galaxy evolution.

2.1 Introduction

The heavy-element abundance in galaxies is a key physical property for understanding galaxy evolution. Metals are formed in massive stars and are dispersed into the interstellar medium (ISM) via mass-loss processes. Hence, metallicity provides an important record of the star formation history of a galaxy. Galaxies and their chemical abundances, however, do not evolve as closed systems where metals are dispersed into the ISM as gas is converted into stars. Rather, they are modulated by inflow of unenriched gas (e.g., Kewley et al. 2010) and a complex "feedback" mechanism where supernovae and stellar winds influence the ISM by inducing outflows of gas into the intergalactic medium (IGM) and regulating star formation through reheating (Larson 1974; Larson & Dinerstein 1975; Kauffmann & Charlot 1998; Somerville & Primack 1999; Springel & Hernquist 2003).

A simple "closed-box" model in which feedback is not considered predicts a correlation between two fundamental parameters−mass and metallicity (van den Bergh 1962; Schmidt 1963; Searle & Sargent 1972; Erb et al. 2006). The pioneering work of Lequeux et al. (1979) first showed this correlation in local irregular galaxies. Many subsequent efforts have focused on the relation between luminosity and metallicity (Skillman et al. 1989; Zaritsky et al. 1994; Garnett et al. 1997; Lamareille et al. 2004; Salzer et al. 2005) where luminosity is taken as a proxy for mass because of the difficulty in inferring galaxy masses from observables. Early attempts to extend this relation to intermediate redshifts found that the luminosity-metallicity (LZ) relation at earlier epochs was consistent with the local universe (Kobulnicky et al. 1999; Carollo & Lilly 2001). However, many recent investigations

have provided compelling evidence for evolution of the LZ relation over cosmological times (Kobulnicky & Koo 2000; Pettini et al. 2001; Kobulnicky et al. 2003; Kobulnicky & Kewley 2004; Maier et al. 2004; Shapley et al. 2004, 2005). Luminosities of galaxies evolve along with their chemical abundances on cosmological timescales and disentangling the contribution for each has posed difficulties in these studies.

Evolution in the LZ relation implies an evolution in the more fundamental mass-metallicity (MZ) relation. Development of more sophisticated models for stellar population synthesis (Bruzual & Charlot 2003) and gaseous nebula (Ferland 1996; Charlot & Longhetti 2001) allowed Tremonti et al. (2004, hereafter T04) to establish and quantify the local MZ relation for $\sim 53,000$ star-forming galaxies from the Sloan Digital Sky Survey (SDSS). They found that metallicity increases linearly with stellar mass for galaxies having masses between $10^{8.5} M_{\odot}$ and $10^{10.5} M_{\odot}$ and flattens out at higher masses. They attribute this depletion of metals in less massive galaxies to ubiquitous galactic winds that strip metals more effectively from galaxies with shallow potential wells, dispersing them into the IGM. Alternatively, it has been suggested that low mass systems have ongoing star formation and have yet to convert much of their gas into stars and therefore are less evolved, less metal-rich systems as compared to more massive galaxies which have undergone rapid star formation (Brooks et al. 2007; de Rossi et al. 2007; Mouchine et al. 2008). Finally, a varying stellar mass distribution has also emerged as a possible explanation for the observed MZ relation (Köppen et al. 2007).

Cosmological hydrodynamic simulations (Brooks et al. 2007; Oppenheimer & Davé 2008) have predicted an evolution in the MZ relation and recent observations at intermediate redshifts ($z \sim 0.7$) have provided strong evidence for an evolution. Using the Gemini Deep Deep Survey, Savaglio et al. (2005) first showed the MZ relation beyond the local universe for galaxies at $z = 0.4 - 1.0$. Their relation intersects the local relation at $M \sim 10^{10.4} M_{\odot}$ but is ~ 0.3 dex lower at $M \sim 10^{9.3} M_{\odot}$, implying a much steeper slope. They conclude that the slope of the MZ relation must become flatter over time. Cowie & Barger (2008) found a difference > 0.2 dex for a redshift range of $0.475 < z < 0.9$ with a similar slope. More

recently, Lamareille et al. (2009) find a flatter slope in the MZ relation out to $z \sim 0.9$ and an average difference in metallicity of ~ 0.2 dex. To date, the MZ relation has been extended beyond $z \sim 3$ (Shapley et al. 2005; Erb et al. 2006; Maiolino et al. 2008; Pérez-Montero et al. 2009; Mannucci et al. 2009). All these studies have shown evidence of evolution but rigorous quantitative analysis has been hampered by disparate results and small sample sizes leaving the MZ relation at higher redshifts quantitatively uncertain.

In this paper we present results of our study determining the mass-metallicity and luminosity-metallicity relation for galaxies in the redshift range of $0.75 < z < 0.82$. We infer metallicities from gas phase oxygen abundances using strong line diagnostics (Pagel et al. 1979; Kewley & Dopita 2002; Kewley & Ellison 2008, hereafter KE08). We make use of publicly available data from the Deep Extragalactic Evolutionary Probe 2 (DEEP2, Davis et al. 2003). We measure the MZ and LZ relations from 1,348 galaxies, a substantial increase in the number of objects studied in this redshift range to date. We note that a large sample of galaxies with metallicity and stellar mass determinations in such small redshift range is ideal for reliably constraining the MZ relation at a specific redshift. In § 2.2 we present our criteria for selection of galaxies and properties of our selected sample. In § 2.3 we describe our method for determining masses, our correction for underlying Balmer absorption and our method for determining masses. In § 2.4 we present our derived MZ and LZ relations. In § 2.5 we present a discussion of our results. Here we compare the MZ and LZ relation and infer the B-band luminosity and evolution as a function of stellar mass and we compare our MZ relation with relations derived by other authors at similar redshfits. We summarize our results in § 2.6. Where necessary, we adopt the standard cosmology $(H_0, \Omega_m, \Omega_\Lambda) = (70\, km\, s^{-1}\, Mpc^{-1}, 0.3, 0.7)$.

2.2 The Data

2.2.1 DEEP2 Survey Data

Our $z \sim 0.8$ sample comes from the DEEP2 (Deep Extragalactic Evolutionary Probe 2) survey. The DEEP2 team used the DEIMOS (Faber et al. 2003) multi-object spectrograph on the Keck telescope to measure spectra for galaxies in 4 fields covering 3.5 deg^2 down to a limiting magnitude of $R_{AB} = 24.1$. The survey contains spectra for $\sim$50,000 galaxies, the majority of which are in the redshift range $0.7 < z < 1.4$. The relatively high-resolution ($R \geq 5000$) spectra cover the nominal spectral range 6500-9100$\mathring{A}$. For this study, we used the third data release[1] data and the 1-d spectra were obtained from the Horne extraction (Horne 1986).

BRI photometry was obtained by the DEEP2 team for these objects from imaging carried out using the CFH12K camera on the 3.6 m Canada France Hawaii Telescope (Coil et al. 2004). For a subsample of the data, K_s-band photometry was available in addition to the BRI photometry. These data were obtained using the Wide Field Infrared Camera on the 5m Hale telescope at Mt. Palomar (Bundy et al. 2006). All magnitudes in this study are in the AB system.

2.2.2 Data Selection

From the 46,337 unique objects in the survey, we begin by selecting 31,656 galaxies for which we have secure redshift determinations from the DEEP2 team ($Q \geq 3$, see website for more details). For our determination of metallicity, we use the R_{23} strong line diagnostic, first calibrated by Pagel et al. (1979). We apply a more recent R_{23} calibration based on the stellar population synthesis and photoionization model calibrations from Kewley & Dopita (2002), and updated in Kobulnicky & Kewley (2004). In the text, we refer to this calibration as KK04. The R_{23} method is a parameterization of metallicity as function of the ratio of

[1] http://www.deep.berkeley.edu/DR3/

Table 2.1. Sample Selection

Selection Criteria	Total	Blue	Red
Total number of unique objects	46,337	-	-
Galaxies with secure redshift determination	31,656	-	-
Galaxies with redshifts $0.75 < z < 0.82$	4,198	3,323	875
Rest-frame wavelength cover $3720 - 5020\mathring{A}$	2,738	2,152	586
Measured metallicities	2,504	2,117	387
SN $H\beta > 3$	2,168	1,996	172
$EW(H\beta) > 4\mathring{A}$	1,973	1,902	71
$\sigma_{R23} < 2$	1,751	1,702	49
Robust continuum	1,713	1,665	48
Not AGN	1,679	1,631	48
Blue star forming galaxies	1,631	1,631	0

Note. — The first column gives the particular selection criteria and the second column gives the total number of galaxies that meet this and all criteria above it in the table. The third and fourth column splits the total number of galaxies into blue and red sub-samples as defined by equation 2.1.

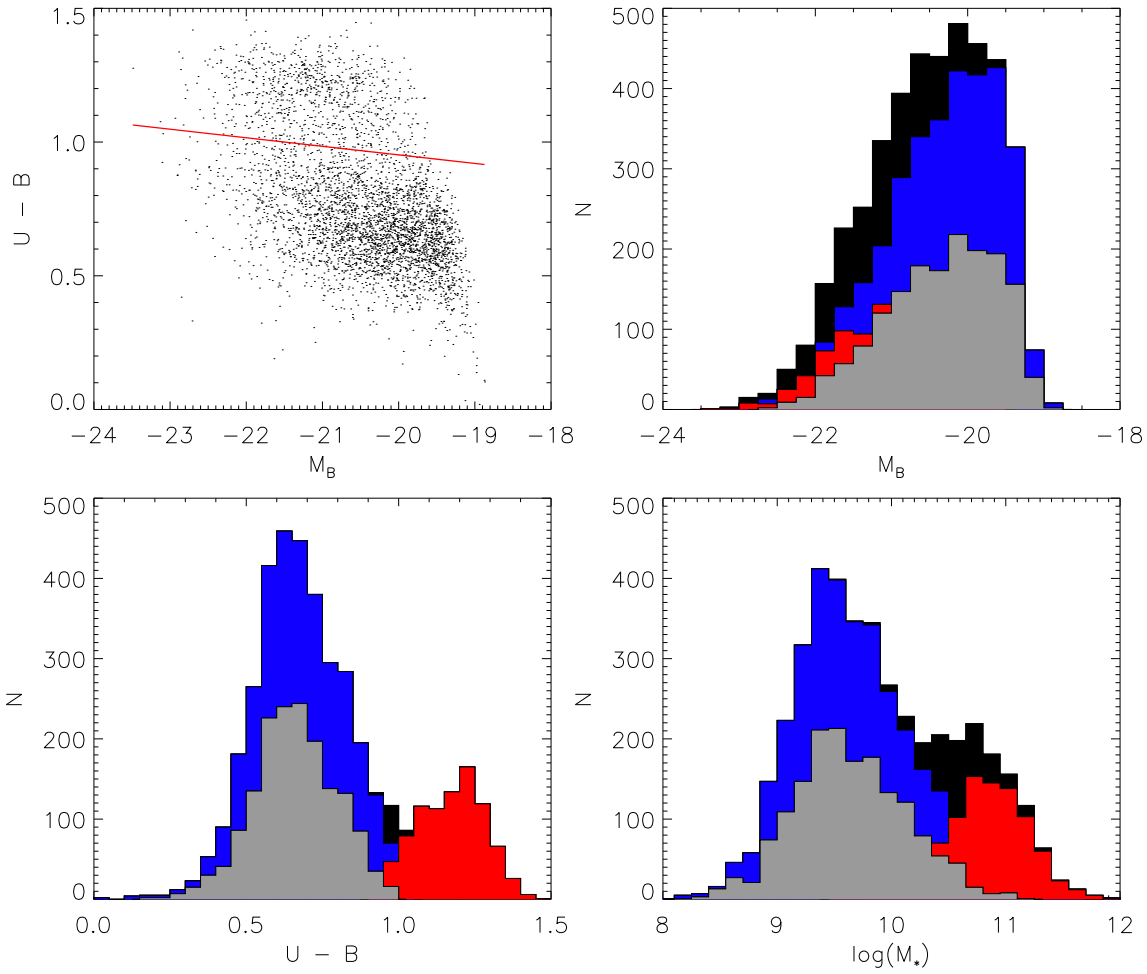

Figure 2.1 The top left panel shows the color magnitude diagram of the full sample of 4,198 galaxies with the required wavelength coverage from which we make our selection. The red line is the blue-red color division given by equation 2.1. The black histogram in each of the other three panels is for the full sample. The blue and red histograms are for the blue and red galaxies within the full sample and the grey histogram is for our selected sub-sample of 1,631 galaxies. The top right panel shows the distribution of the absolute B-band magnitude. The bottom left panel shows the color distribution and bottom right panel shows the mass distribution.

the oxygen nebular emission ([OII]λ3727 doublet, [OIII]λ4959 and [OIII]λ5007) to $H\beta$. The method is formally defined in § 2.3.3. Given the nominal spectral range of the DEEP2 survey, we can sufficiently bracket the required emission lines within the $0.75 < z < 0.82$ redshift range. Due to a varying object position on the slitmask, the actual spectral range

varies from object to object and we require that the spectra cover the wavelength range of $3720 - 5020\mathring{A}$, leaving us with 2,738 galaxies. We were unable to measure the metallicity in 234 galaxies due to our inability to fit the oxygen or $H\beta$ emission lines, leaving us with 2,504 galaxies.

We calculate the R_{23} ratios using the continuum normalized flux (see Appendix for full description). In the appendix we show that the pseudo-EW is equal, to within the errors, to the equivalent width and refer to it hereafter as the EW. The errors on our equivalent width and line ratio determination come from propagating the measurement uncertainties in the spectrum. In selecting galaxies for analysis, we require that the S/N $H\beta > 3$, $EW(H\beta) > 4\mathring{A}$ and the error in the R_{23} line ratio be less than 2. At high metallicities, the line strength of the [OII] and [OIII] line diminishes due to the effectiveness of line cooling of the HII region. In order to avoid biasing our MZ relation to lower metallicities we do not place a S/N cut on these lines. We normalize the line flux to the continuum by fitting a polynomial to the underlying continuum and dividing the spectrum by this fit. We require that the fit to the continuum be $1\sigma_c$ above the continuum, where σ_c is the standard deviation of the line-subtracted spectrum (see appendix for more detail). These cuts leave us with 1,713 galaxies.

Strong-line methods of metallicity determination assume a star forming population of galaxies and are not applicable to AGN. We identify all galaxies with $log(R_{23}) > 1$ as AGN and remove them from our sample (Kewley et al., in prep). Furthermore, using the color separation for blue and red galaxies parameterized by Willmer et al. (2006) for the DEEP2 survey, Weiner et al. (2007) conclude that a very small fraction of blue galaxies have AGN whereas at least half of the red galaxies show evidence of AGN emission. Similar to T04, we select the blue star forming galaxies to analyze, as described in the following section. We remove the red galaxies from our sample and are left with 1,631 blue emission line galaxies. The first and second column of Table 2.1 summarizes our selection. The median for $EW(H\beta)$, S/N $H\beta$ and σ_{R23} of our selected sample is 12.1, 10.0 and 0.65 respectively.

Table 2.2. Median Properties of the DEEP2 Galaxies

Sample	$U-B$	M_B	Mass $log(M/M_\odot)$
DEEP2 Full	0.72	-20.4	9.80
DEEP2 Red	1.18	-21.1	10.85
DEEP2 Blue	0.67	-20.2	9.62
DEEP2 Selected	0.66	-20.3	9.59

Note. — The median properties of the data. In the first column we identify the four samples. The next three columns give the median $U-B$ color, absolute B-band magnitude and mass for each of these samples.

2.2.3 Properties of Selected Sample

Willmer et al. (2006) studied the red and blue galaxy luminosity functions by dividing the DEEP2 sample at the trough of the bimodal $U-B$ color distribution. The U- and B-band absolute magnitudes are synthesized by relating the observed magnitudes to spectral energy distributions (SEDs) of nearby galaxies and inferring a rest-frame absolute magnitude from this SED. We follow a similar procedure and synthesize the U- and B-band absolute magnitude using the filters of Buser (1978) and Ažusienis & Straižys (1969) respectively. The red and blue galaxy color division found by Willmer et al. (2006) is given by

$$U-B = 1.0 - 0.032(M_B + 21.5). \tag{2.1}$$

The color division has been converted to AB magnitudes using Table 1 from Willmer et al. (2006). In column three and four of Table 2.1 we examine the cuts from our selection with respect to the galaxy color.

The top left panel of Figure 2.1 shows the color-magnitude diagram and the solid red line is the color division given by equation 2.1. The other three panels give the absolute B-band magnitude, stellar mass (derived in § 2.3.1) and $U-B$ color distribution. The black

histogram gives the full sample of 4,198 DEEP2 galaxies between $0.75 < z < 0.82$. We refer to this sample as the DEEP2 Full sample. Using the $U - B$ color division, we split the DEEP2 Full sample into sub-samples of red and blue galaxies. The histograms of these sub-samples are plotted in red and blue and we refer to these sub-samples as the DEEP2 Red and DEEP2 Blue samples respectively. The grey histogram is the distribution of our selected sample of 1,631 galaxies described in § 2.2.2 and we refer to this as our DEEP2 Selected sample. The median properties of these samples are given in Table 2.2.

The absolute B-band magnitude distribution in the top right panel of Figure 2.1 shows a range of $-19.0 > M_B > -23$ for the DEEP2 Full sample. Faber et al. (2007) showed that luminosity functions derived for blue galaxies from the DEEP2 data have a $M_B^* = -21.15$ in our selected redshift range. Our DEEP2 Selected sample consists of galaxies around the knee of the blue galaxy luminosity function (Schechter 1976) with $\sim$15% (245/1631) of our galaxies brighter than M_B^*. The bottom left panel of Figure 2.1 shows that the $U - B$ color range is $0 < U - B < 1.5$ for the DEEP2 Full sample. The color division between red and blue is at $U - B \sim 1$ and the bimodal distribution is clearly highlighted by the well separated peaks in the blue and red histograms. The bimodal color distribution separates red early-type galaxies from blue late-type star forming galaxies (Strateva et al. 2001; Hogg et al. 2003; Baldry et al. 2004; Willmer et al. 2006). The mass distribution shown in the bottom right panel of Figure 2.1 reflects this bimodality, whereby the red galaxies in our sample are not only brighter, but more massive and separated from the lower mass blue galaxies.

By comparing the histograms and median properties in Figure 2.1, it is clear that the DEEP2 Red sample of galaxies are brighter and more massive than the DEEP2 Blue sample. However, when comparing the histograms and median properties of our DEEP2 Selected sample, which is comprised solely of blue galaxies, with the DEEP2 Blue sample, there is no selection bias towards the brighter or more massive galaxies as one may expect given the selection criteria. We conclude from the comparison of the properties of the DEEP2 Selected

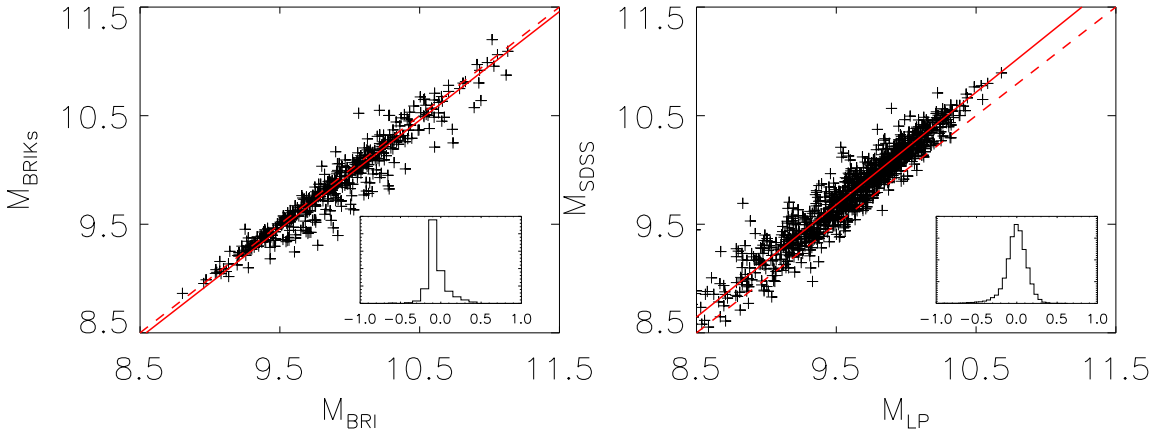

Figure 2.2 Comparison of stellar masses estimates. The left panel shows the mass estimates using BRI-band photometry (M_{BRI}, x-axis) as compared with $BRIK_s$-band photometry (M_{BRIKs}, y-axis). The right panel compares mass estimates made using Le Phare (M_{LP}, x-axis) and those provided by the MPA/JHU team (M_{SDSS}, y-axis). The dashed line in each plot is the one-to-one correspondence of the two data sets. The solid line is a bisector fit to the data. The sub-panel in each of the plots shows a histogram of the differences between the two estimates with -0.04 and 0.19 dex added as corrections to the M_{BRI} and M_{LP} mass estimates respectively.

and DEEP2 Blue sample that our selected galaxies are representative of the population of blue star forming of galaxies in the DEEP2 survey at $0.75 < z < 0.8$.

2.3 Data Analysis

2.3.1 Stellar Mass Determination

We estimate galaxy stellar masses by comparing photometry with stellar population synthesis models in order to determine the mass-to-light ratio (Bell et al. 2003; Fontana et al. 2004). We use the Le Phare[2] code developed by Arnouts, S. & Ilbert, O. to estimate the galactic stellar mass. Le Phare is a set of FORTRAN routines developed to determine the photometric redshifts of galaxies. If the redshift is known, it can be held fixed while other physical parameters of the galaxy are determined (i.e. stellar mass) by SED fitting.

[2] *http://www.cfht.hawaii.edu/~arnouts/LEPHARE/cfht_lephare/lephare.html*

The stellar templates of Bruzual & Charlot (2003) and an IMF described by Chabrier (2003) are used to synthesize magnitudes. The 27 models span three metallicities and seven exponentially decreasing star formation models (SFR $\propto e^{-t/\tau}$) with $\tau = 0.1, 0.3, 1, 2, 3, 5, 10, 15$ and 30 Gyrs. We apply the extinction law of Calzetti et al. (2000) allowing E(B-V) to range from 0 to 0.6 and stellar population ages ranging from 0 to 13 Gyrs. Ilbert et al. (2009) provide a more detailed description of how the physical parameters are estimated.

We are able to determine stellar masses using BRI and K_s-band data for 454 of our selected galaxies. In order to test for systematic variation in the stellar mass determination for the remaining sample of galaxies with only BRI photometry, we compare the stellar masses for our 454 galaxies determined with BRI and K_s-band data with stellarmasses determined for the same galaxies with just the BRI bands. The left panel of Figure 2.2 shows the comparison. The x-axis is the mass determination from BRI band data and the y-axis is the mass determination from $BRIK_s$-band data. The dashed line is the one-to-one correspondence and the solid line is a linear bisector fit to the data.

We perform a bootstrap linear fit by taking the bisector of the X vs Y and Y vs X regression using the routine *boot_xyfit.pro* from the IDL astronomy users library. Bootstrapping is a non-parametric statistical method of inferring errors whereby errors are calculated from the distribution of the fitted parameters for many fits to randomly selected subsample of the data. In order to minimize the covariance between the slope and intercept, we zero point the data by subtracting 10 from the logarithm of the stellar mass. The linear fit is given by

$$X_{BRIK_s} = (-0.042 \pm 0.006) - (1.00 \pm 0.01) X_{BRI}, \tag{2.2}$$

where $X_{BRI} = M_{BRI} - 10, X_{BRIK_s} = M_{BRIK_s} - 10$ and M_{BRI} and M_{BRIK_s} are the stellar masses determined by using three and four bands respectively. The slope is consistent

with unity. To first order, the absence of the K_S-band data results in only a ~ 0.04 dex overestimate of the stellar mass.

The DEEP2 galaxies with K_s-band data from the full sample are generally brighter and more massive than our selected galaxies, while the color distribution is consistent with our selected sample. The K_s-band data for our selected sample span the full range of mass, color and absolute B-band magnitude and the medians are 9.81, 0.68 and -20.7 respectively. To check for any systematic variations with galaxy properties we fit half of the data that is below the median in mass, color and magnitude respectively and find that the fits are all consistent within the errors. When K_s-band photometry is unavailable, we subtract 0.04 dex from the mass to correct for the systematic overestimate. After applying this correction, there is a 0.12 dex dispersion between the one-to-one correspondence of the two mass estimates.

We have redetermined the local MZ and LZ relations from $\sim 21,000$ galaxies in the SDSS data release 7 (see appendix). We compared our stellar mass determination using Le Phare with those determined by the MPA/JHU team from fitting the photometry and a Kroupa IMF (Kroupa 2001). Both methods use stellar population synthesis to fit the photometry and we expect the estimates to only vary by a constant offset. The right panel of Figure 2.2 shows this comparison. The dashed line is the one-to-one correspondence and the solid line is a bootstrap linear bisector fit to the data as described earlier. The linear fit is given by

$$X_{LP} = (0.198 \pm 0.001) + (1.035 \pm 0.003) X_{SDSS}, \tag{2.3}$$

where $X_{LP} = M_{LP} - 10$ and $X_{SDSS} = M_{SDSS} - 10$. M_{LP} and M_{SDSS} are the stellar masses determined using Le Phare and those provided by the MPA/JHU team, respectively. As before, to minimize the covariance of the slope and intercept, we zero point the data by subtracting 10 from the masses. The slope is near unity and to first order the estimates differ by only a constant offset of 0.198 dex (a factor of ~ 1.6). Taking into account this

constant offset, there is a 0.14 dex dispersion in the one-to-one correspondence between the two mass estimates.

For local galaxies it has been shown that the errors between photometric and dynamical mass are typically ~ 0.2 dex (Drory et al. 2004). In this study, we observe galaxies at $z \sim 0.8$ and therefore expect even greater errors in the photometric determination of mass. Moreover, Conroy et al. (2009) have shown that additional uncertainties in estimates of physical parameters from stellar population synthesis modeling result from the choice of IMF, dust model and spectral libraries. However, the full impact of these effects on the absolute calibration of the physical parameters are still not well understood. Therefore, when investigating evolution of the MZ relation, we take care to have a consistent relative calibration of the physical parameters between the samples. The absolute calibration remains uncertain.

2.3.2 Correction for Stellar Balmer Aborption

When measuring EWs it is necessary to make a correction for underlying stellar absorption in the Balmer lines. Kobulnicky & Phillips (2003) have estimated an average correction of $2\mathring{A}$ in the $EW(H\beta)$ for the underlying Balmer absorption using 22 galaxies from the spectroscopic galaxy atlas of Kennicutt (1992). The galaxies in the Kennicutt atlas have a spectral resolutions of 5-8$\mathring{A}$. We expect the effects of Balmer absorption to be greater in galaxy spectra with lower resolution because the flux of the narrow emission line is spread over a broader region of the absorption trough. Presumably for this reason, Cowie & Barger (2008) find a correction of $1\mathring{A}$ by stacking spectra observed using DEIMOS onboard Keck with a spectral resolution of $3.5\mathring{A}$. The DEEP2 data have also been obtained using DEIMOS but with a smaller spectral resolution of $1.4\mathring{A}$.

Unfortunately, the low S/N in our data does not allow us to investigate the Balmer absorption in individual galaxy spectra. However, the strength of the Balmer absorption is a function of the age of the stellar population and is therefore expected to correlate with physical parameters of the galaxy such as stellar mass. In order to investigate the effects

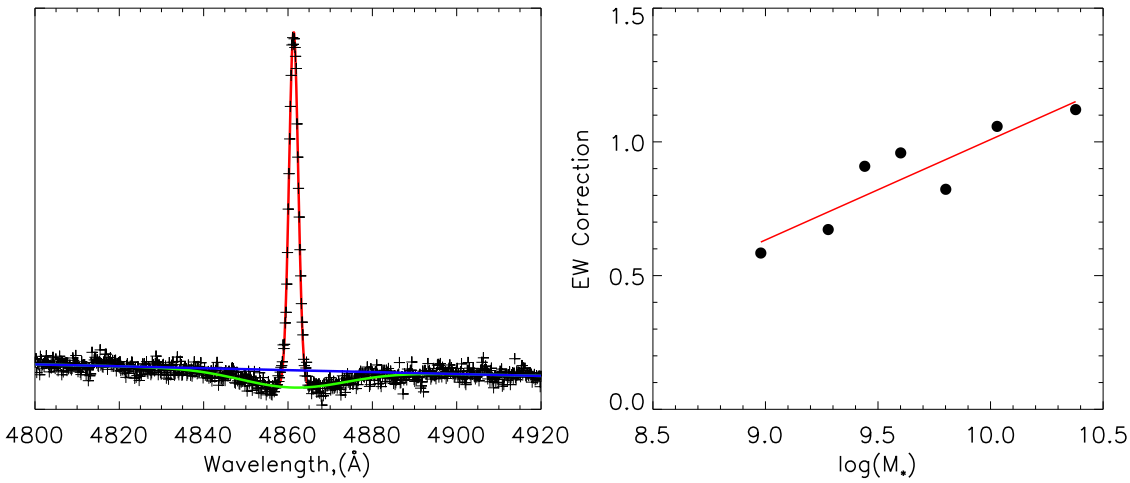

Figure 2.3 The left panel shows an example of a stacked spectra. The red curve is a fit to the $H\beta$ emission, the green curve is a fit to the $H\beta$ absorption and the blue line is a fit to the continuum. The are of the region bracketed by the absorption on the bottom, emission on the sides and continuum at the top is the correction factor to the $EW(H\beta)$. The right panel shows this correction for $H\beta$ absorption as a function of stellar mass for data sorted into 7 mass bins. The red line is a linear parameterization of the correction as a function of stellar mass.

of stellar absorption on our measurement we stack our spectra in bins of stellar mass and examine the effect of the Balmer absorption on the $EW(H\beta)$.

We stack our spectra into 7 mass bins. We normalize each spectrum to the continuum by dividing by the median value of the continuum between $4800-4815\AA$ and $4900-4915\AA$. We then stack ~ 230 spectra in each mass bin by interpolating all spectra to have the same wavelength vector and take the median of the flux corresponding to each wavelength element. We get similar results if we take the mean rather than the median. The left panel of Figure 2.3 shows an example of a stacked spectrum. We see that the $H\beta$ emission line sits on a broad absorption trough. The $EW(H\beta)$ correction accounts for the integrated flux of the emission line (red curve) that lies below the continuum (blue curve) and would not be included when measuring the $EW(H\beta)$ in lower S/N spectra due to the absorption (green curve). To obtain a correction, we measure the $EW(H\beta)$ for the stacked spectrum and a corrected spectrum with the absorption removed. The right panel shows the correction to

the $EW(H\beta)$ as a function of stellar mass. The red line is a linear least-square fit given by

$$EW_{corr} = (1.01 \pm 0.05) + (0.38 \pm 0.08)x, \tag{2.4}$$

where $x = log(M_*) - 10$. EW_{corr} is the amount added to the $EW(H\beta)$ to correct for underlying absorption. The median correction to the $EW(H\beta)$ in our sample is 0.9. We note that this correction does not significantly effect our derived MZ relation owing to the fact that the median correction of 0.9 $\mathring{A}$ is small compared to the median $EW(H\beta)$ of 12.1 $\mathring{A}$. This small correction translates to a median increase of 0.04 dex in metallicity.

We perform a simple test in order to assess the effect of varying the spectral resolution on the Balmer absorption correction. We convolve our stacked spectra with gaussians of varying widths. We find that the Balmer correction is sensitive to the spectral resolution. The correction increases with smaller spectral resolution and the slope of the correction with respect to stellar mass flattens. We speculate that the larger correction found by Kobulnicky & Phillips (2003) may be attributed to the lower spectral resolution of their data. In a future study, using higher quality data we hope to quantitatively establish the magnitude of this effect.

2.3.3 Metallicity Determination

We use the strong line diagnostics of KK04 as presented in KE08 in order to obtain an estimate of galaxy gas-phase metallicities. The diagnostics are based on the Kewley & Dopita (2002) R_{23} theoretical calibrations. In both diagnostics the metallicity is determined using the R_{23} and O_{32} ratios. We calculate these ratios from our EWs such that

$$R_{23} = \frac{EW([OII]) + EW([OIII])}{EW(H\beta)} \tag{2.5}$$

and

$$O_{32} = \frac{EW([OIII])}{EW([OII])}, \tag{2.6}$$

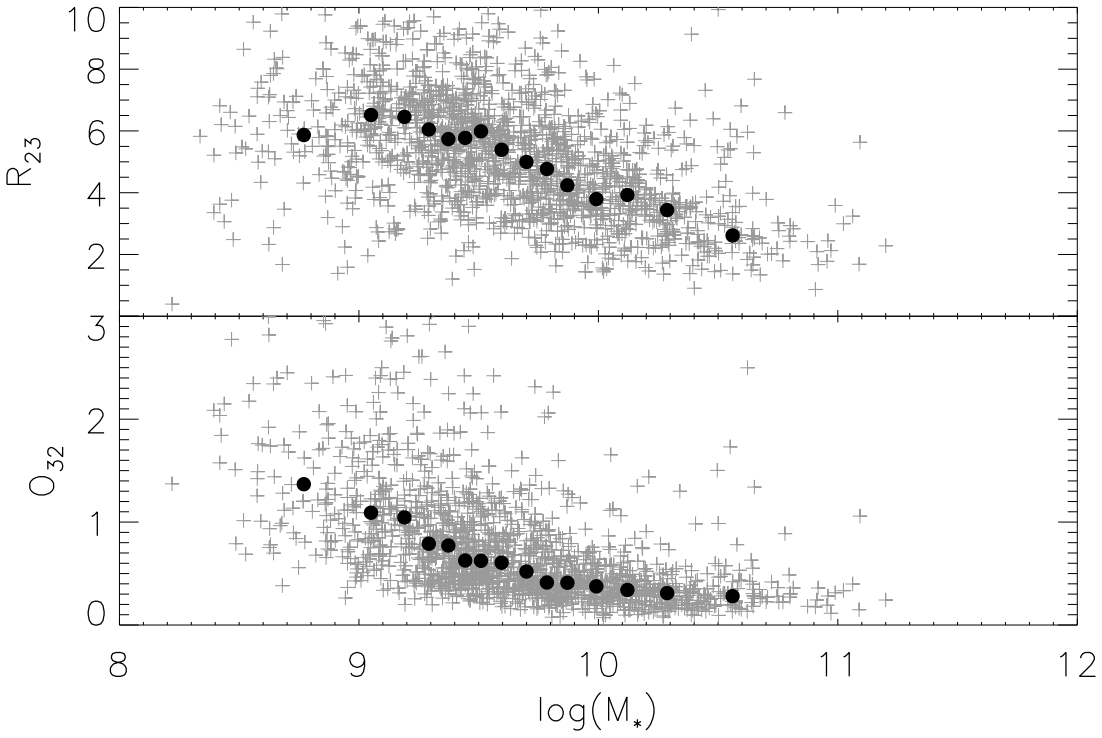

Figure 2.4 The R_{23} (top) and O_{32} (bottom) line ratios as a function of stellar mass. The grey pluses are the unbinned data and the black filled circles are the data binned into 15 mass bins where each bin has equal number of data points.

where $EW([OII])$ is for the [OII] doublet and $EW([OIII])$ is taken to be 1.33 $\times$ $EW([OIII]\lambda5007)$. We have used the assumption that the ratio of the fluxes of $[OIII]\lambda5007$ to $[OIII]\lambda4959$ is 3 (Osterbrock 1989). We have fitted the $[OIII]\lambda4959$ line because the widths of the $H\beta, [OIII]\lambda4959$ and $[OIII]\lambda5007$ line fits are tied in order to increase the S/N of the fit, as described in the appendix, but the S/N in the $EW([OIII]\lambda5007)$ is higher and the $EW([OIII]\lambda4959)$ is inferred from theoretical considerations for the metallicity determination.

We use equations A4 and A6 given in the appendix of KE08 to derive the ionization parameter and metallicity respectively. The R_{23} method for determining metallicities is known to be sensitive to the ionization parameter. The ionization parameter characterizes the ionization state of the gas and quantitatively represents the number of ionizing photons

per second per unit area divided by the hydrogen density. The ionization parameter has the units of velocity and can be thought of as the maximum velocity of the ionization front through the nebula. The metallicity and ionization parameter are interdependent. In order to obtain a consistent measurement of the metallicity and ionization parameter an iterative scheme is used, the details of which are provided in the appendix of KE08. Furthermore, all metallicities used in this study for comparison that are not explicitly calculated using the KK04 calibration are converted to be consistent using the conversions provided in KE08.

Figure 2.4 shows the R_{23} (top) and O_{32} (bottom) line ratios for our sample. The grey pluses are the individual measurements and the black filled circles are the data sorted into 15 mass bins of equal number of data points. The median values of the R_{23} and O_{32} line ratios are 5.1 and 0.6 and median errors are 0.6 and 0.06 respectively. Both the R_{23} and O_{32} line ratios are sensitive to the metallicity and the relation between stellar mass and the line ratios can be attributed to the relation between stellar mass and metallicity.

Metallicity is not a monotonic function of R_{23}, but rather is doubly valued for a given ratio. A particular value of R_{23} corresponds to two different metallicities, one on the higher metallicity branch and one on the lower metallicity branch. The peak of the R_{23} ratio occurs at $12 + log(O/H) \approx 8.4$. This degeneracy is due to the fact that on the lower branch R_{23} scales with metallicity because the intensity of the collisionally excited [OII] and [OIII] lines scales with the abundance. On the upper branch, nebular cooling, which results from collisional excitation followed by photon emission, effectively cools the nebula decreasing the electron temperature leading to a decrease in the rate of collisional excitation of the [OII] and [OIII] lines. In order to break this degeneracy, generally other line ratios such as [NII]/H_α are used. However, in our sample, these lines are not observed and the metallicity is assumed to lie on the upper branch. This assumption breaks down at lower masses. Looking at the R_{23} mass relation in Figure 2.4, a turnover appears to occur at about $log(M_*) \sim 9.2$ and we revisit this issue in § 2.4.

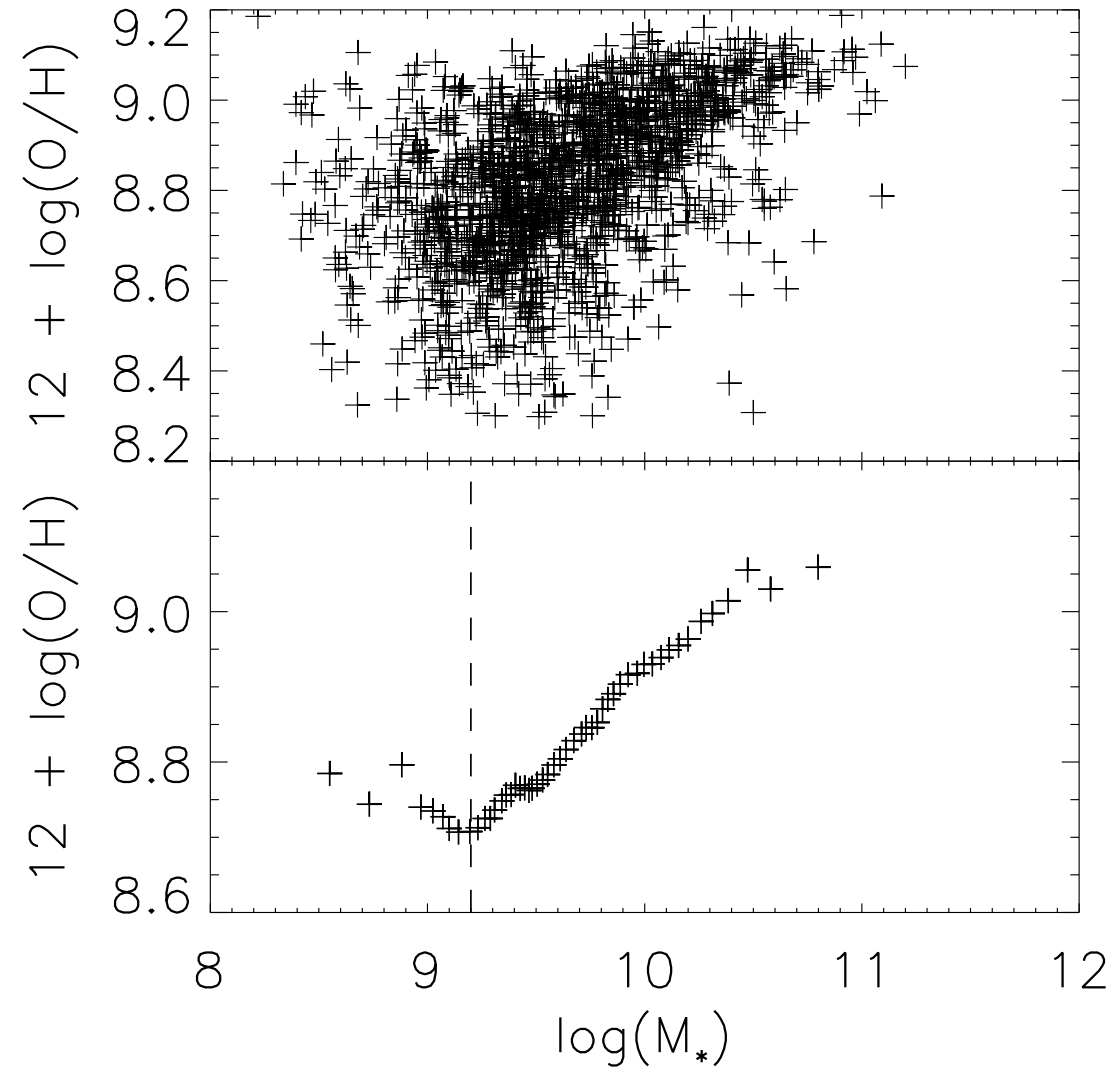

Figure 2.5 The mass and metallicity for the DEEP2 sample. The top panel shows the metallicity plotted against mass for the 1,631 galaxies in our sample. The bottom panel is a boxcar averaged smoothing of the data displayed in the top panel binned by mass. We attribute the break in the slope at $M \sim 10^{9.2} M_{\odot}$ to the misplacement of galaxies on the upper branch of the KK04 metallicity diagnostic. The vertical dashed line ($M = 10^{9.2} M_{\odot}$) in the lower panel is our lower limit cutoff mass used in determining the MZ relation for the DEEP2 sample.

2.4 Mass-Metallicity and Luminosity-Metallicity Relations

From our measured EWs and photometry, we can estimate both the gas-phase oxygen abundances and stellar masses for the galaxies in our sample. From the Spearman rank

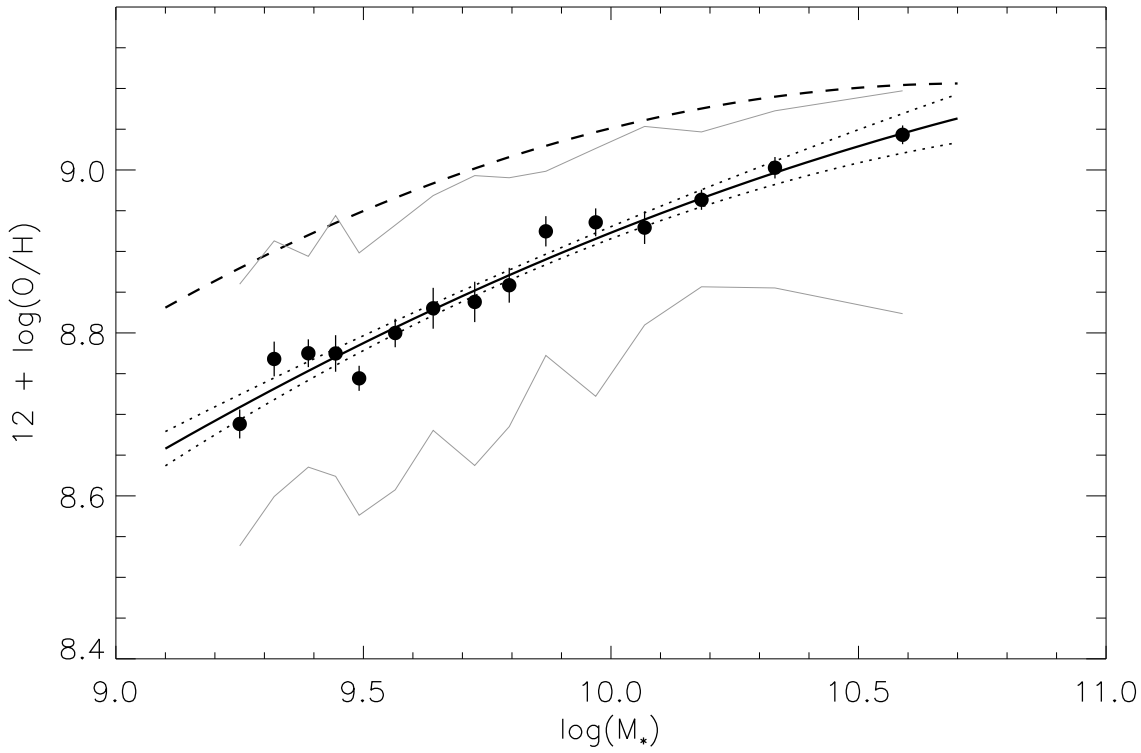

Figure 2.6 The MZ relation derived from the DEEP2 sample. The black data points are the median of the mass and metallicity sorted into 15 bins. The bootstrapped errors are determined by randomly selecting galaxies from within each mass bin and determining the median for this subsample. The error bar then is the standard deviation of the distribution of median values. The grey lines are the 16% and 84% contours of the data. The solid curve is a quadratic fit to the data and the dotted curves around the quadratic fit are the 1σ uncertainty in the fit determined from bootstrapping the errors. The dashed curve is the local MZ relation from the appendix of this paper.

test, we conclude with over 99% confidence that we have a positive correlation between mass and metallicity and luminosity and metallicity. This confidence in our observed correlation justifies a fit to the data.

2.4.1 The Mass-Metallicity Relation

The top panel of Figure 2.5 shows stellar mass and metallicity measured for our sample of 1,631 galaxies. The bottom panel shows binned data with a boxcar smoothing. In

determining the metallicity, we have assumed that all galaxies fall on the upper branch of the KK04 metallicity diagnostic. T04 have shown that in the local universe the MZ relation extends down to a stellar mass of $M_* = 10^{8.5} M_\odot$ with no break in the slope. We work under the assumption that the MZ relation at $z \sim 0.8$ extends to at least $M_* \sim 10^9 M_\odot$ with no break in slope. Under this assumption, we interpret the break in the slope at $M_* = 10^{9.2} M_\odot$ observed in the bottom panel of Figure 2.5 to be caused by the misplacement of lower branch galaxies on the upper branch. This turnover mass is further evidenced by the the R_{23} ratio as a function of stellar mass seen Figure 2.4. We take a lower mass limit, indicated by the vertical dashed line in the bottom panel of Figure 2.5, of $M_* = 10^{9.2} M_\odot$ to fit our MZ relation. We note that 283 of our 1,631 galaxies fall below this limit, leaving us with 1,348 galaxies from which we determine the MZ relation.

We parameterize the MZ relation with a quadratic function of the form

$$12 + log(O/H) = A + Bx + Cx^2, \tag{2.7}$$

where $x = log(M_*) - 10$. Our data and fit residuals are not normally distributed so we apply a standard non-parametric bootstrapping technique in determining the fit parameters and errors. One of the underlying assumptions of the bootstrapping method is that the observed distribution reasonably approximates the parent distribution. Under this assumption and the assumption of independence of the sample, properties determined from many independent random subsamples of the data should be normally distributed. We begin by randomly selecting, with replacement, 1,348 galaxies from our sample of 1,348 galaxies. Meaning, within a random subsample some data points may be selected more than once while others may not be selected at all. We then bin these randomly selected galaxies by sorting them into 15 equally populated mass bins. The mass and metallicity in each bin is determined by taking the median of the data in the bin. We perform a least-square quadratic fit to the binned data using the routine *poly_fit.pro* in IDL. We randomly resample and fit the data 10,000 times and take the mean and standard deviation of this

distribution of fitted parameters, which are normally distributed, as the fit parameters and errors for the MZ relation.

The MZ relation is best fitted by

$$12 + log(O/H) = 8.923 + 0.24\,x - 0.06\,x^2, \tag{2.8}$$

with the 1σ errors in each of the parameters in equation 10.5 given by $\sigma_A = 0.007, \sigma_B = 0.01$ and $\sigma_C = 0.03$. Figure 4.8 shows the DEEP2 MZ relation at $z \sim 0.8$ compared to the local MZ relation from SDSS (see appendix). The black filled circles are the data sorted into 15 mass bins. Each bin contains ~ 90 data points and the errors on the data are determined by randomly selecting ~ 90 data points in each bin and taking the median of the subsample. We take the standard deviation of this distribution as the error in each bin. We note that these errors characterize the distribution of metallicities within each mass bin but do not take into account measurement uncertainties in the metallicity determination. The grey lines are the 16% and 84% percentile contours of the data. The large dispersion at the high mass end is due to the large interval in mass covered by the highest mass bins.

Overall, we find that the high-mass ($M > 10^{10.5} M_\odot$) DEEP2 galaxies have similar metallicities (within the errors of ± 0.05 dex) to local galaxies at the same stellar mass. At lower masses ($M < 10^{10.5} M_\odot$), the DEEP2 galaxies have lower metallicities than the SDSS sample for a given stellar mass, up to a $\Delta log(O/H) \sim 0.15$ dex.

2.4.2 The Luminosity-Metallicity Relation

Figure 2.7 shows the LZ relation derived from the DEEP2 sample and the local sample from SDSS. Similar to the MZ relation, the LZ relation is determined for galaxies with $M_* > 10^{9.2} M_\odot$. The filled circles are the median metallicities in 15 luminosity bins. The solid curve is a linear fit to the binned data and is parameterized by the equation

$$12 + log(O/H) = (8.909 \pm 0.006) - (0.117 \pm 0.008) X_B, \tag{2.9}$$

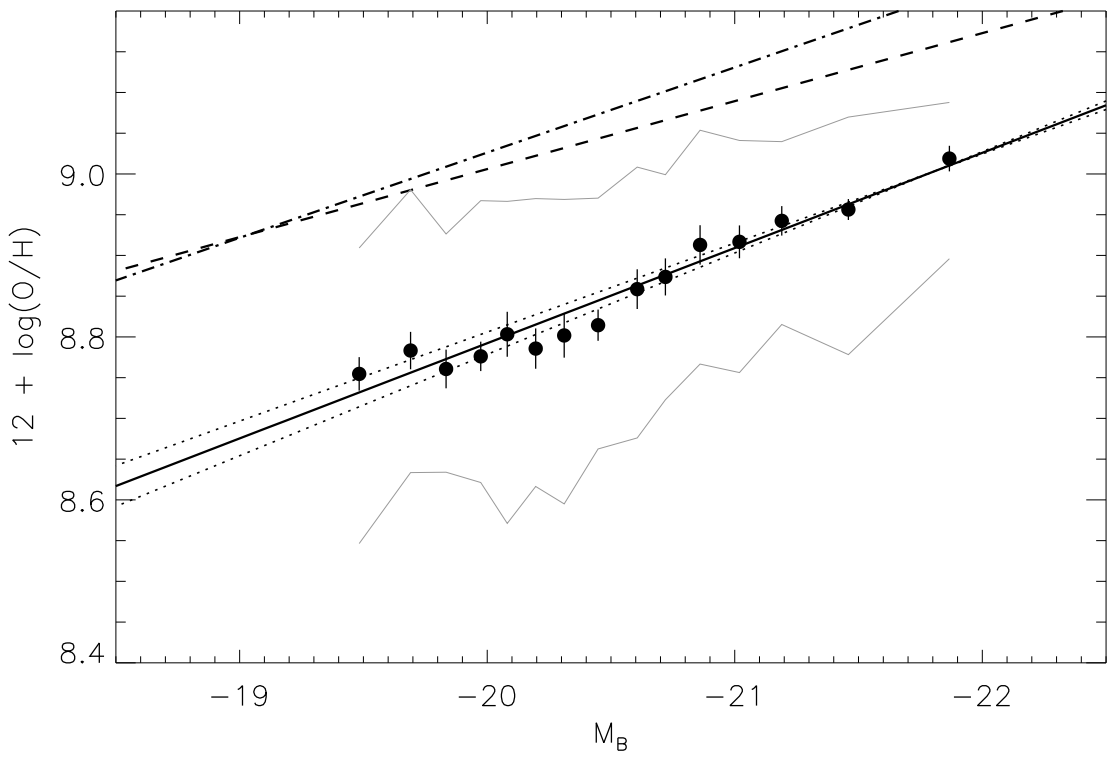

Figure 2.7 The LZ relation derived from the DEEP2 sample. The black data points are the median of the M_B and metallicity sorted into 15 luminosity bins. The solid line is a linear fit to the data and the dotted lines are the 1σ uncertainty of the fit determined from bootstrapping errors. The grey lines are the 16% and 84% percentile contours of the data. The dashed line is the local LZ relation from the appendix of this paper.

where $X_B = M_B + 21$. The errors in the fit and binned data of the LZ relation are derived in the same manner as for the MZ relation. The grey lines are the 16% and 84% percentile contours of the data. The dashed curve is the local LZ relation from SDSS taken from the appendix of this paper. The fit made is over the full range of magnitudes ($-21 < M_B < -18$) of the local LZ relation. However, the local LZ relation appears to turn over at $M_B < -21$. The dot-dashed curve is a fit to the linear part of the local LZ relation with $M_B > -21$. The slope of this fit and the DEEP2 LZ relation are consistent to within the errors. KK04 find that the slope of the LZ relation for $z = 0.6 - 0.8$ and $z = 0.8 - 1.0$ are -0.117 ± 0.017

and -0.134 ± 0.032 respectively. To within the errors, the slopes derived by KK04 agree with DEEP2 and local LZ relation slopes as well.

2.5 Discussion

In this section we will discuss our key assumptions (§ 2.5.1), the evolution of the B-band luminosity as a function of stellar mass in the population of blue galaxies (§ 2.5.2) and compare our determination of the MZ relation with other authors (§ 2.5.3).

2.5.1 Assumptions

We list and address some key assumptions made in this paper:

1. All galaxies with $M_* \geq 10^{9.2} M_\odot$ are on the upper branch of the R_{23} diagnostic. At the lower mass end of the DEEP2 MZ relation the dispersion is small and consistent with the dispersion found in the local MZ relation (T04). This small dispersion suggests that at $z \sim 0.8$, the vast majority of galaxies with $M_* > 10^{9.2} M_\odot$ are on the upper metallicity branch of the R_{23} diagnostic. Additionally, T04 have observed a continuous slope down to $M_* \sim 10^{8.5} M_\odot$. A breakdown of this assumption would result in the R_{23} measure of metallicity in low metallicity galaxies to be significantly overestimated ($\sim$ 1dex) resulting in a flattening of the MZ relation at lower masses. This flattening is observed to occur at $M_* = 10^{9.2} M_\odot$ and given the small dispersion, we hypothesize that misplacement on the upper branch is minor above this mass. Near infrared spectroscopy to obtain additional line ratios for a representative subsample of DEEP2 galaxies is needed to test this hypothesis.

2. Metals are instantaneously recycled. This approximation was first introduced by Schmidt (1963). The approximation is valid when metals produced in massive stars, such as oxygen, are considered and if the SFR is not subject to extreme variations on short timescale (Pagel 1997). From their study of DEEP2 galaxies since $z = 1.1$, Noeske et al. (2007b) determine that the dominant form of evolution is a gradual decline in star formation.

3. We have attempted to remove AGN using empirical limits on the R_{23} ratio and the color bimodality. This removes most of the galaxies whose emission is dominated by AGN, but composite galaxies in our sample may be blue and not exceed the empirical R_{23} limit. AGN contamination in composite galaxy spectra increases the R_{23} ratio due to the high $[OIII]/H\beta$ ratio. On the upper metallicity branch of the R_{23} diagnostic, the metallicity is a monotonically decreasing function of R_{23}. Therefore, AGN contamination will lower the metallicity estimate. However, due to their relatively small numbers in the DEEP2 blue galaxy sample (Weiner et al. 2007) and the small dispersion in the MZ relation, AGN contamination is likely to play a minor role in the MZ relation (Lamareille et al. 2009). Near infrared spectroscopy to obtain additional AGN-sensitive emission-line ratios is required to verify this assumption.

4. Since its introduction by Salpeter (1955), the initial stellar mass function (IMF) - describing the mass distribution of stars at birth - has largely been taken to be universal and invariant. Indirect evidences for variations in the local IMF have been provided by the comparison of $H\alpha$ emission to the far-ultraviolet flux (Meurer et al. 2009) and the $H\alpha$ flux to broadband color index (Hoversten & Glazebrook 2008). Comparisons of the rate of luminosity evolution to that of color evolution provides indirect observational evidence for a possible redshift evolution in the IMF (van Dokkum 2008). Furthermore, IMF variations have been cited as the possible cause of the MZ relation (Köppen et al. 2007). We work under the assumption that the IMF is universal.

5. MZ and LZ relation studies assume that the absence of low surface brightness galaxies (LSBGs) do not significantly bias the determination of the MZ and LZ relations. Impey & Bothun (1997) point out that LSBGs will be absent in magnitude limited surveys. However, by comparing photometry in overlapping fields where both CFHT and Hubble Space Telescope imaging is available, no galaxies brighter than the magnitude limit of $R_{AB} = 24.1$ are found to be lost due to low surface brightness (Simard et al. 2002; Willmer

et al. 2006). Melbourne et al. (2007) come to similar conclusions regarding the loss of low surface brightness galaxies from deep imaging in the GOODS-N field.

2.5.2 B-band Luminosity Evolution

In many previous studies, luminosity has been taken as a proxy for mass (Kobulnicky & Koo 2000; Pettini et al. 2001; Garnett 2002; Kobulnicky et al. 2003; Kobulnicky & Kewley 2004; Maier et al. 2004; Shapley et al. 2004, 2005). However, it has been recognized that the evolution in the LZ relation cannot straightforwardly be attributed to metallicity evolution, but that luminosity evolution must also be considered. By comparing figures 4.8 and 2.7, we see that the offset in metallicity in the MZ relation is significantly smaller than the offset in the LZ relation. Lamareille et al. (2009) (among others) suggest that the differential evolution in the LZ and MZ relation results from an evolution in the mass-to-light ratio. They estimate the evolution such that

$$\Delta M_B = a^{-1} \times [\Delta log(O/H)^M - \Delta log(O/H)^L], \tag{2.10}$$

where a is the slope of the LZ relation and $\Delta log(O/H)^M$ and $\Delta log(O/H)^L$ are the differences in metallicity at a fixed stellar mass and fixed B-band magnitude in the MZ and LZ relations, respectively. Equation 2.10 assumes that the metallicity evolution is characterized by the MZ relation and that additional evolution inferred from the LZ relation is due to evolution of the luminosity.

We estimate the evolution of the B-band luminosity as a function of stellar mass from equation 2.10. We take the difference between the local and DEEP2 LZ relation, $\Delta log(O/H)^L$, to be the average difference between the binned DEEP2 data and the fit to the local LZ relation over all magnitudes (see Figure 2.7). Consequently, $\Delta log(O/H)^L = 0.20 \pm 0.03$ dex and $a = -0.11$. We take $\Delta log(O/H)^M$ to be the difference between the

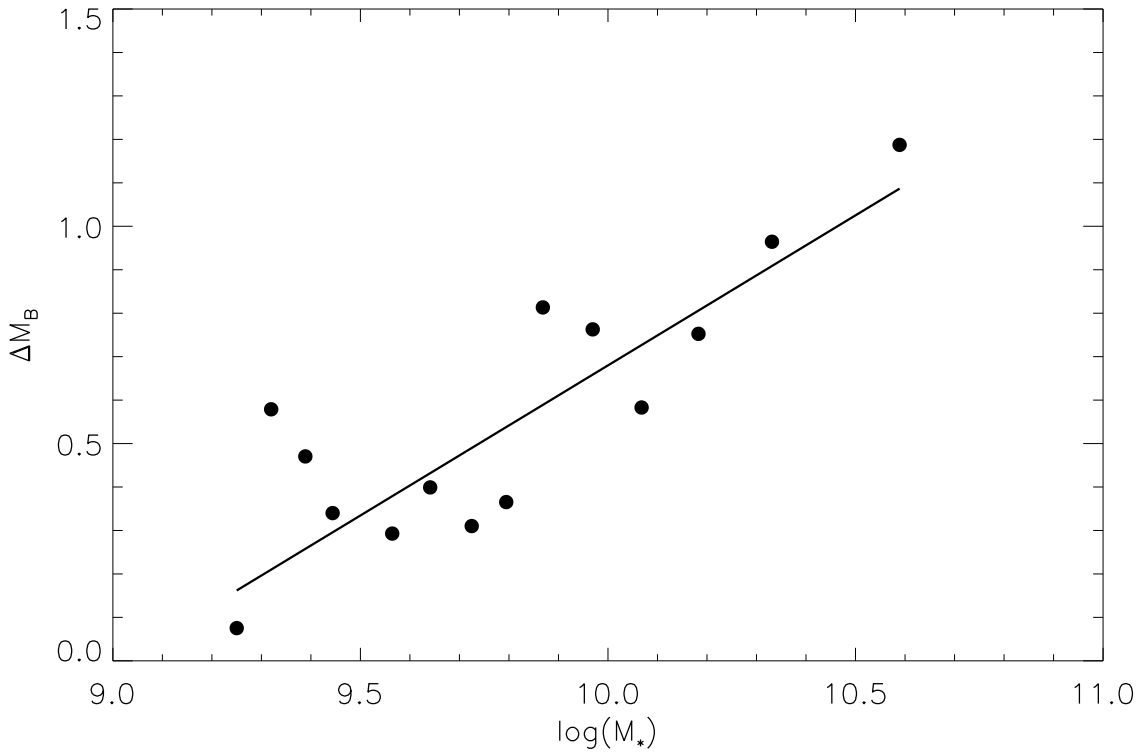

Figure 2.8 The B-band luminosity evolution inferred from the comparison of our MZ and LZ relations. The black data points are determined by taking the difference between the binned DEEP2 data and the fit to the local MZ relation and plugging it into equation 2.10. The line is from combining equations 2.10 and 2.11.

DEEP2 binned data and local MZ relation fit. The difference is parameterized by

$$\Delta log(O/H)^M = (0.12 \pm 0.01) - (0.08 \pm 0.02)x, \tag{2.11}$$

where $x = log(M_*) - 10$. Here we have performed a linear least-squares fit using *poly_fit.pro* and the errors are determined from the residuals of the fit and do not account for observational uncertainties.

Figure 2.8 shows the B-band luminosity evolution inferred from our comparison of the DEEP2 MZ and LZ relations. Combining equation 2.10 and 2.11 we get

$$\Delta M_B = (0.68 \pm 0.06) + (0.7 \pm 0.1)x, \tag{2.12}$$

the B-band luminosity evolution of blue star forming galaxies between $z \sim 0.8$ and the local galaxy population as a function of stellar mass. This is shown in Figure 2.8 by the solid line.

It has been shown that the luminosity functions of blue galaxies evolves with time (Ilbert et al. 2005; Blanton 2006; Willmer et al. 2006; Faber et al. 2007). These studies conclude that M_B^* has dimmed by ~ 1 mag since $z \sim 0.8$, consistent with the evolution observed in our sample at the higher stellar mass end. Noeske et al. (2007b) show that the star formation as a whole was higher at $z \sim 1$ and that the star formation rate gradually declines with galaxies spending 67% of their lifetime since $z = 1$ with SFR that are within a factor 2 of their average and 95% of their time within a factor of 4. In an accompanying letter, Noeske et al. (2007a) find that initial onset and rate of decline in star formation are functions of redshift and galaxy mass with less massive galaxies having later initial onsets with a lower rate of decline and consider this an important component of downsizing (Cowie et al. 1996). The absolute B-band luminosity is a tracer of star formation and the observed differential evolution with respect to stellar mass shown in Figure 2.8 may be attributed to this type of downsizing.

2.5.3 Comparison of MZ Relations

There are considerable difficulties in making a comparison of the MZ relation owing to the varying quality and type of data and the different methodologies and sample selections. The systematic differences among strong-line metallicity calibrations have been investigated by KE08. They derived conversions that reach agreement among calibrations to within ± 0.05 dex in metallicity. KE08 conclude that while absolute metallicity values are uncertain, relative metallicities (such as MZ relations) can be reliably compared, providing that the metallicities have been converted into the same base calibration.

Though offsets between different metallicity calibrations can now be removed, the systematic effects on differing measurements of stellar mass have yet to be fully explored. Moreover, comparisons between spectral and photometric methods have not been rigorously

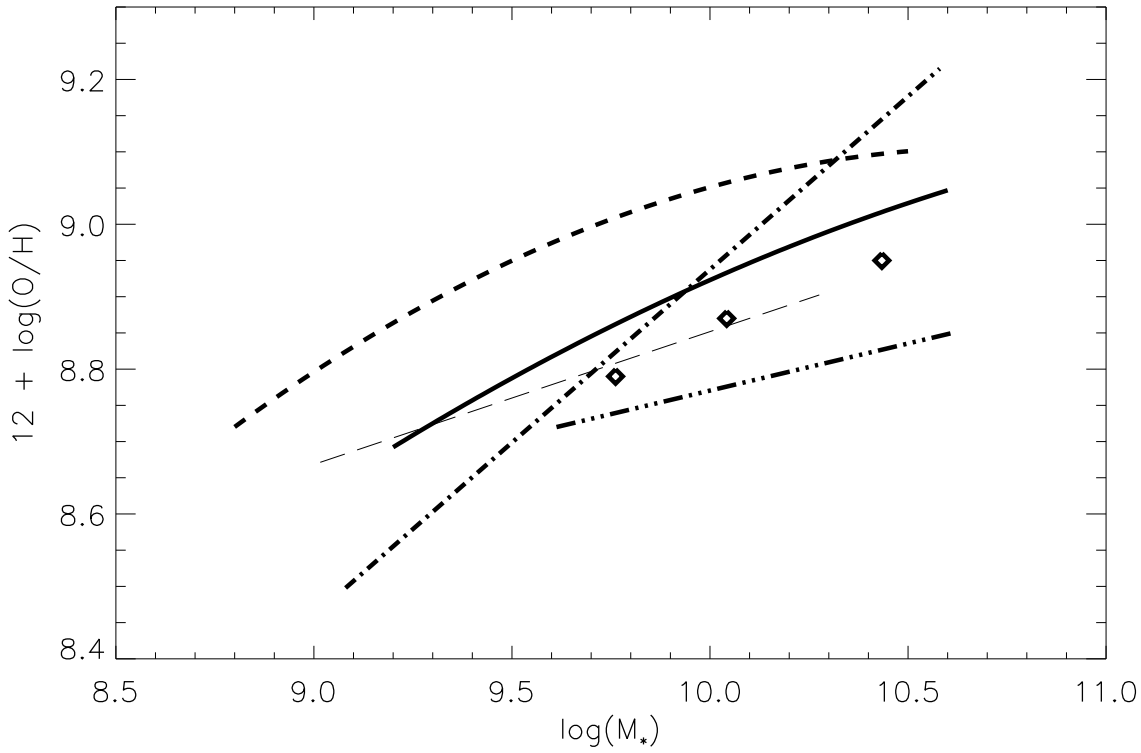

Figure 2.9 A comparison of the MZ relation derived by several authors. The solid line in this figure is our MZ relation derived for galaxies with $z = 0.75 - 0.82$. The short dashed curve is the local MZ relation for galaxies with $z = 0.04 - 0.1$ from the appendix of this paper. The long dashed curve is the MZ relation for galaxies with $z = 0.6 - 0.8$ from Lamareille et al. (2009). The dot-dashed curve is for galaxies with $z = 0.4 - 0.98$ from Savaglio et al. (2005). The triple dot-dashed curve is for galaxies with $z = 0.475 - 0.9$ from Cowie & Barger (2008). Metallicities and masses have been converted to be consistent amongst the samples. The relations only cover the stellar mass range over which they were determined.

investigated and the systematic effects of the photometric bands used in determining stellar mass remain uncertain. These problems are further compounded by the fact that many of the selection criteria in these studies may be a function of redshift (i.e. S/N of flux or EW, minimum values of flux or EW, color, etc.) and therefore the samples from which the MZ relations are determined may not be comparable even if similar selections are used.

Several authors have investigated the MZ relation covering the redshift interval examined in this study ($z = 0.75 - 0.82$). Figure 2.9 compares our MZ relation (solid curve) with

previously derived relations from Savaglio et al. (2005) (dot-dashed), Cowie & Barger (2008) (triple dot-dashed) and Lamareille et al. (2009) (long dashed line). All metallicities have been converted to the KK04 calibration using the conversions in KE08. We have attempted to make the stellar masses consistent with ours by converting all the determinations to the Chabrier IMF used in this study. The relations plotted only cover the stellar mass range over which they were determined.

The first attempt to investigate the MZ relation at intermediate redshifts was made by Savaglio et al. (2005) using the Gemini Deep Deep Survey. This sample consists of 28 galaxies from the Gemini Deep Deep Survey with emission in [OII], $H\beta$ and [OIII] at the 3σ level covering the redshift range of $z = 0.40 - 0.98$. This sample consists of galaxies designated as late (7/28) and intermediate type (21/28). This sample is augmented with 28 galaxies from the Canada France Redshift Survey (Lilly et al. 1995).The dot-dashed fit in Figure 2.9 is a linear bisector fit of the S05 mass and metallicity. Though Savaglio et al. establish a MZ relation at higher redshifts, the small sample size and selection in addition to the fitting method does not allow us to make a direct comparison with our determination.

Lamareille et al. (2009) study the evolution of the MZ relation by splitting their sample into three redshift ranges. They find that the most massive galaxies undergo the most evolution at $z \sim 0.8$, implying that the slope of the MZ relation flattens out at higher redshfits. However, L09 do not find a strong Spearman rank correlation coefficient, thus hindering a rigorous statistical analysis. The relation shown in Figure 2.9 (long-dashed line) is a linear fit to average metallicities in 4 mass bins for ~ 130 galaxies in the redshift range of $z = 0.6 - 0.8$. The galaxies are selected to have $S/N > 4$ in the flux of the [OII], $H\beta$ and [OIII] emission lines. The flattening of the slope at higher redshifts may possibly be a consequence of the S/N cut on the [OII] and [OIII] lines. These cuts may be a function of redshift and bias against higher metallicity galaxies generally found at higher stellar masses. At lower masses, the MZ relation of L09 is in agreement with our determination.

Cowie & Barger (2008) study the evolution of the MZ relation by splitting their sample into a low-z and mid-z redshift interval. The two intervals are $0.05 < z < 0.475$ and

$0.475 < z < 0.9$ and have a median redshift of 0.44 and 0.75 respectively. The low-z and mid-z samples have 35 and 154 galaxies respectively. They find that there is a 0.25 dex difference in the metallicity in the mid-z sample as compared with the local relation and that the metallicity increases by 0.13 dex between the mid-z and low-z sample. The triple dot-dashed line in Figure 2.9 shows the mid-z relation.

A major source of discrepancy between our determination and Cowie et al. can be attributed to the fitting procedure. Figure 31 of Cowie et al. shows that the spread in metallicity becomes larger as metallicity decreases. This may result from the greater uncertainty in determining metallicity from the R_{23} diagnostic which becomes less sensitive to metallicity around the R_{23} local maximum ($12 + log(O/H) \sim 8.4$) (see C08 figure 23 or KK04 figure 7 for example). In a least-square fit, data that are further away from the fitted relation have a greater influence in determining the best fit. Looking at figure 63 of C08 shows that the median of the metallicity in 4 mass bins is systematically higher than the fitted relation. With the diamonds in figure 2.9, we plot the median of the MZ relation for the mid-z sample sorted into 3 mass bins (L. Cowie, private communication). We fit our relation to the median metallicity in 15 mass bins as described in § 2.4. The MZ relation determined from the median of the C08 data is more comparable to our determination. Given the many uncertainties discussed in comparing the MZ relation, the agreement between the relation of L09, C08 and our determination from DEEP2 is promising.

Our MZ relation comparisons highlight the need for consistent sample selection and MZ relation fitting techniques when comparing MZ relations at the same or different redshifts.

2.6 Summary

We have conducted a study of the mass-metallicity and luminosity-metallicity relation at $z \sim 0.8$ using the 1,348 galaxies from the DEEP2 survey. This large sample has allowed us to establish the mass-metallicity and luminosity-metallicity relation at $z \sim 0.8$ with greater

statistical significance than previous studies in this redshift regime. Such a large sample within a small redshift range is essential for avoiding evolution effects in luminosity or metallicity that may influence luminosity-metallicity and mass-metallicity relations derived over a larger redshift interval.

We have obtained stellar masses by inferring a SED from our photometry and fitting it with current stellar population synthesis models. We have determined the gas-phase oxygen abundance in a consistent manner from strong-line methods. We summarize our main results as follows:

1. We find a clear correlation between mass and metallicity at $z \sim 0.8$, consistent with previous work (Savaglio et al. 2005; Cowie & Barger 2008; Lamareille et al. 2009). The level of chemical enrichment achieved by galaxies is a function of stellar mass. At $z \sim 0.8$, galaxies with $M_* \sim 10^{10.6} M_\odot$ have metallicities that are lower by 0.05 dex as compared to the local sample, which is within the errors of the metallicity calibration conversions. The metallicity difference between $z \sim 0.8$ and local galaxies rises to 0.15 dex at $M_* \sim 10^{9.2} M_\odot$.

2. There is a clear correlation between luminosity and metallicity at $z \sim 0.8$, as shown in previous work. The level of chemical enrichment achieved by galaxies is a function of luminosity. The metallicity at a given luminosity at $z \sim 0.8$ is 0.20 dex lower than the local sample due to the combination of metallicity and luminosity evolution with redshift.

3. The offset in the LZ relation between $z \sim 0.8$ and local galaxies is significantly larger than the offset observed in the MZ relation between these two redshifts. We attribute this difference to evolution in the mass-to-light ratio between $z \sim 0.8$ and $z \sim 0$. We infer a luminosity evolution that scales with stellar mass and is consistent with determinations from studies of blue galaxy luminosity functions.

Both the luminosity and metallicity evolution are a function of stellar mass, consistent with the downsizing scenario of galaxy evolution. In a subsequent paper, we will examine the origin of the mass-metallicity relation and its evolution over cosmological timescales.

References

Ažusienis, A., & Straižys, V. 1969, Soviet Astronomy, 13, 316

Baldry, I. K., Glazebrook, K., Brinkmann, J., Ivezić, Ž., Lupton, R. H., Nichol, R. C., & Szalay, A. S. 2004, ApJ, 600, 681

Bell, E. F., McIntosh, D. H., Katz, N., & Weinberg, M. D. 2003, ApJ, 585, L117

Blanton, M. R. 2006, ApJ, 648, 268

Brooks, A. M., Governato, F., Booth, C. M., Willman, B., Gardner, J. P., Wadsley, J., Stinson, G., & Quinn, T. 2007, ApJ, 655, L17

Bruzual, G., & Charlot, S. 2003, MNRAS, 344, 1000

Bundy, K., et al. 2006, ApJ, 651, 120

Buser, R. 1978, A&A, 62, 411

Calzetti, D., Armus, L., Bohlin, R. C., Kinney, A. L., Koornneef, J., & Storchi-Bergmann, T. 2000, ApJ, 533, 682

Carollo, C. M., & Lilly, S. J. 2001, ApJ, 548, L153

Chabrier, G. 2003, PASP, 115, 763

Charlot, S., & Longhetti, M. 2001, MNRAS, 323, 887

Coil, A. L., Newman, J. A., Kaiser, N., Davis, M., Ma, C.-P., Kocevski, D. D., & Koo, D. C. 2004, ApJ, 617, 765

Conroy, C., Gunn, J. E., & White, M. 2009, ApJ, 699, 486

Cowie, L. L., & Barger, A. J. 2008, ApJ, 686, 72

Cowie, L. L., Songaila, A., Hu, E. M., & Cohen, J. G. 1996, AJ, 112, 839

Davis, M., et al. 2003, in SPIE, ed. P. Guhathakurta, Vol. 4834, 161–172

de Rossi, M. E., Tissera, P. B., & Scannapieco, C. 2007, MNRAS, 374, 323

Drory, N., Bender, R., & Hopp, U. 2004, ApJ, 616, L103

Erb, D. K., Shapley, A. E., Pettini, M., Steidel, C. C., Reddy, N. A., & Adelberger, K. L. 2006, ApJ, 644, 813

Faber, S. M., et al. 2003, in Society of Photo-Optical Instrumentation Engineers (SPIE) Conference Series, Vol. 4841, Society of Photo-Optical Instrumentation Engineers (SPIE) Conference Series, ed. M. Iye & A. F. M. Moorwood, 1657–1669

Faber, S. M., et al. 2007, ApJ, 665, 265

Ferland, G. J. 1996, Hazy, A Brief Introduction to Cloudy 90, ed. G. J. Ferland

Fontana, A., et al. 2004, A&A, 424, 23

Garnett, D. R. 2002, ApJ, 581, 1019

Garnett, D. R., Shields, G. A., Skillman, E. D., Sagan, S. P., & Dufour, R. J. 1997, ApJ, 489, 63

Hogg, D. W., et al. 2003, ApJ, 585, L5

Horne, K. 1986, PASP, 98, 609

Hoversten, E. A., & Glazebrook, K. 2008, ApJ, 675, 163

Ilbert, O., et al. 2009, ApJ, 690, 1236

—. 2005, A&A, 439, 863

Impey, C., & Bothun, G. 1997, ARA&A, 35, 267

Kauffmann, G., & Charlot, S. 1998, MNRAS, 294, 705

Kennicutt, Jr., R. C. 1992, ApJS, 79, 255

Kewley, L. J., & Dopita, M. A. 2002, ApJS, 142, 35

Kewley, L. J., & Ellison, S. L. 2008, ApJ, 681, 1183

Kewley, L. J., Rupke, D., Jabran Zahid, H., Geller, M. J., & Barton, E. J. 2010, ApJ, 721, L48

Kobulnicky, H. A., Kennicutt, Jr., R. C., & Pizagno, J. L. 1999, ApJ, 514, 544

Kobulnicky, H. A., & Kewley, L. J. 2004, ApJ, 617, 240

Kobulnicky, H. A., & Koo, D. C. 2000, ApJ, 545, 712

Kobulnicky, H. A., & Phillips, A. C. 2003, ApJ, 599, 1031

Kobulnicky, H. A., et al. 2003, ApJ, 599, 1006

Köppen, J., Weidner, C., & Kroupa, P. 2007, MNRAS, 375, 673

Kroupa, P. 2001, MNRAS, 322, 231

Lamareille, F., et al. 2009, A&A, 495, 53

Lamareille, F., Mouhcine, M., Contini, T., Lewis, I., & Maddox, S. 2004, MNRAS, 350, 396

Larson, R. B. 1974, MNRAS, 169, 229

Larson, R. B., & Dinerstein, H. L. 1975, PASP, 87, 911

Lequeux, J., Peimbert, M., Rayo, J. F., Serrano, A., & Torres-Peimbert, S. 1979, A&A, 80, 155

Lilly, S. J., Le Fevre, O., Crampton, D., Hammer, F., & Tresse, L. 1995, ApJ, 455, 50

Maier, C., Meisenheimer, K., & Hippelein, H. 2004, A&A, 418, 475

Maiolino, R., et al. 2008, A&A, 488, 463

Mannucci, F., et al. 2009, MNRAS, 398, 1915

Melbourne, J., Phillips, A. C., Harker, J., Novak, G., Koo, D. C., & Faber, S. M. 2007, ApJ, 660, 81

Meurer, G. R., et al. 2009, ApJ, 695, 765

Mouchine, M., Gibson, B. K., Renda, A., & Kawata, D. 2008, ArXiv e-prints

Noeske, K. G., et al. 2007a, ApJ, 660, L47

—. 2007b, ApJ, 660, L43

Oppenheimer, B. D., & Davé, R. 2008, MNRAS, 387, 577

Osterbrock, D. E. 1989, Astrophysics of gaseous nebulae and active galactic nuclei, ed. D. E. Osterbrock

Pagel, B. E. J. 1997, Nucleosynthesis and Chemical Evolution of Galaxies, ed. Pagel, B. E. J.

Pagel, B. E. J., Edmunds, M. G., Blackwell, D. E., Chun, M. S., & Smith, G. 1979, MNRAS, 189, 95

Pérez-Montero, E., et al. 2009, A&A, 495, 73

Pettini, M., Shapley, A. E., Steidel, C. C., Cuby, J.-G., Dickinson, M., Moorwood, A. F. M., Adelberger, K. L., & Giavalisco, M. 2001, ApJ, 554, 981

Salpeter, E. E. 1955, ApJ, 121, 161

Salzer, J. J., Lee, J. C., Melbourne, J., Hinz, J. L., Alonso-Herrero, A., & Jangren, A. 2005, ApJ, 624, 661

Savaglio, S., et al. 2005, ApJ, 635, 260

Schechter, P. 1976, ApJ, 203, 297

Schmidt, M. 1963, ApJ, 137, 758

Searle, L., & Sargent, W. L. W. 1972, ApJ, 173, 25

Shapley, A. E., Coil, A. L., Ma, C.-P., & Bundy, K. 2005, ApJ, 635, 1006

Shapley, A. E., Erb, D. K., Pettini, M., Steidel, C. C., & Adelberger, K. L. 2004, ApJ, 612, 108

Simard, L., et al. 2002, ApJS, 142, 1

Skillman, E. D., Kennicutt, R. C., & Hodge, P. W. 1989, ApJ, 347, 875

Somerville, R. S., & Primack, J. R. 1999, MNRAS, 310, 1087

Springel, V., & Hernquist, L. 2003, MNRAS, 339, 289

Strateva, I., et al. 2001, AJ, 122, 1861

Tremonti, C. A., et al. 2004, ApJ, 613, 898

van den Bergh, S. 1962, AJ, 67, 486

van Dokkum, P. G. 2008, ApJ, 674, 29

Weiner, B. J., et al. 2007, ApJ, 660, L39

Willmer, C. N. A., et al. 2006, ApJ, 647, 853

Zahid, H. J., Kewley, L. J., & Bresolin, F. 2011, ApJ, 730, 137

Zaritsky, D., Kennicutt, Jr., R. C., & Huchra, J. P. 1994, ApJ, 420, 87

Chapter 3

The Chemical Evolution of Star-Forming Galaxies Over the Last 11 Billion Years

Note: This chapter originally appeared as Zahid, H.J., Geller, M.J., Kewley, L.J., Hwang, H.S., Fabricant, D.G., & Kurtz, M.J., 2013, ApJ 771, L19. This is work is based on data from the SHELS survey (PI M. Geller). I analyzed the data and I am the primary author of this work.

Abstract

We calculate the stellar mass-metallicity relation at five epochs ranging to $z \sim 2.3$. We quantify evolution in the shape of the mass-metallicity relation as a function of redshift; the mass-metallicity relation flattens at late times. There is an empirical upper limit to the gas-phase oxygen abundance in star-forming galaxies that is independent of redshift. From examination of the mass-metallicity relation and its observed scatter we show that the flattening at late times is a consequence of evolution in the stellar mass where galaxies enrich to this empirical upper metallicity limit; there is also evolution in the fraction of galaxies at a fixed stellar mass that enrich to this limit. The stellar mass where metallicities begin to saturate is ~ 0.7 dex smaller in the local universe than it is at $z \sim 0.8$.

3.1 Introduction

Gas dynamics and star formation regulate the gas-phase oxygen abundance (metallicity) of star-forming galaxies. Oxygen in the universe forms in the late stage evolution of massive stars. Oxygen dispersed into the interstellar medium (ISM) by supernovae and stellar winds increases the metallicity of galaxies as they increase their stellar mass. Observations suggest that in most star-forming galaxies at $z \lesssim 2$, the increase in stellar mass is dominated by cosmological inflows of gas from the intergalactic medium (Noeske et al. 2007; Whitaker et al. 2012, among others). At the same time, outflows of gas are ubiquitously observed in star-forming galaxies out to $z \sim 3$ (Weiner et al. 2009; Chen et al. 2010; Steidel et al. 2010). Because metallicity is established by the interplay of gas flows and star-formation, observations of the chemical evolution of galaxies provides important constraints for these physical processes in models of galaxy evolution (e.g. Davé et al. 2011; Zahid et al. 2012b; Møller et al. 2013).

The mass-metallicity (MZ) relation is a measure of the average gas-phase oxygen abundance as a function of stellar mass. Lequeux et al. (1979) first observed the relation between stellar mass and metallicity in nearby irregular and blue compact galaxies. From the analysis of $\sim 50,000$ star-forming galaxies in the Sloan Digital Sky Survey, Tremonti et al. (2004) establish the MZ relation in the local universe. Subsequent efforts show that the MZ relation extends to low stellar masses ($\sim 10^7 M_{\odot}$; Lee et al. 2006; Zahid et al. 2012a; Berg et al. 2012) and out to *at least* $z \sim 3$ (Savaglio et al. 2005; Erb et al. 2006; Maiolino et al. 2008; Mannucci et al. 2009; Zahid et al. 2011; Foster et al. 2012; Yabe et al. 2012; Pérez-Montero et al. 2013; Yuan et al. 2013, among others), with indications that it may extend to even higher redshifts (Laskar et al. 2011; Møller et al. 2013). The metallicities of galaxies increase with stellar mass and the metallicities at all stellar masses decrease with redshift. Because of systematic uncertainties and a lack of sufficiently large samples of galaxies with well determined metallicities at intermediate and high redshifts, evolution in the shape of the MZ relation is not well known.

A robust determination of the evolution of the MZ relation requires consistent measurements of the metallicities *and* stellar masses of galaxies. Here we bring together a homogeneously analyzed sample of galaxies with well determined MZ relations to investigate the evolution of the MZ relation to $z \sim 2.3$. In Section 3.2 we describe the data and the methods applied to determine metallicities and stellar masses. In Section 3.3 we present the MZ relation and its scatter and quantify its evolution. We discuss our results in Section 3.4 and conclude with a summary in Section 3.5. We assume the standard cosmology $(H_0, \Omega_m, \Omega_\Lambda) = (70 \text{ km s}^{-1} \text{ Mpc}^{-1}, 0.3, 0.7)$ and a Chabrier (2003) IMF.

3.2 Data and Methods

3.2.1 The Data

We derive the MZ relation at $z = 0.08, 0.29$ and 0.78 using data from the Sloan Digital Sky Survey DR7 (SDSS; Abazajian et al. 2009), the Smithsonian Hectospec Lensing Survey (SHELS; Geller et al. 2005, Hwang et al., in prep) and the Deep Extragalactic Evolutionary Probe 2 Survey DR3 (DEEP2; Davis et al. 2003), respectively. The MZ relation at $z = 1.41$ and 2.26 are determined by Yabe et al. (2012) and Erb et al. (2006), respectively. We determine the stellar masses of galaxies in their sample using our method (see Section 3.2.2) and adopt their metallicity estimates but convert them for consistency with our measurements of metallicity in the $z < 1$ samples (see Section 3.2.3).

Our primary selection criteria for galaxies in the $z < 1$ samples are the signal-to-noise (S/N) ratios of strong emission lines. Foster et al. (2012) show that the derived MZ relation does not vary significantly with S/N cuts on most of the strong emission lines used in this study, though S/N cuts on the [OIII]λ5007 line can lead to a significant bias. The requisite lines for determining metallicity in the $z < 1$ samples are [OII]λ3727, Hβ and [OIII]λ5007 (see Section 3.2.3). We require a S/N > 3 in the [OII]λ3727 and Hβ emission lines. Additionally, in the SDSS and SHELS sample we use the Hα and [NII]λ6584 emission lines in selecting star-forming galaxies and apply the same S/N criteria.

The SDSS spectroscopic sample consists of $\sim 900,000$ galaxies primarily in the redshift range of $0 < z < 0.3$. We adopt emission line fluxes measured by the MPA/JHU[1] group and determine the stellar masses from the *ugriz*-band photometry. AGN are removed from the sample using the [OIII]/Hβ vs. [NII]/Hα diagram (i.e. the BPT method, Baldwin et al. 1981; Kauffmann et al. 2003; Kewley et al. 2006). We require an aperture covering fraction $\gtrsim 20\%$(Kewley et al. 2005) and select galaxies with $z < 0.12$. Our final sample consists of $\sim 51,000$ star-forming galaxies in the redshift range of $0.02 < z < 0.12$

The SHELS survey consists of $\sim 25,000$ galaxies in the F1 (Hwang et al., in prep) and F2 (Geller et al. 2005; Hwang et al. 2012; Geller et al. 2012) regions of the Deep Lens Survey (Wittman et al. 2002) spanning the redshift range of $0 < z < 0.8$. We determine stellar masses from the *ugriz*-band SDSS photometry and remove AGN using the BPT method. Our sample consists of 3,577 star-forming galaxies in the redshift range $0.2 < z < 0.38$.

The DEEP2[2] survey (Davis et al. 2003) consists of $\sim 50,000$ galaxies spanning the redshift range of $0.7 < z < 1.4$. We determine stellar masses from *BRI*-band photometry with additional K_s-band photometry for half of the sample. This sample differs slightly from the sample we analyzed in Zahid et al. (2011). For consistency with the SDSS and SHELS analysis, we use stellar population synthesis models to remove Balmer absorption. Additionally, we limit AGN contamination by removing 17 x-ray galaxies in the sample (Goulding et al. 2012). Our final sample consists of 1,254 star-forming galaxies in the redshift range $0.75 < z < 0.82$.

Yabe et al. (2012) and Erb et al. (2006) measure the MZ relation at $z \sim 1.4$ and $z \sim 2.3$, respectively. Yabe et al. (2012) determine the MZ relation from the stacked spectra of 71 objects with significant detections of Hα and Erb et al. (2006) determine the MZ relation from the stacked spectra of 87 UV-selected star-forming galaxies. The MZ relations determined by Erb et al. (2006) and Yabe et al. (2012) are subject to some systematic uncertainties (see Section 3.2.3) that we are currently unable to quantify. We include these data to demonstrate that the best data currently available at high redshift are

[1] http://www.mpa-garching.mpg.de/SDSS/DR7/
[2] http://deep.ps.uci.edu/DR3/

qualitatively consistent with the main conclusions of this study based *solely* on the $z < 1$ samples.

3.2.2 Stellar Mass Determination

We measure stellar masses for the five samples using the Le Phare[3] code developed by Arnouts & Ilbert. We determine the mass-to-light ratio by fitting the SED with stellar population synthesis models and we scale the luminosity by the mass-to-light ratio to yield a stellar mass estimate (see Bell et al. 2003). We use the stellar templates of Bruzual & Charlot (2003) and a Chabrier (2003) IMF. The models have two metallicities and seven exponentially decreasing star formation models (SFR $\propto e^{-t/\tau}$) with $\tau = 0.1, 0.3, 1, 2, 3, 5, 10, 15$ and 30 Gyrs. We apply the extinction law of Calzetti et al. (2000) allowing E(B−V) from 0 to 0.6 and a stellar population age range from 0 to 13 Gyrs. For each of our samples, the age never exceeds the age of the universe at the median redshift of the sample.

We adopt the median of the mass distribution as our estimate of the stellar mass. We compare the stellar masses we determine for our SDSS sample with those derived by the MPA/JHU group. We find a 0.17 dex dispersion after correcting for a systematic offset between the two methods. This dispersion is consistent with the observational uncertainty in the photometry.

3.2.3 Metallicity Determination

Ratios of the strength of collisionally excited emission lines to recombination lines are both theoretically and empirically calibrated for determining metallicity. A long-standing astrophysical problem is that the absolute metallicity determined from theoretical calibrations is typically $\sim$ 0.3 dex higher than metallicities determined using empirical calibration methods. However, we emphasize that our analysis requires a robust *relative* estimate of the metallicity, which the various metallicity diagnostics deliver (Kewley &

[3] $http://www.cfht.hawaii.edu/\sim arnouts/LEPHARE/cfht\_lephare/lephare.html$

Ellison 2008). Kewley & Ellison (2008) provide a table of formulae allowing for conversion of metallicities into various baseline methods.

We determine metallicities from the $R23$ line ratio calibrated by Kobulnicky & Kewley (2004, hereafter KK04). A major advantage of this method is that it explicitly solves and corrects for the ionization parameter. The relevant ratios of measured emission line intensities are

$$R23 = \frac{[\mathrm{OII}]\lambda 3727 + [\mathrm{OIII}]\lambda 4959, 5007}{\mathrm{H}\beta} \tag{3.1}$$

and

$$O32 = \frac{[\mathrm{OIII}]\lambda 4959, 5007}{[\mathrm{OII}]\lambda 3727}. \tag{3.2}$$

We assume that the ratio of the fluxes of [OIII]λ5007 to [OIII]λ4959 is 3 (Osterbrock 1989) and adopt a value of 1.33 times the [OIII]λ5007 when summing the [OIII]λ5007 and [OIII]λ4959 line strengths. The $R23$ method is sensitive to the ionization state of the gas and the $O32$ ratio is used to correct for variations. We apply this method to the SDSS, SHELS and DEEP2 data. The galaxies in this study all lie on the upper metallicity branch (see Zahid et al. 2011).

At higher redshifts the requisite lines for determination of the $R23$ ratio are rarely observed. Pettini & Pagel (2004, hereafter PP04) calibrate

$$N2 = ([\mathrm{NII}]\lambda 6584/\mathrm{H}\alpha) \tag{3.3}$$

to yield the metallicity. The advantage of this diagnostics is that the lines are closely spaced and easily observed in a single spectroscopic setting. However, diagnostics using [NII]λ6584 are known to depend on the ionization parameter (Kewley & Dopita 2002) and the N/O ratio which is not constant with metallicity (e.g. Pérez-Montero & Contini 2009). These effects may evolve with redshift (Kewley et al., in prep). Therefore, an MZ relation based on this diagnostics may be systematically biased. Both Erb et al. (2006) and Yabe et al. (2012) determine metallicities using the PP04 $N2$ calibration. We convert metallicities determined

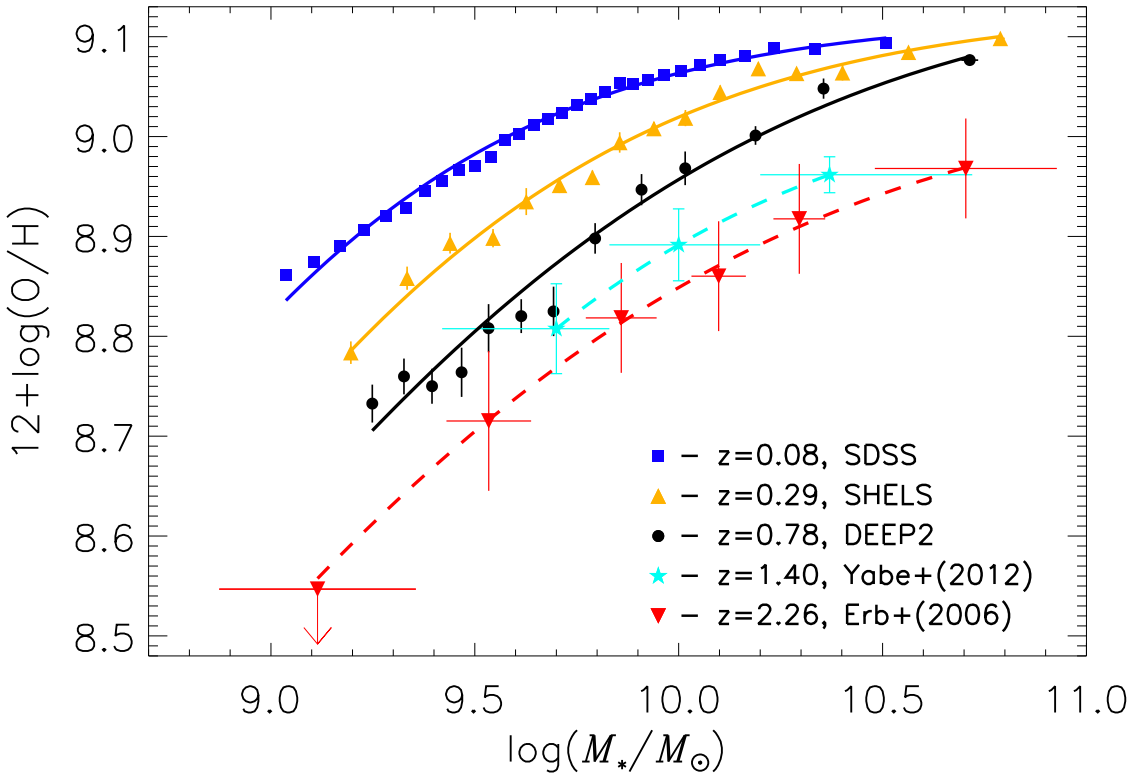

Figure 3.1 The MZ relation at five epochs ranging to $z \sim 2.3$. The curves are fits to the data defined by Equation 4.6. The solid curves indicate metallicities determined using the KK04 strong-line method and the dashed curves indicate metallicities converted using the formulae of Kewley & Ellison (2008).

from the PP04 $N2$ diagnostic to the KK04 diagnostic using the conversion formulae given in Kewley & Ellison (2008).

3.3 Results

3.3.1 The MZ Relation

Figure 10.1 shows the MZ relations at five epochs. We determine the MZ relation for the SDSS, SHELS and DEEP2 samples by binning the data. We sort galaxies into equally populated bins of stellar mass and plot the median stellar mass and metallicity for each bin. The MZ relation of Yabe et al. (2012) and Erb et al. (2006) is determined from

Table 3.1. MZ Relation Fit

Sample	Redshift	Z_o	$\log(M_o/M_\odot)$	γ	Calibration
SDSS	0.08	9.121 ± 0.002	8.999 ± 0.005	0.85 ± 0.02	KK04
SHELS	0.29	9.130 ± 0.007	9.304 ± 0.019	0.77 ± 0.05	KK04
DEEP2	0.78	9.161 ± 0.026	9.661 ± 0.086	0.65 ± 0.07	KK04
Y12	1.40	9.06 ± 0.36	9.6 ± 0.8	0.7 ± 1.5	PP04
E06	2.26	9.06 ± 0.27	9.7 ± 0.9	0.6 ± 0.7	PP04

Note. — The sample and median redshift are given in columns 1 and 2, respectively. The fit parameters from Equation 4.6 are given in columns 3-5. Column 6 indicates the strong line method used for deriving metallicity. We convert PP04 metallicities to the KK04 calibration using the formulae from Kewley & Ellison (2008).

stacked spectra sorted by stellar mass. The errors for the $z < 1$ data are determined from bootstrapping. For the $z > 1$ data the errors are determined from the dispersion in the stacked spectra.

We fit the MZ relation using the function defined by Moustakas et al. (2011). The functional form of the MZ relation fit is

$$12 + \log(\mathrm{O/H}) = Z_o - \log\left[1 + \left(\frac{M_*}{M_o}\right)^{-\gamma}\right]. \tag{3.4}$$

This function is desirable because it is monotonic unlike the commonly used quadratic fit (e.g. Tremonti et al. 2004; Zahid et al. 2011) which turns over at high stellar masses. Furthermore, the parameters of the fit reflect our physical intuition of chemical evolution and are more straightforward to interpret physically (see discussion in appendix of Moustakas et al. 2011). In Equation 4.6, Z_o is the asymptotic metallicity where the MZ relation flattens, M_o is the characteristic mass where the MZ relation begins to flatten and γ is the power law slope of the MZ relation for $M_* << M_o$. The fitted value of Z_o is subject to uncertainties in the absolute calibration of the metallicity diagnostic, though the relative values are robust (see Section 3.2.3). We do not probe stellar masses where $M_* << M_o$. Therefore the power

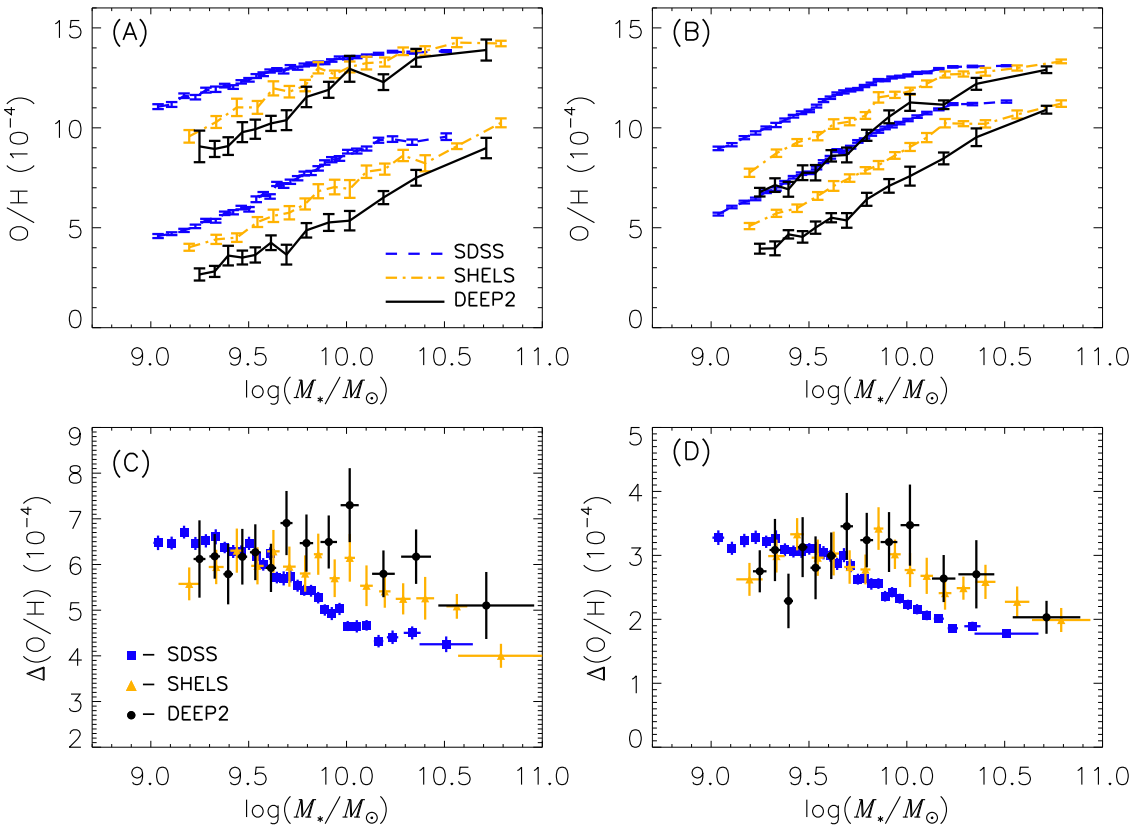

Figure 3.2 Limits containing the central (A) 85% and (B) 50% of the metallicity distribution and the difference between the upper and lower limits for the central (C) 85% and (D) 50% of the galaxy metallicity distribution as a function of stellar mass for the $z < 1$ samples. For clarity the metallicity is plotted on a linear scale.

law slope of the MZ relation at the low mass end, γ, is not well constrained. Table 1 lists the fitted parameters. We propagate the observational uncertainties to the parameter errors.

3.3.2 Scatter in the MZ Relation

The scatter in the metallicity distribution as a function of stellar mass and redshift provides important additional constraints for the chemical evolution of galaxies. In Figure 5.5 we plot the scatter in the MZ relation. We note that we have converted the metallicity to linear units for clarity. In Figures 5.5A and 5.5B we plot the limits containing the central 85% and 50% of the galaxy metallicity distribution, respectively, as a function of stellar mass.

The errors bars are determined from bootstrapping the sample distribution. In Figures 5.5C and 5.5D we plot the scatter in the MZ relation (defined as the difference between the upper and lower limits of the 85% and 50% contour, respectively) as a function of stellar mass. The error bars are the bootstrapped errors on the limits added in quadrature.

3.4 Discussion

3.4.1 Evolution of the MZ Relation

Figure 10.1 shows that at a fixed stellar mass (over the stellar mass range $10^9 M_\odot \lesssim M_* \lesssim 10^{11} M_\odot$) the average metallicity of the star-forming galaxy population increases as a function of cosmic time since $z \sim 2.3$. However, the evolution is mass dependent; thus the shape of the MZ relation evolves with time. There is a greater metallicity evolution in lower mass galaxies since $z \sim 0.8$ as compared to more massive galaxies. The smaller difference in the MZ relation for massive galaxies since $z \sim 0.8$ is due to flattening of the MZ relation at higher stellar masses.

Figures 5.5A and 5.5B show that the flattening in the MZ relation at late times results from a mass dependent flattening of the upper envelope of the metallicity distribution. The stellar mass where galaxy metallicities saturate decreases at late times. The statistically significant evolution of M_o to lower stellar masses at late times (see Table 1) quantifies this effect. The metallicity distribution in Figure 5.5A and 5.5B also shows that there is an empirical upper metallicity limit. Z_o in Equation 4.6 quantifies the upper metallicity limit. Within the observational uncertainties, Z_o is constant to $z \sim 2.3$.

Analytical models provide a physical interpretation of Z_o and the observed effect of metallicity saturation. In a closed-box model of chemical evolution where no gas enters or leaves the system, the gas-phase oxygen abundance can evolve to arbitrarily high values. However, galaxies do not evolve as closed boxes. More realistically, in an inflow model of chemical evolution where star formation is fueled by inflowing, pristine gas, the gas-phase

oxygen abundance saturates at a metallicity equivalent to the nucleosynthetic stellar yield[4] (Edmunds 1990). In this case, the amount of oxygen produced by massive stars is balanced by the amount of oxygen locked-up forever in low mass stars. When outflows are included in analytical models, the upper metallicity limit can *potentially* be reduced to an effective stellar yield (e.g. Edmunds 1990). This yield depends on the composition of the outflow, which is not yet well constrained by observations. The constancy of Z_o suggests that the metallicity of outflows, at a fixed stellar mass, has not evolved significantly since $z \sim 2.3$.

Figures 5.5A and 5.5B show that the fraction of saturated galaxies at a fixed stellar mass increases at late times. Thus massive galaxies in Figures 5.5C and 5.5D have smaller scatter in their metallicity distribution at late times. The straightforward interpretation of the data is that at early times ($z \sim 0.8$) the scatter in star-forming galaxy metallicities is nearly constant as a function of stellar mass. As galaxies evolve, metallicity saturation occurs first in the most massive galaxies and later at lower stellar masses. The stellar mass where the metallicity saturates and the fraction of saturated galaxies at a fixed stellar mass evolves with redshift. The data show that metallicity saturation leads to a decrease in the scatter with time (Figures 5.5C and 5.5D). Therefore, the observed scatter in the MZ relation at $z \sim 0.8$ is likely to be a lower limit to the scatter in the MZ relation at higher redshifts.

3.4.2 Comparison with Previous Observational Studies

Evolution in the shape of the MZ relation has previously been reported (Savaglio et al. 2005; Maiolino et al. 2008; Zahid et al. 2011). At a fixed stellar mass, there is relatively greater enrichment in less massive galaxies since $z \sim 0.8$. Our results provide a robust quantification of this evolution.

Galaxies are observed to form in "downsizing" such that massive galaxies form earlier and more rapidly than low mass systems and the star-forming population of galaxies is

[4]For reference, the saturation metallicity (i.e. gas-phase oxygen abundance) in Figure 5.5 converted to mass density units is ~ 0.013. Typical theoretical values of the nucleosynthetic stellar yield of oxygen in the same units vary between 0.01 and 0.02.

dominated by less massive galaxies at later times (Cowie et al. 1996). Flattening of the slope of the MZ relation at late times has been interpreted as the chemical version of galaxy downsizing (Savaglio et al. 2005; Maier et al. 2006; Maiolino et al. 2008; Zahid et al. 2011). We show that flattening of the MZ relation is due to a redshift evolution in the stellar mass where the metallicities of galaxies begin to saturate. This is probably due to gradual depletion of gas reservoirs at late times for galaxies at a fixed stellar mass. In this case, the flattening of the slope of the MZ relation can be interpreted without the need to invoke downsizing.

Moustakas et al. (2011) study the MZ relation to $z \sim 0.75$ using a sample of $\sim 3,000$ galaxies drawn from the AGN and Galaxy Evolution Survey (AGES, Kochanek et al. 2012). In contrast to our results, they find that the shape of the MZ relation does not evolve in a mass-dependent way for galaxies with stellar masses $> 10^{9.8} M_{\odot}$. They base their conclusion on an MZ relation which is only derived for the most massive galaxies at intermediate redshifts. At $z \sim 0.6$, the lowest stellar mass bin has a median stellar mass of $10^{10.6} M_{\odot}$ as compared to $10^{9.2} M_{\odot}$ for the DEEP2 galaxy sample at $z \sim 0.8$. Thus the shape of the MZ relation at intermediate redshifts is not well constrained by the data. However, a direct comparison of the data suggests that systematic differences in sample selection may be the source of the discrepancy. The MZ relation measured by Moustakas et al. (2011) at $z \sim 0.3$ is significantly flatter for galaxies with $M_* > 10^{10.2} M_{\odot}$ as compared to the relation we derive from the SHELS sample at the same redshift. Moustakas et al. (2011) select galaxies with well measured [OIII]λ5007. Foster et al. (2012) show that a S/N cut on the [OIII]λ5007 emission line leads to a flattening of the MZ relation for massive galaxies because metal-rich galaxies have weak oxygen emission and low ionization parameter (Zahid et al. 2012a). A systematic bias against massive, metal-rich galaxies could lead to an underestimate of the relation for massive galaxies and may explain the lack of evolution in the shape reported by Moustakas et al. (2011).

3.5 Summary and Conclusions

We investigate the evolution of the mass-metallicity relation and its shape using five samples spanning the redshift range of $0 \lesssim z \lesssim 2.3$. We calculate the stellar masses and metallicities for all five samples using as consistent a methodology as is currently possible. Our conclusions are primarily based on the three $z < 1$ galaxy samples at $z = 0.08, 0.29$ and 0.78 for which we have metallicities measured in individual galaxies. We show that the MZ relation at $z = 1.4$ and 2.26 determined from stacked spectra are consistent with the main conclusions of this study which are:

- The metallicities of star-forming galaxies at a fixed stellar mass decrease at all stellar mass $\gtrsim 10^9 M_\odot$ as a function redshift.
- The MZ relation since $z \sim 0.8$ evolves in a mass dependent manner such that the shape of the MZ relation changes with redshift.
- Galaxy metallicities saturate. The stellar mass where galaxy metallicities saturate and the fraction of galaxies with saturated metallicities at a fixed stellar mass evolves. Thus there is a mass dependent decrease in the scatter and a flattening of the MZ relation at late times.
- We attribute the flattening of the MZ relation at late times to an empirical upper limit in the gas-phase oxygen abundance for star-forming galaxies which does not evolve significantly.

We quantify evolution in the shape of the MZ relation out to $z \sim 0.8$. The multiplexing capability of the new generation of near-infrared spectrographs will allow us to rigorously establish the MZ relation for $z > 1$ galaxies.

References

Abazajian, K. N., et al. 2009, ApJS, 182, 543

Baldwin, J. A., Phillips, M. M., & Terlevich, R. 1981, PASP, 93, 5

Bell, E. F., McIntosh, D. H., Katz, N., & Weinberg, M. D. 2003, ApJS, 149, 289

Berg, D. A., et al. 2012, ApJ, 754, 98

Bruzual, G., & Charlot, S. 2003, MNRAS, 344, 1000

Calzetti, D., Armus, L., Bohlin, R. C., Kinney, A. L., Koornneef, J., & Storchi-Bergmann, T. 2000, ApJ, 533, 682

Chabrier, G. 2003, PASP, 115, 763

Chen, Y.-M., Tremonti, C. A., Heckman, T. M., Kauffmann, G., Weiner, B. J., Brinchmann, J., & Wang, J. 2010, AJ, 140, 445

Cowie, L. L., Songaila, A., Hu, E. M., & Cohen, J. G. 1996, AJ, 112, 839

Davé, R., Finlator, K., & Oppenheimer, B. D. 2011, MNRAS, 416, 1354

Davis, M., et al. 2003, in SPIE, ed. P. Guhathakurta, Vol. 4834, 161–172

Edmunds, M. G. 1990, MNRAS, 246, 678

Erb, D. K., Shapley, A. E., Pettini, M., Steidel, C. C., Reddy, N. A., & Adelberger, K. L. 2006, ApJ, 644, 813

Foster, C., et al. 2012, A&A, 547, A79

Geller, M. J., Dell'Antonio, I. P., Kurtz, M. J., Ramella, M., Fabricant, D. G., Caldwell, N., Tyson, J. A., & Wittman, D. 2005, ApJ, 635, L125

Geller, M. J., Diaferio, A., Kurtz, M. J., Dell'Antonio, I. P., & Fabricant, D. G. 2012, AJ, 143, 102

Goulding, A. D., et al. 2012, ApJS, 202, 6

Hwang, H. S., Geller, M. J., Kurtz, M. J., Dell'Antonio, I. P., & Fabricant, D. G. 2012, ApJ, 758, 25

Kauffmann, G., et al. 2003, MNRAS, 346, 1055

Kewley, L. J., & Dopita, M. A. 2002, ApJS, 142, 35

Kewley, L. J., & Ellison, S. L. 2008, ApJ, 681, 1183

Kewley, L. J., Groves, B., Kauffmann, G., & Heckman, T. 2006, MNRAS, 372, 961

Kewley, L. J., Jansen, R. A., & Geller, M. J. 2005, PASP, 117, 227

Kobulnicky, H. A., & Kewley, L. J. 2004, ApJ, 617, 240

Kochanek, C. S., et al. 2012, ApJS, 200, 8

Laskar, T., Berger, E., & Chary, R.-R. 2011, ApJ, 739, 1

Lee, H., Skillman, E. D., Cannon, J. M., Jackson, D. C., Gehrz, R. D., Polomski, E. F., & Woodward, C. E. 2006, ApJ, 647, 970

Lequeux, J., Peimbert, M., Rayo, J. F., Serrano, A., & Torres-Peimbert, S. 1979, A&A, 80, 155

Maier, C., Lilly, S. J., Carollo, C. M., Meisenheimer, K., Hippelein, H., & Stockton, A. 2006, ApJ, 639, 858

Maiolino, R., et al. 2008, A&A, 488, 463

Mannucci, F., et al. 2009, MNRAS, 398, 1915

Møller, P., Fynbo, J. P. U., Ledoux, C., & Nilsson, K. K. 2013, MNRAS, 430, 2680

Moustakas, J., et al. 2011, ArXiv e-prints

Noeske, K. G., et al. 2007, ApJ, 660, L43

Osterbrock, D. E. 1989, Astrophysics of gaseous nebulae and active galactic nuclei, ed. D. E. Osterbrock

Pérez-Montero, E., & Contini, T. 2009, MNRAS, 398, 949

Pérez-Montero, E., et al. 2013, A&A, 549, A25

Pettini, M., & Pagel, B. E. J. 2004, MNRAS, 348, L59

Savaglio, S., et al. 2005, ApJ, 635, 260

Steidel, C. C., Erb, D. K., Shapley, A. E., Pettini, M., Reddy, N., Bogosavljević, M., Rudie, G. C., & Rakic, O. 2010, ApJ, 717, 289

Tremonti, C. A., et al. 2004, ApJ, 613, 898

Weiner, B. J., et al. 2009, ApJ, 692, 187

Whitaker, K. E., van Dokkum, P. G., Brammer, G., & Franx, M. 2012, ApJ, 754, L29

Wittman, D. M., et al. 2002, in Society of Photo-Optical Instrumentation Engineers (SPIE) Conference Series, Vol. 4836, Society of Photo-Optical Instrumentation Engineers (SPIE) Conference Series, ed. J. A. Tyson & S. Wolff, 73–82

Yabe, K., et al. 2012, PASJ, 64, 60

Yuan, T.-T., Kewley, L. J., & Richard, J. 2013, ApJ, 763, 9

Zahid, H. J., Bresolin, F., Kewley, L. J., Coil, A. L., & Davé, R. 2012a, ApJ, 750, 120

Zahid, H. J., Dima, G. I., Kewley, L. J., Erb, D. K., & Davé, R. 2012b, ApJ, 757, 54

Zahid, H. J., Geller, M. J., Kewley, L. J., Hwang, H. S., Fabricant, D. G., & Kurtz, M. J. 2013, ApJ, 771, L19

Zahid, H. J., Kewley, L. J., & Bresolin, F. 2011, ApJ, 730, 137

[t

Chapter 4

The FMOS-Cosmos Survey of Star-Forming Galaxies at $z \sim 1.6$ II. The Mass-Metallicity Relation and the Dependence on Star Formation Rate and Dust Extinction

Note: This chapter is currently under review by the Astrophysical Journal. The main co-authors are D. Kashino and J. Silverman along with many people from the COSMOS collaboration. The data were taken by J. Silverman and myself. I am the primary author of this work.

Abstract

We investigate the relationships between stellar mass, gas-phase oxygen abundance (metallicity), star formation rate, and dust content of star-forming galaxies at z$\sim$1.6 using Subaru/FMOS spectroscopy in the COSMOS field. The mass-metallicity relation at $z \sim 1.6$ is significantly steeper than the relation observed in the local Universe. The most massive galaxies at $z \sim 1.6$ ($\sim 10^{11} M_{\odot}$) are enriched to the level observed in massive galaxies in the local Universe. The mass-metallicity relation we measure at $z \sim 1.6$ supports the suggestion of an empirical upper metallicity limit that does not significantly evolve with redshift. We find an *anti*-correlation between metallicity and star formation rate for galaxies at a fixed

stellar mass at $z \sim 1.6$ which is similar to trends observed in the local Universe. We do not find a relation between stellar mass, metallicity and star formation rate that is independent of redshift; our data suggest that there is redshift evolution in this relation. We examine the relation between stellar mass, metallicity and dust extinction. We find that at a fixed stellar mass dustier galaxies tend to be more metal rich. From examination of the stellar masses, metallicities, SFRs and dust extinctions we conclude that stellar mass is most closely related to dust extinction.

4.1 Introduction

Near-infrared multi-object spectrographs placed on 8 - 10 m class telescopes have recently opened up the redshift desert ($1 < z < 2$) for spectroscopic exploration. This redshift range is particularly important since it marks the epoch where galaxies transition from the peak of cosmic star-formation to the more quiescent build-up of stellar mass that we see in galaxies today (Hopkins & Beacom 2006, and references therein). Understanding of the physical processes responsible for this transition is crucial for building a coherent picture of galaxy evolution. In this series of papers, we report on the first results of our recent survey of star-forming galaxies at $1.4 < z < 1.7$. We present the sample and survey design in Silverman et al. (In Preparation, hereafter Paper III) and the spectroscopically measured, extinction corrected star formation rates (SFRs) in Kashino et al. (2013, hereafter Paper I). Here we present on the relation between stellar mass, gas-phase oxygen abundance, SFR and dust extinction for our sample.

The gas-phase oxygen abundance (metallicity) is a crucial diagnostic of galaxy evolution. Oxygen is the most abundant heavy element produced in massive stars and comprises half the mass of heavy elements in the Universe. Therefore, the abundance of oxygen is an excellent proxy of chemical evolution. Oxygen is dispersed into the interstellar medium (ISM) of galaxies by massive stars through stellar winds and supernovae. The mass of oxygen in the ISM accumulates as galaxies build-up stellar mass. However, metallicity is

a measure of the amount of oxygen *relative* to hydrogen. Therefore, it is not simply an accumulated record of star-formation but also a sensitive tracer of gas flows. The inflow of pristine gas can dilute the abundance of oxygen and decrease the metallicity but inflows also fuel star-formation leading to the synthesis of heavy elements. At the same time, feedback from massive stars is one of the primary mechanisms by which gas is expelled from galaxies (e.g. Mathews & Baker 1971; Larson 1974). It is clear that outflows can transport metals out of galaxies (Renzini 1997; Martin et al. 2002; Kirby et al. 2011; Bordoloi et al. 2011; Newman et al. 2012; Zahid et al. 2012b). However, the impact that outflows have on metallicity remains uncertain since composition of outflowing material is not well constrained observationally.

Using observations of 8 local star-forming galaxies, Lequeux et al. (1979) first showed that metallicity increases with stellar mass. In subsequent years samples have grown considerably. Tremonti et al. (2004) establish a tight (~ 0.1 dex scatter) mass-metallicity (MZ) relation in the local universe by examining $\sim 50,000$ galaxies from the SDSS with stellar masses ranging from $10^{8.5} \gtrsim M_*/M_\odot \gtrsim 10^{11}$. The relation has since been extended down to $\sim 10^6 M_\odot$ (Lee et al. 2006; Zahid et al. 2012a; Berg et al. 2012). Surveys of distant galaxies have made it possible to study the MZ relation at intermediate (Savaglio et al. 2005; Maier et al. 2005; Zahid et al. 2011; Pérez-Montero et al. 2013; Zahid et al. 2013a) and high redshifts (Erb et al. 2006; Maiolino et al. 2008; Mannucci et al. 2009; Laskar et al. 2011; Yabe et al. 2012; Yuan et al. 2013; Kulas et al. 2013). At a fixed stellar mass, galaxies are less enriched at higher redshifts. While the origin of this relation is still debated, measurements of the chemical evolution of galaxies provide important constraints for the processes of star formation and gas flows in models of galaxy evolution (e.g., Brooks et al. 2007; Finlator & Davé 2008; Davé et al. 2011; Zahid et al. 2012b; Torrey et al. 2013; Lilly et al. 2013; Zahid et al. 2014).

While almost all studies conclude that the gas in galaxies becomes more metal-rich as the Universe evolves, some studies also report a flattening of the the MZ relation for massive galaxies at late times (Savaglio et al. 2005; Maier et al. 2005; Maiolino et al. 2008; Zahid et al.

2011, 2013a). Many of these works (Savaglio et al. 2005; Maier et al. 2006; Maiolino et al. 2008; Zahid et al. 2011) attribute this flattening to galaxy downsizing (Cowie et al. 1996), i.e. the process by which star formation becomes more dominant in lower mass systems at late times. However, we show that flattening of the slope of the MZ relation is more consistent with the process of metallicity saturation rather than strictly a consequence of downsizing (Zahid et al. 2013a). In this study, we revisit this issue and extend our analysis to $z \sim 1.6$.

In the local Universe, the metallicity at a fixed stellar mass appears to be correlated with SFR (Ellison et al. 2008; Lara-López et al. 2010; Mannucci et al. 2010; Yates et al. 2012; Andrews & Martini 2013). Mannucci et al. (2010) suggest that the relation between stellar mass, metallicity and SFR that minimizes the scatter for local galaxies does not evolve out to $z \sim 2.5$. However, several studies have shown that this relation is dependent on methodology (Yates et al. 2012; Andrews & Martini 2013). We examine the relation between stellar mass, metallicity and SFR at $z \sim 1.6$ applying a consistent methodology throughout.

The paper is organized as follows: In Section 4.2 and 4.3 we describe our data and methodology, respectively. In Section 4.4 we examine emission line diagnostics using a subset of our sample where we have both J and H-band observations. In Section 4.5 we present the main results of our study and we discuss potential systematic issues in our measurements in Section 4.6. In Section 4.7 we discuss our results and we present a summary in Section 4.8. When necessary we adopt a standard cosmology with $(H_0, \Omega_m, \Omega_\Lambda) = (70$ km s^{-1} Mpc^{-1}, 0.3, 0.7) and a Chabrier (2003) IMF.

4.2 Data

4.2.1 FMOS-COSMOS Observations

Details of the survey design and observations are presented in Paper III. Here we summarize the most relevant aspects. We emphasize that when necessary measured quantities are

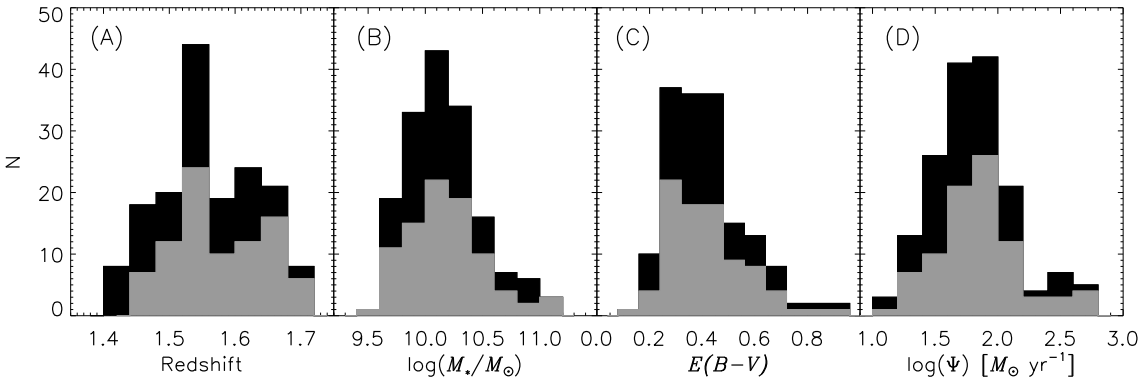

Figure 4.1 The (A) redshift, (B) stellar mass, (C) nebular $E(B-V)$ and (D) SFR distribution of our sample of galaxies at $z \sim 1.6$. The black histogram shows the distribution for our sample of 162 Hα detected galaxies. The gray histogram shows the distribution for the subsample of 85 Hα detected galaxies that are observed both in J and H-band.

converted from the Salpeter (1955) IMF used in Paper I and III to the Chabrier (2003) IMF used in this work. This is done for consistency with our previous metallicity studies.

Our observations are carried out using the near-infrared Fiber Multi-Object Spectrograph (FMOS; Kimura et al. 2010) on the Subaru Telescope. FMOS has 400 1.2" fibers distributed over a 30' diameter circular field-of-view. We operate the spectrograph in cross-beam switching mode. Two fibers are allocated to each object. The spectrograph dithers between two positions such that one of the two fibers is always on source while the other fiber is used for sky subtraction. This procedure allows us to observe $\sim$ 200 galaxies with simultaneous sky observations for optimal sky subtraction. An OH-airglow suppression filter blocks the strongest atmospheric emission lines (Iwamuro et al. 2001). Our observations are taken using the high resolution mode which has a spectral resolution of $R \sim 2200$. At this resolution, the [NII]λ6584 and Hα lines are well resolved in star-forming galaxies (see Figure 1 in Kashino et al. 2013) and contamination from narrow sky lines is minimized. For galaxies at $1.4 < z < 1.7$, we can observe Hα and Hβ in the H-long (1.60 - 1.80 μm) and J-long (1.11 - 1.35 μm) bands, respectively.

We primarily target star-forming galaxies in the redshift range of $1.4 < z < 1.7$ in the central square degree of the COSMOS field (Scoville et al. 2007). We preselect galaxies

using robust photometric redshifts from the catalog of Ilbert et al. (2010). These redshifts are based on 30 bands of photometry ranging from the UV to the mid-infrared. In order to efficiently target star-forming galaxies, we require K_s-band magnitudes < 23. For the majority of the sample we use an sBzK selection (Daddi et al. 2004) using the catalog of McCracken et al. (2010). A significant number of objects however, were selected based on stellar mass and photo-z (see Paper III). To minimize AGN contamination, we exclude galaxies which have x-ray detections. We revisit this issue in Section 4.4 and 4.6.

The H-band observations of 796 galaxies were carried out over 6 nights in March 2012 and 2 nights in January 2013. Each galaxy was observed for ~ 5 hours allowing us to reach a 3σ flux limit of 4×10^{-17} ergs s^{-1} cm^{-2} corresponding to a unobscured SFR limit of $\sim 5 M_{\odot}$ yr^{-1}. A subsample of galaxies with Hα detections satisfying signal-to-noise (S/N) > 3 were observed in the J-band in order to obtain measurements of Hβ and [OIII]λ5007. These observations were carried out in March 2012, December 2012 and February 2013 with an on source integration time of ~ 5 hours.

All data were reduced with the FMOS Image-Based Reduction Package (Fibre-pac; Iwamuro et al. 2012). In cross-beam switching mode, the sky is observed simultaneously along with the target. Initial sky subtraction is performed by differencing the fiber pair. Next the detector cross talk and bias difference between the quadrants are corrected and the flat fielding is performed. After the bad pixels are rejected, the image is corrected for distortion and the residual sky is subtracted. The images from multiple exposures are combined to produce a single spectrum per object. The wavelength is calibrated based on the Th-Ar spectral images taken just before the science exposure with a typical accuracy of > 1 pixel (~ 1Å in high resolution mode). The flux calibration is carried out using flux standard stars that are observed simultaneously with other scientific targets.

From our observations we selected 168 galaxies with significant Hα detections (S/N > 3). A subsample of 89 galaxies also have corresponding J-band observations. For the metallicity analysis we remove galaxies whose Hα emission is near the edge of the detector and therefore [NII]λ6584 is not observed. Our final sample consists of 162 star-forming

galaxies observed in the H-band band with significant (S/N > 3) detections of Hα emission and a subsample of 87 galaxies with corresponding J-band observations. The measured physical properties of both these samples are shown in Figure 8.1. Figure 8.1 shows that the subsample of galaxies for which we have J-band observations is representative of the larger H-band sample.

4.2.2 The Local Sample

The local sample of galaxies is from Sloan Digital Sky Survey (SDSS York et al. 2000). Here, we adopt the same sample used in Zahid et al. (2013a). The parent SDSS DR7 spectroscopic sample consists of $\sim 900,000$ galaxies primarily in the redshift range of $0 < z < 0.3$ (Abazajian et al. 2009). We adopt emission line fluxes measured by the MPA/JHU[1] group. From repeat observations, the MPA/JHU group determine that the formal uncertainties are underestimated. We scale the uncertainties of the line fluxes by the factors they recommend[2]. We require an aperture covering fraction $\gtrsim 20\%$ to avoid biasing our metallicity estimate (Kewley et al. 2005). Ellison et al. (2008) show that metallicities are correlated to galaxy size and therefore aperture effects may bias the MZ relation. However, the MZ relation we derive does not strongly depend on the minimum covering fraction we apply in selecting the sample. This could result form the fact that massive galaxies, which are most affected by aperture effects, tend to have shallow metallicity gradients. Integral field surveys of local galaxies currently underway will definitely address systematic biases related to covering fractions. We select galaxies in a limited redshift range with $z < 0.12$ to minimize evolutionary effects.

Our primary selection criteria for galaxies is the S/N ratios of strong emission lines. We require a S/N > 3 in the [OII]λ3727, Hβ, Hα and [NII]λ6584 emission lines. S/N cuts made to [OII]λ3727, Hβ, Hα and [NII]λ6584 emission lines do not significantly bias the MZ relation derived for local galaxies (Foster et al. 2012). Foster et al. (2012) show that S/N

[1] http://www.mpa-garching.mpg.de/SDSS/DR7/
[2] http://www.mpa-garching.mpg.de/SDSS/DR7/raw_data.html

cuts on the [OIII]λ5007 line can lead to a significant bias in the MZ relation. Therefore we make no S/N cut on the [OIII]λ5007 line.

Metallicities are determined from line flux ratios under the assumption that massive stars produce the EUV radiation field that ionized the nebular gas. Therefore, metallicities determined in galaxies where active galactic nuclei (AGN) contribute significantly to the ionizing radiation are not reliable. AGN are removed from the sample using the [OIII]/Hβ vs. [NII]/Hα line flux ratio diagram (i.e. the BPT method, Baldwin et al. 1981; Kauffmann et al. 2003; Kewley et al. 2006). Star-forming galaxies are well separated from AGN in the [OIII]/Hβ vs. [NII]/Hα line flux ratio diagram and her we apply the separation given in Kewley et al. (2006) to remove AGN. Galaxies with

$$\log([\mathrm{OIII}]/\mathrm{H}\beta) < 0.61/[\log([\mathrm{NII}]/\mathrm{H}\alpha) - 0.05] + 1.3 \tag{4.1}$$

are defined as star-forming. Here, [OIII], Hβ, [NII] and Hα are the emission line strengths of [OIII]λ5007, Hβ, [NII]λ6584 and Hα, respectively.

Our final sample consists of $\sim 51,000$ star-forming galaxies in the redshift range of $0.02 < z < 0.12$.

4.3 Methods

4.3.1 Metallicity Determination

Collisionally excited emission lines are the primary coolant in HII regions. Their line strengths scale with temperatures and metallicity. Therefore, flux ratios of collisionally excited emission lines to recombination emission lines can be used to estimate metallicity. Various ratios have been calibrated either empirically or theoretically to yield estimates of the gas-phase oxygen abundance. Different calibrations applied to the same galaxies can give metallicities that range up to ~ 0.6 dex (Kewley & Ellison 2008). Thus, there is great uncertainty in the absolute metallicity scale with empirically calibrated diagnostics typically

yielding metallicities that are ~ 0.3 dex smaller than theoretically calibrated diagnostics. It is beyond the scope of this paper to go into details of various diagnostics and possible resolutions. We refer the reader to detailed discussions of this issue presented in Kewley & Ellison (2008). However, we note that despite the uncertainty in absolute metallicities, Kewley & Ellison (2008) find that relative metallicities determined using various diagnostics are robust. This is fortunate since we are able to apply the same method for determining metallicity in both our local sample from SDSS and our sample of galaxies at $z \sim 1.6$.

We determine metallicities using the commonly used $N2$ diagnostic calibrated by Pettini & Pagel (2004, PP04 hereafter). Here, $N2$ is defined as the log of the emission line ratio between [NII]λ6584 and Hα. The advantage of this ratio is that the lines are closely spaced in wavelength and therefore can be easily observed simultaneously in the H-band for galaxies at $1.4 < z < 1.7$. Additionally, because we are taking a flux ratio and the lines are only separated by ~ 20Å, no extinction correction is required. PP04 calibrate the line ratio using a semi-empirical approach. At lower metallicities they empirically determine metallicities from temperature sensitive auroral lines. This method is known as the "direct" method and it provides a well established metallicity scale below solar metallicities. However, the [OIII]λ4363 auroral line used in determining metallicities with the "direct" method is extremely weak. Because the line strength decreases exponentially with increasing metallicity it is not observed in metal-rich HII regions. PP04 use photoionization modeling of individual HII regions to calibrated metallicities in metal-rich regions where the direct method can not be applied. We apply the linear calibration given by

$$12 + \log(\mathrm{O/H}) = 8.90 + 0.57 \times N2. \tag{4.2}$$

The calibration is valid for $-2.5 < N2 < -0.3$. The formal statistical errors of the slope and intercept are 0.03 and 0.04, respectively, and the intrinsic dispersion is 0.18 dex. We note that PP04 also provide a quadratic calibration of the N2 ratio. While the quadratic calibration gives a quantitatively different MZ relation, the major conclusions of this work

rely on the relative accuracy of the diagnostics and are independent of the particular calibration. Throughout this work, we provide the measured N2 values along with the inferred metallicities.

PP04 also calibrate the $O3N2$ line ratio which is defined as $\log\{([\mathrm{OIII}]/\mathrm{H}\beta)/([\mathrm{NII}]/\mathrm{H}\alpha)\}$. Here, [OIII] refers to the line flux of [OIII]λ5007 and [NII] refers to the line flux of [NII]λ6584. The metallicity calibration for this ratio is

$$12 + \log(\mathrm{O/H}) = 8.73 - 0.32 \times O3N2. \tag{4.3}$$

Because the $N2$ and $O3N2$ line ratios are calibrated using the same data, they should be consistent. However, several studies of high redshift galaxies have reported systematic differences in the metallicities determined using this ratio (e.g. Erb et al. 2006; Yabe et al. 2012). Since we measure the [OIII] and Hβ lines in a subset of our galaxies, we are able to asses the consistency of these two ratios at $z \sim 1.6$ (see Section 4.4.2).

Several authors have calibrated the $N2$ ratio independently (Denicoló et al. 2002; Nagao et al. 2006; Marino et al. 2013). While the calibrations vary systematically, they are all consistent with a monotonically increasing, quasi-linear relation between metallicity and $N2$. We emphasize that while the absolute metallicity is uncertain and varies systematically depending on the calibration applied, the relative metallicities determined from $N2$ are robust over the range of metallicities explored in this study. The results and conclusions of this study rely on the relative metallicities being accurate. In Table 6.1 we provide the measured $N2$ ratio and the metallicities derived using the PP04 calibration.

4.3.2 Mass Determination

For the SDSS sample we determine the stellar masses from the *ugriz*-band photometry (Stoughton et al. 2002). The stellar masses for the FMOS sample are determined from 30 band UV to IR photometry (Capak et al. 2007).

We use the Le Phare[3] code developed by Arnouts, S. & Ilbert, O. to estimate stellar masses. We estimate the stellar masses of galaxies by comparing photometry with stellar population synthesis models in order to determine the mass-to-light (M/L) ratio. The M/L ratio is then used to scale the observed luminosity (Bell et al. 2003; Fontana et al. 2004). Magnitudes are synthesized from the stellar templates of Bruzual & Charlot (2003) and we use a Chabrier (2003) IMF. The 27 models have two metallicities and seven exponentially decreasing star formation models (SFR $\propto e^{-t/\tau}$) with $\tau = 0.1, 0.3, 1, 2, 3, 5, 10, 15$ and 30 Gyrs. We apply the extinction law of Calzetti et al. (2000) allowing E(B−V) to range from 0 to 0.6 and the stellar population ages range from 0 to 13 Gyrs. Conroy et al. (2009) estimate that systematic errors in stellar mass are $\sim$ 0.3 dex for local galaxies. We have applied a consistent procedure for measuring the stellar masses for our different samples in order to mitigate systematic uncertainties and derive a relatively robust estimate.

We use the Kennicutt (1998) relation between the synthesized UV luminosity and SFR to correct for the emission line contributions to the photometry. This treatment accounts for Hα, Hβ and [OII]λ3727 and [OIII]λ4959, 5007 (Ilbert et al. 2010). We have determined stellar masses using broadband photometry and therefore the emission line correction are small. In Zahid et al. (2011) we compare this method with the method used by the MPA/JHU group to determine stellar masses of the SDSS galaxies. We find that the dispersion between the two methods is 0.14 dex which is consistent with the observational uncertainties. The stellar mass distribution of our sample is plotted in Figure 8.1B.

4.3.3 E(B-V) Determination

For the local sample we measure dust extinction from the Balmer decrement. For case B recombination with electron temperature $T_e = 10^4$K and electron density $n_e = 10^2$ cm^{-3}, the intrinsic Hα/Hβ ratio is expected to be 2.86 (Hummer & Storey 1987). We obtain the intrinsic color excess, $E(B-V)$ using the extinction curve of Calzetti et al. (2000). Groves et al. (2012) suggest that Hβ equivalent widths and line fluxes provided in the SDSS DR7

[3] *http://www.cfht.hawaii.edu/~arnouts/LEPHARE/cfht_lephare/lephare.html*

are underestimated due to improper correction for Hβ absorption. We apply the correction they recommend. The typical correction is small, reducing the $E(B-V)$ by ~ 0.03.

We detect Hβ in very few individual galaxies at $z \sim 1.6$. Therefore, we are not able to measure extinction from the Balmer decrement in individual galaxies. In Paper I we determine stellar reddening, $E_{star}(B-V)$, from the observed B_J-z color (Daddi et al. 2007). We average our FMOS-COSMOS spectra in three bins of $E_{star}(B-V)$. We measure the Hβ and Hα line fluxes and derive the Balmer decrement and nebular reddening, $E_{neb}(B-V)$, from these average spectra. We determine the average factor $f = 0.83$ which relates stellar reddening to nebular reddening, i.e. $E_{neb}(B-V) = E_{star}(B-V)/f$. We convert the stellar reddening determined from the observed $B_J - z$ color of individual galaxies into a nebular reddening, $E_{neb}(B-V)$, using our correction factor, f. The extinction correction, $A_{\mathrm{H}\alpha}$, ranges between $0.6 \sim 1.7$. Hereafter, all references to $E(B-V)$ are to $E_{neb}(B-V)$ derived from the stellar extinction using the $f = 0.83$ factor. The $E(B-V)$ distribution is plotted in Figure 8.1C.

4.3.4 SFR Determination

For the SDSS sample Brinchmann et al. (2004) measure SFRs from the Balmer lines but apply an aperture correction based on the galaxy colors measured inside and outside the fiber. Salim et al. (2007) improve this correction by comparing SFRs determined from Balmer lines with SFRs determined from UV photometry. We emphasize that aperture corrections to the SFR are important since the 3" SDSS fibers typically cover less than half of the galaxy light (Kewley et al. 2005; Zahid et al. 2013c). The aperture corrected SFRs are made available by the MPA/JHU group in the DR7 and we adopt them in this work. We convert the SFRs to a Chabrier IMF by subtracting 0.05 dex from the DR7 measurements.

We measure SFRs for galaxies at $z \sim 1.6$ from extinction corrected Hα luminosities using the calibration from Kennicutt (1998). The measurements in Paper I are based on the Salpeter (1955) IMF. We scale down these measurements by a factor of 1.7 for consistency with the Chabrier (2003) IMF we use in this work. The cosmology adopted in Paper I is

$\Omega_m = 0.25$ and $\Omega_\Lambda = 0.75$. This differs from the cosmology adopted in this work ($\Omega_m = 0.3$, $\Omega_\Lambda = 0.7$). We scale the SFRs used in this work down by a factor of 0.035 dex to convert between the two cosmologies. The FMOS fibers are 1.2" and therefore do not typically fully cover most galaxies at $z \sim 1.6$ under typical seeing conditions. We correct for fiber losses by applying an aperture correction to the data. The aperture correction is derived by convolving *HST/ACS I*-band images with the seeing conditions of our observation and extracting 1.2" aperture flux and comparing it to total flux. This procedure assumes that the Hα and UV emission have the same spatial distribution. The Hα flux is scaled by the aperture correction factor which ranges between $1.2 \sim 5$ with a typical value of ~ 2.

The SFR distribution of our sample is shown in Figure 8.1D.

4.3.5 Averaging Spectra

In star-forming galaxies the [NII] emission line is significantly weaker than Hα. Because the line scales with metallicity, it is more likely to be detected in metal-rich galaxies and is detected in only a small fraction of our sample. In order to derive an unbiased MZ relation, we rely on stacking multiple spectra sorted by stellar mass in order to measure an average [NII]/Hα ratio. We find that [NII] can be measured with reasonable S/N in even the least massive (lowest metallicity) galaxies in our sample by stacking ~ 16 spectra.

We tried various methods for stacking the data including error weighted averages, medians and stacking of spectra normalized to luminosity or SFR. In each case, the MZ relation we derive was statistically consistent. We adopt the procedure described below because it yields the smallest χ^2 fit of the MZ relation.

We sort galaxies into bins of stellar mass and average the spectra. We convert the observed frame flux vector of each observation to the rest-frame flux vector using the measured redshift. We then interpolate the flux and error spectrum of each galaxy using a 0.5Å per pixel sampling. This wavelength sampling corresponds to the observed frame single pixel resolution of FMOS (1.25Å) for galaxies at $z = 1.5$. Before averaging over the multiple observations we perform two cuts. First, we remove pixels in regions contaminated

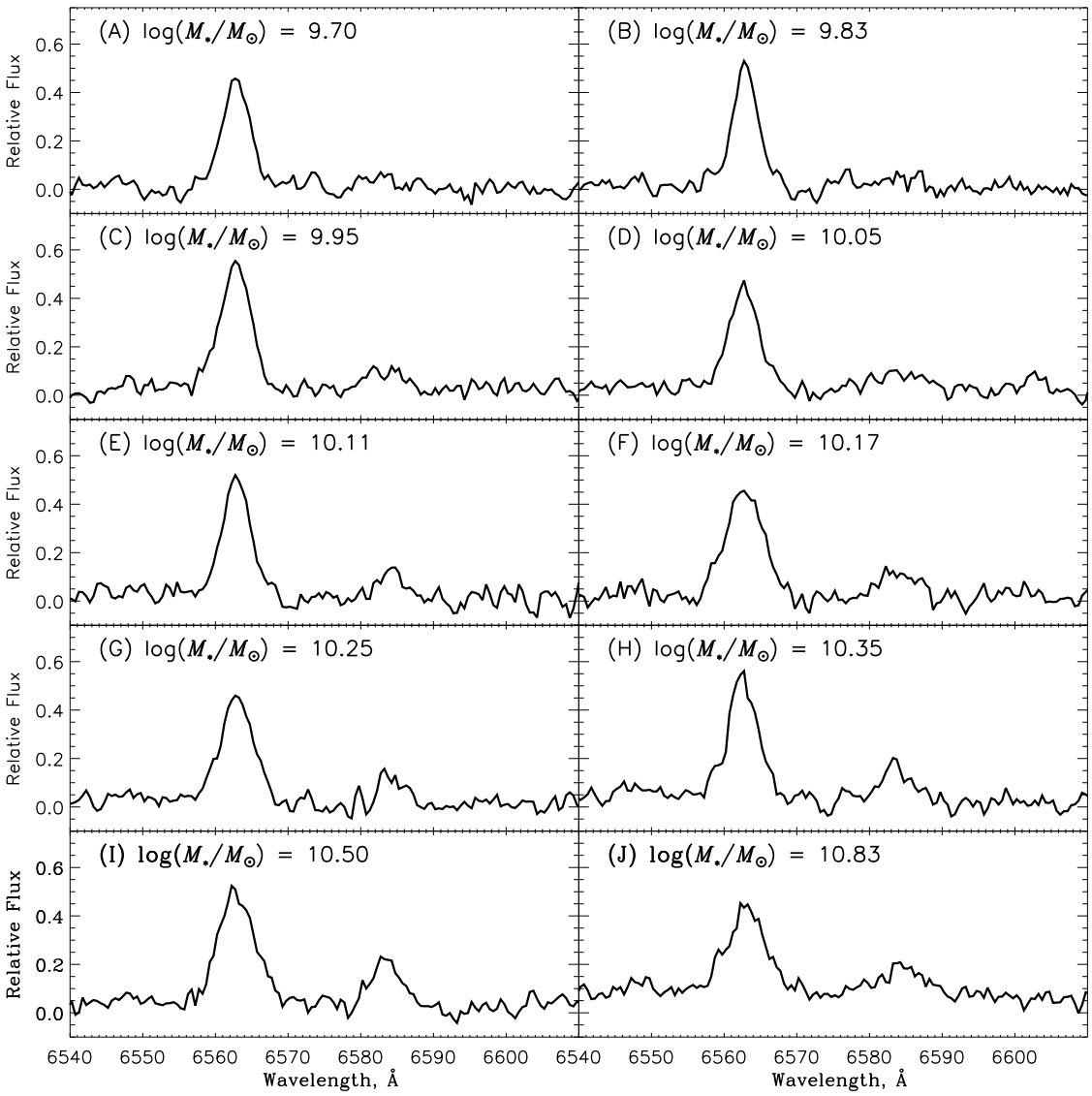

Figure 4.2 The FMOS spectra sorted and averaged in 10 stellar mass bins. The median stellar mass of each bin is listed in each panel.

by strong residual sky lines. These regions are easily identified in the error spectrum by their relatively large errors. This cut typically removes $\sim 10\%$ of the data in each resampled pixel bin. Second, we calculate a resistant mean using *resistant_mean.pro* routine in IDL which is part of the robust statistics package in the Astronomy Users Library. We clip all data that is 5 median absolute deviations from the median of the distribution of each pixel.

This procedure typically cuts out $\sim 2\%$ of the data. Our results are not sensitive to the specific level adopted for the two cuts. The error of each resolution element in the average is determined from the observational uncertainties of the individual pixels in each spectra added in quadrature. Figure 4.2 shows the stacked spectra.

A serious concern is that the data cuts we have applied may bias the MZ relation we derive in Section 4.5.1. In order to assess the impact of our cuts on the MZ relation we apply each of the cuts described above in turn. The MZ relation we derive by averaging the data without applying any cuts is statistically consistent with relation we derive with the cuts applied. The average error in the metallicity we measure from the average spectra when no cuts are applied is $\bar{\sigma} = 0.11$ dex and the χ^2 of the fit to the MZ relation is 2.9. By removing $\sim 10\%$ of the data in regions contaminated by strong sky lines we reduce the average error in the metallicity to $\bar{\sigma} = 0.036$ dex and derive an improved fit with $\chi^2 = 2.4$. Finally, by using the resistant mean and removing $\sim 2\%$ of the data the average errors remain the same but the derived fit is improved to $\chi^2 = 1.6$. We conclude that the procedure we apply in removing data does not bias our derived relation but does significantly reduce the errors in metallicity and improve the fit of the MZ relation.

4.3.6 Line Fitting

We fit emission lines using the *MPFIT* package of routines implemented in IDL (Markwardt 2009). The [NII]λ6584 and Hα line are simultaneously fit with a gaussian profile. We first subtract away the continuum by fitting a line to the pixels in 40Å windows on either side of the emission lines. We then perform a χ^2 minimization to fit the width, amplitude and central wavelength of each emission line. The line widths of the [NII]λ6584 and Hα emission lines are forced to be the same. We adopt the area of the gaussian determined from the fit parameters as our estimate of the line flux. We propagate the observational uncertainties to the fit parameters and flux estimates.

For a subset of our galaxies we have J-band observations of the [OIII]λ5007 and Hβ emission lines. We follow an identical procedure for estimating line fluxes for these lines

as we do for [NII] and Hα but with one notable exception. Balmer absorption arising in the atmospheres of intermediate-mass A-type stars can lead to underestimates of the Hβ emission line flux. This is because the emission line sits in an absorption trough which leads to a flux decrement (e.g., see Figure 3 in Zahid et al. 2011). We correct for this underlying absorption by fitting the continuum using stellar population synthesis models. Here we combine our J-band and H-band observations. We average our 87 spectra in five stellar mass bins. We mask out emission lines and fit the continuum in the average spectra with a linear combination of Bruzual & Charlot (2003) models convolved to the FMOS instrument resolution.

Figure 4.3 shows the Balmer absorption correction factor derived by comparing the fluxes measured with and without an absorption correction. The absorption correction factor is defined as $F(\mathrm{H}\beta)_{corr}/F(\mathrm{H}\beta)$. Here $F(\mathrm{H}\beta)_{corr}$ and $F(\mathrm{H}\beta)$ are the Hβ line fluxes measured from our stacked data with and without an absorption correction, respectively. The linear fit is given by

$$F(\mathrm{H}\beta)_{corr}/F(\mathrm{H}\beta) = 1.09 + 0.30\,[\log(M_*/M_\odot) - 10] \tag{4.4}$$

The Hβ emission line Balmer absorption correction ranges from $1 \sim 1.5$ for galaxies in our sample with a median of 1.27. For the BPT analysis in the following section, we apply the absorption correction given by Equation 4.4 to individual galaxies. The absorption correction for Hα is small ($\lesssim 2\%$, see Paper I). Thus, we make no correction for Hα absorption.

We derive the formal errors by propagating the observational uncertainties of each pixel through to the fit parameters from which we determine line fluxes. These errors are then propagated to the line ratios and metallicities in the standard way. The formal errors only reflect the quality of the data and do not account for the intrinsic scatter in the line flux ratios due to the intrinsic scatter in the MZ relation (Zahid et al. 2012a). Within each stellar mass bin we estimate the intrinsic scatter in the metallicities by bootstrapping the

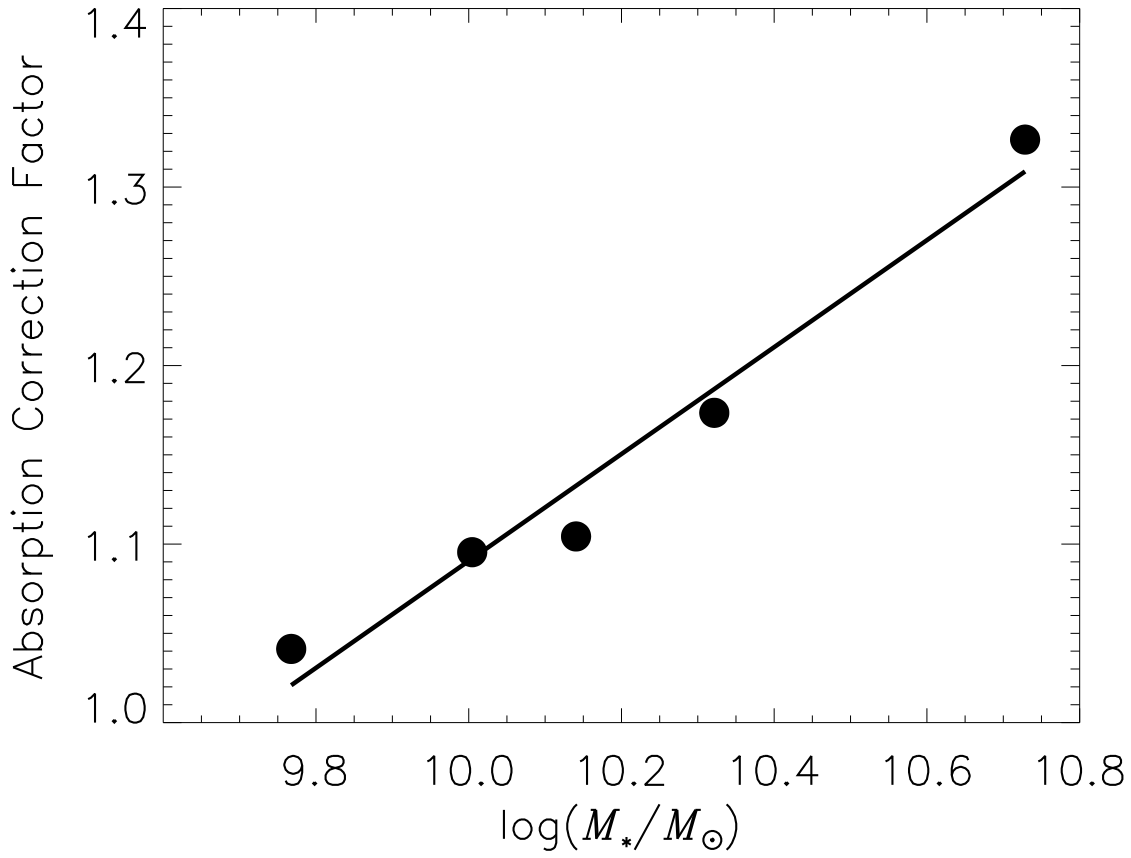

Figure 4.3 The factor by which the Hβ line flux corrected for Balmer absorption is greater than the Hβ line flux without an absorption correction. The factor is determined from average galaxy spectra sorted in five bins of stellar mass.

data. In each bin of stellar mass, we randomly select, with replacement, N spectra and average using the procedure described above. Here N is the number of spectra in each bin of stellar mass (see Table 6.1). We perform this procedure 1000 times for each of the mass bins, determining the line fluxes and metallicities from the average spectra each time. Given the small number of spectra in each mass bin (~ 16), it is unlikely that we are sampling the full scatter in line fluxes and metallicities. The scatter derived using the bootstrap therefore is a lower limit to the intrinsic scatter.

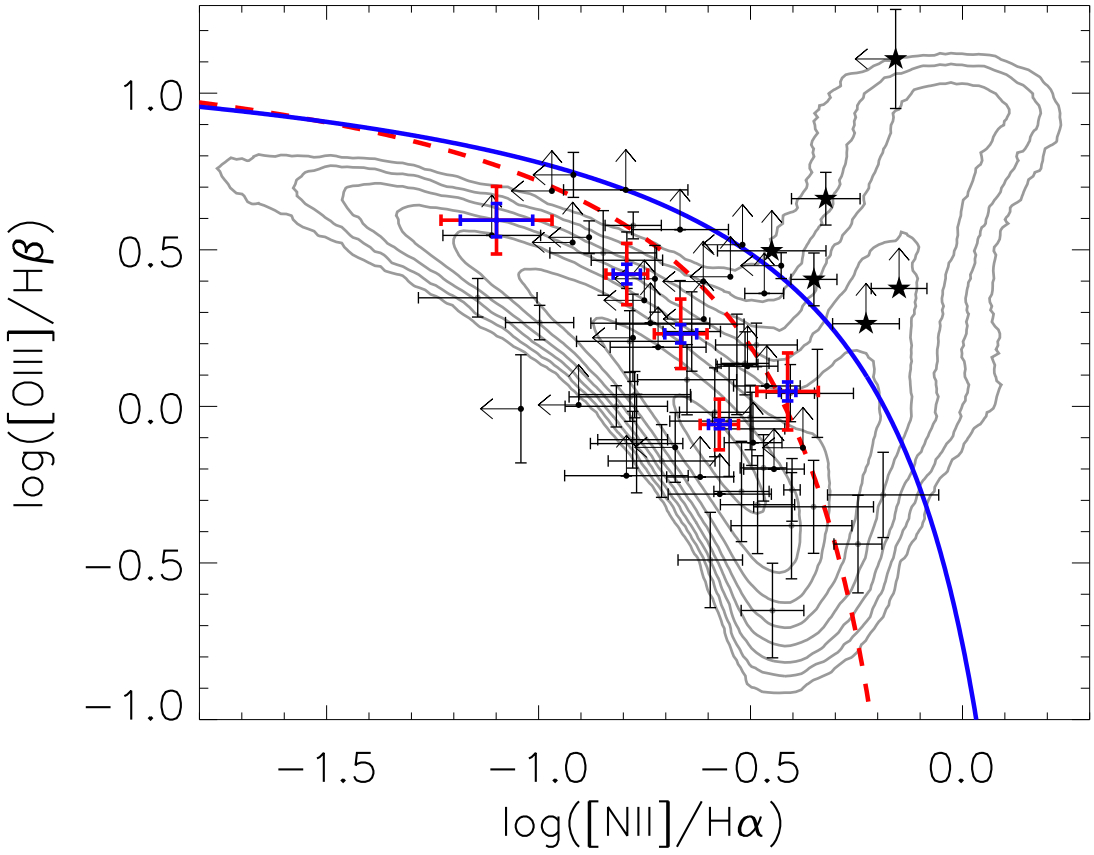

Figure 4.4 The [OIII]/Hβ vs [NII]/Hα diagram for the subsample of our galaxies with both J and H-band observations. Individual galaxies are shown by black. The objects denoted by stars are identified as AGN by their location on this diagram. We also plot the line fluxes determined from spectra averaged in five mass bins. The blue and red errors bars are the formal and bootstrapped errors, respectively. The gray contours are the distribution of $\sim 93,000$ local galaxies in the SDSS. The red curve is the empirical separation between purely star-forming galaxies and composites and AGN in the local Universe (Kewley et al. 2006). The blue curve is the separation at $z \sim 1.6$ (Kewley et al. 2013b).

4.4 Emission Line Diagnostics

4.4.1 AGN Contamination

The [OIII]/Hβ vs. [NII]/Hα diagnostic diagram is commonly used to classify galaxies as star-forming or active galactic nuclei (AGN Baldwin et al. 1981; Kauffmann et al. 2003;

Kewley et al. 2006). The line flux of [OIII]λ5007 relative to Hβ is plotted against the line flux of [NII]λ6584 relative to Hα. Recently, Kewley et al. (2013a) suggest that the physical conditions of the ISM and radiation field evolve with redshift, thus leading to a cosmic evolution of the locus of star-forming and AGN galaxies on the [OIII]/Hβ vs. [NII]/Hα diagnostic diagram. By comparing their theoretical models to observations, Kewley et al. (2013b) derive a redshift dependent classification given by

$$\begin{aligned} \log([OIII]/\mathrm{H}\beta) &= \frac{0.61}{\log([NII]/\mathrm{H}\alpha) - 0.02 - 0.1833z} \\ &\quad +1.2 + 0.03z. \end{aligned} \tag{4.5}$$

Galaxies below and above the dividing line defined by Equation 4.5 are classified as star-forming and AGN, respectively.

In Figure 4.4 we plot the [OIII]/Hβ vs. [NII]/Hα line ratios for 72 individual galaxies with Hα and [OIII]λ5007 detections. We also plot the ratios for average spectra of 87 galaxies sorted into 5 mass bins. The emission line properties are determined from averaging 16 or 17 spectra in each stellar mass bin. The blue error bars are the formal observational uncertainties and the red error bars are the bootstrapped errors which estimate the intrinsic scatter of the data. The red dashed and blue solid curves are the local and $z \sim 1.6$ classification determined from Equation 4.5, respectively. We find that our sample of galaxies have excitation that is nearly consistent with the locus of local star-forming galaxies (cf. contours and red dashed line). Comparison with the $z \sim 1.6$ classification line reveals that most of our galaxies lie well within the star-forming sequence. The six galaxies denoted by stars are identified as AGN. For our sample we find that $8\% \pm 3\%$ of the sample is AGN. This value is consistent with the estimates of Stott et al. (2013) for galaxies at $z \sim 1.5$.

We are not able to assess AGN contamination for the full sample since we have J-band observations and significant detection of [OIII]λ6584 for only a fraction of our sample (72/162). In order to assess the potential impact of AGN contamination on our measurement of the MZ relation. We determine the MZ relation for the 87 galaxies where we have J and

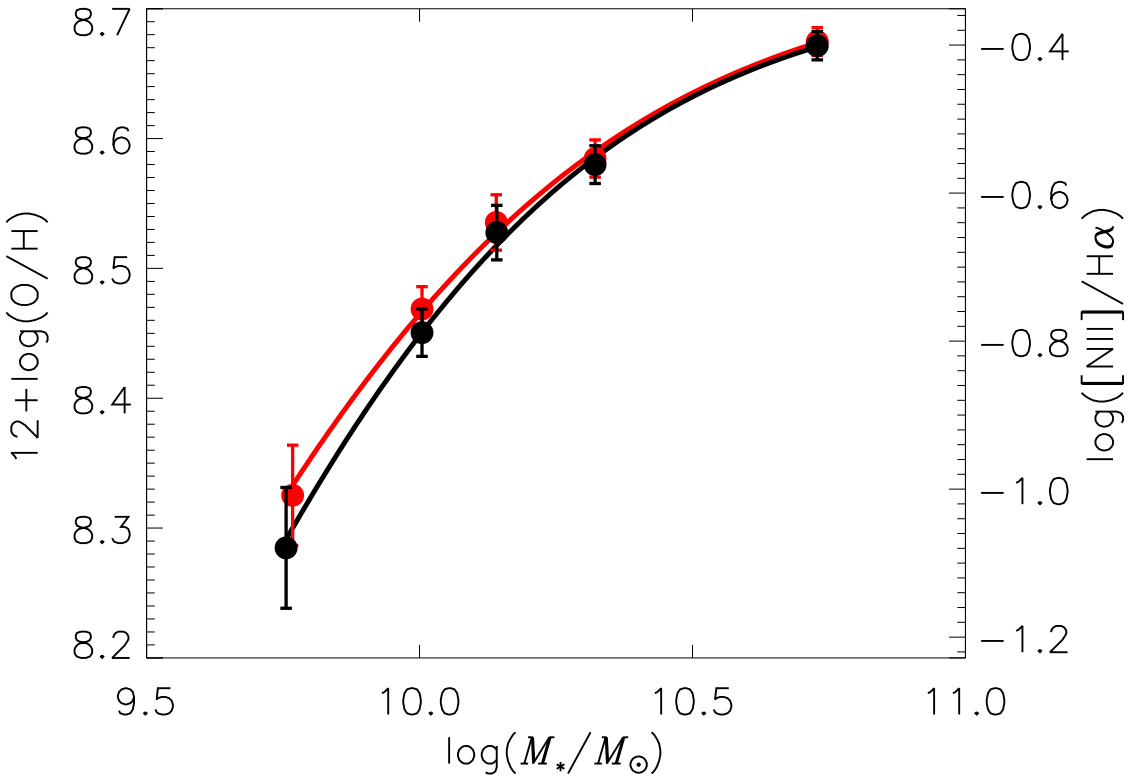

Figure 4.5 A comparison of the MZ relation for our sample of 87 galaxies with J and H-band observations. The red curve is determined from the full sample and the black curve is determined by from a subsample of 81 galaxies where the six galaxies identified as AGN in Figure 4.4 are removed. The impact of AGN contamination appears to be negligible.

H-band observations and compare this to the same sample with the 6 galaxies identified as AGN removed. Figure 4.5 shows the MZ relation determined for the sample with (red points and curve) and without (black points and curves) the 6 galaxies identified as AGN removed. In this J-band observed subsample, AGN contamination leads to a slight overestimate of the metallicity for the least massive galaxies. However, the two relations are consistent within the observational errors and we conclude that AGN contamination is not significant in our sample. Throughout the rest of the paper, we remove the six galaxies identified as AGN. The results presented in Section 4.5 are based on analysis of 156 galaxies.

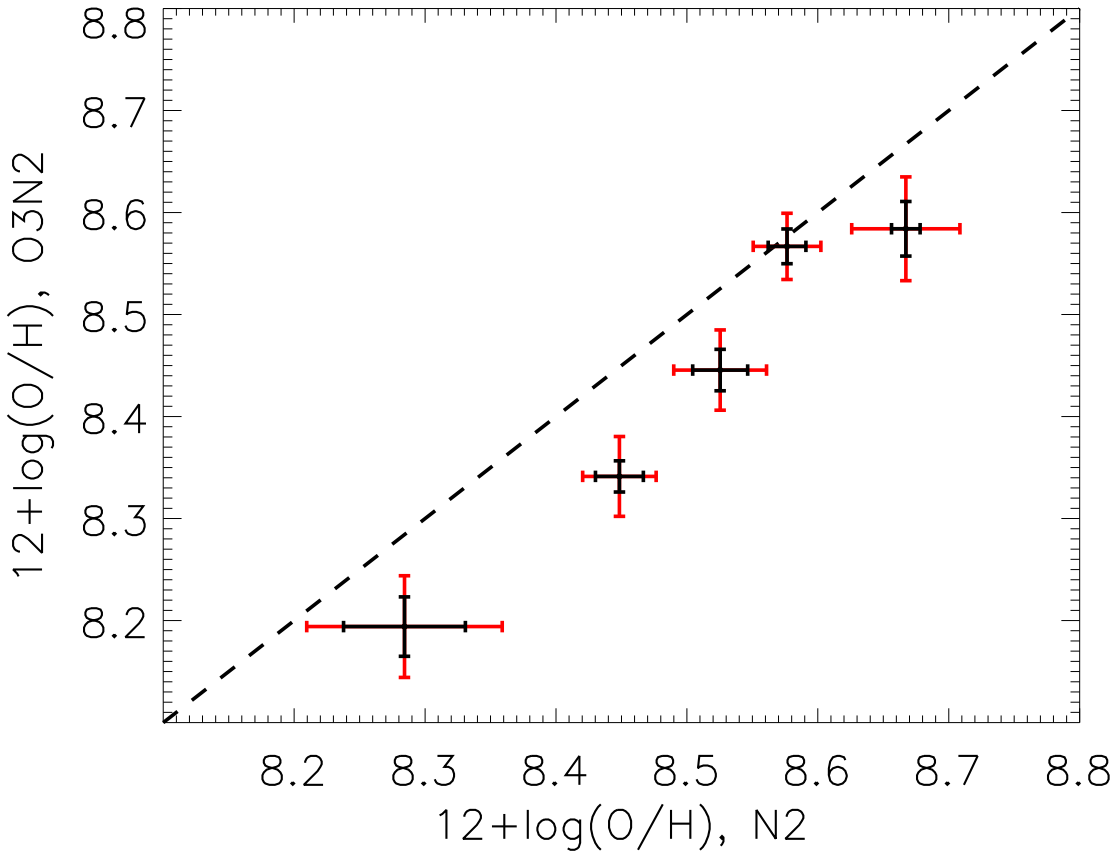

Figure 4.6 A comparison of the metallicity determined from the $N2$ and $O3N2$ calibration of PP04 for the subsample of our galaxies with both J and H-band observations. The metallicities are determined from spectra averaged in five mass bins. The black and red errors bars are the formal and bootstrapped errors, respectively. The dashed line is the one-to-one agreement.

4.4.2 Metallicity Comparison

In Figure 4.6 we compare metallicities determined using the $N2$ and $O3N2$ diagnostics for the 81 galaxies for which we have both $J-$band and $H-$band spectroscopy. The data are sorted in the same manner as the previous section. The metallicities derived from the $O3N2$ diagnostic are systematically lower than those determined using the $N2$ diagnostic. This is result is consistent with Erb et al. (2006) and Yabe et al. (2012) who also find that the

$O3N2$ diagnostic gives systematically lower metallicities than the $N2$ diagnostic in high redshift galaxies.

The $O3N2$ and the $N2$ diagnostic of Pettini & Pagel (2004) are calibrated to the same data and in the local Universe these two calibrations provide consistent results (e.g. Kewley & Ellison 2008). However, Figure 4.6 demonstrates that at higher redshifts, the two diagnostics are not consistent. The offset is even larger when using the more recent calibration of the $O3N2$ and $N2$ diagnostic provided by Marino et al. (2013). The systematic offset in metallicity between the two diagnostics is attributed to changing physical conditions of the ISM in high redshift galaxies (Erb et al. 2006; Kewley et al. 2013b; Cullen et al. 2014). In particular, a harder ionizing radiation field in high redshift galaxies is consistent with the $O3N2$ systematically offsetting to lower metallicities when compared with $N2$ (Kewley et al., In Preparation). In higher redshift galaxies, the high sensitivity of the $O3N2$ diagnostic to the ionization parameter makes it a poor indicator of metallicity (Kewley et al., In Preparation). The $N2$ diagnostic provides a more robust estimate and is the one adopted in this study. From our analysis we conclude that the $O3N2$ diagnostic should not be used to determine metallicities for galaxies outside the local Universe.

4.5 Results

4.5.1 The Mass-Metallicity Relation

In Figure 4.7 we plot the metallicity as a function of stellar mass for individual galaxies in the sample. The metallicities are determined from the fitted $N2$ ratio using the PP04 calibration. The black points are the galaxies where [NII]λ6584 is measured with S/N$>$ 3. The error bars only reflect the observational uncertainties and do not account for the 0.18 dex intrinsic dispersion of the metallicity calibration. The red points are galaxies for which we have adopted an 3σ upper limit for the [NII]λ6584 line flux. As Figure 4.7 demonstrates, we are more likely to not detect [NII]λ6584 in less massive galaxies. In Paper I we show that the less massive galaxies in our sample have lower SFRs. The greater number of

Table 4.1. FMOS-COSMOS MZ Relation Data

Stellar Mass $\log(M_*/M_\odot)$	$N2$ $\log([NII]/\mathrm{H}\alpha)$	12+log(O/H) PP04	$\log(\Psi)$ $[M_\odot\ \mathrm{yr}^{-1}]$	$E(B-V)$ Nebular	N
9.70	-0.951 ± 0.066	8.358 ± 0.038	1.175 ± 0.048	0.267 ± 0.012	16
9.83	-0.909 ± 0.060	8.382 ± 0.034	1.258 ± 0.059	0.279 ± 0.021	16
9.95	-0.783 ± 0.038	8.454 ± 0.022	1.397 ± 0.051	0.342 ± 0.020	16
10.05	-0.733 ± 0.038	8.482 ± 0.021	1.415 ± 0.056	0.357 ± 0.024	16
10.11	-0.678 ± 0.043	8.514 ± 0.024	1.509 ± 0.046	0.351 ± 0.034	16
10.17	-0.676 ± 0.034	8.515 ± 0.019	1.512 ± 0.076	0.403 ± 0.030	16
10.25	-0.647 ± 0.033	8.531 ± 0.019	1.702 ± 0.044	0.442 ± 0.032	15
10.35	-0.548 ± 0.024	8.587 ± 0.014	1.699 ± 0.054	0.466 ± 0.019	15
10.50	-0.435 ± 0.022	8.652 ± 0.013	1.824 ± 0.057	0.525 ± 0.037	15
10.83	-0.419 ± 0.023	8.661 ± 0.013	2.206 ± 0.093	0.679 ± 0.044	15

Note. — Column 1 gives the median stellar mass for each of the ten mass bins. Column 2 and 3 are the fitted $N2$ ratio and corresponding 12+log(O/H) using the PP04 calibration, respectively. The errors only represent the observational uncertainties and do not include the 0.18 dex intrinsic dispersion of the metallicity calibration. Column 4 and 5 are the median SFR and median $E(B-V)$ in each bin, respectively. The number of spectra averaged in each bin, N, is given in Column 6.

Table 4.2. MZ Relation Fit

Sample	Redshift	Z_o	$\log(M_o/M_\odot)$	γ
SDSS	0.08	8.704 ± 0.001	8.57 ± 0.01	0.65 ± 0.01
COSMOS	1.55	8.740 ± 0.042	9.93 ± 0.09	0.88 ± 0.18

Note. — The fits shown in Figure 4.8 and parameterized by Equation 4.6.

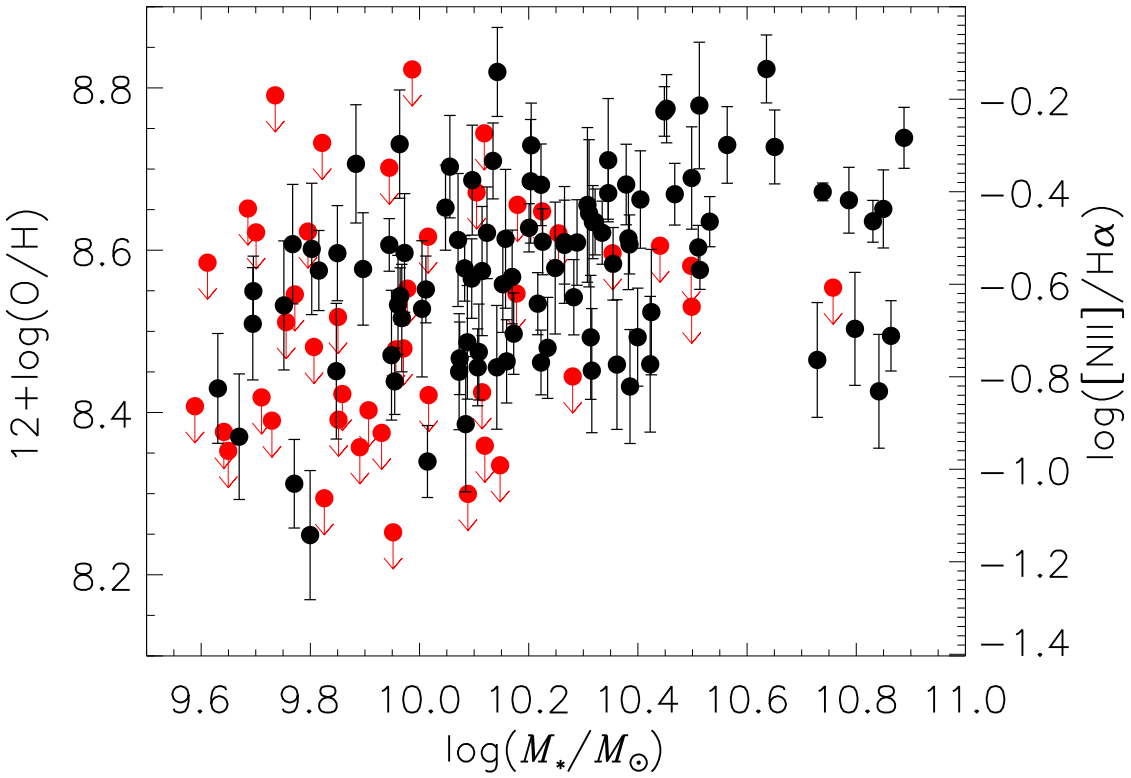

Figure 4.7 The metallicity measured in individual galaxies as a function of stellar mass. The black data points are galaxies with [NII]λ6584 measured with S/N$>$ 3. The red points are galaxies for which we have adopted 3σ upper limit for the [NII]λ6584 flux.

non-detections in less massive galaxies is likely due to their lower SFRs. Strong sky lines contaminate $\sim$ 10% of the spectra and the small number of non-detections at higher stellar masses are likely due to strong sky line contamination.

Figure 4.7 shows that some less massive galaxies in our sample are metal-rich. The observed scatter in Figure 4.7 is the lower limit to the true scatter. Metal-rich galaxies are found across the whole stellar mass range probed in this study. This is consistent with the distribution metal-rich galaxies observed in the local Universe (Zahid et al. 2012a). It is important to note that we have adopted a 3σ upper limit for [NII]λ6584 in galaxies. The number of galaxies with upper limits on metallicity is substantially larger at the lower mass end of the distribution. This suggests that the scatter likely increases as a function of stellar

mass (see also Zahid et al. 2012a). Here we have used the $N2$ diagnostic for determining metallicity and it is important to bear in mind that saturation of the diagnostic likely contributes in part to the nearly constant upper metallicity envelope of the distribution in Figure 4.7.

Figure 4.7 demonstrates that our observations do not have sufficient sensitivity to provide an unbiased probe of metallicities in galaxies at stellar masses $M_* \lesssim 10^{10.3} M_\odot$. The S/N of [NII]$\lambda$6584 is a function of both SFR and metallicity. Since these physical properties are both strongly correlated with stellar mass, this leads to bias in the MZ relation determined from individual galaxies in our sample. We therefore rely on averaging spectra in order to increase the S/N of our measurement and determine a less biased MZ relation.

Our analysis is based on averaging spectra sorted into ten bins of stellar mass. There are 15 or 16 spectra in each of the mass bins. The stellar mass adopted is the median stellar mass in each bin. The metallicity is determined from the $N2$ line ratio determined from averaged spectra. The Hα line is detected and SFRs are measured in individual objects without the necessity to stack (Paper I). The SFR adopted is the median SFR in each bin. The data are summarized in Table 6.1.

Figure 4.8 shows the MZ relation at $z \sim 1.6$ (black curve). The black points are the metallicities determined from the average spectra. The black error bars are the formal observational uncertainties determined by propagating the observational uncertainty in each pixel of the individual spectra. At a fixed stellar mass, there is intrinsic scatter in the metallicity distribution of galaxies (Tremonti et al. 2004; Zahid et al. 2012a). The red error bars are the standard deviation of the bootstrapped metallicity distribution in each bin of stellar mass and provide an estimate of the intrinsic scatter. Figure 4.8 shows that in each of the stellar mass bins the observational uncertainties are always smaller than the intrinsic scatter.

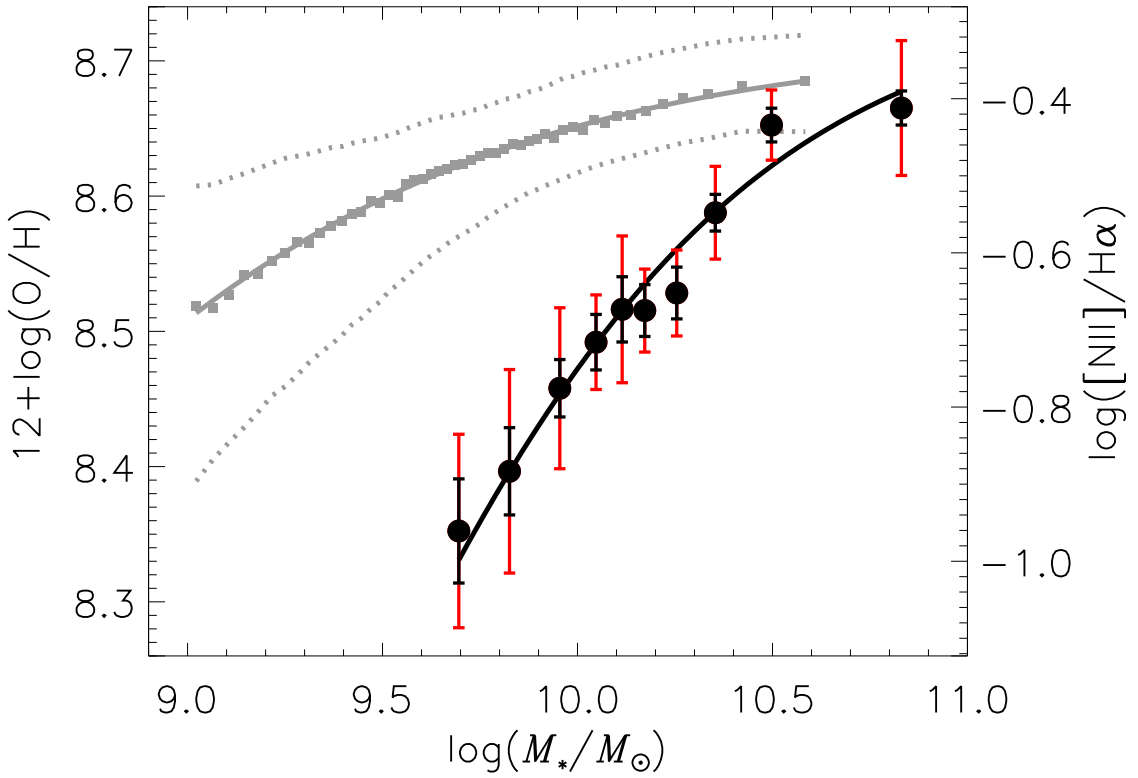

Figure 4.8 The MZ relation determined from our sample of galaxies at $z \sim 1.6$. The black points are metallicities determined from spectra averaged in ten mass bins. The black and red errors bars are the formal and bootstrapped errors, respectively. The black curve is a fit to the $z \sim 1.6$ MZ relation as described by Equation 4.6. The gray data points are the median metallicities in 50 bins of stellar mass for galaxies in our local fiducial sample from SDSS. The solid gray curve is a fit to the local relation and the dotted lines denote the interval containing the central 68% of galaxies.

We fit the MZ relation using the logarithmic form suggested by Moustakas et al. (2011). The MZ relation is parameterized as

$$12 + \log(\mathrm{O/H}) = Z_o - \log\left[1 + \left(\frac{M_*}{M_o}\right)^{-\gamma}\right]. \tag{4.6}$$

This function is preferred to a polynomial fit since it encapsulates much of our intuition regarding chemical evolution (see Moustakas et al. 2011; Zahid et al. 2013a). In this parameterization, Z_o is the asymptotic metallicity where the MZ relation flattens, M_o is the

characteristic stellar mass where the relation begins to flatten and γ is the power-law slope of the MZ relation for stellar masses $<< M_o$. The parameters are determined using a χ^2 minimization as implemented in the *MPFIT* package in IDL (Markwardt 2009). The MZ relation at $z \sim 1.6$ is shown by the black curve. The fiducial local MZ relation is determined from $\sim 50,000$ SDSS galaxies and is shown by the gray curve. For the local relation, we sort the data into 50 bins of stellar mass and take the median metallicity in each bin. The error bars are smaller than the data points. The dotted curves contain the central 68% of the galaxy distribution. We determine the MZ relation for the local sample using the same diagnostic (i.e. $N2$ calibrated by PP04) as applied to the $z \sim 1.6$ data. The observational uncertainties are propagated through and the fit parameters and errors are given in Table 10.1.

In Section 4.4.1 and Figure 4.5 we examine the MZ relation for our subsample for which we have J-band observations and are able to assess AGN contamination. The black curve in Figure 4.5 is the MZ relation with six galaxies identified as AGN removed from the sample. The fit to the MZ relation in Figure 4.5 is consistent with the relation we derive in Figure 4.8.

4.5.2 The Stellar Mass, Metallicity and SFR Relation

The metallicities of galaxies are governed by gas flows and star formation. Recent work shows that in local galaxies there appears to be an *anti*-correlation between the SFR and metallicity at a fixed stellar mass (Ellison et al. 2008; Mannucci et al. 2010; Andrews & Martini 2013); at least at lower stellar masses (see Yates et al. 2012). One possible explanation for this trend is that while inflows of gas dilute the gas-phase abundance and lower metallicities, they also fuel star-formation and lead to elevated SFRs. Motivated by this physical picture, Mannucci et al. (2010) propose that the parameterization of the relation between stellar mass, metallicity and SFR that minimizes the scatter in local galaxies is independent of redshift. They refer to this as the "fundamental metallicity relation" (FMR). In their analysis, the lower metallicities of intermediate and high redshift

Table 4.3. FMOS-COSMOS Stellar Mass, Metallicity and SFR Relation

Stellar Mass $\log(M_*/M_\odot)$	$N2$ $\log([NII]/\mathrm{H}\alpha)$	12+log(O/H) PP04	$\log(\Psi)$ $[M_\odot\ \mathrm{yr}^{-1}]$	N
		Low-SFR		
9.82	-0.803 ± 0.042	8.442 ± 0.024	1.155 ± 0.027	26
10.11	-0.660 ± 0.031	8.524 ± 0.018	1.415 ± 0.023	26
10.36	-0.534 ± 0.022	8.595 ± 0.013	1.614 ± 0.034	26
		High-SFR		
9.89	-0.916 ± 0.040	8.378 ± 0.023	1.397 ± 0.033	26
10.16	-0.683 ± 0.027	8.511 ± 0.015	1.665 ± 0.031	26
10.56	-0.477 ± 0.015	8.628 ± 0.009	1.999 ± 0.090	26

Note. — The same as Table 6.1 but split into two bins of SFR as described in the text.

galaxies are compensated by their higher SFRs such that galaxies out to $z \sim 2.5$ are consistent with local FMR. However, it is clear that the FMR is highly dependent on methodology (Yates et al. 2012; Andrews & Martini 2013). Therefore, applying a consistent methodology is important. We determine stellar masses, metallicities and SFRs for local galaxies and our sample at $z \sim 1.6$ by applying as consistent a methodology as is currently possible in order to test the validity of the FMR.

The scatter in the local MZ relation is correlated with the SFR (Ellison et al. 2008; Mannucci et al. 2010; Yates et al. 2012; Andrews & Martini 2013). We can examine the relation between stellar mass, metallicity and SFR for our sample at $z \sim 1.6$ because we have SFRs determined from the Hα luminosity in individual galaxies. We average the spectra by first sorting the data into three bins of stellar mass and then dividing the data in each bin of stellar mass into two bins of SFR. The metallicity and SFR in each bin of stellar mass and SFR is determined from 26 galaxies.

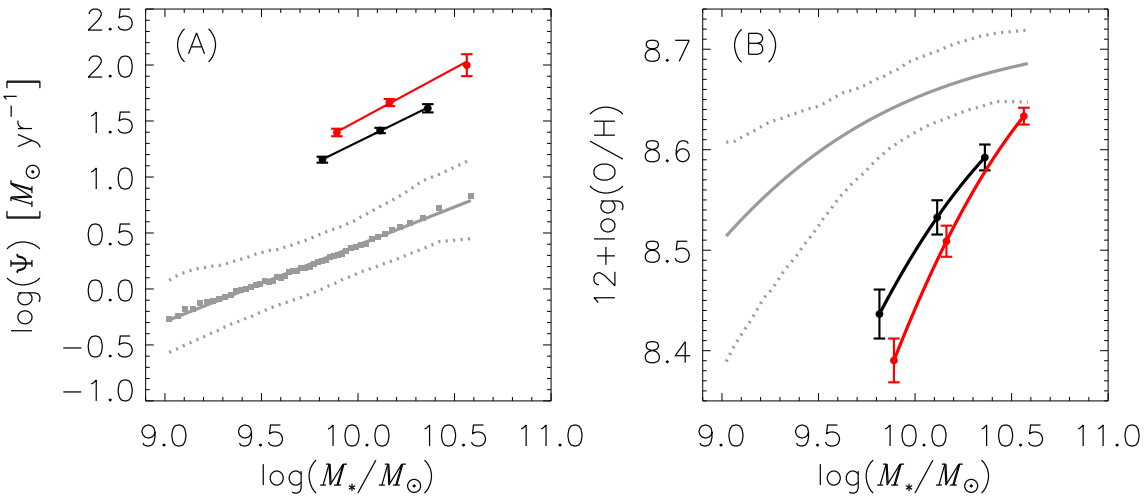

Figure 4.9 (A) The relation between stellar mass and SFR. The black and red points are the median SFRs for galaxies that are first sorted into three mass bins and then two SFR bins. The solid black and red lines are linear fits to the relation between stellar mass and SFR for the high and low SFR bins, respectively. The gray points are the median SFRs sorted into 50 bins of stellar mass for star-forming galaxies in our local fiducial sample. The solid line is a fit to the relation between stellar mass and SFR and the dotted line is denotes the interval containing central 68% of galaxies. (B) The MZ relation for the sample divided into bins of stellar mass and SFR for the same data shown in (A). The black and red points are the metallicities in bins of stellar mass and SFR. The black and red curves are fits to the high and low SFR data, respectively. The gray curve is the fit to the local MZ relation and the dotted line denotes the interval containing the central 68% of galaxies.

In Figure 4.9A we plot the median SFR in each bin. The error bars are the bootstrapped errors on the median and are analogous to the standard error on the mean. The red and black curves in Figure 4.9 are linear fits with a slope of 0.93 ± 0.13 and 0.85 ± 0.08, respectively. The local stellar mass - SFR relation is shown in gray. The local relation is determined by taking the median SFR in 50 bins of stellar mass. The solid gray line is a fit to the local relation. The dotted gray curves indicate the limits containing the central 68% of the galaxy distribution. The slope of the local relation is 0.68 ± 0.01 and does not differ significantly (2σ) from the slope of the $z \sim 1.6$ relation. However, the slope of the relation is dependent on sample selection (cf. Peng et al. 2010).

Table 4.4. FMOS-COSMOS Stellar Mass, Metallicity and E(B-V) Relation

Stellar Mass $\log(M_*/M_\odot)$	$N2$ $\log([NII]/\mathrm{H}\alpha)$	12+log(O/H) PP04	E(B-V) Nebular	N
Low-E(B-V)				
9.77	-0.963 ± 0.046	8.351 ± 0.026	0.259 ± 0.008	26
10.11	-0.734 ± 0.027	8.482 ± 0.015	0.325 ± 0.012	26
10.38	-0.564 ± 0.019	8.579 ± 0.011	0.464 ± 0.015	26
High-E(B-V)				
9.95	-0.782 ± 0.036	8.454 ± 0.020	0.342 ± 0.012	26
10.16	-0.622 ± 0.031	8.545 ± 0.018	0.446 ± 0.008	26
10.64	-0.395 ± 0.018	8.675 ± 0.010	0.637 ± 0.024	26

Note. — The same as Table 6.1 but split into two bins of $E(B-V)$ as described in the text.

In Figure 4.9B we show the MZ relation for the data sorted into bins of SFR. The MZ relation shown by the red and black curve correspond to the high and low SFR bins, respectively, shown in Figure 4.9A. The gray curve is the local MZ relation. The metallicities of high SFR galaxies (red curve) are systematically lower than the metallicities of low SFR galaxies (black curve). At a fixed stellar mass, the metallicity is *anti*-correlated to the SFR. This is similar to trends seen in local galaxies at lower stellar masses (e.g. Mannucci et al. 2010). It is important to note that while the slope of the stellar mass - SFR relation is similar for local and $z \sim 1.6$ galaxies, the MZ relation for the same galaxies is significantly steeper. This has important implications for the FMR proposed by (Mannucci et al. 2010). We examine this issue in detail in Section 4.7.3.

4.5.3 The Stellar Mass, Metallicity and E(B-V) Relation

A strong correlation is observed between metallicity and dust in the local Universe (Heckman et al. 1998; Boissier et al. 2004; Asari et al. 2007; Garn & Best 2010; Xiao et al. 2012; Zahid

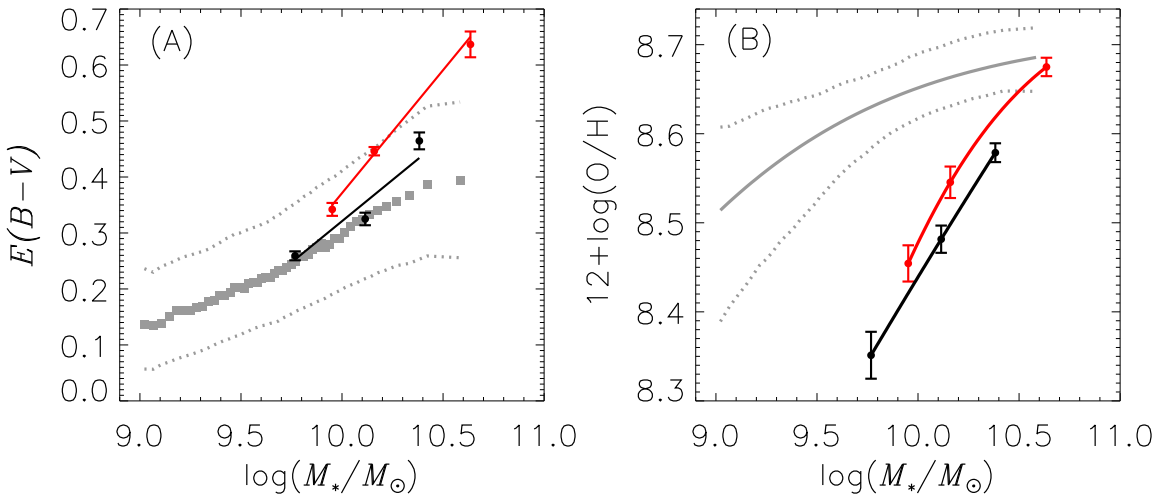

Figure 4.10 (A) The relation between stellar mass and $E(B-V)$. The black and red points are the median nebular $E(B-V)$ for galaxies that are first sorted into three mass bins and then two $E(B-V)$ bins. The solid black and red lines are linear fits to the relation between stellar mass and $E(B-V)$ for the high and low $E(B-V)$ bins, respectively. The gray points are the median $E(B-V)$ sorted into 50 bins of stellar mass for star-forming galaxies in our local fiducial sample. The solid line is a fit to the relation between stellar mass and SFR and the dotted lines denote the interval containing central 68% of galaxies. (B) The MZ relation for the sample divided into bins of stellar mass and $E(B-V)$ for the same data shown in (A). The black and red points are the metallicities in bins of stellar mass and $E(B-V)$. The black and red curves are fits to the high and low SFR data, respectively. The gray curve is the fit to the local MZ relation and the dotted line denotes the interval containing the central 68% of galaxies.

et al. 2012b, 2013c). Reddy et al. (2010) indirectly examine the relation between dust obscuration and metallicity at $z \sim 2$. They find that the L_{IR}/L_{UV} ratio, which is taken as a proxy for dust, scales with stellar mass. They combine the relation between stellar mass and L_{IR}/L_{UV} ratio with the relation between stellar mass and metallicity from Erb et al. (2006) to derive a relation between metallicity and L_{IR}/L_{UV} ratio, i.e. dust extinction.

In Figure 4.10 we examine the relation between stellar mass, metallicity and $E(B-V)$. We average the spectra by first sorting the data into three bins of stellar mass and then divide the data in each bin of stellar mass into two bins of $E(B-V)$. The metallicity and $E(B-V)$ in each bin is determined from 26 galaxies. In Figure 4.10A the $E(B-V)$ value

is the median of the 26 galaxies in each bin and the errors are bootstrapped. The red and black points correspond to the high and low $E(B-V)$ bins, respectively. The gray squares are the median $E(B-V)$ values in 50 bins of stellar mass for the local sample of galaxies. The dotted lines denotes the interval containing 68% of the galaxy distribution.

In Figure 4.10B we plot the metallicity determined in bins of stellar mass and $E(B-V)$. The red and black points and curves correspond to the high and low $E(B-V)$ sample, respectively. Figure 4.10B shows that galaxies with higher $E(B-V)$ (red points) also have higher metallicity. At a fixed stellar mass, the metallicity is correlated with dust extinction. Similar trends are observed in the local sample (e.g., Zahid et al. 2012b, 2013c). This correlation is perhaps not that surprising since dust is composed of metals.

4.6 Systematic Issues in the Measurements

Before turning to a discussion of our results, we highlight some of the systematic issues in our measurements. Current and future spectroscopic surveys should be able to address many of these issues.

The fit to the MZ relation presented in Section 4.5.1 is strongly constrained by the two highest stellar mass bins. In Figure 4.8, the bin at $M_* \sim 10^{10.5} M_\odot$ is above the relation. Figure 4.7 shows that there is a lack of intermediate and low metallicity objects for galaxies in this mass range. If we exclude the bin at $M_* \sim 10^{10.5} M_\odot$, the fitted Z_o and $\log(M_o/M_\odot)$ are 8.75 ± 0.06 and 9.94 ± 0.15, respectively. These values are consistent with values given in Table 10.1. Excluding the second to highest stellar mass bin in our fit does not change any of the conclusions of this paper. However, if we exclude the highest stellar mass bin the two fits are not consistent. The saturation metallicity, Z_o, and turnover mass, M_o, are both strongly dependent on the highest mass bin. While the analysis presented in Figure 4.4 suggests that AGN contamination does not significantly affect high mass galaxies, the conclusions remain tentative since we are unable to assess the AGN contribution in the full FMOS sample we have used to determined the MZ relation.

Our sample presented here is selected primarily using the sBzK selection in order to maximize detections. In the future, our FMOS survey will use a more simple mass selection in order to understand sample bias. While the sBzK selection is not significantly biased against dusty galaxies because the reddening vector moves objects parallel to the selection cut (Daddi et al. 2004), our effective sensitivity of 4×10^{-17} ergs s^{-1} cm^{-2} may not reach deep enough to observe Hα in objects that are heavily obscured by dust. To increase likelihood of detection, for the majority of the sample we imposed a second selection criteria that required obscured SFRs of $\sim 5M_{\odot}$ yr^{-1} based on UV luminosities. This introduces bias against heavily obscured objects. In Paper III we quantify the bias in our selection. In Figure 4.10 we show that at the metallicity is correlated with dust extinction. Thus, if our sample is biased against heavily obscured objects, we may be missing many metal-rich galaxies in our sample $z \sim 1.6$. This bias is likely to be mass dependent and effect our measurement of the MZ relation at high stellar masses. However, galaxies with heavy dust obscuration also tend to have higher SFRs. The relation between SFR and metallicity is opposite to the relation between dust extinction and metallicity and therefore these two effects may offset each other. The relation between stellar mass, metallicity, dust extinction and SFR are complicated and more complete spectroscopic samples are required in order to assess any bias that may be present in our measurements.

The observed anti-correlation between metallicity and SFR (e.g. Mannucci et al. 2010) may lead to an overestimate of the MZ relation at low stellar masses. This is because the galaxies with SFRs falling below our detection limit are preferentially found at lower stellar masses and because of the anti-correlation between metallicity and SFR, these low SFR galaxies also tend to have high metallicities. This type of bias would result in an artificial steepening of the MZ relation.

One of the primary challenges with spectroscopically accessing the redshift desert ($1 \lesssim z \lesssim 2$) is that optical emission lines are redshifted into the near-infrared. The near-infrared is significantly contaminated by strong atmospheric emission lines, making observations of faint emission lines extremely difficult. This is compounded by detector

throughput and sensitivities that are significantly below optical detectors. Because of these difficulties, we are not able to observe faint emission lines such as [NII]λ6584 in a significant number of individual galaxies. Instead, we must rely on averaging many spectra in order to achieve the S/N necessary to detect weak emission lines. This may be problematic since the properties of galaxies that we are measuring are not necessarily linear with line strength. For example, the [NII]λ6584 line strength scales exponentially with metallicity and therefore simply averaging spectra may bias our measurement. To address this particular issue, we have measured the relation using the median of the stacked spectra, rather than average to test for any systematic bias. The two methods yield consistent results. Furthermore, we examine the bias in local star-forming galaxies by sorting galaxies into 50 bins of stellar mass and then averaging the line flux of [NII]λ6584 and Hα before determining metallicity. We find a very small offset ($\sim$ 0.01 dex) between the MZ relation from first averaging the line fluxes as compared to the standard method we have adopted in this work. One possible explanation for this may be that the while the line flux ratio is correlated to metallicity, the SFR is anti-correlated to metallicity. Thus, while higher metallicity objects have higher [NII]/Hα ratios, the lower metallicity objects have higher fluxes due to higher SFRs. However, we emphasize that for line ratios that are doubly valued with metallicity such as $R23$, this problem may be exacerbated. Testing whether a systematic offset exists at higher redshift requires a large sample of galaxies with individual detections of metallicity sensitive lines. Future spectroscopic surveys should deliver this.

For many objects, the redshift is determined from a single, low S/N emission line. Comparisons with other spectroscopic samples suggests that a fraction of our line detections ($\sim$ 10%) are either spurious or misidentifications (see Paper III). In the case of improper line identification, we systematically underestimate the metallicity since there is no corresponding [NII]λ6584 emission. This is largely a problem affecting the lowest stellar mass galaxies in our sample and we expect that our estimates of the metallicity are systematically underestimated at low stellar masses. However, because we have selected

our sample using robust photometric redshifts, this only effects a small fraction of our sample and therefore should not be a significant bias in our measurement.

We have used the local calibrations for metallicity and applied them to high redshift data. Several authors have shown that evolving ISM conditions may lead to evolution in key emission line diagnostics (Erb et al. 2006; Hainline et al. 2009; Rigby et al. 2011; Yabe et al. 2012; Kewley et al. 2013a). Typically, these studies have argued for evolving ISM conditions on the basis of the [OIII]/Hβ vs. [NII]/Hα diagram. However, the metallicities of galaxies are also dependent on conditions of the ISM (e.g. Kewley & Dopita 2002). In this study, we have shown that the metallicities determined using the $N2$ and $O3N2$ line ratios are inconsistent despite being calibrated to the same data in the local Universe (PP04). In order to assess the impact of these variations on metallicity, deep observations of full optical spectra in a large sample of galaxies are necessary.

In Zahid et al. (2013a) we attribute the flattening of the MZ relation for massive galaxies to the physical effect of metallicity saturation. In that study, we determine metallicities using the $R23$ diagnostic. Photoionization modeling suggests that this metallicity diagnostic saturates at metallicities significantly higher than the maximum metallicity observed in star-forming galaxies (Kewley & Dopita 2002). However, the $N2$ diagnostic is prone to saturation at significantly lower metallicities (Kewley & Dopita 2002). The saturation of $N2$ suggests that metallicities may be higher than those that we have measured here. However, we emphasize that the flattening observed in the local MZ relation is present using several different diagnostics (see Kewley & Ellison 2008). Moreover, the high $N2$ ratios are only observed in the most massive galaxies and therefore saturation may only effect a small fraction of the most massive galaxies. Since we have applied the same diagnostic to both or local and $z \sim 1.6$ sample, we have mitigated uncertainties in the relative metallicities.

In Figure 4.9 we examine the relation between stellar mass, metallicity and SFR. Similar to the local Universe, there appears to be an anti-correlation between metallicity and SFR at a fixed stellar mass. We measure SFR from the Hα line flux and metallicity is determined from the $N2$ ratio. While SFR is directly dependent on the Hα line flux, the metallicity is

inversely dependent on the Hα line flux. The errors are correlated in the same way as the observed trends. This could potentially produce an artificial trend in our measurement of the stellar mass, metallicity and SFR relation for galaxies at $z \sim 1.6$. However, we note that for local galaxies such trends persist even when completely independent line diagnostics are used. For example, similar trends are observed when SFRs are determined from Balmer lines and metallicities are determined from the [NII]λ6584/[OII]λ3727 ratio (Andrews & Martini 2013). In this case, the two measurements are independent and the effect in local galaxies can not be attributed to correlated errors. It remains to be seen whether trends persist when using independent diagnostics for higher redshift samples.

In Figure 4.10 we examine the relation between stellar mass, dust extinction and metallicity. The trends observed in the relation at $z \sim 1.6$ are similar to those observed in local galaxies. Namely, at a fixed stellar mass, dust extinction is correlated to metallicity. However, we are currently not able to apply a consistent methodology when examining these two samples because Hβ is detected in only a small fraction of our sample. We instead rely on dust extinction determined from the continuum extinction measured from the $B - z$ color. We convert this to nebular extinction using the factor we derive in Paper I. While this may apply to population on average, this may not be applicable to individual galaxies. Future surveys with higher sensitivity and broader wavelength coverage should be able to establish the validity of this approach and robustly establish the relation between stellar mass, dust extinction and metallicity.

4.7 Discussion

4.7.1 Comparison of the MZ Relation with Previous High-z Studies

Yabe et al. (2012) report on the MZR at $z \sim 1.4$ based on FMOS observations conducted in low resolution mode. The initial sample is K-band selected with a secondary selection for galaxies expected to have Hα flux $> 10^{-16}$ ergs s^{-1} cm^{-2} based on rest-frame UV emission. They derive an MZR by stacking the spectra of 71 galaxies that have significant

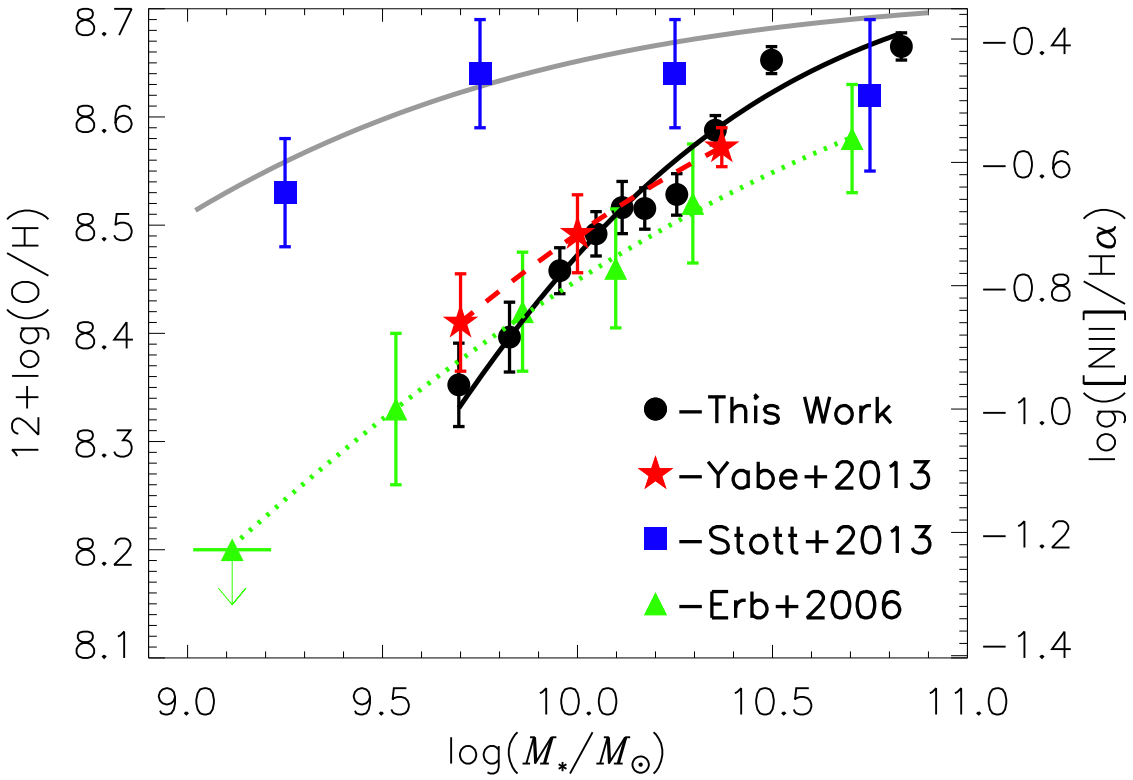

Figure 4.11 A comparison of the MZ relation we measure at $z \sim 1.6$ with the measurement at $z \sim 1.4$ from Yabe et al. (2012). The black filled circles and curve are our measurements. The red stars are measurements from Yabe et al. (2012).
.

Hα detections in 3 mass bins. In order to make a robust comparison, both the stellar masses and metallicities must be determined in a consistent manner. Yabe et al. (2012) derive metallicities from the $N2$ using the PP04 calibration. However, we find that the stellar mass estimates are systematically offset mostly (but not completely) due to the different IMFs adopted. We recalculate the stellar masses applying our methodology using photometry provided by K. Yabe. We compare our derived stellar masses with those calculated by Yabe et al. (2012). Our mass estimates are systematically lower by 0.28 dex. For consistency, we subtract 0.28 dex from the stellar masses derived by Yabe et al. (2012) when plotting the MZR.

Figure 4.11 shows a direct comparison between the MZR derived by Yabe et al. (2012, red stars) and the MZR we measure (black solid curve and filled circles). Our data extend ~ 0.5 dex higher in stellar mass. The MZR we derive is systematically steeper, though over the stellar mass range probed by Yabe et al. (2012) the metallicities in the individual bins are consistent within the errors. As we noted in Section 4.6, some small fraction of the galaxies have misidentified Hα. Including these galaxies in the average leads to an underestimate of the metallicity. The misidentification of Hα largely effects the least massive galaxies in the sample. This may explain the lower metallicities we measure in the lowest mass bin. Given the differences in sample size (156 compared to 71 galaxies) and observational modes (high resolution compared to low resolution) we consider the good agreement in the two measurements to be reassuring.

In Figure 4.11 we also plot the MZ relation from Erb et al. (2006, green triangles). Erb et al. (2006) average the spectra of 87 star-forming galaxies at $z \sim 2.3$ in five bins of stellar mass. We have recalculated their stellar masses using the same methodology applied to our $z \sim 1.6$ sample in order to ensure a consistent comparison (see Zahid et al. 2012b). The Erb et al. (2006) sample is flatter than the relation we derive for our sample at $z \sim 1.6$. At the low mass end, our metallicities may be underestimated. This may explain part of the discrepancy (see Section 4.6). At the high mass end, it is possible that metallicities determined by Erb et al. (2006) may be underestimated. The sample of Erb et al. (2006) is UV selected Lyman break galaxies and therefore biased against dusty objects. In Figure 4.10 we show that dust extinction and metallicity are correlated. The UV selected samples are likely to be missing the dustier, metal-rich massive galaxies and therefore the average metallicity derived by Erb et al. (2006) may be underestimated in the highest mass bins.

Henry et al. (2013) have examined the MZ relation for low mass galaxies at $z \sim 1.8$. The data demonstrate a clear decline in metallicity at lower stellar masses (down to $\sim 10^8 M_{\odot}$). The relation they derive is consistent with our measurements. However, we note that due the faintness of low mass galaxies, the observational uncertainties are large and therefore do not provide a strong validation of the MZ relation we derive.

Recently, Stott et al. (2013) report a MZ relation for a combined sample of galaxies at $z = 0.84$ and $z = 1.47$. They determine the metallicity from stacking spectra 103 galaxies into four bins of stellar mass. The blue squares in Figure 4.11 are their measurements of the MZ relation. The primary conclusion of Stott et al. (2013) is that the MZ relation does not evolve with redshift (compare their data with local relation shown by the gray curve in Figure 4.11). They argue that the more than dozen previous studies reporting an evolution in the MZ relation are biased. They cite the higher SFRs probed in previous studies and selection bias in UV selected samples as the origin of the reported evolution.

Figure 4.11 clearly demonstrates that the lack of evolution in the MZ relation reported by Stott et al. (2013) is not supported by our data. The potential sources of bias provided by Stott et al. (2013) do not strictly apply to our data. Our sample is based on the sBzK selection which is significantly less biased against dusty objects as compared to UV selections. This is because in color-color space, the effect of dust is to move objects parallel to the selection criteria (Daddi et al. 2004). Furthermore, this effect should be most pronounced for massive galaxies and low mass galaxies are unlikely to be severely dust obscured. A second source of bias suggested by Stott et al. (2013) is that previous studies probe significantly higher average SFRs. We note that our observations are carried using FMOS on Subaru operated in high resolution mode. This setup is identical to the observational setup used by Stott et al. (2013). However, our observations are significantly deeper as we observe a single pointing position per night whereas Stott et al. (2013) observed six positions in a night. Our observations have a sensitivity limit that is nearly an order of magnitude deeper than the observations of Stott et al. (2013) and therefore we are able to to observe galaxies with significantly lower SFRs. We conclude that our sample does not suffer significantly from the type of bias suggested by Stott et al. (2013). We consider the redshift evolution of the MZ relation to be real.

4.7.2 Evolution of the MZ relation

In Zahid et al. (2013a) we examine the evolution of the MZ relation. Our analysis is primarily based on three large samples at $z < 1$ for which we are able to measure metallicities in individual galaxies using the same metallicity calibration (i.e. Kobulnicky & Kewley 2004). In Zahid et al. (2013a), we fit the MZ relation using the parameterization given in Equation 4.6 and conclude that the shape of the MZ relation evolves significantly with redshift such that it flattens at late times. In an "open-box" model of galaxy chemical evolution where star formation is primarily fueled by cosmological accretion and is capable of driving large scale galaxy winds which expel metals from the ISM, the gas-phase oxygen abundance may not exceed the effective yield.[4] We argue that the flattening of the MZ relation is primarily driven by massive galaxies enriching to the effective yield. We show that upper metallicity limit, Z_o, does not to evolve significantly out to *at least* $z \sim 0.8$ (Zahid et al. 2013a). Furthermore, we show that the flattening of the relation can be primarily understood as an evolution in M_o, the stellar mass at which the MZ relation begins to flatten. M_o is ~ 0.7 dex lower in the local universe as compared to $z \sim 0.8$ (Zahid et al. 2013a).

The MZ relation we derive at $z \sim 1.6$ is consistent with the evolution observed in the MZ relation at $z < 1$. Table 10.1 gives the fit parameters for the local and $z \sim 1.6$ relation[5]. Within the observational uncertainties, the saturation metallicity, Z_o, does not evolve since $z < 1.6$ and M_o is ~ 1.3 dex larger at $z \sim 1.6$. The lack of evolution in the saturation metallicity places constraints on the metallicity of outflows and oxygen yields in star-forming galaxies. Detailed comparison of the evolution with analytical and numerical models is needed to rigorously establish this. The lack of evolution in Z_o and the evolution

[4]The nucleosynthetic yield is the mass of oxygen formed per unit SFR. In the presence of outflows, some metals may be lost and the effective yield is the mass of oxygen produced minus the mass of oxygen lost in the wind per unit SFR.

[5]The fit parameters given in Table 10.1 can not be directly compared to those provided in Zahid et al. (2013a). Because of the different spectral ranges covered by the data, we are required to apply different metallicity calibrations in determining metallicities. Systematic differences between various metallicity calibrations are well documented, though relative metallicities are found to be robust (e.g. Kewley & Ellison 2008)

of M_o to larger masses means that only the most massive galaxies at $z \sim 1.6$ achieve the level of enrichment observed in the local universe. However, our interpretation remains tentative due to possible saturation of the $N2$ diagnostic (see Section 4.6).

The high gas-phase abundance of massive star-forming galaxies at $z \sim 1.6$ is consistent with observations which indicate super-solar metallicities for the stellar populations of massive early-type galaxies (e.g. Gallazzi et al. 2005; Thomas et al. 2005; Panter et al. 2008; Conroy et al. 2013). Analysis of the stellar population ages of these massive early type galaxies indicates old stellar populations ($\gtrsim 10$ Gyr). This implies that these galaxies formed stars in the distant past from gas enriched to the level observed in massive star-forming galaxies in the local universe. More to the point, Panter et al. (2008) show that the most massive early-type galaxies exhibit super-solar stellar metallicities that do not evolve out to $z \gtrsim 2$. In contrast, less massive galaxies show significant evolution since $z \sim 2$ with the least massive galaxies showing the greatest evolution. The stellar metallicity evolution trends observed by Panter et al. (2008) are consistent with the evolution observed in the gas-phase oxygen abundance of the star-forming galaxy population since $z \sim 1.6$, i.e. a steepening of the MZ relation at higher redshift. *The chemical evolution of star-forming galaxies may be characterized by an upper metallicity limit that does not evolve with redshift. This upper limit is achieved in progressively lower stellar mass galaxies as the Universe evolves.* This evolution is likely driven by the decreasing gas fraction of galaxies with time.

4.7.3 The Stellar Mass, Metallicity and SFR Relation

Ellison et al. (2008) first showed the *anti*-correlation between specific SFR and metallicity at a fixed stellar masses. Subsequently, this relation has been examined by several authors (e.g. Mannucci et al. 2010; Yates et al. 2012; Andrews & Martini 2013, and others). These studies show that for SDSS galaxies, the scatter around the MZ relation is somehow correlated to the SFR. In particular, Mannucci et al. (2010) find that at a fixed stellar mass, the metallicity is *anti*-correlated to the SFR. They parameterize the metallicity as a function of stellar

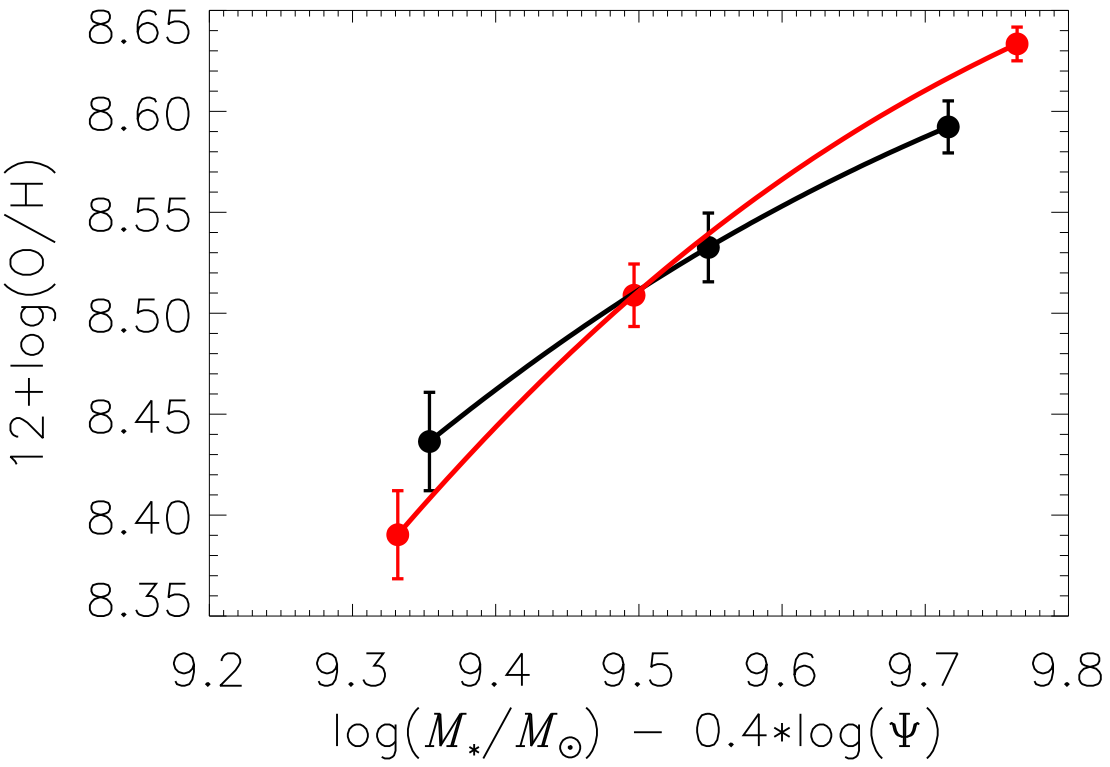

Figure 4.12 Following the approach of Mannucci et al. (2010), we plot metallicity against the combination of stellar mass and SFR that minimizes the scatter for our sample at $z \sim 1.6$. The data are the same as in Figure 4.9.

mass and SFR, i.e. $\mu_\alpha = \log(M_*/M_\odot) - \alpha\log(\Psi)$. They find that $\alpha = 0.32$ minimizes the scatter in the local MZR. They argue that the relation between metallicity and μ_α does not evolve for galaxies with $z < 3$ and refer to this relation as the "fundamental metallicity relation" (FMR). For the FMR, the lower metallicities observed in high redshift galaxies are compensated by their higher SFRs. However, the relation is dependent on methodology (Yates et al. 2012; Andrews & Martini 2013). There is no consensus regarding the evolution of the relation between stellar mass, metallicity and SFR and therefore the validity of the FMR remains tentative (e.g Niino 2012; Pérez-Montero et al. 2013; Sánchez et al. 2013; Cullen et al. 2014).

The analysis of the FMR we present differs from Mannucci et al. (2010) in one significant manner. Unlike Mannucci et al. (2010) who determine SFRs from dust corrected Hα luminosity in the fiber, we instead adopt the aperture and dust corrected SFRs provided by the MPA/JHU group in the SDSS DR7. This is very important as aperture corrections for SFRs are significant for local galaxies (see Zahid et al. 2013c). For the SDSS sample used in this study the aperture corrected SFRs are on average 0.5 dex larger than SFRs determined from Hα flux measured in the aperture. This is because the typical fiber covering fraction for galaxies in our local sample is $\sim$ 30%. For the Mannucci et al. (2010) sample, the average difference is 0.7 dex. The larger difference is because they do not apply a minimum covering fraction in selecting their sample. This difference is significant and substantially impacts the FMR. The FMR with aperture corrected SFRs is offset by 0.22 dex from the FMR determined using SFRs calculated from the Hα flux in the fiber.

If we calculate metallicities for our sample using the Maiolino et al. (2008) $N2$ calibration, which is the one used in Mannucci et al. (2010), and apply the exact same selection and methodology in analyzing the local SDSS sample as Mannucci et al. (2010), we find significantly better agreement between galaxies in the local Universe and at $z \sim 1.6$. However, we still find that the our sample at $z \sim 1.6$ is a steeper relation that is not fully consistent with the local FMR within the errors. The standard interpretation of the FMR is that it reflects short timescale responses to gas flows (Mannucci et al. 2010). Inflows of pristine gas decrease the gas-phase oxygen abundance but also lead to an increase in SFR. In this sense, it is a relation between global, integrated properties of galaxies. However, the SDSS SFRs measured without aperture corrections are not reflective of the global SFR in SDSS galaxies and therefore not the appropriate measurement for deriving relations based on global properties. It is beyond the scope of this paper to examine the FMR in detail. We simply note that if we use SDSS SFRs without aperture corrections, we find better agreement between the local FMR and the relation at $z \sim 1.6$. This agreement is likely to be misleading. For the following analysis however, we use the aperture corrected SDSS SFRs.

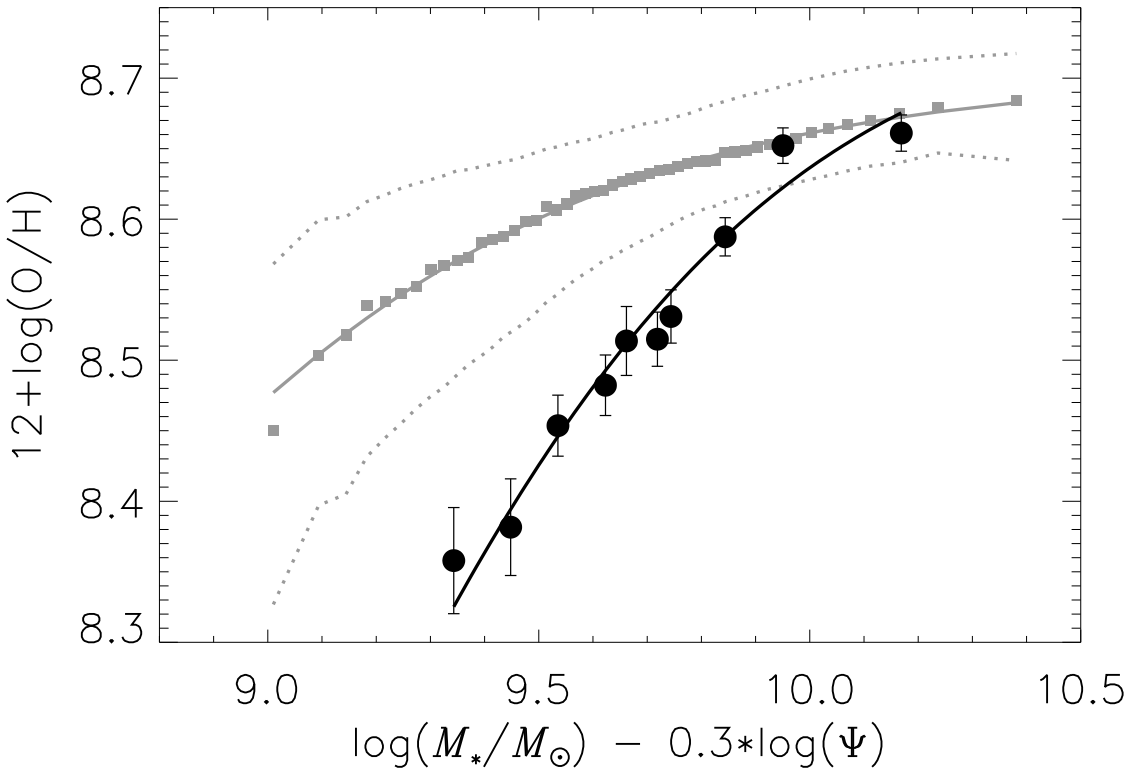

Figure 4.13 The FMR for our local fiducial sample (gray curve and squares) and our $z \sim 1.6$ sample (black curve and circles). The gray dotted lines denote the interval containing the central 68% of local galaxy distribution.

In Figure 4.9 we examine the relation between stellar mass, metallicity and SFR. Similar to trends reported by Mannucci et al. (2010, and others) for local SDSS galaxies, we find that at a fixed stellar mass, metallicity is *anti*-correlated to the SFR. Following the approach of Mannucci et al. (2010), we determine the value α that minimizes the scatter in metallicity for our $z \sim 1.6$ sample. In Figure 4.12 we plot the metallicity as a function μ_α for galaxies shown in Figure 4.9. Because of the small sample size, we find that the derived value of α is dependent on the number of bins. We conclude that for our sample of galaxies at $z \sim 1.6$ the scatter is minimized for $\alpha \sim 0.4 - 0.5$.

We find that for local galaxies $\alpha = 0.30$ minimizes the scatter in metallicities when they are measured using the $N2$ ratio. This same value is independently derived by Andrews &

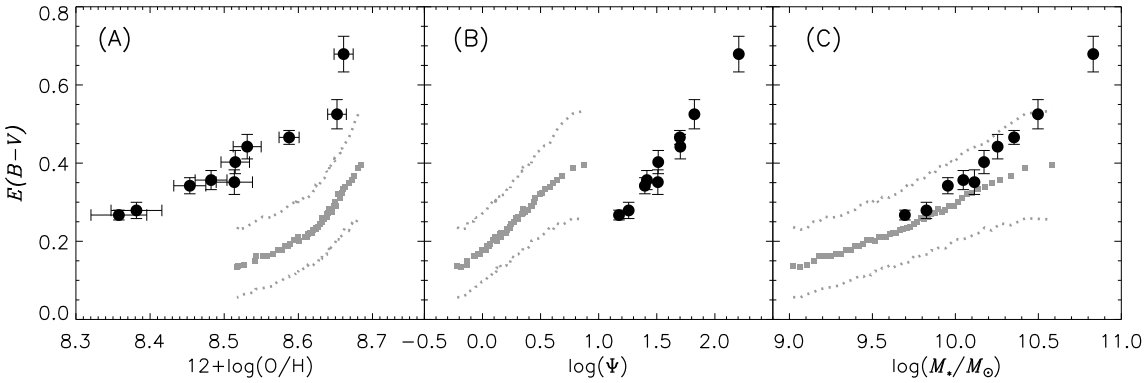

Figure 4.14 The relation between $E(B-V)$ and (A) metallicity, (B) SFR and (C) stellar mass. The black points are galaxies at $z \sim 1.6$ and the gray squares are the median values of $E(B-V)$ in 50 bins of stellar mass. The dotted line denotes the interval containing the central 68% of the distribution of local galaxies.

Martini (2013). In Figure 4.13 we plot the metallicities of local (gray curve) and $z \sim 1.6$ (black curve) galaxies as a function of the μ_α that minimizes the scatter in the local relation.

Our data do not support a relation between stellar mass, metallicity and SFR that is independent of redshift, i.e. the FMR of Mannucci et al. (2010). When the metallicities of galaxies at $z \sim 1.6$ are plotted against the μ_α that minimizes the scatter in the local relation, a single relation is not observed (Figure 4.13). *The data support significant evolution in the relation between stellar mass, metallicity and SFR.* We emphasize that this is largely due to the use of aperture corrected SFRs for local galaxies.

4.7.4 The Stellar Mass, Metallicity, SFR and Dust

Understanding the distribution of dust as a function of cosmic time and galaxy properties is critical. Several recent studies have focused on the dust properties of local galaxies (e.g., Garn & Best 2010; Xiao et al. 2012; Zahid et al. 2013c). Garn & Best (2010) derive a relation between dust extinction and stellar mass. On average the magnitude of extinction, $A_{H\alpha}$, varies between 0 and 2 for galaxies in the SDSS. Garn & Best (2010) perform a principal component analysis of dust extinction, stellar mass, metallicity and SFR. From PCA, they conclude that the dominant physical property related to dust extinction in

galaxies is stellar mass. The secondary correlations between dust extinction, metallicity and SFR are primarily due to the correlation of all three of these properties to stellar mass. At a fixed stellar mass dust extinction and metallicity are correlated in our sample of galaxies at $z \sim 1.6$ (see Figure 4.10). However, we note that this relation is significantly weaker than the relation between stellar mass and dust extinction. The straightforward interpretation is that galaxies increase their dust content as they build their stellar mass.

We examine the relation between dust extinction, stellar mass, metallicity and SFR for our sample at $z \sim 1.6$ with the local relation. In Figure 4.14 we plot the dust extinction as a function of (A) metallicity, (B) SFR and (C) stellar mass. The black points are the $z \sim 1.6$ sample sorted into 10 bins of stellar mass and the gray squares are the local sample sorted into 50 bins of stellar mass. Figure 4.14A and B clearly demonstrate that dust extinction as a function of metallicity and SFR, respectively, are significantly offset from the local relation. In contrast, the relation between dust extinction and stellar mass is similar for galaxies local galaxies and $z \sim 1.6$ galaxies (see also Paper I).

The primary difference in the relation between stellar mass and dust extinction at $z \sim 1.6$ as compared to the local Universe is at the high mass end. At $z \sim 1.6$, massive galaxies exhibit larger extinction as compared to local galaxies. This may be due to the distribution of dust within galaxies or to a greater dust content in galaxies at $z \sim 1.6$. Wild et al. (2011) show that the line-to-continuum extinction is greater for galaxies with higher stellar mass surface densities. They interpret this as an effect related to the dust distribution around young stars. In contrast, if the dust content is greater, this may be related to the higher SFRs of galaxies at $z \sim 1.6$. Zahid et al. (2013b) suggest that dust efflux by outflows may explain the distribution of dust in local star-forming galaxies. In this scenario, dust is slowly effluxed from galaxies by continuous interaction of dust with the radiation field generated by ongoing star-formation. The timescale of dust efflux is significantly longer than the timescale of dust production and therefore galaxies accumulate dust. The dust content of galaxies in this scenario is a balance between dust production and dust efflux. A generic prediction of this model is that massive galaxies which form stars more rapidly also

have greater dust content. This is because, on average, they form their stars over a shorter period of time and do not have as much time to efflux dust from their ISM.

4.8 Summary and Conclusions

We derive the mass-metallicity relation using spectroscopic observations of ~ 160 galaxies at $z \sim 1.6$. These galaxies are observed as part of our ongoing survey of star-forming galaxies in the redshift desert. These data constitute the largest high-resolution spectroscopic sample of star-forming galaxies at $z > 1.4$ for which we can measure star formation rates and metallicities from optical emission lines. The main results and conclusions of our analysis are:

- There is a strong relation observed between stellar mass and metallicity for star-forming galaxies at $z \sim 1.6$. The shape of the mass-metallicity relation evolves with redshift and is steeper at early times. The most massive galaxies ($M_* \sim 10^{11} M_\odot$) in our sample at $z \sim 1.6$ have enriched to the level observed in the local Universe. Less massive galaxies ($M_* \sim 10^{9.5} M_\odot$) have metallicities that are > 0.25 dex lower at $z \sim 1.6$ as compared to the local Universe.

- The data support our previous results showing that the evolution of the shape in the mass-metallicity relation is a consequence of galaxies enriching to an empirical upper metallicity limit. The stellar mass where galaxies enrich to this upper metallicity limit is ~ 1.3 dex larger at $z \sim 1.6$ than in the local Universe. Our analysis suggests that the upper metallicity limit does not evolve significantly since $z \sim 1.6$.

- At a fixed stellar mass, metallicity is *anti*-correlated to the star formation rate such that, on average, galaxies with higher star formation rates tend to have lower metallicities. Similar trends are observed in the local Universe.

- Our data do not support a relation between stellar mass, metallicity and SFR that is independent of redshift (i.e. Mannucci et al. 2010). We observe significant evolution in

the relation between stellar mass, metallicity and star formation rate when comparing the local data with our $z \sim 1.6$ sample.

- We find that at a fixed stellar mass, dustier galaxies tend to have higher metallicities. We examine the relation between dust extinction and stellar mass, metallicity and SFR for galaxies at $z \sim 1.6$. By comparing these relations with the same relations for local galaxies, we conclude that stellar mass is closely related to the dust content of galaxies.

A consistent picture for the chemical evolution of star-forming galaxies since $z \sim 2$ is emerging. Our analysis and conclusions are based on averaging spectra from many galaxies. Measurements of metallicities in mass-selected individual galaxy samples using multiple diagnostics will be useful for assessing systematic issues. In particular, we are limited by our ability to detect only the strongest emission lines. This contributes to incorrect assignments of redshift and limited control over AGN contamination. The effect of these systematic issues needs to be quantified and corrected. Deeper near-infrared spectroscopic surveys with greater wavelength coverage should allow us to do this soon.

References

Abazajian, K. N., et al. 2009, ApJS, 182, 543

Andrews, B. H., & Martini, P. 2013, ApJ, 765, 140

Asari, N. V., Cid Fernandes, R., Stasińska, G., Torres-Papaqui, J. P., Mateus, A., Sodré, L., Schoenell, W., & Gomes, J. M. 2007, MNRAS, 381, 263

Baldwin, J. A., Phillips, M. M., & Terlevich, R. 1981, PASP, 93, 5

Bell, E. F., McIntosh, D. H., Katz, N., & Weinberg, M. D. 2003, ApJS, 149, 289

Berg, D. A., et al. 2012, ApJ, 754, 98

Boissier, S., Boselli, A., Buat, V., Donas, J., & Milliard, B. 2004, A&A, 424, 465

Bordoloi, R., et al. 2011, ApJ, 743, 10

Brinchmann, J., Charlot, S., White, S. D. M., Tremonti, C., Kauffmann, G., Heckman, T., & Brinkmann, J. 2004, MNRAS, 351, 1151

Brooks, A. M., Governato, F., Booth, C. M., Willman, B., Gardner, J. P., Wadsley, J., Stinson, G., & Quinn, T. 2007, ApJ, 655, L17

Bruzual, G., & Charlot, S. 2003, MNRAS, 344, 1000

Calzetti, D., Armus, L., Bohlin, R. C., Kinney, A. L., Koornneef, J., & Storchi-Bergmann, T. 2000, ApJ, 533, 682

Capak, P., et al. 2007, ApJS, 172, 99

Chabrier, G. 2003, PASP, 115, 763

Conroy, C., Graves, G., & van Dokkum, P. 2013, ArXiv e-prints

Conroy, C., Gunn, J. E., & White, M. 2009, ApJ, 699, 486

Cowie, L. L., Songaila, A., Hu, E. M., & Cohen, J. G. 1996, AJ, 112, 839

Cullen, F., Cirasuolo, M., McLure, R. J., Dunlop, J. S., & Bowler, R. A. A. 2014, MNRAS, 440, 2300

Daddi, E., Cimatti, A., Renzini, A., Fontana, A., Mignoli, M., Pozzetti, L., Tozzi, P., & Zamorani, G. 2004, ApJ, 617, 746

Daddi, E., et al. 2007, ApJ, 670, 156

Davé, R., Finlator, K., & Oppenheimer, B. D. 2011, MNRAS, 416, 1354

Denicoló, G., Terlevich, R., & Terlevich, E. 2002, MNRAS, 330, 69

Ellison, S. L., Patton, D. R., Simard, L., & McConnachie, A. W. 2008, ApJ, 672, L107

Erb, D. K., Shapley, A. E., Pettini, M., Steidel, C. C., Reddy, N. A., & Adelberger, K. L. 2006, ApJ, 644, 813

Finlator, K., & Davé, R. 2008, MNRAS, 385, 2181

Fontana, A., et al. 2004, A&A, 424, 23

Foster, C., et al. 2012, A&A, 547, A79

Gallazzi, A., Charlot, S., Brinchmann, J., White, S. D. M., & Tremonti, C. A. 2005, MNRAS, 362, 41

Garn, T., & Best, P. N. 2010, MNRAS, 409, 421

Groves, B., Brinchmann, J., & Walcher, C. J. 2012, MNRAS, 419, 1402

Hainline, K. N., Shapley, A. E., Kornei, K. A., Pettini, M., Buckley-Geer, E., Allam, S. S., & Tucker, D. L. 2009, ApJ, 701, 52

Heckman, T. M., Robert, C., Leitherer, C., Garnett, D. R., & van der Rydt, F. 1998, ApJ, 503, 646

Henry, A., et al. 2013, ArXiv e-prints

Hopkins, A. M., & Beacom, J. F. 2006, ApJ, 651, 142

Hummer, D. G., & Storey, P. J. 1987, MNRAS, 224, 801

Ilbert, O., et al. 2010, ApJ, 709, 644

Iwamuro, F., et al. 2012, PASJ, 64, 59

Iwamuro, F., Motohara, K., Maihara, T., Hata, R., & Harashima, T. 2001, PASJ, 53, 355

Kashino, D., et al. 2013, ApJ, 777, L8

Kauffmann, G., et al. 2003, MNRAS, 346, 1055

Kennicutt, Jr., R. C. 1998, ARA&A, 36, 189

Kewley, L. J., & Dopita, M. A. 2002, ApJS, 142, 35

Kewley, L. J., Dopita, M. A., Leitherer, C., Davé, R., Yuan, T., Allen, M., Groves, B., & Sutherland, R. 2013a, ApJ, 774, 100

Kewley, L. J., & Ellison, S. L. 2008, ApJ, 681, 1183

Kewley, L. J., Groves, B., Kauffmann, G., & Heckman, T. 2006, MNRAS, 372, 961

Kewley, L. J., Jansen, R. A., & Geller, M. J. 2005, PASP, 117, 227

Kewley, L. J., Maier, C., Yabe, K., Ohta, K., Akiyama, M., Dopita, M. A., & Yuan, T. 2013b, ApJ, 774, L10

Kimura, M., et al. 2010, PASJ, 62, 1135

Kirby, E. N., Martin, C. L., & Finlator, K. 2011, ApJ, 742, L25

Kobulnicky, H. A., & Kewley, L. J. 2004, ApJ, 617, 240

Kulas, K. R., et al. 2013, ArXiv e-prints

Lara-López, M. A., et al. 2010, A&A, 521, L53+

Larson, R. B. 1974, MNRAS, 169, 229

Laskar, T., Berger, E., & Chary, R.-R. 2011, ApJ, 739, 1

Lee, H., Skillman, E. D., Cannon, J. M., Jackson, D. C., Gehrz, R. D., Polomski, E. F., & Woodward, C. E. 2006, ApJ, 647, 970

Lequeux, J., Peimbert, M., Rayo, J. F., Serrano, A., & Torres-Peimbert, S. 1979, A&A, 80, 155

Lilly, S. J., Carollo, C. M., Pipino, A., Renzini, A., & Peng, Y. 2013, ApJ, 772, 119

Maier, C., Lilly, S. J., Carollo, C. M., Meisenheimer, K., Hippelein, H., & Stockton, A. 2006, ApJ, 639, 858

Maier, C., Lilly, S. J., Carollo, C. M., Stockton, A., & Brodwin, M. 2005, ApJ, 634, 849

Maiolino, R., et al. 2008, A&A, 488, 463

Mannucci, F., Cresci, G., Maiolino, R., Marconi, A., & Gnerucci, A. 2010, MNRAS, 408, 2115

Mannucci, F., et al. 2009, MNRAS, 398, 1915

Marino, R. A., et al. 2013, ArXiv e-prints

Markwardt, C. B. 2009, in Astronomical Society of the Pacific Conference Series, Vol. 411, Astronomical Data Analysis Software and Systems XVIII, ed. D. A. Bohlender, D. Durand, & P. Dowler, 251

Martin, C. L., Kobulnicky, H. A., & Heckman, T. M. 2002, ApJ, 574, 663

Mathews, W. G., & Baker, J. C. 1971, ApJ, 170, 241

McCracken, H. J., et al. 2010, ApJ, 708, 202

Moustakas, J., et al. 2011, ArXiv e-prints

Nagao, T., Maiolino, R., & Marconi, A. 2006, A&A, 459, 85

Newman, S. F., et al. 2012, ApJ, 761, 43

Niino, Y. 2012, ApJ, 761, 126

Panter, B., Jimenez, R., Heavens, A. F., & Charlot, S. 2008, MNRAS, 391, 1117

Peng, Y.-j., et al. 2010, ApJ, 721, 193

Pérez-Montero, E., et al. 2013, A&A, 549, A25

Pettini, M., & Pagel, B. E. J. 2004, MNRAS, 348, L59

Reddy, N. A., Erb, D. K., Pettini, M., Steidel, C. C., & Shapley, A. E. 2010, ApJ, 712, 1070

Renzini, A. 1997, ApJ, 488, 35

Rigby, J. R., Wuyts, E., Gladders, M. D., Sharon, K., & Becker, G. D. 2011, ApJ, 732, 59

Salim, S., et al. 2007, ApJS, 173, 267

Salpeter, E. E. 1955, ApJ, 121, 161

Sánchez, S. F., et al. 2013, A&A, 554, A58

Savaglio, S., et al. 2005, ApJ, 635, 260

Scoville, N., et al. 2007, ApJS, 172, 1

Stott, J. P., et al. 2013, ArXiv e-prints

Stoughton, C., et al. 2002, AJ, 123, 485

Thomas, D., Maraston, C., Bender, R., & Mendes de Oliveira, C. 2005, ApJ, 621, 673

Torrey, P., Vogelsberger, M., Genel, S., Sijacki, D., Springel, V., & Hernquist, L. 2013, ArXiv e-prints

Tremonti, C. A., et al. 2004, ApJ, 613, 898

Wild, V., Charlot, S., Brinchmann, J., Heckman, T., Vince, O., Pacifici, C., & Chevallard, J. 2011, MNRAS, 417, 1760

Xiao, T., Wang, T., Wang, H., Zhou, H., Lu, H., & Dong, X. 2012, MNRAS, 421, 486

Yabe, K., et al. 2012, PASJ, 64, 60

Yates, R. M., Kauffmann, G., & Guo, Q. 2012, MNRAS, 422, 215

York, D. G., et al. 2000, AJ, 120, 1579

Yuan, T.-T., Kewley, L. J., & Richard, J. 2013, ApJ, 763, 9

Zahid, H. J., Bresolin, F., Kewley, L. J., Coil, A. L., & Davé, R. 2012a, ApJ, 750, 120

Zahid, H. J., Dima, G. I., Kewley, L. J., Erb, D. K., & Davé, R. 2012b, ApJ, 757, 54

Zahid, H. J., Geller, M. J., Kewley, L. J., Hwang, H. S., Fabricant, D. G., & Kurtz, M. J. 2013a, ApJ, 771, L19

Zahid, H. J., Kewley, L. J., & Bresolin, F. 2011, ApJ, 730, 137

Zahid, H. J., Torrey, P., Kudritzki, R., Kewley, L., Dave, R., & Geller, M. 2013b, ArXiv e-prints

Zahid, H. J., Torrey, P., Vogelsberger, M., Hernquist, L., Kewley, L., & Davé, R. 2014, Ap&SS, 349, 873

Zahid, H. J., Yates, R. M., Kewley, L. J., & Kudritzki, R. P. 2013c, ApJ, 763, 92

Chapter 5

The Metallicities of Low Stellar Mass Galaxies and the Scatter in the Mass-Metallicity Relation

Note: This chapter originally appeared as Zahid, H.J., Bresolin, F., Kewley, L.J., Coil, A.L., & Dave, R. 2012, Apj, 750, 120. This work was primarily based on publicly available data from the Deep Extragalactic Evolutionary Probe 2 (DEEP2) and Sloan Digital Sky Survey (SDSS) surveys. I am the primary author of this work.

Abstract

In this investigation we quantify the metallicities of low mass galaxies by constructing the most comprehensive census to date. We use galaxies from the SDSS and DEEP2 survey and estimate metallicities from their optical emission lines. We also use two smaller samples from the literature which have metallicities determined by the direct method using the temperature sensitive [OIII]λ4363 line. We examine the scatter in the local mass-metallicity (MZ) relation determined from $\sim$20,000 star-forming galaxies in the SDSS and show that it is larger at lower stellar masses, consistent with the theoretical scatter in the MZ relation determined from hydrodynamical simulations. We determine a lower limit for the scatter in metallicities of galaxies down to stellar masses of $\sim 10^7$ $M_\odot$ that is only slightly smaller than the expected scatter inferred from the SDSS MZ relation and significantly larger than what is previously established in the literature. The average metallicity of star-forming galaxies increases with stellar mass. By examining the scatter in the SDSS MZ relation,

we show that this is mostly due to the lowest metallicity galaxies. The population of low mass, metal-rich galaxies have properties which are consistent with previously identified galaxies that may be transitional objects between gas-rich dwarf irregulars and gas-poor dwarf spheroidals and ellipticals.

5.1 Introduction

The metallicity of a galaxy is a key physical parameter for understanding its history and evolution. Starting with Pagel et al. (1979), the practice of estimating gas-phase abundances from optical emission lines has allowed for significant advances in the study of galaxy evolution. Metals are produced in stars and returned to the interstellar medium (ISM) through stellar mass loss. In this way, the metallicity provides a record of the star formation history. However, the gas-phase abundance is modulated by gas flows where feedback processes can drive enriched gas out of galaxies and accretion of both primordial and enriched material can influence the gas-phase abundance. Observations of the relation between metallicity and other physical properties of galaxies and the evolution of these relations can place important constraints on the physical processes governing galaxy evolution.

The mass-metallicity (MZ) and luminosity-metallicity (LZ) relation was first observed by Lequeux et al. (1979) using nearby dwarf galaxies. Using ∼50,000 galaxies from the SDSS, Tremonti et al. (2004) have established the relation for the local population of star-forming galaxies down to stellar masses of $\log(M_*) \sim 10^{8.5}$ $M_\odot$. The MZ relation has also been observed at higher redshifts (Erb et al. 2006; Cowie & Barger 2008; Lamareille et al. 2009; Mannucci et al. 2009; Zahid et al. 2011, among others). From the scatter in the MZ and LZ relation, many authors conclude that the fundamental correlation is between stellar mass and metallicity, such that lower mass galaxies have lower metallicity (e.g. Tremonti et al. 2004; Zahid et al. 2011). Tremonti et al. (2004) attribute this effect to stellar wind driven mass loss enabled by the shallow potential wells in low mass galaxies. However,

Dalcanton et al. (2004) argue that observations of the local MZ relation are also consistent with metal-poor infall of gas.

Several authors have suggested that gas flows alone cannot explain the MZ relation. Using smoothed particle hydrodynamical simulations, Brooks et al. (2007) have argued that in addition to mass loss driven by UV heating and supernova feedback, a mass dependent star formation efficiency can help to explain the origin and evolution of the MZ relation. In this scenario, due to lower star formation efficiencies, low mass galaxies have yet to convert much of their gas reservoir into stars and therefore are less metal-rich. Alternatively, Köppen et al. (2007) suggest that the MZ relation may result from variations of the initial mass function. They argue that in low mass galaxies the initial mass function does not extend to high stellar masses due to the low levels of star formation, thus resulting in fewer massive stars forming and less chemical enrichment.

The metallicities of low mass galaxies ($M_* \lesssim 10^{8.5}$ $M_\odot$) may provide important clues to the origin of the MZ relation which may help to distinguish between the various proposed scenarios. Many authors have investigated the metallicities of nearby dwarf galaxies (Searle & Sargent 1972; Skillman et al. 1989; Kennicutt & Skillman 2001; Lee et al. 2003; Hidalgo-Gámez et al. 2003; van Zee & Haynes 2006; Zhao et al. 2010, among others) but few have focused on the MZ relation (Tamura et al. 2001; Lee et al. 2006; Vaduvescu et al. 2007). Lee et al. (2006) extend the MZ relation by 2.5 orders of magnitude in stellar mass. Their main conclusion is that the scatter in the MZ relation is similar over 5 orders of magnitude.

Recent observations of low mass, metal-rich galaxies present a challenge to this conclusion (Gu et al. 2006; Dellenbusch et al. 2007; Peeples et al. 2008; Petropoulou et al. 2011). In particular, Peeples et al. (2008) focus on a population of metal-rich dwarf galaxies from the SDSS which they consider outliers to the MZ relation. They identify these galaxies as objects nearing the end of their star formation activity and transitioning from dwarf spirals and irregulars to dwarf spheroidals and ellipticals, consistent with the scenario discussed by Grebel et al. (2003). However, citing possible systematic overestimates in the derived metallicities, Berg et al. (2011) refute this result. Due to the small number of

observations, it remains unclear whether there is a population of low stellar mass, metal-rich galaxies. A population of galaxies, such as these, would present an important new test for chemical evolution models and cosmological simulations while providing stronger constraints for the physical mechanisms governing the MZ relation and galaxy evolution.

Here we examine the metallicities in galaxies spanning stellar masses from $10^6 \lesssim \mathrm{M}_*/\mathrm{M}_\odot \lesssim 10^{10}$. In Section 5.2 we present the data and selection criteria used and in Section 5.3 we discuss our determination of stellar mass from photometry and metallicity from optical spectra. We examine the scatter in the MZ relation determined from $\sim 20,000$ SDSS galaxies in Section 5.4 and in Section 5.5 we focus on the metallicities of low mass galaxies. In Section 5.6 we investigate systematic uncertainties in our mass and metallicity determinations. We present the main results of this study, the scatter in the MZ relation at low stellar masses in Section 5.7. The physical properties of these galaxies are examined in Section 5.8 and in Section 5.9 we provide a discussion. We give a summary of our results in Section 5.10. When necessary we adopt the standard cosmology $(H_0, \Omega_m, \Omega_\Lambda) = (70$ km s^{-1} Mpc^{-1}, 0.3, 0.7).

5.2 Data Sample

5.2.1 The SDSS Sample

The SDSS DR7 consists of ∼900,000 galaxies spanning a redshift range of $0 < z < 0.7$ (Abazajian et al. 2009). The survey has a Petrosian magnitude limit of $r_P = 17.8$ and the spectra cover the nominal range of 3900 - 9100Å. For each object five bands of photometry, *ugriz*, is available (Stoughton et al. 2002). We use the publicly available emission line fluxes measured by the MPA-JHU group[1]. We determine the local MZ relation from ∼20,000 galaxies using the sample selection of Zahid et al. (2011). Hereafter, we refer to this relation as the SDSS MZ relation.

[1]http://www.mpa-garching.mpg.de/SDSS/DR7/

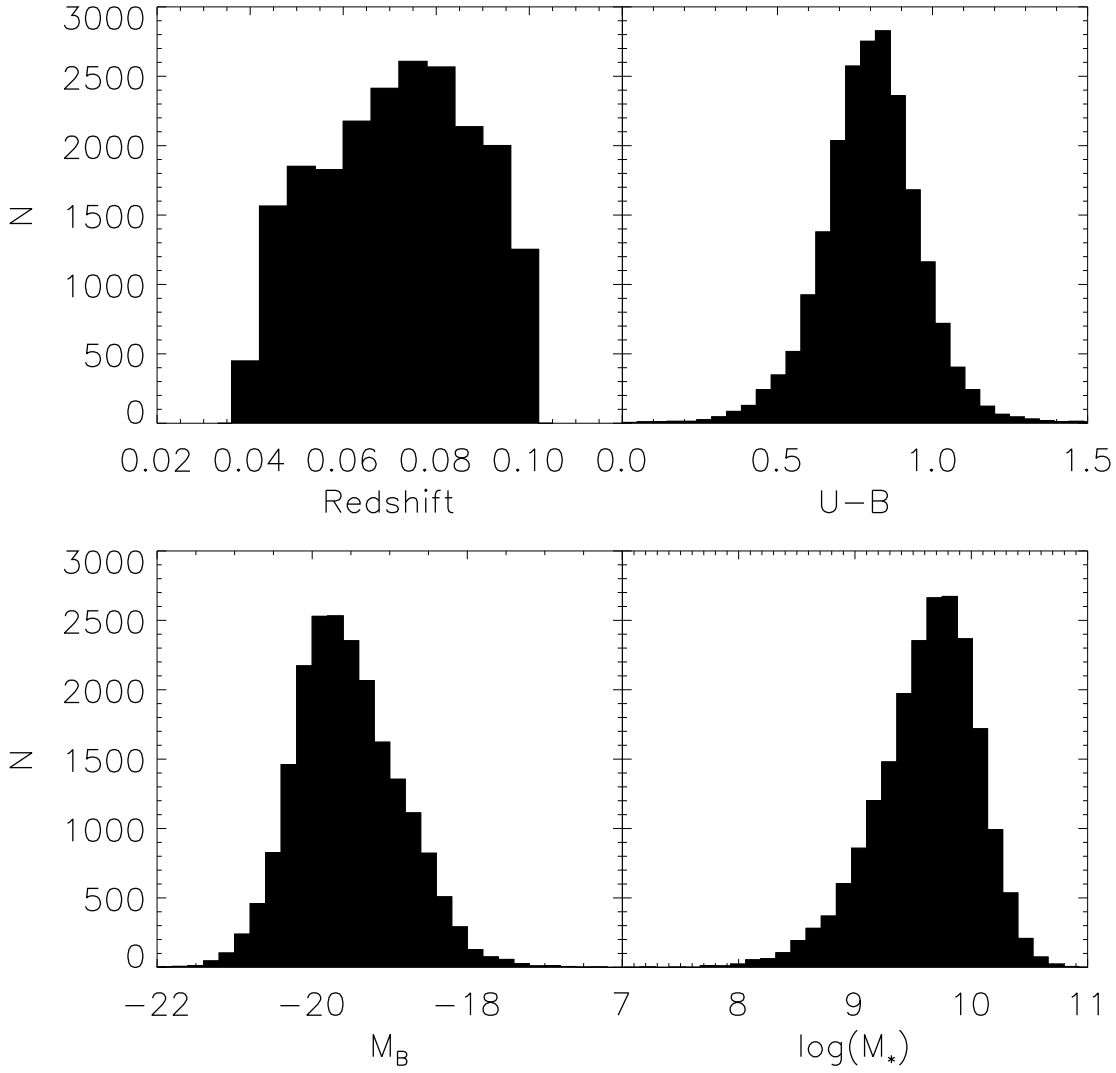

Figure 5.1 The distribution of redshift (top left), U−B color (top right), absolute B-band magnitude (bottom left) and stellar mass (bottom right) for our selected sample of ∼20,000 SDSS galaxies.

We first distinguish star-forming galaxies from AGN using the scheme of Kewley et al. (2006). In order to avoid aperture effects, we require a g-band fiber aperture covering fraction $> 30\%$ and impose a lower redshift limit of 0.04 (Kewley et al. 2005). The median covering fraction for the selected sample is 38%. Kewley et al. (2006) find that the SDSS

sample is incomplete at higher redshifts and in order to minimize evolutionary effects we impose an upper limit redshift cutoff of z = 0.1.

We require that the S/N Hβ > 3, $\sigma_{R23} < 2$ and equivalent width of Hβ be greater than $4\mathring{A}$. Here, σ_{R23} is the error in the R23 parameter which is the sum of the flux in the [OIII]$\lambda 4959, 5007$ + [OII]$\lambda 3727$ divided by the Hβ flux. We find that the measured relation is not strongly dependent on the values adopted for these cuts and we select in this manner to be consistent with previous studies. In the selected sample, the median S/N of Hα and Hβ are 37 and 21, respectively.

Figure 5.1 shows the distribution of redshift, U−B color, absolute B-band magnitude and stellar mass for our selected sample. This particular selection gives us a pure star-forming galaxy sample in a narrow redshift range. It covers 2 orders of magnitude in stellar mass and has a color distribution consistent with blue star-forming galaxies.

5.2.2 Dwarf Galaxies Sample

Many measurements of metallicities of dwarf galaxies can be found in the literature. We use the samples of Lee et al. (2006, see references therein), Gil de Paz et al. (2003) and Peeples et al. (2008). Lee et al. (2006) extend the SDSS MZ relation by 2.5 decades in stellar mass. Their sample is taken from the literature and consists of 27 dwarf galaxies. Using the models of Bell & de Jong (2001), they derive masses from the $B - K$ color and scale them to a Chabrier (2003) IMF. In this study we use the 21 galaxies in the Lee et al. (2006) sample for which there are metallicities determined by the direct method and we adopt their stellar mass determination.

Gil de Paz et al. (2003) compile a sample of blue compact dwarf (BCD) galaxies. These galaxies are selected on basis of color, morphology and luminosity such that: $\mu_B - \mu_R < 1, \mu_B < 22$ mag arcsec^{-2} and $M_K > -21$ mag. Here, μ_B and μ_R are the peak surface brightness in B and R-band, respectively and M_K is the K-band magnitude. Zhao et al. (2010) investigate the LZ relation for blue compact dwarfs using B and R-band photometry from this compilation with additional K$_s$-band photometry obtained from

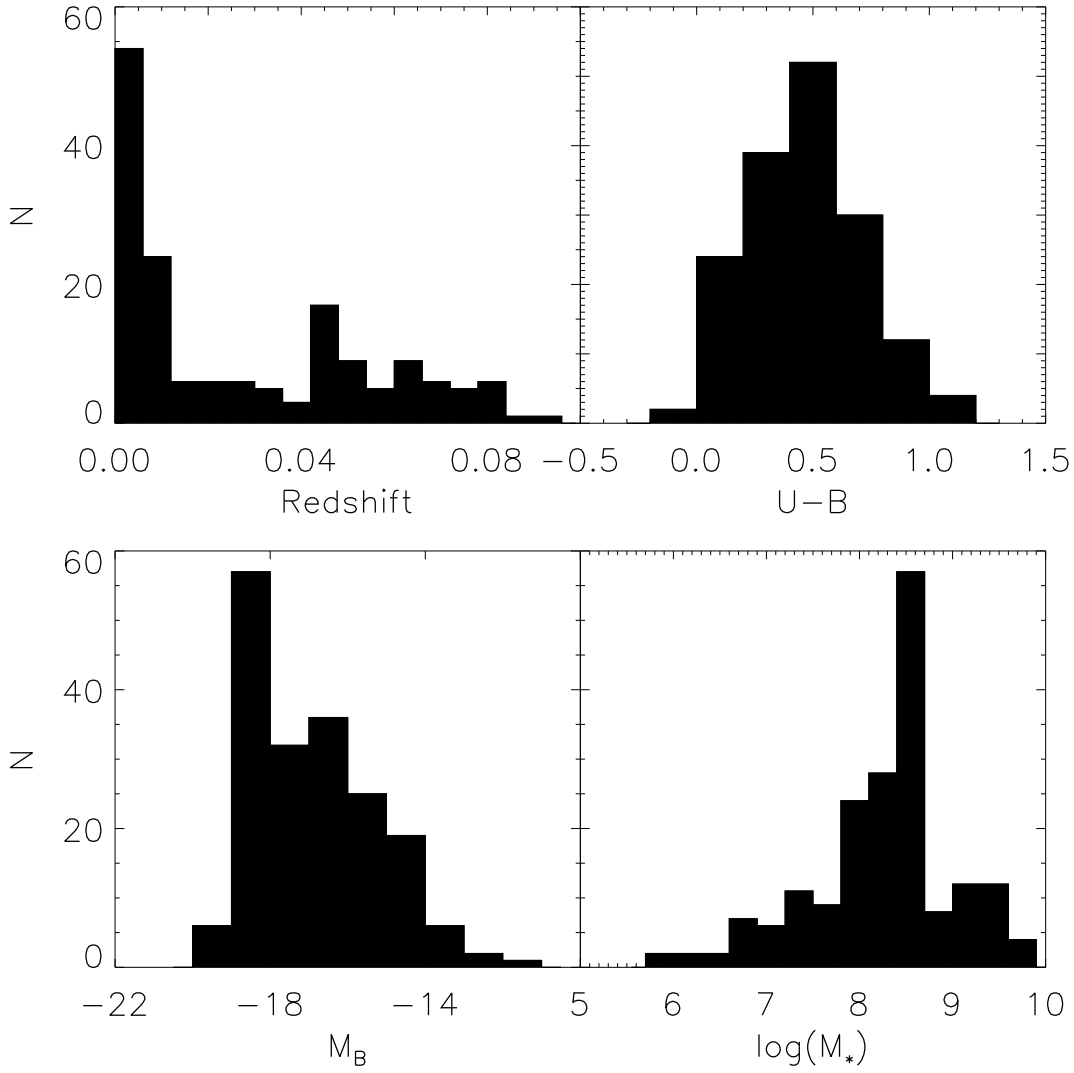

Figure 5.2 The distribution of redshift (top left), U−B color (top right), absolute B-band magnitude (bottom left) and stellar mass (bottom right) for our sample of dwarf galaxies. For the 21 dwarf galaxies from Lee et al. (2006) we do not have redshift or color data.

several sources (Jarrett et al. 2000; Noeske et al. 2003, 2005; Vaduvescu et al. 2007). We determine, for the first time, the stellar masses from the photometry as described in Section 5.3.2. Of the 80 galaxies in the Zhao et al. (2010) sample, we select 66 with detections of [OIII]λ4363, allowing for metallicities to be determined using direct method. Similar to Lee et al. (2006), the metallicities of the Zhao et al. (2010) sample are compiled from

the literature and may suffer from aperture effects. However, by comparing abundances measured from several different sources in a subsample of the galaxies, Zhao et al. (2010) conclude that the effect is small. Both these samples with metallicities determined from the direct method reveal a population of low mass, metal-poor galaxies (see Section 5.5.1).

Peeples et al. (2008) examine the outliers from the mass-metallicity relation. Their sample consists of 41 metal-rich dwarf galaxies from the SDSS. We use the Peeples et al. (2008) sample but adopt the flux values of Berg et al. (2011) for the four galaxies they reexamined. Given the strict selection criteria of Peeples et al. (2008), the "very low mass" sample of galaxies (which have $\log(M_*) \lesssim 9$) only consists of 17 galaxies. In order to investigate possible systematic effects in the determination of metallicities of low stellar mass galaxies, we supplement the Peeples et al. (2008) sample of 17 galaxies with 56 low mass, metal-rich galaxies taken from the SDSS sample described in Section 5.2.1. We refer to these 56 galaxies as the supplemental SDSS sample. These galaxies have stellar masses $<10^{8.8} M_\odot$ and have high metallicities determined by three different diagnostics, making them outliers from the SDSS MZ relation. We use several independent methods of metallicity determination (i.e. Yin et al. 2007; Kobulnicky & Kewley 2004; Kewley & Dopita 2002, see Section 5.3.1) in order to mitigate systematic effects that may result in overestimates of the metallicity with any one method.

Figure 5.2 shows the distribution of redshift, U−B color, absolute B-band magnitude and stellar mass for the dwarf galaxies sample.

5.2.3 The DEEP2 Sample

We probe significantly fainter objects than is possible with the SDSS by analyzing galaxies from the DEEP2 survey (Davis et al. 2003). This allows us to probe deeper to find low stellar mass objects otherwise not observed in shallow broadband surveys. The majority of galaxies in our parent sample come from observations of the Extended Groth Strip. The DEEP2 team used the DEIMOS multi-object spectrograph on the 10m Keck telescope to target galaxies in 4 fields covering 3.5 square-degrees down to a limiting magnitude of

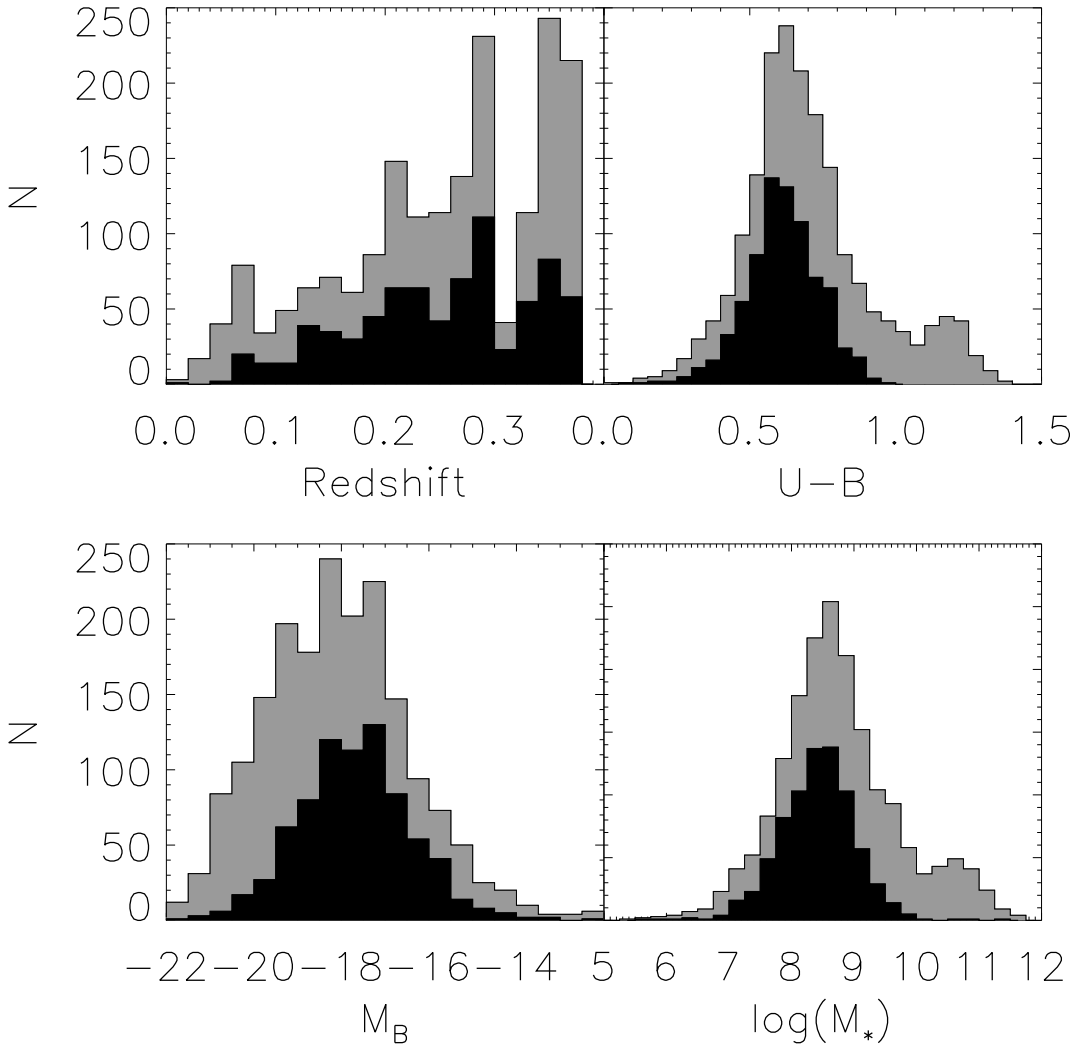

Figure 5.3 The distribution of the parent (grey histogram) and selected (black histogram) sample of galaxies from the DEEP2 survey. The redshift distribution (top left) of the selected sample is roughly consistent with the parent sample. Our selection picks out the bluer (top right), less luminous (bottom left) and less massive (bottom right) galaxies as compared to the parent sample.

$R_{AB} = 24.1$. They primarily target galaxies in the redshift range of $0.7 < z < 1.4$. In order to maximize efficiency of finding high redshift galaxies, a color preselection approximately given by: B-R $<$ 2.35$\times$(R-I) - 0.45, R-I $>$ 1.15, or B-R $<$ 0.5 was applied for galaxies in

fields 2-4. Galaxies in the Extended Groth Strip region (field 1) were targeted without a photometric redshift color pre-selection (Coil et al. 2004).

The moderately high-resolution (R$\sim$ 5000) spectra have a nominal spectral coverage of $6500 - 9100$Å. BRI-band photometry for these galaxies was obtained by the DEEP2 team using the CFH12K camera on the 3.6 m Canada France Hawaii Telescope (Coil et al. 2004) and for 54% of our selected sample of galaxies K_s-band photometry is available from the Hale telescope at Mt. Palomar (Bundy et al. 2006). In this study, we use the third release of the data[2].

In order to estimate metallicities, we use the [NII]λ6584 and Hα emission lines. These lines are observed in the DEEP2 data in the redshift range of $0 < z < 0.38$. We measure the uncalibrated flux of these emission lines by taking the area of a least-square gaussian fit. In many cases, the [NII] line can be very weak (S/N < 3), so we simultaneously fit two gaussians with a single gaussian line-width to both emission lines. We use the same method to measure the [SII]$\lambda 6717, 6731$ lines. We also measure the equivalent widths using the method outlined in the appendix of Zahid et al. (2011). The error in the fitted line flux and equivalent width comes from propagating the measurement uncertainties in the spectrum. The median signal-to-noise (S/N) in our sample for Hα is 22.

From the parent sample of 2,065 galaxies within the requisite redshift range, we select 777 galaxies for this analysis. In our selected sample, 695 are found in the Extended Groth Strip (field 1). By examining the photometric imaging, we find that 51 of the sources are star-forming knots in larger galaxies; these sources are removed from the sample. We select galaxies that have a reduced-χ^2 of the fit less than 2 and a S/N of Hα greater than 3. We also require that the 68% confidence interval of our stellar mass estimate be smaller than 0.3 dex. These selections remove 1172 galaxies from the parent sample. Initially, we apply no S/N cut on the [NII]λ6584 line in order to avoid biasing against low metallicity objects. We remove 5 galaxies from the sample that have log([NII]/Hα) greater than maximum star-forming ratio of -0.3 (e.g. Kewley et al. 2006). Following Weiner et al. (2007) who suggest

[2]http://deep.berkeley.edu/DR3/

that a substantial fraction of red emission line galaxies in the DEEP2 survey may be AGN contaminated, we remove 60 red galaxies using the blue and red galaxy color division for DEEP2 galaxies from Willmer et al. (2006).

Figure 5.3 shows the properties of the parent (grey histogram) and selected sample (black histogram). The redshift range of the parent and selected sample are comparable. Similar to our selection of SDSS galaxies, our selection of the DEEP2 data picks out the late-type blue star-forming galaxies which are generally less bright and less massive than early-type red galaxies. The U−B, M_B and mass distributions in Figure 5.3 reflects our selection.

5.3 Methods

5.3.1 Mass Determination

We estimate galaxy stellar masses by comparing photometry with stellar population synthesis models in order to determine the mass-to-light ratio which we use to scale the observed luminosity (Bell et al. 2003; Fontana et al. 2004). Magnitudes are synthesized from the stellar templates of Bruzual & Charlot (2003) and an IMF described by Chabrier (2003). The 27 models span seven exponentially decreasing star formation models (SFR $\propto e^{-t/\tau}$) with $\tau = 0.1, 0.3, 1, 2, 3, 5, 10, 15$ and 30 Gyrs and two metallicities (0.4 and $1Z_{\odot}$). The stellar population ages range from 0 to 13 Gyrs and we apply the extinction law of Calzetti et al. (2000) allowing E(B−V) to range from 0 to 0.6. The median statistical error for the derived stellar masses, determined from propagating the uncertainty in the photometry, is 0.15 dex. Though systematic effects can be significant (Drory et al. 2004; Conroy et al. 2009), in all the samples except for the 21 galaxies from Lee et al. (2006), we have consistently measured the stellar masses giving us a robust relative measure. The U and B-band absolute magnitudes for galaxies in the SDSS, DEEP2 and Zhao et al. (2010) samples are synthesized using this same procedure.

Emission line contributions are accounted for by taking the Kennicutt (1998) relation between the SFR and the UV luminosity which is synthesized as part of the mass determination procedure. In our sample, making no correction for the emission line contributions does not alter our mass determinations significantly. We adopt the median of the mass distribution and take the 68% confidence interval as a measure of the error. In Zahid et al. (2011) we compare this method with the one used by the MPA/JHU group to determine stellar masses of the SDSS galaxies. We find that the results differ by a constant offset of $\sim$0.2 dex and that the dispersion between the two methods is 0.14 dex.

5.3.2 Metallicity Determination

The galaxies used in this study are not homogeneously observed. We therefore require several methods for determination of metallicities which we discuss here. Furthermore, different systematic uncertainties are associated with the various methods of metallicity determination, so when possible we use several methods for the same galaxy in order to assess and mitigate these uncertainties (see Section 5.6.2).

Metallicities for the dwarf galaxies sample from Lee et al. (2006) and Zhao et al. (2010) are determined using the direct method (Section 5.3.2). For the SDSS and DEEP2 galaxies we determine metallicities using the empirically calibrated method of Yin et al. (2007, Section 5.3.2). To address systematic bias and uncertainties we apply both empirically and theoretically calibrated methods in determining the scatter in the metallicities of local star-forming galaxies from SDSS. We also derive empirical corrections for metallicities determined from the [NII]λ6584 using the empirically calibrated N/O ratio (Section 5.3.2 and Section 5.6.2).

Electron Temperature Method

The "direct" or electron temperature (T_e) method relies on measurements of the temperature sensitive auroral lines (e.g. [OIII]λ4363, [N II]λ5755). These lines provide tight constraints on the electron temperature and allow for straightforward determination

of the gas-phase abundance. The metallicities are calculated using the iterative scheme presented by Izotov et al. (2006). Due to temperature fluctuations and gradients, the O^+ and O^{2+} ions reside in different zones of the HII region. T_e([OIII]) is determined for the O^{2+} ion from the [OIII]λ4363 line and a linear conversion is applied to determine the temperature in the region of O^+, T_e([OII]). Contributions from higher ionization states are considered negligible and the gas-phase abundance is taken as the sum of the abundance in the two zones.

This method suffers from several drawbacks making its use impractical in many cases. The [OIII]λ4363 line is on the order of 100 times weaker than the strong oxygen emission lines (e.g. [OII]λ3727, [OIII]λ5007) observed in optical spectra thus necessitating high S/N measurements. In most cases, this method can only be applied to nearby galaxies where high S/N spectra are available. Due to efficient cooling of HII regions by metals, the line can only be observed in low metallicity HII regions (< 0.5 $Z_\odot$). Finally, in the presence of temperature gradients and fluctuations within HII regions, several authors have argued that the T_e method may lead to underestimates of the metallicity (e.g. Stasińska 2002, 2005; Bresolin et al. 2006; Peña-Guerrero et al. 2011), although recent work by Bresolin et al. (2009) and has shown good agreement between direct abundances of extragalactic HII regions and stellar metallicities for blue supergiants (see also Kudritzki et al. 2012).

Empirically Calibrated Method

Semi-empirically calibrated methods rely on calibrating strong-line ratios to metallicities determined from the combination of the T_e method along with detailed photoionization modeling. The [NII]λ6584 to Hα ratio is shown to be strongly correlated to gas-phase oxygen abundance. Pettini & Pagel (2004) have calibrated this ratio to nearby HII regions. They have parameterized the linear relation as

$$12 + \log(\mathrm{O/H}) = 8.90 + 0.57 \times N2 \tag{5.1}$$

where $N2 = \log([\mathrm{NII}]\lambda6584/\mathrm{H}\alpha)$. This relation is valid in the range of $-2.5 < N2 < -0.3$ and has 1σ intrinsic scatter of 0.18 dex.

The linear relation between $N2$ and metallicity parameterized by Pettini & Pagel (2004) is poorly constrained at metallicities below $12 + \log(\mathrm{O/H}) \sim 7.7$. Yin et al. (2007) place stronger constraints at lower metallicities on the relation between metallicity and $N2$ by using a sample $\sim$ 700 galaxies from the SDSS along with values found in the literature using only metallicities determined from the T_e method, thus providing a purely empirical calibration. They parameterize the linear relation as

$$12 + \log(\mathrm{O/H}) = 9.263 + 0.836 \times N2. \tag{5.2}$$

Their relation is valid in the range of $-2.5 < N2 < -0.5$ and has a 1σ intrinsic scatter of 0.16 dex. In this study, we are investigating low mass galaxies in the local universe and therefore find it desirable to have a metallicity diagnostic appropriately constrained at low metallicities. When determining metallicities from $N2$, we adopt the parameterization of Yin et al. (2007). In the appendix we compare this parameterization with Pettini & Pagel (2004) at low stellar masses.

Theoretically Calibrated Method

A third class of metallicity diagnostics relies solely on calibration of strong-line ratios using photoionization models. These methods are not susceptible to observational limitations imposed by empirical calibrations relying on the faint $[\mathrm{OIII}]\lambda4363$ line. Therefore, the model metallicities are well constrained and the parameterization is well defined over a broad range.

The methods of Kobulnicky & Kewley (2004) and Kewley & Dopita (2002) calibrate strong-line ratios to metallicities determined using photoionization models. Kobulnicky & Kewley (2004) rely on the $R23$ diagnostic, which is the sum of the flux of $[\mathrm{OII}]\lambda3727$, 3729 and $[\mathrm{OIII}]\lambda4959, 5007$ normalized to the Hβ flux. Though Kobulnicky & Kewley (2004)

apply explicit corrections for the ionization parameter variations, there still may be some systematic effects that are uncorrected. Therefore, we also use the Kewley & Dopita (2002) method which relies on the $N2O2$ ratio which is the [NII]λ6584 to [OII]λ3727, 3729 flux ratio. This diagnostic is shown to be independent of the ionization parameter. Finally, for the SDSS sample of galaxies we also use the Tremonti et al. (2004) method which relies on fitting theoretical models of integrated galaxy spectra to the most prominent optical lines. For a review of these methods, we refer the reader to the appendix of Kewley & Ellison (2008). We provide conversions between two commonly used $R23$ diagnostics and the direct method in the appendix of this paper.

Nitrogen to Oxygen Ratio

In order to investigate the effect of enhanced nitrogen enrichment with respect to oxygen, we measure the nitrogen abundance from emission line fluxes. N/O is empirically calibrated using star-forming galaxies in the SDSS with direct measurements of ionic abundances by Amorín et al. (2010). The calibration is given by

$$\log(\mathrm{N/O}) = -0.86 + 1.94 \times N2S2 + 0.55 \times N2S2^2, \tag{5.3}$$

where

$$N2S2 = \log\left(\frac{[\mathrm{NII}]\lambda 6584}{[\mathrm{SII}]\lambda 6717, 6731}\right). \tag{5.4}$$

[SII] is strongly correlated to [OII] and due to less uncertainty in the reddening correction, the relation between N/O and [NII]/[SII] shows less dispersion (~ 0.1 dex) than the relation between N/O and [NII]/[OII].

5.3.3 Ionization Parameter

The ionization parameter characterizes the level of ionization of the gas in an HII region. The ionization parameter is defined as

$$q = \frac{F_i}{n}, \tag{5.5}$$

where F_i is the flux of ionizing photons per unit area and n is the number density of hydrogen atoms. The ionization parameter has units of velocity and can be thought of as the maximum velocity attainable by an ionization front driven by the local radiation field. The ionization parameter can best be constrained observationally by comparing two ionization states of single species. A commonly used diagnostic for measuring the ionization parameter is the $O32$ parameter defined as

$$O32 = \log\left(\frac{[\mathrm{OIII}]\lambda 4959, 5007}{[\mathrm{OII}]\lambda 3727, 3729}\right). \tag{5.6}$$

However, Kewley & Dopita (2002) have shown that the [OIII]/[OII] ratio is not only dependent on the ionization parameter, but is also sensitive to metallicity.

Conversely, many of the strong line diagnostics are sensitive to the ionization parameter. One approach to disentangling the relationship between metallicity and the ionization parameter is to assign an initial guess of the metallicity in order to constrain the ionization parameter. Using this estimate of the ionization parameter, a second, more accurate estimate of the metallicity can be obtained. This process can be iterated until the values of both the ionization parameter and metallicity converge.

We measure the ionization parameter and metallicity using the Kobulnicky & Kewley (2004) diagnostic. This method uses the iterative scheme described above. The ionization parameter is determined from the $O32$ line ratio and the metallicity is determined from the

$R23$ line ratio, defined as

$$R23 = \log\left(\frac{[\mathrm{OIII}]\lambda 4959, 5007 + [\mathrm{OII}]\lambda 3727, 3729}{\mathrm{H}\beta}\right). \tag{5.7}$$

For details of how metallicity and ionization parameter are determined see the appendix of Kewley & Ellison (2008).

5.3.4 Star Formation Rates

The star formation rates (SFRs) for the SDSS samples were made available in the DR7. These SFRs are measured using the technique of Brinchmann et al. (2004) who empirically correct for aperture effects. Salim et al. (2007) found that in galaxies with low level star formation, the SFRs were overestimated using this technique. Salim et al. (2007) correct this overestimate and this has been applied to the SFRs provided in the DR7.

For the DEEP2 and Zhao et al. (2010) samples we use the conversion of Kennicutt (1998) to determine SFRs from Hα luminosities. This is given by

$$\mathrm{SFR}\ (\mathrm{M}_\odot\ \mathrm{yr}^{-1}) = 4.6 \times 10^{-42}\ \mathrm{L}_{\mathrm{H}\alpha}\ (\mathrm{ergs\ s}^{-1}), \tag{5.8}$$

where $\mathrm{L}_{\mathrm{H}\alpha}$ is the Hα luminosity and the pre-factor has been scaled down by a factor 1.7 to convert from a Salpeter (1955) to a Chabrier (2003) IMF. For the DEEP2 data we scale the uncalibrated Hα fluxes to the photometry and for the Zhao et al. (2010) sample, Hα luminosities are determined by Gil de Paz et al. (2003) from narrow-band Hα filter images. We correct for dust extinction in both these samples using the E(B$-$V) derived from the SED fit when determining stellar mass.

5.4 The SDSS MZ Relation and its Scatter

We determine the SDSS MZ relation from ∼20,000 galaxies with metallicities determined using the $N2$ method given by Equation 5.2. In Figure 10.1, we show the MZ relation and its

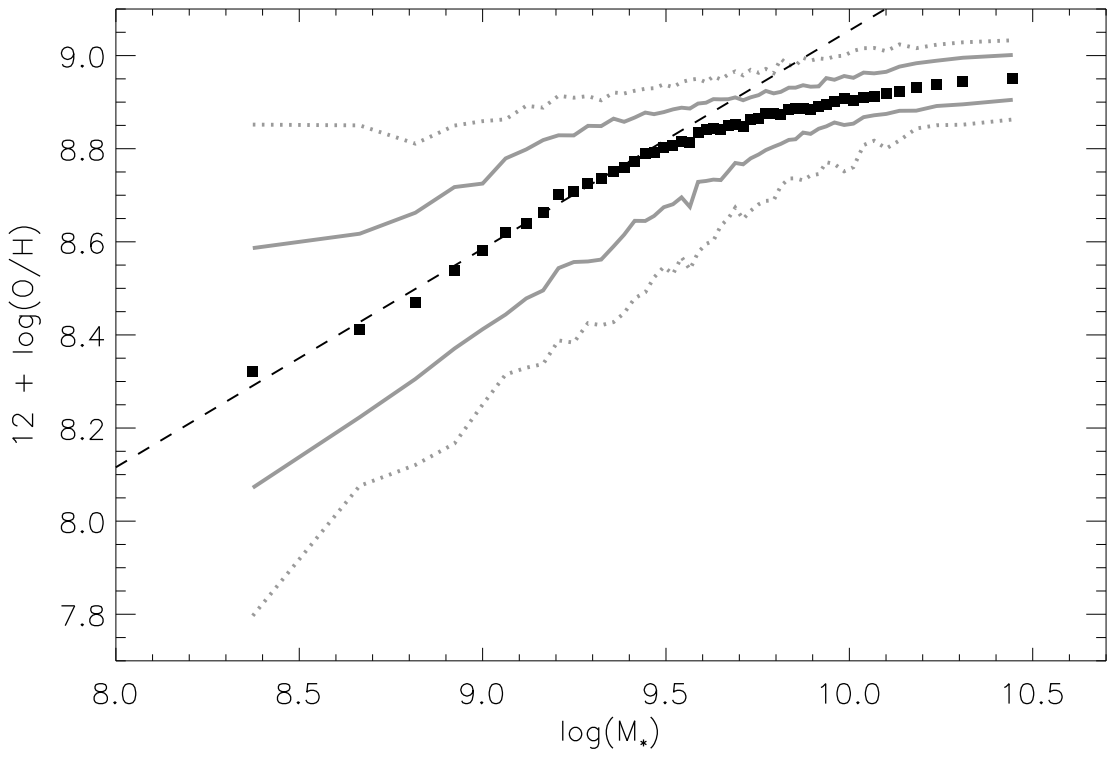

Figure 5.4 The mass metallicity relation for SDSS galaxies. The black squares are median metallicity in 50 bins of stellar mass determined from ∼20,000 galaxies in the SDSS. The dashed line is a fit to the linear portion of the MZ relation ($\log(M_*) \lesssim 9.4$). The solid and dotted gray curves are the 68 and 95 percent contours of the distribution.

scatter. We note that throughout this paper, when referring to the scatter in metallicities, we explicitly mean to refer to the range of observed metallicities at a fixed stellar mass. The relation is determined by sorting the data into 50 equally populated bins of stellar mass and taking the median mass and metallicity in each bin. The relation is plotted by the black squares and the scatter is shown by the solid and dotted grey curves which are the 68 and 95% contours of the distribution, respectively. For galaxies at a fixed stellar masses $< 10^{9.5} M_\odot$ the scatter is symmetric. At higher stellar masses, the distribution is skewed towards lower metallicity galaxies (with a skewness near -1). A large part of this skewness can be attributed to the saturation of strong-line methods at high metallicities (Kewley & Dopita 2002). Additional skewness may also be the result of a physical upper limit to the

metallicity attainable by a galaxy, though this is not well established and separating out these two effects is beyond the scope of this work.

The dashed line in Figure 10.1 is a linear fit to the data. The turnover observed in Figure 10.1 is due to a combination of a real turnover in metallicities as a function of stellar mass and saturation of the $N2$ parameter at high metallicities. We only fit to the linear portion of the SDSS MZ relation below the turnover ($12 + \log(\mathrm{O/H}) \lesssim 8.8$). The fit is performed by minimizing the square of the residuals and is parameterized as

$$12 + \log(\mathrm{O/H}) = (8.585 \pm 0.003) + (0.47 \pm 0.01) X_M. \tag{5.9}$$

Here, $X_M = log(M_*) - 9$ and M_* is the stellar mass in solar mass units. We fix the zero-point at a stellar mass of $10^9 M_\odot$ in order to reduce the covariance between the slope and intercept. The errors in the fit are assessed by bootstrapping the sample. We note that we consider this fitted MZ relation as the fiducial relation for later comparisons with the data.

Lee et al. (2006) examine the MZ relation for 27 low mass galaxies and conclude that the scatter is similar over five decades of stellar mass. However, using $\sim 20,000$ galaxies from SDSS (Figure 10.1), it becomes clear that the scatter increases substantially for lower stellar mass galaxies down to stellar mass of $\sim 10^{8.5}$ $\mathrm{M}_\odot$. We test whether the larger scatter at lower stellar masses is real or an artifact of the method used in determining metallicities. We examine the scatter as a function of stellar mass using several diagnostic methods of metallicity determination. We quantify the scatter in the MZ relation as the magnitude of the interval containing 95% of the data for a given stellar mass bin.

Figure 5.5 shows the scatter as a function of stellar mass for several diagnostics. Tremonti et al. (2004) determine the MZ relation from ∼50,000 galaxies in the SDSS. The solid black line is the scatter in their determination of the MZ relation. We have subtracted 0.2 dex from their mass determination for consistency with our measurements of stellar mass (Zahid et al. 2011). The green dot-dashed, red triple dot-dashed and blue dotted curves are the scatter for the MZ relation, with the Zahid et al. (2011) selection,

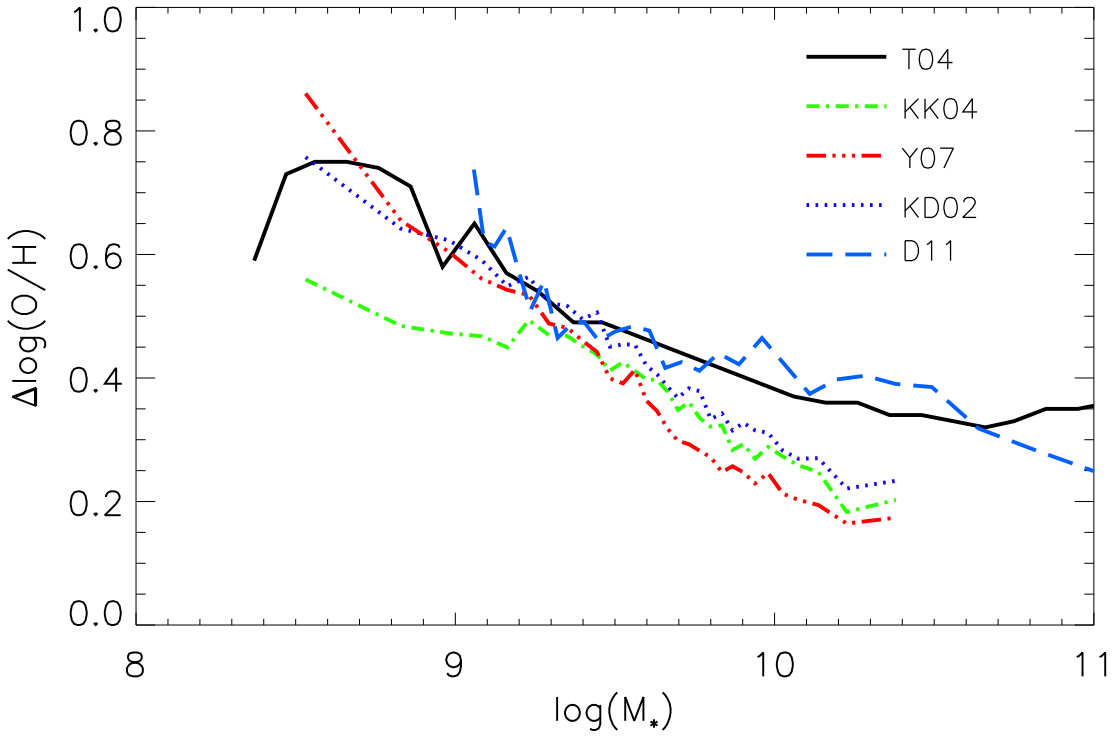

Figure 5.5 The width of the metallicity interval containing 95% of the data in each mass bin as a function of stellar mass for different metallicity diagnostics. The solid black line is the data taken from Tremonti et al. (2004). The dot-dashed green curve, triple dot-dashed red curve and the dotted blue curve are the Zahid et al. (2011) selected data with metallicities determined using the Kobulnicky & Kewley (2004), Yin et al. (2007) and Kewley & Dopita (2002) diagnostics, respectively. The blue long-dashed curve is the theoretical scatter from hydrodynamical simulations using a momentum conserving wind model (Davé et al. 2011b).

determined using the diagnostics of Kobulnicky & Kewley (2004), Yin et al. (2007) and Kewley & Dopita (2002), respectively. The blue long-dashed curve is the theoretical scatter determined from cosmological hydrodynamical simulations (Davé et al. 2011a, more details in Section 5.9).

Strong line methods, in particular diagnostics using $N2$, are known to saturate at high metallicities. This is partly responsible for the low scatter observed at high stellar masses for the MZ relations determined from the $N2$ diagnostic (red curve). However, the trend of decreasing scatter in the MZ relation is continuous and is observed across all stellar

masses, in particular at lower stellar masses where the strong-line diagnostics are not saturated. The mean relative errors in the $N2$, $N2O2$ and $R23$ line ratios used in the Yin et al. (2007), Kewley & Dopita (2002) and Kobulnicky & Kewley (2004) diagnostics are 0.02, 0.05 and 0.04 dex, respectively. The observational uncertainties of the $N2O2$ and $R23$ line ratios increase with stellar mass due to the diminishing line strength of the oxygen lines at higher metallicity. Even at high stellar masses, the observational uncertainties are substantially smaller than the observed scatter and we note that for SDSS galaxies, systematic uncertainties associated with strong-line methods dominate over the observational uncertainties (Kewley & Ellison 2008). In general, the magnitude of the observed scatter in Figure 5.5 is significantly larger than either the observational or systematic uncertainties and we attribute this to intrinsic scatter in metallicities of galaxies at a fixed stellar mass.

In Figure 10.1 we see that the reason the scatter is larger at lower stellar mass is due to the fact that the metallicity of the most enriched galaxies in any given stellar mass bin decreases with a much more shallow slope than the least enriched galaxies. When comparing the high mass end to the low mass end of the MZ relation in Figure 10.1, we see that the metallicities of the most enriched galaxies only decrease by $\sim$0.2 dex over 2 decades of stellar mass, whereas the metallicities of the least enriched galaxies decrease by $\sim$1 decade.

5.5 Metallicities of Low Mass Galaxies

In this section we extend our study of the scatter in the MZ relation to low mass galaxies. Because different methods have been applied in determining the metallicities of metal-poor and metal-rich galaxies, we present them separately in Sections 5.1 and 5.2, respectively.

5.5.1 Metal-Poor Dwarf Galaxies

We plot the mass and metallicity of the sample of dwarf galaxies taken from Lee et al. (2006) and Zhao et al. (2010) in Figure 5.6. The metallicities for this sample have been

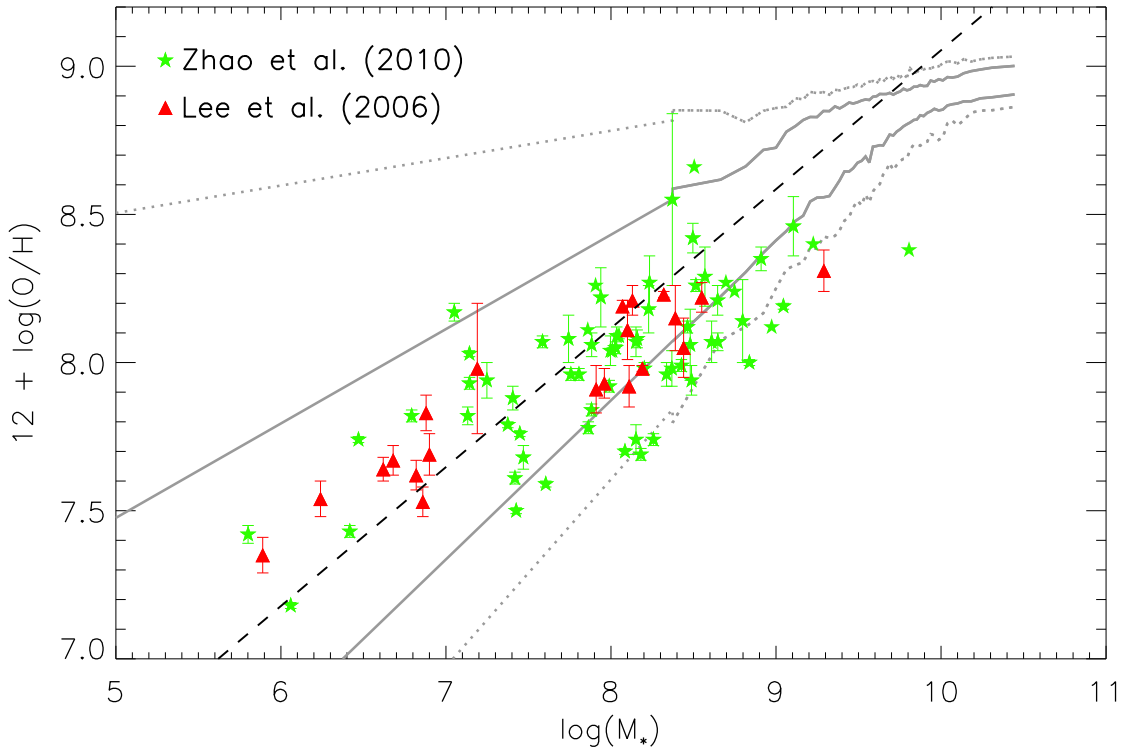

Figure 5.6 The MZ relation for 21 dwarf irregular galaxies(red triangles) from the sample of Lee et al. (2006) and 66 compact blue galaxies (green stars) from the sample of Zhao et al. (2010).

determined using the direct method (see Section 5.3.2). The fiducial MZ relation is plotted as the dashed line. In Figure 5.6 we linearly extrapolate the 68 (solid line) and 95% (dotted line) contours to lower masses by fitting the contours in the linear portion of the fiducial relation ($8.5 \lesssim \log(M_*) \lesssim 9.4$). We extrapolate the observed scatter to investigate whether at the low mass end the scatter is consistent with the expectation from the fiducial relation.

The slope of the MZ relation determined from this sample alone is 0.27 ± 0.02. The fit and error have been determined by a bootstrapping method. The slope differs significantly (9σ) from the slope of the fiducial relation (0.47 ± 0.01, see Equation 10.5) determined from the $N2$ method as shown in Figure 10.1. We note that the $N2$ method used in determining the fiducial relation is calibrated to be on the same absolute scale as the direct method. The metallicities of the 87 dwarf galaxies plotted in Figure 5.6 deviate strongly from the

distribution inferred from the SDSS MZ relation such that no low mass, metal-rich galaxies are observed. The smaller scatter observed in low stellar mass galaxies was noted by Lee et al. (2006).

The small scatter observed in these data could be a result of selection bias attributable to the direct method of metallicity determination. The [OIII]λ4363 line becomes too weak to observe at $\sim$0.5 $Z_{\odot}$ (12 + log(O/H)$\sim$8.5) and above. This is because the [OIII]λ4363 line strength is anti-correlated to metallicity, such that lower metallicity objects have stronger emission. These observational effects could lead to an artificial suppression of the scatter. In particular, the fact that all the galaxies in the sample have 12 + log(O/H) $\lesssim$ 8.5 and that the highest metallicity galaxy observed at a given stellar mass is a strong function of stellar mass likely results from observational biases associated with the direct method.

5.5.2 Metal-Rich Galaxies from SDSS and DEEP2

In Figure 5.7 we plot the masses and metallicities of the DEEP2 galaxies along with the sample from Peeples et al. (2008) and our supplemental SDSS sample. The metallicities for these galaxies are determined from the $N2$ calibration of Yin et al. (2007) given in Equation 5.2. For 31% (240/770) of the DEEP2 sample of galaxies [NII]λ6584 is not detected at a 3σ level. For these galaxies we adopt a 3σ upper limit value for [NII]λ6584 when determining the metallicity. The dashed line is the extension of the fit to the linear portion of the SDSS MZ relation as seen in Figure 5.6. The 68 (solid line) and 95% (dotted line) contours of the fiducial relation have been extrapolated for stellar masses below log(M_*) $\lesssim$ 8.5. The median observational uncertainty in the metallicities of the detected DEEP2 galaxies is 0.05 and for the Peeples et al. (2008) and SDSS supplemental sample it is 0.008 dex.

Opposite to the behavior of the [OIII]λ4363 line, the [NII]λ6584 line becomes stronger at higher metallicities. The fixed magnitude limit of the DEEP2 survey means that at lower stellar masses only the strongest [NII]λ6584 emitters will be be detected. This effect can be seen in Figure 5.7 where the lowest metallicity object observed at a given mass increases in metallicity with decreasing stellar mass. This is opposite to the observational

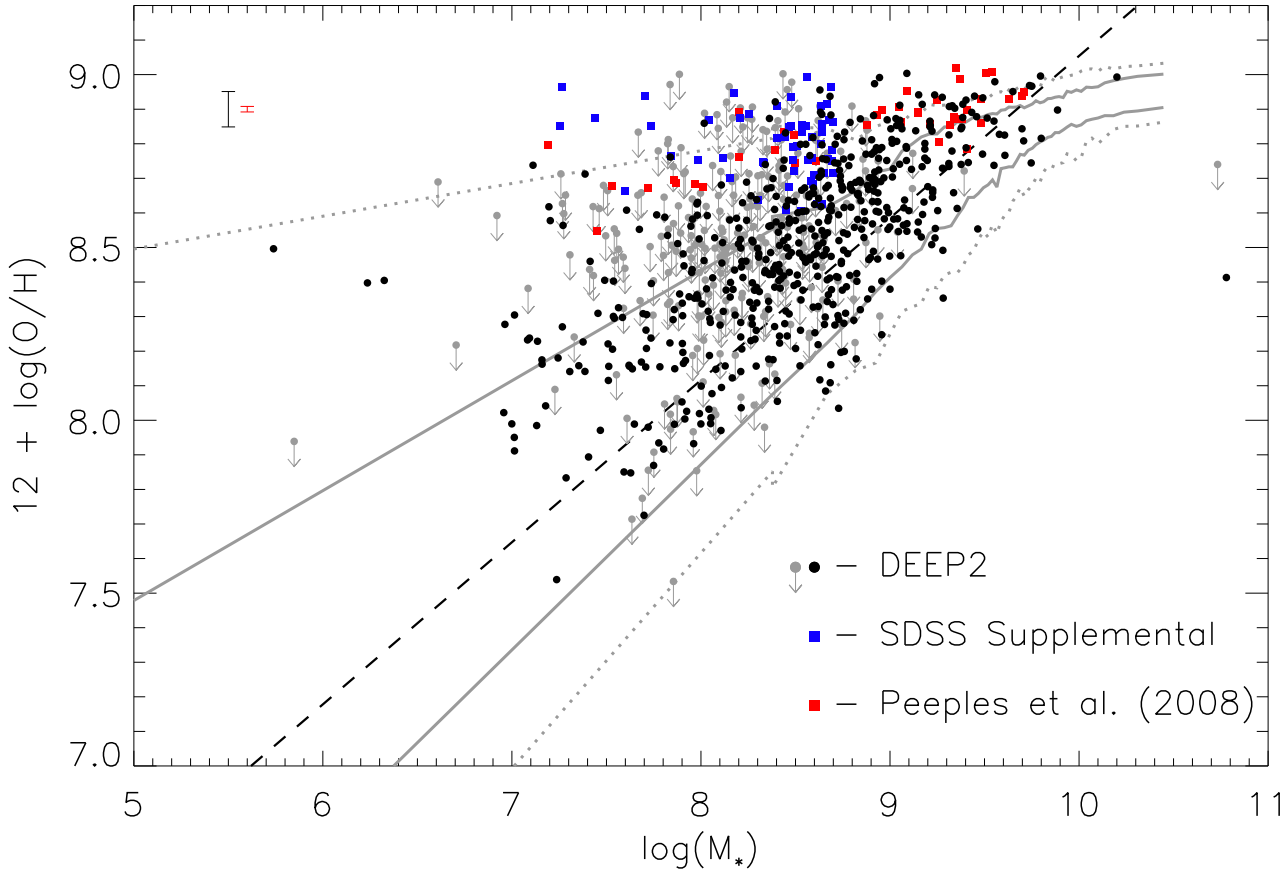

Figure 5.7 The mass and metallicity for our sample of metal-rich galaxies. The black points are 534 galaxies from the DEEP2 survey. The gray arrows are an additional 248 galaxies from DEEP2 where we only measure upper limits. These upper limits are determined by adopting a 3σ upper limit for non-detected [NII]λ6584. The red and blue squares are galaxies from the SDSS taken from Peeples et al. (2008) and our supplemental SDSS sample, respectively. The median error in the metallicities of the detected DEEP2 and SDSS sample of galaxies are 0.05 and 0.008 dex and are shown by the black and red error bars in the top left, respectively. The dashed line is the fit to the SDSS MZ relation take from Figure 5.6. The solid and dotted gray lines are the 68 and 95% contours of the SDSS MZ relation. The fit and contours have been extended down to lower masses by linearly extrapolating the contour from the linear portion of the SDSS MZ relation ($\log(M_*) \lesssim 9.4$).

bias present in the samples of Lee et al. (2006) and Zhao et al. (2010) which have direct method metallicities.

These data for the first time reveal a population of low mass, metal-rich galaxies down to stellar masses of $\sim 10^6$ $M_\odot$. By combining two methods in determining metallicity which have the opposite observational bias, we find a significantly higher scatter in the metallicities of low mass galaxies than previously reported. Because of incompleteness and sample bias, we cannot reliably determine the MZ relation or quantify its scatter at low stellar masses. In Section 5.7 we derive a lower limit for the observed scatter in the metallicities of low stellar mass galaxies.

5.6 Systematic Uncertainties in Mass and Metallicity

5.6.1 Stellar Mass Estimates

Our apparently low mass, metal-rich objects could be higher mass galaxies with systematically underestimated stellar masses. This could possibly result from heavy obscuration due to dust. For our sample of 94 metal-rich galaxies from SDSS, we determine the extinction from the Balmer decrement. The mean E(B−V) for our sample is 0.29 ± 0.12. We do not observe Hβ in our DEEP2 sample and therefore determine the extinction from the SED fit. The mean E(B−V) for our DEEP2 sample is 0.26 ± 0.16. Our metal-rich sample of galaxies have values of extinction consistent with star-forming galaxies in the local universe (e.g. Jansen et al. 2001) and are not found to suffer from heavy extinction. Moreover, our method for determining stellar masses corrects for extinction and we remove galaxies from our sample that have stellar mass estimates that have 68% confidence intervals > 0.3 dex.

The velocity dispersion of a galaxy has been shown to correlate with the stellar mass with some scatter (e.g. Kassin et al. 2007). Therefore, low velocity dispersion can be taken as an indication of low stellar mass. The line-of-sight velocity dispersion for the DEEP2 sample is given by Weiner et al. (2006) as

$$\sigma_{disp} = \frac{c}{\lambda_{obs}} (\sigma_{obs} - \sigma_{inst})^{1/2}, \tag{5.10}$$

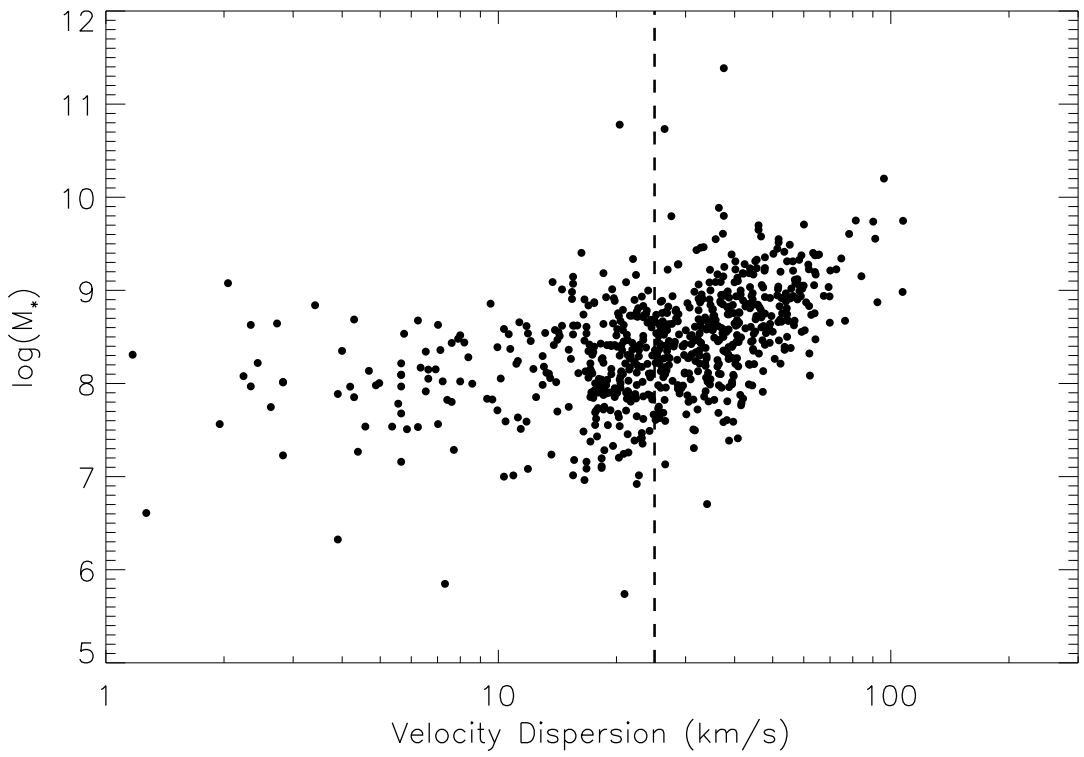

Figure 5.8 The stellar mass plotted against the velocity dispersion for our sample of DEEP2 galaxies. The velocity dispersion below 25 km/s (dashed line) has large errors due to instrumental resolution.

where σ_{disp} is the velocity dispersion given in km s^{-1}, λ_{obs} is the observed wavelength and σ_{obs} and σ_{inst} are the observed line width and instrumental resolution, respectively. For the DEEP2 sample, the velocity dispersion is primarily determined from the Hα emission line. For the DEEP2 data the instrumental resolution is 0.56Å (Weiner et al. 2006). The velocity dispersion becomes unreliable when $\sigma_{disp} > c\sigma_{inst}/\lambda_{obs}$ due to the fact that small errors in the line width translate to large errors in the velocity dispersion (Weiner et al. 2006).

Figure 5.8 shows that the stellar mass is correlated to the velocity dispersion, as expected. The median velocity dispersion of our DEEP2 sample is 26 km s^{-1}. Below $\sim$25 km s^{-1}, shown by the vertical dashed line, galaxies have unreliable determination of the velocity dispersion due to their small line widths but are still consistent with low stellar

masses. We are not able to perform the same comparison for our sample of galaxies from SDSS because of the lower instrumental resolution of that survey.

5.6.2 Metallicity Estimates

Recently, Berg et al. (2011) have reexamined four of the metal-rich galaxies from the sample of Peeples et al. (2008). Using new spectroscopic observations along with detailed comparisons with photoionization models, Berg et al. (2011) conclude that the metallicities of the four galaxies have been overestimated. They attribute this overestimate of the oxygen abundance to high N/O and to low ionization.

The Ionization Parameter

We gain a handle on the ionization level of the gas by examining the ionization parameter (see Section 5.3.3 for derivation). In Figure 5.9 we have plotted the ionization parameter as a function of stellar mass. The red points plot the sample from Peeples et al. (2008) with the four galaxies investigated by Berg et al. (2011) circled. For half of the Peeples et al. (2008) sample, the [OII] doublet is not observed. For these data we have used the [SII]λ6717, 6731 line as a proxy. The [SII] flux is strongly correlated to the [OII] flux owing to their similar ionization potential and primary origin. We derive a linear relation between the [SII] and [OII] dereddened line flux from $\sim$20,000 galaxies in the Zahid et al. (2011) sample and use this to infer the [OII] line flux when only [SII] is observed. The rms in the relation is 0.16 dex. These objects are shown by the red stars in Figure 5.9. The dashed black curve is the ionization parameter for the SDSS sample binned by stellar mass and the gray solid and dotted curves are the 68 and 95% contours, respectively.

We are not able to ascertain the distribution of ionization parameter for our DEEP2 sample due to inability to measure the same line at two ionization stages (e.g. [OII] and [OIII]). It may be that our sample of DEEP2 galaxies have low ionization, though this is not a general feature of low mass, metal-rich galaxies. Future observations may shed light on this issue.

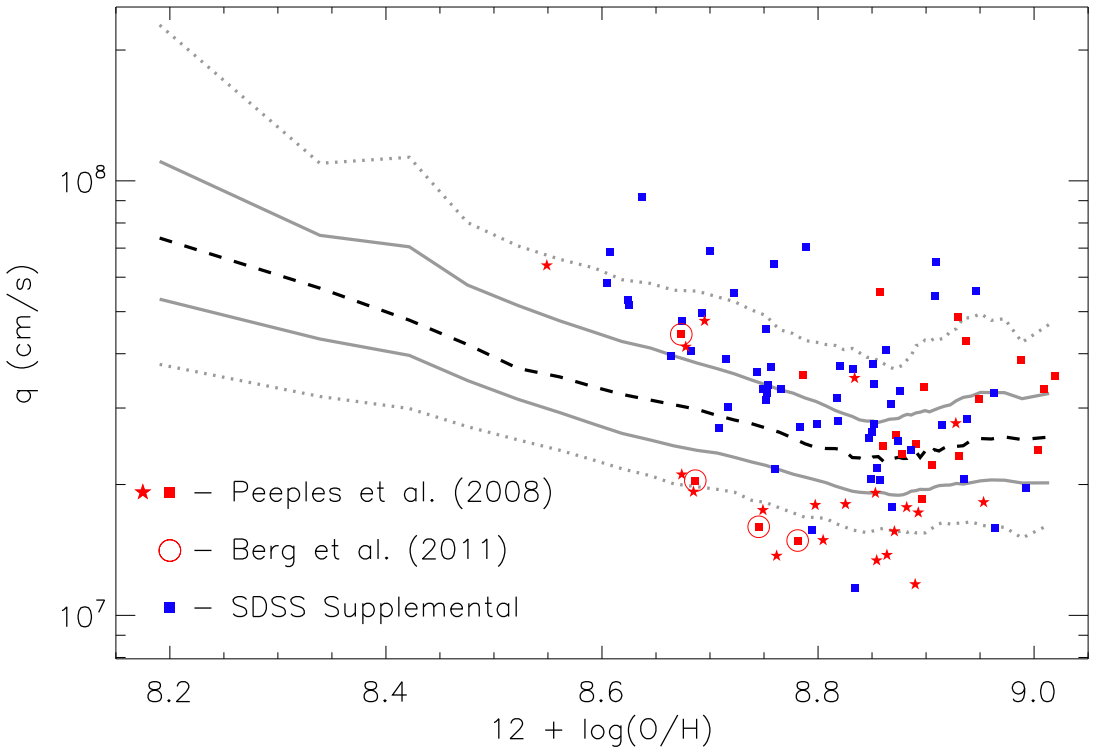

Figure 5.9 The ionization parameter plotted against stellar mass. The Peeples et al. (2008) sample for which [OII]λ3727, 3729 is observed is plotted by the red squares. When [OII] is not observed, we use [SII] as a proxy. These galaxies are plotted by red stars. The 56 galaxies comprising our supplemental sample are plotted by the blue squares. The $O32$ value for SDSS sample taken from Zahid et al. (2011) is plotted by the dashed line. The data is sorted into 50 bins of stellar mass and the median $O32$ value is taken in each bin. The 68 and 95% contours of the data are plotted by the solid and dotted gray curves.

Consistent with the findings of Berg et al. (2011), we find that three of the four galaxies that they investigated have ionization parameters that are lower than the larger SDSS sample. However, many of the galaxies in the supplemental SDSS sample (blue points) and the sample of Peeples et al. (2008, red points) appear to have ionization parameters consistent with the larger SDSS sample from Zahid et al. (2011). This suggests that though low ionization may be an issue for some of the low mass, metal-rich galaxies, it is not generally the case.

Empirical Correction for Nitrogen Enhancement

For our metal-rich sample we use the [NII]λ6584 line to measure the oxygen abundance. Nitrogen is known to have a primary component, formed mostly in massive stars, and a secondary component, formed in low and intermediate mass stars. Oxygen on the other hand is a primary element. Oxygen abundances inferred from $N2$ line ratio are known to depend on nitrogen to oxygen ratio (N/O) (Storchi-Bergmann et al. 1994; Denicoló et al. 2002; Pérez-Montero & Contini 2009). The secondary production of nitrogen is dependent on the amount of oxygen already present in the star through the CNO cycle, producing a larger N/O at higher metallicity. Similarly, this dependence leads to a low dispersion in the N/O ratio at low metallicities (Edmunds & Pagel 1978; Alloin et al. 1979) with the dispersion increasing at higher metallicities (Pérez-Montero & Contini 2009).

We determine N/O using Equation 5.3. For the DEEP2 sample we do not have flux calibrated data, so we substitute in the equivalent widths of [NII] and [SII] lines when determining $N2S2$. Kobulnicky & Phillips (2003) and Zahid et al. (2011) have demonstrated that substituting equivalent widths for line fluxes when measuring line ratios does not introduce significant errors. Figure 5.10 shows the N/O plotted as a function of stellar mass. The nitrogen abundances of the Peeples et al. (2008) and supplemental SDSS samples are elevated relative to the DEEP2 sample. This is consistent with the generally higher metallicities of the Peeples et al. (2008) and supplemental SDSS samples as compared to the DEEP2 sample (see Figure 5.7) and due to metallicity dependency of secondary production, an independent measure of these galaxies having high metallicities.

We derive an empirical correction for enhanced nitrogen abundance by comparing the difference between direct method metallicities with those measured using the strong line method. We select all star-forming galaxies in the SDSS sample that have S/N $>$ 5 detections of [OII]$\lambda 3727, 3729$, [OIII]$\lambda 4363, 4959, 5007$, Hβ and [SII]$\lambda 6717, 6731$. There are 627 galaxies that meet this criteria. We measure the oxygen abundance using the strong line calibration of Yin et al. (2007), the direct method as parameterized by Izotov et al. (2006) and N/O using the calibration of Amorín et al. (2010). In Figure 5.11 we plot the

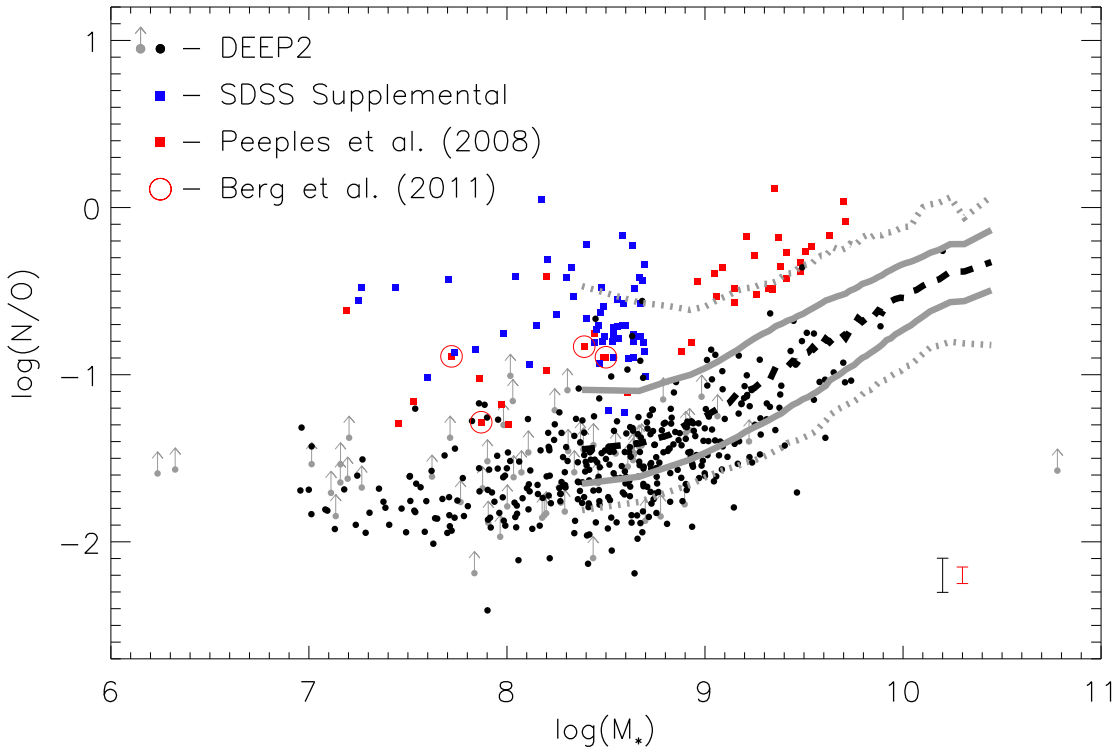

Figure 5.10 N/O plotted as a function of stellar mass. The black points are 373 galaxies from the DEEP2 sample. For 59 galaxies in the DEEP2 sample, we observe [SII] with S/N < 3. For these galaxies we have adopted a 3σ limit for the [SII] EW. These data give a lower limit for N/O and are plotted by the gray arrows. The red and blue squares are the Peeples et al. (2008) and our supplemental sample, respectively. The four galaxies circled are the ones reexamined by Berg et al. (2011). The median error for the nitrogen abundance of 0.1 and 0.05 dex for the DEEP2 and SDSS sample are shown by the black and red error bar in the bottom right corner, respectively.

difference in metallicity between the strong line method and the direct method as a function of N/O. The strong line method increasingly overestimates the metallicity with respect to the direct method as a function of N/O for this sample.

We have determined the errors in $\Delta\log(\mathrm{O/H})$ by adding in quadrature the errors from the strong line and direct method metallicities. The median error in $\Delta\log(\mathrm{O/H})$ and N/O is 0.09 and 0.03 dex, respectively. The direct method metallicities dominate the errors in $\Delta\log(\mathrm{O/H})$ owing to the weakness of the [OIII]λ4363 line. We fit a linear

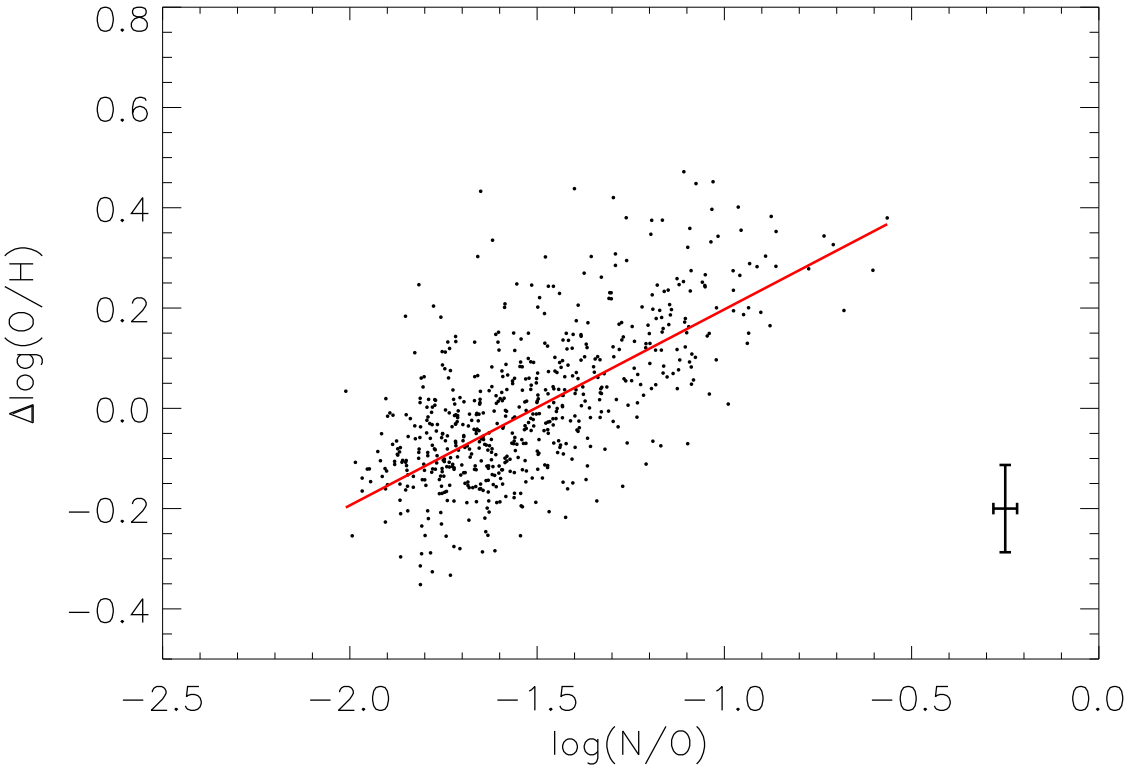

Figure 5.11 The difference in metallicity between the strong line method and the direct method plotted against N/O. The sample is 627 galaxies from the SDSS DR7 with emission lines of interest detected with a S/N > 5. The red line is a linear fit to the data taking into account errors in both coordinates. The median error in the metallicity difference and N/O is 0.09 and 0.03 dex, respectively.

relationship to the data using the MPFITEXY routine which takes into account errors in both coordinates (Williams et al. 2010). The MPFITEXY routine depends on the MPFIT package (Markwardt 2009). The linear fit is given by

$$\Delta\log(\mathrm{O/H}) = (0.64 \pm 0.03) + (0.42 \pm 0.02) \times \log(\mathrm{N/O}) \tag{5.11}$$

and is plotted by the red line in Figure 5.11. The rms of the fit to the data is 0.11 dex, with 0.07 dex attributable to the observational uncertainties.

Correction Overestimates

In making the correction for N/O, we have assumed that the direct method provides the most reliable metallicity estimate and therefore have corrected our strong line metallicities. We offer some words of caution in making this type of correction. The correction has been derived as a function of N/O. The galaxies used in deriving the empirical correction mostly lie in the region between $-2.0 < \log(\mathrm{N/O}) < -1.0$ (see Figure 5.12). We have extrapolated the correction for galaxies with $\log(\mathrm{N/O}) > -1.0$, where most of the galaxies from the Peeples et al. (2008) and our supplemental SDSS sample lie.

In applying this correction, we have assumed that the direct method provides the most reliable metallicity measure. However, temperature fluctuations and gradients in HII regions may lead to underestimates of the metallicity with the direct method (Stasińska 2002, 2005; Bresolin et al. 2006). The [OIII]λ4363 line strength increases with temperature. In the presence of fluctuations or gradients the inferred temperature may be biased towards higher temperatures in which case it would not be representative of the HII regions, especially in global spectra (Kobulnicky et al. 1999).

5.7 Scatter in MZ Relation at Low Masses

In Figure 5.12 we apply our derived empirical correction for enhanced nitrogen enrichment to the data. Even with the correction for enhanced N/O, low mass, metal-rich galaxies remain. The empirical correction for N/O brings the metallicities of the four galaxies investigated by Berg et al. (2011) down to $12 + \log(\mathrm{O/H}) \sim 8.4$-$8.5$ (circled galaxies in Figure 5.12). The low ionization in three of the four galaxies would further reduce the metallicity estimate. Berg et al. (2011) conclude that the metallicities of their four galaxies probably lie in the range of $7.9 < 12 + \log(\mathrm{OH}) < 8.4$. Our analysis supports this conclusion. However, the same analysis applied to the rest of the galaxies in this study also supports the conclusion that *not all of the low mass, metal-rich galaxies have overestimated metallicities.*

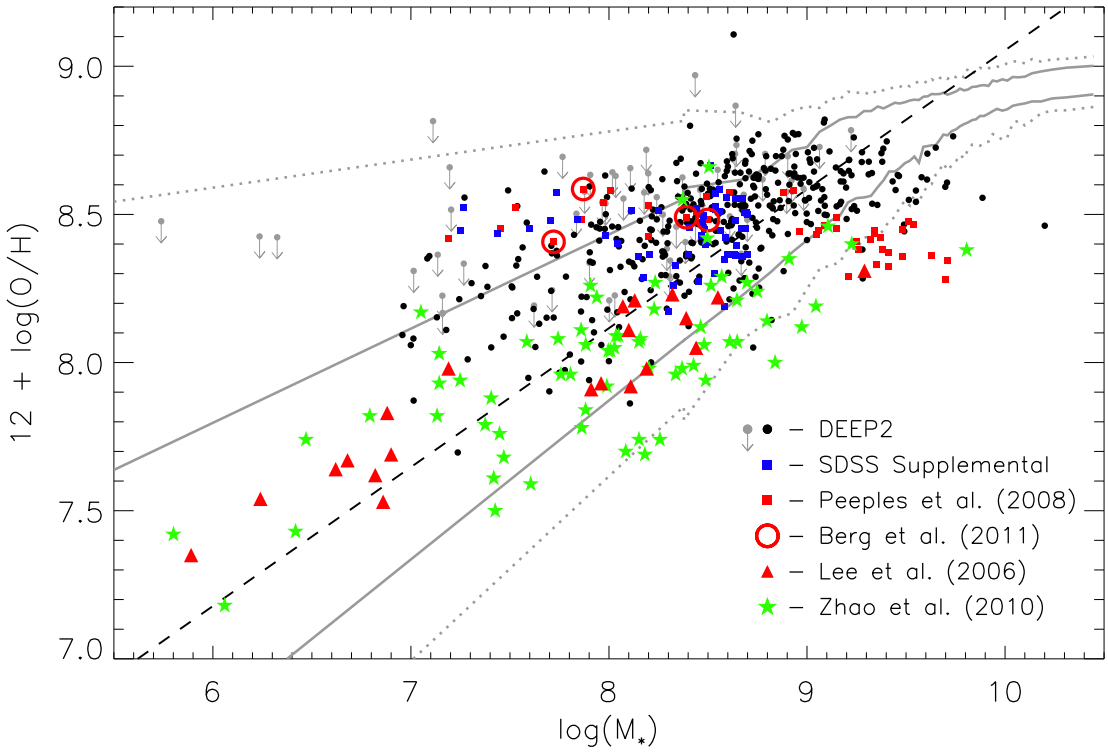

Figure 5.12 The metallicity plotted against stellar mass. For the DEEP2 (black dots and gray arrows), Peeples et al. (2008, red squares) and supplemental (blue squares) sample we have determined metallicities using the $N2$ diagnostic. We apply an empirical correction to these data for enhanced nitrogen enrichment given in Equation 5.11. We also plot the samples of Lee et al. (2006, red triangles) and Zhao et al. (2010, green stars) for which metallicities have been determined using the direct method.

For galaxies above $10^9\,M_\odot$, Figure 5.12 suggests that we may be overcorrecting for N/O. Because of this potential overcorrection and the fact that the sample is incomplete, the scatter at low stellar masses could only be *larger* than what we observe. We consider Figure 5.12 to display a lower limit to the intrinsic scatter in metallicities as a function of stellar mass. The observed scatter down to 10^7 $M_\odot$ is only slightly lower than what is inferred from the SDSS MZ relation.

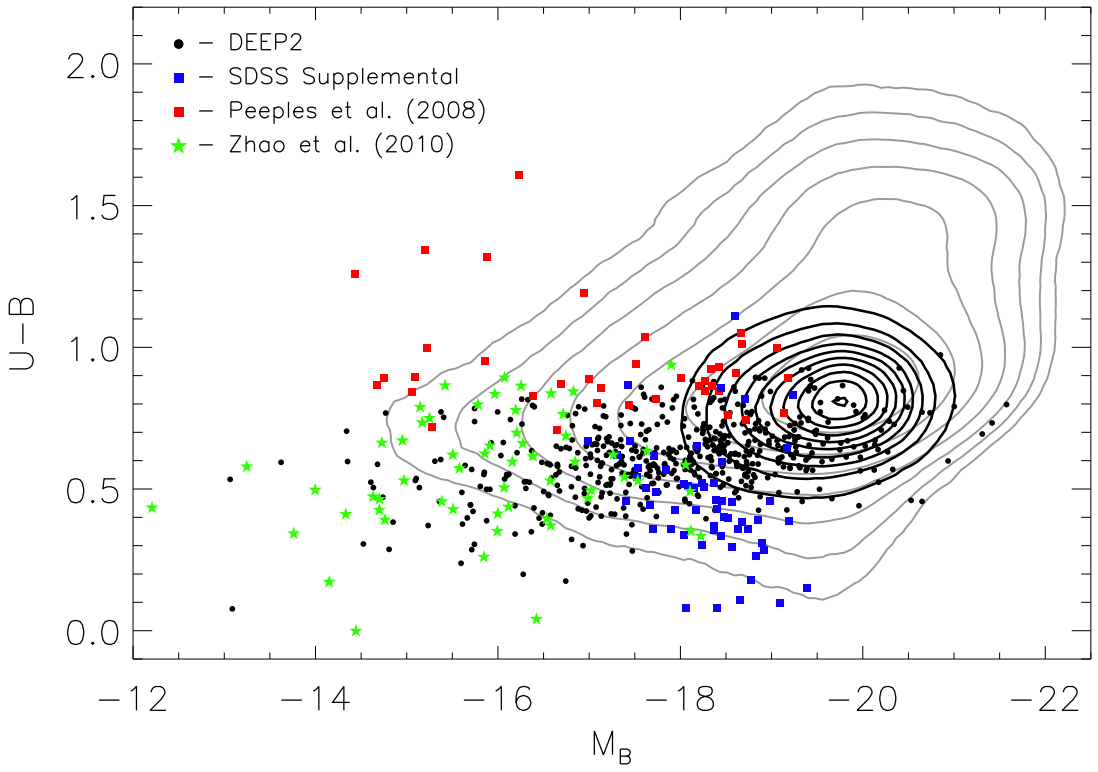

Figure 5.13 The color-magnitude diagram of our sample of galaxies. The DEEP2 and Zhao et al. (2010) sample are plotted in black dots and green stars, respectively. The Peeples et al. (2008) and supplemental low mass, metal-rich sample from SDSS are plotted by the red and blue square, respectively. The black contours are for the main SDSS sample of star-forming galaxies taken from Zahid et al. (2011). The gray contours for $\sim 200,000$ galaxies in the SDSS.

5.8 Physical Properties

We explore some of the physical properties of the low mass galaxies and compare them with typical galaxies in the SDSS sample to understand their physical nature.

5.8.1 Galaxy Colors, SFRs and Equivalent Widths

The color-magnitude diagram is shown in Figure 5.13. The low mass galaxies have lower luminosities than the main sample of SDSS galaxies (black contours) and tend to be slightly bluer in color. The Peeples et al. (2008) galaxies (red squares) appear to be the reddest

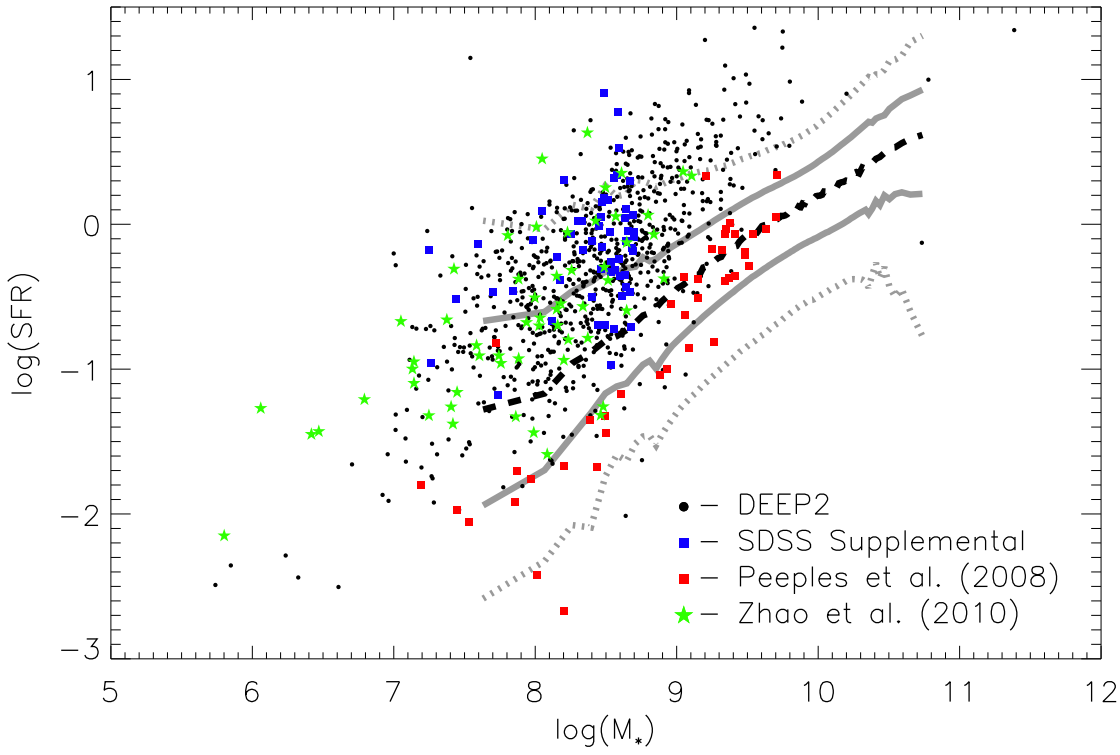

Figure 5.14 The SFR plotted as a function of stellar mass. The DEEP2 and Zhao et al. (2010) sample are plotted in black dots and green stars, respectively. The Peeples et al. (2008) and supplemental low mass, metal-rich sample from SDSS are plotted by the red and blue square, respectively. The black dashed curve is the median SFR in 100 bins of stellar mass for $\sim 140,000$ star-forming galaxies in the SDSS. The 68 and 95% contours are shown by the solid an dotted gray curves, respectively

galaxies of all the samples. The metal-rich galaxies from the DEEP2 survey and the supplemental sample from SDSS appear to have colors that are consistent with the galaxies from the sample of Zhao et al. (2010), which are blue compact dwarf galaxies selected on the basis of their color. The gray contours are for $\sim 200,000$ galaxies from SDSS selected to be non-AGN using the BPT diagram and have $z < 0.1$. The red sequence is shown by the locus of galaxies in the top right of the figure. Some of the galaxies of Peeples et al. (2008) have colors consistent with the red sequence, supporting the conclusion that these are transitionary objects.

In Figure 6.4 we examine the SFRs as a function of stellar mass. High mass galaxies tend to have higher SFRs. The SFRs of Peeples et al. (2008) sample generally are lower than the other samples, consistent with their redder colors. The distribution of SFRs for the DEEP2, Zhao et al. (2010) and supplemental SDSS samples appear to be similar. The black dashed curve is the SFRs for $\sim 140,000$ star-forming galaxies in the SDSS sorted into 100 stellar mass bins. These data are selected to have a S/N>5 in Hα and Hβ, $z < 0.1$ and are required to be classified as star-forming in the BPT diagram. In general, the data used in this study appeare to be biased towards higher SFRs relative to the local galaxies from SDSS. For the DEEP2 data, this is partly a result of redshift evolution in the SFRs as these data have $z \lesssim 0.4$. This plot illustrates some of the bias in the samples used in this study. A more complete sample is required to probe galaxies with lower SFRs.

In Figure 5.15 we plot the metallicities of our galaxies against the equivalent width of Hα (EW Hα). Here we have not applied our correction for elevated N/O as this may be an overestimate and does not affect the interpretation. The EW Hα is a measure of the Hα line flux divided by the underlying continuum. The flux of Hα is a proxy of star formation and the underlying continuum is dominated by the emission of the older, low and intermediate mass stars. This population probed by the underlying continuum of Hα dominates the stellar mass of a galaxy. The EW Hα represents a measure of the amount of star formation normalized to stellar mass and therefore changes with time. We choose to plot EW Hα instead of specific star formation rate because it is a directly observable quantity and is not subject to the uncertainties in stellar mass and star formation rate. There appears to be a trend in each of the samples separately such that galaxies with lower EW Hα tend to have higher metallicities.

5.8.2 Physical Nature of Low Mass Galaxies

The blue colors observed the low mass galaxies are typical of dwarf galaxies. Schombert et al. (1995) find that their sample of dwarf spiral galaxies have colors that are bluer than the normal early-type spirals despite their low star formation rates (see also Hidalgo-Gámez

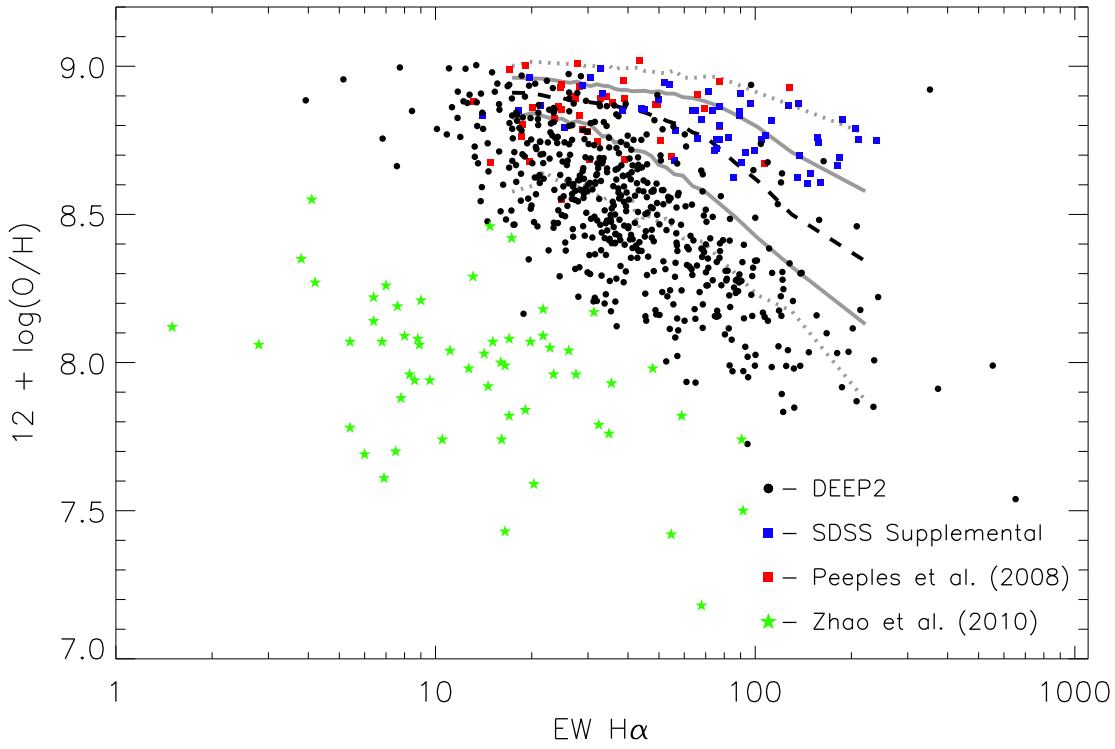

Figure 5.15 The metallicity as a function of the equivalent width of Hα (EW Hα). The DEEP2 and Zhao et al. (2010) sample are plotted in black dots and green stars, respectively. The Peeples et al. (2008) and the supplemental low mass, metal-rich sample from SDSS are plotted by the red and blue square, respectively. The median metallicity in 50 bins of EW Hα for the SDSS sample taken from Zahid et al. (2011) is plotted by the dashed black curve. The 68 and 95% contours are shown by the solid an dotted gray curves. The equivalent width is observed to strongly decrease with increasing metallicity.

2004). These colors are also consistent with those observed in quiescent gas-rich dwarf galaxies (van Zee et al. 1997). Peeples et al. (2008) sample of galaxies are, in general, the reddest galaxies. This is consistent with the lower SFRs observed in those galaxies.

Blue colors are a general property observed in star-forming galaxies. Blue colors imply a population of young, high mass stars which tend to dominate the luminosity output of a galaxy. The fact that blue colors are observed in these dwarf galaxies even though many exhibit low levels of star formation as inferred from the Hα line luminosity suggests that even low levels of localized star formation in low stellar mass systems can dominate the

color. Peeples et al. (2008) observe that many of their galaxies are dominated by blue cores. In the supplemental SDSS sample, a few galaxies also have blue cores, though in the majority of galaxies star formation appears to be more widespread.

One of the most interesting features of our sample of galaxies is the relation between metallicity and EW Hα as seen in Figure 5.15. A similar trend is observed in the DEEP2, SDSS and Zhao et al. (2010) sample such that the highest metallicity objects in each sample have the lowest EWs. However, though the three samples have a similar range in EWs, they are somewhat segregated in metallicity such that they cluster into what appears to be distinct populations. In Figure 5.15, there appears to be a continuum between the DEEP2 and SDSS data, but a gap in metallicity between the Zhao et al. (2010) sample. We hypothesize that a complete census of low mass galaxies cover the full range of observed metallicities and EW Hα.

The low and high metallicity sample of galaxies investigated in this study have similar masses, colors, SFRs and EW Hα. This implies that these galaxies likely have similar stellar populations. Under this assumption, the most straight-forward interpretation of Figure 5.15 would be that the differing metallicities in the samples is due to the gas content of the galaxies, such that the lower metallicity galaxies at a given EW Hα are more gas rich. This is consistent with the interpretation of Dellenbusch et al. (2007) and Peeples et al. (2008).

5.9 Discussion

Understanding and quantifying the scatter in the MZ relation is crucial to uncovering the origin of the MZ relation. Observations of low mass, metal-rich galaxies help shed light on this issue but also present us with a recently discovered population of galaxies requiring further investigation and characterization.

The MZ relation at low stellar masses has only been studied by a few authors (Tamura et al. 2001; Lee et al. 2006; Vaduvescu et al. 2007; Petropoulou et al. 2011). These studies

have been hampered by a small number of observations owing to the faintness of low stellar mass galaxies and selection biases. Lee et al. (2006) conclude that MZ relation extends to lower metallicities with no increase in the scatter. We have shown that the scatter in the MZ relation increases substantially ($\sim$0.4 dex) over the 2 decades of stellar mass observed in the SDSS MZ relation (Figure 5.5).

By examining data from the DEEP2 and SDSS surveys, we are able to identify low mass, metal-rich galaxies that appear to be consistent with the increasing scatter implied by the SDSS MZ relation (Figure 10.1). The observations of low mass, metal-rich galaxies challenge the notion that the MZ relation extends to low stellar masses with no increase in the scatter as found by Lee et al. (2006). Furthermore, given their low stellar masses and shallow potential wells implied by the velocity dispersion (see Figure 5.8), it is difficult to understand these galaxies in the context of the canonical explanation for the MZ relation which argues that shallow potential wells in lower mass galaxies prevent them from enriching due to loss of metals through galactic scale outflows (e.g. Tremonti et al. 2004).

The MZ relation is observationally well established in both the local (e.g. Tremonti et al. 2004) and high redshift universe (e.g. Erb et al. 2006; Mannucci et al. 2009). The MZ relation shows that the median (or mean) metallicity of star-forming galaxies increases as a function of stellar mass. Our results suggest that in the local universe this is largely driven by a more rapid decline in the metallicity of the most metal-poor galaxies relative to metal-rich galaxies at lower stellar masses (see Figure 5.7 or 5.12). This observed trend puts stronger constraints on theoretical chemical evolution models attempting to reproduce the MZ relation.

In Figure 5.5, we have compared the scatter in the MZ relation from several diagnostics with the theoretical scatter taken from the smoothed particle hydrodynamical simulations of Davé et al. (2011a,b). Davé et al. (2011a) investigate the MZ relation using several prescriptions for winds. Their simulations include a no wind model, two constant wind models (with velocities of 340 and 680 km s^{-1}) and a momentum driven wind such that the wind speed scales with the velocity dispersion of the galaxy. The constant wind models

have considerably higher scatter at low stellar masses than the observations and the no wind model generally shows less scatter than the observations. The momentum driven wind model best characterizes the observational data and the scatter predicted by this model is shown in Figure 5.5. The overall normalization is a free parameter in the models but in addition to the scatter, the shape and slope of the local MZ relation (from Tremonti et al. 2004) are also well fit by this model (Davé et al. 2011a, see their Figure 1). The predicted scatter in the models deviates most strongly at lower stellar masses. Therefore, the scatter in the MZ relation at lower masses will provide important tests for theoretical models of chemical evolution. However, current simulations (e.g. Davé et al. 2011a,b) do not resolve galaxies with stellar masses below $10^9\,M_\odot$ and we await higher resolution simulations to make this comparison.

From their simulations, Davé et al. (2011a) argue that galaxies evolve around an equilibrium MZ relation. Large scale gas flows perturb galaxies from equilibrium and the scatter in the MZ relation is a quantitative measure of the time it takes to return to equilibrium which, in their simulations, is reestablished through infall of gas. They argue if the dilution time of the gas (gas mass divided by inflow rate) is small compared to the dynamical time of the galaxy (at the virial radius), then the scatter will be small. Within this framework, our observations suggest that the timescales for galaxies to equilibrate once they are perturbed are longer at lower stellar masses (i.e. the dilution time is longer than the dynamical time at lower stellar masses).

In the local universe, the SFRs of star-forming galaxies are (anti-)correlated to the metallicity in the sense that the higher metallicity objects at a given stellar mass have lower SFRs (Ellison et al. 2008; Mannucci et al. 2010; Davé et al. 2011a). For our low mass samples, this trend is only weakly present in the data (see Figure 6.4). Specifically, the scatter in the MZ relation at low stellar masses can be *slightly* reduced if SFRs are accounted for in the manner presented in Mannucci et al. (2010). However, the SDSS supplemental sample and some of the DEEP2 galaxies appear to have both high metallicities and SFRs, inconsistent with the observed trend at higher stellar masses. The full implication of this

correlation is still not well understood, though it is probably related to the gas content which regulates both the gas-phase abundance and the SFR. The fact that this effect is relatively weak in lower mass galaxies suggests that the relative contribution of various physical mechanisms governing the metallicities of low mass galaxies may differ from higher mass galaxies.

Our analysis supports the conclusion that the sample of low mass, metal-rich galaxies appear to be "transitional" dwarf galaxies nearing the end of their star formation (Grebel et al. 2003; Peeples et al. 2008). This interpretation suggests that metal-rich galaxies have low gas fractions relative to other dwarf galaxies of similar stellar mass and the low gas fractions are largely responsible for the high gas-phase oxygen abundance observed. Dellenbusch et al. (2007) come to similar conclusions for their smaller sample of low luminosity, metal-rich galaxies. In this evolutionary scenario, these galaxies would represent the link between the gas-rich dwarf irregulars and the gas-deficient dwarf spheroidals and ellipticals. The bluer galaxies in the supplemental SDSS sample would be at an earlier evolutionary stage in this transition, where star formation is more widespread than the Peeples et al. (2008) sample but gas content is lower than their low metallicity counterparts. Accurate determinations of the gas content of low mass, metal-rich galaxies are important to test and establish this scenario.

The environment of these low mass galaxies may play a crucial role in determining their chemical properties. Both observations and simulations have suggested that galaxies in dense environments tend to have metallicities over and above those expected from the correlation of stellar mass and the environment (Cooper et al. 2008; Davé et al. 2011a). Moreover, the stripping away of gas from low mass galaxies in high density environments, either through ram pressure stripping or interactions, has been cited as the possible explanation for high metallicities (Boselli et al. 2008; Petropoulou et al. 2011). However, Peeples et al. (2008) conclude that their galaxies are fairly isolated and the DEEP2 and supplemental SDSS sample of galaxies, at least in projection, do not appear to be in high

density environments though further investigation into the environments of low mass, metal-rich galaxies is necessary.

In order for ram pressure stripping to occur effectively it is estimated that $P_{ram} \sim \rho_{\rm IGM} v^2 > \sigma^2 \rho_{\rm gas}/3$ (Gunn & Gott 1972). Here, $P_{\rm ram}$ is the ram pressure, $\rho_{\rm IGM}$ is the gas density of the intergalactic medium (IGM), v is the velocity of the galaxy through the IGM, σ is the velocity dispersion and $\rho_{\rm gas}$ is the gas density of the galaxy. Typical IGM densities ($n_{\rm H} < 10^{-5}$ cm^{-3}) are likely not sufficient to remove significant amounts of gas. However, as Grebel et al. (2003) argue, a combination of tidal effects along with ram pressure stripping as dwarf galaxies pass near giant galaxies or dense regions of the IGM (if the medium is inhomogeneous) is the most plausible mechanism for gas removal. In this scenario, even if dwarf galaxies are not currently found in high density environments, previous encounters could remove gas from the ISM and any subsequent star formation would lead to elevated levels of enrichment due to the low gas fractions.

The blue cores and low SFRs of many of the metal-rich galaxies suggests that star formation is not widespread throughout the galaxy. Localized star formation opens up the possibility that the high metallicities observed in some of these galaxies may be a result of the nebular emission dominated by individual HII regions. In this case, the inferred metallicity may not be indicative of the global metallicity of the galaxy. Gu et al. (2006) were the first to observe a metal-rich dwarf galaxy. From detailed photometric and spectral analysis of IC 225, they find that there are two photometric cores in this galaxy that are spatially separated; the off-nuclear core being bluer than the blue nucleus. From the redshifts of the line emission and absorption, they conclude that the line emission originates from the off-nuclear core. Follow up kinematic study of the nuclear region of IC 225 using integral field spectroscopy have confirmed this result (Miller & Rudie 2008).

In most star-forming galaxies, the gas-phase oxygen abundance is determined from emission lines integrated over many star-forming regions and hence considered to reflect the global metallicity. If, in these low mass systems, the emission lines are dominated by a single region, the metallicity determined from these lines may not reflect the global gas-

phase abundance. Spatially resolved spectroscopic studies of the metal-rich dwarf galaxies will help to establish whether the high metallicities observed are representative of global metallicities or are localized to individual HII regions. If the latter is true, determining at what stellar masses this effect becomes pronounced and the systematic effects this has on metallicity studies of galaxies is crucial.

5.10 Summary

In this contribution, we have investigated the metallicities of low mass galaxies. Our data comes from culling the literature and from identifying low mass galaxies in the SDSS and DEEP2 survey. We summarize our main findings as follows:

1. We examine the scatter in the local stellar mass-metallicity relation determined from ∼20,000 galaxies in the SDSS. We find that the scatter increases with decreasing stellar mass. We observe this trend using several diagnostic methods of metallicity determination mitigating the systematic effects and uncertainties associated with any particular diagnostic. The theoretical scatter taken from smoothed particle hydrodynamical simulations with momentum driven winds is also examined and found to be consistent with the observed scatter (see Figure 5.5).

2. The low stellar mass MZ relation derived from galaxies with metallicities determined using the direct method shows a smaller range of metallicities than the SDSS MZ relation. We attribute this lower observed scatter to selection bias in galaxies with metallicities determined by the direct method. Using the $N2$ strong-line diagnostic method, we provide observations of low mass, metal-rich galaxies. We examine systematic uncertainties of enhanced nitrogen enrichment and variations in the ionization parameter to help establish the metal-richness of these low mass galaxies. The results challenge the notion that the scatter in the low stellar mass-metallicity relation is small and constant with stellar mass. Due to incompleteness of our sample

and the possibility that our empirical correction for elevated N/O is overcorrecting the data, we give a lower limit to the scatter at low stellar masses (see Figure 5.12).

3. Low mass, metal-rich objects have been identified in the literature as the transitional objects between gas rich dwarf irregulars and gas poor dwarf spheroidals and ellipticals (Dellenbusch et al. 2007; Peeples et al. 2008). We examine the physical properties of these low mass galaxies and find that they are generally consistent with this scenario.

Further observations are required to understand these recently discovered population of galaxies. In particular, accurate gas mass determinations will help to establish these low mass, metal-rich galaxies as gas poor. Spatially resolved spectroscopy of individual galaxies will help to determine if the metallicities inferred from the emission lines are indicative of the global metallicities. The effects that nitrogen enhancement and low ionization parameter have on metallicities are not well understood. A firm observational basis is required for deriving empirical corrections. Finally, detailed investigations into the environments of these galaxies may shed light on physical mechanisms leading to their ostensibly high metallicities and their roles within the sequence of galaxy evolution.

References

Abazajian, K. N., et al. 2009, ApJS, 182, 543

Alloin, D., Collin-Souffrin, S., Joly, M., & Vigroux, L. 1979, A&A, 78, 200

Amorín, R. O., Pérez-Montero, E., & Vílchez, J. M. 2010, ApJ, 715, L128

Bell, E. F., & de Jong, R. S. 2001, ApJ, 550, 212

Bell, E. F., McIntosh, D. H., Katz, N., & Weinberg, M. D. 2003, ApJ, 585, L117

Berg, D. A., Skillman, E. D., & Marble, A. R. 2011, ArXiv e-prints

Boselli, A., Boissier, S., Cortese, L., & Gavazzi, G. 2008, ApJ, 674, 742

Bresolin, F., Gieren, W., Kudritzki, R.-P., Pietrzyński, G., Urbaneja, M. A., & Carraro, G. 2009, ApJ, 700, 309

Bresolin, F., Pietrzyński, G., Urbaneja, M. A., Gieren, W., Kudritzki, R.-P., & Venn, K. A. 2006, ApJ, 648, 1007

Brinchmann, J., Charlot, S., White, S. D. M., Tremonti, C., Kauffmann, G., Heckman, T., & Brinkmann, J. 2004, MNRAS, 351, 1151

Brooks, A. M., Governato, F., Booth, C. M., Willman, B., Gardner, J. P., Wadsley, J., Stinson, G., & Quinn, T. 2007, ApJ, 655, L17

Bruzual, G., & Charlot, S. 2003, MNRAS, 344, 1000

Bundy, K., et al. 2006, ApJ, 651, 120

Calzetti, D., Armus, L., Bohlin, R. C., Kinney, A. L., Koornneef, J., & Storchi-Bergmann, T. 2000, ApJ, 533, 682

Chabrier, G. 2003, PASP, 115, 763

Coil, A. L., Newman, J. A., Kaiser, N., Davis, M., Ma, C.-P., Kocevski, D. D., & Koo, D. C. 2004, ApJ, 617, 765

Conroy, C., Gunn, J. E., & White, M. 2009, ApJ, 699, 486

Cooper, M. C., et al. 2008, MNRAS, 383, 1058

Cowie, L. L., & Barger, A. J. 2008, ApJ, 686, 72

Dalcanton, J. J., Yoachim, P., & Bernstein, R. A. 2004, ApJ, 608, 189

Davé, R., Finlator, K., & Oppenheimer, B. D. 2011a, MNRAS, 416, 1354

Davé, R., Oppenheimer, B. D., & Finlator, K. 2011b, ArXiv e-prints

Davis, M., et al. 2003, in SPIE, ed. P. Guhathakurta, Vol. 4834, 161–172

Dellenbusch, K. E., Gallagher, III, J. S., & Knezek, P. M. 2007, ApJ, 655, L29

Denicoló, G., Terlevich, R., & Terlevich, E. 2002, MNRAS, 330, 69

Drory, N., Bender, R., & Hopp, U. 2004, ApJ, 616, L103

Edmunds, M. G., & Pagel, B. E. J. 1978, MNRAS, 185, 77P

Ellison, S. L., Patton, D. R., Simard, L., & McConnachie, A. W. 2008, ApJ, 672, L107

Erb, D. K., Shapley, A. E., Pettini, M., Steidel, C. C., Reddy, N. A., & Adelberger, K. L. 2006, ApJ, 644, 813

Fontana, A., et al. 2004, A&A, 424, 23

Gil de Paz, A., Madore, B. F., & Pevunova, O. 2003, ApJS, 147, 29

Grebel, E. K., Gallagher, III, J. S., & Harbeck, D. 2003, AJ, 125, 1926

Gu, Q., Zhao, Y., Shi, L., Peng, Z., & Luo, X. 2006, AJ, 131, 806

Gunn, J. E., & Gott, III, J. R. 1972, ApJ, 176, 1

Hidalgo-Gámez, A. M. 2004, Revista Mexicana de Astronomía y Astrofísica, 40, 37

Hidalgo-Gámez, A. M., Sánchez-Salcedo, F. J., & Olofsson, K. 2003, A&A, 399, 63

Izotov, Y. I., Stasińska, G., Meynet, G., Guseva, N. G., & Thuan, T. X. 2006, A&A, 448, 955

Jansen, R. A., Franx, M., & Fabricant, D. 2001, ApJ, 551, 825

Jarrett, T. H., Chester, T., Cutri, R., Schneider, S., Skrutskie, M., & Huchra, J. P. 2000, AJ, 119, 2498

Kassin, S. A., et al. 2007, ApJ, 660, L35

Kennicutt, Jr., R. C. 1998, ARA&A, 36, 189

Kennicutt, Jr., R. C., & Skillman, E. D. 2001, AJ, 121, 1461

Kewley, L. J., & Dopita, M. A. 2002, ApJS, 142, 35

Kewley, L. J., & Ellison, S. L. 2008, ApJ, 681, 1183

Kewley, L. J., Groves, B., Kauffmann, G., & Heckman, T. 2006, MNRAS, 372, 961

Kewley, L. J., Jansen, R. A., & Geller, M. J. 2005, PASP, 117, 227

Kobulnicky, H. A., Kennicutt, Jr., R. C., & Pizagno, J. L. 1999, ApJ, 514, 544

Kobulnicky, H. A., & Kewley, L. J. 2004, ApJ, 617, 240

Kobulnicky, H. A., & Phillips, A. C. 2003, ApJ, 599, 1031

Köppen, J., Weidner, C., & Kroupa, P. 2007, MNRAS, 375, 673

Kudritzki, R.-P., Urbaneja, M. A., Gazak, Z., Bresolin, F., Przybilla, N., Gieren, W., & Pietrzyński, G. 2012, ApJ, 747, 15

Lamareille, F., et al. 2009, A&A, 495, 53

Lee, H., Grebel, E. K., & Hodge, P. W. 2003, A&A, 401, 141

Lee, H., Skillman, E. D., Cannon, J. M., Jackson, D. C., Gehrz, R. D., Polomski, E. F., & Woodward, C. E. 2006, ApJ, 647, 970

Lequeux, J., Peimbert, M., Rayo, J. F., Serrano, A., & Torres-Peimbert, S. 1979, A&A, 80, 155

Mannucci, F., Cresci, G., Maiolino, R., Marconi, A., & Gnerucci, A. 2010, MNRAS, 408, 2115

Mannucci, F., et al. 2009, MNRAS, 398, 1915

Markwardt, C. B. 2009, in Astronomical Society of the Pacific Conference Series, Vol. 411, Astronomical Data Analysis Software and Systems XVIII, ed. D. A. Bohlender, D. Durand, & P. Dowler, 251

Miller, B. W., & Rudie, G. 2008, in IAU Symposium, Vol. 245, IAU Symposium, ed. M. Bureau, E. Athanassoula, & B. Barbuy, 311–312

Noeske, K. G., Papaderos, P., Cairós, L. M., & Fricke, K. J. 2003, A&A, 410, 481

—. 2005, A&A, 429, 115

Pagel, B. E. J., Edmunds, M. G., Blackwell, D. E., Chun, M. S., & Smith, G. 1979, MNRAS, 189, 95

Peña-Guerrero, M. A., Peimbert, A., Peimbert, M., & Ruiz, M. T. 2011, ArXiv e-prints

Peeples, M. S., Pogge, R. W., & Stanek, K. Z. 2008, ApJ, 685, 904

Pérez-Montero, E., & Contini, T. 2009, MNRAS, 398, 949

Petropoulou, V., Vílchez, J., Iglesias-Páramo, J., Papaderos, P., Magrini, L., Cedrés, B., & Reverte, D. 2011, ApJ, 734, 32

Pettini, M., & Pagel, B. E. J. 2004, MNRAS, 348, L59

Salim, S., et al. 2007, ApJS, 173, 267

Salpeter, E. E. 1955, ApJ, 121, 161

Schombert, J. M., Pildis, R. A., Eder, J. A., & Oemler, Jr., A. 1995, AJ, 110, 2067

Searle, L., & Sargent, W. L. W. 1972, ApJ, 173, 25

Skillman, E. D., Kennicutt, R. C., & Hodge, P. W. 1989, ApJ, 347, 875

Stasińska, G. 2002, in Revista Mexicana de Astronomia y Astrofisica, vol. 27, Vol. 12, Revista Mexicana de Astronomia y Astrofisica Conference Series, ed. W. J. Henney, J. Franco, & M. Martos, 62–69

Stasińska, G. 2005, A&A, 434, 507

Storchi-Bergmann, T., Calzetti, D., & Kinney, A. L. 1994, ApJ, 429, 572

Stoughton, C., et al. 2002, AJ, 123, 485

Tamura, N., Hirashita, H., & Takeuchi, T. T. 2001, ApJ, 552, L113

Tremonti, C. A., et al. 2004, ApJ, 613, 898

Vaduvescu, O., McCall, M. L., & Richer, M. G. 2007, AJ, 134, 604

van Zee, L., & Haynes, M. P. 2006, ApJ, 636, 214

van Zee, L., Haynes, M. P., & Salzer, J. J. 1997, AJ, 114, 2497

Weiner, B. J., et al. 2007, ApJ, 660, L39

—. 2006, ApJ, 653, 1027

Williams, M. J., Bureau, M., & Cappellari, M. 2010, MNRAS, 409, 1330

Willmer, C. N. A., et al. 2006, ApJ, 647, 853

Yin, S. Y., Liang, Y. C., Hammer, F., Brinchmann, J., Zhang, B., Deng, L. C., & Flores, H. 2007, A&A, 462, 535

Zahid, H. J., Bresolin, F., Kewley, L. J., Coil, A. L., & Davé, R. 2012, ApJ, 750, 120

Zahid, H. J., Kewley, L. J., & Bresolin, F. 2011, ApJ, 730, 137

Zhao, Y., Gao, Y., & Gu, Q. 2010, ApJ, 710, 663

Chapter 6

A Census of Oxygen in Star-Forming Galaxies: An Empirical Model Linking Metallicities, Star Formation Rates and Outflows

Note: This chapter originally appeared as Zahid, H.J., Dima G.I., Kewley, L.J., Erb, D.K., & Dave, R. 2012, ApJ, 757, 54. I am the primary author of this work.

Abstract

In this contribution we present the first census of oxygen in star-forming galaxies in the local universe. We examine three samples of galaxies with metallicities and star formation rates at $z = 0.07, 0.8$ and 2.26, including the SDSS and DEEP2 surveys. We infer the total mass of oxygen produced and mass of oxygen found in the gas-phase from our local SDSS sample. The star formation history is determined by requiring that galaxies evolve along the relation between stellar mass and star formation rate observed in our three samples. We show that the observed relation between stellar mass and star formation rate for our three samples is consistent with other samples in the literature. The mass-metallicity relation is well established for our three samples and from this we empirically determine the chemical evolution of star-forming galaxies. Thus, we are able to simultaneously constrain the star formation rates and metallicities of galaxies over cosmic time allowing us to estimate the mass of oxygen locked up in stars. Combining this work with independent measurements

reported in the literature we conclude that the loss of oxygen from the interstellar medium of local star-forming galaxies is likely to be a ubiquitous process with the oxygen mass loss scaling (almost) linearly with stellar mass. We estimate the total baryonic mass loss and argue that only a small fraction of the baryons inferred from cosmological observations accrete onto galaxies.

6.1 Introduction

A complete theory of galaxy formation and evolution will have to be able to self-consistently account for, among other physical processes, the star formation and chemical evolution of galaxies. Our understanding of galaxy evolution is rooted in the currently accepted cosmological model in which large-scale structure in the universe traces out the cosmic web of dark matter and growth of the universe is accelerated by dark energy. In this theoretical framework, a hierarchical formation of galaxies is favored in which larger galaxies form as the dark matter halos within which they are embedded merge over time. It remains uncertain what epoch in cosmic history this is the dominant mode of growth. However, recent observations of strong correlations observed between fundamental galaxy parameters (e.g. mass, age, size, luminosity, baryonic content and angular momentum) have lead some to question the stochastic nature of the hierarchical formation scenario (Disney et al. 2008; Nair et al. 2010). One possible resolution is that galaxies and groups of galaxies gather matter early on followed by quiescent, isolated evolution (Peebles & Nusser 2010). The evolution of galaxies may be simpler than a hierarchical formation model suggests.

A large number of studies have recently revealed that there exists a tight relation between stellar mass and star formation rates (SFRs) out to $z \sim 2$ (Noeske et al. 2007b; Salim et al. 2007; Daddi et al. 2007; Elbaz et al. 2007; Pannella et al. 2009; Elbaz et al. 2011, among others). We refer to this as the MS relation. All these studies find the slope of the relation to be near unity and a 1σ scatter of $\lesssim 0.3$ dex. The relation and its small scatter is taken as evidence that secular processes, such as gas accretion, are the dominant mechanism for star

formation with mergers playing a minor role. In particular, Noeske et al. (2007b) suggest that the presence of an MS relation with constant scatter at several epochs implies that star formation is gradually declining with galaxies spending 67% (95%) of their star formation lifetime within a factor of $\sim$2 (4) of their average SFR.

Several studies have applied the observational constraints imposed by the MS relation and its evolution to uncover star formation histories of galaxies. Noeske et al. (2007a) show that their model of "staged" galaxy evolution accounts for the observed relation. In their model, less massive galaxies have later onset of initial star formation with longer timescales of exponential decay. Similar models result if star-forming galaxies are assumed to lie on the MS relation at all epochs. Several studies have focused on this simpler approach of continuity of star formation along MS relation. Conroy & Wechsler (2009) combine this approach with abundance matching to dark matter halos, concluding that mergers play a minor role in mass growth of galaxies. Using this approach, Peng et al. (2010) are able to explain the shape and evolution of the observed stellar mass function for star-forming galaxies. Papovich et al. (2011) apply this technique to understand the gas accretion process at high redshifts. Leitner & Kravtsov (2011) use this technique to show that gas recycling is sufficient to fuel the observed star formation in the local universe and Leitner (2012) argue that most star-forming galaxies in the local universe formed at $1 < z < 2$.

The chemical evolution of the gas-phase of star-forming galaxies is largely constrained by observations of the mass-metallicity (MZ) relation. Lequeux et al. (1979) were the first to show that the metallicities of galaxies increase with stellar mass. The MZ relation is well established in the local universe (Tremonti et al. 2004) and has been observed for intermediate (Savaglio et al. 2005; Cowie & Barger 2008; Zahid et al. 2011; Moustakas et al. 2011) and high redshift galaxies (Erb et al. 2006a; Mannucci et al. 2009). The shape of the MZ relation is observed to be relatively constant with evolution in the zero point such that galaxies at earlier redshifts are found to have lower gas-phase abundance.

The metal content of galaxies is governed by the processes of star formation and large scale gas flows. Outflowing gas has directly been observed in starburst galaxies (Rupke

et al. 2005; Martin 2006; Tremonti et al. 2007; Rich et al. 2010; Tripp et al. 2011) and is found to be a ubiquitous phenomena in higher redshift star-forming galaxies (Shapley et al. 2003; Weiner et al. 2009; Steidel et al. 2010). A recent survey of the halos of galaxies conducted by Tumlinson et al. (2011) reveals that large reservoirs of oxygen are found to exist in the circum-galactic medium (CGM) of all star-forming galaxies. They conclude that the CGM of star-forming galaxies contains a substantial amount of gas and metals, perhaps far exceeding the gas within the galaxies themselves. In this study we use our census of oxygen to quantify the loss of metals and gas from the ISM of normal local star-forming galaxies.

Census techniques have proven to be crucial in our understanding of cosmological evolution. A well constrained inventory of the energy content of the universe is one of the greatest triumphs of modern cosmology. By comparing a census of the observed baryons in the local universe to the expected cosmological density, Fukugita et al. (1998, among others) showed that the vast majority of baryons are not observed. This is one of the missing baryons problems. A second related problem is that the amount of baryons within galaxies is not in accord with expectations inferred from the properties of the dark matter halos within which they are embedded (e.g Bell et al. 2003b). Theoretical cosmological models suggest that the missing baryons are to be found in the warm-hot intergalactic medium (WHIM) (Cen & Ostriker 1999; Davé et al. 2001). Baryons in this phase may or may not be associated with galaxies and it remains unclear what fraction of the baryons accreted onto galaxies and were later ejected.

In this study we present a self-consistent, empirically constrained census model of oxygen in star-forming galaxies. The data used in this study are presented in Section 6.2 and the methods used in deriving the stellar masses, metallicities and SFRs of galaxies are discussed in Section 6.3. We parameterize the SFRs of galaxies as a function of stellar mass and redshift in Section 6.4 by examining the MS relation at several redshifts. We describe the various components of our oxygen census in Section 6.5. We develop our self-consistent empirical models for the star formation and chemical history of galaxies in

Section 6.6 and 6.7, respectively, by imposing the continuity condition that galaxies build up their stellar mass by evolving along the empirical relation between stellar mass and SFR with the metallicity inferred from the MZ relation at several redshifts. In Section 6.8 we present the results of our census and in Section 6.9 we discuss systematics and uncertainties in our approach. We provide a discussion of our results in Section 6.10 and a summary of our results in Section 6.11. For this study we adopt the standard cosmology $(H_0, \Omega_m, \Omega_\Lambda) = (70\,km\,s^{-1}\,Mpc^{-1}, 0.3, 0.7)$.

6.2 The Data and Sample Selection

In this section we describe the local sample of galaxies from SDSS (Section 6.2.1), our intermediate redshift sample from DEEP2 (Section 6.2.2) and a high redshift sample from Erb et al. (2006a, Section 6.2.3). Galaxies are primarily selected such that the chemical properties can be determined from their spectra. The binned data are given in a Table 6.1.

6.2.1 The SDSS Sample

We draw our local sample from the SDSS DR7 which consists of ∼900,000 galaxies spanning a redshift range of $0 < z < 0.7$ (Abazajian et al. 2009). The survey has a Petrosian limiting magnitde of $r_P = 17.8$ covering 8,200 deg^2. The spectra have a nominal spectral range of 3900 - 9100Å and a spectral resolution of R $\sim$ 2000. We make use of the *ugriz*-band photometry available for each object (Stoughton et al. 2002) and the publicly released emission line fluxes measured by the MPA-JHU group[1]. We refer to the sample presented here as the "metallicity selected SDSS sample".

We correct for dust extinction in the emission lines by inferring a reddening correction from the Balmer decrement. For case B recombination with electron temperature $T_e = 10^4$K and electron density $n_e = 10^2$ cm^{-3}, the intrinsic Hα/Hβ ratio is expected to be 2.86 (Osterbrock 1989). We get the intrinsic color excess, E(B−V), and the correction for dust attenuation using the extinction law of Cardelli et al. (1989) and a corresponding $R_v = 3.1$.

[1] http://www.mpa-garching.mpg.de/SDSS/DR7/

We note that the results of this study are not dependent on our choice of a particular extinction law.

We select a pure star-forming sample of local emission line galaxies from the SDSS DR7. We first distinguish star-forming galaxies from AGN by constraining the ionizing radiation source using the [OIII]λ5007, [NII]λ6584, Hβ and Hα emission lines (Baldwin et al. 1981; Veilleux & Osterbrock 1987; Kauffmann et al. 2003; Kewley et al. 2006). In particular, we remove galaxies using the equation given in Kewley et al. (2006) where

$$\log([\mathrm{OIII}]/\mathrm{H}\beta) > 0.61/\left(\log([\mathrm{NII}]/\mathrm{H}\alpha) - 0.05\right) + 1.3. \tag{6.1}$$

In order to avoid aperture effects, we require a g-band fiber aperture covering fraction $> 30\%$ in addition to imposing a lower redshift limit of 0.04 (Kewley et al. 2004). The median covering fraction for the metallicity selected SDSS sample is 38%. Kewley et al. (2006) find that the SDSS sample is incomplete at higher redshifts and in order to minimize evolutionary effects we also impose an upper limit redshift cutoff of $z = 0.1$.

In order to establish comparable samples, galaxies in the local sample are selected from SDSS using the same selection criteria as the DEEP2 sample. In particular, galaxies are selected to have S/N of H$\beta > 3$, $\sigma_{R23} < 2$ and equivalent width of H$\beta > 4$Å. Here, σ_{R23} is the error in the $R23$ parameter which is the ratio of the oxygen nebular emission ([OII]λ3727 doublet and [OIII]$\lambda 4959, 5007$) to Hβ. These particular selection criteria gives us a sample of $\sim$20,000 star-forming galaxies in the limited redshift range of $0.04 < z < 0.1$.

6.2.2 The DEEP2 Sample

Our sample of intermediate redshift star-forming galaxies is taken from the DEEP2 survey (Davis et al. 2003). Details of sample selection and properties are given in Zahid et al. (2011), here we summarize the data selection. The survey consists of $\sim$45,000 galaxies targeted mostly in the redshift range of $0.7 > z > 1.4$ by applying a color preselection using BRI-band photometry (Coil et al. 2004). The survey has a limiting magnitude of

$R_{AB} = 24.1$ and covers 3.5 deg^2. The spectra have a nominal spectral range of 6500 - 9100Å and a resolution of R $\sim$ 5000. The emission line equivalent widths are measured in Zahid et al. (2011) and we adopt the same values here.

The sample selection is based on the spectral and photometric properties of the galaxies. We reduce AGN contamination by first requiring that $\log(R23) < 1$ (Kewley et al., in prep). Using the color separation for blue and red galaxies parameterized by Willmer et al. (2006), Weiner et al. (2007) conclude that only a small fraction of blue galaxies in DEEP2 appear to harbor AGN whereas a large fraction of red emission line galaxies show evidence of AGN emission. We further limit AGN contamination by removing 48 galaxies in the sample that are classified as red galaxies using the color division of Willmer et al. (2006).

Given the nominal spectral coverage, the redshift range of galaxies in our sample is limited by the necessity to simultaneously observe both the [OII]λ3727 doublet and the [OIII]λ5007 emission lines which are required for chemical analysis. We further require that the S/N H$\beta > 3$, the error of the $R23$ emission line ratio, σ_{R23}, be less than 2 and that equivalent width of H$\beta > 4$Å. Finally, due to ambiguity in the metallicity determination of DEEP2 galaxies at low stellar masses (see Section 6.3.2) we also remove all galaxies with $M_* < 10^{9.2} M_\odot$. This selection criteria gives us a sample of 1348 star-forming galaxies in the limited redshift range of $0.75 < z < 0.82$.

6.2.3 The E06 Sample

Erb et al. (2006a, E06 hereafter) determine the MZ relation from 87 star-forming galaxies at $z \sim 2.2$ selected from a larger sample of 114 galaxies described in Erb et al. (2006b). The galaxies are selected on the basis of their rest-frame UV colors and redshifts are determined from their UV spectra. All galaxies in the sample have $UGRK$-band photometry. Most also have J-band photometry and 32 galaxies have been observed at 3.6, 4.5, 5.4 and 8.0 μm with IRAC onboard the Spitzer Space Telescope. Hα spectra were obtained using NIRSPEC on the Keck II telescope.

Table 6.1. Data

$\log(M_*/M_\odot)$	12 + log(O/H)	E(B−V)	$\log(\Psi)$
	SDSS		
8.51	8.707 ± 0.004	0.11 ± 0.02	-0.20 ± 0.02
8.82	8.736 ± 0.006	0.13 ± 0.02	-0.12 ± 0.02
8.97	8.787 ± 0.007	0.15 ± 0.02	-0.19 ± 0.02
9.08	8.819 ± 0.008	0.16 ± 0.02	-0.20 ± 0.02
9.17	8.859 ± 0.007	0.18 ± 0.02	-0.19 ± 0.02
9.23	8.875 ± 0.006	0.19 ± 0.01	-0.14 ± 0.01
9.30	8.900 ± 0.006	0.20 ± 0.01	-0.12 ± 0.01
9.36	8.920 ± 0.006	0.22 ± 0.01	-0.10 ± 0.01
9.41	8.923 ± 0.006	0.23 ± 0.01	-0.07 ± 0.01
9.45	8.946 ± 0.006	0.24 ± 0.01	-0.06 ± 0.01
9.49	8.947 ± 0.006	0.24 ± 0.01	-0.03 ± 0.01
9.54	8.969 ± 0.006	0.27 ± 0.01	-0.02 ± 0.01
9.57	8.977 ± 0.004	0.26 ± 0.01	-0.01 ± 0.01
9.61	8.993 ± 0.006	0.27 ± 0.01	0.03 ± 0.01
9.64	8.989 ± 0.005	0.28 ± 0.01	0.05 ± 0.01
9.68	9.007 ± 0.004	0.28 ± 0.01	0.07 ± 0.01
9.71	9.010 ± 0.004	0.30 ± 0.01	0.09 ± 0.01
9.75	9.022 ± 0.004	0.30 ± 0.01	0.11 ± 0.01
9.78	9.035 ± 0.003	0.32 ± 0.01	0.13 ± 0.01
9.81	9.037 ± 0.004	0.33 ± 0.01	0.16 ± 0.01
9.85	9.048 ± 0.003	0.33 ± 0.01	0.17 ± 0.01

The metallicity for these galaxies is determined from the emission line ratio of [NII]λ6584 to Hα. The [NII]λ6584 line is sensitive to metallicity with the strength of the line decreasing with decreasing metallicity. The S/N of the individual galaxy spectra is insufficient to measure the weak [NII]λ6584 line. In order to increase the S/N of their spectra and to increase the chance of detecting [NII] emission line at low metallicites, E06 stack 14 or 15 individual galaxy spectra binned by stellar mass into 6 composite spectra. The [NII]λ6584 and Hα emission line fluxes and metallicities are measured from these composite spectra.

Table 6.1—Continued

$\log(M_*/M_\odot)$	12 + log(O/H)	E(B−V)	log(Ψ)
9.88	9.056 ± 0.003	0.36 ± 0.01	0.22 ± 0.01
9.92	9.059 ± 0.003	0.36 ± 0.01	0.24 ± 0.01
9.95	9.068 ± 0.003	0.38 ± 0.01	0.27 ± 0.01
10.00	9.061 ± 0.003	0.39 ± 0.01	0.32 ± 0.01
10.04	9.081 ± 0.002	0.40 ± 0.01	0.34 ± 0.01
10.09	9.084 ± 0.003	0.43 ± 0.01	0.40 ± 0.01
10.15	9.088 ± 0.002	0.44 ± 0.01	0.47 ± 0.01
10.24	9.086 ± 0.003	0.47 ± 0.01	0.53 ± 0.01
10.39	9.095 ± 0.002	0.52 ± 0.01	0.73 ± 0.01
	DEEP2		
9.25	8.69 ± 0.02	0.17 ± 0.03	0.35 ± 0.03
9.32	8.76 ± 0.02	0.19 ± 0.02	0.32 ± 0.02
9.39	8.78 ± 0.02	0.20 ± 0.03	0.37 ± 0.03
9.44	8.77 ± 0.02	0.21 ± 0.03	0.39 ± 0.03
9.49	8.74 ± 0.01	0.21 ± 0.03	0.43 ± 0.03
9.56	8.80 ± 0.02	0.23 ± 0.03	0.49 ± 0.03
9.64	8.83 ± 0.02	0.24 ± 0.04	0.54 ± 0.04
9.72	8.84 ± 0.02	0.26 ± 0.03	0.60 ± 0.03
9.79	8.86 ± 0.02	0.27 ± 0.05	0.60 ± 0.05
9.87	8.92 ± 0.02	0.31 ± 0.05	0.72 ± 0.05
9.97	8.94 ± 0.02	0.33 ± 0.03	0.77 ± 0.03
10.07	8.93 ± 0.02	0.35 ± 0.03	0.82 ± 0.03

6.3 Methods

In this section we discuss our methods for determining stellar masses (Section 6.3.1), metallicities (Section 6.3.2) and SFRs (Section 6.3.3).

6.3.1 Stellar Mass

We use the Le Phare[2] code developed by Arnouts, S. & Ilbert, O. to estimate the galactic stellar mass. This code estimates the stellar masses of galaxies by comparing photometry with stellar population synthesis models in order to determine the mass-to-light ratio which is then used to scale the observed luminosity (Bell et al. 2003b; Fontana et al. 2004). We synthesize magnitudes from the stellar templates of Bruzual & Charlot (2003) and use a Chabrier (2003) IMF. The 27 models have two metallicities and seven exponentially decreasing star formation models (SFR $\propto e^{-t/\tau}$) with $\tau = 0.1, 0.3, 1, 2, 3, 5, 10, 15$ and 30 Gyrs. We apply the extinction law of Calzetti et al. (2000) allowing E(B−V) to range from 0 to 0.6 and the stellar population ages range from 0 to 13 Gyrs. The median statistical error for the derived stellar masses, determined from propagating the uncertainty in the photometry, is 0.15 dex. Though systematic effects may be large (Drory et al. 2004; Conroy et al. 2009), we have consistently measured the stellar masses for our different samples giving us a robust relative measure (Swindle et al. 2011, R. Swindle, private comm.).

We account for emission line contributions by taking the Kennicutt (1998a) relation between the synthesized UV luminosity and SFR and the emission lines. This treatment accounts for Hα, Hβ and [OII]λ3727 and [OIII]λ4959, 5007 (Ilbert et al. 2010). In our sample, making no correction for the emission line contributions does not significantly alter our mass determinations. We adopt the median of the mass distribution and take the 68% confidence interval as a measure of the error. In Zahid et al. (2011) we compare this method with the method used by the MPA/JHU group to determine stellar masses of the SDSS galaxies. We find that the two estimates differ by a constant offset of ∼0.2 dex and that the dispersion between the two methods is 0.14 dex.

[2] $http://www.cfht.hawaii.edu/\sim arnouts/LEPHARE/cfht\_lephare/lephare.html$

Table 6.1—Continued

$\log(M_*/M_\odot)$	12 + log(O/H)	E(B−V)	$\log(\Psi)$
10.18	8.96 ± 0.01	0.38 ± 0.03	0.92 ± 0.03
10.33	9.00 ± 0.01	0.43 ± 0.02	0.98 ± 0.02
10.59	9.04 ± 0.01	0.53 ± 0.04	1.29 ± 0.04
		E06	
9.14	<8.55	0.14 ± 0.09	1.40 ± 0.14
9.56	8.72 ± 0.07	0.21 ± 0.07	1.41 ± 0.05
9.89	8.82 ± 0.06	0.28 ± 0.08	1.60 ± 0.06
10.12	8.86 ± 0.06	0.33 ± 0.07	1.52 ± 0.08
10.32	8.92 ± 0.06	0.39 ± 0.09	1.78 ± 0.06
10.73	8.97 ± 0.05	0.52 ± 0.06	1.96 ± 0.06

Note. — The stellar mass (column 1), metallicity determined from the diagnostic of Kobulnicky & Kewley (2004, column 2), fitted E(B−V) from Equation 9.1 (column 3) and SFR(column 4) for the SDSS, DEEP2 and E06 samples. For the E06 sample the metallicity has been converted from Pettini & Pagel (2004) to Kobulnicky & Kewley (2004) using the conversion constants in Kewley & Ellison (2008). DEEP2 and E06 sample we have corrected for dust extinction when determining SFRs from the Balmer lines using the E(B−V) values given in column 3. For the DEEP2 and SDSS data the values are the median in bins of stellar mass. The errors are determined from bootstrapping and are analogous to the standard error on the mean. For the E06 sample, the errors are the standard error of the mean. Each data bin is equally populated such that the SDSS, DEEP2 and E06 samples contain ~ 700, ~ 90 and ~ 15 galaxies in each bin, respectively. Electronic version available upon request.

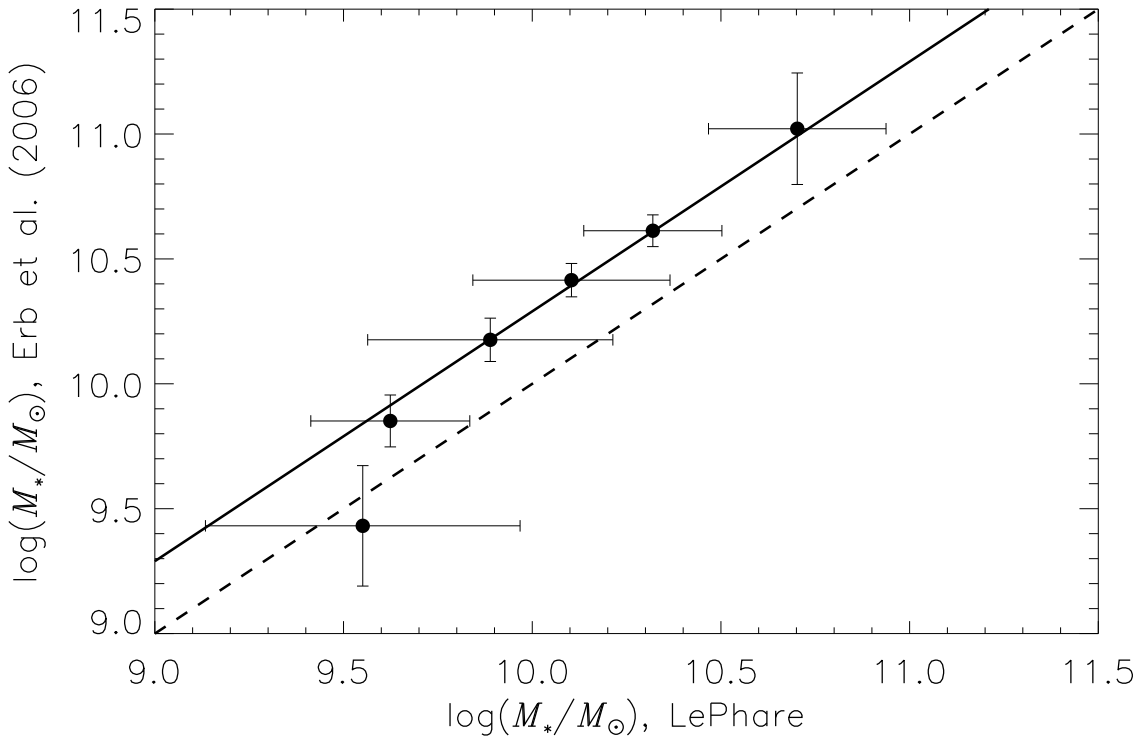

Figure 6.1 The stellar mass determined by Erb et al. (2006c) plotted against our determination using Le Phare. The dashed line is the one-to-one agreement and the solid line is offset by 0.29 dex. In the five higher mass bins, the stellar mass estimates used in E06 are greater by a factor of 2 (0.29 dex).

E06 measure stellar masses using a similar method of comparing photometry with stellar population synthesis models (Erb et al. 2006c). However, an important difference is that they measure the "total" stellar mass, which is the integral of the SFR over the lifetime of the galaxy. They find that this stellar mass is $\sim 10 - 40\%$ higher than the instantaneous (or what they term "current living") stellar mass. However, most mass estimates found in the literature are generally the instantaneous and not "total" stellar mass. We recalculate the stellar masses for their individual galaxies and bin the data according to their original binning. In Figure 6.1 we compare the mass estimates for each of their 6 bins. The x-axis shows our mass estimate and y-axis is the original mass estimate from E06. The error

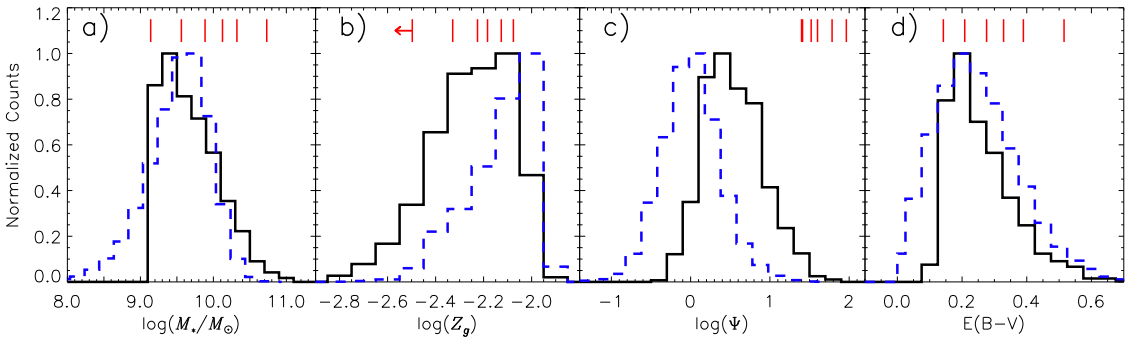

Figure 6.2 A histogram of the a) stellar mass, b) metallicity, c) SFR ($M_\odot$ yr^{-1}) and d) the fitted E(B−V) for the DEEP2 (solid black) and SDSS (dashed blue) samples. The values for the 6 binned data points of E06 are shown by the red ticks.

bar represents the rms dispersion of stellar masses in each mass bin. For the five higher mass bins, we find that there is a constant offset such that the E06 estimates are 0.29 dex higher than our estimate. For the lowest mass bin, there appears to be a near one-to-one agreement, though the 0.29 dex offset is within the errors. This is most likely due to the fact that the lowest mass galaxies are younger and therefore have a much closer agreement between their instantaneous and "total" stellar mass. Moreover, we do not concern ourselves too much with the lowest mass bin as the metallicity measure is only an upper limit for this bin. Since we do not rebin the E06 data in determining the metallicity we adopt their stellar mass values but subtract 0.29 dex to make them consistent with our estimates.

Figure 8.1a shows the distribution of the stellar masses for all three samples.

6.3.2 Metallicity

We use two strong-line methods to determine the metallicity of galaxies in our sample. In this section we only present the parameterization of the calibration and defer a detailed discussion of the methods until Section 6.8.3. For the SDSS and DEEP2 sample we determine metallicities using the calibration of Kobulnicky & Kewley (2004). This method

relies on the $R23$ and $O32$ parameters which are defined as

$$R23 = \frac{[\mathrm{OII}]\lambda 3727 + [\mathrm{OIII}]\lambda 4959, 5007}{\mathrm{H}\beta} \tag{6.2}$$

and

$$O32 = \frac{[\mathrm{OIII}]\lambda 4959, 5007}{[\mathrm{OII}]\lambda 3727}. \tag{6.3}$$

Here the ratio implies the ratio of the measured line intensities. We have used the assumption that the ratio of the fluxes of [OIII]λ5007 to [OIII]λ4959 is 3 (Osterbrock 1989). Due to the higher S/N of the [OIII]λ5007 line, for the sum of the [OIII]λ4959 and [OIII]λ5007 flux we adopt a value of 1.33 times the [OIII]λ5007 flux.

The $R23$ strong-line method is known to be sensitive to the ionization parameter. The ionization parameter characterizes the ionization state of the gas and quantitatively represents the number of ionizing photons per second per unit area divided by the hydrogen density. The ionization parameter can be constrained by measuring the ratio of the line intensity of the same element at two ionization stages. The method of Kobulnicky & Kewley (2004) does this explicitly by using the $O32$ line ratio. Because both the metallicity and ionization parameter are interdependent, an iterative scheme is used, the details of which are provided in the appendix of Kewley & Ellison (2008). In particular we use equations A4 and A6.

The DEEP2 data are not flux calibrated so we use the line equivalent widths with a correction applied for Balmer absorption (Zahid et al. 2011). For consistency we determine the SDSS metallicities using line equivalent widths as well. Several studies have established that line equivalent widths can be substituted for line fluxes when measuring metallicities if data are not flux calibrated or a reliable reddening estimate is unavailable (Kobulnicky & Phillips 2003; Moustakas et al. 2010; Zahid et al. 2011). In particular, we test this on our SDSS sample and find that the dispersion between the metallicities measured using equivalent widths and dereddened line fluxes is $\sim$0.05 dex which is less than intrinsic

uncertainties of the strong-line method. The average difference in the MZ relation derived using the two methods is < 0.01 dex.

One issue with using the $R23$ method is that metallicity is not a monotonic function of $R23$. For a particular value of the $R23$ parameter there are two possible values of metallicity known as the upper and lower branch metallicity. This degeneracy is generally alleviated by employing a second metallicity diagnostic that relies on line ratios that are monotonic with metallicity. For our SDSS sample of galaxies, the use of [NII]/$H\alpha$ reveals that the vast majority ($\sim$99%) of galaxies are on the upper branch. For our DEEP2 sample, the nominal wavelength coverage of the spectra does not allow us to simultaneously observe the $R23$ lines and [NII]/Hα. We assume all galaxies with $M_* > 10^{9.2} M_\odot$ lie on the upper metallicity branch (for more details see Figure 5 in Zahid et al. 2011).

The calibration of Kobulnicky & Kewley (2004) is based on theoretical photoionization models. Empirical methods rely on calibrating strong-line ratios to metallicities determined using temperature sensitive auroral lines. E06 determine metallicities using the empirical calibration of Pettini & Pagel (2004). The metallicity is given by

$$12 + \log(\mathrm{O/H}) = 8.90 + 0.57 \times N2 \tag{6.4}$$

where $N2 = \log([\mathrm{NII}]\lambda 6584/\mathrm{H}\alpha)$. Using $\sim 28,000$ galaxies from the SDSS DR4, Kewley & Ellison (2008) derive constants for converting between various diagnostics. We use these conversion constants to consistently determine metallicities for all three samples using both the theoretical and empirical calibrations of Kobulnicky & Kewley (2004) and Pettini & Pagel (2004).

The metallicity of a galaxy is traditionally defined as a number density of oxygen relative to hydrogen and is given as $12 + \log(\mathrm{O/H})$. For this study we require the mass density of oxygen relative to hydrogen. We convert number density to mass density using the relation

$$\log(Z_g) \quad = \quad 12 + \log(\mathrm{O/H}) - \tag{6.5}$$

$$
\begin{aligned}
& 12 - \log\left(\frac{M_O/M_H}{XM_H + YM_{He}}\right) \\
= \quad & \log(\mathrm{O/H}) - \log\left(\frac{15.999/1.0079}{0.75 \cdot 1.0079 + 0.25 \cdot 4.0026}\right).
\end{aligned}
$$

For the remainder of the paper, Z_g refers to the gas-phase *mass* density of oxygen relative hydrogen. Also, when referring to metallicity or gas-phase oxygen abundance we mean to refer to Z_g.

Figure 8.1b shows the distribution of the metallicities for all three samples.

6.3.3 Star Formation Rate

The SFRs for the SDSS sample are derived by the MPA/JHU group using the technique of Brinchmann et al. (2004) with additional improvements given by Salim et al. (2007). The strong emission lines of each galaxy are fit using the nebular emission models of Charlot & Longhetti (2001). All emission lines contribute to constraining the dust attenuation, though the largest contribution comes from the Hα/Hβ ratio. At the median redshift of the SDSS, about a 1/3 of the galaxy light is contained within the 3" fiber. In order to account for losses, Brinchmann et al. (2004) derive an aperture correction which was improved upon by Salim et al. (2007). We convert from a Kroupa to Chabrier IMF by dividing by 1.06.

We estimate the SFRs for the DEEP2 and E06 sample from the Hβ and Hα emission lines, respectively. In order to reliably estimate the SFR, it is necessary to make a correction to the Balmer line flux due to dust extinction. Since the nominal wavelength coverage of both the DEEP2 and E06 spectra do not allow us to observe multiple order Balmer lines, we are not able to derive a correction from the Balmer decrement. Garn & Best (2010) have shown that for a sample of star-forming galaxies from the SDSS the extinction determined from the Hα/Hβ ratio can be predicted from the stellar mass, Hα luminosity or metallicity of the galaxy with a dispersion of $\sim$0.1 dex. The relation between stellar mass and dust extinction found by Garn & Best (2010) is shown to be valid out to $z \sim 1.5$ (Sobral et al. 2012) and a relation between dust extinction, stellar mass and metallicity is also observed in galaxies at $z \sim 2$ (Reddy et al. 2010).

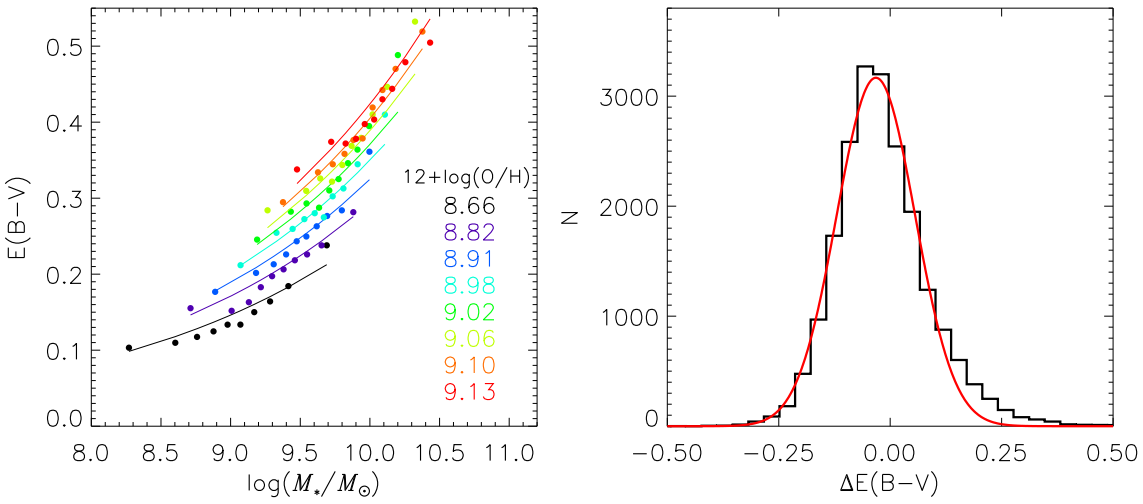

Figure 6.3 A fit to E(B−V) as function of stellar mass and metallicity. The left panel shows the E(B−V) sorted into 8 color-coded bins of metallicity and plotted as function of stellar mass. The underlying curves are the fitted relation given by Equation 9.1 and color-coded by metallicity. The right panel shows a histogram of the residuals between the observed E(B−V) and those determined from the fitted relation.

Xiao et al. (2012) obtain a slightly better fit (dispersion of 0.07 dex) by incorporating galaxy inclination and using a different parameterization. We determine E(B−V) for our sample of SDSS galaxies from the Balmer decrement assuming the Cardelli et al. (1989) extinction law and parameterize E(B−V) as a function of stellar mass and metallicity using a similar formulation to Xiao et al. (2012). The color excess is given by

$$\mathrm{E(B-V)} = (p_0 + p_1 Z^{p_2}) \times M^{p_3}, \tag{6.6}$$

where $Z = 10^{(12+\log(\mathrm{O/H})-8)}$ and $M = M_*/10^{10}$. The metallicities are derived using the calibration of Kobulnicky & Kewley (2004). We perform a non-linear least square fit using the MPFIT[3] set of routines (Markwardt 2009). The data are weighted by their 1σ statistical uncertainties and the errors are propagated to the parameters. The fit returns $p_0 = 0.12 \pm 0.01$, $p_1 = 0.041 \pm 0.006$, $p_2 = 0.77 \pm 0.06$ and $p_3 = 0.240 \pm 0.002$. The left

[3]http://purl.com/net/mpfit

panel of Figure 6.3 shows the mean E(B−V) binned by stellar mass and color coded by metallicity. The fit to these binned data are shown by the color coded curves. The right panel shows the residuals between the observed and fitted color excess. There is a slight tail to the distribution owing to the lower quality of the fit to the high stellar mass, high metallicity and high color excess data. The rms dispersion between the observations and the fit is ∼0.11 dex.

We measure the SFRs for the DEEP2 sample of galaxies using the Hβ luminosity. In order to obtain a flux calibration, we integrate the DEEP2 spectra over the I-band filter response and compare to the observed I-band magnitude. This gives us an estimate for the conversion between counts on the detector and flux given in ergs s^{-1}. This procedure accounts for both throughput and slit losses assuming that the line-to-continuum emission ratio is constant inside and outside of the slit. This assumption is reasonable as slit losses are generally small because the vast majority of DEEP2 galaxies have effective radius smaller than the 1" slit width (Weiner et al. 2007). We linearly fit the flux calibrated continuum in a 80Å window about the Hβ emission line and scale the equivalent width by the continuum to obtain a Hβ flux.

We use the extinction law of Cardelli et al. (1989) and the fitted E(B−V) values given by Equation 9.1 to correct the observed Hβ flux in the DEEP2 sample for dust attenuation. We obtain the luminosity from the flux using the relation $L(\mathrm{H}\beta) = F_{\mathrm{H}\beta} \times 4\pi D_L^2$ where $F_{\mathrm{H}\beta}$ is the dereddened Hβ flux and D_L is the luminosity distance determined from the redshift. We determine the SFR from the Kennicutt (1998a) relation between SFR and Hα luminosity given by

$$\mathrm{SFR} = 7.9 \times 10^{-42} L(\mathrm{H}\alpha)[\mathrm{ergs\ s}^{-1}]. \tag{6.7}$$

We take $L(\mathrm{H}\alpha) = 2.86 \times L(\mathrm{H}\beta)$ and scale the SFR from Salpeter to Chabrier IMF by dividing by 1.7.

E06 infer their SFRs from the Hα luminosity corrected for dust extinction using the E(B−V) determined from SED fitting. A factor of 2 aperture correction was applied and

the SFRs were determined using the Kennicutt (1998a) relation converted to a Chabrier IMF. We redetermine the SFRs for their 87 galaxies by applying an extinction correction determined from Equation 9.1 to their observed Hα luminosities. Following E06, we apply a factor of 2 aperture correction to the observed luminosity. We determine the SFR from Equation 6.7 and bin data according to E06.

Figure 8.1c shows the distribution of the SFRs for all three samples.

6.4 Galactic Stellar Mass Growth

6.4.1 The Observed Relation between Stellar Mass and SFR

In Figure 6.4 we plot the MS relation for the SDSS (blue squares), DEEP2 (black circles) and E06 (red triangles) star-forming galaxies at redshifts of $z = 0.07, 0.78$ and 2.26, respectively. For the SDSS, DEEP2 and E06 samples the median SFR is determined in bins of stellar masses. For the SDSS, DEEP2 and E06 samples there are ~ 700, ~ 90 and ~ 15 galaxies in each data bin. The flattening in the relation observed at lower stellar masses is due to incompleteness (see below) such that the lower SFR galaxies fall out of our selected samples at lower stellar masses. Down to $\log(M_*) \sim 9.2$ for the SDSS and DEEP2 sample and $\log(M_*) \sim 9.5$ for the E06 sample the relation between stellar mass and SFR is well described by a power law.

For the SDSS and DEEP2 samples the error bars plotted on the data points indicate the interval containing 68% of the data within each mass bin. For the E06 sample the error bars indicate the standard deviation of the distribution within each mass bin. The median scatter in the SFRs is 0.25, 0.27 and 0.24 dex for the SDSS, DEEP2 and E06 samples, respectively. The scatter in the three samples is comparable and is roughly constant with stellar mass. The observed scatter in our samples is comparable to the $\lesssim 0.3$ dex found in studies examining the M_*-SFR relation out to $z \sim 2$ (Salim et al. 2007; Elbaz et al. 2007; Noeske et al. 2007b; Daddi et al. 2007; Pannella et al. 2009).

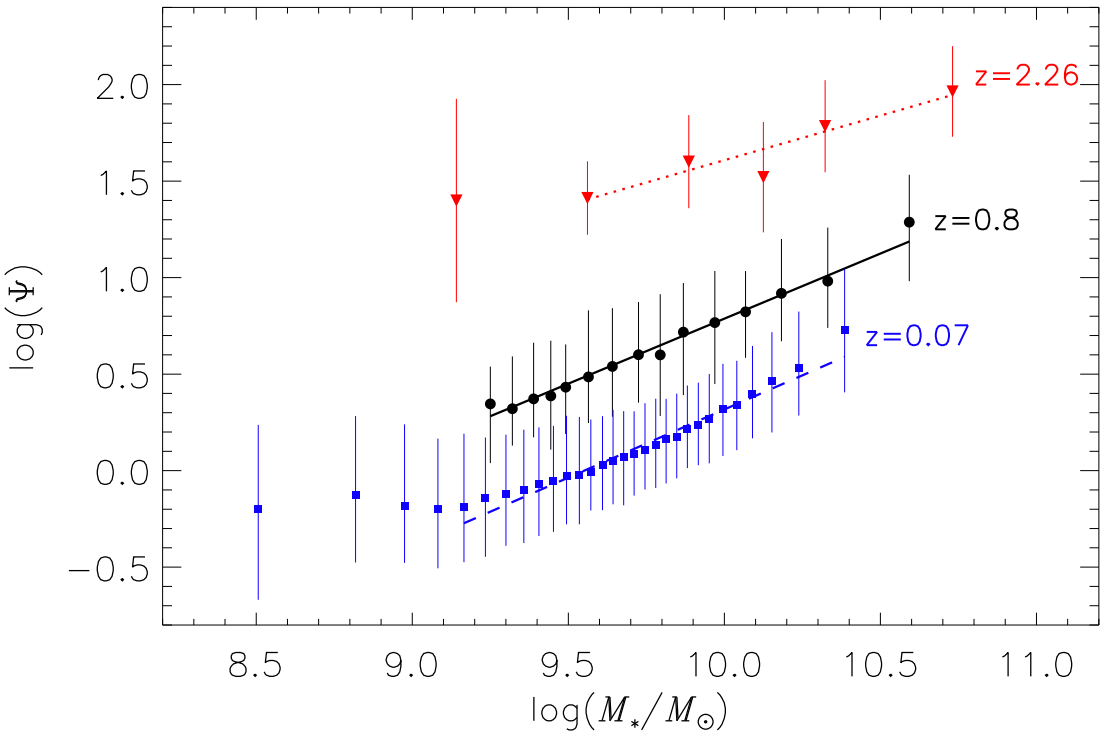

Figure 6.4 The logarithm of the SFR ($M_\odot$ yr^{-1}) plotted in bins of stellar mass for the SDSS (blue squares), DEEP2 (black circles) and E06 (red triangles) samples. For the SDSS and DEEP2 sample the median SFR is plotted and the error bars indicate the interval containing 68% of the data. For the E06 sample the median is plotted and the error bars are the standard deviation of the distribution. The dashed blue, solid black and dotted red lines are fits to the to the observed MS relation for the SDSS, DEEP2 and E06 samples, respectively. The fit parameters are given in Table 6.2.

We fit a linear relation between $\log(\Psi)$ and $\log(M_*/M_\odot)$ in the mass range where the samples are monotonically declining using the *linfit.pro* routine in IDL. The form of the fit is given by

$$\log(\mathrm{SFR}) = \delta + \gamma \cdot [\log(M_*/M_\odot) - 10], \tag{6.8}$$

where δ is the logarithm of the SFR at $10^{10} M_\odot$ and γ is the power law index. The dashed blue, solid black and dotted red lines in Figure 6.4 are the fits to the SDSS, DEEP2 and E06 samples, respectively. We give the fit parameters and the errors in Table 6.2. The

Table 6.2. Mass-SFR Relation

Sample	redshift	δ	γ
SDSS	0.07	0.317 ± 0.003	0.71 ± 0.01
DEEP2	0.78	0.787 ± 0.009	0.67 ± 0.02
E06	2.26	1.608 ± 0.028	0.46 ± 0.07

Note. — The fitted MS relation for our three samples as parameterized by Equation 6.8.

errors for the SDSS and DEEP2 fit parameters are bootstrapped. The errors for the E06 sample are determined from propagating the standard error of each data bin, $\sigma/\sqrt{n}$, where σ is the standard deviation of the distribution and n is the number of objects in each bin. The power law index of the relation is consistent (within the small errors) for the SDSS and DEEP2 samples. We have applied a factor of 2 aperture corrections to all galaxies in the E06 sample. This correction is likely overcorrecting the lower mass galaxies which could explain the shallower slope observed in the MS relation. The zero point of the MS relation shows evolution to higher values with increasing redshift.

6.4.2 Sample Incompleteness

In all three of our samples the MS relation flattens out at lower stellar masses (see Figure 6.4). The galaxies in all three of the samples are selected such that chemical properties can be determined from the spectra. Determining chemical properties from the emission lines of star-forming galaxies generally requires high S/N observations and therefore samples with determined metallicities are more susceptible to incompleteness. We demonstrate that the observed flattening is due to incompleteness by comparing our sample of ∼20,000 galaxies for which we have well determined metallicities with a larger, more complete sample of SDSS star-forming galaxies.

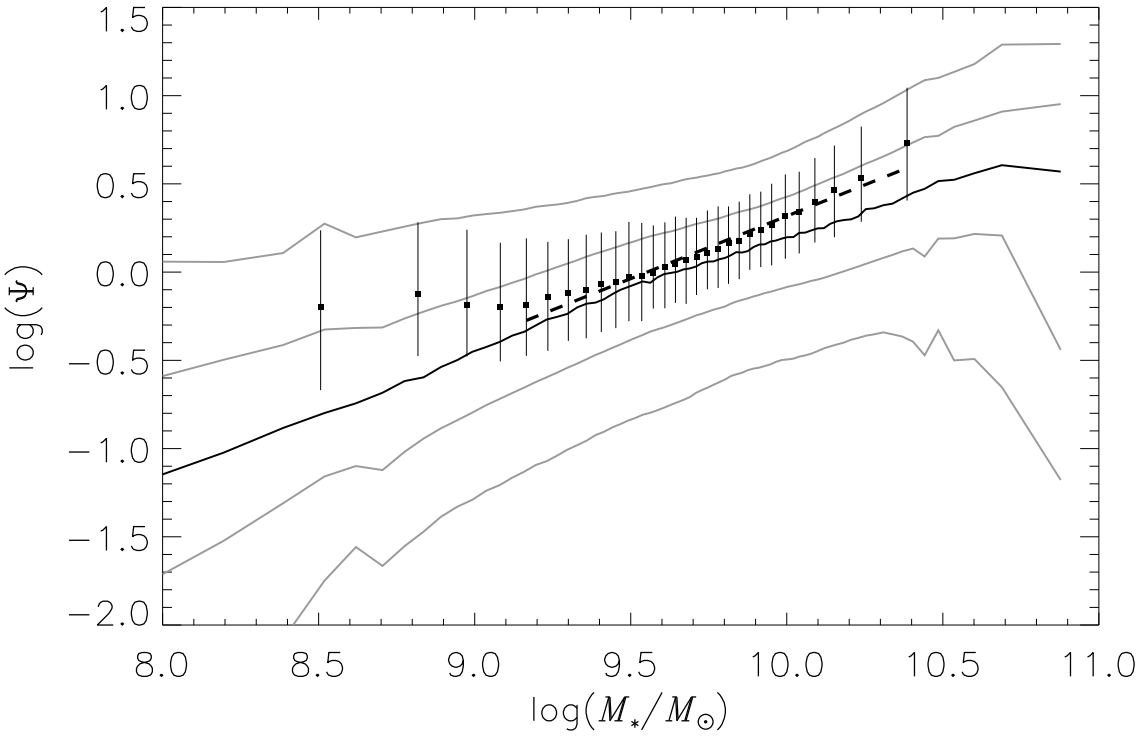

Figure 6.5 The SFR ($M_{\odot}$ yr^{-1}) plotted against stellar mass for our metallicity selected SDSS sample (black points) along with larger comparison sample from SDSS. The black points and error bars are the observed MS relation and its scatter for our metallicity selected SDSS sample. The dashed black line is our fitted relation given by Equation 6.8 with parameters given in Table 6.2. The solid black curve is the MS relation for our larger comparison sample and the gray lines are the 68 and 95% contours.

We select the larger comparison sample by first removing AGN using the [OIII]/Hβ vs. [NII]/Hα diagram (Kauffmann et al. 2003; Kewley et al. 2006) and imposing the similar redshift restrictions ($z < 0.1$) as our metallicity selected SDSS sample. This gives us a parent sample ∼200,000 star-forming galaxies. The aperture corrected SFRs given in the SDSS DR7 rely on a Bayesian technique principally fitting Hα and Hβ lines to determine extinction corrected SFRs (Brinchmann et al. 2004; Salim et al. 2007). We select galaxies from the parent sample by requiring a S/N of 5 in the Hα and Hβ emission lines. This gives us a sample of ∼140,000 star-forming galaxies with $z < 0.1$ and detections of Hα and Hβ.

We note that the distribution of SFRs in our comparison sample are largely independent of choice of S/N cuts and therefore the observed incompleteness in our metallicity selected SDSS sample likely results from our limit on the equivalent width of Hβ.

Figure 6.5 shows the SFRs for both our metallicity selected SDSS sample of galaxies and the larger comparison sample. The black data points with error bars and dashed line are the same as in Figure 6.4. The solid black line is the median SFRs of our comparison sample sorted into 75 bins of stellar mass and the gray curves are the 68 and 95% contours of the data. The MS relation in the larger comparison sample has a slope of 0.65 which is sightly more shallow than our metallicity selected SDSS sample. This slope is consistent with the slope determined by Salim et al. (2007) for MS relation of SDSS galaxies. The zero point of the larger sample is slightly lower as compared to our metallicity selected SDSS sample. Over the range where we fit the MS relation, the difference in the SFRs for the two samples is < 0.1 dex and both relations show similar scatter.

From this comparison it is clear that the flattening observed in the MS relation in Figure 6.4 is due to incompleteness. The slightly higher zero point of our metallicity selected SDSS sample suggests that there is a slight bias against low star-forming galaxies over all mass ranges. This is consistent with our expectation that the higher S/N and equivalent width of Hβ required in the spectra for chemical analysis selects against galaxies with weak lines and low levels of star formation. Despite this selection effect, Figure 6.5 demonstrates that incompleteness does not significantly bias our determination of the MS relation.

Noeske et al. (2007b) examine the MS relation for DEEP2 galaxies in the redshift range of $0.2 < z < 1$. They determine SFRs from the 24 μm flux and add in the SFRs determined from the DEEP2 emission lines with no extinction correction to account for unobscured star formation. They determine the fit to the MS relation in the range where their sample is $>95\%$ complete. The MS relation determined by Noeske et al. (2007b, but see Dutton et al. (2010)) at $z = 0.78$ is consistent with our determination for our DEEP2 sample at the same redshift, despite the fact that our sample is selected differently and we have determined SFRs from extinction corrected emission lines. Our correction for dust extinction relies on the

correlation between extinction, stellar mass and metallicity (Section 6.4.3). This necessarily introduces a correlation between stellar mass and SFR. The fact that the MS determined from our DEEP2 sample is consistent within the errors to the relation fit by Noeske et al. (2007b) implies that our dust correction is not introducing a *spurious* correlation between stellar mass and SFR. Furthermore, we conclude that the MS relation we determine at $z = 0.78$ from our DEEP2 sample is not biased due to incompleteness.

The completeness of the E06 sample at $z = 2.26$ is much more uncertain. This sample is UV-selected which may bias against star-forming galaxies with low levels of star formation if they are present at this redshift. However, we note that the observed relation determined from the E06 sample is consistent within the errors to the zero point and scatter found by Daddi et al. (2007) using a highly complete sample at $z \sim 2$ and Pannella et al. (2009) who use radio stacking to determine SFRs. This suggests that the observed MS relation in the E06 sample is not significantly biased.

6.4.3 Parameterization of SFR

With a well defined MS relation at several redshifts, we can parameterize the SFR as a function of mass and redshift. We seek a parameterization where the variables of mass and redshift are separated such that the SFR is given by

$$\Psi(M_*, z) = \psi_o(z) \cdot f(M_*). \tag{6.9}$$

Here $\Psi(M_*, z)$ is the SFR as a function of stellar mass and redshift, $\psi_o(z)$ is the zero point which evolves with redshift and $f(M_*)$ is the relation between stellar mass and SFR. This definition explicitly assumes that the slope of the relation between stellar mass and SFR has no time dependency.

As discussed in Section 6.4.1, the SFR as a function of stellar mass is well fit by a power law in stellar mass with an index near unity. We therefore parameterize the stellar mass

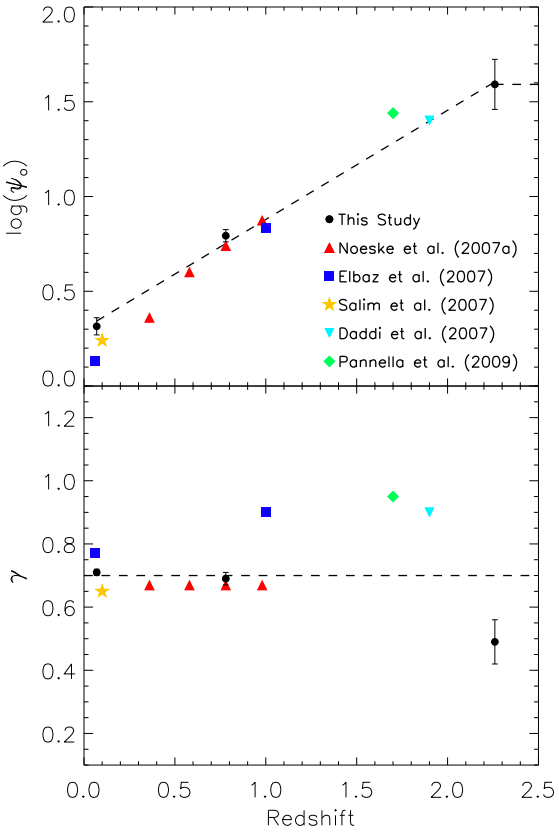

Figure 6.6 The SFR ($M_\odot$ yr^{-1}) for a $10^{10}M_\odot$ galaxy (ψ_o, top panel) and the power law index of the MS relation (γ, bottom panel) as a function of redshift for our data (black points) alongside several values from the literature. The data come from Noeske et al. (2007b, red triangles), Elbaz et al. (2007, blue squares), Salim et al. (2007, yellow star), Daddi et al. (2007, cyan triangle) and Pannella et al. (2009, green diamond). The dashed line in the top panel is the fit for ψ_o as a function of redshift for our three samples given by Equation 6.11. The dashed line in the bottom panel is our adopted value of 0.7 for the power law index of the MS relation, γ.

dependency as

$$f(M_*) = (M_*/10^{10}M_\odot)^\gamma, \tag{6.10}$$

where the only free parameter, γ, is the power law index of the relation. With this definition for $f(M_*)$, the zero point, $\psi_o(z)$, is the SFR of a $10^{10}M_\odot$ galaxy. The zero point of the relation as a function of redshift, as we show below, is well fit by an exponential and we

parameterize it as

$$\psi_o(z) = \alpha \cdot \exp(\beta z). \tag{6.11}$$

Here, α is the zero point at $z = 0$ and β determines the rate of exponential increase with redshift.

Figure 6.6 shows a compilation taken from the literature for the values of γ (bottom panel) and ψ_o (top panel) as defined in Equations 6.10 and 6.11, respectively. For comparison, data from this study are plotted as black points on these plots. We have converted the stellar masses and SFRs for the data shown in Figure 6.6 such that they are consistent with the (Chabrier 2003) IMF. The data selection and method of SFR determination vary. In the local universe, Salim et al. (2007) derive SFRs by fitting the UV/optical broad-band SED. Elbaz et al. (2007) adopt the Brinchmann et al. (2004) aperture corrected SFRs given in the DR4. At $0.2 < z < 1$, the measurements of Noeske et al. (2007b)[4] have SFRs determined from a combination of uncorrected emission line fluxes and 24 μm fluxes. At $z \sim 1$, Elbaz et al. (2007) determine SFRs from the infrared luminosity inferred from the 24 μm flux. At $z \sim 2$, Daddi et al. (2007) determine SFRs from dust corrected UV luminosities and Pannella et al. (2009) determine SFRs from stacking analysis of the radio continuum.

Despite the differences in methodology, our determination of the zero point, ψ_o (top panel Figure 6.6), is remarkably consistent with values found in the literature. In the local universe, we find a marginally higher zero point, which is due to incompleteness (see Section 6.4.2). At $z = 0.78$ we determine the same relation (within the errors) as Noeske et al. (2007b). At $z = 2.26$ the relation determined from the E06 sample is consistent with the higher redshift data. Out to $z \sim 1$, the slope of the MS relation, γ (bottom panel of Figure 6.6), are consistent in most of the studies. At $z > 1$ the slopes show some variation, though the variation is only about $\pm 35\%$. We note that in this study, our results are not

[4]We have taken the parameters of the Noeske et al. (2007b) MS relation from the compilation of Dutton et al. (2010).

sensitive to the adopted value of γ because the redshift evolution of the SFR is significantly greater than the magnitude of the variation introduced by a $\pm 35\%$ change in γ.

In order to derive $\Psi(M_*, z)$, we need to determine values for the three free parameters, α, β and γ. For the SDSS and DEEP2 samples the slopes are consistent (within the errors) and we adopt a constant value of 0.7 for γ in Equation 6.10 (see also Whitaker et al. 2012). This is shown by the dashed line in the bottom panel of Figure 6.6. To determine α and β we fit a line of the form

$$\log[\psi_o(z)] = \log(\alpha) + 0.434\,\beta z, \tag{6.12}$$

to our data. The fit is shown by the dashed line in the top panel of Figure 6.6. We note that we have fit only to our data, but the fit is more or less consistent with all the studies compiled from the literature. At $z > 2.26$ we assume that ψ_o is flat noting that our results are not strongly dependent on this extrapolation because in our model most of the stellar mass growth in star-forming galaxies in the local universe occurs at $z < 2.26$ (see also Leitner 2012).

With both $\psi_o(z)$ and $f(M_*)$ determined, we can parameterize the SFRs of star-forming galaxies as a function of stellar mass and redshift by entering the fitted results back into Equation 9.2. The SFR as a function of stellar mass and redshift is given by

$$\Psi(M_*, z) = 2.00 \cdot \exp(1.33z) \left(\frac{M_*}{10^{10}}\right)^{0.7} [M_\odot\,\mathrm{yr}^{-1}]. \tag{6.13}$$

In Figure 6.7 we show the fitted relation plotted over the observations. Though the fitted slope of the MS relation at $z = 2.26$ was shallower (see Table 6.2), the data is still reasonably well described by the relation given in Equation 6.13.

6.5 Inventory of Oxygen

In this study we compare an estimate of the total amount of oxygen produced with the amount found in the ISM and stars of local star-forming galaxies. We focus on oxygen

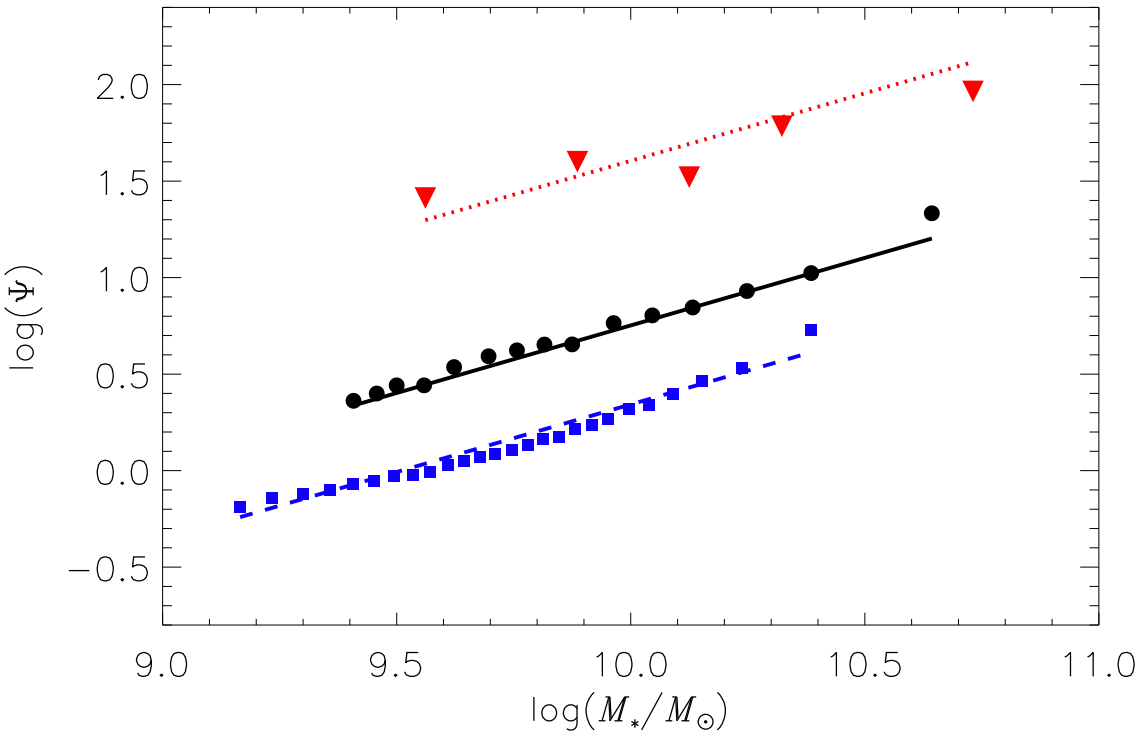

Figure 6.7 The fitted relation for the SFR ($M_\odot$ yr^{-1}) as function of redshift, $\Psi(M_*, z)$, given by Equation 6.13 plotted over our three samples.

because it is a primary element produced in massive stars that end their lives as Type II supernovae. Oxygen is the most abundant element produced and therefore the easiest to measure from strong nebular emission lines originating in the ISM of galaxies. Oxygen production depends only weakly on the initial metallicity (Thomas et al. 1998; Kobayashi et al. 2006) and is considered a robust tracer of total metal production. We assume that oxygen production is independent of metallicity. The rate of oxygen production is then simply given by

$$\frac{dM_T^o}{dt} = P_o \, \Psi. \tag{6.14}$$

Here M_T^o is the mass of oxygen produced in solar mass units, P_o is a constant representing the mass of newly synthesized oxygen per solar mass of gas converted to stars and Ψ is the

SFR. We can estimate the total oxygen production by integrating Equation 6.14. This is given by

$$M_T^o(t > t_i) = P_o \int_{t_i}^{t} \Psi(t')\, dt'. \tag{6.15}$$

The amount of oxygen produced between some initial time, t_i, and some later time, t, is proportional to the total amount of star formation during that epoch. This equation implies that $M_T^o \propto M_*$, where M_T^o is the *total* amount of oxygen produced in a galaxy and M_* is the stellar mass of the galaxy. Ψ is explicitly parameterized as a function of redshift (see Equation 6.13) which we convert into a function time by assuming the conversion between redshift and time using the IDL routine *galage.pro*.

The second component of our oxygen census is the oxygen found in the ISM. We define the global gas-phase oxygen mass abundance such that $Z_g = M_g^o/M_g$. Here, M_g and M_g^o are the mass of gas and the mass of oxygen in the gas-phase, respectively, given in solar mass units. The total oxygen mass in the gas-phase is given by rewriting this equation such that $M_g^o = Z_g\, M_g$. Both Z_g and M_g are measured quantities.

The final component of our census of oxygen in star-forming galaxies is the oxygen locked up in stars. Assuming that the gas in galaxies is well mixed and mass return from stars is instantaneous, the rate at which oxygen is locked up in stars is given by

$$\frac{dM_*^o}{dt} = (1 - R)\, Z_g\, \Psi. \tag{6.16}$$

Here M_*^o is the mass of oxygen going into stars in solar mass units and R is a constant representing the fraction of gas that is returned to the ISM through various stellar mass loss processes. We can integrate Equation 6.16 to get the total amount of oxygen locked up in low mass stars. This is given by

$$M_*^o(t > t_i) = (1 - R) \int_{t_i}^{t} Z_g(t')\, \Psi(t')\, dt'. \tag{6.17}$$

M_*^o represents the amount of oxygen in the ISM that gets forever locked up in low mass stars in the time between t_i and t. Similar to Ψ, Z_g is a explicitly a function of redshift which we convert into a function of time. In Sections 6.6 and 6.7 we develop an empirically constrained, self-consistent approach for determining $\Psi(t)$ and $Z_g(t)$, respectively.

6.6 Tracing Galaxies through Cosmic Time

One interpretation of the MS relation and its evolution is that most star formation is driven largely by secular processes such as gas accretion and mergers do not play a significant role (e.g. Noeske et al. 2007b; Dutton et al. 2010; Elbaz et al. 2011). Under the assumption that stellar mass build up is a purely secular process, we can trace stellar mass evolution of galaxies by assuming that

$$\frac{dM_*}{dt} = (1 - R)\,\Psi. \tag{6.18}$$

Here $\frac{dM_*}{dt}$ is the time rate of change of stellar mass, R is the return fraction which accounts for gas that is formed into stars but then returned to the ISM via various mass loss processes (e.g. supernovae and stellar winds) and Ψ is the SFR. For simplicity we assume that R is a constant (see Section 6.9 and the Appendix for more discussion).

If we further assume the continuity condition that star-forming galaxies *evolve along the MS relation* and SFRs are a (determined) function of stellar mass and redshift (see Equation 6.13), it is straightforward to integrate Equation 9.3 in order to determine the stellar mass as a function of redshift. This is given by

$$M_*(t) = M_{*,i} + (1 - R) \int_{t_i}^{t} \Psi(M_*,\, t')\, dt'. \tag{6.19}$$

Here $M_*(t)$ is the stellar mass at some redshift, $t < t_i$. $M_{*,i}$ is the stellar mass at some initial time, t_i, and the integral of $\Psi(M_*, t)$ represents the gain in stellar mass, modulo the return fraction R, from some initial time t_i to some later time t. If $M_{*,i}$ is set to an arbitrarily low value ($10^6 M_\odot$) and the upper limit of the integral is the current epoch, then

t_i is simply the formation time. This is similar to the staged model of Noeske et al. (2007a) such that lower stellar mass star-forming galaxies in the local universe begin forming their stars at later times.

Equation 6.19 is a simple, yet powerful tool for identifying star-forming galaxies at lower redshifts with their progenitors at higher redshifts under the assumption of secular evolution (i.e. no contribution from merging) and that the SFRs are a known function of stellar mass and redshift (see Equation 6.13); the latter being observationally determined. Similar approaches have been developed in the literature and we direct the reader to Leitner (2012) for a detailed discussion of the implications of such a model for stellar mass growth. Because of the stellar mass dependence of Ψ and the fact that SFR is measured in units of solar masses per year and not solar masses per redshift, Equation 9.3 does not have a straightforward analytical solution and thus requires numerical integration. The integration of Equation 9.3 gives both the stellar mass and star formation history of the galaxy.

6.7 Galactic Chemical Evolution

The three data samples used in this study have been selected because they all have well determined MZ relations. The MZ relation for the SDSS and DEEP2 samples are determined by Zahid et al. (2011) and for the E06 sample by Erb et al. (2006a). We convert the metallicity, traditionally quoted as a number density given by 12 + log(O/H), to gas-phase mass abundance using the simple linear conversion given by Equation 6.6.

In Figure 6.8 we plot the MZ relation for our three data samples. The MZ relation for the SDSS and DEEP2 sample are determined using the calibration of Kobulnicky & Kewley (2004, Figure 6.8a) and the for the E06 sample using the calibration of Pettini & Pagel (2004, Figure 6.8b). Kewley & Ellison (2008) have shown that while various calibrations give relatively accurate measurements of the metallicity, there are systematic differences. We apply the conversions constants they derive in order to convert between the two calibrations shown in Figure 6.8. The shape of the MZ relation determined from the two

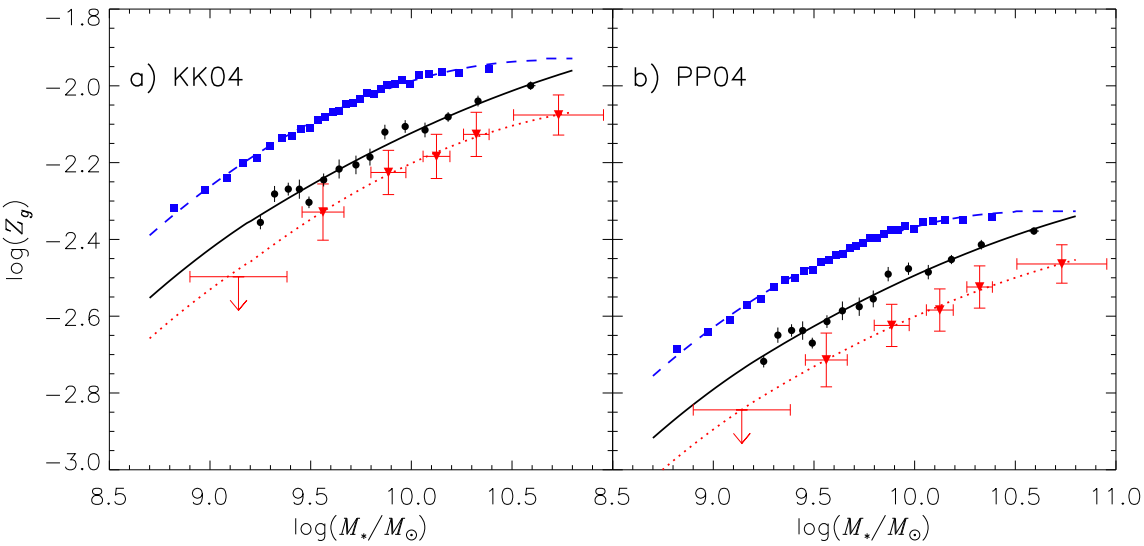

Figure 6.8 The MZ relation determined using the calibration of a) Kobulnicky & Kewley (2004) and b) Pettini & Pagel (2004). The metallicity is given as the mass abundance of oxygen relative to hydrogen. The blue, black and red curves are the MZ relations determined for the local sample from SDSS, the intermediate redshift sample from DEEP2 (Zahid et al. 2011) and the high redshift sample from Erb et al. (2006a), respectively. The metallicities for the SDSS and DEEP2 data are originally determined using the Kobulnicky & Kewley (2004) diagnostic and the metallicity of the Erb et al. (2006a) sample is originally determined using the Pettini & Pagel (2004) diagnostic. When necessary, the metallicities have been converted using the coefficients given by Kewley & Ellison (2008).

calibrations is very similar. The main difference being the 0.35 dex higher abundances of the Kobulnicky & Kewley (2004) calibration with respect to the calibration of Pettini & Pagel (2004). In this study we adopt the average of the two calibrations for our determination of metallicities. In Section 6.8.3 we provide a more detailed discussion of the calibrations uncertainties.

We use the observed MZ relations to determine the gas-phase mass abundance as a function of stellar mass and redshift. The three samples in this study suggest that the MZ relation evolves linearly with time. Moustakas et al. (2011) investigate the MZ relation evolution out to $z = 0.75$ and suggest that it evolves linearly with redshift. In this study we assume linear evolution with time but note that assuming linear evolution with redshift

has only minor quantitive effects on our results and has no effect on our interpretation. We further assume a constant offset between the three relations at $\log(M_*/M_\odot) < 9.2$. The MZ relation in the local universe is shown to extend to low stellar masses (Lee et al. 2006; Zahid et al. 2012) and we linearly extrapolate the three relations to lower stellar masses when necessary.

In summary, we determine the gas-phase mass abundance of oxygen at arbitrary redshifts and stellar masses by linearly interpolating between the three observed relations shown in Figure 6.8. We linearly interpolate both in *time* and *stellar mass* in order to determine $Z_g(M_*, z)$.

6.8 A Census of Oxygen

There are three components to our oxygen census: total oxygen produced, amount of oxygen locked up in stars and the amount of oxygen in the gas-phase. To put this in context, we begin our census by noting the basic balance equation for oxygen. In a closed-box system with no inflows or outflows of gas, the oxygen balance is given by

$$\begin{aligned} dM_g^o &= P_o\,\Psi - Z_g\,\Psi + R\,Z_g\,\Psi \\ &= P_o\,\Psi - (1-R)\,Z_g\,\Psi \end{aligned} \tag{6.20}$$

As before, M_g^o is the mass of oxygen in the gas-phase, Z_g is the gas-phase mass abundance of oxygen and is defined as $Z_g = M_g^o/M_g$, where M_g is the gas mass. Ψ is the SFR. R and P_o are the gas return fraction and mass of newly synthesized oxygen per unit stellar mass, respectively. The first term on the right-hand side of Equation 6.20 represents the total mass of oxygen produced, the second term represents the amount that goes into stars and the third term represents the amount that is subsequently returned through mass loss. The stellar yield, y, is related to the nucleosynthetic yield and gas fraction by $y = P_o/(1-R)$. We introduce this basic balance equation to place the census of oxygen in star-forming galaxies

that follows within the context of simple chemical evolution models. For a more detailed discussion of these chemical evolution models we refer the reader to Edmunds (1990).

6.8.1 Total Oxygen Production

The total amount of oxygen produced by the stars within a galaxy is simply given by

$$M_T^o = P_o \frac{M_*}{1-R}. \tag{6.21}$$

The quantity $M_*/(1-R)$ represents the total amount of gas converted into stars. Several simplifying assumptions go into Equation 6.21: 1) The IMF is constant, 2) gas is instantaneously returned and 3) the oxygen yield is independent of metallicity. In Section 6.8 we discuss systematics and uncertainties associated with each of these assumptions.

6.8.2 Oxygen in the Gas-Phase

The total mass of oxygen in the gas-phase in local star-forming galaxies is given by $M_g^o = Z_g\, M_g$, where M_g^o is the mass of oxygen in the gas-phase. Unfortunately, direct gas mass measurements are available for only a few galaxies in our local sample. We therefore estimate the gas mass of local galaxies using the observed relation between gas fraction and stellar mass for star-forming galaxies. Peeples & Shankar (2011) compile gas mass estimates (HI + H_2, with correction for helium) from several sources in the literature and give the binned cold gas fraction as a function of stellar mass (see Table 2 in their paper). The values are compiled from the data sets of McGaugh (2005), Leroy et al. (2008) and Garcia-Appadoo et al. (2009).

In Figure 6.9 we plot the log of the gas fraction, f_g, as a function of stellar mass. The gas fraction is defined such that $f_g = M_g/M_*$[5]. The stellar mass estimates of Peeples & Shankar (2011) are taken from MPA/JHU catalog and we make a 0.2 dex correction for consistency (Zahid et al. 2011). The error bars are the 1σ uncertainties on the mean of

[5]We have adopted the convention of Peeples & Shankar (2011) in defining f_g. This differs from the traditional definition of the gas fraction given by $f_g = M_g/(M_* + M_g)$.

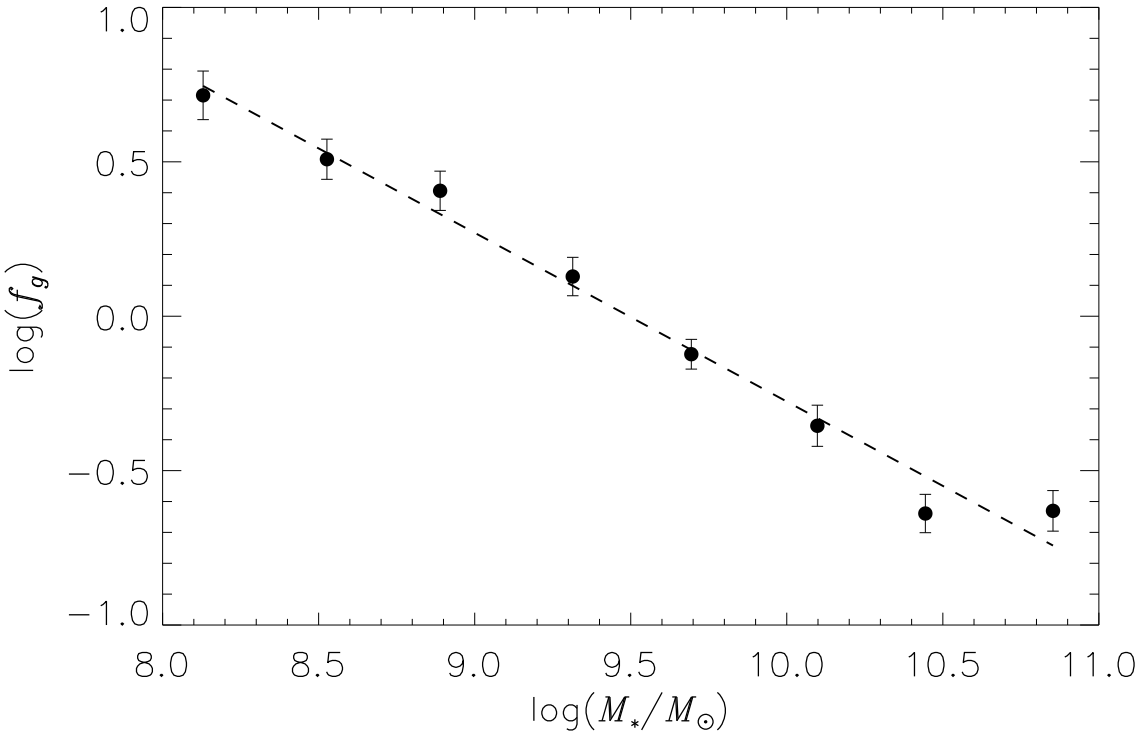

Figure 6.9 The gas fraction as a function of stellar mass for star-forming galaxies taken from the compilation of Peeples & Shankar (2011). The dashed line is a fit to the relation and is given by Equation 6.22.

$\log(f_g)$. The dashed line is a fit to the relation given by

$$\log(f_g) = (-0.28 \pm 0.03) - (0.55 \pm 0.03) \cdot [\log(M_*/M_\odot) - 10]. \tag{6.22}$$

The errors in the parameters come from propagating the uncertainties in the mean of $\log(f_g)$. When calculating gas mass, we add 0.1 dex to the fitted relation at all stellar masses to account for ionized gas (see Table 1.1 in Tielens 2005). Using this relation, the gas mass is given by $M_g = f_g M_*$. We note that the gas fractions given by Equation 6.22 are greater than values inferred from inversion of the Schmidt-Kennicutt relation (see Figure 2 in Peeples & Shankar 2011). Using gas fractions determined from inverting the Schmidt-Kennicutt

relation would therefore lower the estimate of the mass of oxygen in the gas-phase and increase the oxygen deficit presented in Section 6.8.4.

We can straightforwardly estimate the mass of oxygen in the gas-phase of local star-forming galaxies from observed quantities by combining the relation for f_g given in Equation 6.22 with the MZ relation for local star-forming galaxies shown in Figure 6.8. This is given by $M_g^o = Z_g f_g M_*$.

6.8.3 Oxygen Locked Up in Stars

The most difficult component of our oxygen census to estimate is the oxygen locked up in stars. The total amount of oxygen produced by stars and the amount of oxygen found in the gas-phase of galaxies can be inferred from the *present-day* physical quantities of the stellar mass and gas-phase abundance. However, the oxygen locked up in stars is an accumulated property that is dependent on the star formation and chemical history. The amount of oxygen locked up in stars between some initial redshift t_i and some later redshift t is analytically given by

$$M_*^o(t > t_i) = (1 - R) \int_{t_i}^{t} Z_g(t')\, \Psi(t')\, dt'. \tag{6.23}$$

We have parameterized both the SFR (see Section 6.4) and gas-phase oxygen abundance (see Section 6.7) as a function of stellar mass and time and are therefore able to empirically constrain the total amount of oxygen locked up in stars by simply carrying out a numerical integration of Equation 6.23.

We simultaneously determine the star formation and stellar mass history of a galaxy using Equation 6.19. We set $M_{*,i} = 10^6 M_\odot$ and carry the integral from t_i out to $t = 12.5$ Gyr [6]. Higher values of t_i correspond to younger, lower stellar mass star-forming galaxies in the local universe. We show the stellar mass history of three galaxies ($t_i = 2.4, 4.0$ and 6.4 Gyr) in Figure 6.10a and star formation history in Figure 6.10b assuming $R = 0.35$.

[6] We set the upper limit of the integral to a time corresponding to a redshift of $z = 0.07$ rather than $z = 0$ because this is the median redshift of our local sample from SDSS.

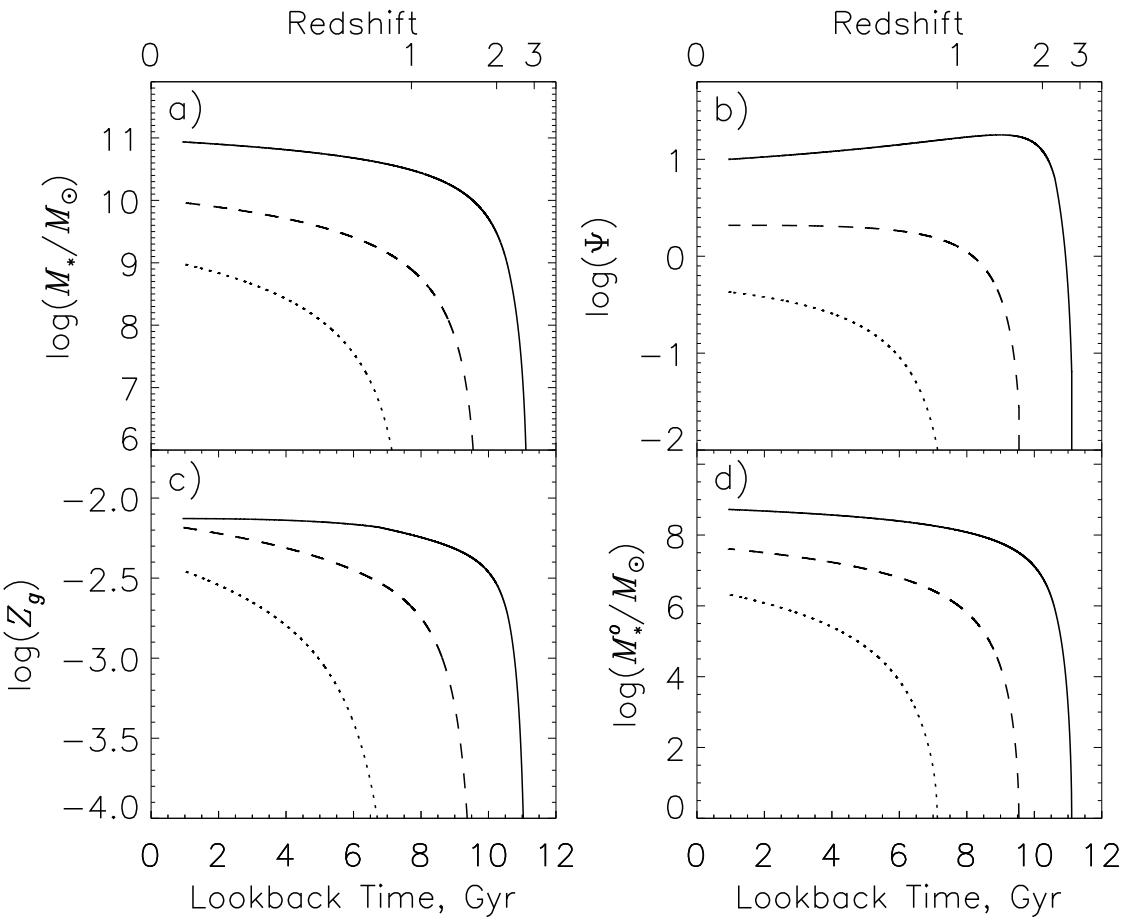

Figure 6.10 The a) stellar mass, b) SFR ($M_\odot$ yr^{-1}), c) gas-phase oxygen abundance and d) the mass of oxygen locked up in stars determined from our models as a function of look back time and redshift. The solid, dashed and dotted curves are galaxies that have a stellar mass of $10^{11}, 10^{10}$ and $10^9 M_\odot$ in the local universe (z = 0.07).

The stellar mass history as a function of redshift allows us to determine the metallicity as a function of redshift for each galaxy using the procedure described in Section 6.7. We plot the chemical history in Figure 6.10c. Entering the star formation history, $\Psi(t)$ (Figure 6.10b), and the chemical history, $Z_g(t)$ (Figure 6.10c), into Equation 6.23, we can determine the mass of oxygen locked up in stars as a function of redshift. This is shown in Figure 6.10d.

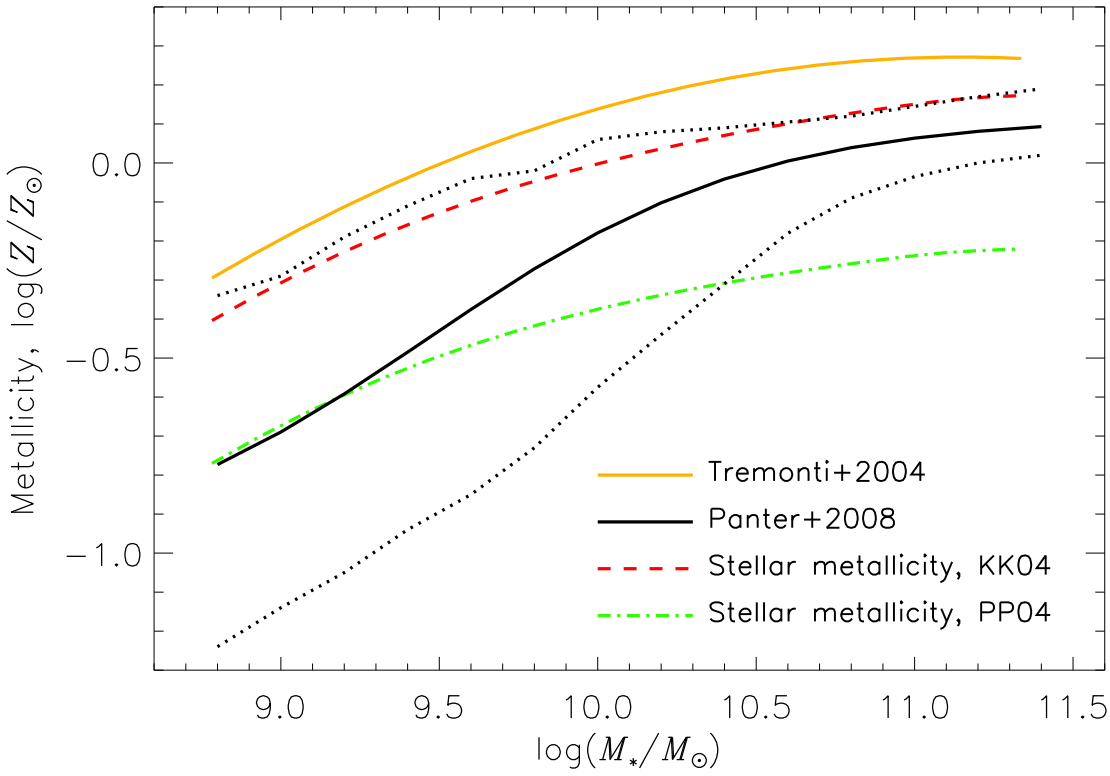

Figure 6.11 The stellar mass−stellar metallicity relation for local star-forming galaxies. The solid black curve is the fitted relation determined by Panter et al. (2008) and the dotted curves are the 16 and 84% contours of the distribution. The red dotted and green dot-dashed curves plot the stellar metal content of local star-forming galaxies calculated from Equation 6.24 using the Kobulnicky & Kewley (2004) and Pettini & Pagel (2004) abundance calibrations, respectively. For reference (c.f. Panter et al. 2008, Figure 6), the solid yellow curve plots the MZ relation from Tremonti et al. (2004).

Gallazzi et al. (2005) and Panter et al. (2008) examine the stellar mass−stellar metallicity relation determined from stellar population modeling of SDSS spectra. Both groups derive a consistent relation which implies that the imprint of the MZ relation from earlier epochs is observed in stellar populations of galaxies today. In Figure 6.11 we compare the metallicity of stars from our model analysis to that observed by Panter et al. (2008) using $\sim 300,000$ galaxies in SDSS. We estimate the mass-weighted stellar metallicity from our model of the star formation and chemical histories of galaxies (see Figure 6.10b and c,

respectively). In particular we compute

$$Z_*(M_*) = \frac{\int_{t_i}^{t} \Psi(t')Z(t')dt'}{\int_{t_i}^{t} \Psi(t')dt'} = \frac{\int_{t_i}^{t} \Psi(t')Z(t')dt'}{M_*}, \tag{6.24}$$

where Z_* is the mass-weighted stellar metallicity as a function of current stellar mass, M_*. We compare directly to the mass-weighted stellar metallicity relation observed and parameterized by Panter et al. (2008, see Equation 1 and Figure 6). In Figure 6.11 the Panter et al. (2008) fitted relation is plotted by the solid black curve and the 16 and 84% contours of the distribution are shown by the dotted black curve.

As can be seen from Equation 6.24, our estimate of the metal content of stars is dependent on the choice of gas-phase abundance diagnostic. In Figure 6.11 we plot the mass-weighted stellar metallicity for both the Kobulnicky & Kewley (2004, red dashed curve) and Pettini & Pagel (2004, green dot-dashed curve) calibration. For reference the MZ relation from Tremonti et al. (2004) is plotted by the yellow curve and for consistency we adopt the solar metallicity value of $12+\log(\mathrm{O/H})_\odot = 8.87$ used by Panter et al. (2008). Estimates from the two different abundance diagnostics converted into stellar metallicities using Equation 6.24 envelope the relation from Panter et al. (2008). In this study we have adopted a metallicity calibration that is an average of the Kobulnicky & Kewley (2004) and Pettini & Pagel (2004) calibration (see Section 6.7). Within the systematic uncertainties, our estimate of stellar metallicities using Equation 6.24 and the observed stellar metallicities from Panter et al. (2008) are consistent.

6.8.4 The Oxygen Deficit

In Figure 6.12a-c we plot the mass of oxygen for our three census components. We plot the total mass of oxygen produced (blue curve), the mass of oxygen in the gas-phase (black curve) and the mass of oxygen locked up in stars (red curve) as a function of stellar mass for star-forming galaxies in the local universe. The solid, dotted and dashed curves are used to illustrate the effect varying the parameters has on different components of the census.

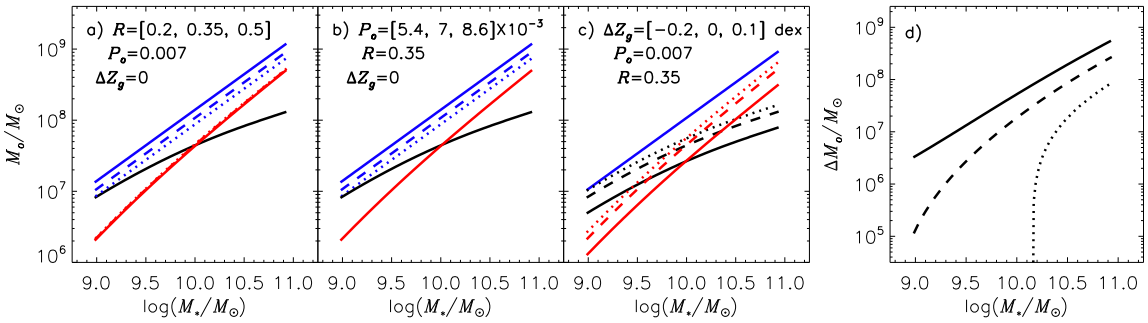

Figure 6.12 The census model of oxygen determined by a) varying the return fraction, b) the oxygen yield and c) the zero point of the oxygen abundance calibration while keeping the other two parameters constant, respectively. a-c) The total oxygen produced (blue line), oxygen found in the gas (black) and stellar phase (red) are plotted as a function of stellar mass for local star-forming galaxies. In a-c) we display the three values adopted for the varying parameter along with the constant values adopted for the other two parameters. The solid, dotted and dashed lines indicate how the mass of oxygen varies for the three different census components when adopting the three different values for the varying parameter. d) The oxygen deficit which is defined as the total oxygen produced minus the oxygen found in the gas and stellar phase. The oxygen deficit is the same for the oxygen masses determined in a-c).

The three free parameters in our model are the return fraction, R, the oxygen yield, P_o, and a constant offset in metallicity (which we refer to as ΔZ_g) since the zero point varies depending on the calibration. Figure 6.12a-c demonstrates the dependencies of the various components of our census on the free parameters of the model. In Figure 6.12a-c we vary R, P_o and ΔZ_g, respectively, while keeping the other two parameters fixed. The three values adopted for the varying parameter and the adopted values of the constant parameters are shown in a-c. In Figure 6.12a we see that variations in R mainly affects the total amount of oxygen produced with a small effect on the amount of oxygen locked up in stars. Figure 6.12b shows that varying P_o only affects the total amount of oxygen produced and Figure 6.12c demonstrates that varying ΔZ_g affects both the stellar and gas-phase components of the census, but has no effect on the total amount of oxygen produced.

For a closed-box model, the total mass of oxygen produced equals the mass of oxygen found in the gas-phase and stars. However if metals are lost from the system, the equality

will not hold. Thus we have

$$\Delta M^o = M_T^o - M_g^o - M_*^o, \tag{6.25}$$

where, as before, M_T^o is the total mass of oxygen produced and M_g^o and M_*^o is the mass found in the gas-phase and stars, respectively. ΔM^o, which we refer to as the oxygen deficit, represents the total amount of oxygen produced that is unaccounted for by the gas-phase and stellar components. In Figure 6.12d we plot the oxygen deficit which is the same for the three cases shown in Figure 6.12a-c. *The variation in the parameters are degenerate such that the oxygen deficit depends only on the variation in the quantity* $\Delta Z_g(1-R)/P_o$*, effectively reducing our three free parameters to one free parameter.* We note that the stellar yield, y, is given by $y = P_o/(1-R)$. Therefore, our model is only sensitive to the changes in the zero point of the metallicity relative to the stellar yield. Higher (lower) values of $\Delta Z_g/y$ correspond to a smaller (larger) oxygen deficit. To first order, this is true for all models of chemical evolution relying on these quantities.

If we assume that all oxygen in galaxies originates from the stars within the galaxy, the oxygen deficit cannot be negative because a negative value would imply that there is more oxygen in the gas and stars than was produced by the galaxy. A physical model of the oxygen deficit requires a combination of the free parameters ($\Delta Z_g(1-R)/P_o$) that yield $\Delta M^o \geq 0$. The dotted line in Figure 6.12d gives a negative oxygen deficit at $M_* \lesssim 10^{10} M_\odot$, implying this is an unphysical model.

The functional form of the oxygen deficit with respect to stellar mass varies according to $\Delta Z_g(1-R)/P_o$. However, a generic feature of the oxygen deficit is that it monotonically increases with stellar mass and is substantial at high stellar masses regardless of our particular choice of $\Delta Z_g(1-R)/P_o$. In the case where the oxygen deficit is substantial at all stellar masses (solid curve in Figure 6.12), we have $\Delta M^o \propto M_*^\alpha$ with a near unity value of for the exponent ($\alpha = 1.14$). When the oxygen deficit is large at all stellar masses (solid curve in Figure 6.12), the oxygen deficit does not strongly depend on the shape of the MZ relation or the shape of the relation between gas fraction and stellar mass. At more

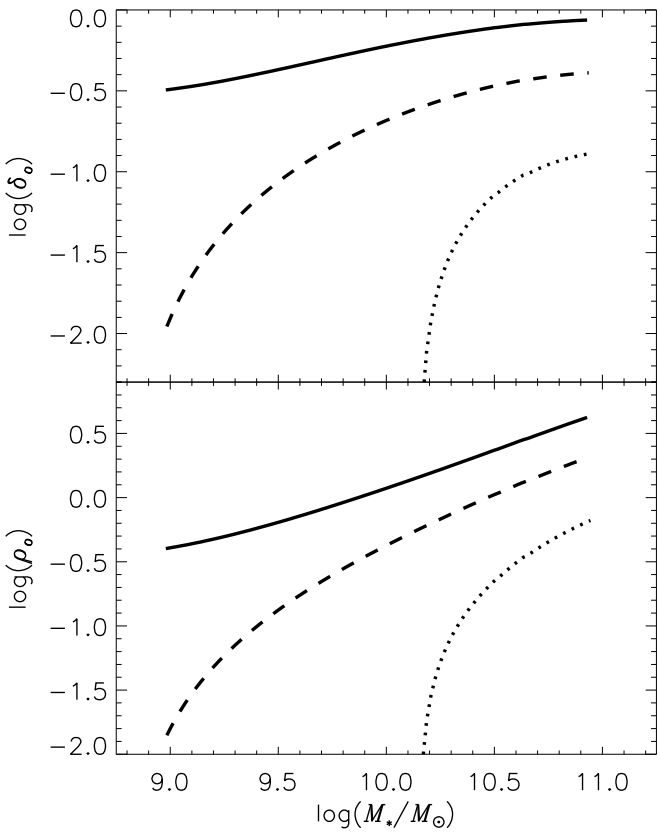

Figure 6.13 The top panel shows the oxygen deficit relative to the mass of oxygen in the gas and stellar phase and the bottom panel shows the oxygen deficit relative to only the mass of oxygen in the gas-phase. The oxygen deficit is the same as in Figure 6.12d and the solid, dotted and dashed lines indicate the different oxygen deficit derived by varying the free parameters.

moderate values of $\Delta Z_g(1-R)/P_o$ examined in our models (dashed curve in Figure 6.12), the relation between the oxygen deficit and stellar mass is more complicated. In Section 6.9.1 we argue that a model where the oxygen deficit is large at all stellar masses and is nearly proportional the stellar mass is most consistent with independent observations of oxygen in the halos of star-forming galaxies.

In Figure 7.3 we plot the fractional oxygen deficit. In the top panel we plot the logarithm of δ_o, which we define as

$$\delta_o = \frac{\Delta M^o}{M_*^o + M_g^o}. \tag{6.26}$$

δ_o is the oxygen deficit relative to the total oxygen content of the galaxy. In the bottom panel we plot the logarithm of ρ_o, which we define as

$$\rho_o = \Delta M^o / M_g^o. \tag{6.27}$$

δ_o is an important quantity reflecting key physical processes governing chemical evolution of galaxies but cannot be determined for individual galaxies as the fraction of oxygen locked up stars cannot be measured. ρ_o does not account for oxygen locked up in stars, but can be determined from observable quantities and is therefore an important parameter for comparison with observations.

6.9 Systematics and Uncertainties

We have derived the oxygen deficit by comparing the total oxygen produced with the amount found in the gas-phase and stars of galaxies. We have derived the oxygen deficit on the basis of observed relations that are determined from large samples of galaxies. Star formation rates and metallicities of individual galaxies are subject to stochastic variations resulting from physical processes that are not fully understood. The results of our study are valid in a statistical sense and do not necessarily apply to any individual galaxy.

Large stochastic variations in the star formation rates and metallicities of galaxies does pose a problem for our approach since we assume galaxies evolve along the observed MS and MZ relations. The tight relation between stellar mass and SFR and the small scatter suggest that the SFRs of star-forming galaxies in the local universe do not vary rapidly over their lifetime and that mergers play a minor role (e.g. Noeske et al. 2007b; Dutton et al. 2010; Elbaz et al. 2011). Though the observed scatter in metallicities increases at the low stellar mass end of the local MZ relation (Zahid et al. 2012), the 1σ scatter is $\lesssim 0.2$ dex (Tremonti et al. 2004). The main source of uncertainty then is likely not associated with our approach but rather with parameters of our model and other simplifying assumptions which we discuss below.

6.9.1 The Return Fraction and Instantaneous Recycling Approximation

The fraction of gas returned to the ISM is mass dependent and therefore sensitive to the particular choice of an IMF, with theoretical values ranging between $\sim 20 - 50\%$. We have adopted this range in Figure 6.12a. The physical mechanism regulating mass loss in stars varies by stellar mass. In low mass stars, stellar winds during the red-giant branch and asymptotic giant-branch are the dominant mechanism. In intermediate mass stars winds during the asymptotic giant branch phase dominate and for high mass stars, both stellar winds and supernovae contribute to stellar mass loss (Jungwiert et al. 2001, and references therein).

The return fraction is important in our models in that it sets the total amount of star formation required for a galaxy to have a particular current stellar mass. The total amount of gas converted into stars, M_{gs}, in a galaxy with a current stellar mass of M_* is given by $M_{gs} = M_*/(1 - R)$. A galaxy with $R = 0.5$ will, to first-order, form 40% more stars than a galaxy with $R = 0.3$ to achieve the same stellar mass. Because the amount of oxygen produced is directly proportional to the total amount of star formation, there will be a commensurate increase in total oxygen production.

We have also adopted the instantaneous recycling approximation (IRA) introduced by Tinsley (1980). The IRA assumes that the gas is returned to the ISM immediately following star formation. It is shown that the IRA works well for high mass stars whose lifetimes are short compared to star formation time scales. Oxygen is a primary element, mainly produced in Type II supernovae. In our models, the lifetimes of massive stars responsible for oxygen enrichment and gas mixing timescales are significantly shorter than the timescales of star formation and therefore the IRA is reasonable in regards to oxygen production. However, the gas return from Type II supernovae accounts for 10-20% of the gas returned to the ISM and a larger fraction is returned on longer timescales from intermediate and low mass stars (see Jungwiert et al. 2001).

Examining various IMFs, Leitner & Kravtsov (2011) show that the majority of stellar mass loss occurs in the first 1-2 Gyrs (c.f. their Figure 1). Noeske et al. (2007b, among

others) argue that the MS relation implies that for most star-forming galaxies the SFR gradually declines. The gradual decline in SFRs is a generic feature of models assuming the continuity condition that galaxies build up stellar mass evolving along the observed MS relation (e.g. Peng et al. 2010; Leitner & Kravtsov 2011; Leitner 2012, this work). The IRA can be reasonably applied in situations where the SFR is not changing rapidly with redshift because though the current generations of stars being formed will return majority of their gas in 1-2 Gyrs, the total gas return will be an integration over previous generations. If the SFR is not rapidly varying, the return fraction will reach a relatively constant value within a few Gyrs.

In the Appendix we apply a time dependent treatment for gas return in determining the oxygen deficit. We no longer assume the IRA so that oxygen is not instantaneously recycled nor is the return fraction a constant. We show that our results are not sensitive to time dependencies in the return rate and adopting a constant and instantaneous return of gas is valid.

6.9.2 The Oxygen Yield

The production of oxygen in our models is defined by the oxygen yield, P_o. The oxygen yield represents the total amount of newly synthesized oxygen per unit stellar mass of star formation. Following Henry et al. (2000), we formally define the integrated oxygen yield as

$$P_o = \int_{m_l}^{m_u} m p_o(m) \phi(m) dm. \tag{6.28}$$

Here m_l and m_u are the lower and upper limits of the mass range of stars formed, respectively, $p_o(m)$ is the mass fraction of oxygen synthesized by a star of stellar mass m and $\phi(m)$ is the normalized IMF. Uncertainties in P_o arise from uncertainties in the stellar yields, the IMF and the mass range of integration. Here we discuss only the stellar oxygen yields. For a more complete review of uncertainties in stellar yields of various elements see Romano et al. (2010).

The dependence of the oxygen yield on the IMF is clear from examination of Equation 6.28. The relative weight of stars in different mass ranges assuming different IMFs are given by Romano et al. (2005, Table 1). The relative weight of $8-40M_{\odot}$ stars is a factor 1.6 higher for the Chabrier IMF as compared to the Salpeter IMF, highlighting the uncertainties in the oxygen yields associated with the assumption of the IMF. These uncertainties are further exacerbated by the possibility of a varying IMF. Kroupa & Weidner (2003) argue that the integrated galactic initial mass function (IGIMF), the stellar mass distribution function for all stars within a galaxy, is an integration of the stellar IMF over the embedded cluster mass function, ECMF. There exists an empirical relation between the ECMF and the observed SFR, leading to a dependence of the IGIMF on the observed SFR. Peeples & Shankar (2011) show several models for the stellar yield, taking into consideration these variations.

Almost all oxygen in the universe is produced in massive stars ($m \gtrsim 8M_{\odot}$). Using detailed models of Type II supernovae explosions, Woosley & Weaver (1995) provide the nucleosynthetic yields for stars in the mass range of $11 - 40M_{\odot}$ and for a range of metallicities. Thielemann et al. (1996) present similar model calculations but in the mass range of $13-25M_{\odot}$. Thomas et al. (1998) compare these two models finding good agreement between the oxygen yields except at high stellar masses where the yields calculated by Woosley & Weaver (1995) saturate. Henry et al. (2000) calculate the integrated oxygen yield using the models of Maeder (1992), Woosley & Weaver (1995) and the Thielemann et al. (1996) models updated to include contributions from 40 and $70M_{\odot}$ stars (Nomoto et al. 1997). Assuming a Salpeter IMF and a range of upper and lower masses Henry et al. (2000) find that the oxygen yields range between $0.004 - 0.016$ (see their Table 2). Using more sophisticated models, Kobayashi et al. (2006) calculate nucleosynthetic yields by assuming a range of metallicities, explosion energies (supernovae and hypernovae) and metallicity dependent mass loss. They calculate the integrated oxygen yield using a Salpeter IMF and a lower and upper mass limit of 0.07 and $50M_{\odot}$, respectively. They find that the oxygen yield is weakly dependent on metallicity and ranges between $0.006-0.008$. In Figure 6.12b, we adopt a range of $0.0056 - 0.0091$ for the oxygen yield.

6.9.3 The Abundance Calibration

The uncertainty in the absolute nebular abundance calibration is a long-standing problem in observational astronomy. Kewley & Ellison (2008) show that the metallicity can vary by as much as 0.7 dex when using different abundance diagnostics for the same set of galaxies. This poses serious problems for understanding galactic chemical evolution. The uncertainties are largely due to method of calibration used in establishing the diagnostic. Empirical methods rely on calibrating strong line ratios using HII regions and galaxies with metallicities determined using the so-called direct method which uses temperature sensitive auroral lines. (e.g. Pettini & Pagel 2004). Empirical methods have several limitations and theoretical calibrations of strong-line ratios using photoionization models have also been developed (e.g. Kewley & Dopita 2002; Kobulnicky & Kewley 2004; Tremonti et al. 2004). Detailed discussions of strengths and weaknesses of the various methods and calibrations can be found in Kewley & Ellison (2008) and Moustakas et al. (2010), we summarize the salient points here.

Peimbert (1967) points out that temperature fluctuations within nebular regions may lead to overestimates of the temperature. Temperature fluctuations are thought to be more problematic in metal-rich HII regions, where efficient line-cooling may lead to temperature inhomogeneities and strong temperature gradients (Garnett 1992). These overestimates of nebular temperatures lead to underestimates of the metallicity with the direct method (Stasińska 2002, 2005; Bresolin et al. 2006) and temperature inhomogeneities among the HII regions within a galaxy also pose problems for metallicity determinations based on global spectra (Kobulnicky et al. 1999). A second, and perhaps more pernicious problem is the distribution of electrons within an HII region may not follow a Boltzmann distribution but rather may be κ-distributed (a well known particle distribution in plasma physics). A κ-distribution of electrons may account for the discrepant temperatures and metallicities inferred from auroral lines (Nicholls et al. 2012).

Empirical calibrations require observations of extremely faint auroral lines. In particular, the [OIII]λ4363 line is on the order of 100 times weaker than the strong optical oxygen lines

(e.g. [OII]λ3727, [OIII]λ5007). Furthermore, the line strength diminishes with increasing metallicity, due to efficient line cooling, and is only observed in low metallicity HII regions ($\lesssim 0.5Z_{\odot}$). The high S/N spectra required to observe the auroral lines taken together with temperature inhomogeneities within individual HII regions suggests that samples used to calibrate empirical methods may be biased and unreliable, particularly at higher metallicities.

Theoretical methods rely solely on photoionization models to calibrate strong-line ratios. These methods are not susceptible to observational limitations imposed by empirical calibrations and metallicities are well constrained and parameterization is well defined over the full range of observed line ratios. The absolute calibration of metallicities are model dependent and uncertainties are subject to the simplifying assumptions of the model. Indirect evidence suggests that these methods systematically overestimate the metallicity (e.g. Bresolin et al. 2009a; Kudritzki et al. 2012).

The metallicities in our samples are determined using either the theoretical diagnostic of Kobulnicky & Kewley (2004, SDSS and DEEP2) or the empirical diagnostic of Pettini & Pagel (2004, E06). These two methods differ by a constant offset of ~ 0.3 dex. For our metallicity diagnostic we therefore adopt the average of the metallicities determined using these two methods.

Kewley & Ellison (2008) have shown that the relative estimates of the metallicity are robust for various diagnostics. However, the absolute calibration varies significantly and the shape of the MZ relation can change depending on the calibration adopted (see Figure 2 of Kewley & Ellison 2008). In our models, the oxygen deficit is sensitive to the shape of the MZ relation only in the case when the oxygen deficit is small. As we show in the following section, our model showing a large oxygen deficit (the solid line in Figure 6.12d) is most consistent with observations of oxygen in the halos of star-forming galaxies. Furthermore, the shapes of the MZ relations determined from the calibration of Kobulnicky & Kewley (2004) and Pettini & Pagel (2004) are consistent within the errors (see Figure 6.8) despite the

fact that the two diagnostics are calibrated independently using a theoretical and empirical calibration, respectively.

6.9.4 Depletion onto Dust Grains

Some uncertainty in the absolute metallicity scale is associated with depletion of metals onto dust. Several authors have inferred ~ 0.1 dex depletion of oxygen onto dust grains (Jenkins 2004; Cartledge et al. 2006; Peimbert & Peimbert 2010). However, in NGC 300 the agreement between the gradient inferred from A and B supergiants and that from emission lines suggests that there is very little, if any dust depletion in this galaxy (Bresolin et al. 2009a). It is likely that dust depletion ranges between $0 \sim 0.1$ dex and perhaps is dependent on physical properties of galaxies such as metallicity or stellar mass.

The oxygen deficit we estimate is sensitive to the gas-phase abundance only at small oxygen deficits. If we assume a constant relative level of depletion (e.g. ~ 0.1 dex), the effects of dust depletion on the oxygen deficit is more pronounced in lower mass galaxies which have a smaller oxygen deficit. However, low mass galaxies may also have lower levels of depletion as NGC300[7] indicates. By comparing to independent observations of the mass of oxygen found in the halos of star-forming galaxies, we argue in Section 6.10.1 that a model with a large oxygen deficit is favored. In the case of a large oxygen deficit (solid curve in Figure 6.12), assuming that oxygen is depleted onto dust by 0.1 dex changes the oxygen deficit by 0.7 dex at a stellar mass of $10^9 M_\odot$ and by 0.15 dex at a stellar mass of $10^{11} M_\odot$. This level of dust depletion in our model with a large oxygen deficit does not alter the conclusions of this paper. Given the large uncertainties on how dust depleted oxygen is in HII region and systematic uncertainties of our metallicity calibration, we make no explicit correction for this effect. In Figure 6.12c, we vary the adopted metallicity by [-0.2, +0.1] dex.

[7]The stellar mass of NGC300 is $\sim 10^9 M_\odot$ (Kent 1987).

6.9.5 Abundance Gradients

It is well established that star-forming galaxies in the local universe have spatial abundance gradients such that the central regions of galaxies are more metal rich than their outskirts (e.g. Zaritsky et al. 1994). In our estimate for the amount of oxygen in the gas-phase (see Section 6.8.2) we adopt an oxygen abundance determined from nebular emission within the 3 arc second SDSS fiber aperture. We determine the oxygen abundance of local galaxies from data selected to have a covering fraction of $> 30\%$ which is shown to be sufficient for reproducing the global abundance (Kewley et al. 2005). We reproduce the global luminosity weighted abundance whereas an unbiased method for estimating the gas-phase metal content of galaxies would be to use a global metallicity estimator that reflects the average total gas-phase abundance (i.e. a gas mass weighted abundance). However, given current observations it is not possible to assess what biases are introduced by adopting a luminosity weighted abundance for estimating gas-phase metal content. Surveys of abundance gradients in nearby galaxies currently under way along with a new generation of radio instruments capable of measuring the gas content of large samples of galaxies will likely resolve this issue.

We speculate that the luminosity weighted oxygen abundance is likely to overestimate the gas mass weighted abundance. In star-forming galaxies where luminosity is dominated by young stars the luminosity weighted abundance reflects the abundance of star-forming gas. The Schmidt-Kennicutt relation for star formation relates the star formation surface density to the gas surface density by $\Sigma_{SFR} \propto \Sigma_{gas}^{1.4}$ (Kennicutt 1998b). Because of the non-linear relation between the two quantities, the luminosity weighted metallicity will not be consistent with the gas mass weighted metallicity but instead will be biased towards higher gas surface density regions which tend to lie in the central, metal-rich regions of galaxies. Therefore, the average metallicity of the gas is likely to be lower than the inferred luminosity weighted abundance used in this study for estimating the oxygen mass in the gas-phase. However, given that observations comparing the gas mass and luminosity weighted

abundances are currently not feasible, we do not attempt to make a correction for this effect.

6.10 Discussion

The census of oxygen for star-forming galaxies has been determined from the observationally constrained star formation and chemical histories. In Section 6.8 we derive the oxygen deficit determined by comparing the expected total production of oxygen with what is currently found in the gas and stellar phases. We note that oxygen deficit represents the *net* deficit of oxygen accounted for by the stars and gas and excludes oxygen that may be expelled from the ISM and subsequently recycled back into the galaxies as some models predict (e.g Davé et al. 2011).

One advantage to determining mass loss in the manner presented in this study is that a detailed physical mechanism governing mass loss is not required. The feedback processes thought to be responsible for mass loss have proven to be notoriously difficult to model and disentangling the various contributions observationally is challenging given that the physical mechanisms are not clearly understood (for review see Veilleux et al. 2005). Here we discuss some of the implications of our observational constraints on mass loss and future prospectives for our models and results.

6.10.1 Outflows

Galactic outflows are a key physical process governing galaxy evolution (Veilleux et al. 2005). In the nearby universe they are commonly observed in starburst and post-starburst galaxies (e.g Rupke et al. 2005; Martin 2006; Tremonti et al. 2007; Rich et al. 2010; Tripp et al. 2011) and are ubiquitous in higher redshift star-forming galaxies (e.g Shapley et al. 2003; Weiner et al. 2009; Rubin et al. 2010; Steidel et al. 2010). The outflowing gas and metals may remain gravitationally bound to galaxies in which case the material should be found to reside in the hot halos or it may escape the galaxy potential well altogether.

The oxygen deficit may be partially resolved by oxygen present in the outer disks and hot halos of galaxies. Several studies have found flat abundance gradients in the outer disks of star-forming galaxies (Bresolin et al. 2009b; Werk et al. 2010, 2011; Bresolin et al. 2012). The amount of oxygen observed in the outer disks cannot be reconciled with the low levels of star formation and transport of metals from the inner disk is the most likely scenario explaining the flat abundance gradients though the physical mechanism for the transport of metals to outer disks is not clearly understood. Oxygen has also been observed in absorption in the halos of star-forming galaxies (Chen & Mulchaey 2009; Prochaska et al. 2011). In a survey of 42 galaxies conducted using the *Cosmic Origins Spectrograph* onboard the Hubble Space Telescope, Tumlinson et al. (2011) report ubiquitous detection of OVI in the halos of star-forming galaxies. They conclude that the mass of heavy elements and gas in the circum-galactic medium (CGM) may far exceed whats found within the galaxies themselves. From the column density of OVI, they estimate that the CGM of $10^{9.5} - 10^{11.5} M_{\odot}$ stellar mass galaxies (out to 150 kpc) contains at least $\sim 10^{7} M_{\odot}$ of oxygen, where they have assumed an ionization correction factor of 0.2 to account for oxygen in all ionization states.

In Figure 6.14 we plot the oxygen deficit along with the lower limit mass estimate of Tumlinson et al. (2011) shown by the red dot-dashed line. At a stellar mass of $10^{9.5} M_{\odot}$, our model showing the largest oxygen deficit (solid curve) is consistent with the lower limit estimates of Tumlinson et al. (2011). These independent results rule out all except the highest oxygen deficit model (solid line in Figure 6.14). *A model with significant and ubiquitous outflows in star-forming galaxies is required for consistency with independent observations.* As discussed in Section 6.7.4, our models suggest that in the case of significant outflows the oxygen deficit will scale (nearly) linearly with stellar mass. A linear scaling is consistent with the result found by Kirby et al. (2011) from their analysis of metal mass loss in Milky Way dwarf galaxies. At $10^{11} M_{\odot}$, our model exceeds the lower limit estimate of Tumlinson et al. (2011) by ~ 2 orders of magnitude.

Gas propelled to high velocities may escape from galaxies all together. Estimates of the escape fraction of outflowing material have been difficult to determine accurately mainly

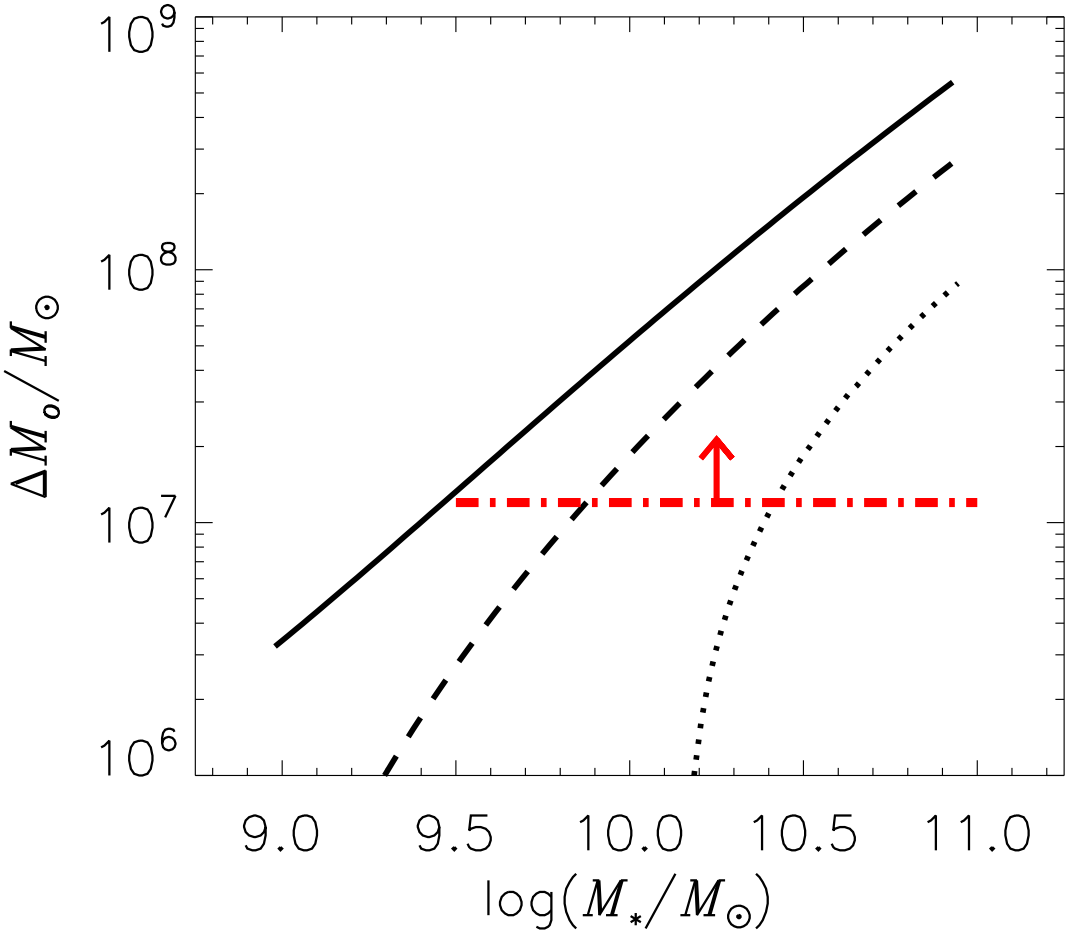

Figure 6.14 The oxygen deficit with the lower limit of observed oxygen mass in the halos of star-forming galaxies from Tumlinson et al. (2011). The oxygen deficit is the same as in Figure 6.12d and the solid, dotted and dashed lines indicate the different oxygen deficit derived by varying the free parameters.

due to lack of constraints on halo drag (Veilleux et al. 2005). It may be that detailed estimates of the oxygen mass in the CGM of galaxies will account for the $\sim$ 2 orders of magnitude greater oxygen deficit at $M_* \sim 10^{11} M_\odot$ implied by our models as compared to lower limit estimates of Tumlinson et al. (2011). However, if the oxygen deficit is not resolved by oxygen found in the halos of galaxies, a natural reservoir for the remainder of the oxygen deficit would be the intergalactic medium (IGM). This scenario is consistent

with theoretical models where large scale galactic outflows transport metals from the galaxy to the IGM (e.g. Springel & Hernquist 2003; Oppenheimer & Davé 2006; Kobayashi et al. 2007; Oppenheimer et al. 2012). However, the kinematics of oxygen in the CGM of local star-forming galaxies suggest that most of the oxygen is gravitationally bound (Tumlinson et al. 2011).

A common method of estimating the escape fraction is to compare the outflow velocity to the escape velocity of the gravitational potential well of the galaxy. Early theoretical work suggested that mass loss occurs only in galaxies with shallow potential wells (e.g. Larson 1974; Dekel & Silk 1986; Mac Low & Ferrara 1999; Ferrara & Tolstoy 2000). However, recent observational and theoretical work has suggested that mass loss driven by AGN or star formation occurs in significantly higher mass galaxies as well (Strickland et al. 2004; Murray et al. 2005; Weiner et al. 2009; Steidel et al. 2010; Fischer et al. 2010; Feruglio et al. 2010; Sturm et al. 2011; Aalto et al. 2012).

It is not clear whether low-mass or high-mass galaxies are responsible for the IGM enrichment. Though low mass galaxies may lose a larger fraction of their metals, they may not be a significant source of IGM enrichment due to their low rates of metal production (Martin et al. 2002; Kirby et al. 2011). On the other hand, due to the deep potential wells of large galaxies, metals may not be efficiently ejected into the IGM. If the latter is true, our model would predict that the CGM and/or outer disks of massive star-forming galaxies ($10^{11} M_{\odot}$) should contain substantially greater quantities of oxygen than their lower mass counterparts ($10^{9} M_{\odot}$). Surveys of the CGM and studies of the outer disks of star-forming galaxies currently underway will provide important clues to resolving the oxygen deficit implied by our models.

6.10.2 Baryonic Mass Loss

One possible interpretation of the oxygen deficit is that it has been driven out of the galaxy ISM by galactic outflows. If oxygen is expelled via outflows, we expect an even larger mass of gas expelled since outflowing gas will not be pure oxygen. We can estimate the *total*

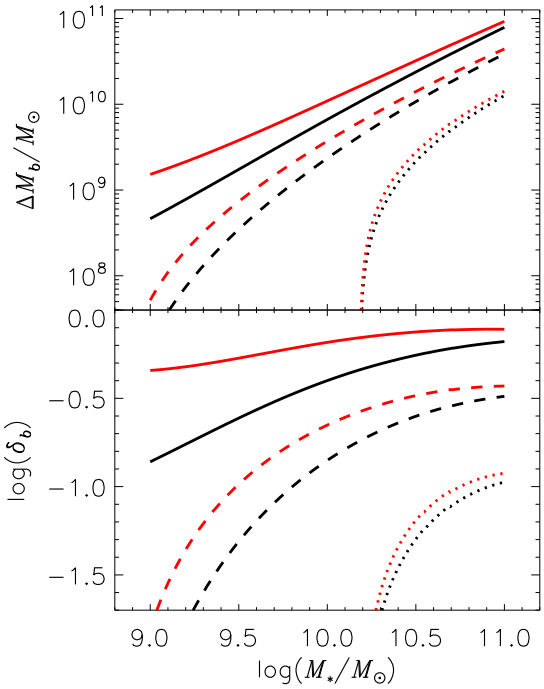

Figure 6.15 The top panel is the inferred baryonic mass loss and the bottom panel is the baryonic mass loss relative to the stellar and gas mass. The oxygen deficit is the same as in Figure 6.12d and the solid, dotted and dashed lines indicate the different oxygen deficit derived by varying the free parameters. The black and red curves are determined by adopting an enriched outflow (Equation 6.29) and uniform wind model (Equation 6.31), respectively.

baryonic mass loss in two ways. First, we adopt an enriched wind model assuming that the metallicity of outflowing gas is equal to the Type II SNe oxygen yield (see Section 6.8.2). We adopt a value for $P_o = 0.007$ which is $\sim 1.6 Z_\odot$. This value is consistent with estimates of Martin et al. (2002) for the metallicity of a starburst driven wind in NGC 1569. Assuming outflows are enriched, we can estimate the total baryonic mass loss by the dividing the oxygen deficit by the oxygen yield. This is given by

$$\Delta M_b = \frac{M_T^o - M_g^o - M_*^o}{P_o} = \frac{\Delta M_o}{P_o}. \tag{6.29}$$

ΔM_b is the total amount of baryonic mass loss and ΔM_o is the oxygen deficit.

We also derive an upper limit estimate of the total baryonic mass loss by assuming a uniform wind model. In the uniform wind model, the metallicity of the outflowing gas is the same as the ISM. In general, the metallicity of the outflowing gas is lower than the yield and therefore more gas is required to outflow in this model in order to yield the oxygen deficit derived in Section 6.7.4. In the uniform wind model estimate P_o in Equation 6.29 is replaced by a SFR weighted metallicity, Z_ψ. The SFR weighted metallicity and the total baryon loss are given by

$$Z_\psi = \frac{\int_{t_i}^{t} \Psi Z_g dt}{\int_{t_i}^{t} \Psi dt} \tag{6.30}$$

and

$$\Delta M_{b\psi} = \frac{\Delta M_o}{Z_\psi}, \tag{6.31}$$

and $\Delta M_{b\psi} > \Delta M_b$.

In the top panel of Figure 6.15 we plot the total baryonic mass loss as a function of stellar mass for galaxies in the local universe. The black and red curves are estimates adopting an enriched outflow (Equation 6.29) and uniform wind model (Equation 6.31), respectively. In the bottom panel of Figure 6.15 we plot the logarithm of δ_b which we define as

$$\delta_b = \frac{\Delta M_b}{M_g + M_*}. \tag{6.32}$$

δ_b is the ratio of the total baryonic mass loss to the baryonic mass of the galaxy, where the baryonic mass of the galaxy (gas + stellar). δ_b represents the ratio of the mass of gas to be cycled in and out of the galaxy compared to the current baryonic mass of the galaxy.

In the currently accepted cosmological model (ΛCDM), the universal baryon fraction is precisely determined from the cosmic microwave background, the observed baryon acoustic oscillations and the Hubble constant. The universal baryon and dark matter density revealed by these observations is given by $\Omega_b = 0.0456 \pm 0.0016$ and $\Omega_c = 0.227 \pm 0.014$, respectively (Komatsu et al. 2011). Studies attempting to account for the baryons find that only a

fraction of the expected baryons are observed in the low-redshift universe (Fukugita et al. 1998; Fukugita & Peebles 2004; Nicastro et al. 2005; Sommer-Larsen 2006; Shull et al. 2011).

Only about a tenth of the baryons are found in the stars and gas of galaxies (Bell et al. 2003a). While the Lyα forest at low redshifts can account for another $\sim$ 30% (Penton et al. 2004; Sembach et al. 2004), the majority of baryons are still missing. Some cosmological simulations favor the warm-hot intergalactic medium (WHIM) as the repository of the missing baryons (e.g Cen & Ostriker 1999; Davé et al. 2001; Cen & Ostriker 2006; Oppenheimer et al. 2012). However, observations of the hot gas at $10^5 - 10^7$K comprising the WHIM remain tentative and no compelling evidence for the detection of this phase yet exists (Bregman 2007). The distribution of the WHIM material is unknown and hot halos of massive galaxies are considered as a possible reservoir for substantial fraction of the missing baryons (Cen & Ostriker 2006; Tang et al. 2009; Kim et al. 2009), though this remains controversial (Anderson & Bregman 2010).

An open question is what fraction of the missing baryons were ejected from galaxies through feedback processes and what fraction never accreted in the first place. We can compare our estimates of the total baryonic mass that can be associated with galaxies (baryonic mass plus the baryonic mass loss) with the expected baryon content of galaxies and their halos inferred from cosmological estimates. The stellar-to-halo mass (SHM) relation parameterizes the relationship between stellar mass of galaxies and the dark matter halos in which they reside. Moster et al. (2010) develop a statistical approach whereby halos and subhalos are populated in an N-body simulations with the requirement that the observed stellar mass function be reproduced. They parameterize the SHM as

$$\frac{M_*}{M_h} = 2\left(\frac{M_*}{M_h}\right)_0 \left[\frac{M_h}{M_1}^{-\beta} + \frac{M_h}{M_1}^{-\gamma}\right]^{-1}. \tag{6.33}$$

Here M_h is the halo mass and $\left(\frac{M_*}{M_h}\right)_0$, M_1, β and γ are free parameters. The relation evolves with redshift and the parameters are given by

$$\begin{aligned} \log M_1(z) &= 1.07 \cdot (1+z)^{0.019} \\ \left(\frac{M_*}{M_h}\right)_0 (z) &= 0.0282 \cdot (1+z)^{-0.72} \\ \gamma(z) &= 0.556 \cdot (1+z)^{-0.26} \end{aligned}$$

and

$$\beta(z) = 1.06 + 0.17z. \tag{6.34}$$

We can estimate the expected baryon content of galaxies from the universal ratio of baryonic to dark matter given by $f_{bc} = \Omega_b/\Omega_c = 0.201 \pm 0.014$.

Figure 6.16 demonstrates the missing baryon problem for galaxies. The dashed cyan line is the current total baryonic (gas + stellar) mass content of galaxies plotted as a function of stellar mass. The dot-dashed blue line is the expected total baryonic mass content of galaxies assuming the universal baryonic to dark matter ratio and the SHM relation of Moster et al. (2010) and is given by $M_b = f_{bc}\, M_h$. The solid black and red curves are the sum of the baryonic mass and the baryonic mass loss using the two estimates given by Equations 6.29 and 6.31. The solid black and red curves can be interpreted as estimates of the baryon content associated with galaxies and are the amount of baryons currently found in local star-forming galaxies plus what was once in the galaxies but has since been cycled out through outflows.

The baryon content associated with galaxies is still substantially lower than the inferred content from cosmology. The straightforward interpretation of Figure 6.16 is that the missing baryons were never accreted onto local star-forming galaxies and unless a large reservoir of gas is found in the halos of star-forming galaxies it is likely that the missing

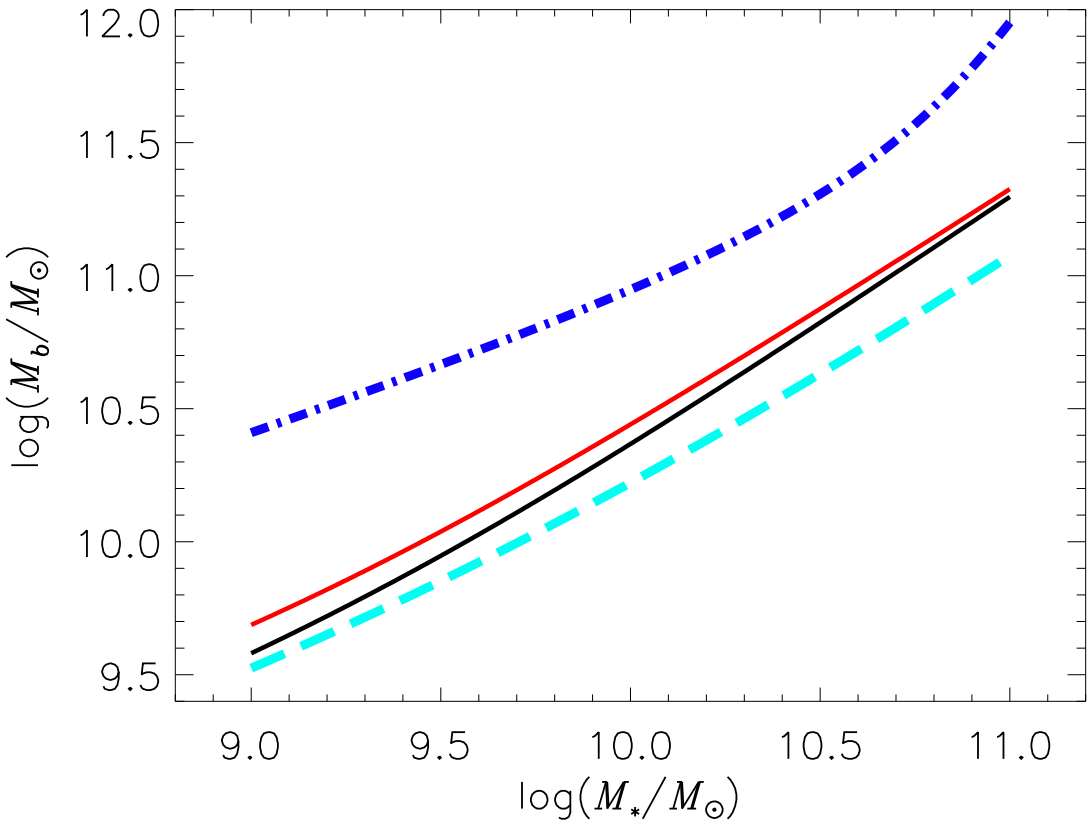

Figure 6.16 The dashed cyan curve is the total baryonic (gas + stellar) mass of galaxies in the local universe. The dot-dashed blue line is the inferred baryon content from cosmological fraction and is given by $f_{bc}\, M_h$. The solid black and red lines are the total baryonic mass plus the baryon mass loss for an enriched wind model (Equation 6.29) and uniform wind model (Equation 6.31), respectively. In our estimate we have adopted the oxygen deficit given by the solid curve in Figure 6.12d.

baryons reside in the IGM. Using observationally motivated constraints for the mass and radii of hot halos, Anderson & Bregman (2010) come to a similar conclusion.

From our estimate of the baryon mass loss we can derive an effective mass loading factor, η, which is given by

$$\eta = \frac{\Delta M_b}{M_*/(1-R)}. \tag{6.35}$$

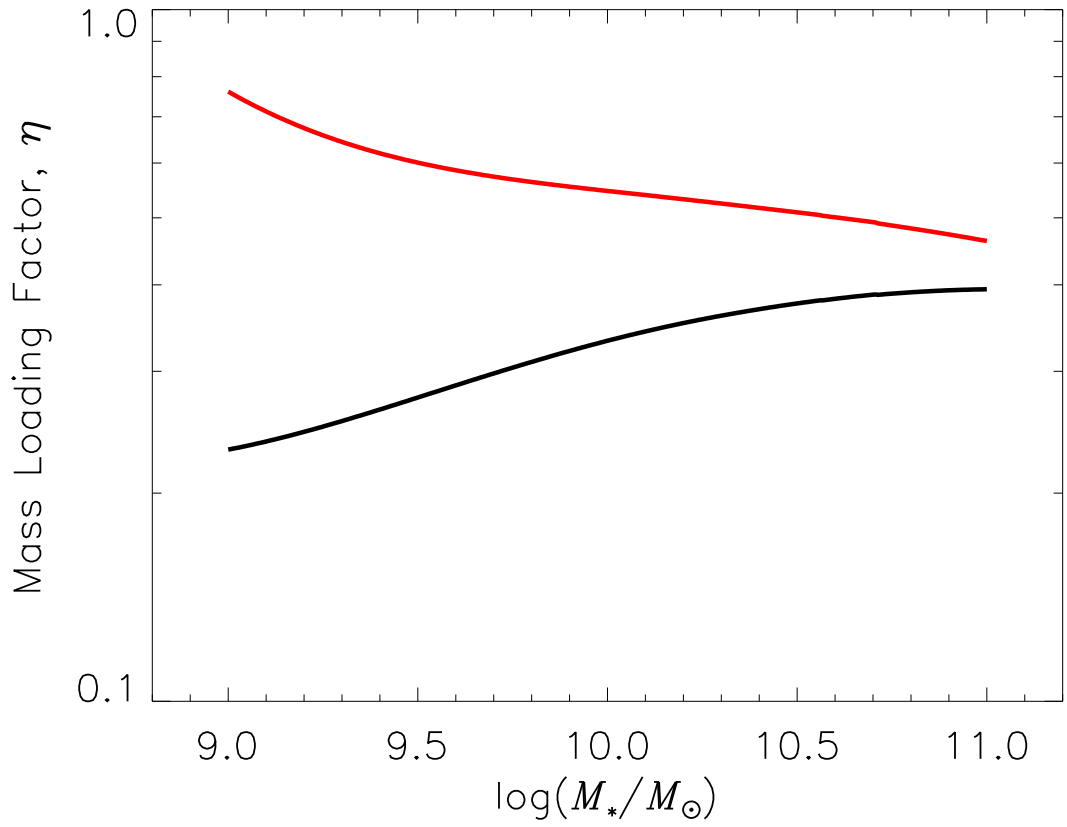

Figure 6.17 The effective mass loading parameter given in Equation 6.35 plotted against stellar mass. The red and black curves give the effective mass loading factor for our upper and lower limit estimates of the total baryon mass loss, respectively.

The quantity ΔM_b is the total amount of baryonic mass loss and $M_*/(1-R)$ represents the *total* amount of star formation. In the literature the instantaneous mass loading factor is defined as $\eta_i = \dot{M}_w/\dot{M}_*$. The instantaneous mass loading factor is the mass loss rate divided by the SFR. The effective mass loading as we have defined it in Equation 6.35 is the instantaneous mass loading factor, η_i, averaged over the star formation history. In Figure 6.17 we plot the effective mass loading factor as a function of stellar mass. Here, we have adopted $R = 0.5$. Assuming a smaller value for R would lower the estimate. Even adopting

our upper limit estimates of baryon mass loss, the effective mass loading for star-forming galaxies in the local universe is < 1.

6.10.3 Future Prospects

A complete and self-consistent theory of galaxy evolution will require a detailed account of galaxy growth and chemical evolution along with physical mechanisms governing these processes. In this contribution we present empirical models attempting to self-consistently integrate chemical evolution and galaxy growth. Our self-consistent approach is complementary to cosmological simulations and semi-analytical models and the self-consistent census approach presented here should be compared with those models. Both theoretical and observational advances are crucial to constraining the model results developed in this study. The method of analysis used in this study provides useful tests for consistency of a diverse set of observations and theories related to chemical properties of galaxies. Here we address future prospects for improvement.

One of the greatest outstanding astrophysical problems is the large uncertainty in the absolute calibration of the nebular abundances scale. High S/N observations of large sample of HII regions covering a broad range of physical parameters will be extremely important in statistically establishing and testing diagnostics. Such observations will be crucial in developing empirical calibrations relying on recombination lines which are thought to be less susceptible to effects of temperature variations associated with auroral lines (Esteban et al. 2002; Peimbert & Peimbert 2005; Bresolin 2007). A complementary approach will be to use the recently developed wide-field integral field spectrographs to observe nearby HII regions in order to understand the discrepancy between empirically and theoretically calibrated strong-line methods. A well calibrated diagnostic applied to large data sets investigating the MZ relation at higher redshifts and to lower stellar masses will provide important constraints for our understanding of chemical evolution and our census of oxygen in the stellar and gas-phase.

Theoretical models incorporating stellar rotation and mass loss into computations of nucleosynthesis for stars at all masses are yet to be developed (Romano et al. 2010). Current models of stellar nucleosynthesis are not yet able to explain the full diversity of chemical abundance patterns observed. While the oxygen yields are much better constrained by models owing to its primary origin, there is still a factor of $\sim$ 2 discrepancy. A single, self-consistent model of nucleosynthesis able to reproduce the abundance ratios observed in the Milky Way and other nearby galaxies will likely alleviate some of the discrepancy, thus constraining the total oxygen production in star-forming galaxies.

Part of the uncertainty in chemical evolution models rests on the assumption of a particular IMF (Romano et al. 2005). Adopting a constant IMF is problematic for galaxies, where even a constant stellar IMF, could lead to variations in the integrated galactic IMF (Kroupa & Weidner 2003) and studies of the IMF from integrated measurements of star-forming galaxies indirectly indicate variations (Hoversten & Glazebrook 2008; Lee et al. 2009; Meurer et al. 2009). A varying IMF would have important implications for chemical evolution models (e.g. Romano et al. 2005; Köppen et al. 2007; Calura et al. 2010). Despite the mounting evidence, no direct evidence of IMF variations in star-forming galaxies is currently available leading to a lack of consensus on the constancy of the IMF. Distinguishing whether a universal IMF or IGIMF formulation provides a better description of large scale star formation will be important for chemical evolution studies of galaxies. Large statistical studies of the integrated properties of galaxies observed over cosmic time, in particular observations of the FUV and FIR properties which are now becoming available, will be useful in establishing any systematic variations of the IMF. In our study, tighter constraints on the IMF will alleviate much of the uncertainty in the total amount of oxygen produced and the return fraction.

Total gas masses are required to measure the absolute content of metals within galaxies from observed relative abundances. In the local universe, large surveys of atomic and molecular gas have been conducted (Helfer et al. 2003; Walter et al. 2008; Leroy et al. 2009; Saintonge et al. 2011). Molecular gas at higher redshifts has also been detected in star-

forming galaxies (Daddi et al. 2008, 2010; Tacconi et al. 2010). The next generation of radio and sub-mm observatories such as the Atacama Large Millimeter/submillimeter Array and the Square Kilometer Array will revolutionize the study of cold gas in the universe allowing us to probe larger samples to far greater depths. Currently, we are only able to estimate the total oxygen in the gas-phase of local star-forming galaxies. Measurements of cold gas in nearby and distant star-forming galaxies taken together with a well calibrated gas-phase metallicity diagnostic will allow us to track the total mass, not just relative abundance, of oxygen in the gas-phase of star-forming galaxies over cosmic time.

The structure, content and chemical composition of outflowing gas is highly uncertain. Understanding the physical properties of galactic winds is crucial for estimating the total mass of gas outflowing from galaxies. Observations reveal that galaxy scale outflows have a complicated multiphase structure (see Veilleux et al. 2005) and observations suggest that structure and composition vary in each of the phases (e.g. Tripp et al. 2011). Multi-wavelength observations are required. The cold gas component can be observed in absorption lines of neutral and low ionization state metals and the current generation of integral field spectrographs on 8-10m class telescopes and wide-field integral field spectrographs on 4m class telescopes will provide census of galactic scale outflows in local galaxies and presence of galactic winds in the distant universe. Hotter phases can be observed using space-based UV spectrometers such as the *Cosmic Origins Spectrograph* (COS) onboard Hubble. A crucial but inaccessible phase is the so-called wind fluid which drives the stellar winds. A hard x-ray telescope with high spatial resolution and sensitivity is required to observe this phase. For the foreseeable future, astronomers will likely have to rely on detailed theoretical models and indirect observations to understand the wind fluid.

COS will also provide important insight into the circum-galactic and warm-hot ionized mediums, both thought to be important repositories of baryons. Studies of these regions will begin to reveal the baryonic content of the hot haloes and intergalactic medium surrounding galaxies. Observations of these regions along with a census of baryons associated with galaxies will be crucial to potentially identifying the large fraction of missing baryons in the

local universe and resolving this long-standing problem (Bregman 2007). A benchmark for these studies is to resolve the oxygen deficit in star-forming galaxies presented here.

In this study we have applied the best theoretical and observational constraints available in undertaking a census of oxygen in star-forming galaxies. We are unable to draw any strong quantitative conclusions from the models developed owing to the large uncertainties associated with both our adopted model parameters and observational inputs. Nonetheless, this study represents one of the first attempts to self-consistently account for the stellar mass growth and chemical evolution of galaxies. As theoretical and observational advances allow for ever greater constraints, we hope the approach taken in this study will prove to be an important ingredient in testing and developing a fully self-consistent theory of galaxy evolution.

6.11 Summary

In this study, we have consistently incorporated chemical evolution in the framework of stellar mass growth in order to conduct a census of oxygen in local star-forming galaxies. We are able to estimate the total oxygen production from total amount of star formation inferred from the current stellar mass. The mass of oxygen in the gas-phase is constrained by the observed MZ relation in the local universe and the relation between gas fraction and stellar mass. The most difficult to constrain observationally is the amount of oxygen locked up stars. Our empirical models self-consistently incorporate stellar mass growth and chemical evolution, thus allowing us to track the metallicity of the gas from which stars are formed over cosmological timescales and giving us empirical constraints on the oxygen mass locked up in stars. The main results of this study are given below.

1. We conduct a census of oxygen and show that the amount of oxygen in the stellar and gas phase of galaxies does not fully account for the total amount of oxygen produced. We conclude that the most straight-forward interpretation of the oxygen deficit is that

oxygen has been expelled from galaxies by outflows. Our results establish the need for ejective feedback in normal star-forming galaxies.

2. We compare our oxygen deficit with the observed lower limit of oxygen found in the CGM of star-forming galaxies and conclude that oxygen mass loss is a ubiquitous process in star-forming galaxies. Furthermore, the oxygen deficit in our preferred model scales with stellar mass and we predict that either more massive galaxies should be found to contain a greater mass of oxygen in their halos or that oxygen escapes the galaxy potential well altogether and therefore massive galaxies contribute for IGM enrichement.

3. We estimate the total amount of mass lost from the ISM of star-forming galaxies and find that it is a small fraction of the total baryon content expected from the cosmological baryon density. We conclude that only a small fraction of the total baryons in the universe ever cycled through star-forming galaxies.

Our empirical model provides an important test of self-consistency for many physical processes governing galaxy evolution. Future theoretical and observational advances will provide ever increasing constraints on the census of oxygen in star-forming galaxies and our models provide important benchmarks with which to compare theory and observation.

References

Aalto, S., Garcia-Burillo, S., Muller, S., Winters, J. M., van der Werf, P., Henkel, C., Costagliola, F., & Neri, R. 2012, A&A, 537, A44

Abazajian, K. N., et al. 2009, ApJS, 182, 543

Anderson, M. E., & Bregman, J. N. 2010, ApJ, 714, 320

Baldwin, J. A., Phillips, M. M., & Terlevich, R. 1981, PASP, 93, 5

Bell, E. F., McIntosh, D. H., Katz, N., & Weinberg, M. D. 2003a, ApJ, 585, L117

—. 2003b, ApJS, 149, 289

Bregman, J. N. 2007, ARA&A, 45, 221

Bresolin, F. 2007, ApJ, 656, 186

Bresolin, F., Gieren, W., Kudritzki, R.-P., Pietrzyński, G., Urbaneja, M. A., & Carraro, G. 2009a, ApJ, 700, 309

Bresolin, F., Kennicutt, R. C., & Ryan-Weber, E. 2012, ApJ, 750, 122

Bresolin, F., Pietrzyński, G., Urbaneja, M. A., Gieren, W., Kudritzki, R.-P., & Venn, K. A. 2006, ApJ, 648, 1007

Bresolin, F., Ryan-Weber, E., Kennicutt, R. C., & Goddard, Q. 2009b, ApJ, 695, 580

Brinchmann, J., Charlot, S., White, S. D. M., Tremonti, C., Kauffmann, G., Heckman, T., & Brinkmann, J. 2004, MNRAS, 351, 1151

Bruzual, G., & Charlot, S. 2003, MNRAS, 344, 1000

Calura, F., Recchi, S., Matteucci, F., & Kroupa, P. 2010, MNRAS, 406, 1985

Calzetti, D., Armus, L., Bohlin, R. C., Kinney, A. L., Koornneef, J., & Storchi-Bergmann, T. 2000, ApJ, 533, 682

Cardelli, J. A., Clayton, G. C., & Mathis, J. S. 1989, ApJ, 345, 245

Cartledge, S. I. B., Lauroesch, J. T., Meyer, D. M., & Sofia, U. J. 2006, ApJ, 641, 327

Cen, R., & Ostriker, J. P. 1999, ApJ, 514, 1

—. 2006, ApJ, 650, 560

Chabrier, G. 2003, PASP, 115, 763

Charlot, S., & Longhetti, M. 2001, MNRAS, 323, 887

Chen, H.-W., & Mulchaey, J. S. 2009, ApJ, 701, 1219

Coil, A. L., Newman, J. A., Kaiser, N., Davis, M., Ma, C.-P., Kocevski, D. D., & Koo, D. C. 2004, ApJ, 617, 765

Conroy, C., Gunn, J. E., & White, M. 2009, ApJ, 699, 486

Conroy, C., & Wechsler, R. H. 2009, ApJ, 696, 620

Cowie, L. L., & Barger, A. J. 2008, ApJ, 686, 72

Daddi, E., et al. 2010, ApJ, 713, 686

Daddi, E., Dannerbauer, H., Elbaz, D., Dickinson, M., Morrison, G., Stern, D., & Ravindranath, S. 2008, ApJ, 673, L21

Daddi, E., et al. 2007, ApJ, 670, 156

Davé, R., et al. 2001, ApJ, 552, 473

Davé, R., Finlator, K., & Oppenheimer, B. D. 2011, MNRAS, 416, 1354

Davis, M., et al. 2003, in SPIE, ed. P. Guhathakurta, Vol. 4834, 161–172

Dekel, A., & Silk, J. 1986, ApJ, 303, 39

Disney, M. J., Romano, J. D., Garcia-Appadoo, D. A., West, A. A., Dalcanton, J. J., & Cortese, L. 2008, Nature, 455, 1082

Drory, N., Bender, R., & Hopp, U. 2004, ApJ, 616, L103

Dutton, A. A., van den Bosch, F. C., & Dekel, A. 2010, MNRAS, 405, 1690

Edmunds, M. G. 1990, MNRAS, 246, 678

Elbaz, D., et al. 2007, A&A, 468, 33

—. 2011, A&A, 533, A119

Erb, D. K., Shapley, A. E., Pettini, M., Steidel, C. C., Reddy, N. A., & Adelberger, K. L. 2006a, ApJ, 644, 813

Erb, D. K., Steidel, C. C., Shapley, A. E., Pettini, M., Reddy, N. A., & Adelberger, K. L. 2006b, ApJ, 647, 128

—. 2006c, ApJ, 646, 107

Esteban, C., Peimbert, M., Torres-Peimbert, S., & Rodríguez, M. 2002, ApJ, 581, 241

Ferrara, A., & Tolstoy, E. 2000, MNRAS, 313, 291

Feruglio, C., Maiolino, R., Piconcelli, E., Menci, N., Aussel, H., Lamastra, A., & Fiore, F. 2010, A&A, 518, L155

Fischer, T. C., Crenshaw, D. M., Kraemer, S. B., Schmitt, H. R., & Trippe, M. L. 2010, AJ, 140, 577

Fontana, A., et al. 2004, A&A, 424, 23

Fukugita, M., Hogan, C. J., & Peebles, P. J. E. 1998, ApJ, 503, 518

Fukugita, M., & Peebles, P. J. E. 2004, ApJ, 616, 643

Gallazzi, A., Charlot, S., Brinchmann, J., White, S. D. M., & Tremonti, C. A. 2005, MNRAS, 362, 41

Garcia-Appadoo, D. A., West, A. A., Dalcanton, J. J., Cortese, L., & Disney, M. J. 2009, MNRAS, 394, 340

Garn, T., & Best, P. N. 2010, MNRAS, 409, 421

Garnett, D. R. 1992, AJ, 103, 1330

Helfer, T. T., Thornley, M. D., Regan, M. W., Wong, T., Sheth, K., Vogel, S. N., Blitz, L., & Bock, D. C.-J. 2003, ApJS, 145, 259

Henry, R. B. C., Edmunds, M. G., & Köppen, J. 2000, ApJ, 541, 660

Hoversten, E. A., & Glazebrook, K. 2008, ApJ, 675, 163

Ilbert, O., et al. 2010, ApJ, 709, 644

Jenkins, E. B. 2004, Origin and Evolution of the Elements, 336

Jungwiert, B., Combes, F., & Palouš, J. 2001, A&A, 376, 85

Kauffmann, G., et al. 2003, MNRAS, 346, 1055

Kennicutt, Jr., R. C. 1998a, ARA&A, 36, 189

—. 1998b, ApJ, 498, 541

Kent, S. M. 1987, AJ, 93, 816

Kewley, L. J., & Dopita, M. A. 2002, ApJS, 142, 35

Kewley, L. J., & Ellison, S. L. 2008, ApJ, 681, 1183

Kewley, L. J., Geller, M. J., & Jansen, R. A. 2004, AJ, 127, 2002

Kewley, L. J., Groves, B., Kauffmann, G., & Heckman, T. 2006, MNRAS, 372, 961

Kewley, L. J., Jansen, R. A., & Geller, M. J. 2005, PASP, 117, 227

Kim, J.-h., Wise, J. H., & Abel, T. 2009, ApJ, 694, L123

Kirby, E. N., Martin, C. L., & Finlator, K. 2011, ApJ, 742, L25

Kobayashi, C., Springel, V., & White, S. D. M. 2007, MNRAS, 376, 1465

Kobayashi, C., Umeda, H., Nomoto, K., Tominaga, N., & Ohkubo, T. 2006, ApJ, 653, 1145

Kobulnicky, H. A., Kennicutt, Jr., R. C., & Pizagno, J. L. 1999, ApJ, 514, 544

Kobulnicky, H. A., & Kewley, L. J. 2004, ApJ, 617, 240

Kobulnicky, H. A., & Phillips, A. C. 2003, ApJ, 599, 1031

Komatsu, E., et al. 2011, ApJS, 192, 18

Köppen, J., Weidner, C., & Kroupa, P. 2007, MNRAS, 375, 673

Kroupa, P., & Weidner, C. 2003, ApJ, 598, 1076

Kudritzki, R.-P., Urbaneja, M. A., Gazak, Z., Bresolin, F., Przybilla, N., Gieren, W., & Pietrzyński, G. 2012, ApJ, 747, 15

Larson, R. B. 1974, MNRAS, 169, 229

Lee, H., Skillman, E. D., Cannon, J. M., Jackson, D. C., Gehrz, R. D., Polomski, E. F., & Woodward, C. E. 2006, ApJ, 647, 970

Lee, J. C., et al. 2009, ApJ, 706, 599

Leitner, S. N. 2012, ApJ, 745, 149

Leitner, S. N., & Kravtsov, A. V. 2011, ApJ, 734, 48

Lequeux, J., Peimbert, M., Rayo, J. F., Serrano, A., & Torres-Peimbert, S. 1979, A&A, 80, 155

Leroy, A. K., et al. 2009, AJ, 137, 4670

Leroy, A. K., Walter, F., Brinks, E., Bigiel, F., de Blok, W. J. G., Madore, B., & Thornley, M. D. 2008, AJ, 136, 2782

Mac Low, M.-M., & Ferrara, A. 1999, ApJ, 513, 142

Maeder, A. 1992, A&A, 264, 105

Mannucci, F., et al. 2009, MNRAS, 398, 1915

Markwardt, C. B. 2009, in Astronomical Society of the Pacific Conference Series, Vol. 411, Astronomical Data Analysis Software and Systems XVIII, ed. D. A. Bohlender, D. Durand, & P. Dowler, 251

Martin, C. L. 2006, ApJ, 647, 222

Martin, C. L., Kobulnicky, H. A., & Heckman, T. M. 2002, ApJ, 574, 663

McGaugh, S. S. 2005, ApJ, 632, 859

Meurer, G. R., et al. 2009, ApJ, 695, 765

Moster, B. P., Somerville, R. S., Maulbetsch, C., van den Bosch, F. C., Macciò, A. V., Naab, T., & Oser, L. 2010, ApJ, 710, 903

Moustakas, J., Kennicutt, Jr., R. C., Tremonti, C. A., Dale, D. A., Smith, J.-D. T., & Calzetti, D. 2010, ApJS, 190, 233

Moustakas, J., et al. 2011, ArXiv e-prints

Murray, N., Quataert, E., & Thompson, T. A. 2005, ApJ, 618, 569

Nair, P. B., van den Bergh, S., & Abraham, R. G. 2010, ApJ, 715, 606

Nicastro, F., et al. 2005, Nature, 433, 495

Nicholls, D. C., Dopita, M. A., & Sutherland, R. S. 2012, ApJ, 752, 148

Noeske, K. G., et al. 2007a, ApJ, 660, L47

—. 2007b, ApJ, 660, L43

Nomoto, K., Hashimoto, M., Tsujimoto, T., Thielemann, F.-K., Kishimoto, N., Kubo, Y., & Nakasato, N. 1997, Nuclear Physics A, 616, 79

Oppenheimer, B. D., & Davé, R. 2006, MNRAS, 373, 1265

Oppenheimer, B. D., Davé, R., Katz, N., Kollmeier, J. A., & Weinberg, D. H. 2012, MNRAS, 420, 829

Osterbrock, D. E. 1989, Astrophysics of gaseous nebulae and active galactic nuclei, ed. D. E. Osterbrock

Pannella, M., et al. 2009, ApJ, 698, L116

Panter, B., Jimenez, R., Heavens, A. F., & Charlot, S. 2008, MNRAS, 391, 1117

Papovich, C., Finkelstein, S. L., Ferguson, H. C., Lotz, J. M., & Giavalisco, M. 2011, MNRAS, 412, 1123

Peebles, P. J. E., & Nusser, A. 2010, Nature, 465, 565

Peeples, M. S., & Shankar, F. 2011, MNRAS, 417, 2962

Peimbert, A., & Peimbert, M. 2005, in Revista Mexicana de Astronomia y Astrofisica Conference Series, Vol. 23, Revista Mexicana de Astronomia y Astrofisica Conference Series, ed. S. Torres-Peimbert & G. MacAlpine, 9–14

Peimbert, A., & Peimbert, M. 2010, ApJ, 724, 791

Peimbert, M. 1967, ApJ, 150, 825

Peng, Y.-j., et al. 2010, ApJ, 721, 193

Penton, S. V., Stocke, J. T., & Shull, J. M. 2004, ApJS, 152, 29

Pettini, M., & Pagel, B. E. J. 2004, MNRAS, 348, L59

Prochaska, J. X., Weiner, B., Chen, H.-W., Mulchaey, J., & Cooksey, K. 2011, ApJ, 740, 91

Reddy, N. A., Erb, D. K., Pettini, M., Steidel, C. C., & Shapley, A. E. 2010, ApJ, 712, 1070

Rich, J. A., Dopita, M. A., Kewley, L. J., & Rupke, D. S. N. 2010, ApJ, 721, 505

Romano, D., Chiappini, C., Matteucci, F., & Tosi, M. 2005, A&A, 430, 491

Romano, D., Karakas, A. I., Tosi, M., & Matteucci, F. 2010, A&A, 522, A32

Rubin, K. H. R., Weiner, B. J., Koo, D. C., Martin, C. L., Prochaska, J. X., Coil, A. L., & Newman, J. A. 2010, ApJ, 719, 1503

Rupke, D. S., Veilleux, S., & Sanders, D. B. 2005, ApJS, 160, 115

Saintonge, A., et al. 2011, MNRAS, 415, 32

Salim, S., et al. 2007, ApJS, 173, 267

Savaglio, S., et al. 2005, ApJ, 635, 260

Sembach, K. R., Tripp, T. M., Savage, B. D., & Richter, P. 2004, ApJS, 155, 351

Shapley, A. E., Steidel, C. C., Pettini, M., & Adelberger, K. L. 2003, ApJ, 588, 65

Shull, J. M., Smith, B. D., & Danforth, C. W. 2011, ArXiv e-prints

Sobral, D., Best, P. N., Matsuda, Y., Smail, I., Geach, J. E., & Cirasuolo, M. 2012, MNRAS, 420, 1926

Sommer-Larsen, J. 2006, ApJ, 644, L1

Springel, V., & Hernquist, L. 2003, MNRAS, 339, 289

Stasińska, G. 2002, in Revista Mexicana de Astronomia y Astrofisica, vol. 27, Vol. 12, Revista Mexicana de Astronomia y Astrofisica Conference Series, ed. W. J. Henney, J. Franco, & M. Martos, 62–69

Stasińska, G. 2005, A&A, 434, 507

Steidel, C. C., Erb, D. K., Shapley, A. E., Pettini, M., Reddy, N., Bogosavljević, M., Rudie, G. C., & Rakic, O. 2010, ApJ, 717, 289

Stoughton, C., et al. 2002, AJ, 123, 485

Strickland, D. K., Heckman, T. M., Colbert, E. J. M., Hoopes, C. G., & Weaver, K. A. 2004, ApJ, 606, 829

Sturm, E., et al. 2011, ApJ, 733, L16

Swindle, R., Gal, R. R., La Barbera, F., & de Carvalho, R. R. 2011, AJ, 142, 118

Tacconi, L. J., et al. 2010, Nature, 463, 781

Tang, S., Wang, Q. D., Lu, Y., & Mo, H. J. 2009, MNRAS, 392, 77

Thielemann, F.-K., Nomoto, K., & Hashimoto, M.-A. 1996, ApJ, 460, 408

Thomas, D., Greggio, L., & Bender, R. 1998, MNRAS, 296, 119

Tielens, A. G. G. M. 2005, The Physics and Chemistry of the Interstellar Medium, ed. Tielens, A. G. G. M.

Tinsley, B. M. 1980, Fund. Cosmic Phys., 5, 287

Tremonti, C. A., et al. 2004, ApJ, 613, 898

Tremonti, C. A., Moustakas, J., & Diamond-Stanic, A. M. 2007, ApJ, 663, L77

Tripp, T. M., et al. 2011, Science, 334, 952

Tumlinson, J., et al. 2011, Science, 334, 948

Veilleux, S., Cecil, G., & Bland-Hawthorn, J. 2005, ARA&A, 43, 769

Veilleux, S., & Osterbrock, D. E. 1987, ApJS, 63, 295

Walter, F., Brinks, E., de Blok, W. J. G., Bigiel, F., Kennicutt, Jr., R. C., Thornley, M. D., & Leroy, A. 2008, AJ, 136, 2563

Weiner, B. J., et al. 2009, ApJ, 692, 187

—. 2007, ApJ, 660, L39

Werk, J. K., Putman, M. E., Meurer, G. R., & Santiago-Figueroa, N. 2011, ApJ, 735, 71

Werk, J. K., Putman, M. E., Meurer, G. R., Thilker, D. A., Allen, R. J., Bland-Hawthorn, J., Kravtsov, A., & Freeman, K. 2010, ApJ, 715, 656

Whitaker, K. E., van Dokkum, P. G., Brammer, G., & Franx, M. 2012, ApJ, 754, L29

Willmer, C. N. A., et al. 2006, ApJ, 647, 853

Woosley, S. E., & Weaver, T. A. 1995, ApJS, 101, 181

Xiao, T., Wang, T., Wang, H., Zhou, H., Lu, H., & Dong, X. 2012, MNRAS, 421, 486

Zahid, H. J., Bresolin, F., Kewley, L. J., Coil, A. L., & Davé, R. 2012, ApJ, 750, 120

Zahid, H. J., Kewley, L. J., & Bresolin, F. 2011, ApJ, 730, 137

Zaritsky, D., Kennicutt, Jr., R. C., & Huchra, J. P. 1994, ApJ, 420, 87

Chapter 7

Empirical Constraints for the Magnitude and Composition of Galactic Winds

Note: This chapter originally appeared as Zahid, H.J, Torrey, P., Vogelsberger, M., Hernquist, L., Kewley L., & Davé, R. 2014, Ap&SS, 349, 873. I am the primary author of this work.

Abstract

Galactic winds are a key physical mechanism for understanding galaxy formation and evolution, yet empirical and theoretical constraints for the character of winds are limited and discrepant. Recent empirical models find that local star-forming galaxies have a deficit of oxygen that scales with galaxy stellar mass. The oxygen deficit provides unique empirical constraints on the magnitude of mass loss, composition of outflowing material and metal reaccretion onto galaxies. We formulate the oxygen deficit constraints so they may be easily implemented into theoretical models of galaxy evolution. We parameterize an effective metal loading factor which combines the uncertainties of metal outflows and metal reaccretion into a single function of galaxy virial velocity. We determine the effective metal loading factor by forward-fitting the oxygen deficit. The effective metal loading factor we derive has important implications for the implementation of mass loss in models of galaxy evolution.

7.1 Introduction

Galaxy scale winds are fundamental to galaxy evolution. The observed baryon content of galaxies is substantially below the cosmic baryon fraction (Papastergis et al. 2012). To account for this deficit, galaxy formation theories require mechanisms to reduce the efficiency with which galaxies grow (e.g., Springel & Hernquist 2003a). Consequently, strong feedback which is capable of launching galactic scale outflows is central to semi-analytic and hydrodynamical galaxy formation models (e.g., Somerville & Primack 1999; Springel & Hernquist 2003a; Schaye et al. 2010; Davé et al. 2011b; Vogelsberger et al. 2013, plus many others). In simulations, energy and/or momentum injected by massive stars is capable of driving gas out of galaxies. Although these outflows are primarily required to regulate the growth of galaxies, they also drive metals out of the interstellar medium (ISM). Outflows reduce the metal content in galaxies and contribute to the enrichment of the circumgalactic and intergalactic medium (e.g. Springel & Hernquist 2003a; Oppenheimer & Davé 2006; Davé et al. 2011b).

Despite the need for outflows to regulate the growth of galaxies, the physical properties of galactic scale winds are poorly determined observationally. The lack of understanding is partly due to the complex multi-phase structure of the gas, which can only be characterized in detail with observations over a broad range of wavelengths (Veilleux et al. 2005). While absorption line studies permit direct measurements of outflow velocities (e.g. Heckman et al. 2000; Rupke et al. 2005; Weiner et al. 2009; Chen et al. 2010; Erb et al. 2012; Martin et al. 2012; Rubin et al. 2013), estimates of the magnitude of mass loss in winds are much more difficult to obtain. Moreover, the metallicity of the wind material is constrained by only a few observations (e.g., Martin et al. 2002).

In the absence of a complete understanding of the character of outflows, theories employ wind prescriptions that are tuned to reproduce the observed properties of the galaxy population (e.g., the galaxy stellar mass function). This is typically achieved by assuming that a constant amount of energy or momentum is injected per unit star formation

and that the wind speed scales in proportion to galaxy escape velocity (Martin 2005). However, in detail, the normalization and scaling of outflows vary significantly between implementations. For example, the galaxy stellar mass functions derived by Davé et al. (2011b) and Puchwein & Springel (2013) both provide satisfactory fits to the stellar mass function of local galaxies; this is in spite of mass loading factors that have normalization offsets of an order of magnitude for low stellar mass (i.e. $M_* \sim 10^9 M_\odot$) systems. The uncertainties in our understanding of the physical properties of galactic winds are further complicated by numerical approximations that vary substantially from one simulation code to another (e.g Vogelsberger et al. 2012; Kereš et al. 2012; Sijacki et al. 2012; Torrey et al. 2012; Nelson et al. 2013).

Gas outflows deplete the heavy element content of galaxies. Typically it is assumed that the wind material has the same metallicity as the ambient ISM. However, the actual wind metallicity relative to the ISM may be greater if it is primarily comprised of supernova ejecta or substantially depressed if a sufficient amount of metal-poor gas is entrained as the wind propagates out of the galaxy. The total amount of metals ejected from the ISM will be proportional to the magnitude and metallicity of the outflowing gas, modulo the amount of metals ejected and subsequently reaccreted. In the absence of direct measurements characterizing these physical processes, we must rely on empirical constraints for the total metal loss in the local galaxy population to infer the properties of outflows and reaccretion.

We provide empirical constraints for outflows that can be easily implemented in galaxy formation models. In Section 7.2 we review the empirical oxygen mass loss estimates of Zahid et al. (2012) and the formalism for outflows typically employed in galaxy formation models. In Section 7.3 we introduce an effective metal loading factor which describes the loss of heavy elements from galaxies under the influence of both galactic outflows and inflows and derive the best fit for the effective metal loading factor by forward-fitting the empirical oxygen mass loss estimates. In Section 7.4 we directly compare our fit with parameterizations of outflows currently used in galaxy formation models and summarize

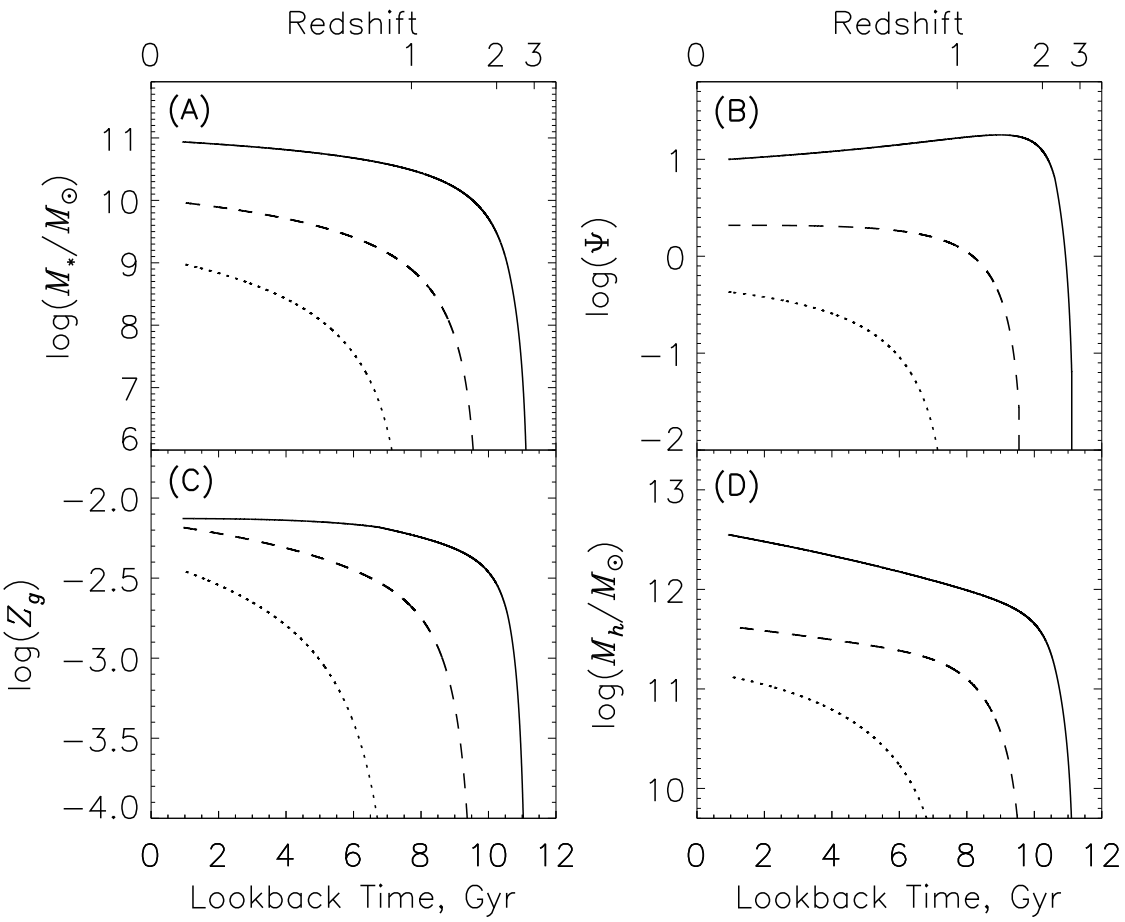

Figure 7.1 Panels (A) and (B): Stellar mass and star formation history tracks for three example model star-forming galaxies as required by the multi-epoch observations of the MS relation, respectively. Panel (C): Chemical history tracks for the model galaxies determined from multi-epoch observations of the MZ relation. Panel (D): Halo mass tracks inferred from the inversion of the stellar mass-halo mass function of Behroozi et al. (2012).

our results in Section 7.5. We adopt a standard cosmology $(H_0, \Omega_m, \Omega_\Lambda) = (70$ km s^{-1} Mpc^{-1}, 0.3, 0.7 and a Chabrier (2003) initial mass function (IMF).

7.2 Formalism

7.2.1 The Oxygen Budget

Estimates for the total oxygen budget of local star-forming galaxies is provided by Zahid et al. (2012). We briefly summarize the formalism here. The oxygen balance can be characterized as:

$$M_T^o = M_g^o + M_*^o + \Delta M^o, \tag{7.1}$$

where M_T^o is the total oxygen mass produced by stellar evolution, M_g^o is the mass of oxygen currently in the ISM, M_*^o is the mass of oxygen locked up in stars, and ΔM^o is the remaining unaccounted for oxygen which resides in the intergalactic medium (IGM) and/or circumgalactic medium (CGM). Three of the four terms in this equation can be empirically constrained.

The total mass of oxygen produced is $M_T^o = yM_*/(1-R)$. Here, y is the total mass of oxygen formed per unit mass of star formation and the factor $M_*/(1-R)$ is the total integrated stellar mass. This is the current mass in stars, M_*, increased by a factor $1/(1-R)$ to account for gas recycling. Here R is fraction of mass that forms into stars and is later returned back to the ISM by stellar winds and supernovae. This fraction can range between 0.2 - 0.5 depending on the choice of IMF (Leitner & Kravtsov 2011; Zahid et al. 2012). In this work we adopt $R = 0.35$. The mass of oxygen in the ISM is $M_g^o = Z_g M_g$, where M_g is the galaxy gas mass and Z_g is the gas-phase oxygen abundance. The total oxygen mass locked up in stars is

$$M_*^o = (1-R) \int Z_g(t)\ \Psi(t)\ dt. \tag{7.2}$$

Here $\Psi(t)$ is the star formation rate (SFR) as a function of time. Evaluating Equation 7.2 requires constraints on the chemical and star formation histories of the local star-forming galaxy population. Empirically, stellar mass growth and chemical evolution are constrained by the fact that galaxies evolve along a redshift dependent stellar mass-SFR (MS) relation,

$\Psi = \Psi(z, M_*)$, and that galaxies evolve along a redshift-dependent mass-metallicity (MZ) relation, $Z_g = Z_g(z, M_*)$.

In Zahid et al. (2012), multi-epoch observations are used to define the MS and MZ relation tracks which star-forming galaxies follow. Figures 10.5A and 10.5B show the stellar mass and star formation history tracks of three model galaxies assuming evolution along the MS relation. Figure 10.5C shows the gas-phase abundance tracks required by the observed MZ relation at several epochs and the stellar mass growth inferred from the MS relation. The mass locked up in stars is estimated by evaluating Equation 7.2. Using empirical estimates for M_T^o, M_g^o and M_*^o we can determine ΔM^o from Equation 7.1. The oxygen deficit, ΔM^o, represents the magnitude of oxygen mass loss that has occurred to ensure that local galaxies fall along the observed MZ relation.

Systematic uncertainties in the parameters required for conducting the oxygen census yield a range of possibilities for the oxygen deficit as a function of galaxy stellar mass (see Zahid et al. 2012). We adopt the oxygen deficit that is consistent with independent estimates of the oxygen content of hot halos of star-forming galaxies (Tumlinson et al. 2011). The empirically determined oxygen deficit is

$$\Delta M^o(M_*) = 4.48 \times 10^7 \left(\frac{M_*}{10^{10} M_\odot} \right)^{1.13} \; [M_\odot]. \tag{7.3}$$

A robust conclusion of Zahid et al. (2012) is that oxygen mass loss is more significant for massive galaxies. We note that the estimates of Tumlinson et al. (2011) are lower limits and the total oxygen mass in halos may be larger by a factor of a few (J. Werk, private communication; Werk et al. 2013). This would lead to a commensurate increase in the derived oxygen deficit.

The key step for parameterizing the oxygen loss for use in galaxy formation models is to cast the deficit in terms of quantities related to the galaxy potential well. We determine the halo mass of galaxies in our model, $M_h = M_h(z, M_*)$, using the stellar mass - halo mass

relation of Behroozi et al. (2012)[1]. Our model of stellar mass growth taken together with the redshift dependent stellar mass - halo mass relation allows us to track the evolution of the galaxy potential well as a function of redshift. Figure 10.5D shows the halo mass as a function of time for the three model galaxies. The evolving virial velocity of each galaxy is easily derived from the halo mass as a function of redshift and stellar mass and is given by Equation 19 in Peeples & Shankar (2011, and references therein). In Section 7.3, we model the effective metal loading factor as a function of virial velocity and forward-fit this model to the observed oxygen deficit.

7.2.2 Ejecting Oxygen from Galaxies

Our primary goal in this contribution is to provide the new empirical constraints on galaxy mass loss from Zahid et al. (2012) in a form that is directly applicable in galaxy formation models. The oxygen mass loss can be accounted for by enriched material that is ejected from the galaxy into the CGM and/or the IGM. In either case, the oxygen mass loss is caused by galactic outflows. We note that most semi-analytic models and hydrodynamic simulations of galaxy formation rely on star formation driven winds as the primary (if not only) mass loss mechanism that operates in low-mass galaxies ($M_* \lesssim 10^{11} M_\odot, M_h \lesssim 10^{12} M_\odot$). These winds originate from deep within the galactic potential wells and are a form of "ejective" feedback. They regulate the growth of galaxies and are also thought to be primary mechanism for metal loss in star-forming galaxies. While black hole growth may also drive winds (e.g. Rupke & Veilleux 2011), we do not consider black hole driven feedback here since it is likely to be prevalent in only the most massive galaxies (e.g. Hopkins et al. 2006, 2008; Somerville et al. 2008).

A general form of the oxygen deficit integrated over the lifetime of a galaxy is

$$\Delta M^o = \int \left[Z_w(t) \dot{M}_w(t) - Z_{acc}(t) \dot{M}_{acc}(t) \right] dt, \tag{7.4}$$

[1]The relation is not directly invertible and we use tables provided by P. Behroozi (private communication).

where Z_w, $\dot{M}_w$, Z_{acc} and $\dot{M}_{acc}$ are the wind metallicity, wind mass loss rate, accretion metallicity and accretion rate, respectively. None of the terms inside the integral on the right hand side of Equation 7.4 are well constrained observationally. In the following section we present our primary result; a parameterization of the oxygen deficit that combines the uncertainties of each of the terms in Equation 7.4.

Often in galaxy formation models two basic assumptions are made regarding galactic outflows. First, it is assumed that the mass loss rate from star-formation driven winds is directly proportional to the star formation rate. This relationship is parameterized in the mass loading factor, η_w, such that $\dot{M}_w = \eta_w \Psi$. The mass loading factor is tuned so that models reproduce basic properties of the galaxy population. Second, the wind metallicity is parameterized by a metal loading factor, γ_w, such that $Z_w = \gamma_w Z_g$. In uniform wind models it is assumed that the metallicity of the outflowing wind material is identical to that of the ambient ISM from which the wind is launched. The metal loading factor in many models of galaxy formation is set to unity though there is no compelling observational evidence to suggest that this is the case.

7.3 Effective Metal Loading Factor

To take advantage of the empirical constraints on ΔM^o described in Section 7.2, we can rewrite the oxygen deficit as

$$\Delta M^o = \int \zeta(t)\ \Psi(t)\ Z_g(t) dt \tag{7.5}$$

where

$$\zeta = \eta_w \gamma_w - \eta_{acc} \gamma_{acc} \tag{7.6}$$

is the effective metal loading factor. In this form, the metallicity of the wind and accreted material are expressed in terms the ISM metallicity using the relative metallicity parameters γ_w and γ_{acc}. Similarly, the rate of mass ejection in the wind and the rate of mass accretion

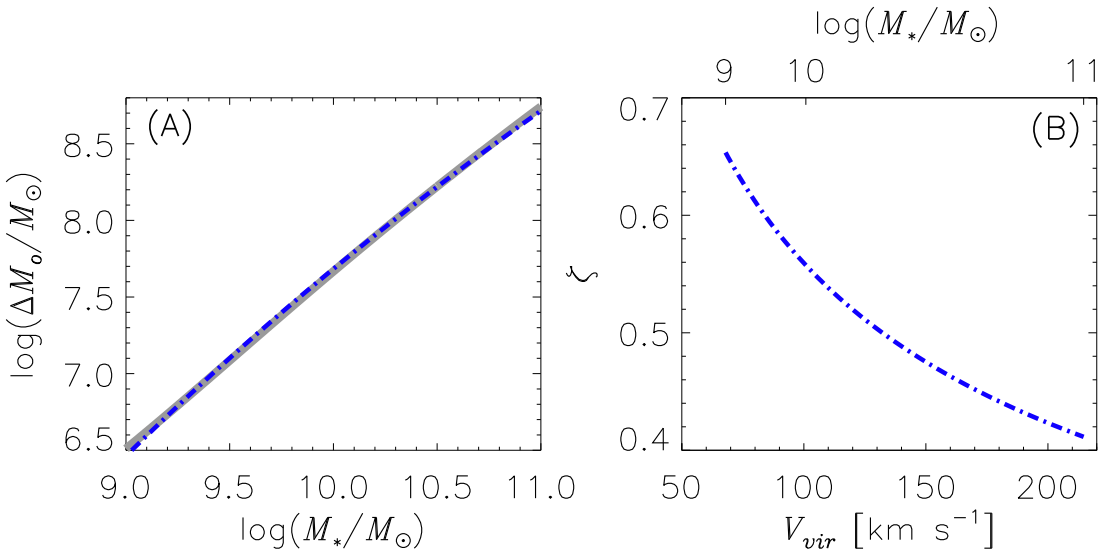

Figure 7.2 Panel (A): Forward-fit of the effective metal loading factor given by Equation 10.14. The oxygen deficit (Equation 7.3) is shown by the solid grey curve.The best fit model is given by the dot-dashed blue curve. Panel (B): Effective mass loading factor derived from panel (A) plotted as a function of virial velocity.

are expressed in terms of the star formation rate using the relative mass loading parameters η_w and η_{acc}. The advantage of the formulation presented in Equation 7.5 is that we have empirical constraints on the oxygen deficit, ΔM^o, the metallicity, Z_g, and the star formation rate, Ψ, leaving only the effective metal loading factor undetermined. Thus, by adopting a functional form for the effective metal loading factor we can forward-fit the oxygen deficit to derive the best fit parameters. The key step taken here is combining our uncertainty about the mass loading, η, and relative metallicity, γ, into a single function which can be empirically constrained.

A best fit effective metal loading factor can be derived based on Equation 7.5 by comparing to the empirically determined oxygen deficit (see Section 7.2.1). To facilitate the fitting procedure, we parameterize the effective metal loading factor as

$$\zeta(V_{vir}) = \alpha \left(\frac{100 \text{ km s}^{-1}}{V_{vir}} \right)^{\beta} \tag{7.7}$$

Table 7.1 Mass Loading Factors

Model	α	β
Peeples & Shankar (2011)	0.53	2
Vogelsberger et al. (2013)	50	2
Puchwein & Springel (2013)	10	2
Okamoto et al. (2010)	13	2
Davé et al. (2011b)	2.25	1
Hopkins et al. (2012)	7	1.1

where α and β set the normalization and slope, respectively. The power law functional form is adopted because a similar functional form is used to parameterize wind mass loading factors in galaxy formation models. We determine the best-fit parameter values by minimizing the residuals between the empirically derived oxygen deficit given by Equation 7.3 and the oxygen deficit we calculate from integrating Equation 7.5 using the same empirical model of stellar mass growth, halo mass growth and chemical evolution as described in Section 7.2.1. The best fit parameters are $\alpha = 0.57$ and $\beta = 0.41$ and the best-fit result for the effective metal loading factor is shown by the blue dot-dashed curve in Figure 7.2.

The effective metal loading factor we present can be straightforwardly applied as an empirical constraint for mass loss in simulations. Equation 7.6 can be solved for any factor(s) that is (are) not constrained within the simulation. If the best-fit effective metal loading factor parameterized by Equation 10.14 is adopted, the solution for any unconstrained factor(s) in Equation 7.6 will necessarily be consistent with the empirical mass loss constraints based on the oxygen deficit of Zahid et al. (2012). As empirical constraints for metal loss in galaxies improve, the approach presented here provides a straightforward methodology for implementing empirical constraints within theoretical models.

7.4 Discussion

Constraining the cycling of gas and metals in and out of galaxies is key for understanding the chemical evolution of the universe. The properties of gas cycling are defined by four

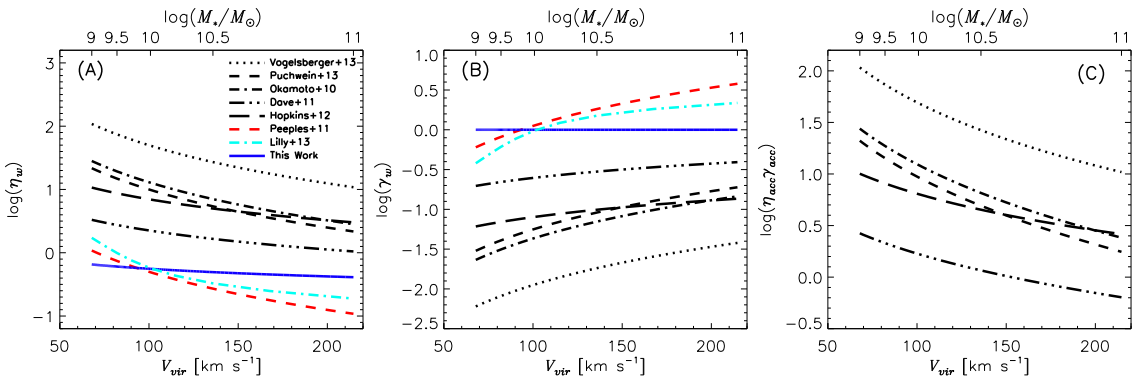

Figure 7.3 (A) Comparison of various mass-loading factors compiled from the literature. The mass loading factors that are implemented in various theoretical models are shown by the black curves. The empirically derived mass-loading factors are shown by the colored curves. Under the assumption of a uniform wind and negligible metal accretion, the metal loading factor we derive reduces to the mass loading factor. The solid blue curve is our metal loading factor assuming $\gamma_w = 1$ and $\eta_{acc}\gamma_{acc} << \eta_w\gamma_w$. (B) The metallicity of outflowing material for the various mass loading factors such that galaxies are consistent with the derived oxygen deficit and galaxies in theoretical models fall on the local MZ relation under the assumption that metal reaccretion is negligible. (C) The metal reaccretion efficiency assuming a uniform wind model ($\gamma_w = 1$) for various mass loading factors such that galaxies are consistent with the derived oxygen deficit and fall on the local MZ relation. Under these assumptions the metal reaccretion efficiencies of (Peeples & Shankar 2011) and (Lilly et al. 2013) are negative for massive galaxies which is unphysical and so are not plotted.

quantities; the wind and accretion mass loading (η_w and η_{acc}, respectively) and the relative metallicity of outflowing and inflowing gas with respect to the ISM metallicity (γ_w and γ_{acc}, respectively). In the absence of direct observational constraints, the magnitude of the mass loading factors in models of galaxy formation are constrained by the baryonic mass function. The oxygen deficit, which is set by the cumulative effect of oxygen ejection and reaccretion, provides independent constraints on the metallicity of outflows and inflows. However, the magnitude and composition of both outflows and inflows are only *relatively* constrained by the observations and therefore are subject to significant degeneracies. In consideration of these uncertainties, the effective metal loading factor we derive combines the uncertainties of the mass loading and composition of outflows with the efficiency of metal reaccretion into a single empirically constrained function of halo virial velocity.

Galaxies have baryonic content well below the simple prediction of the cosmological baryon fraction (e.g. Papastergis et al. 2012). Thus, massive outflows are required in simulations in order to reproduce the observed distribution of stellar masses in galaxies (Springel & Hernquist 2003b). Variable wind models, where mass loading scales with host galaxy properties, are successful at reproducing a broader range of observations (e.g. Oppenheimer & Davé 2006; Finlator & Davé 2008; Davé et al. 2011b,a; Hopkins et al. 2012; Puchwein & Springel 2013). In contrast, empirically derived mass loading factors are principally constrained by the metal content of galaxies (e.g. Peeples & Shankar 2011; Lilly et al. 2013). Figure 7.3A shows mass loading factors found in the literature plotted as a function of galaxy virial velocity. Mass loading factors applied in theoretical models are indicated by the black curves (i.e. Okamoto et al. 2010; Davé et al. 2011b; Hopkins et al. 2012; Puchwein & Springel 2013; Vogelsberger et al. 2013) and empirically derived mass loading factors are indicated by the colored curves (i.e. This work; Peeples & Shankar 2011; Lilly et al. 2013)[2]. The functions are summarized in Table 1. Based on our empirical constraints from the oxygen census, we have derived the effective metal loading factor and not the mass loading factor in Section 7.3. We plot the effective metal loading factor from this work in Figure 7.3A under the assumption that $\gamma_w = 1$ and $\eta_w \gamma_w >> \eta_{acc} \gamma_{acc}$ in which case $\eta_w = \zeta$ in Equation 7.6.

Figure 7.3A demonstrates that there is a large discrepancy between empirically derived mass loading factors and those currently applied in theoretical models. The discrepancy results from the different observational constraints and set of assumptions adopted in theoretically and empirically motivated studies of mass loss. Theoretical mass loading factors are primarily constrained by the observed baryonic mass content of dark matter halos. Because galaxies are baryon deficient relative to the cosmological baryon fraction, massive outflows are required. However, interaction and coupling between the multi-phase outflowing material with pristine, infalling gas from the IGM is currently not well understood and this interaction may suppress initial gas accretion on galaxies (van de Voort

[2]The mass loading factor derived by Lilly et al. (2013) cannot be parameterized by a power law in virial velocity (Equation 10.14) and therefore the model parameters do not appear in Table 1.

et al. 2011). In contrast, empirically derived mass loading factors attempt to produce the observed metal content of galaxies (e.g. the MZ relation). The primary assumption being that the reaccretion of metals ejected from the galaxy ISM is negligible. However, this is taken as a matter of convenience since efficiency of reaccretion is not observationally constrained.

In light of the observational uncertainties and varying set of assumptions, several possibilities exist for alleviating the discrepancy between theoretically and empirically derived mass loading factors :

1. Some form of feedback suppresses initial gas accretion onto dark matter halos and/or galaxies (see van de Voort et al. 2011). In this case, massive outflows are not required in order to reproduce the baryonic mass distribution of galaxies and theoretical mass loading factors in Figure 7.3A are unrealistically large.

2. The metallicity of outflowing gas is extremely low (i.e. $\gamma_w << 1$). While a large amounts of gas are expelled from galaxies, only a small fraction of the metals in the ISM are carried by the outflowing material. If we assume metal reaccretion is negligible (i.e. $\eta_{acc}\gamma_{acc} << 1$), then we can solve Equation 10.14 for the metallicity outflowing gas such that $\gamma_w = \zeta/\eta_w$. In Figure 7.3B we plot this for the various mass loading factors. Vogelsberger et al. (2013), for example, find that they need $\gamma_w < 1$ in order to simultaneously reproduce the galaxy stellar mass function and the MZ relation of local galaxies. The wind metallicity required in their simulations such that they are consistent with observed MZ relation of local galaxies (assuming $\eta_{acc}\gamma_{acc} << 1$) is shown by the dotted curve in Figure 7.3B.

3. Metal reaccretion is very efficient ($\gamma_{acc}\eta_{acc} >> 1$). Massive outflows may expel a large mass of metals but metals are able to preferentially accrete back onto galaxies (e.g. Davé et al. 2011a). Equation 10.14 can be solved for the metal reaccretion efficiency such that $\eta_{acc}\gamma_{acc} = \gamma_w\gamma_w - \zeta$. We plot the metal reaccretion efficiency in Figure 7.3C sssuming that outflowing gas has the metallicity of the ISM ($\gamma_w = 1$).

Most likely a combination of factors will likely contribute to resolving the discrepancy. Quantifying the properties of gas flows in Equation 7.4 is a key step for understanding the formation and evolution of galaxies. The effective metal loading factor derived in Section 7.3 provides straightforward way to apply empirical constraints in future theoretical models investigating mass loss and the apparent discrepancy.

7.5 Summary and Conclusions

We provide an important new parameterization for the empirical determination of the mass of oxygen expelled from star-forming galaxies first presented in Zahid et al. (2012). We present these constraints in the form of an effective metal loading factor which combines the uncertainties of outflows and inflows into a single factor. The effective metal loading factor is fit to the empirical determination of the mass of oxygen expelled from star-forming galaxies. This formulation provides joint constraints on the composition and magnitude of galaxy scale outflows. These constraints are parameterized as a function of halo virial velocity and thus may be straightforwardly implemented in theoretical models of galaxy evolution.

We show that there is large discrepancy between theoretical and empirical constraints for mass loss in galaxies. The discrepancy is due to a differing set of observational constraints and assumptions adopted in the empirical and theoretical approaches, respectively. Possibilities for resolving the discrepancy are: 1) initial gas accretion onto dark matter halos is significantly suppressed; 2) outflows are extremely metal-poor (see also Vogelsberger et al. 2013; Torrey et al. 2013); 3) metal reaccretion is extremely efficient; 4) all of the above. Our formulation of the empirical constraints on composition and magnitude of galaxy scale outflows may be implemented in theoretical models in order to explore these issues.

Our estimates of the mass of oxygen expelled from star-forming galaxies over their lives scales with galaxy stellar mass (Zahid et al. 2012). This may be a result of outflows driven by dust which operate more efficiently in massive galaxies (Zahid et al. 2013b). Recent

observations of an empirical upper limit for the gas-phase abundance in galaxies that is independent of redshift suggests that wind composition does not evolve significantly (Zahid et al. 2013a). Therefore, the derived effective metal loading factor may be applicable to the galaxy population over much of cosmic time. We anticipate the empirical estimates we derive for the effective metal loading factor will be useful for constraining outflows in cosmological simulations. Future observations characterizing the physical properties of galaxy winds will provide important information for removing degeneracies between outflow composition and metal reaccretion.

References

Behroozi, P. S., Wechsler, R. H., & Conroy, C. 2012, ArXiv e-prints

Chabrier, G. 2003, PASP, 115, 763

Chen, Y.-M., Tremonti, C. A., Heckman, T. M., Kauffmann, G., Weiner, B. J., Brinchmann, J., & Wang, J. 2010, AJ, 140, 445

Davé, R., Finlator, K., & Oppenheimer, B. D. 2011a, MNRAS, 416, 1354

Davé, R., Oppenheimer, B. D., & Finlator, K. 2011b, ArXiv e-prints

Erb, D. K., Quider, A. M., Henry, A. L., & Martin, C. L. 2012, ApJ, 759, 26

Finlator, K., & Davé, R. 2008, MNRAS, 385, 2181

Heckman, T. M., Lehnert, M. D., Strickland, D. K., & Armus, L. 2000, ApJS, 129, 493

Hopkins, P. F., Cox, T. J., Kereš, D., & Hernquist, L. 2008, ApJS, 175, 390

Hopkins, P. F., Hernquist, L., Cox, T. J., Di Matteo, T., Robertson, B., & Springel, V. 2006, ApJS, 163, 1

Hopkins, P. F., Quataert, E., & Murray, N. 2012, MNRAS, 421, 3522

Kereš, D., Vogelsberger, M., Sijacki, D., Springel, V., & Hernquist, L. 2012, MNRAS, 425, 2027

Leitner, S. N., & Kravtsov, A. V. 2011, ApJ, 734, 48

Lilly, S. J., Carollo, C. M., Pipino, A., Renzini, A., & Peng, Y. 2013, ArXiv e-prints

Martin, C. L. 2005, ApJ, 621, 227

Martin, C. L., Kobulnicky, H. A., & Heckman, T. M. 2002, ApJ, 574, 663

Martin, C. L., Shapley, A. E., Coil, A. L., Kornei, K. A., Bundy, K., Weiner, B. J., Noeske, K. G., & Schiminovich, D. 2012, ApJ, 760, 127

Nelson, D., Vogelsberger, M., Genel, S., Sijacki, D., Kereš, D., Springel, V., & Hernquist, L. 2013, MNRAS, 429, 3353

Okamoto, T., Frenk, C. S., Jenkins, A., & Theuns, T. 2010, MNRAS, 406, 208

Oppenheimer, B. D., & Davé, R. 2006, MNRAS, 373, 1265

Papastergis, E., Cattaneo, A., Huang, S., Giovanelli, R., & Haynes, M. P. 2012, ApJ, 759, 138

Peeples, M. S., & Shankar, F. 2011, MNRAS, 417, 2962

Puchwein, E., & Springel, V. 2013, MNRAS, 428, 2966

Rubin, K. H. R., Prochaska, J. X., Koo, D. C., Phillips, A. C., Martin, C. L., & Winstrom, L. O. 2013, ArXiv e-prints

Rupke, D. S., Veilleux, S., & Sanders, D. B. 2005, ApJS, 160, 115

Rupke, D. S. N., & Veilleux, S. 2011, ApJ, 729, L27

Schaye, J., et al. 2010, MNRAS, 402, 1536

Sijacki, D., Vogelsberger, M., Kereš, D., Springel, V., & Hernquist, L. 2012, MNRAS, 424, 2999

Somerville, R. S., Hopkins, P. F., Cox, T. J., Robertson, B. E., & Hernquist, L. 2008, MNRAS, 391, 481

Somerville, R. S., & Primack, J. R. 1999, MNRAS, 310, 1087

Springel, V., & Hernquist, L. 2003a, MNRAS, 339, 289

—. 2003b, MNRAS, 339, 312

Torrey, P., Vogelsberger, M., Genel, S., Sijacki, D., Springel, V., & Hernquist, L. 2013, ArXiv e-prints

Torrey, P., Vogelsberger, M., Sijacki, D., Springel, V., & Hernquist, L. 2012, MNRAS, 427, 2224

Tumlinson, J., et al. 2011, Science, 334, 948

van de Voort, F., Schaye, J., Booth, C. M., Haas, M. R., & Dalla Vecchia, C. 2011, MNRAS, 414, 2458

Veilleux, S., Cecil, G., & Bland-Hawthorn, J. 2005, ARA&A, 43, 769

Vogelsberger, M., Genel, S., Sijacki, D., Torrey, P., Springel, V., & Hernquist, L. 2013, ArXiv e-prints, 1305.2913

Vogelsberger, M., Sijacki, D., Kereš, D., Springel, V., & Hernquist, L. 2012, MNRAS, 425, 3024

Weiner, B. J., et al. 2009, ApJ, 692, 187

Werk, J. K., Prochaska, J. X., Thom, C., Tumlinson, J., Tripp, T. M., O'Meara, J. M., & Peeples, M. S. 2013, ApJS, 204, 17

Zahid, H. J., Dima, G. I., Kewley, L. J., Erb, D. K., & Davé, R. 2012, ApJ, 757, 54

Zahid, H. J., Geller, M. J., Kewley, L. J., Hwang, H. S., Fabricant, D. G., & Kurtz, M. J. 2013a, ApJ, 771, L19

Zahid, H. J., Torrey, P., Kudritzki, R., Kewley, L., Dave, R., & Geller, M. 2013b, ArXiv e-prints

Zahid, H. J., Torrey, P., Vogelsberger, M., Hernquist, L., Kewley, L., & Davé, R. 2014, Ap&SS, 349, 873

Chapter 8

The Observed Relation between Stellar Mass, Dust Extinction and Star Formation Rate in Local Galaxies

Note: This chapter originally appeared as Zahid, H.J., Yates, R.M., Kewley, L.J., & Kudritzki, R.P. 2013, ApJ, 763, 92. This work is based on publicly available data from the Sloan Digital Sky Survey (SDSS). I am the primary author of this work.

Abstract

In this study we investigate the relation between stellar mass, dust extinction and star formation rate (SFR) using $\sim$150,000 star-forming galaxies from the SDSS DR7. We show that the relation between dust extinction and SFR changes with stellar mass. For galaxies at the same stellar mass dust extinction is *anti*-correlated with the SFR at stellar masses $< 10^{10} M_{\odot}$. There is a sharp transition in the relation at a stellar mass of $10^{10} M_{\odot}$. At larger stellar masses dust extinction is *positively* correlated with the SFR for galaxies at the same stellar mass. The observed relation between stellar mass, dust extinction and SFR presented in this study helps to confirm similar trends observed in the relation between stellar mass, metallicity and SFR. The relation reported in this study provides important new constraints on the physical processes governing the chemical evolution of galaxies. The *anti*-correlation between SFR and stellar mass for galaxies with stellar masses $> 10^{10} M_{\odot}$

is shown to extend to the population of quiescent galaxies suggesting that the physical processes responsible for the observed relation between stellar mass, dust extinction and SFR may be related to the processes leading to the shut down of star formation in galaxies.

8.1 Introduction

Dust is a fundamental constituent of galaxies. Dust is formed from processed stellar material returned back to the interstellar medium (ISM) either through supernovae or stellar winds. Massive stars ($\gtrsim 8M_{\odot}$) which end their lives as Type II supernovae (SNe) and the AGB phase of intermediate mass stars ($1 \lesssim M_{\odot} \lesssim 8$) are considered to dominate stellar dust production in star-forming galaxies while dust in the ISM may also be formed *in situ* from accretion of enriched gas processed by stars (Dwek 1998). Dust is formed from metals and therefore, not surprisingly, a strong correlation is observed between dust and the gas-phase oxygen abundance both in the local universe (Heckman et al. 1998; Boissier et al. 2004; Asari et al. 2007; Garn & Best 2010; Xiao et al. 2012; Zahid et al. 2012b) and at high redshifts (Reddy et al. 2010).

Lequeux et al. (1979) first observed a relation between stellar mass and gas-phase oxygen abundance in star-forming galaxies. Using $\sim 53,000$ galaxies, Tremonti et al. (2004) have since established a tight relation between stellar mass and the gas-phase oxygen abundance for star-forming galaxies in the local universe. This so-called mass-metallicity (MZ) relation has been observed at low stellar masses (Lee et al. 2006; Zahid et al. 2012a) and out to high redshifts (Savaglio et al. 2005; Erb et al. 2006; Cowie & Barger 2008; Maiolino et al. 2008; Mannucci et al. 2009; Lamareille et al. 2009; Zahid et al. 2011; Moustakas et al. 2011; Yabe et al. 2011). The metallicity is strongly correlated with stellar mass and the shape of the MZ relation is relatively constant with redshift. Over cosmic time the metallicities of galaxies at a fixed stellar mass evolve as galaxies become more enriched at late times.

The MZ relation is shaped by several important physical processes. Oxygen, the most abundant metal in the ISM, is primarily produced in massive stars which end their lives

as Type II SNe, subsequently returning enriched material back to the ISM. However, the observed gas-phase oxygen abundance is also subject to large scale gas flows. Pristine inflowing gas and enriched outflows can both reduce the gas-phase abundance within a galaxy. In pristine inflows the metal content is diluted whereas outflows physically remove metals from the ISM. If the outflowing gas is enriched to levels beyond the ambient ISM, either due to the direct escape of metal-rich ejecta from SNe or to preferential entrainment of metals in galactic winds, the average galaxy metallicity will decline. Tremonti et al. (2004) argue that the enriched outflows which more easily escape the shallow potential wells of low mass galaxies are responsible for the observed MZ relation. Because both inflows and outflows have a similar observational consequence, it has proven difficult to disentangle the effects of gas flows from observations of metallicity alone (see Dalcanton 2007). In this context, the dust content of galaxies may provide important leverage in breaking the degeneracy of these two effects owing to the fact that the observed extinction in galaxies is dependent only on the amount of dust along the line-of-sight and cannot be diluted by inflows of pristine gas. In this study we examine the relation between stellar mass, dust extinction and SFR for star-forming galaxies in the local universe in order to better constrain the physical processes responsible for chemical evolution of galaxies.

In addition to the MZ relation, a tight relation between the stellar mass and SFR of galaxies is observed to exist out to $z \sim 2.5$ (Noeske et al. 2007; Elbaz et al. 2007; Daddi et al. 2007; Pannella et al. 2009; Whitaker et al. 2012). The slope and scatter of the stellar mass-SFR (MS) relation are constant and independent of redshift and the overall normalization evolves such that at a fixed stellar mass galaxies at later times have lower SFRs. The fixed slope and scatter in the MS relation suggest that quiescent processes such as cosmological gas accretion are largely responsible for stellar mass growth since $z \sim 2.5$. Understanding how the scatter in the MS relation is populated and how quiescent galaxies move off the MS relation will provide important constraints for galaxy evolution. In this study we examine the dust properties of galaxies along the MS relation to shed light on this issue.

The MZ relation and its second parameter dependencies have been investigated by several groups. Most notable is the relation between stellar mass, metallicity and SFR. Ellison et al. (2008) show that there exists a correlation between metallicity and specific star formation rate (sSFR) for galaxies at a fixed stellar mass. The relationship between stellar mass, metallicity and SFR was subsequently investigated by Mannucci et al. (2010) who show that at a fixed stellar mass the SFR is *anti*-correlated with metallicity. They argue for a "fundamental metallicity relation" between stellar mass, metallicity and SFR. The lower metallicities observed in star-forming galaxies at early times are balanced by the higher SFRs in these galaxies such that the "fundamental metallicity relation" does not evolve out to $z \sim 2$. Lara-López et al. (2010) have independently found a "fundamental plane" relating the stellar mass, metallicity and SFR of galaxies which appears to match the observational data to $z \sim 3.5$.

The observed relation between stellar mass, metallicity and SFR does depend on methodology and sample selection. Yates et al. (2012) reexamine the "fundamental metallicity relation" and find that while at lower stellar masses the SFR is *anti*-correlated to metallicity, the relation reverses at higher stellar masses such that a *positive* correlation is observed. Yates et al. (2012) argue that the "twist" in the relation is a result of gas-rich mergers at higher stellar masses which fuel a starburst leading to gas exhaustion and quenching of star formation. Subsequent gas accretion at levels too low to efficiently form large amounts of stars leads to metallicity dilution in these systems thus giving rise to the observed correlation.

In order to shed light on the stellar mass, metallicity and SFR relation and to understand the physical properties of galaxies populating the MS relation we examine the relation between stellar mass, dust extinction and SFR. In Section 8.2 we describe our sample and in Section 8.3 we present our results. We provide a detailed discussion of selection and aperture effects in Section 8.4. In Section 8.5 we provide a brief discussion and in Section 8.6 we summarize the main results of the paper. Throughout this work we adopt the

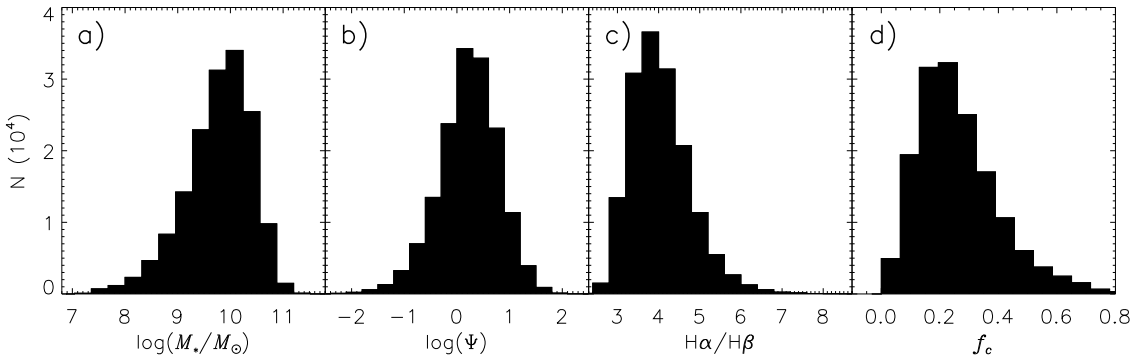

Figure 8.1 The distribution of a) stellar mass, b) SFR ($M_\odot$ yr^{-1}), c) Balmer decrement and d) g-band fiber covering fraction for the SN8 sample.

standard cosmology $(H_0, \Omega_m, \Omega_\Lambda) = (70$ km s^{-1} Mpc^{-1}, 0.3, 0.7) and a Chabrier (2003) IMF.

8.2 Data and Methods

We draw our sample from the SDSS DR7 which consists of $\sim 870,000$ unique galaxies spanning a redshift range of $0 < z < 0.7$ (Abazajian et al. 2009). The survey has a Petrosian limiting magnitude of $r_P = 17.8$ covering 8,200 deg^2. The spectra have a nominal spectral range of 3900 - 9100Å and a spectral resolution of R $\sim$ 2000. Both the stellar masses, which are determined from the *ugriz*-band photometry (Stoughton et al. 2002), and the emission line fluxes are measured by the MPA-JHU group[1]. We adopt the DR7 values in this work but subtract 0.2 dex from the stellar masses for consistency with our previous work where stellar masses are estimated using a different set of routines (see Zahid et al. 2011). The SFRs in the DR7 are derived using the technique of Brinchmann et al. (2004) with additional improvements given by Salim et al. (2007). The SFRs are determined from fitting prominent emission lines in the spectra with the largest contribution coming from Hα and Hβ and are corrected for dust and aperture effects.

[1]http://www.mpa-garching.mpg.de/SDSS/DR7/

The emission line fluxes are measured by the MPA/JHU group (see Tremonti et al. 2004). Balmer absorption is prominent in the atmospheres of A stars. For integrated spectra of galaxies a correction for Balmer absorption is required in order to estimate the emission line strength of Balmer lines. The emission lines are continuum subtracted and corrected for stellar absorption by fitting a linear combination of the Charlot & Bruzual 2008 stellar population synthesis models (Charlot & Bruzual, in prep). We have scaled the emission line uncertainties of Hα and Hβ by 2.473 and 1.882, respectively, as recommended by the MPA/JHU group.

From the parent sample, we select a pure star-forming sample of emission line galaxies. We first distinguish star-forming galaxies from AGN by constraining the ionizing radiation source using the [OIII]λ5007, [NII]λ6584, Hβ and Hα emission lines (Baldwin et al. 1981; Kauffmann et al. 2003; Kewley et al. 2006). Following Kewley et al. (2006), we remove galaxies where

$$\log([\mathrm{OIII}]/\mathrm{H}\beta) > 0.61/\left(\log([\mathrm{NII}]/\mathrm{H}\alpha) - 0.05\right) + 1.3. \tag{8.1}$$

This selection yields a sample of $388,000$ galaxies. In order to obtain a robust estimate of the Balmer decrement we require that the signal-to-noise (S/N) of the Hα and Hβ line be greater than 8. These selection criteria yield a sample of $\sim 157,000$ star-forming galaxies. We refer to this selected sample as the SN8 sample.

Groves et al. (2012) find that the Hβ equivalent widths and line fluxes may be systematically underestimated due to an overcorrection for Hβ absorption. They argue that this systematic underestimate in the Hβ line flux leads to a 0.1 mag overestimate of A_v. In this study we are investigating the relation between stellar mass, dust extinction and SFR. Groves et al. (2012) conclude that the Hα and Hγ lines do not suffer from the same systematic errors in the absorption correction. In order to asses whether the effect of this possible systematic uncertainty qualitatively changes the relation between stellar mass, dust extinction and SFR, we also determine dust extinction from the Hα/Hγ ratio. We require a S/N$>$ 3 in the Hγ line when determining the dust extinction from the Hα/Hγ

ratio. Most galaxies in the SN8 sample ($> 99\%$) have a S/N > 3 in Hγ. We determine the dust extinction from the Hα/Hγ ratio in Section 8.4.1 in order to assess any systematic effects due to improper subtraction of Hβ Balmer absorption.

We measure dust extinction from the Balmer decrement. For case B recombination with electron temperature $T_e = 10^4$K and electron density $n_e = 10^2$ cm^{-3}, the intrinsic Hα/Hβ and Hα/Hγ ratio are expected to be 2.86 and 6.11, respectively (Hummer & Storey 1987). We obtain the intrinsic color excess, E(B$-$V), and the correction for dust attenuation using the extinction law of Cardelli et al. (1989) and a corresponding $R_v = 3.1$. We note that the results of this study are largely independent of our choice of extinction law as the relation presented only relies on relative values of extinction. From the color excess we determine the visual extinction measured in magnitudes from $A_v = R_v$ E(B$-$V).

In Figure 8.1 we show the distribution of stellar masses, SFRs, Balmer decrement and fiber covering fractions for the SN8 sample. We estimate the g-band fiber covering fraction, f_c, by comparing the photometric and fiber g-band magnitude. The g-band covering fraction is an estimate of the fraction of the galaxy luminosity contained within the fiber. The median covering fraction for the SN8 sample is 0.24 (see Figure 8.1d). We determine that selection and aperture effects do not significantly bias the observed relation between stellar mass, dust extinction and SFR presented below. In Section 8.4 we discuss selection and aperture effects in detail.

8.3 The Dust and Metallicity Properties of Star-Forming Galaxies

In Section 8.3.1 we present the relation between stellar mass, dust extinction and SFR. For comparison, we present the relation between stellar mass, metallicity and SFR in Section 8.3.2.

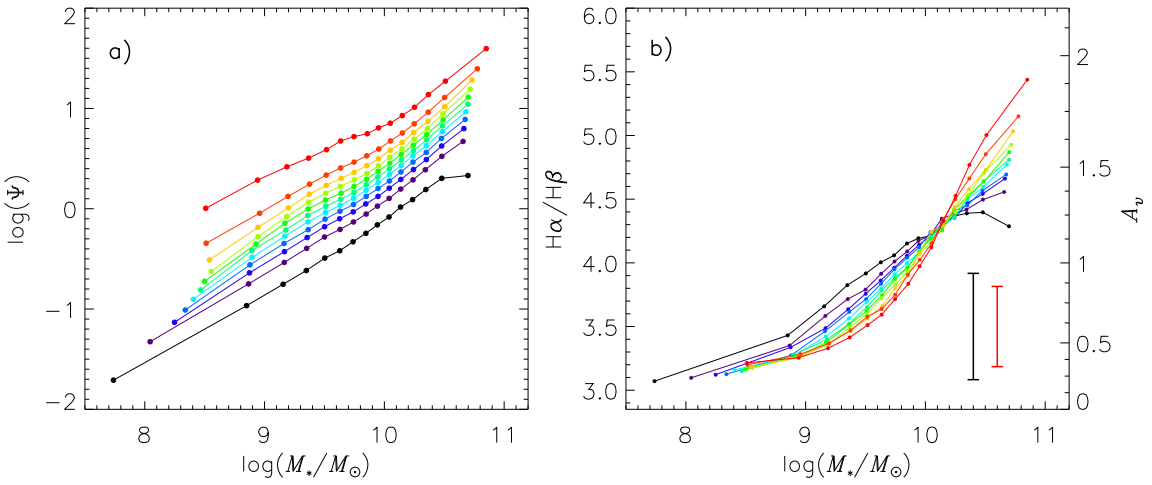

Figure 8.2 The observed relation between stellar mass, dust extinction and SFR ($M_\odot$ yr^{-1}). a) Undeciles of the SFR as a function of stellar mass. b) The median Balmer decrement and visual extinction (in magnitudes, see text for details) sorted into bins of stellar mass and SFR. The colors correspond to undeciles of the SFR shown in a). The black error bars show the median 1σ dispersion of the data in each bin and the red error bars show the observational uncertainty.

8.3.1 The Stellar Mass, Dust Extinction and SFR Relation

In Figure 9.1 we show the relation between stellar mass, dust extinction and SFR. Hereafter, we refer to the stellar mass, dust extinction and SFR relation as the MDSR. The data are first sorted into 16 equally populated bins of stellar mass and then each mass bin is sorted into 11 equally populated bins of SFR. Each bin contains $\sim$ 890 galaxies. In Figure 9.1a the different color curves correspond to undeciles[2] of the SFR as a function of stellar mass. In Figure 9.1b we show the median dust extinction sorted into bins of stellar mass and SFR. Again the curves are color coded to match the undeciles of SFR shown in Figure 9.1a (e.g. red curves correspond to the median dust extinction in the highest SFR bin and the black curve the median dust extinction in the lowest SFR bin in each stellar mass bin, respectively). The median 1σ scatter of the Balmer decrement within each bin is 0.42

[2]Each of eleven equal groups into which a population can be divided according to the distribution of values of a particular variable.

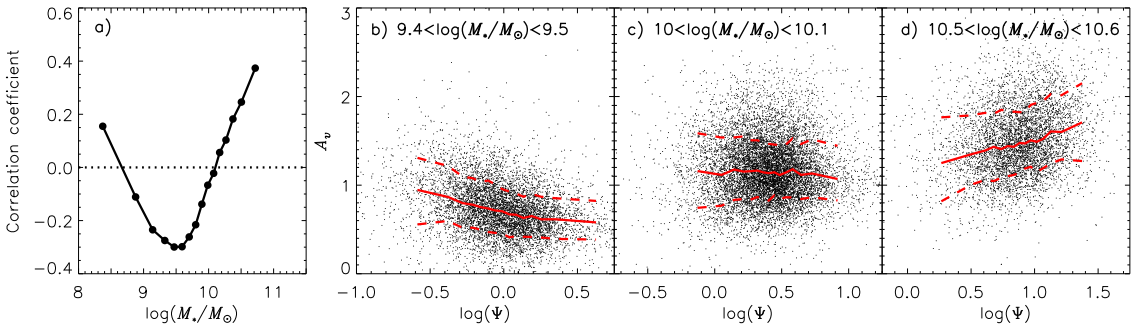

Figure 8.3 a) The Spearman rank correlation coefficient between SFR ($M_\odot$ yr^{-1}) and dust extinction in 16 equally populated bins of stellar mass. The dotted line marks the zero point. b-d) Dust extinction plotted as a function of SFR for galaxies in three of the stellar mass bins shown in a). The range of stellar masses are shown in the text of each panel. The red curves are the median dust extinction in 15 bins of SFR and the dashed curves are the 68% contours of the data.

with 0.32 attributable to observational uncertainty. Given the large number of data points within each bin, the median standard error of the Balmer decrement for each bin is 0.01.

There are several notable features present in Figure 9.1. There is a general trend for the extinction to increase with stellar mass (e.g. Brinchmann et al. 2004). Older, higher stellar mass galaxies typically have greater extinction which is most likely due to the greater number of stars in these galaxies evolving through the AGB phase or ending their lives as supernovae (see Dwek 1998). Perhaps more interesting is the relation between extinction and SFR at a fixed stellar mass. At stellar masses $< 10^{10} M_\odot$ the dust content of galaxies is *anti*-correlated with the SFR such that galaxies with high SFRs tend to have less dust extinction. At a stellar mass of $\sim 10^{10} M_\odot$ (or $A_v \sim 1.2$) there is a sharp transition and at larger stellar masses the extinction is *positively* correlated with the SFR. Figure 9.1 shows two projections of the 3-dimensional MDSR. The reversal of the trend between SFR and dust extinction at a fixed stellar mass can be thought of as a twist in the two dimensional surface defining the relation between stellar mass, dust extinction and SFR.

The twist is also present in the data without binning in SFR. In Figure 8.3 we plot the correlation coefficient between SFR and dust extinction in bins of stellar mass. The data

are binned into 16 equally populated bins of stellar mass, same as in Figure 9.1. In the stellar mass range of $8.5 \gtrsim \log(M_*/M_\odot) \gtrsim 10$ the data show a negative correlation. At $10^{10} M_\odot$ there is a transition to a positive correlation. We demonstrate this visually for the unbinned data in Figure 8.3b-d by showing the relation between dust extinction and SFR in three of the stellar mass bins. At the lowest stellar masses there is evidence for another transition to a positive correlation but the sparsity of data at low stellar masses does not allow us to draw any strong conclusions.

Both Garn & Best (2010) and Xiao et al. (2012) have studied the dust properties of star-forming galaxies in the SDSS. Neither of these studies report the observed twist in the relation between stellar mass, dust extinction and SFR. However, these studies do not examine the relation between dust extinction and SFR at a fixed stellar mass. Both studies employ a principal component analysis (PCA) on the full sample. PCA is a useful statistical technique for assessing the relative contribution of various correlated parameters. PCA finds the orthogonal linear combinations of the variables that maximize the variance in the data. However, traditional PCA techniques assume a linear relation between the variables. The twist is not obvious using PCA because the relation of dust extinction and SFR is opposite at lower stellar masses as compared to higher stellar masses, thus "canceling out" in PCA. PCA performed on a sub-sample of the data in restricted range of stellar mass does reveal the twist between dust extinction and SFR (see Figure 8.3).

8.3.2 The Stellar Mass, Metallicity and SFR Relation

In Figure 8.4a we show the relation between stellar mass, metallicity and SFR. Hereafter we refer to this relation as the MZSR. The MZSR is determined using the sample and methodology of Yates et al. (2012). The data are binned into mass bins of width 0.15 dex and SFR bins of width 0.3 dex. The mean metallicity determined from the Bayesian method of Tremonti et al. (2004) are plotted for each bin and the different color curves correspond to the various SFR bins. The center of each SFR bin is given in the legend of the figure. We refer the reader to Yates et al. (2012) for more details on methodology and sample selection.

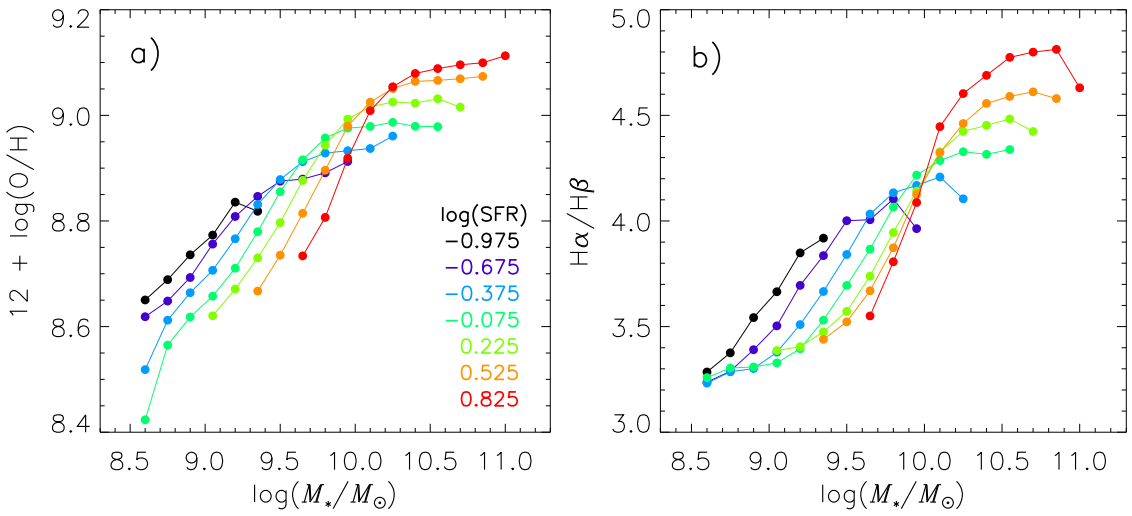

Figure 8.4 The observed relation between a) stellar mass, metallicity and SFR ($M_{\odot}$ yr^{-1}, c.f. Figure 1 of Yates et al. 2012) and b) stellar mass, Balmer decrement and SFR using the T2 sample from Yates et al. (2012). The data are the a) mean metallicities and b) mean Balmer decrements in constant width bins of stellar mass and SFR. The curves are color-coded corresponding to the different SFR bins shown in the legend (the value given for the SFR is the bin center).

We present Figure 8.4 to draw attention to the qualitative similarities in the observed MZSR as compared to the observed MDSR (Figure 9.1). At a fixed stellar mass there exists an *anti*-correlation between the metallicity and SFR for galaxies with stellar masses $\lesssim 10^{10} M_{\odot}$. At a stellar masses $\gtrsim 10^{10} M_{\odot}$ the trend reverses and a *positive* correlation is observed between metallicity and SFR at a fixed stellar mass. As can be seen in Figure 8.4b, the twist in the MDSR is also present in the Yates et al. (2012) data.

The *anti*-correlation between metallicity and SFR at lower stellar masses is significantly stronger than the *anti*-correlation between dust extinction and SFR. We determine the correlation coefficient between SFR and metallicity for ~ 7400 galaxies in the stellar mass range of $9.4 < \log(M_*/M_{\odot}) < 9.5$. The metallicities are taken from the DR7 and are determined using the Bayesian technique of Tremonti et al. (2004). The sample correlation coefficient between the aperture corrected SFR and metallicity is $r = -0.41$. Using the SFR determined from the observed Hα luminosity in the fiber the Spearman rank correlation

coefficient between SFR and metallicity is $r = -0.15$. The *anti*-correlation between stellar mass and metallicity is still present when using Hα fiber SFRs (e.g. Mannucci et al. 2010), however the strength of the correlation is diminished.

Metallicity is a measure of oxygen relative to hydrogen whereas dust extinction is dependent on the absolute number of absorbers within the line of sight. To first order, the observed dust extinction, unlike metallicity, is independent of the gas fraction. The stronger correlation between SFR and metallicity as compared to SFR and dust extinction and much of the difference in the MZSR as compared to the MDSR seen in Figure 8.4 is likely due to a correlation between the gas fraction and SFR. Higher gas fractions may sustain higher SFRs while also diluting the metallicity, thus strengthening the *anti*-correlation between metallicity and SFR observed at stellar masses $< 10^{10} M_{\odot}$. Measurements of gas masses in a large sample of star-forming galaxies should provide important insight into the relationship between metallicity and dust.

8.4 Systematic, Selection and Aperture Effects

In this section we investigate possible systematic issues with improper subtraction of Hβ absorption (Section 8.4.1), biases in the observed MDSR associated with our method of sample selection (Section 8.4.2) and systematic effects of measuring global physical properties of galaxies from emission lines observed within a limited aperture (Section 8.4.3). We conclude that selection and aperture effects are not significant in our determination of the MDSR.

8.4.1 Systematic Effects in the Hβ Absorption Correction

In Figure 8.5 we plot the MDSR with dust extinction determined from the Hα/Hγ ratio. The relation presented in Figure 8.5 displays the same characteristics as Figure 9.1b. An *anti*-correlation between dust extinction and SFR at stellar masses $< 10^{10} M_{\odot}$ and a positive correlation at higher stellar masses. We observe a $\sim$ 0.1 magnitude greater extinction

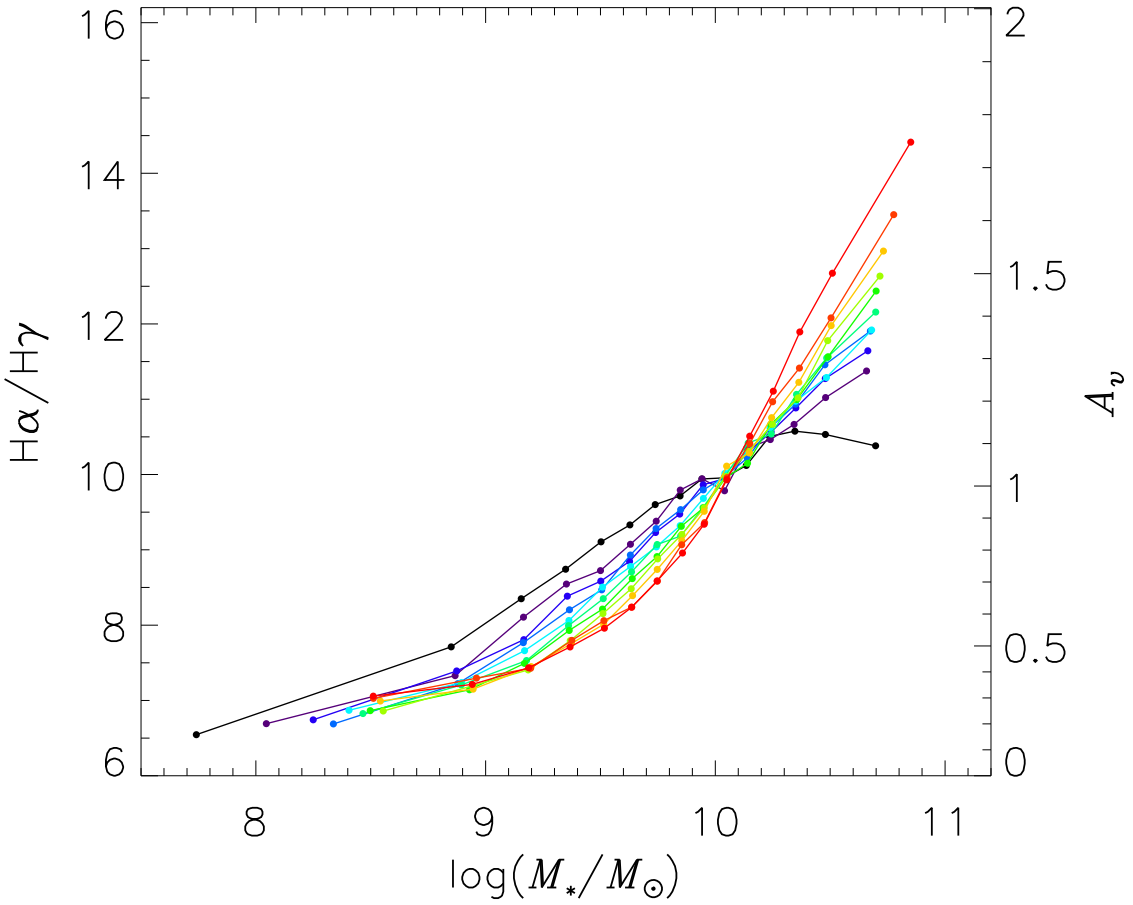

Figure 8.5 The observed relation between stellar mass, dust extinction and SFR ($M_\odot$ yr^{-1}). Similar to Figure 9.1b but with dust extinction determined from the Hα/Hγ ratio.

when determining A_v from Hα/Hβ as compared to Hα/Hγ. Groves et al. (2012) find a similar offset and by comparing SDSS DR7 data with DR4 data. They attribute the difference in extinction determined from Hα/Hβ and Hα/Hγ to a systematic error in the subtraction of the underlying Hβ Balmer absorption. While systematic effects in subtracting the underlying Hβ absorption may affect the absolute measurement of A_v, we conclude that the observed twist in the MDSR is not affected. A comparison of Figure 8.5 with Figure 9.1b shows that a greater difference in A_v is observed at higher stellar masses and SFRs. The overestimation of A_v appears to be correlated with the stellar mass and SFR.

8.4.2 Selection Effects

We select star-forming galaxies from the parent sample using the BPT method which allows us to identify and remove galaxy spectra dominated by AGN emission (see Section 8.2). We require a S/N > 8 in the Hα and Hβ emission line fluxes in order to obtain a robust estimate of the SFR and Balmer decrement from which we measure the extinction. The strength of the Balmer lines scales with number of UV ionizing photons originating from massive stars and therefore is a good indicator of the SFR (Kennicutt 1998). We may bias our sample by selecting galaxies above a fixed S/N threshold because galaxies with low levels of star formation will have weak Balmer lines that may not meet our S/N requirement. This selection criteria could lead to a spurious MDSR if the bias is mass dependent.

In order to investigate the bias introduced by our S/N requirement we compare the distribution of SFR as a function of stellar mass for the SN8 sample with a sample selected requiring a S/N > 3 in the Hα and Hβ emission lines. We refer to this sample as the SN3 samples. The SN3 sample consists of $\sim 259,000$ galaxies and contains a factor of ~ 1.6 more galaxies than the SN8 sample. In Figure 8.6 we plot the distribution of SFRs in 30 bins of stellar mass for the SN8 (black curves) and SN3 (red curves) samples. The median of the SFR distribution (solid curves) of the SN3 sample is typically $\sim$0.1 dex lower than the SN8 sample except at the highest stellar masses where the difference is larger.

We are interested in determining the MDSR for the star-forming sequence of galaxies as identified by Noeske et al. (2007, and many others). The population of star-forming galaxies out to $z \sim 2$ is characterized by a near unity slope and constant scatter in the relation between stellar mass and SFR that is independent of redshift (Noeske et al. 2007; Elbaz et al. 2007; Daddi et al. 2007; Pannella et al. 2009; Whitaker et al. 2012). In the SN8 and SN3 sample, the scatter in the SFR distribution increases at higher stellar masses and a population of massive, low SFR galaxies is present in the distribution shown in Figure 8.6. By examining the sersic index of galaxies on the stellar mass-SFR diagram, Wuyts et al. (2011) show that this region of the diagram is populated by quiescent galaxies best described by de Vaucouleurs profiles. Decreasing our S/N threshold slightly broadens and

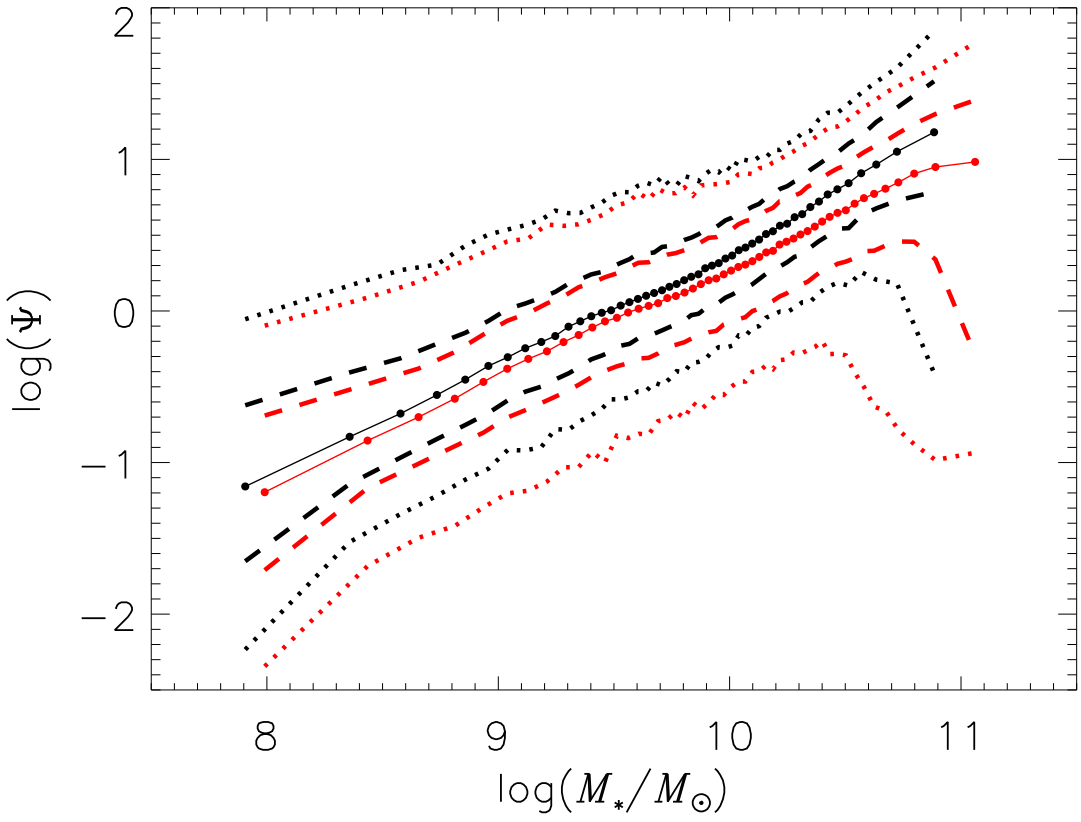

Figure 8.6 The SFR ($M_\odot$ yr^{-1}) distribution for the SN8 (black curves) and SN3 (red curves) samples. The median SFR in 30 equally populated bins of stellar mass are shown by the filled circles and solid curves. The 68% and 95% contours of the distribution are shown by the dashed and dotted curves, respectively.

shifts the distribution of SFRs at all stellar masses and selects a greater number of massive, quiescent galaxies.

In Figure 8.7 we reexamine the stellar mass, dust extinction and SFR relation using our SN3 sample. The greatest difference in the MDSR determined from the SN3 sample as compared to the SN8 sample is for galaxies with stellar masses $\gtrsim 10^{10} M_\odot$ and is attributable to the greater number of quiescent galaxies in the sample. We conclude that our S/N selection criterion does not strongly select against the star-forming sequence of galaxies. The S/N criterion of the SN8 sample does not completely remove quiescent galaxies from

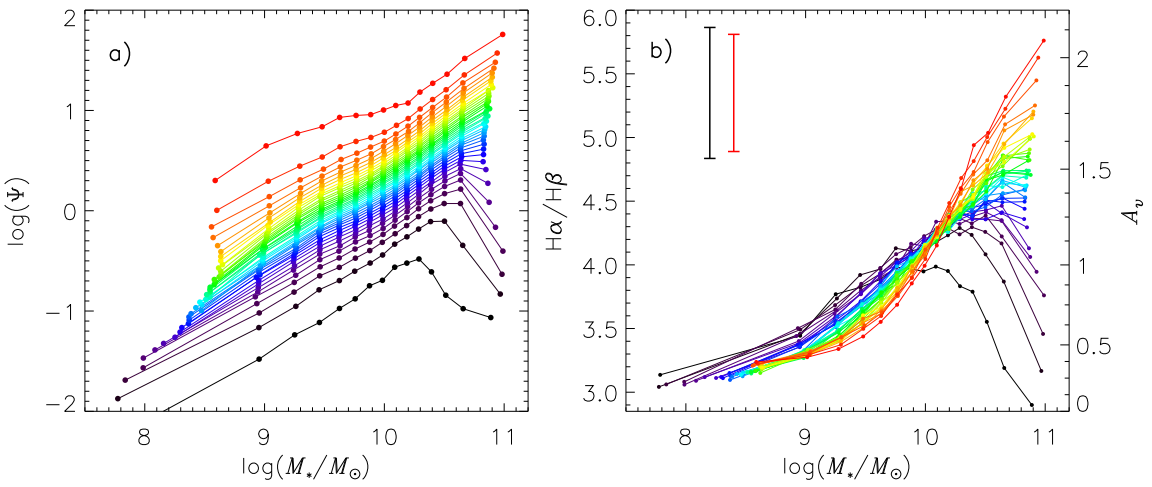

Figure 8.7 The MDSR for the SN3 sample.

the sample, though they constitute a small fraction of the sample. Thus, selection bias is not a significant. Comparison with the SN3 sample suggests that the downturn in the relation between stellar mass and dust extinction observed in the highest mass, lowest SFR bin of the SN8 sample is a consequence of the presence of quiescent galaxies in the sample (see Figure 9.1a). This suggests that twist observed in the MDSR and the *anti*-correlation between SFR and dust extinction is related to the shutting down of star formation in galaxies.

We apply a higher S/N threshold in order to emulate selection effects that may be present in high redshift data. The "twist" in the MDSR is *clearly* observed in the MDSR when the S/N threshold for Hα and Hβ emission is < 20. At a S/N$\gtrsim 25$, there is no longer a "twist" in the MDSR. In the SDSS data 74% of the galaxies are removed when a S/N> 25 is required. At a fixed stellar mass this selection criterion preferentially removes low SFR galaxies. This demonstrates that incompleteness in SFR may bias the observed MDSR and care must be taken when investigating the MDSR in higher redshift samples.

8.4.3 Aperture Effects

We investigate aperture effects associated with measurements of the SFR and the Balmer decrement.

Star Formation Rate

The SFRs used in this study are derived by the MPA/JHU group using the technique developed by Brinchmann et al. (2004, hereafter B04). B04 model the stellar continuum and absorption lines using Bruzual & Charlot (2003) stellar population synthesis models. They model the emission lines using the CLOUDY photoionization code (Ferland 1996) and Charlot & Longhetti (2001) nebular emission models. Dust attenuation is largely constrained using the Balmer decrement with small contributions from other emission lines. This procedure gives the SFR within the 3" fiber aperture. B04 apply a fiber aperture correction in order to obtain the total SFR. The correction is derived by calculating the dependency of SFR on color within the fiber. The SFR outside the fiber is accounted for by assuming that the color dependency of the SFR is the same inside and outside the fiber (see B04 for more details).

Salim et al. (2007) derive dust corrected SFRs for $\sim 50,000$ galaxies in the local universe by fitting the UV and optical spectral energy distribution (SED) with a library of stellar population synthesis models. The SFRs determined from the SED are not subject to aperture effects. Salim et al. (2007) show that the aperture and dust corrected SFRs derived by B04 for the sample of star-forming galaxies (i.e. those with Hα detected with S/N > 3) agree with those determined from the UV and optical SED. There is a systematic difference of 0.02 dex (when 3σ outliers are excluded) and the scatter in the two methods is accounted for by the uncertainty of each method. Salim et al. (2007) conclude that for star-forming galaxies the UV-based SFRs agree remarkably well with the aperture corrected SFRs derived by B04. For the star-forming galaxies in the SN8 sample, the SFRs made available in the DR7 and used in this study are robust against aperture bias.

The MDSR derived in this study is dependent on how the SFR is measured. To demonstrate the need for an aperture correction, we also determine the SFR from the dust corrected Hα luminosity observed in a 3" fiber aperture using the conversion of Kennicutt (1998). We refer to the SFR determined from the observed Hα luminosity as the Fiber SFR and explicitly refer to the aperture corrected SFRs as the DR7 SFR. The relation between

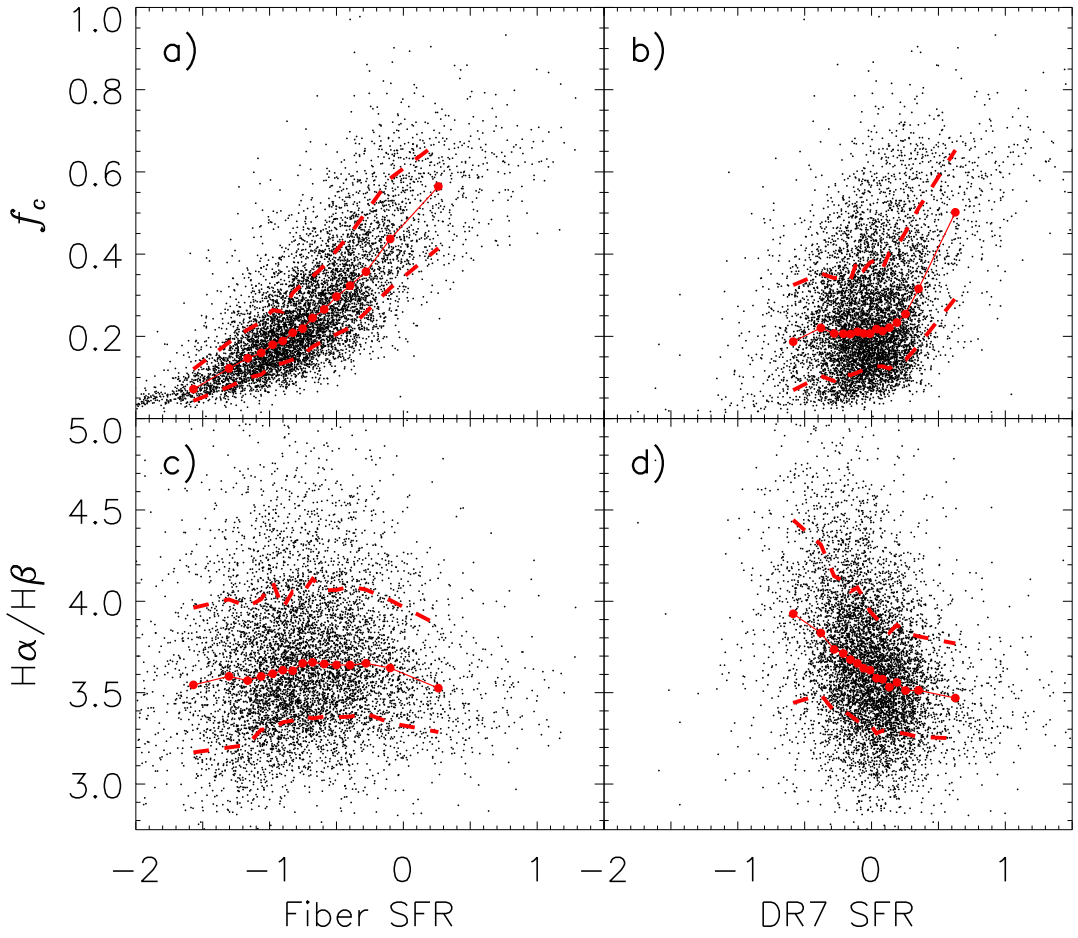

Figure 8.8 Relation between covering fraction, f_c, and a) Hα SFRs and b) aperture corrected SFRs ($M_\odot$ yr^{-1}). The relation between Balmer decrement and c) Hα SFR and d) aperture corrected SFRs. The data are the SN8 sample in a limited mass range ($9.4 < \log(M_*/M_\odot) < 9.5$). The median covering fraction plotted by the solid red curve in 15 bins of a) Hα SFRs and b) aperture corrected SFRs. The median Balmer decrement plotted by the solid red curve in 15 bins of c) Hα SFRs and d) aperture corrected SFRs. The 68% contours of the distributions are shown by the dashed red curves.

stellar mass, dust extinction and Fiber SFR is qualitatively different at lower stellar masses when compared to the same relation using DR7 SFRs. At a fixed stellar mass, the Fiber SFRs are not *anti*-correlated with dust extinction at stellar masses $< 10^{10} M_\odot$. We attribute the different relation observed between dust extinction and SFR at lower stellar masses to aperture effects resulting from the use of Fiber SFRs rather than the DR7 SFRs. In

Figure 8.8a we show the distribution of aperture covering fraction for galaxies as a function of Fiber SFR in a narrow mass range ($9.4 < \log(M_*/M_\odot) < 9.5$). The fiber covering fraction is strongly correlated with the Fiber SFR. In Figure 8.8c we show that Fiber SFRs and Balmer decrements are weakly (positively) correlated at Fiber SFRs < 0 but show a negative correlation at higher Fiber SFRs.

In Figure 8.8b and d we show the distribution of covering fraction and Balmer decrement, respectively, plotted as a function of DR7 SFRs. The Balmer decrement is not strongly correlated with DR7 SFRs. This interval contains $\sim$75% of data. At higher DR7 SFRs there is a positive correlation between the SFR and covering fraction. The correlation between covering fraction and DR7 SFR at higher stellar masses arises because the sample is not volume limited and we have applied a fixed S/N threshold. We observe a similar relation between stellar mass, dust extinction and SFR using the volume limited sample of Zahid et al. (2011) which is comprised of data selected in a redshift range of $0.04 < z < 0.1$. No correlation between covering fraction and DR7 SFR is observed in the volume limited sample in the mass range investigated in Figure 8.8. However, restricting the redshift range removes a substantial number of low and high mass galaxies. Because the effect of not selecting a volume limited sample is not significant and does not change our conclusions, we do not apply this additional criterion in selecting data.

By comparing Figure 8.8c and d we show that not including an aperture correction for SFR results in a spurious correlation between Balmer decrement and SFR. Figure 8.8 highlights the importance of applying an aperture correction to SDSS SFRs when examining global trends in order to avoid systematic bias in relations between SFR and other physical properties.

Balmer Decrement

Several studies have reported variations in dust extinction with galactocentric radius (e.g. Holwerda et al. 2005; Boissier et al. 2007; Tamura et al. 2009; Muñoz-Mateos et al. 2009). However, Kewley et al. (2005) find little evidence for systematic variation between nuclear

and global extinction for covering fractions $> 20\%$. Here we test possible biases that may result from aperture effects in determining the Balmer decrement.

If strong negative dust gradients exist in galaxies then the measured Balmer decrement will be biased towards larger values of extinction in galaxies with small covering fractions. In this case, the measured Balmer decrement will not reflect the global dust properties. We first test for any bias by plotting the Balmer decrement as a function of the aperture covering fraction. In Figure 8.9 we plot the Balmer decrement as a function of aperture covering fraction for data in a narrow mass range. For data in the stellar mass range of $9.4 < \log(M_*/M_\odot) < 9.5$, the Balmer decrement is not strongly correlated to the aperture covering fraction.

We also apply a more global test for potential bias in the Balmer decrement due to aperture effects. We divide the SN8 sample into two equally populated subsamples. Sample S1 is comprised of galaxies that have covering fraction less than the median covering fraction of the SN8 sample ($f_c < 0.24$). Sample S2 is the complementary sample with covering fraction greater than the median covering fraction. Each sample has $\sim$74,000 galaxies.

We want to examine the bias in the Balmer decrement associated *only* with the covering fraction. While in small bins of stellar mass, the aperture corrected SFR is not strongly correlated to covering fraction (see Figure 8.8b), the SFRs and stellar masses across the whole sample are correlated to the covering fraction. The correlation of the SFR and stellar mass with covering fraction is a consequence of the fact that SDSS is a magnitude limited survey and we have selected our sample using a fixed S/N threshold. Therefore we must take care to remove second order correlations between Balmer decrement and covering fraction resulting from correlations between covering fraction, SFR and stellar mass. We do this by randomly selecting subsets of the S1 and S2 data that are matched to have an identical SFR and stellar mass distributions (in bins of 0.05 dex width). We refer to these as the S1s and S2s subsamples. The S1s and S2s subsamples are comprised of $\sim 39,000$ galaxies each. Figure 8.10a and b show the stellar mass and SFR distribution for S1s and S2s in gray. The stellar mass and SFR distributions of the S1s and S2s are representative of the SN8

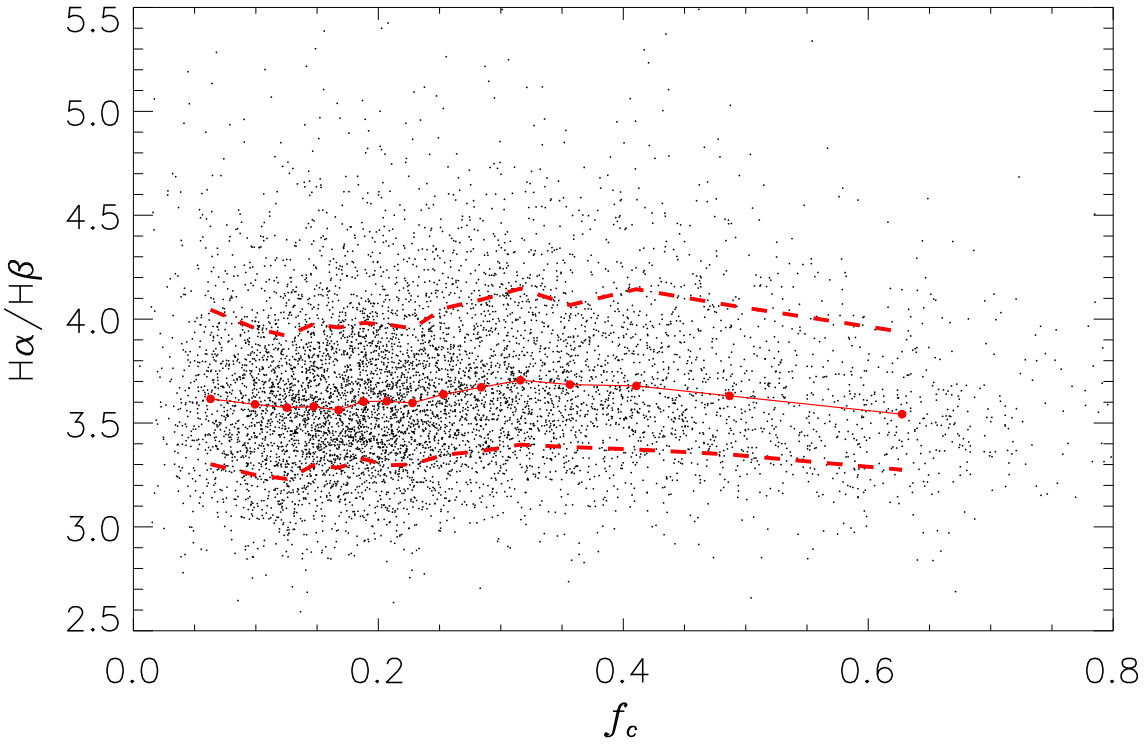

Figure 8.9 The Balmer decrement plotted against the aperture covering fraction, f_c. The black data points are taken from the SN8 sample in a limited mass range ($9.4 < \log(M_*/M_\odot) < 9.5$). The median Balmer decrement is plotted by the solid red curve in 15 bins of aperture covering fraction, f_c. The 68% contours of the distributions are shown by the dashed red curves.

sample and are identical for the S1s and S2s sample by design. Figure 8.10c and d show the distribution of the Balmer decrement and covering fraction for the S1s (red histogram) and S2s (blue histogram) samples, respectively.

In Figure 8.11 we show the distribution of the logarithm of the Balmer decrement for the S1s (red histogram) and S2s (blue histogram) samples. The data are nearly log-normally distributed. The median observational uncertainties in the Balmer decrement for the S1s and S2s samples are 0.34 and 0.28, respectively. The S1s sample ($f_c < 0.24$) has a slightly broader distribution as compared to the S2s sample. The greater width of the S1s distribution may be due to the larger observational uncertainties of the S1s sample. Despite

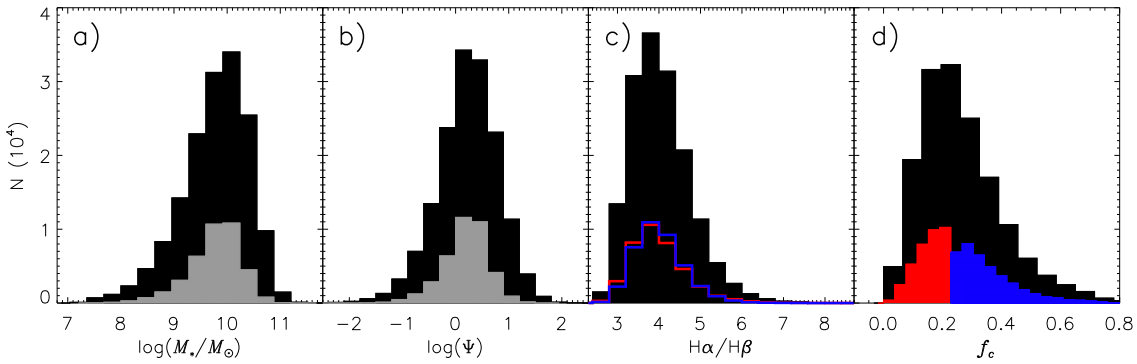

Figure 8.10 The black histograms are for the SN8 sample and are the same as Figure 8.1. The stellar mass and SFR ($M_\odot$ yr^{-1}) distribution are identical for the S1s and S2s sample and are shown by the gray histograms. The distribution of the c) Balmer decrement and d) covering for the S1s and S2s samples are shown by the red and blue histograms, respectively.

the very different distribution in covering fraction, the distribution of Balmer decrement in the S1s and S2s samples are very similar. If there were a strong bias in the measured Balmer decrement due to aperture effects, we would expect a relative shift in the distribution of the Balmer decrement for the S1s and S2s samples. We conclude that aperture effects do not significantly bias the measurement of the dust extinction in the SN8 sample.

The Balmer decrement measured in the fiber is a flux-weighted average over many HII regions. We perform a simple calculation to test whether the similarity in the S1s and S2s Balmer decrement distribution is consistent with the extinction observed in nearby galaxies. Muñoz-Mateos et al. (2009) measure the radial attenuation profile for galaxies in the Spitzer Infrared Nearby Galaxies Survey sample. The typical (median) radial attenuation gradient measured is -0.023 mags/kpc. We convert this gradient measured in magnitudes of extinction into a gradient in Balmer decrement assuming the (Cardelli et al. 1989) extinction curve. We adopt an exponential profile for Hα surface brightness with a fiducial scale length of 4 kpc. Using these values we determine the flux-weighted Balmer decrement as a function of fiber covering fraction. We find that for the fiducial values of radial attenuation gradient and Hα scale length, the Blamer decrement is overestimated by $\sim 5\%$ when the covering fraction is 5% (the minimum for the SN8 sample) and a 4% overestimate when

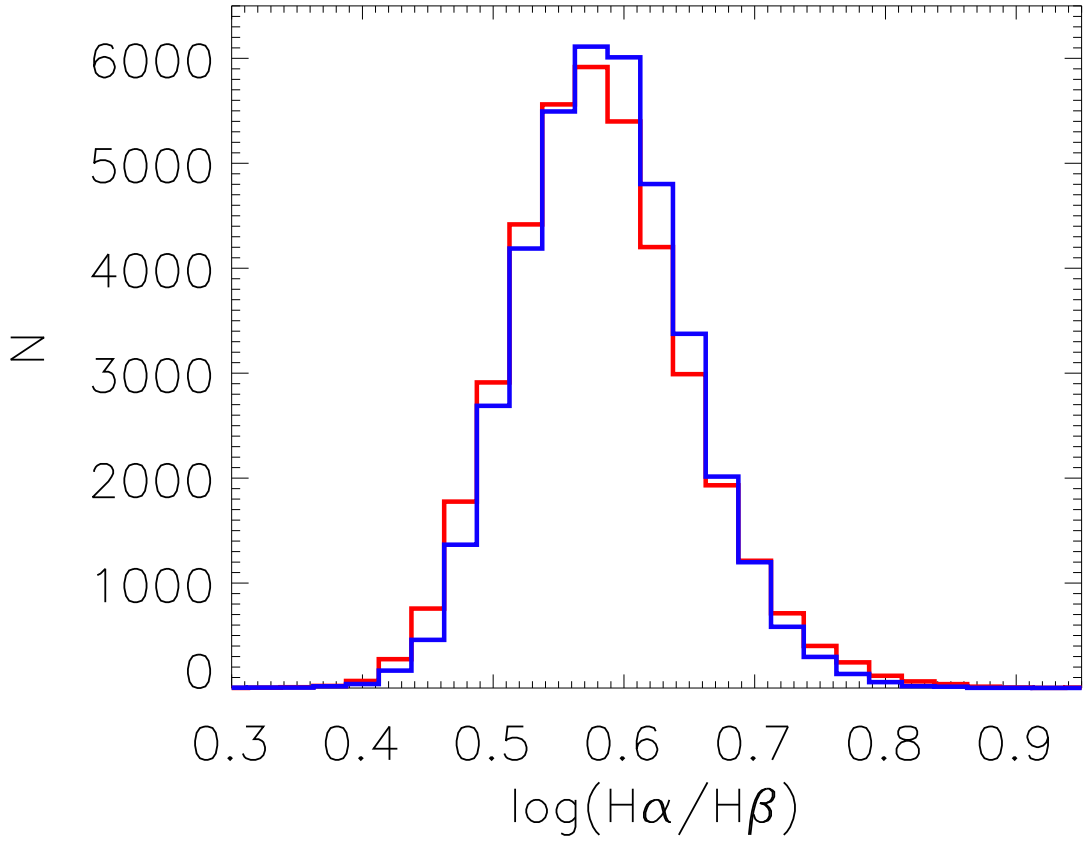

Figure 8.11 Distribution of the logarithm of the Balmer decrement for the S1s (red) and S2s (blue) samples.

the covering fraction is 20%. The median covering fraction of the S1s and S2s samples is 16% and 33%, respectively. The relative systematic error in the Balmer decrement between these two covering fraction is $\sim$ 1%. The calculated values for the relative error do not depend strongly on scale length adopted but do increase if a steeper attenuation gradient is adopted (e.g. relative error of 5% for an attenuation gradient of -0.1 mags/kpc). We conclude that distribution of Balmer decrement shown in Figure 8.11 is consistent with the typical (shallow) gradients found in local spiral galaxies (e.g. Muñoz-Mateos et al. 2009).

As we have shown in this section, the measured dust extinction and SFRs are not significantly biased by aperture effects. However, because aperture effects are present in

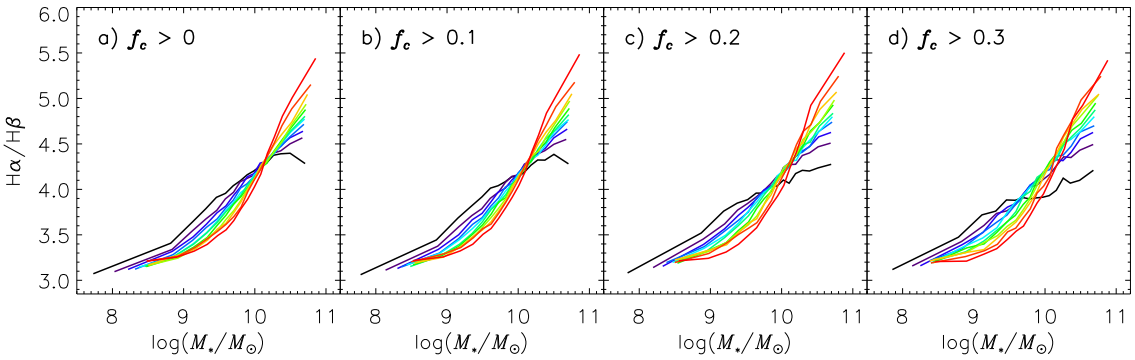

Figure 8.12 The MDSR for the SN8 sample but with a minimum aperture covering fraction requirement of a) 0, b) 0.1, c) 0.2 and d) 0.3.

the SDSS sample in a complicated way, we also test whether the observed MDSR is effected by aperture bias. In Figure 8.12 we plot the MDSR by applying an increasing minimum aperture covering fraction requirement. In Figure 8.12a-d we apply a minimum covering fraction of 0, 0.1, 0.2 and 0.3 in selecting data and determine the MDSR using ∼157,000, ∼143,000, ∼98,000 and ∼52,000 galaxies, respectively. A very similar MDSR is observed in Figure 8.12a-d. We conclude that selection and aperture effects are not significant in our determination of the MDSR.

8.5 Discussion

In this contribution we have presented the MDSR for local star-forming galaxies. The physics of dust production, destruction and evolution are not well understood (for review see Draine 2003) and it is beyond the scope of this study to make detailed considerations of these processes. It is well established that dust forms from metals and therefore it is not surprising that a strong correlation between dust and metals is observed (e.g. Garn & Best 2010). Zahid et al. (2012b) derive a relation between stellar mass, metallicity and dust extinction. They show that the dust extinction increases with *both* stellar mass and metallicity. That is, dust extinction increases with stellar mass and at a fixed stellar mass, the metallicity and dust extinction are positively correlated. The correlation between stellar

mass, dust extinction and metallicity is also evident from PCA (Garn & Best 2010; Xiao et al. 2012).

The MDSR shows similar trends as the MDZR. While dust extinction can be easily estimated from the Balmer decrement, metallicity is substantially more difficult physical quantity to measure. Various methods have been developed to determine the gas-phase oxygen abundance from the emission line properties of star-forming galaxies (for review of methods see Kewley & Ellison 2008). The most commonly used methods rely on theoretically or empirically calibrating ratios of strong collisionally excited emission lines to recombination lines. However, these so-called strong line methods suffer from various systematic uncertainties. In particular, Kewley & Ellison (2008) show that the metallicity determined for the same sample of galaxies can differ by up to $\sim$0.6 dex depending on the choice of calibration. Thus the observed MDSR presented in this study helps to independently establish the observed MDZR presented in Yates et al. (2012).

The observed MZ relation and its second parameter dependencies serve as a Rosetta stone for understanding the physical processes responsible for the chemical evolution of galaxies. Because dust is formed from metals, we favor a common physical origin for the twist observed in both the MDSR presented in this study and the MDZR investigated by Yates et al. (2012). While dust may be destroyed, metals can not and therefore the observed MDSR can not be explained by destruction processes unless the similarities in the MDSR and MDZR are taken to be coincidental. Moreover, given that metals are locked up in dust, we may expect an opposite trend in the MDSR and MDZR if dust destruction is the responsible mechanism since the destruction of dust grains should liberate the constituent metals, thus increasing the gas-phase abundance. The metallicities of galaxies are set by a balance between star formation and gas flows. Dust extinction is, to first order, insensitive to the infall of metal-poor gas and cannot be diluted. Therefore the observed twist in the MDSR and the MDZR can not *solely* be explained as a consequence of gas dilution. We consider differential mass loss in galaxies which is related to the SFR a natural explanation of the observed twist in the MDSR and MDZR.

Whitaker et al. (2012) study the relation between stellar mass and SFR out to $z = 2.5$. They conclude that the dust attenuation observed in star-forming galaxies increases with stellar mass. They find that for galaxies with stellar masses $\gtrsim 10^{10} M_{\odot}$ dusty, blue galaxies populate the upper envelope of the scatter in the MS relation. Conversely, red low-dust galaxies have lower observed SFRs and are interpreted to possibly be in the process of shutting down star formation. They show that the MS relation at $1 < z < 1.5$ for red galaxies has a shallower slope than the MS relation for blue galaxies. It is possible that at lower stellar masses the two relations cross such that a similar trend of a reverse in the correlation between SFR and dust attenuation at a fixed stellar mass may be present in the high redshift population of star-forming galaxies (see Figure 4 of Whitaker et al. 2012). However, due to incompleteness no firm conclusions can be drawn regarding the correlation between SFR and dust attenuation at low stellar masses.

The results of our study are consistent with the interpretation of Whitaker et al. (2012). In particular, decreasing our S/N threshold to S/N > 3 (Section 8.4.2) results in the inclusion of a significant fraction of quiescent galaxies as identified by the sersic index analysis of Wuyts et al. (2011). Figure 8.7 shows continuity in the correlation between dust extinction and SFR observed at stellar masses $> 10^{10} M_{\odot}$. This suggests that the physical mechanism responsible for the correlation between SFR and dust extinction at higher stellar masses and the twist in the MDSR and MZSR may be related to the physical processes leading to the shut down of star formation and the migration of galaxies to the red sequence.

8.6 Summary

In this study we have investigated the relation between stellar mass, SFR and dust extinction. We conclude that:

- Our analysis is consistent with the conclusions of Garn & Best (2010) that the strongest correlation in the data is the *positive* correlation between stellar mass, SFR and dust extinction.

- The relation between SFR and dust extinction *at a fixed stellar mass* is mass dependent. At a fixed stellar mass, an *anti*-correlation between the SFR and dust extinction is observed for galaxies with stellar masses $< 10^{10} M_{\odot}$. There is a sharp transition at a stellar mass of $10^{10} M_{\odot}$. In galaxies with larger stellar masses there is a *positive* correlation between the SFR and dust extinction at a fixed stellar mass.

- The relation between stellar mass, metallicity and SFR (see Yates et al. 2012) shows the same trends as the relation between stellar mass, dust extinction and SFR. Unlike metals, dust can not be diluted by inflows of pristine gas. The observed stellar mass, dust extinction and SFR relation provides important new constraints for understanding the physical processes governing chemical evolution of galaxies.

- Quiescent galaxies are observed to populate the high mass, low SFR part of the stellar mass - SFR diagram. When including quiescent galaxies in the sample we find continuity in the correlation between dust extinction and SFR at stellar masses $> 10^{10} M_{\odot}$. The physical processes responsible for the relation between stellar mass, dust extinction and SFR at the high mass end may be related to the physical processes leading to the shutdown of star formation.

In a forthcoming paper we develop a model incorporating momentum driven outflows as a possible explanation for the observed relation between stellar mass, dust extinction and SFR presented here.

References

Abazajian, K. N., et al. 2009, ApJS, 182, 543

Asari, N. V., Cid Fernandes, R., Stasińska, G., Torres-Papaqui, J. P., Mateus, A., Sodré, L., Schoenell, W., & Gomes, J. M. 2007, MNRAS, 381, 263

Baldwin, J. A., Phillips, M. M., & Terlevich, R. 1981, PASP, 93, 5

Boissier, S., Boselli, A., Buat, V., Donas, J., & Milliard, B. 2004, A&A, 424, 465

Boissier, S., et al. 2007, ApJS, 173, 524

Brinchmann, J., Charlot, S., White, S. D. M., Tremonti, C., Kauffmann, G., Heckman, T., & Brinkmann, J. 2004, MNRAS, 351, 1151

Bruzual, G., & Charlot, S. 2003, MNRAS, 344, 1000

Cardelli, J. A., Clayton, G. C., & Mathis, J. S. 1989, ApJ, 345, 245

Chabrier, G. 2003, PASP, 115, 763

Charlot, S., & Longhetti, M. 2001, MNRAS, 323, 887

Cowie, L. L., & Barger, A. J. 2008, ApJ, 686, 72

Daddi, E., et al. 2007, ApJ, 670, 156

Dalcanton, J. J. 2007, ApJ, 658, 941

Draine, B. T. 2003, ARA&A, 41, 241

Dwek, E. 1998, ApJ, 501, 643

Elbaz, D., et al. 2007, A&A, 468, 33

Ellison, S. L., Patton, D. R., Simard, L., & McConnachie, A. W. 2008, ApJ, 672, L107

Erb, D. K., Shapley, A. E., Pettini, M., Steidel, C. C., Reddy, N. A., & Adelberger, K. L. 2006, ApJ, 644, 813

Ferland, G. J. 1996, Hazy, A Brief Introduction to Cloudy 90, ed. G. J. Ferland

Garn, T., & Best, P. N. 2010, MNRAS, 409, 421

Groves, B., Brinchmann, J., & Walcher, C. J. 2012, MNRAS, 419, 1402

Heckman, T. M., Robert, C., Leitherer, C., Garnett, D. R., & van der Rydt, F. 1998, ApJ, 503, 646

Holwerda, B. W., Gonzalez, R. A., Allen, R. J., & van der Kruit, P. C. 2005, AJ, 129, 1381

Hummer, D. G., & Storey, P. J. 1987, MNRAS, 224, 801

Kauffmann, G., et al. 2003, MNRAS, 346, 1055

Kennicutt, Jr., R. C. 1998, ARA&A, 36, 189

Kewley, L. J., & Ellison, S. L. 2008, ApJ, 681, 1183

Kewley, L. J., Groves, B., Kauffmann, G., & Heckman, T. 2006, MNRAS, 372, 961

Kewley, L. J., Jansen, R. A., & Geller, M. J. 2005, PASP, 117, 227

Lamareille, F., et al. 2009, A&A, 495, 53

Lara-López, M. A., et al. 2010, A&A, 521, L53+

Lee, H., Skillman, E. D., Cannon, J. M., Jackson, D. C., Gehrz, R. D., Polomski, E. F., & Woodward, C. E. 2006, ApJ, 647, 970

Lequeux, J., Peimbert, M., Rayo, J. F., Serrano, A., & Torres-Peimbert, S. 1979, A&A, 80, 155

Maiolino, R., et al. 2008, A&A, 488, 463

Mannucci, F., Cresci, G., Maiolino, R., Marconi, A., & Gnerucci, A. 2010, MNRAS, 408, 2115

Mannucci, F., et al. 2009, MNRAS, 398, 1915

Moustakas, J., et al. 2011, ArXiv e-prints

Muñoz-Mateos, J. C., et al. 2009, ApJ, 701, 1965

Noeske, K. G., et al. 2007, ApJ, 660, L43

Pannella, M., et al. 2009, ApJ, 698, L116

Reddy, N. A., Erb, D. K., Pettini, M., Steidel, C. C., & Shapley, A. E. 2010, ApJ, 712, 1070

Salim, S., et al. 2007, ApJS, 173, 267

Savaglio, S., et al. 2005, ApJ, 635, 260

Stoughton, C., et al. 2002, AJ, 123, 485

Tamura, K., Jansen, R. A., & Windhorst, R. A. 2009, AJ, 138, 1634

Tremonti, C. A., et al. 2004, ApJ, 613, 898

Whitaker, K. E., van Dokkum, P. G., Brammer, G., & Franx, M. 2012, ApJ, 754, L29

Wuyts, S., et al. 2011, ApJ, 742, 96

Xiao, T., Wang, T., Wang, H., Zhou, H., Lu, H., & Dong, X. 2012, MNRAS, 421, 486

Yabe, K., et al. 2011, ArXiv e-prints

Yates, R. M., Kauffmann, G., & Guo, Q. 2012, MNRAS, 422, 215

Zahid, H. J., Bresolin, F., Kewley, L. J., Coil, A. L., & Davé, R. 2012a, ApJ, 750, 120

Zahid, H. J., Dima, G. I., Kewley, L. J., Erb, D. K., & Dave, R. 2012b, ArXiv e-prints

Zahid, H. J., Kewley, L. J., & Bresolin, F. 2011, ApJ, 730, 137

Zahid, H. J., Yates, R. M., Kewley, L. J., & Kudritzki, R. P. 2013, ApJ, 763, 92

Chapter 9

The Slow Flow Model of Dust Efflux in Local Star-Forming Galaxie

Note: This chapter originally appeared as Zahid, H.J., Torrey, P., Kudritzki, R.P., Kewley, L., Dave, R., & Geller, M.J 2013, MNRAS, 436, 1852. I am the primary author of this work.

Abstract

We develop a dust efflux model of radiation pressure acting on dust grains which successfully reproduces the relation between stellar mass, dust opacity and star formation rate observed in local star-forming galaxies. The dust content of local star-forming galaxies is set by the competition between the physical processes of dust production and dust loss in our model. The dust loss rate is proportional to the dust opacity and star formation rate. Observations of the relation between stellar mass and star formation rate at several epochs imply that the majority of local star-forming galaxies are best characterized as having continuous star formation histories. Dust loss is a consequence of sustained interaction of dust with the radiation field generated by continuous star formation. Dust efflux driven by radiation pressure rather than dust destruction offers a more consistent physical interpretation of the dust loss mechanism. By comparing our model results with the observed relation between stellar mass, dust extinction and star formation rate in local star-forming galaxies we are able to constrain the timescale and magnitude of dust loss. The timescale of dust loss is long

and therefore dust is effluxed in a "Slow Flow". Dust loss is modest in low mass galaxies but massive galaxies may lose up to 70 $\sim$ 80% of their dust over their lifetime. Our Slow Flow model shows that mass loss driven by dust opacity and star formation may be an important physical process for understanding normal star-forming galaxy evolution.

9.1 Introduction

9.1.1 Background

Dust is a fundamental constituent of the interstellar medium (ISM) of galaxies. Dust forms from material recycled back to the ISM through stellar winds or supernovae. The AGB phase of intermediate mass stars ($1 \lesssim M_{\odot} \lesssim 8$) and massive stars ($\gtrsim 8M_{\odot}$) which end their lives as Type II supernovae (SNe) are considered the dominant source of stellar dust production in star-forming galaxies while dust in the ISM may also form *in situ* from accretion of enriched gas processed by stars (Dwek 1998). Dust forms from metals and a strong correlation between gas-phase oxygen abundance and dust content is observed in local (Heckman et al. 1998; Boissier et al. 2004; Asari et al. 2007; Garn & Best 2010; Xiao et al. 2012; Zahid et al. 2012b) and high redshifts galaxies (Reddy et al. 2010; Domínguez et al. 2013).

Dust is composed of heavy elements and therefore the chemical and dust properties of galaxies should evolve consistently. The heavy element content of star-forming galaxies is characterized by a strong relation between the stellar mass and average gas-phase oxygen abundance (Lequeux et al. 1979; Tremonti et al. 2004). This so-called mass-metallicity relation (MZR) extends to low stellar mass galaxies ($\sim 10^7 M_{\odot}$ Lee et al. 2006; Zahid et al. 2012a; Berg et al. 2012) and is observed at intermediate (Savaglio et al. 2005; Cowie & Barger 2008; Zahid et al. 2011; Moustakas et al. 2011; Zahid et al. 2013a) and high redshifts (Erb et al. 2006; Mannucci et al. 2009; Laskar et al. 2011). The metallicity at all stellar masses increases with time and the high mass end of the relation flattens at late times as galaxies enrich to an empirical upper limit in the gas-phase abundance (Zahid et al. 2013a).

Examination of the second parameter dependencies of the MZR has revealed a correlation between stellar mass, metallicity and star formation rate (Ellison et al. 2008; Lara-López et al. 2010; Mannucci et al. 2010; Yates et al. 2012; Andrews & Martini 2013). We refer to this relation as the MZSR. For less massive galaxies, Lara-López et al. (2010) and Mannucci et al. (2010) find that metallicity is *anti*-correlated to SFR at a fixed stellar mass. However, the relation between stellar mass, metallicity and SFR is dependent on methodology (Yates et al. 2012; Andrews & Martini 2013). Like Mannucci et al. (2010) and Lara-López et al. (2010), Yates et al. (2012) find a similar relation for low mass galaxies. However, they show that for massive galaxies the metallicity and SFR are *positively* correlated at a fixed stellar mass. Thus, there is a "twist" in the relation between stellar mass, metallicity and SFR. Not surprisingly, in these same galaxies, a similar twist is observed in the relation between stellar mass, dust extinction and SFR (Zahid et al. 2013c). Dust is formed from metals and we argue for a common physical origin for both relations.

Recent observations indicate that stellar mass growth of most star-forming galaxies is dominated by secular evolution over the last ∼10 billion years. A strong correlation between stellar mass and SFR is observed out to at least $z \sim 2.5$ (Noeske et al. 2007b; Salim et al. 2007; Elbaz et al. 2007; Daddi et al. 2007; Pannella et al. 2009; Whitaker et al. 2012; Reddy et al. 2012) and is found to be independent of environment (Peng et al. 2010; Wijesinghe et al. 2012; Koyama et al. 2013). The small scatter (~ 0.25 dex) of the relation is independent of redshift suggesting that secular processes such as cosmological gas accretion dominate over mergers in building up the stellar mass of galaxies since at least $z \sim 2-3$. The observed stellar mass-SFR relation (MSR) places strong constraints on the star formation histories of galaxies (Noeske et al. 2007a; Conroy & Wechsler 2009; Leitner 2012; Zahid et al. 2012b). The observed MSR at several epochs implies that the majority of local star-forming galaxies are best characterized by continuous star formation histories. The observations demand that the majority of local star-forming galaxies maintain SFRs that do not vary significantly from their mean SFRs over most of their lifetime (Noeske et al. 2007b).

The well defined MSRs and MZRs observed over cosmological time provide purely empirical constraints for continuous stellar mass growth and chemical enrichment of galaxies as they evolve (see Zahid et al. 2012b). We attempt to understand trends in the metal and dust distribution of local galaxies in the context of this empirical framework. We develop a model where trends in the metal and dust distribution are naturally explained as a consequence of star-formation and large scale galactic gas flows. Recent theoretical considerations suggest that momentum, unlike energy which can be radiated away, may be the primary driver of large scale gas flows (Murray et al. 2005). Dust plays a crucial role since radiation couples to dust over a large and continuous range of wavelengths (Draine 2003) and provides a convenient mechanism for momentum transfer between the radiation field and the gas (e.g. Murray et al. 2005).

The potential importance of radiation pressure acting on dust in the context of galactic mass loss is well recognized. Chiao & Wickramasinghe (1972) suggest that under the influence of radiation pressure, dust may escape galaxies along magnetic field lines. Ferrara (1993) posits that dusty diffuse clouds embedded in a anisotropic radiation field will feel a net acceleration due to radiation pressure. Davies et al. (1998) argue that driven by an imbalance between radiation and gravitational forces, disk galaxies may expel a large fraction (90%) of dust produced over $\sim$ 1Gyr timescales. Dynamical coupling of dust and gas through collisions or coulomb interactions could provide a mechanism for transferring momentum from the radiation field to the gas (Draine 2004). Using cosmological simulations, Aguirre et al. (2001) show that the IGM could be enriched by the expulsion of dust and gas driven by radiation pressure. Several models incorporating dust driven winds have recently been considered in the literature (Zhang & Thompson 2010; Zu et al. 2011; Sharma et al. 2011; Sharma & Nath 2012; Chattopadhyay et al. 2012; Wise et al. 2012).

9.1.2 A Model of Dust Driven Outflows

We develop a numerical model of radiation pressure acting on dust grains leading to an expulsion of dust and metals as an explanation for the observed relation between stellar mass, dust extinction and SFR in SDSS galaxies shown in Figure 9.1 (Zahid et al. 2013c). We refer to this relation as the MDSR. The relation between dust extinction and SFR changes with stellar mass. For galaxies at the same stellar mass dust extinction is *anti*-correlated with the SFR at stellar masses $< 10^{10} M_{\odot}$. There is a sharp transition in the relation at a stellar mass of $10^{10} M_{\odot}$. In massive galaxies dust extinction is *positively* correlated with the SFR for galaxies at the same stellar mass.

The model we develop to reproduce the MDSR assumes the following:

1. At a fixed stellar mass the current SFR is *anti*-correlated to the age of the galaxy.

2. The rate of dust production is proportional to the rate at which mass is recycled by stars.

3. The rate of dust loss is dependent on the amount of dust present and the rate at which high energy photons are produced.

4. The timescale of dust loss is comparable but not identical to the timescale of dust production.

Under these assumptions we propose the following as an interesting physical model explaining the observed MDSR: Radiation pressure driven galactic mass loss (e.g. Murray et al. 2005) is a ubiquitous process in normal star-forming galaxies. Momentum is physically deposited into the ISM by the absorption of high energy photons. Therefore the galactic mass loss rate is proportional to the opacity and SFR (Assumption 3). The main source of opacity in star-forming galaxies is dust and in low mass galaxies dust can accumulate because the opacities, SFRs and therefore galactic mass loss rates are all low. The dust content of a galaxy is proportional to the total amount of stellar mass recycled (Assumption 2). Because stellar mass recycling is a time dependent process, the total amount of stellar

mass recycled in a galaxy is correlated to galaxy age; older galaxies necessarily recycle a greater fraction of their stellar mass. At a fixed stellar mass the current SFR is *anti*-correlated to galaxy age (Assumption 1). Therefore dust opacity is *anti*-correlated with SFR for lower mass galaxies. As galaxies build up stellar mass they accumulate dust. This leads to an increase in their mass loss rate. If the timescale of dust loss is the same as dust production then galaxies should reach an equilibrium where dust loss is balanced by dust production. However, if the timescale over which dust is expelled from the ISM is not *identical* to the timescale of dust production (Assumption 4), then galaxies with high stellar mass recycling rates (SMRRs), and therefore high dust production rates (Assumption 2), may accumulate dust. At a fixed stellar mass the SMRR is positively correlated with the SFR and therefore we expect a similar correlation between the dust content and SFR. A model such as this accounts for all the notable features in the observed MDSR. Because the timescale for dust loss is long, we refer to this as the "Slow Flow" process.

We develop the Slow Flow model by bringing together star formation, chemical evolution and time dependent stellar mass recycling in order to understand the dust properties of local star-forming galaxies. In Section 9.2 we discuss the data and present the observed MDSR. In Section 9.3 and 4 we describe our numerical implementation of Assumptions 1 and 2, respectively. We describe our implementations of Assumptions 3 and 4 and demonstrate that we can reproduce the MDSR in Section 9.5. In Section 9.6 we justify our interpretation of dust loss as dust efflux in a slow flow rather than dust destruction. We revisit the assumptions in Section 9.7. In Section 9.8 we provide a discussion and we conclude with a summary of our model in Section 9.9. Table 9.1 and 9.2 provide a key for frequently used acronyms and symbols, respectively. Throughout this work we adopt the standard cosmology $(H_0, \Omega_m, \Omega_\Lambda) = (70 \text{ km s}^{-1} \text{ Mpc}^{-1}, 0.3, 0.7)$ and a Chabrier (2003) initial mass function (IMF).

Table 9.1 Key for Frequently Used Acronyms

Acronym	Definition
SFR	star formation rate
SFH	star formation history
ISM	interstellar medium
IMF	initial mass function
MZR	the stellar mass-metallicity relation
MSR	the stellar mass-star formation rate relation
SMRR	stellar mass recycling rate
MDSR	the stellar mass-dust extinction-star formation rate relation
MZSR	the stellar mass-metallicity-star formation rate relation

Table 9.2 Key for Frequently Used Symbols

Symbol	Definition
M_*	stellar mass
Ψ	star formation rate
τ	dust opacity
$\dot{M}_R$	mass recycling rate
M_R	total mass of recycled gas
t	time, variable of integration
t_f	formation time of galaxy
S	offset from the observed median relation between stellar mass and star formation rate
f_{mr}	fraction of mass recycled as a function of time for single burst stellar population
$\dot{f}_{mr}$	time derivative of fraction of mass recycled
M_d	mass of dust
Free Parameters	
Δt	timescale of dust loss/destruction
η	efficiency of dust loss in slow flow
α	efficiency of dust loss in fast flow

9.2 Data and Methods

9.2.1 The MDSR

In Zahid et al. (2013c) we present the observed MDSR for $\sim 150,000$ star-forming galaxies in the SDSS DR7 (Abazajian et al. 2009). We summarize the data selection and methodology and refer the reader to Zahid et al. (2013c) for more details. We adopt the stellar masses and SFRs given in the DR7. The stellar masses are determined from the *ugriz*-band photometry (Stoughton et al. 2002). The SFRs are derived by the MPA/JHU group using the technique of Brinchmann et al. (2004) with additional improvements given by Salim et al. (2007). The SFRs are corrected for dust and aperture effects.

We distinguish star-forming galaxies from AGN using the [OIII]λ5007/Hβ vs [NII]λ6584/Hα diagram (Kauffmann et al. 2003a; Kewley et al. 2006). In order to obtain a robust estimate of the Balmer decrement, we require that the signal-to-noise of the Hα and Hβ line be greater than 8. These selection criteria give us a sample of $\sim 150,000$ star-forming galaxies. A detailed analysis of selection effects is presented in Zahid et al. (2013c).

Dust extinction is determined from the Balmer decrement assuming Case B recombination. For a gas with electron temperature $T_e = 10^4$K and electron density $n_e = 10^2$ cm^{-3}, the intrinsic Hα/Hβ ratio is expected to be 2.86 (Osterbrock 1989). We derive the intrinsic colour excess, E(B$-$V), and the correction for dust attenuation using the extinction law of Cardelli et al. (1989) and a corresponding $R_v = 3.1$. From the visual extinction, A_v, we determine the visual optical depth from the relation $\tau_v = A_v/1.086 = R_v$ E(B$-$V)/1.086.

Figure 9.1 (c.f. Figure 2 from Zahid et al. 2013c) shows the observed MDSR for local star-forming galaxies. The $\sim 150,000$ SDSS galaxies in our sample are first sorted into 16 equally populated bins of stellar mass. Each of the 16 bins of stellar mass are then sorted into 11 equally populated bins of SFR. The data plotted in Figure 9.1a and 9.1b are the same (i.e. belong to the same bin of stellar mass and SFR). Figure 9.1a and 9.1b show the

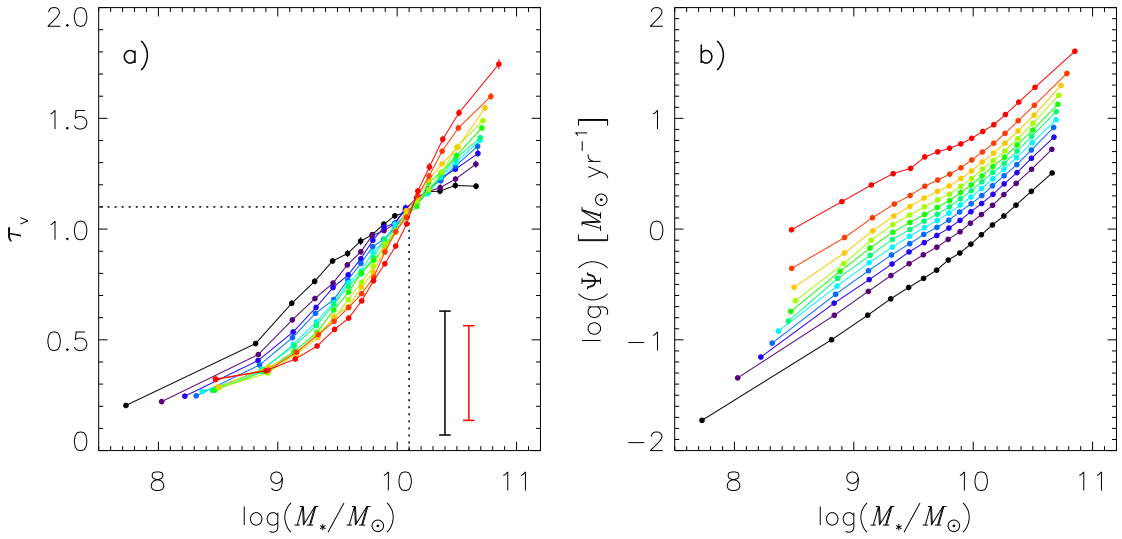

Figure 9.1 The observed relation between stellar mass, dust opacity and SFR for a sample $\sim 150,000$ galaxies from the SDSS DR7. a) The median optical depth derived from the Balmer decrement (see text for details) sorted into bins of stellar mass and SFR. The black and red error bars are the median scatter in each bin and median observational uncertainty, respectively. b) The corresponding SFR in each bin. Each curve is an undecile of the SFR in bins of stellar mass. The standard error for each bin is plotted but is typically smaller than the data point. (This figure is a reproduction of Figure 2 from Zahid et al. 2013c)

median optical depth and median SFR in bins of stellar mass and SFR. In each bin, the median is determined from ~ 890 galaxies. The curves in Figure 9.1a are colour-coded to match the SFRs shown in Figure 9.1b. Each curve is an undecile[1] of the SFR in bins of stellar mass. The red curves correspond to the highest SFR in each bin of stellar mass and the black curves the lowest SFR bin in each bin of stellar mass. The median 1σ scatter of the optical depth binned by stellar mass and SFR (Figure 9.1a) is 0.30 with 0.22 attributable to observational uncertainty. The error of the median optical depth in bins of stellar mass and SFR is determined from bootstrapping and is analogous to the standard error on the mean. The standard error for the optical depth in each bin of stellar mass and SFR is ~ 0.01. The error for each bin is plotted in Figure 9.1a but is typically smaller than the data points.

[1]Each of eleven equal groups into which a population can be divided.

As Figure 9.1 shows, the dust opacity is correlated with stellar mass. Dust is formed from material recycled back into the ISM from stars. Massive galaxies have recycled a larger amount of material and therefore tend to be dustier. More notable is the relation between dust extinction and SFR which changes with stellar mass. For galaxies at the same stellar mass dust extinction is *anti*-correlated with the SFR for galaxies with stellar masses $< 10^{10} M_{\odot}$. At a stellar mass of $10^{10} M_{\odot}$ there is a sharp transition. In massive galaxies dust extinction is *positively* correlated with the SFR for galaxies at the same stellar mass. Yates et al. (2012) see a similar "twist" in the relation between metallicity and SFR for star-forming galaxies in the local universe (for details see Zahid et al. 2013c).

9.2.2 The Stellar Mass, Metallicity and Dust Extinction Relation

Dust is formed from metals and therefore a correlation between metallicity and extinction is expected. Xiao et al. (2012) show that the colour excess is well fit as a function of stellar mass and metallicity. In Zahid et al. (2012b) we derive a fit to the colour excess which is

$$\mathrm{E(B-V)} = (0.12 + 0.041 Z^{0.77}) \times M^{0.24}, \tag{9.1}$$

where $Z = 10^{(12+\log(\mathrm{O/H})-8)}$ and $M = M_{*}/(10^{10} M_{\odot})$. The metallicity is determined from the strong line method of Kobulnicky & Kewley (2004). There is a well known discrepancy between various methods of determining gas-phase metallicities (e.g. Kennicutt et al. 2003; Kewley & Ellison 2008). However, our analysis only requires *relative* accuracy in estimating metallicity which the Kobulnicky & Kewley (2004) calibration delivers (see Kewley & Ellison 2008). The fit is to $\sim 20,000$ SDSS galaxies (for more information on this sample see appendix of Zahid et al. 2011) and the RMS of the fit is 0.11 dex.

9.2.3 Galaxy Age

The spectrum of a galaxy contains a significant amount of information relating to its physical properties and the features of the galaxy spectrum are often interpreted using

evolutionary stellar population synthesis models. The shape of the continuum within a galaxy is directly related to its underlying stellar population and the chemical properties of the stellar population can be inferred from the absorption line features. A standard set of absorption indices have been calibrated for this task (e.g. Worthey et al. 1994). Tojeiro et al. (2007) derive a method, dubbed versatile spectral analysis (VESPA), to determine star formation and metallicity histories of galaxies from the shape of the continuum and standard absorption indices. A catalogue with VESPA applied to the SDSS DR7 galaxies is publicly available (Tojeiro et al. 2009)[2]. In order to estimate the ages of galaxies we adopt the values determined from the stellar population synthesis models of Maraston (2005) with a one-parameter dust model. In the VESPA catalogue, the star formation histories (SFHs) of galaxies are determined in 16 logarithmically spaced bins in lookback time. The total amount of stellar mass formed in each bin is given. We adopt the centre of each bin interval as the lookback time for each bin. The average age of stars for each galaxy is then determined from the mass-weighted lookback time.

9.3 A Model for Stellar Mass Growth

We assume that at a fixed stellar mass the current SFR of galaxies is *anti*-correlated with the age of the stellar population (Assumption 1). Stochasticity in the star-formation process demands that this is not necessarily true for individual galaxies. However, each bin in Figure 9.1 is the median of ~ 890 galaxies. We emphasize that our model assumption *only* applies to galaxies in an average sense; on average, at a fixed stellar mass, galaxies with higher SFRs have formed their stars over a shorter timescale and are necessarily younger.

The observational data support the assumption that in the galaxy population-on average-the SFR is anti-correlated to the age. In Figure 9.2 we plot the relation between stellar mass, SFR and mass-weighted age. These data are a sub-sample of the $\sim 150,000$ SDSS galaxies used to determine the MDSR for which we are able to measure mass-weighted ages using the VESPA models (Tojeiro et al. 2009). The sample is comprised of $\sim 135,000$

[2]http://www-wfau.roe.ac.uk/vespa/

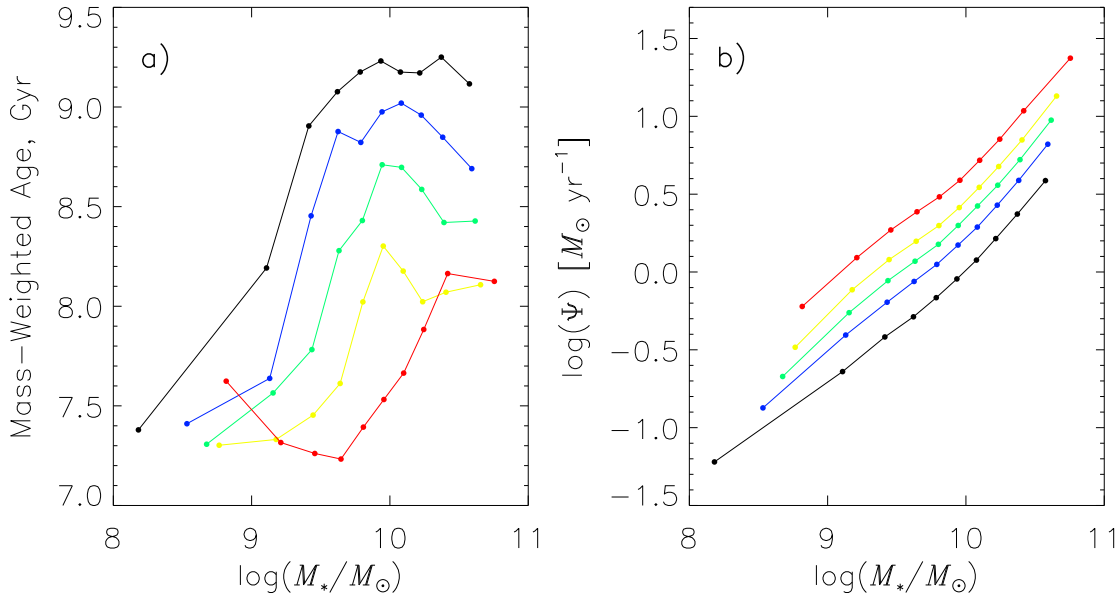

Figure 9.2 a) The mass-weighted age determined from the VESPA models for $\sim 135,000$ galaxies in the SDSS DR7 sorted into bins of stellar mass and SFR. b) The corresponding SFR for each bin of mass-weighted age.

galaxies. We use a binning procedure similar to the one used for deriving the MDSR. The data are first sorted into 10 equally populated bins of stellar mass and then each bin of stellar mass is sorted into 5 equally populated bins of mass-weighted age. Each bin contains ~ 2700 galaxies. Figure 9.2 shows that massive galaxies have older stellar populations (see also Kauffmann et al. 2003b). More importantly, at a fixed stellar mass the age of a galaxy is *anti*-correlated to its SFR.

We implement Assumption 1 numerically by requiring that galaxies evolve along the observed MSR (Noeske et al. 2007b; Salim et al. 2007; Daddi et al. 2007; Elbaz et al. 2007; Pannella et al. 2009; Whitaker et al. 2012, among others). In order to produce an *anti*-correlation between stellar mass and galaxy age, we populate the scatter in the MSR such that galaxies maintain a constant offset as they evolve. Whitaker et al. (2012) show that the intrinsic 1σ scatter in the MSR is ~ 0.25 dex and the slope slightly flattens at higher redshift. There is significant evolution in the zero point. We adopt a constant slope for the

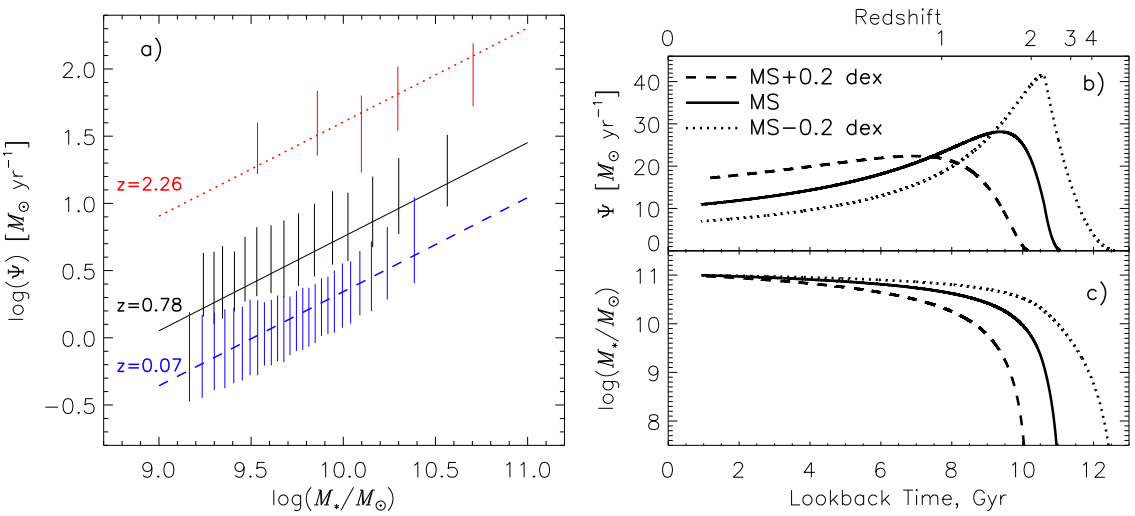

Figure 9.3 a) The MSR at three epochs. The error bars plot the 1σ scatter of the SFR in bins of stellar mass. b) The star formation and c) stellar mass history for three model galaxies determined from integrating Equation 9.5 assuming the SFRs given by Equation 9.2. Each galaxy has a stellar mass of $10^{11} M_{\odot}$ but with different values adopted for the offset from the MSR (S in Equation 9.5).

MSR. Because redshift evolution of the MSR is dominated by evolution in the zero point, our adoption of a constant slope for the MSR does not affect our results.

In Figure 9.3a we plot the MSR at three redshifts. The data at $z = 0.07$ and 0.8 are taken from Zahid et al. (2011) and the $z = 2.26$ data come from Erb et al. (2006). These data are compiled in Table 1 of Zahid et al. (2012b). From these data we derive the SFR as a function of stellar mass and redshift. In Zahid et al. (2012b) we show that the derived relation is consistent with other studies. The SFR as a function of stellar mass and redshift is

$$\Psi(M_*, z) = 2.00 \cdot \exp(1.33z) \left(\frac{M_*}{10^{10}}\right)^{0.7} [M_{\odot}\,\mathrm{yr}^{-1}]. \quad (9.2)$$

Observations of the MSR at higher redshifts suggest that the zero point does not evolve significantly beyond $z > 2.3$ (see Dutton et al. 2010, and references therein) and in our model calculations we assume no evolution in the zero point and stellar mass slope, i.e. $\Psi(M_*, z > 2.26) = \Psi(M_*, 2.26)$. In our numerical implementation we transform $\Psi(M_*, z)$

to $\Psi(M_*, t)$ using the standard conversion between redshift and time implemented in the astronomy users library IDL routine *galage.pro*.

The SFHs of galaxies can be derived from a simple model requiring that galaxies evolve along the mean MSR at all epochs (Leitner 2012; Zahid et al. 2012b). In the simplest analytical model the rate of stellar mass growth is given by

$$\frac{dM_*}{dt} = \Psi - \dot{M}_R, \tag{9.3}$$

where Ψ is the SFR and $\dot{M}_R$ is the rate that mass is recycled to the ISM through various stellar mass loss processes. The stellar mass of a galaxy is then given by

$$M_*(t) = \int_{t_f}^{t} \left[\Psi(t') - \dot{M}_R(t')\right] \, dt' + M_{*,f}. \tag{9.4}$$

Here $M_{*,f}$ is the stellar mass at t_f. If $M_{*,f}$ is set to some arbitrarily low value (in our models $M_{*,f} = 10^6 M_\odot$) then t_f can be interpreted as the formation time of the galaxy. In order to implement Assumption 1, we build on this model by requiring that a galaxy populate the scatter in the MSR such that it maintains a constant offset at all epochs. Analytically this is given by

$$M_*(t) = \int_{t_f}^{t} \left[S\Psi(t') - \dot{M}_R(t')\right] \, dt' + M_{*,f}, \tag{9.5}$$

where S is a constant offset accounting for the scatter in the MSR. The formation time, t_f, and S uniquely define the SFH of a galaxy in our model.

In Figure 9.3b and 9.3c we show the star formation and stellar mass history, respectively, for three model galaxies that all have a stellar mass of $10^{11} M_\odot$ in the local universe ($t = 13$ Gyr in Equation 9.5). The model galaxies in Figure 9.3 evolve such that they have a constant offset relative to the MSR at all epochs ($\log(S)$ = -0.2, 0 and 0.2 in Equation 9.5). The stellar mass as a function of time for these model galaxies is determined from numerically integrating Equation 9.5.

A fundamental feature of this model of stellar mass growth is that higher mass galaxies are older (c.f. Noeske et al. 2007a). Furthermore, at a fixed stellar mass, galaxies with higher SFRs are younger than galaxies with lower SFRs. This can be seen by the comparing the onset of star formation for the three model galaxies in Figure 9.3b. All three galaxies have a stellar mass of $10^{11} M_{\odot}$ but have different times for the initial onset of star formation, t_f. In our model the age of the galaxy $(t - t_f)$ is *anti*-correlated to the offset from the MSR, S. Consequently, at a fixed stellar mass the age of our model galaxies is *anti*-correlated to the current SFR.

9.4 A Model for Dust Formation

Assumption 2 of our model is that the rate of dust production is proportional to the stellar mass recycling rate. A large amount of dust in star-forming galaxies is thought to be produced by massive ($\gtrsim 8 M_{\odot}$) stars that end their lives as supernovae and post main-sequence evolution (AGB phase) of intermediate mass ($1 \lesssim M_{\odot} \lesssim 8$) stars (Dwek 1998). Because all dust forms from heavier elements, dust that may form in the ISM is also dependent on the gas processed and recycled by stars. Dust production is therefore intimately related to the physical process of stellar mass recycling. In our numerical implementation, we adopt the simplest assumption that the dust production rate is directly proportional to the SMRR.

We implement continuous, time dependent stellar mass recycling following Jungwiert et al. (2001). They give the SMRR as

$$\dot{M}_R(t) = \int_0^t \Psi(t') \dot{f}_{mr}(t - t') dt'. \tag{9.6}$$

Here $\dot{M}_R(t)$ is the SMRR as a function of time, $\Psi(t)$ is the SFR and $\dot{f}_{mr}(t)$ is the time derivative of the fraction of mass recycled to the ISM at time t for a single, instantaneous burst stellar population. The rate at which stellar mass is recycled to the ISM is given as a convolution of the SFR with the time derivative of the fractional mass recycled. Jungwiert

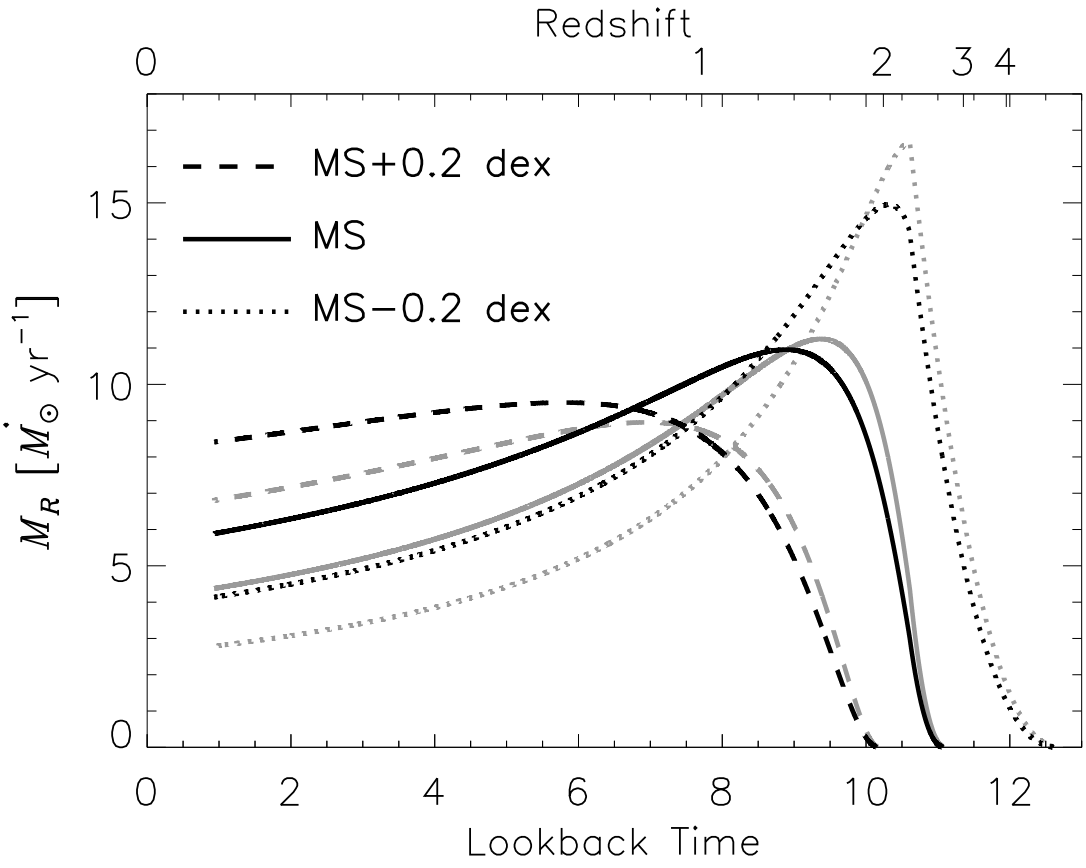

Figure 9.4 The SMRR (black curves) as a function of time for the same three model galaxies in Figure 9.3. The SFRs are given by the grey curves for reference and have been scaled by a factor of 0.4 for ease of comparison.

et al. (2001) parameterize the fractional mass recycled from a single, instantaneous burst stellar population as a function of time by

$$f_{mr}(t) = C_0 \ln\left(\frac{t}{\lambda} + 1\right). \tag{9.7}$$

Both C_0 and λ are constants depending on the particular choice of IMF (values are given in Table 1 of Leitner & Kravtsov 2011). For a Chabrier IMF $C_0 = 0.046$ and $\lambda = 2.76 \times 10^5$ [yrs]. Because there is an interdependency between the SMRR and SFH, we iteratively determine both quantities using Equation 9.5 (Leitner & Kravtsov 2011; Zahid et al. 2012b).

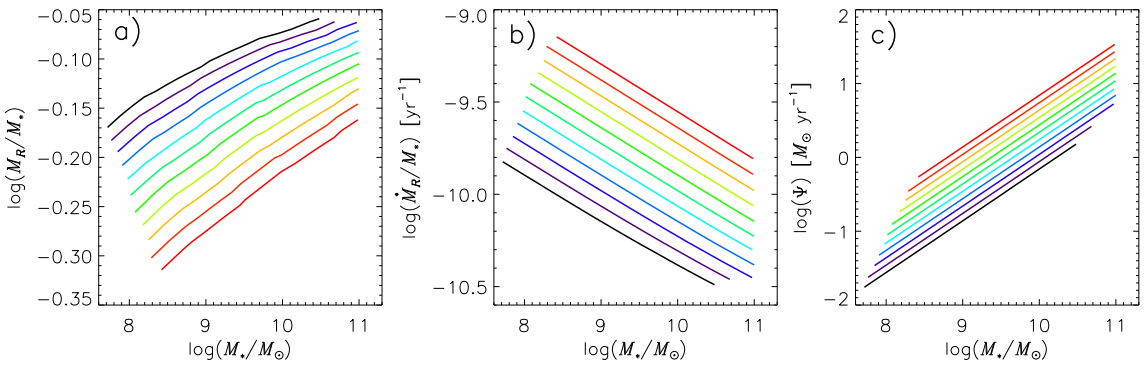

Figure 9.5 The stellar mass recycling properties of model galaxies plotted against stellar mass. a) The total amount of stellar mass recycled divided by the current stellar mass. b) The specific SMRR (the SMRR divided by current stellar mass) and c) the corresponding SFR for each model galaxy.

In Figure 9.4 we plot the SMRR for the three model galaxies shown in Figure 9.3b and 9.3c. Note that due to the convolution, the SMRR is offset in time from the SFR.

9.5 Results: An Analytical Model Reproducing the Observed Relation Between Stellar Mass, Dust Extinction and SFR

9.5.1 Dust Model Outputs

We run our models adopting a range of values for the constant offset from the MSR, S, and formation time, t_f. The 2σ scatter observed in the MSR is ~ 0.5 dex. We run our models for 11 values of S equally spaced such that $-0.5 \leq \log(S) \leq 0.5$. For the formation times we adopt a range of values corresponding to $z < 12$. We use only models with final stellar masses in the range of $8 \lesssim M_*/M_\odot \lesssim 11$. This allows us to explore practically[3] the full range of SFRs and stellar masses observed in our local sample (see right panel of Figure 9.1b). The following analysis is based on 220 model galaxies.

[3]In our models, the maximum mass a galaxy with -0.5 dex offset can form since $z = 12$ is $\sim 10^{10.5} M_\odot$ (see Figure 9.5).

The total amount of stellar mass recycled to the ISM as a function of time is determined by integrating the SMRR over time which is

$$M_R(t) = \int_{t_f}^{t} \dot{M}_R(t')dt'. \tag{9.8}$$

In Figure 9.5a we plot the total amount of stellar mass recycled (normalized to stellar mass) as a function of stellar mass. In Figure 9.5b we show the specific SMRR which is the SMRR divided by stellar mass (analogous to specific SFR) as a function of stellar mass. In Figure 9.5c we show the SFR as a function of stellar mass. In the figure each colour corresponds to a different offset from the MSR. The total amount of mass recycled to the ISM (Figure 9.5a) is *anti*-correlated to the SFR. This is a consequence of the fact that at a fixed stellar mass, galaxies with lower SFRs are older and therefore their stellar populations have had more time to recycle mass back to the ISM through stellar winds and supernovae. Conversely, the SMRR (Figure 9.5b) is *positively* correlated to the SFR. Because the SMRR is related to the SFR through the convolution given in Equation 9.6, at a fixed stellar mass galaxies with higher SFRs also have higher SMRRs.

The *anti*-correlation at a fixed stellar mass between the SFR and total amount of mass recycled and the *positive* correlation between the SMRR and SFR seen in Figure 9.5 is the foundation for the physical model described in Section 9.1.2. We develop an analytical model such that at low stellar masses ($\lesssim 10^{10} M_{\odot}$) the MDSR is governed by the total amount of stellar mass recycled and at higher stellar masses it is related to the current SMRR. Such a model naturally leads to an *anti*-correlation between dust opacity and SFR at lower stellar masses and a *positive* correlation between dust opacity and SFR at higher stellar masses.

9.5.2 The Analytical Slow Flow Model

In order to reproduce the observed MDSR, we develop an analytical model where the observed dust content of the galaxy is a competition between dust production and dust

destruction/efflux. In the discussion that follows we refer to dust efflux and/or destruction as dust loss. The dust production rate is directly proportional to the SMRR (Assumption 2) and the rate of dust loss is proportional to the opacity and the SFR (Assumption 3). The timescale over which dust is lost is not necessarily coincidental with the dust production timescale (Assumption 4). Thus, we introduce a free parameter to account for a temporal offset between production and loss. The "Slow Flow" model is analytically given by

$$M_d(t) \propto \int_{t_f}^{t} \left[\dot{M}_R(t') - \eta\,\tau(t')\,\Psi(t' - \Delta t)\right] dt'. \tag{9.9}$$

Equation 9.9 is the dust balance equation. $M_d(t)$ is the total amount of dust in the galaxy as a function of time. The first term on the right hand side is the dust production term which we assume is proportional to the SMRR, $\dot{M}_R$. The second term on the right hand side represents the rate at which dust is lost; τ is the opacity and Ψ is the SFR. If $t' - \Delta t < t_f$ then $\Psi(t' - \Delta t) = 0$. $\dot{M}_R$ and Ψ are determined from our model of stellar mass growth (Section 9.3) and dust production (Section 9.4). The free parameters of the model are η which is the dust loss efficiency (the dust loss rate per unit SFR) and Δt, the timescale for dust loss.

In Equation 9.9, we do not know τ a priori. For each model galaxy we derive τ as a function of time using the empirical relation given by Equation 9.1 and the observed redshift evolution of the MZR. In the left panel of Figure 9.6 we show the MZR at $z = 0.07, 0.8$ and 2.26 (Zahid et al. 2012b). We have used the Kobulnicky & Kewley (2004) calibration in determining metallicity though we emphasize that our results are independent of our choice of calibration. We determine the metallicity of a galaxy as a function of time by first determining its stellar mass history (see Section 9.3.1 and Figure 9.3c) and then using this to linearly interpolate the observed MZRs in time and stellar mass. This is shown for our three model galaxies in Figure 9.6b. Using the empirical relation between extinction, stellar mass and metallicity given in Equation 9.1 we derive an optical depth as a function of stellar mass and time for the same model galaxies. This is shown in Figure 9.6c.

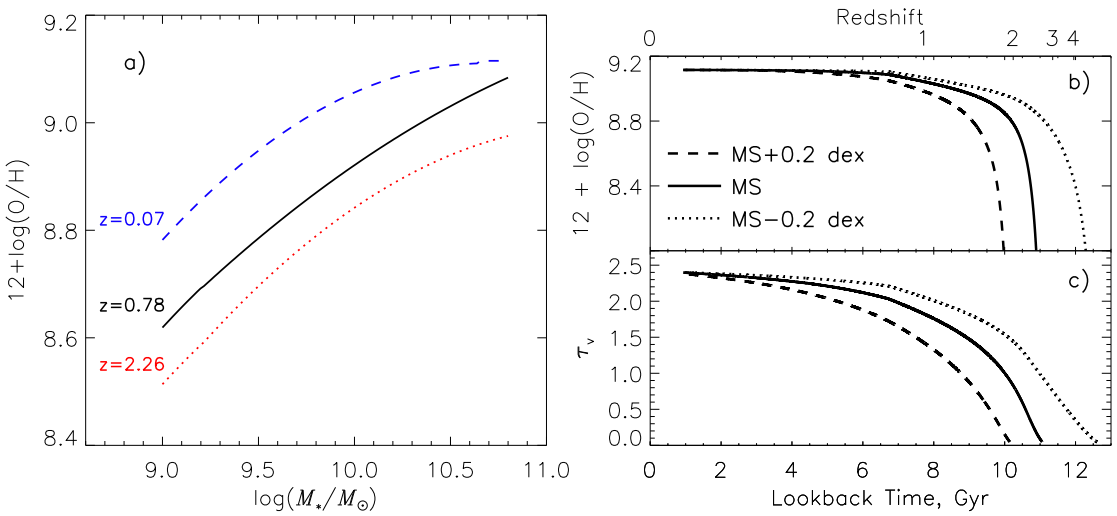

Figure 9.6 a) The MZR at three redshifts (Zahid et al. 2012b). b) The metallicity and c) opacity as a function of time for the same three model galaxies as in Figure 9.3. The metallicites are determined by interpolating between the three MZRs and the opacity is determined from the relation given by Equation 9.1.

In Figure 9.1 we plot the MDSR. The dust content is given by the observed optical depth. Optical depth is given by $\tau = n\sigma_d L$ where n is the volume density of particles, σ_d is the geometric cross section for dust and L is the line-of-sight path length. Our analytical model given in Equation 9.9 is proportional to the total mass of dust in the galaxy. In order to compare with observations we rescale our model such that

$$\tau_{model} = A/M_*^{\beta} \int_{t_f}^{t} \Big[\dot{M}_R(t') - \eta\,\tau_{\rm v}(t')\,\Psi(t'-\Delta t)\Big]\,dt. \tag{9.10}$$

Here a pre-factor A/M_*^{β} is introduced to Equation 9.9. We have the mass of dust $M_d \propto N$ where N is the total amount of dust particles. To first order $N \sim nL^3$ where L^3 represents a volume. If we assume that $M_* \propto L^3$ then we have that $\tau \sim nL \sim N/M_*^{2/3} \sim M_d/M_*^{2/3}$. We set β to 2/3. A is an overall normalization accounting for geometric properties of the dust particles and is determined by normalizing the maximum value of τ in the models to the maximum observed optical depth in Figure 9.1 ($\tau_{max} = 1.9$). The analytical model has four

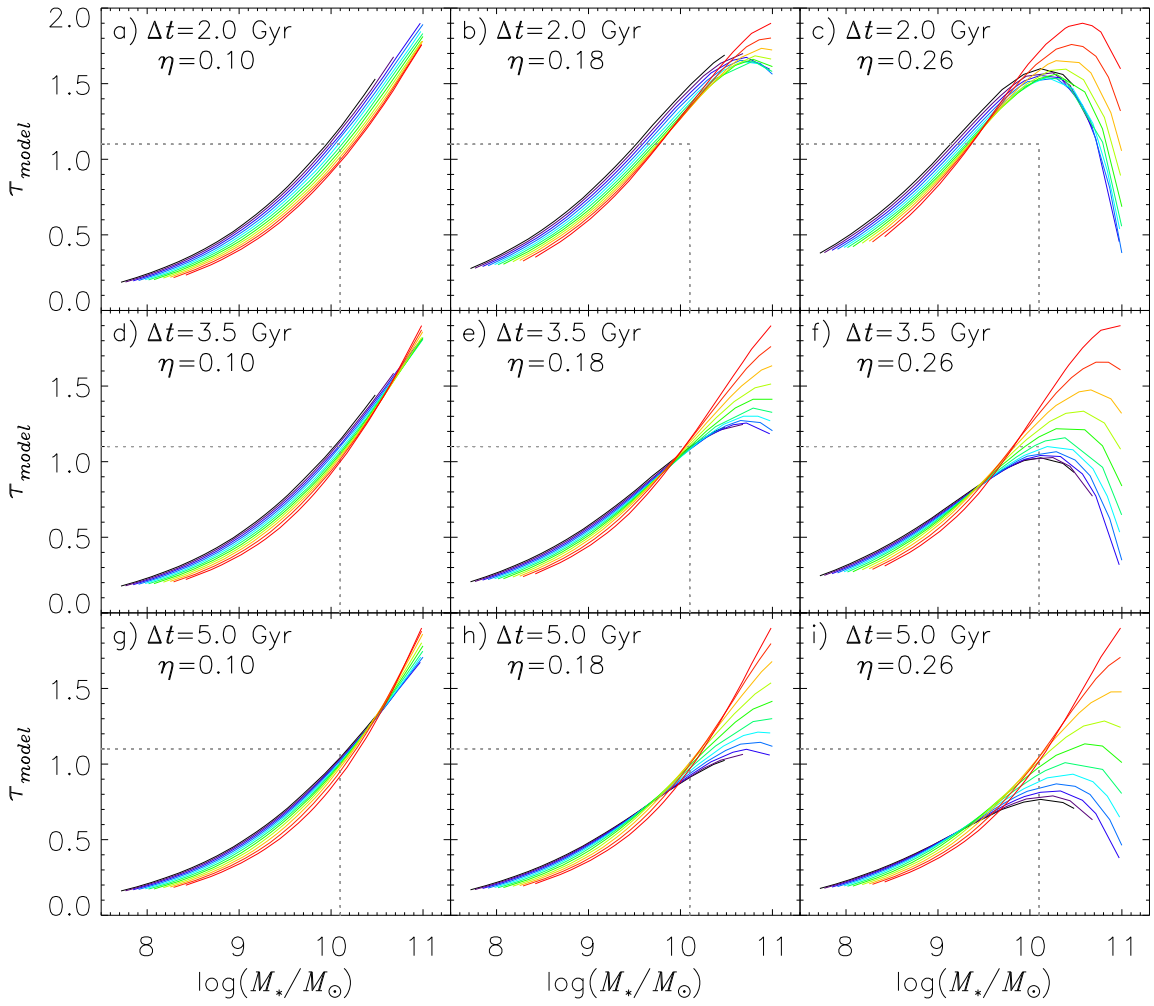

Figure 9.7 The model MDSR as a function of the free parameters η and Δt in Equation 9.10. The colours correspond to the SFRs shown in Figure 9.5c. The dotted lines indicate the stellar mass and opacity at which the twist in the observed MDSR (Figure 9.1) occurs.

degrees of freedom: two constants to make our model output comparable to observations and two free parameters.

9.5.3 The Parameter Space

In Figure 9.7 we plot the MDSR determined from our model given in Equation 9.10 for various choices of the free parameters. We adopt $\eta = [0.10, 0.15, 0.20]$ and $\Delta t = [2.0, 3.5, 5.0]$ Gyr and plot the models in the 3×3 panels of the figure. In each panel the curves plot

τ as a function of stellar mass. τ is determined for each model galaxy by integrating from t_f to $t = 13$ Gyr in Equation 9.10. The curves are colour-coded to match the SFRs shown in Figure 9.5c (e.g. the red curves are the high SFR galaxies and black curves are the low SFR galaxies). Our goal is to reproduce the observed MDSR shown in Figure 9.1.

In Figure 9.7a we see that if $\eta \lesssim 0.1$ and $\Delta t \lesssim 2$ Gyr no twist is observed in the model MDSR. At a fixed stellar mass, galaxies with high SFRs are younger. Stellar mass recycling is a time dependent process and therefore younger galaxies have recycled a smaller fraction of their stellar mass back to the ISM. Because we take dust production to be proportional to the amount of recycled stellar mass, younger galaxies have less dust. When η is small, dust loss is negligible and when Δt is small, the relative amount of dust loss in low and high SFR galaxies, at a fixed stellar mass, is comparable. In this case there is no differential loss of dust in galaxies at a fixed stellar mass. Thus, in Figure 9.7a galaxies that have high SFRs (e.g. red curve) have less dust than galaxies with low SFRs (e.g. black curve) because they have recycled less mass and therefore produced less dust.

The magnitude of the rate of dust loss is set by η. Increasing η decreases the stellar mass at which the twist occurs in the model MDSR. Increasing η also increases the spread of optical depths in galaxies with higher stellar masses independent of the value of Δt adopted. This is seen when comparing rows of Figure 9.7 (η increases from left to right). The dust loss term is (to first order) proportional to $\eta\tau\Psi$. The product of $\eta\tau$ sets the stellar mass at which dust loss becomes significant relative to dust production. Less massive galaxies have smaller τ and therefore increasing η moves the twist to smaller stellar masses. Increasing the value of η also leads to a larger spread in the optical depth at higher stellar masses because η, together with Δt, sets the relative amount of dust lost for galaxies at the same stellar mass.

The maximum value of η is limited by the fact that galaxies cannot lose more dust than they produce. This leads to the requirement that $\eta\tau\Psi \lesssim \dot{M}_R$ or $\eta\tau \lesssim \dot{M}_R/\Psi \sim 0.4$ for a Chabrier IMF. Panels c), f) and i) in Figure 9.7 show that for $\eta = 0.26$ high mass galaxies

lose too much dust when compared to the observations in Figure 9.1. Thus the observations constrain η such that $0.1 < \eta < 0.26$.

The timescale of dust loss is set by Δt and if it is shorter than the timescale of dust production/accumulation then no twist will be observed. For a twist to occur in the model MDSR $\Delta t > 2$ Gyr. Increasing Δt from 2 to 3.5 Gyr decreases the stellar mass at which the twist occurs and slightly increases the spread in the optical depth at higher stellar masses. The timescale of dust loss, Δt, is the same for all galaxies but the timescale of dust production varies according to SFH. At a fixed stellar mass galaxies with higher SFRs have produced a greater fraction of their stars and dust more recently in cosmic time because they are younger (see Figure 9.2). Thus there is a differential accumulation of dust depending on SFH. The differential accumulation of dust occurs on shorter timescales for higher mass galaxies because higher mass galaxies have higher SMRRs. Therefore, increasing Δt moves the twist to smaller stellar masses and slightly increases the spread in optical depth. Increasing Δt from 3 to 5 Gyr does not significantly alter the MDSR because galaxies typically reach a steady state in their SMRR within a few Gyr (see Figure 9.4).

In order to determine the best model parameters we attempt to qualitatively reproduce the observed MDSR shown in Figure 9.1. In particular, we choose parameters that best reproduce the location of the twist and the scatter in dust opacity for massive galaxies. A model with $\eta = 0.17$ and $\Delta t = 3.5$ Gyr best reproduces the observed relation. By varying the parameters we control the stellar mass at which the twist occurs and the relative spread in optical depths observed in high mass galaxies. The spread in the optical depth at low stellar masses (i.e. stellar masses less than the stellar mass where the twist occurs) is independent of our choice of parameters. Because τ is small for lower mass galaxies dust loss is inefficient and the spread in optical depth is set by the difference in age of galaxies at a fixed stellar mass. The model MDSR has a smaller spread in the values of τ at stellar masses $\lesssim 10^{10} M_{\odot}$ when compared to the observed MDSR. Varying the IMF (e.g., using Chabrier Steep instead of Chabrier) or adding an additional dust loss term proportional

the SFR (see below) can ease some of this tension between the model and observations at lower stellar masses.

The amount of dust produced is dependent on our choice of IMF in our model. Therefore, we may expect that the free parameters are as well. We perform a similar analysis using the Chabrier steep IMF which has a steeper high mass slope leading to $\sim 20\%$ less mass loss (see Figure 1 of Leitner & Kravtsov 2011). We are able to reproduce the observed MDSR using the same analytical model. The best value of η is slightly smaller. Δt is independent of our choice of IMF.

9.5.4 Additional Parameters

We include an additional dust loss term to our model that is directly proportional the SFR. The analytical model presented in the previous section accounts for the notable features of the MDSR (Figure 9.1). However, additional physical processes temporally coincidental with the SFR may also be operating in galaxies. It is beyond the scope of this work to produce a model accounting for all possible physical mechanisms affecting the dust content of star-forming galaxies since the physics of dust production and evolution is still not well understood. The additional term added to the model is physically motivated and is meant to indicate the flexibility of the model.

We modify the analytical model for dust production given in Equation 9.9 to include an additional term for dust loss that scales only with the SFR with no time delay. This is given by

$$M_d \propto \int_{t_f}^{t} \left[\dot{M}_R(t') - \eta\, \tau(t')\, \Psi(t' - \Delta t) - \alpha \Psi(t') \right] dt', \tag{9.11}$$

where we have introduced a new free parameter α which is a dust loss efficiency factor analogous to η but for a physical mechanism that operates instantaneously and independent of dust optical depth. The term $\alpha\Psi$ could be interpreted physically as either dust loss or dust destruction. Thermal energy injected from Type II supernovae could drive outflows of dust in bubbles and along filaments of hot gas and/or destroy dust through UV photodissociation,

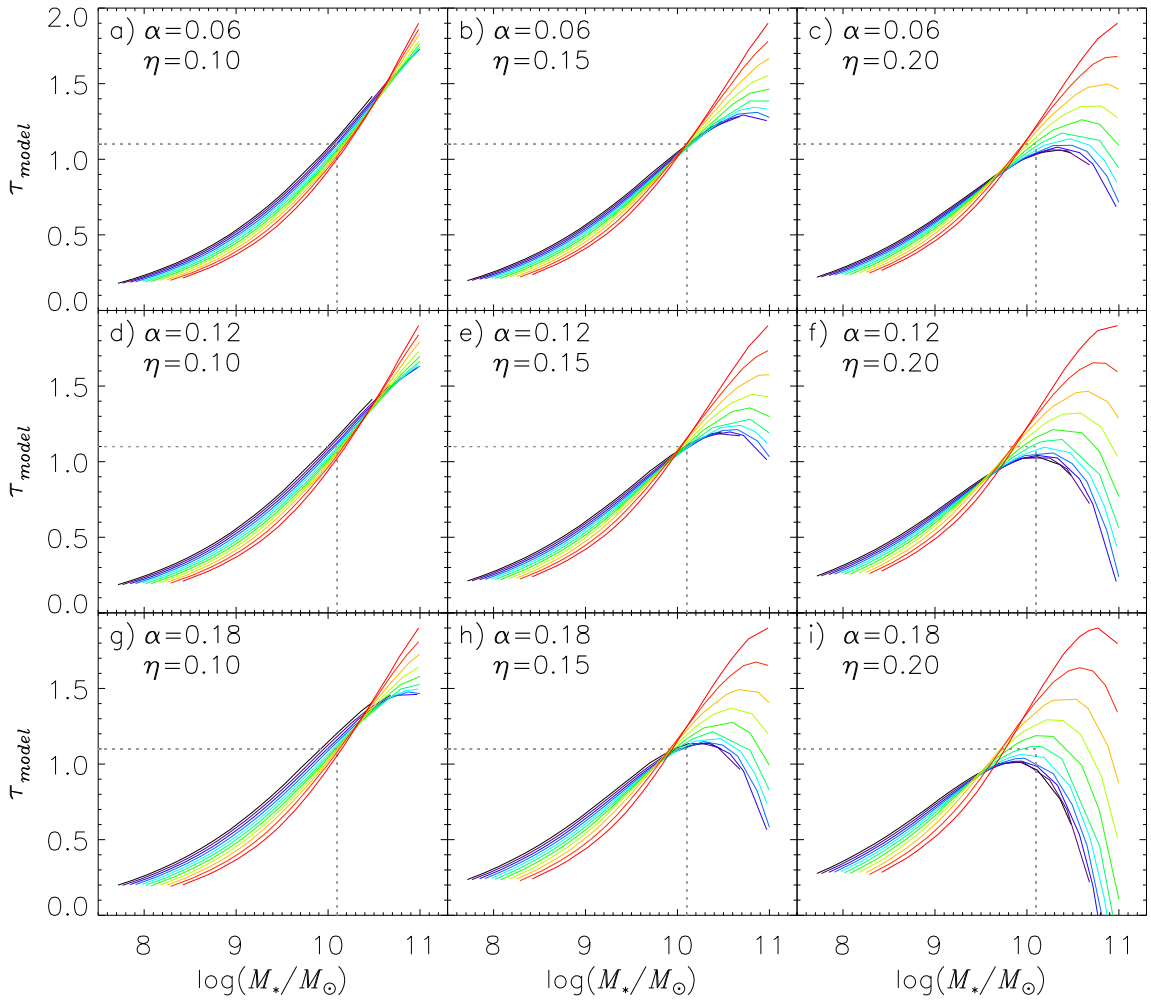

Figure 9.8 The model MDSR as a function of the free parameters η and α in Equation 9.11. The colours correspond to the SFRs shown in Figure 9.5c. The dotted lines indicate the stellar mass and opacity at which the twist in the observed MDSR (Figure 9.1) occurs.

sputtering and/or shocks. Following Equation 9.10, we scale the model given in Equation 9.11 by $A/M_*^{2/3}$.

In Figure 9.8 we plot the MDSR determined from the three parameter model for various choices of the free parameters. Similar to the two parameter model, we find that when $\Delta t \gtrsim 3.5$ Gyr, the model MDSR is insensitive to Δt. We fix $\Delta t = 3.7$ Gyr and we adopt $\eta = [0.10, 0.15, 0.20]$ and $\alpha = [0.05, 0.10, 0.15]$. We plot models with these parameters in the 3×3 panels of the figure. In each panel the curves plot τ as a function of stellar mass.

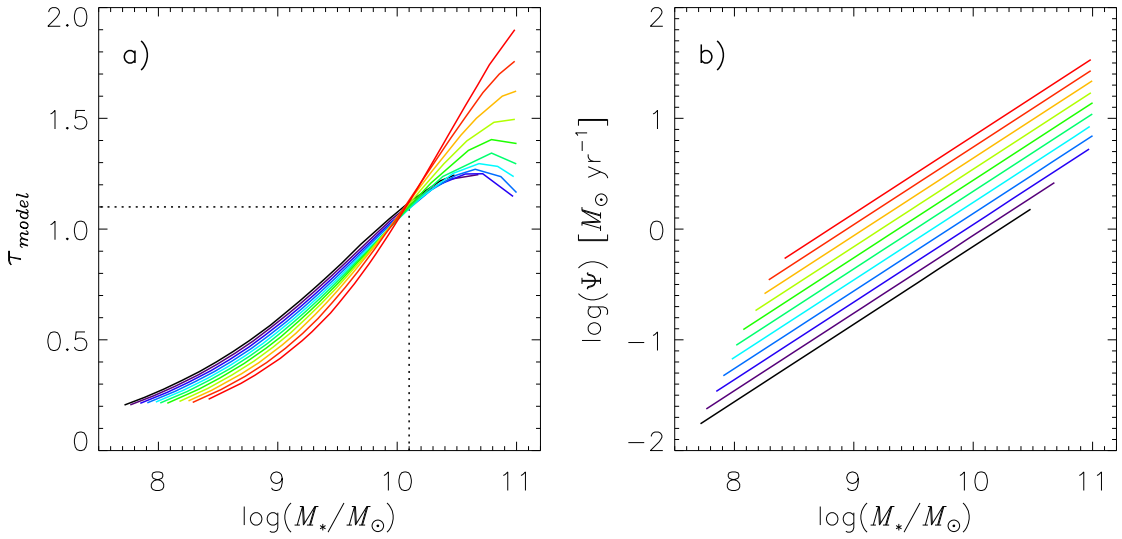

Figure 9.9 a) The "best-fit" model MDSR for the model given by Equation 9.11 with $\eta = 0.14$, $\alpha = 0.12$ and $\Delta t = 3.7$ Gyr. b) The SFRs corresponding to optical depths in shown in a).

As before, the curves are colour-coded to match the SFRs shown in Figure 9.5c (e.g. the red curves are the high SFR galaxies and black curves are the low SFR galaxies).

The new model given by Equation 9.11 gives a MDSR that is qualitatively similar to the model given by Equation 9.9. Increasing η decreases the stellar mass at which the twist occurs independent of α. The effect of α is to increase the spread in optical depth at a fixed stellar mass at *all* stellar masses. In producing the model MDSR, we normalize the relation such that the maximum observed optical depth is 1.9. Increasing the total amount of dust loss across all galaxies also increases the relative amount of dust loss for galaxies at a fixed stellar mass. The increased spread in optical depth in the model at all stellar masses eases some of the tension between the model and observations at low stellar masses.

Galaxies cannot lose more dust than they produce thus, to first-order, $\alpha\Psi + \eta\tau\Psi \lesssim \dot{M}_R$ or $\alpha + \eta\tau \lesssim \dot{M}_R/\Psi \sim 0.4$. In panel f) and i) the value of $\alpha + \eta\tau$ is too large and some galaxies lose more dust than they produce leading to an unphysical negative optical depth. A model with $\eta = 0.14, \alpha = 0.12$ and $\Delta t = 3.7$ Gyr best reproduces the observed MDSR.

The primary result of this paper is shown in Figure 9.9 and can be compared directly to the observed relation shown in Figure 9.1. We note that the model shown in Figure 9.9 is very similar to the best model from Section 9.5.3 (i.e. $\eta = 0.17$, $\Delta t = 3.5$ Gyr and $\alpha = 0$).

9.5.5 Magnitude of Dust Loss

We are unable to estimate dust masses from our model since we derive the optical depth and not dust mass. However, we can estimate the fraction of dust lost (i.e., dust effluxed and/or destroyed) to the amount of dust produced in the model. For the two parameter model (Section 9.5.2) the fraction is given by

$$F_\eta = \frac{\int_{t_f}^{t} \eta\, \tau(t')\, \Psi(t' - \Delta t)\, dt'}{\int_{t_f}^{t} \dot{M}_R(t')\, dt'}. \tag{9.12}$$

The numerator is proportional to the amount of dust lost and the denominator is proportional to the total amount of dust produced. We refer to quantity given by Equation 9.12 as the slow loss term. In Figure 9.10 we plot F_η as a function of stellar mass for the two parameter model. As before, the curves are colour-coded to match the SFRs shown in Figure 9.5c. The fraction of dust lost, F_η, increases with stellar mass because dust loss is dependent on dust opacity and more massive galaxies are dustier. In this case, the magnitude of dust loss in low-mass galaxies is negligible; a property that is consistent with the galaxy formation model of (Wise et al. 2012). At a fixed stellar mass, galaxies with high SFRs lose a smaller fraction of their dust; they are younger and therefore have had less time to lose dust.

We also calculate the fraction of dust lost to dust produced for the three parameter model using Equation 9.12 and

$$F_\alpha = \frac{\int_{t_f}^{t} \alpha\, \Psi(t')\, dt'}{\int_{t_f}^{t} \dot{M}_R(t')\, dt'}. \tag{9.13}$$

The numerator is proportional to the amount of dust lost and the denominator is proportional to the total amount of dust produced. We refer to the quantity given by Equation 9.13 as the fast loss term. We plot F_η, F_α and $F_\eta + F_\alpha$ for our three parameter model discussed in Section 9.5.4 in Figure 9.11a, b and c, respectively. The fraction of dust lost in the slow loss, F_η, for the three parameter model is $\sim 10\%$ less than for our two parameter model because η is $\sim 10\%$ smaller for the three parameter model. The amount of dust lost in the fast loss component is nearly constant with stellar mass because both the dust loss (numerator of Equation 9.13) and dust production (denominator of Equation 9.13) are proportional to the SFR. At a fixed stellar mass galaxies with lower SFRs are older and therefore have recycled a larger amount of their stellar mass back to the ISM. Thus, at a fixed stellar mass, galaxies with low SFRs have formed a greater amount of stars as compared to galaxies with high SFRs since galaxies with high SFRs have recycled a relatively smaller fraction of the material back to the ISM. The amount of dust produced is proportional to the amount of stellar mass recycled. Therefore, at a fixed stellar mass the *anti*-correlation between F_α and SFR is due to the fact that younger galaxies (those with high SFRs) have produced less dust (see Figure 9.5a).

9.6 Dust Efflux as the Physical Basis of the Slow Flow Model

Thus far, dust loss in the Slow Flow model has not been physically interpreted. In particular, the dust loss term parameterized by Equation 9.10 could physically represent dust destruction and/or dust efflux. However, several lines of reasoning support an interpretation of dust efflux over dust destruction as the physical basis of the Slow Flow model.

The observed MZSR provides important constraints for physically interpreting the Slow Flow model developed to reproduce the MDSR. While dust may be destroyed, metals can not and therefore the observed MDSR is unlikely to be explained by destruction processes unless the similar trends observed in the MDSR and MZSR are taken to be coincidental

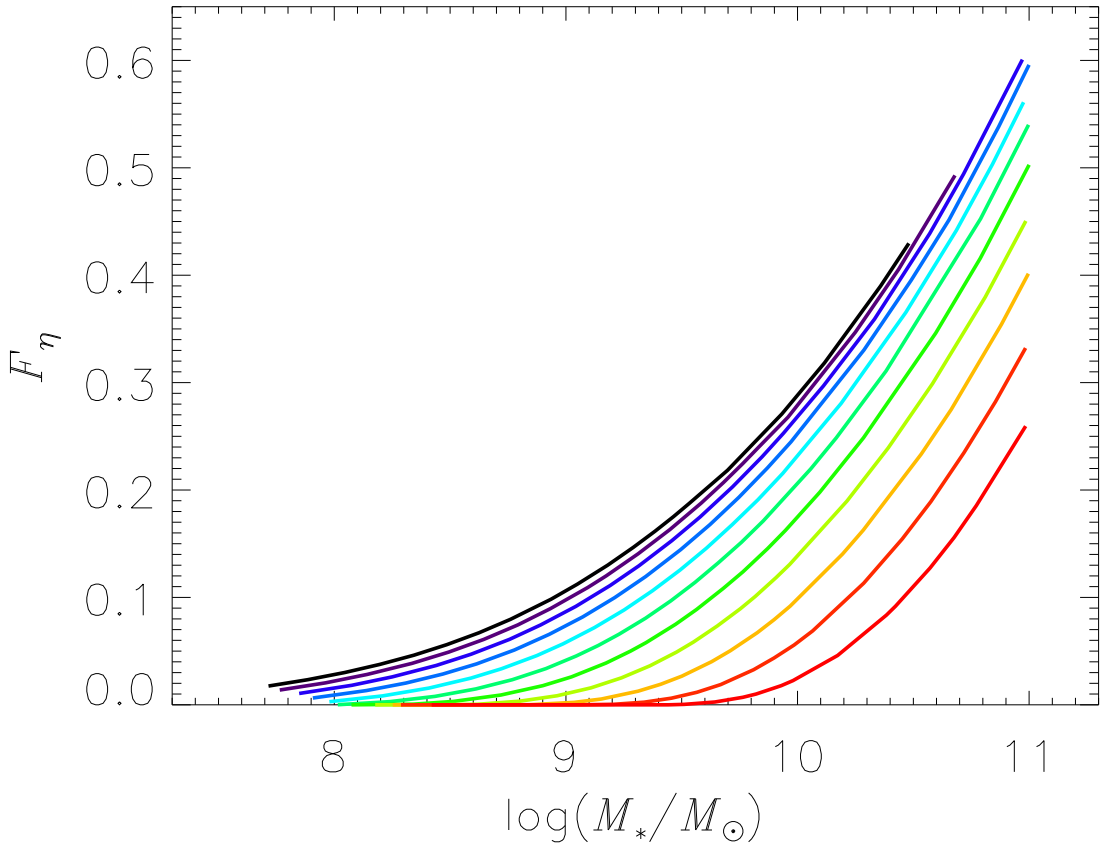

Figure 9.10 The fraction of dust produced that is lost in the Slow Flow for the model given by Equation 9.9. Fractional loss is calculated using Equation 9.12. The colours correspond to the SFRs shown in Figure 9.5c.

(see Zahid et al. 2013c). Furthermore, if dust destruction were responsible for the MDSR we may expect an opposite trend in the MZSR since destruction of dust particles would liberate the constituent metals, thus increasing the gas-phase abundance while decreasing the dust opacity. In light of similar trends in the MZSR derived by Yates et al. (2012), the twist observed in the MDSR may be more naturally explained by dust efflux rather than dust destruction.

It is important to note that the MZSR is dependent on the methodology applied in deriving the physical properties of galaxies (c.f. Mannucci et al. 2010; Yates et al.

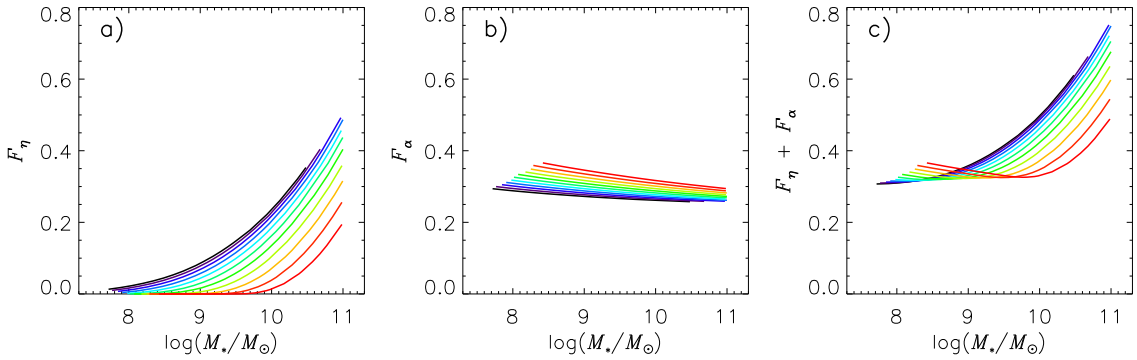

Figure 9.11 Dust loss for the three parameter model given by Equation 9.11. Fractional loss is calculated using a) Equation 9.12 and b) Equation 9.13. c) The sum of the fractional loss given in a) and b). The colours correspond to the SFRs shown in Figure 9.5c.

2012; Andrews & Martini 2013). In particular, there is a well-known and long-standing discrepancy in metallicities derived using various strong-line calibrations (e.g. Kennicutt et al. 2003; Bresolin et al. 2004; Nagao et al. 2006; Kewley & Ellison 2008; Moustakas et al. 2010). For the same galaxies, theoretical calibrations typically yield abundances that are $\gtrsim$ 0.3 dex larger than empirical calibrations (Kewley & Ellison 2008). Much of the discrepancy may be attributed to the method used in calibrating the strong-line ratios. Empirical methods calibrate strong-line ratios against the metallicities derived from temperature sensitive auroral lines (i.e. the "direct" method). Theoretical calibrations instead make use of photoionization and stellar population synthesis models. The qualitatively different MZSRs determined from the SDSS data derived by Mannucci et al. (2010), Yates et al. (2012) and Andrews & Martini (2013) are largely due to the different abundance calibrations applied in deriving the metallicities. Yates et al. (2012) and Andrews & Martini (2013) derive metallicities using purely theoretical and empirical methods, respectively. Mannucci et al. (2010) derive metallicities using a semi-empirical calibration which combines both theoretical and empirical methods.

Detailed discussions regarding the strengths and weaknesses of the various strong-line methods can be found in e.g., Kewley & Ellison (2008) and Moustakas et al. (2010).

Theoretical methods are not susceptible to the observational uncertainties associated with empirical methods and are capable of calibrating metallicities over the full range of observed line ratios. However, theoretical methods are model dependent and are subject the simplifying assumptions and systematic uncertainties associated with the models. In contrast, empirical methods calibrate strong-line ratios against metallicities derived from temperature sensitive auroral lines (e.g. [OIII]λ4363). The direct method provides a well understood scale for metallicity calibration. However, temperature sensitive auroral lines are extremely weak and are typically only observed in HII regions and galaxies with $Z < Z_{\odot}$ and with large observational uncertainties. More to the point, the direct method is known to be susceptible to several systematic issues. Peimbert (1967) points out that temperature fluctuations may lead to systematic underestimates of the metallicity. More recently, the assumption that HII regions are in thermodynamic equilibrium has also been challenged (Nicholls et al. 2012, 2013; Dopita et al. 2013). These authors argue that a breakdown of the assumption of equilibrium leads to an underestimate of the abundance, particularly in metal-rich HII regions. Furthermore, Nicholls et al. (2013) and Dopita et al. (2013) suggest that the use of old atomic data also contributes to the abundance discrepancy. Accounting for these two effects brings theoretically and empirically determined metallicities into good agreement (Dopita et al. 2013).

The suggestion that non-equilibrium electron energy distributions may be at the heart of the abundance discrepancy is promising. Astrophysical plasmas where *in situ* measurements of electron energies can be made have non-equilibrium energy distributions (Nicholls et al. 2012). This suggests that perhaps metallicities determinations based on theoretical models (i.e. Yates et al. 2012) may be more reliable. However, given that non-equilibrium processes remain only one possible solution to the long-standing abundance discrepancy problem, the MZSR derived by Yates et al. (2012) remains uncertain. It is beyond the scope of this paper to investigate these issues in detail but in light of this uncertainty, the physical interpretation based on the observed MZSR of dust efflux as the process responsible for dust loss in the Slow Flow model remains tentative.

Lara-López et al. (2013) examine the relation between stellar mass, specific-SFR and metallicity. They derive a relation similar to MZSR first shown in Yates et al. (2012). However, Lara-López et al. (2013) also examine the HI gas content. They show that for massive galaxies the gas fraction is *positively* correlated with metallicity and SFR. Metallicity is a relative measure of the oxygen to hydrogen abundance in the gas-phase. Therefore, the positive correlation between metallicity, gas fraction and SFR suggests that galaxies with high metallicities and high SFRs may also have greater mass of metals. If the gas and dust are coupled, galaxies may also efflux gas and metals. The observed positive correlation between metallicity, SFR and gas fraction for massive galaxies supports the interpretation of dust efflux over dust destruction. It should be noted that Bothwell et al. (2013) have also examined the relation between stellar mass, metallicity, SFR and HI content and find similar results for less massive galaxies. However, they do not report a positive correlation between metallicity, SFR and HI gas content for massive galaxies though this may be due to systematic effects attributed to the metallicity calibration adopted in that study (see Yates et al. 2012).

The dominant dust destruction mechanisms such as UV photodissociation, sputtering and shocks in star-forming galaxies are dependent on massive stars and therefore the rate of dust destruction should be temporally coincidental with the SFR. However, in order to reproduce the MDSR, a significant temporal offset is required ($\Delta t \sim 3.5$ Gyr), thus favoring an interpretation where dust is effluxed rather than destroyed. In Section 9.5.4, we develop a model with dust loss proportional to only the SFR (Equation 9.11) without a temporal offset. This fast flow term can be more readily interpreted as a dust destruction term. However, we emphasize that this term is not necessary to reproduce the observed MDSR (compare Figure 9.7 and 9.8).

9.7 Model Assumptions

The numerical model we develop in Section 9.3, 9.4 and 9.5 to reproduce the observed MDSR represents one possible implementation. Here we revisit the basic galaxy properties we have assumed. These basic properties are required for any model attempting to reproduce the MDSR in accordance with the physical scenario described in Section 9.1.2.

1. *At a fixed stellar mass the current SFR is anti-correlated to the age of the galaxy.* This assumption is supported by observations which indicate that at a fixed stellar mass the mass-weighted age of stars within a galaxy is *anti*-correlated to its current SFR (see Figure 9.2). An *anti*-correlation between current SFR and galaxy age is the natural consequence of a sufficiently long characteristic timescale associated with the change in the average position of galaxies within the scatter of the MSR. In an accretion driven star formation scenario, the gravitational accretion rate is modulated by dark matter halos and should scale with the halo virial time. By $z = 0$ this is several Gyr which could help explain the observed anti-correlation between current SFR and galaxy age. In any case, we have implemented the observed SFR-age anti-correlation by assuming that galaxies populating the scatter of the MSR maintain a constant offset from the mean relation as they evolve. This is the easiest, albeit most restrictive, implementation to produce the *anti*-correlation between galaxy age and current SFR. It is beyond the scope of this work to explore alternative approaches but we note that any implementations reproducing the *anti*-correlation between galaxy age and current SFR could produce a similar model MDSR.

2. *The rate of dust production is proportional to the rate at which mass is recycled by stars.* We have assumed that the dust production rate is directly proportional to the stellar mass return rate. For reproducing the MDSR the exact nature of the proportionality is not critical so long as at a fixed stellar mass the *relative* quantity of dust produced is larger (smaller) for galaxies that are older (younger) and have returned more (less) stellar mass back to the ISM.

3. *The rate of dust loss is dependent on the amount of dust present and the rate at which high energy photons are produced.* We have implemented this by assuming that the rate of dust loss is proportional to the product of the dust opacity and SFR (see Equation 9.9). A dust loss rate that is given as a product of a quantity that is proportional to the high energy photon production rate and any other physical parameter that scales with the stellar mass (e.g. metallicity, dust mass or stellar mass itself) could produce a similar model MDSR.

4. *The timescale of dust loss is comparable but not identical to the timescale of dust production.* The timescale of dust production is dictated by the evolutionary timescale of intermediate and high mass stars. We have taken the rate of dust production to be directly proportional to the rate of stellar mass recycling. If the dust production timescale is different from the simple assumption made, then the dust loss timescale will change commensurately. This could happen, for example, if one of the populations of stars considered the dominant producers of dust in galaxies (i.e. intermediate mass AGB or type II SN) dominates over another in terms of dust production.

If the four physical conditions enumerated above are representative of the star-forming population of galaxies in the local universe, then a model can be developed that will reproduce the notable features of the observed MDSR shown in Figure 9.1 and in accordance with the physical scenario described in Section 9.1.2. We are not aware of any observational evidence that challenges these physical conditions, though we emphasize that all the physical conditions are not well established either. The physically motivated model developed in this contribution presents an interesting falsifiable hypothesis for the origin of the MDSR.

9.8 Discussion

In Section 9.8.1 we discuss details of our model of stellar mass growth and in Section 9.8.2 we discuss outflows in galaxies. We consider some potential implications of our model in Section 9.8.3.

9.8.1 Stellar Mass Growth and the Scatter in the Stellar Mass - SFR Relation

The *anti*-correlation between galaxy age and SFR at a fixed stellar mass is a fundamental assumption of our model. At stellar masses $\lesssim 10^{10} M_{\odot}$ the *anti*-correlation between dust opacity and SFR is a direct consequence of the *anti*-correlation between age and SFR. Galaxies with low SFRs are older and therefore have had more time to produce and accumulate dust. The remarkable agreement between our model of the MDSR and the observed relation, in addition to indications from the fossil record, suggest that our model of stellar mass growth may be feasible. Thus, further investigation is warranted. The model of stellar mass growth developed in this study begs a very important question: if the scatter in the MSR is temporally correlated, what is the physical mechanism responsible for such a mode of galaxy evolution?

9.8.2 Outflows in Normal Star-Forming Galaxies

In our Slow Flow model dust mass loss scales with the opacity and SFR. Given the (few) Gyr timescales for dust mass loss inferred from our model, we favor radiation pressure acting over long periods of time as the physical basis of the model. Radiation pressure acting on dust grains has been considered both in numerical models (Chiao & Wickramasinghe 1972; Ferrara 1993; Davies et al. 1998; Murray et al. 2005, 2011) and cosmological simulations (Aguirre et al. 2001; Hopkins et al. 2012) as a possible physical mechanism for driving outflows. However, a detailed physical model for a sustained radiation field interacting with dust grains over long periods of time incorporating some degree of dynamical coupling of dust grains to ambient gas remains to be developed. The analytical model presented in this paper provides constraints for a more rigorous physical model.

In our model the dominant mechanism for establishing a twist in the MDSR is radiation driven outflows. A simple back-of-the-envelope estimate of the average outflow velocity can be derived by assuming a distance dust travels before it is out of the line-of-sight, D_d, in a time Δt. The average outflow velocity, $\bar{v}$, is then given by $\bar{v} = D_d/\Delta t$. Adopting a fiducial

value of 10 kpc for D_d and $\Delta t = 3.5$ Gyr determined from our model we get that $\bar{v} \sim 3$ km s^{-1}. If material is ejected and re-accreted back into the galaxies as some models suggest (Davé et al. 2011), then dust may be driven out at substantially higher velocities in which case $\bar{v}$ represents a "drift" velocity at which a net loss of dust occurs.

In the Slow Flow scenario magnetic fields may play an important role in the mass loss process. Chiao & Wickramasinghe (1972) consider a physical scenario of dust driven out of galaxies along magnetic field lines by radiation pressure from stars. They argue that the Larmor radius of charged dust particles in typical ISM conditions is significantly smaller than the disk thickness. Therefore, the motion of dust grains is tied to magnetic field lines. They consider the net outward force from radiation pressure balanced against the drag force from the inter-cloud medium. They calculate the drift velocity is

$$u = 0.82 \left(\frac{0.01 \text{ cm}^{-3}}{n_i} \right) \left(\frac{10^4 \text{ K}}{T} \right)^{1/2} \sin\theta \quad [\text{km s}^{-1}]. \tag{9.14}$$

Here u is the drift velocity, n_i is the number density of particles in the inter-cloud medium, T is the temperature and θ is the inclination angle of the magnetic field with respect to the galactic plane. For the prevailing physical conditions in most star-forming galaxies and assuming a reasonably inclined magnetic field with respect to the galactic plane, the drift velocity of dust grains driven by radiation pressure along magnetic field lines is on the order of a ~ 1 km s^{-1}. This is on the same order of magnitude as the drift velocity inferred from our model.

In our model a large fraction of the dust produced by a galaxy can be expelled in a slow flow (see Figures 9.10 and 9.11a). The degree to which dust is dynamically coupled to the ambient gas in the ISM of galaxies is uncertain. Both collisions of dust particles with gas or coulomb interactions of charged particles with ions could provide a mechanism for transferring momentum from the dust to the gas (Ferrara 1993; Davies et al. 1998; Draine 2004). If the dust and gas are strongly coupled then a significant fraction of the gas in star-forming galaxies could be expelled via the Slow Flow mechanism. In Zahid et al.

(2013c) we argue that the extension of the MDSR to the quiescent population of galaxies suggests that the physical mechanism responsible for the observed MDSR may be related to the shutting down of star-formation in galaxies. The expulsion of large quantities of gas driven by interaction with charged dust particles accelerated by radiation pressure from stars presents a potential physical basis for such a scenario.

From $\sim 110,000$ star-forming galaxies in the SDSS DR7, Yates et al. (2012) have observed a "twist" in the stellar mass, metallicity and SFR relation. The twist occurs at a similar stellar mass as the observed twist in the MDSR of star-forming galaxies. Given that dust and metal content are strongly correlated, we argue that the twist in the stellar mass, metallicity and SFR relation is likely a result of the same physical mechanism responsible for the twist in the dust relation (i.e. the Slow Flow mechanism). At a stellar mass of $\sim 10^{11} M_{\odot}$, low SFR galaxies lose $\sim 50\%$ of dust they produce in the Slow Flow (see Figure 9.10 or 9.11a). This is a factor of ~ 2 more dust than their high SFR counterparts . Similar values for the oxygen mass loss are likely required to explain the twist observed in stellar mass, metallicity and SFR relation. For this to be the case, a relatively strong dynamical coupling between the dust and oxygen in the gas is required.

Taken at face value, the slow flow properties inferred from our model suggest a qualitatively different type of outflow than those observed in starburst, post-starburst and luminous infrared galaxies in the nearby universe (Rupke et al. 2005; Martin 2006; Rich et al. 2010; Tremonti et al. 2007; Sharp & Bland-Hawthorn 2010) or star-forming galaxies at higher redshifts (Shapley et al. 2003; Weiner et al. 2009; Steidel et al. 2010). In these galaxies outflows with velocities on order $\sim$ 1000 km/s are observed driven by energy and/or momentum from vigorous star formation. The mass loading of the wind is typically on order unity or greater. Outflows have also been observed in the stacked spectra of normal star-forming galaxies in the local universe (Chen et al. 2010). In these normal star-forming galaxies, the outflow velocities inferred from the NaD absorption line range from $\sim 120-160$ km s^{-1} .

Hopkins et al. (2012) consider several independent feedback mechanisms in their cosmological simulations. They conclude that multiple feedback processes acting on different spatial and temporal scales are required to produce realistic outflows. In particular they find that in normal star-forming galaxies such as the Milky Way, gas is largely driven out by heating of the ISM by supernovae and shocked stellar winds. Radiation pressure does drive some cold gas out of the ISM but the fraction is small. We note that Hopkins et al. (2012) run their observations over a few orbital periods ($\sim$0.5 Gyr), future simulations run over longer timescales could provide an important test for the model presented here.

Our three parameter model suggests that there is room for additional, independent physical mechanisms for driving out (or destroying) dust in star-forming galaxies. The three parameter model incorporates an additional feedback term that is simply proportional to the SFR. This term could be physically interpreted as energy injection from SN and shocks driven by stellar winds. In this physical picture, thermal energy is deposited directly into the ISM and no coupling between dust and gas is required in order to drive outflows. It may be the case that though a substantial fraction of the *dust* is lost in the slow flow, the coupling of dust and gas is weak leading to very little gas entrainment. Our three parameter model allows for $\sim 30\% - 40\%$ of the dust produced by galaxies at all stellar masses to be driven out by heating of the ISM (see Figure 9.11b) while still producing the twist in the MDSR. The velocity and mass loading of this type of outflow could be significantly larger than the slow flow since the timescale is instantaneous and, to first-order, we expect the ambient dust-to-gas ratio ($\sim$0.01) for the outflowing material.

9.8.3 Mass Transport

Dust driven outflows offer an attractive physical mechanism to explain the dust observed outside of galaxies. Using spectropolarimetric observations, Yoshida et al. (2011) directly observe dust in the wind of M82. Additionally, the presence of dust around galaxies is established by direct observations of polycyclic aromatic hydrocarbon features (Engelbracht et al. 2006; Roussel et al. 2010), in the serendipitous alignment of a galaxy pair where

extended dust disk is observed (Holwerda et al. 2009) and statistical studies of extinction of background galaxies by foreground galaxy halos (Zaritsky 1994; Ménard et al. 2010). Excess reddening is observed on scales ranging from a few kpc to a few Mpc. Fukugita (2011) argues that the total amount of dust produced in the history of the universe is consistent with the amount observed inside and outside of galaxies suggesting that only a small fraction of dust produced is destroyed. From this analysis it is estimated that a large fraction ($\sim 60\%$) of the total dust in the universe is distributed in the halos of galaxies and the intergalactic medium (also see Ménard & Fukugita 2012).

In Zahid et al. (2012b) we conduct a census of oxygen in star-forming galaxies in the local universe. We find that a large fraction of oxygen produced in galaxies is not accounted for by oxygen locked up in stars and in the ISM. The "deficit" of oxygen observed is consistent with the estimated oxygen content of the halos of star-forming galaxies (Tumlinson et al. 2011). A robust conclusion of Zahid et al. (2012b) is that the oxygen deficit scales with stellar mass such that high mass galaxies are missing a larger fraction of their oxygen as compared to lower mass galaxies. The magnitude of dust mass loss and its scaling with stellar mass presented in this study is consistent with the inferred oxygen deficit in local star-forming galaxies. The Slow Flow mechanism may provide a physical basis for understanding the oxygen census of local star-forming galaxies presented in Zahid et al. (2012b).

The physical transport of dust and metals may help to explain several observations. In spiral galaxies, the flat oxygen abundance gradients observed out to several optical radii are inconsistent with *in situ* formation of oxygen (Bresolin et al. 2009b; Werk et al. 2010, 2011; Bresolin et al. 2012). A plausible explanation is the transport of oxygen from the inner parts of galaxies. Such a mechanism would also be consistent with the ubiquitous presence of oxygen in the halos of star forming galaxies (Tumlinson et al. 2011).

The slow flow may also have an effect on local properties of galaxies. Bresolin et al. (2009a) show that the metallicities inferred from temperature sensitive [OIII]λ4363 line and those determined from B and A supergiants by Kudritzki et al. (2008) agree well in NGC 300. If coulomb interactions are responsible for exchange of momentum between dust and

gas, then a preferential loss of more ionized species may occur in dustier HII regions. If this is the case, our model suggests that at higher metallicities, the metallicities inferred for HII regions may be systematically lower than stellar metallicities due to the efficient loss of metals from HII regions with higher dust opacities. However, this would depend on the velocities and timescales of outflows in HII regions which currently are not well constrained. Indication of this effect may already be seen in M81 (Patterson et al. 2012; Kudritzki et al. 2012), the Orion nebula (Simón-Díaz & Stasińska 2011), in the central region of M33 (Urbaneja et al. 2005; U et al. 2009; Bresolin et al. 2010) and in M31 (Zurita & Bresolin 2012).

9.9 Summary

We develop a physically motivated model to reproduce and explain the observed relation between stellar mass, dust opacity and SFR (MDSR). In our model, galaxies continuously evolve along the observed MSR. The scatter in the MSR is populated by galaxies in a temporally correlated manner. As they build up their stellar mass, they produce dust and become more opaque. Radiation from massive stars efficiently couples to dust in systems with high opacity and over long periods of time slowly drives out dust and presumably gas that may be dynamically coupled to the dust. Models for stellar mass growth whereby star-forming galaxies continuously evolve along the MSR and models of radiation pressure acting on dust grains have both been investigated in the literature. This paper is the first to put these together in a self-consistent model. We refer to this self-consistent model incorporating both stellar mass growth and radiation pressure driven outflows, given by Equation 9.10, as the *Slow Flow* model. We summarize the salient features of our model:

- Normal star-forming galaxies evolve along the observed stellar mass-SFR relation. The ~ 0.25 dex 1σ scatter in the relation is temporally correlated for individual galaxies. Thus, for galaxies at the same stellar mass, the age of a galaxy is *anti*-correlated with SFR such that older galaxies have lower *current* SFRs.

- Stellar mass recycling is time dependent and the dust production rate is proportional to the stellar mass recycling rate. At the fixed stellar mass, older galaxies have recycled a larger fraction of their gas back to the ISM and thus produced a greater amount of dust. Also, older galaxies have lower current SFRs at a fixed stellar mass. Therefore, the *anti*-correlation between dust opacity and SFR at stellar masses $\lesssim 10^{10} M_{\odot}$ is naturally explained as an age effect.

- Radiation pressure acting on dust grains over long periods is capable of driving dust out of the ISM of star-forming galaxies. As galaxies grow in stellar mass they become dustier. At a stellar mass $\sim 10^{10} M_{\odot}$ star-forming galaxies become optically thick and radiation efficiently drives dust out of galaxies on a few Gyr timescales.

- The dust production rate is proportional to the stellar recycling rate and thus is *positively* correlated with the SFR. The timescale for dust loss is long and therefore at stellar masses $\gtrsim 10^{10} M_{\odot}$, galaxies with high SFRs accumulate dust more rapidly than they expel it. The accumulation of dust in rapidly star-forming galaxies naturally explains the *positive* correlation between dust opacity and SFR at stellar masses $\gtrsim 10^{10} M_{\odot}$.

The results presented in this paper offer interesting new evidence that outflows of gas and dust play an important role in the evolution of normal star-forming galaxies in the local universe. We demonstrate that considerations for time dependent stellar mass loss are important for understanding the properties of star-forming galaxies. Despite being quite simple, our model gives us a potentially powerful tool for interpreting the observed relation between stellar mass, dust opacity and SFR. A detailed model of the physical processes outlined in this paper needs to be worked out and observations of outflows in normal star-forming galaxies are required to establish and constrain the model.

References

Abazajian, K. N., et al. 2009, ApJS, 182, 543

Aguirre, A., Hernquist, L., Katz, N., Gardner, J., & Weinberg, D. 2001, ApJ, 556, L11

Andrews, B. H., & Martini, P. 2013, ApJ, 765, 140

Asari, N. V., Cid Fernandes, R., Stasińska, G., Torres-Papaqui, J. P., Mateus, A., Sodré, L., Schoenell, W., & Gomes, J. M. 2007, MNRAS, 381, 263

Berg, D. A., et al. 2012, ApJ, 754, 98

Boissier, S., Boselli, A., Buat, V., Donas, J., & Milliard, B. 2004, A&A, 424, 465

Bothwell, M. S., Maiolino, R., Kennicutt, R., Cresci, G., Mannucci, F., Marconi, A., & Cicone, C. 2013, MNRAS, 433, 1425

Bresolin, F., Garnett, D. R., & Kennicutt, Jr., R. C. 2004, ApJ, 615, 228

Bresolin, F., Gieren, W., Kudritzki, R.-P., Pietrzyński, G., Urbaneja, M. A., & Carraro, G. 2009a, ApJ, 700, 309

Bresolin, F., Kennicutt, R. C., & Ryan-Weber, E. 2012, ApJ, 750, 122

Bresolin, F., Ryan-Weber, E., Kennicutt, R. C., & Goddard, Q. 2009b, ApJ, 695, 580

Bresolin, F., Stasińska, G., Vílchez, J. M., Simon, J. D., & Rosolowsky, E. 2010, MNRAS, 404, 1679

Brinchmann, J., Charlot, S., White, S. D. M., Tremonti, C., Kauffmann, G., Heckman, T., & Brinkmann, J. 2004, MNRAS, 351, 1151

Cardelli, J. A., Clayton, G. C., & Mathis, J. S. 1989, ApJ, 345, 245

Chabrier, G. 2003, PASP, 115, 763

Chattopadhyay, I., Sharma, M., Nath, B. B., & Ryu, D. 2012, MNRAS, 423, 2153

Chen, Y.-M., Tremonti, C. A., Heckman, T. M., Kauffmann, G., Weiner, B. J., Brinchmann, J., & Wang, J. 2010, AJ, 140, 445

Chiao, R. Y., & Wickramasinghe, N. C. 1972, MNRAS, 159, 361

Conroy, C., & Wechsler, R. H. 2009, ApJ, 696, 620

Cowie, L. L., & Barger, A. J. 2008, ApJ, 686, 72

Daddi, E., et al. 2007, ApJ, 670, 156

Davé, R., Finlator, K., & Oppenheimer, B. D. 2011, MNRAS, 2110

Davies, J. I., Alton, P., Bianchi, S., & Trewhella, M. 1998, MNRAS, 300, 1006

Domínguez, A., et al. 2013, ApJ, 763, 145

Dopita, M. A., Sutherland, R. S., Nicholls, D. C., Kewley, L. J., & Vogt, F. P. A. 2013, ApJS, 208, 10

Draine, B. T. 2003, ARA&A, 41, 241

—. 2004, Astrophysics of Dust in Cold Clouds (Springer), 213

Dutton, A. A., van den Bosch, F. C., & Dekel, A. 2010, MNRAS, 405, 1690

Dwek, E. 1998, ApJ, 501, 643

Elbaz, D., et al. 2007, A&A, 468, 33

Ellison, S. L., Patton, D. R., Simard, L., & McConnachie, A. W. 2008, ApJ, 672, L107

Engelbracht, C. W., et al. 2006, ApJ, 642, L127

Erb, D. K., Shapley, A. E., Pettini, M., Steidel, C. C., Reddy, N. A., & Adelberger, K. L. 2006, ApJ, 644, 813

Ferrara, A. 1993, ApJ, 407, 157

Fukugita, M. 2011, ArXiv e-prints

Garn, T., & Best, P. N. 2010, MNRAS, 409, 421

Heckman, T. M., Robert, C., Leitherer, C., Garnett, D. R., & van der Rydt, F. 1998, ApJ, 503, 646

Holwerda, B. W., Keel, W. C., Williams, B., Dalcanton, J. J., & de Jong, R. S. 2009, AJ, 137, 3000

Hopkins, P. F., Quataert, E., & Murray, N. 2012, MNRAS, 421, 3522

Jungwiert, B., Combes, F., & Palouš, J. 2001, A&A, 376, 85

Kauffmann, G., et al. 2003a, MNRAS, 346, 1055

—. 2003b, MNRAS, 341, 33

Kennicutt, Jr., R. C., Bresolin, F., & Garnett, D. R. 2003, ApJ, 591, 801

Kewley, L. J., & Ellison, S. L. 2008, ApJ, 681, 1183

Kewley, L. J., Groves, B., Kauffmann, G., & Heckman, T. 2006, MNRAS, 372, 961

Kobulnicky, H. A., & Kewley, L. J. 2004, ApJ, 617, 240

Koyama, Y., et al. 2013, MNRAS

Kudritzki, R.-P., Urbaneja, M. A., Bresolin, F., Przybilla, N., Gieren, W., & Pietrzyński, G. 2008, ApJ, 681, 269

Kudritzki, R.-P., Urbaneja, M. A., Gazak, Z., Bresolin, F., Przybilla, N., Gieren, W., & Pietrzyński, G. 2012, ApJ, 747, 15

Lara-López, M. A., et al. 2010, A&A, 521, L53+

—. 2013, ArXiv e-prints

Laskar, T., Berger, E., & Chary, R.-R. 2011, ApJ, 739, 1

Lee, H., Skillman, E. D., Cannon, J. M., Jackson, D. C., Gehrz, R. D., Polomski, E. F., & Woodward, C. E. 2006, ApJ, 647, 970

Leitner, S. N. 2012, ApJ, 745, 149

Leitner, S. N., & Kravtsov, A. V. 2011, ApJ, 734, 48

Lequeux, J., Peimbert, M., Rayo, J. F., Serrano, A., & Torres-Peimbert, S. 1979, A&A, 80, 155

Mannucci, F., Cresci, G., Maiolino, R., Marconi, A., & Gnerucci, A. 2010, MNRAS, 408, 2115

Mannucci, F., et al. 2009, MNRAS, 398, 1915

Maraston, C. 2005, MNRAS, 362, 799

Martin, C. L. 2006, ApJ, 647, 222

Ménard, B., & Fukugita, M. 2012, ApJ, 754, 116

Ménard, B., Scranton, R., Fukugita, M., & Richards, G. 2010, MNRAS, 405, 1025

Moustakas, J., Kennicutt, Jr., R. C., Tremonti, C. A., Dale, D. A., Smith, J.-D. T., & Calzetti, D. 2010, ApJS, 190, 233

Moustakas, J., et al. 2011, ArXiv e-prints

Murray, N., Ménard, B., & Thompson, T. A. 2011, ApJ, 735, 66

Murray, N., Quataert, E., & Thompson, T. A. 2005, ApJ, 618, 569

Nagao, T., Maiolino, R., & Marconi, A. 2006, A&A, 459, 85

Nicholls, D. C., Dopita, M. A., & Sutherland, R. S. 2012, ApJ, 752, 148

Nicholls, D. C., Dopita, M. A., Sutherland, R. S., Kewley, L. J., & Palay, E. 2013, ApJS, 207, 21

Noeske, K. G., et al. 2007a, ApJ, 660, L47

—. 2007b, ApJ, 660, L43

Osterbrock, D. E. 1989, Astrophysics of gaseous nebulae and active galactic nuclei, ed. D. E. Osterbrock

Pannella, M., et al. 2009, ApJ, 698, L116

Patterson, M. T., Walterbos, R. A. M., Kennicutt, R. C., Chiappini, C., & Thilker, D. A. 2012, MNRAS, 422, 401

Peimbert, M. 1967, ApJ, 150, 825

Peng, Y.-j., et al. 2010, ApJ, 721, 193

Reddy, N. A., Erb, D. K., Pettini, M., Steidel, C. C., & Shapley, A. E. 2010, ApJ, 712, 1070

Reddy, N. A., Pettini, M., Steidel, C. C., Shapley, A. E., Erb, D. K., & Law, D. R. 2012, ApJ, 754, 25

Rich, J. A., Dopita, M. A., Kewley, L. J., & Rupke, D. S. N. 2010, ApJ, 721, 505

Roussel, H., et al. 2010, A&A, 518, L66

Rupke, D. S., Veilleux, S., & Sanders, D. B. 2005, ApJS, 160, 115

Salim, S., et al. 2007, ApJS, 173, 267

Savaglio, S., et al. 2005, ApJ, 635, 260

Shapley, A. E., Steidel, C. C., Pettini, M., & Adelberger, K. L. 2003, ApJ, 588, 65

Sharma, M., & Nath, B. B. 2012, ApJ, 750, 55

Sharma, M., Nath, B. B., & Shchekinov, Y. 2011, ApJ, 736, L27

Sharp, R. G., & Bland-Hawthorn, J. 2010, ApJ, 711, 818

Simón-Díaz, S., & Stasińska, G. 2011, A&A, 526, A48

Steidel, C. C., Erb, D. K., Shapley, A. E., Pettini, M., Reddy, N., Bogosavljević, M., Rudie, G. C., & Rakic, O. 2010, ApJ, 717, 289

Stoughton, C., et al. 2002, AJ, 123, 485

Tojeiro, R., Heavens, A. F., Jimenez, R., & Panter, B. 2007, MNRAS, 381, 1252

Tojeiro, R., Wilkins, S., Heavens, A. F., Panter, B., & Jimenez, R. 2009, ApJS, 185, 1

Tremonti, C. A., et al. 2004, ApJ, 613, 898

Tremonti, C. A., Moustakas, J., & Diamond-Stanic, A. M. 2007, ApJ, 663, L77

Tumlinson, J., et al. 2011, Science, 334, 948

U, V., Urbaneja, M. A., Kudritzki, R.-P., Jacobs, B. A., Bresolin, F., & Przybilla, N. 2009, ApJ, 704, 1120

Urbaneja, M. A., Herrero, A., Kudritzki, R.-P., Najarro, F., Smartt, S. J., Puls, J., Lennon, D. J., & Corral, L. J. 2005, ApJ, 635, 311

Weiner, B. J., et al. 2009, ApJ, 692, 187

Werk, J. K., Putman, M. E., Meurer, G. R., & Santiago-Figueroa, N. 2011, ApJ, 735, 71

Werk, J. K., Putman, M. E., Meurer, G. R., Thilker, D. A., Allen, R. J., Bland-Hawthorn, J., Kravtsov, A., & Freeman, K. 2010, ApJ, 715, 656

Whitaker, K. E., van Dokkum, P. G., Brammer, G., & Franx, M. 2012, ApJ, 754, L29

Wijesinghe, D. B., et al. 2012, MNRAS, 423, 3679

Wise, J. H., Abel, T., Turk, M. J., Norman, M. L., & Smith, B. D. 2012, MNRAS, 427, 311

Worthey, G., Faber, S. M., Gonzalez, J. J., & Burstein, D. 1994, ApJS, 94, 687

Xiao, T., Wang, T., Wang, H., Zhou, H., Lu, H., & Dong, X. 2012, MNRAS, 421, 486

Yates, R. M., Kauffmann, G., & Guo, Q. 2012, MNRAS, 422, 215

Yoshida, M., Kawabata, K. S., & Ohyama, Y. 2011, PASJ, 63, 493

Zahid, H. J., Bresolin, F., Kewley, L. J., Coil, A. L., & Davé, R. 2012a, ApJ, 750, 120

Zahid, H. J., Dima, G. I., Kewley, L. J., Erb, D. K., & Davé, R. 2012b, ApJ, 757, 54

Zahid, H. J., Geller, M. J., Kewley, L. J., Hwang, H. S., Fabricant, D. G., & Kurtz, M. J. 2013a, ApJ, 771, L19

Zahid, H. J., Kewley, L. J., & Bresolin, F. 2011, ApJ, 730, 137

Zahid, H. J., Torrey, P., Kudritzki, R., Kewley, L., Dave, R., & Geller, M. 2013b, ArXiv e-prints

Zahid, H. J., Yates, R. M., Kewley, L. J., & Kudritzki, R. P. 2013c, ApJ, 763, 92

Zaritsky, D. 1994, AJ, 108, 1619

Zhang, D., & Thompson, T. A. 2010, ArXiv e-prints

Zu, Y., Weinberg, D. H., Davé, R., Fardal, M., Katz, N., Kereš, D., & Oppenheimer, B. D. 2011, MNRAS, 412, 1059

Zurita, A., & Bresolin, F. 2012, MNRAS, 427, 1463

Chapter 10

The Universal Relation of Galactic Chemical Evolution: The Origin of the Mass-Metallicity Relation

Note: This chapter has been submitted to the Astrophysical Journal, with co-authors G. Dima, R. Kudritzki, L. Kewley, M. Geller and H.S. Hwang. I am the primary author of this work.

Abstract

We examine the mass-metallicity relation for $z \lesssim 1.6$. The mass-metallicity relation follows a steep slope with a turnover or 'knee' at stellar masses around $10^{10} M_{\odot}$. At stellar masses higher than the characteristic turnover mass, the mass-metallicity relation flattens as metallicities begin to saturate. We show that the redshift evolution of the mass-metallicity relation depends only on evolution of the characteristic turnover mass. The relationship between metallicity and the stellar mass normalized to the characteristic turnover mass is independent of redshift. We find that the redshift independent slope of the mass-metallicity relation is set by the slope of the relationship between gas mass and stellar mass. The turnover in the mass-metallicity relation occurs when the gas-phase oxygen abundance is high enough that the amount of oxygen locked up in low mass stars is an appreciable fraction of the amount of oxygen produced by massive stars. The characteristic turnover mass is the

stellar mass where the stellar-to-gas mass ratio is unity. Numerical modeling suggests that the relationship between metallicity and stellar-to-gas mass ratio is a redshift independent, universal relationship followed by all galaxies as they evolve. The mass-metallicity relation originates from this more fundamental universal relationship between metallicity and stellar-to-gas mass ratio. We test the validity of this universal metallicity relation in local galaxies where stellar mass, metallicity and gas mass measurements are available. The data are consistent with a universal metallicity relation. We derive an equation for estimating the hydrogen gas mass from measurements of stellar mass and metallicity valid for $z \lesssim 1.6$ and predict the cosmological evolution of galactic gas masses.

10.1 Introduction

Gas flows and star formation govern the evolution of galaxies. A key diagnostic of gas flows and star formation in galaxies is the amount of heavy elements relative to hydrogen in the interstellar medium (ISM). Heavy elements are produced by massive stars and are dispersed into the ISM by stellar mass loss processes. Therefore, the ISM metal content is closely linked to the stellar mass of a galaxy. The heavy element abundance is measured relative to hydrogen and therefore also depends on the gas content of galaxies. Understanding the evolution of the gas-phase abundance in terms of gas flows and star formation is fundamental for developing a comprehensive theory of galaxy evolution.

Oxygen is the most abundant heavy element formed in the Universe. Therefore, the abundance of oxygen can be used as a proxy for the production of all heavy elements. The gas-phase oxygen abundance is correlated to the stellar mass in star-forming galaxies. This relation is known as the mass-metallicity (MZ) relation. The MZ relation was first observed in a small sample of nearby galaxies by Lequeux et al. (1979). They showed that galaxy metallicity increases with stellar mass. Subsequently, Tremonti et al. (2004) measure the MZ relation of $\sim 50,000$ star-forming galaxies in the local Universe. They find a tight MZ relation ($\sim$0.1 dex scatter) extending over three orders of magnitude in stellar mass.

The MZ relation is one of the primary observations for measuring the chemical evolution of galaxies. In nearby galaxies, the MZ relation extends down to stellar masses of $\sim 10^6 M_\odot$ (Lee et al. 2006; Zahid et al. 2012a; Berg et al. 2012; Andrews & Martini 2013). A correlation between stellar mass and metallicity is observed not only in gas but also stars (Gallazzi et al. 2005; Kudritzki et al. 2012; Kirby et al. 2013; Conroy et al. 2013; Hosek et al. 2014). The MZ relation is observed out to $z \sim 3$ (Savaglio et al. 2005; Erb et al. 2006; Maiolino et al. 2008; Mannucci et al. 2009; Zahid et al. 2011; Yabe et al. 2012; Zahid et al. 2012b, 2013a,b, and many others) and perhaps beyond (Laskar et al. 2011; Møller et al. 2013). The MZ relation also holds for individual star-forming regions within galaxies (Rosales-Ortega et al. 2012). Observations of the MZ relation reveal that the metallicities of galaxies increase with time. The MZ relation of the most massive galaxies flattens as the Universe evolves (Zahid et al. 2013a). This flattening is a result of an empirical upper limit in galaxy metallicity. The most massive galaxies, even at high redshifts, evolve chemically to this upper metallicity limit (Zahid et al. 2013a,b). The stellar mass where the MZ relation flattens is ~ 0.7 dex lower now than at $z \sim 0.8$ (Zahid et al. 2013a).

It is clear that the MZ relation depends on gas flows and star formation. Still, despite numerous studies of the MZ relation over the last few decades, the physical origin of the MZ relation remains uncertain. Metallicity is defined as the amount of oxygen *relative* to hydrogen. Therefore, an increase in metallicity could result from star formation or metal-poor outflows. In the case of the latter, the metallicity of outflowing material is lower than the ISM metallicity leading to an increase in the amount of oxygen *relative* to hydrogen. Conversely, metallicity can be reduced both by metal-rich outflows or inflows of metal-poor gas. Without clear observational constraints for inflows and outflows, the effects of gas flows and star formation remain degenerate. The MZ relation could possibly be the result of metal-rich outflows (Larson 1974), inefficient star formation in less massive galaxies (Brooks et al. 2007; Finlator & Davé 2008; Calura et al. 2009), metal-poor inflows (Dalcanton et al. 2004), variations in the initial mass function (IMF; Köppen et al. 2007)

or some combination of these physical processes. Uncovering the origin of the MZ relation is crucial for understanding gas flows and star formation in galaxies.

The scatter observed in the MZ relation is correlated with other physical properties. These correlations provide clues to the origin of the MZ relation. Ellison et al. (2008) first showed an anti-correlation between metallicity and specific star formation rate for galaxies at a fixed stellar mass. A relation between stellar mass, metallicity and star formation rate (SFR) is observed in local (Mannucci et al. 2010; Lara-López et al. 2010; Yates et al. 2012; Andrews & Martini 2013) and high redshift galaxies (Zahid et al. 2013b; Yabe et al. 2014; Troncoso et al. 2014). At stellar masses $\lesssim 10^{10.5} M_{\odot}$, galaxies with high SFRs typically have lower metallicities and vice versa. Mannucci et al. (2010) derive a relation between stellar mass, metallicity and SFR that minimizes the scatter of metallicity in the local galaxy population. They argue that the minimum scatter relation between stellar mass, metallicity and SFR that they derive is independent of redshift. They refer to this minimum scatter relation as the fundamental metallicity relation (FMR). For the FMR, the higher SFRs observed in high redshift galaxies account for their lower metallicities. However, the redshift independence of the relation between stellar mass, metallicity and SFR remains tentative (Niino 2012; Pérez-Montero et al. 2013; Sánchez et al. 2013; Zahid et al. 2013b; Ly et al. 2014).

Both the SFR and metallicity are dependent on the gas content. The anti-correlation between metallicity and SFR is likely the result of variations in gas content (Hughes et al. 2012; Lara-López et al. 2013; Bothwell et al. 2013). At a fixed stellar mass, galaxies with higher gas fractions will exhibit elevated SFRs and lower metallicity. Recently, Bothwell et al. (2013) present observations suggesting that the FMR derived by Mannucci et al. (2010) is the result of a relation between stellar mass, metallicity and gas content. In the Bothwell et al. interpretation, the SFR acts as a proxy for gas content in the FMR proposed by Mannucci et al. (2010). Bothwell et al. (2013) are not able to investigate the redshift dependence of the relation between stellar mass, metallicity and gas content due to lack of measurements of cold gas in galaxies outside the local Universe.

Here we model the origin of the MZ relation, its evolution and the dependency of the scatter on SFR. We will show that the fundamental relationship of galactic chemical evolution is the relationship between metallicity and the stellar-to-gas mass ratio. We present the data and methods in Section 10.2 and 10.3, respectively. In Section 10.4 we derive the MZ relation for $z \lesssim 1.6$. We show that the data are consistent with a single metallicity relation that is independent of redshift. In Section 10.5 and 10.6, we interpret our results by examining analytical and numerical models of chemical evolution, respectively. In Section 10.7 we show the observed relationship between metallicity and the stellar-to-gas mass ratio in local galaxies. We provide a discussion in Section 10.8 and a summary of our major results in Section 10.9. We adopt the standard cosmology $(H_0, \Omega_m, \Omega_\Lambda) = (70$ km s^{-1} Mpc^{-1}, 0.3, 0.7) and a Chabrier (2003) IMF.

10.2 Data

We investigate the MZ relation for $z \lesssim 1.6$ using data from the Sloan Digital Sky Survey (SDSS), Smithsonian Hectospec Lensing Survey (SHELS), Deep Extragalactic Evolutionary Probe 2 (DEEP2) and the FMOS-COSMOS survey. The MZ relations examined in this work are previously published in Zahid et al. (2013a,b). In this section we describe the survey samples and selection criteria.

10.2.1 SDSS Data

We derive the local MZ relation using the SDSS DR7 main galaxy sample (Abazajian et al. 2009). The spectroscopic data consists of $\sim 900,000$ galaxies spanning a redshift range of $0 < z < 0.7$. The survey has a limiting magnitude of $r = 17.8$ and covers 8000 deg^2 on the sky (Strauss et al. 2002). The nominal spectral range of the observations is $3800 - 9200$Å with a spectral resolution of $R = 1800 - 2000$. We adopt the line fluxes measured by the MPA/JHU[1] and determine stellar masses from the *ugriz*-band c-model magnitudes. The

[1]http://www.mpa-garching.mpg.de/SDSS/DR7/

line fluxes are corrected for dust extinction using the Cardelli et al. (1989) extinction law assuming a case B recombination Hα/Hβ value of 2.86 (Hummer & Storey 1987).

We derive metallicity from diagnostics based on the ratio of strong nebular emission lines. These strong-line metallicity diagnostics are calibrated under the assumption that stellar ionizing flux is powering nebular emission. The diagnostics are not calibrated to measure metallicities when active galactic nuclei (AGN) are significantly contributing to the ionizing flux. Fortunately, line flux ratios discriminate between star formation and AGN powered nebular emission. Baldwin et al. (1981, BPT) first showed that [NII]λ6584/Hα vs [OIII]λ5007/Hβ diagram could be used to classify galaxies as star-forming or AGN. In order to derive a sample of star-forming galaxies we use the recent classification of Kewley et al. (2006). Galaxies with

$$\log([\mathrm{OIII}]/\mathrm{H}\beta) > 0.61/(\log([\mathrm{NII}]/\mathrm{H}\alpha - 0.05) + 1.3 \tag{10.1}$$

are classified as AGN and are removed from the sample.

Our analysis is based on the emission line fluxes of [OII]λ3727, 3729, Hβ, [OIII]λ5007, Hα and [NII]λ6584. Foster et al. (2012) show that signal-to-noise (S/N) cuts applied to the [OIII]λ5007 lines bias the measured MZ relation. This is because high metallicity galaxies typically have very weak [OIII]λ5007 emission. We apply no S/N selection on the [OIII]λ5007 emission line. We require a S/N$>$ 3 in the line flux measurements of [OII]λ3727, 3729, Hβ, Hα and [NII]λ6584. We apply a lower redshift limit of $z > 0.02$ to ensure that the $[OII]\lambda3727$ is redshifted into the nominal spectral range of the survey. An upper limit redshift of $z < 0.12$ is applied.The 3 arc-second spectroscopic fiber aperture only covers a fraction of the total galaxy flux. We derive the covering fraction by comparing the 3 arc-second fiber flux to the total flux. In order to avoid systematic aperture bias, we require an aperture covering fraction $> 20\%$ as recommended by Kewley et al. (2005). The local selected sample from the SDSS consists of $\sim 51,000$ galaxies.

10.2.2 SHELS Data

The SHELS survey (Geller et al. 2005) consists of $\sim$ 25,000 galaxies ranging from $0 < z < 0.8$ in the F1 (Hwang et al., in preparation) and F2 (Geller et al., in preparation) fields of the Deep Lens Survey (Wittman et al. 2002). The two fields combined cover 8 deg^2 and are observed down to a limiting magnitude of $R = 20.6$. The spectra are taken with Hectospec (Fabricant et al. 2005), a 300 fiber spectrograph mounted on the 6.5 m MMT. The nominal spectral range of the observations is $3700 - 9150\mathring{A}$ with a spectral resolution of $R \sim 3000$. The *ugriz*-band c-model photometry is from the SDSS DR8 (Padmanabhan et al. 2008). Details of emission line equivalent width measurements will be presented in Geller et al. (in preparation).

We select galaxies in the SHELS sample by applying selection criteria similar to the criteria applied to the SDSS sample. AGN are removed from the sample using the Kewley et al. (2006) classification. We require a S/N$>$ 3 for [OII]λ3727, 3729, Hβ, Hα and [NII]λ6584 equivalent widths. The redshift range of the data is restricted to $0.2 < z < 0.38$. The lower redshift limit is set to sufficiently capture evolution between the SDSS and SHELS sample and the upper redshift limit is set by Hα redshifting outside the nominal spectral range. In the restricted redshift range of our metallicity analysis, covering fraction is $> 20\%$ and aperture bias is not an issue. The SHELS sample we select consists of 3577 galaxies.

10.2.3 DEEP2 Data

The DEEP2 survey (Davis et al. 2003) consists of 50,000 galaxies observed in the redshift range of $0.7 < z < 1.4$. We use data from the third data release[2]. The data were observed in four fields covering 3.5 deg^2 down to a limiting magnitude of $R = 24.1$. The spectra were taken with DEIMOS (Faber et al. 2003) mounted on the 10 m Keck Telescope. The nominal spectral range is $6500 - 9100\mathring{A}$ observed at a resolution of $R \sim 5000$. The $BRI-$band photometry was measured from images taken with the CFH12K camera on the 3.6 m Canada-France-Hawaii Telescope (Coil et al. 2004). For about half the galaxies

[2]http://deep.ps.uci.edu/DR3/

in the sample, we have K_s-band photometry from the Wide Field Infrared Camera on the 5 m Hale Telescope (Bundy et al. 2006). Details of the emission line equivalent width measurements can be found in Zahid et al. (2011).

The [OII]$\lambda 3727, 3729$, Hβ and [OIII]$\lambda 5007$ emission lines required for our metallicity analysis are only observed in the redshift range of $0.75 < z < 0.82$. We require a S/N> 3 in the [OII]$\lambda 3727, 3729$ and Hβ emission line equivalent width measurements. Given the nominal spectral range of the data and the redshift of our sample, the Hα and [NII]$\lambda 6584$ emission lines are not observed and we are not able to apply the BPT classification. AGN contamination in the emission line galaxy sample is estimated to be small (Weiner et al. 2007). We identify and remove 17 AGN from the sample using X-ray observations (Goulding et al. 2012). The DEEP2 selected parent sample consists of 1585 galaxies. We refer to this as the parent DEEP2 sample.

10.2.4 FMOS-COSMOS Data

The FMOS-COSMOS survey (Silverman et al., in prep) is an ongoing near-infrared spectroscopic survey of star-forming galaxies in the redshift range of $1.4 < z < 1.7$ found in the central square degree of the COSMOS field (Scoville et al. 2007). The observations are carried out using FMOS (Kimura et al. 2010) mounted on the 8 m Subaru Telescope. Galaxies are observed in the $H-$band (1.6 - 1.80 μm) in high resolution mode with spectral resolution of $R \sim 2200$. A subsample of galaxies are also observed in $J-$band (1.11 - 1.35 μm). In the target redshift range, [NII]$\lambda 6584$ and Hα are observed in the $H-$band and [OIII]$\lambda 5007$ and Hβ are observed in the $J-$band. The COSMOS field has 30 bands of photometry covering UV to IR (Ilbert et al. 2009).

In order to ensure efficient detection, star-forming galaxies are pre-selected in the target redshift range using robust photometric redshifts (Ilbert et al. 2009), an sBzK color selection Daddi et al. (2004) and a K_s-band limiting magnitude of $K_s < 23$. Each FMOS pointing is observed for 5 hours yielding a 3σ line detection limit of 4×10^{-17} ergs s^{-1} cm^{-2} corresponding to an unobscured SFR limit of $\sim 5 M_{\odot}$ yr^{-1}. In all galaxies at least one

emission line is detected with $> 3\sigma$ significance in each individual galaxy spectrum. We identify the strongest observed emission line in our $H-$band observations as Hα.

We derive metallicities using the [NII]λ6584/Hα line flux ratio. Given our sensitivity limit and the typical metallicities and SFRs of galaxies at $z \sim 1.6$, [NII]λ6584 is only detected in a fraction of individual galaxies. To derive an unbiased MZ relation, the spectra are summed in bins of stellar mass before line flux measurements are made. Each summed spectrum is derived from 15 or 16 individual galaxy spectra. Details of the metallicity analysis are presented in Zahid et al. (2013b).

10.2.5 Gas Mass Data

The HI gas mass measurements are taken from the Arecibo Fast Alfa Survey (ALFALFA; Haynes et al. 2011). We use the publicly available data presented in the $\alpha.40$ release[3]. The data consist of $15,855$ detections over a 2800 deg^2 field. Of the observed detections, 95% are associated with extragalactic sources. Nearby galaxies have large uncertainties in their distances which directly impacts the HI mass estimate. We require that galaxies have measured distances > 10 Mpc. Additionally, we select objects which are designated as "Code 1" (HI sources) and have significant detections of the 21 cm line ($S/N > 3$). The HI mass sample is cross-matched to the SDSS DR7 sample by the ALFALFA team. The cross-matched sample we select consists of 6399 galaxies.

In order to measure metallicities using the SDSS spectroscopy we apply additional selection criteria to the cross-matched sample. We require a S/N$>$ 3 for the [OII]$\lambda 3727, 3729$, Hβ, Hα and [NII]λ6584 emission line flux measurements. Because much of the sample consists of nearby galaxies and the sample is small we do not apply a fiber aperture covering fraction selection as is done for the selected SDSS sample described in Section 10.2.1. The final cross-matched sample consists of 2633 galaxies.

Atomic and molecular hydrogen is present in star-forming galaxies. Unfortunately, we do not have direct estimates of the molecular hydrogen content of galaxies in our cross-matched

[3]http://egg.astro.cornell.edu/alfalfa/data/index.php

sample. Instead we account for molecular hydrogen using the observed scaling between atomic and molecular gas mass derived as part of the COLD GASS survey (Saintonge et al. 2011) conducted using the IRAM 30 m telescope. Saintonge et al. (2011) measure the molecular-to-atomic gas mass ratio in 350 local galaxies that are part of the ALFALFA survey. Galaxies are observed until CO is detected or until an upper limit for the molecular gas mass to stellar mass ratio of 1.5% is reached. We estimate H_2 masses from the Saintonge et al. (2011) relation derived from a subset of the data where CO emission was detected. This CO detected subset of galaxies is primarily comprised of star-forming galaxies. Thus, the molecular-to-atomic gas mass ratio derived from this subset is appropriate for our sample. Saintonge et al. (2011) derive the relation

$$\log\left(\frac{M_{H2}}{M_{HI}}\right) = 0.425\,[\log(M_*/M_\odot) - 10.7] - 0.387 \tag{10.2}$$

where M_{H2} and M_{HI} are the molecular and atomic hydrogen mass, respectively. To obtain an estimate of the total hydrogen gas mass of galaxies in our cross-matched sample, we add the molecular hydrogen mass derived from Equation 10.2 to the HI mass measurements from ALFALFA. For galaxies at $M_* \lesssim 10^{10} M_\odot$, the molecular-to-atomic hydrogen mass fraction is $\lesssim 20\%$. For the most massive galaxies in the sample, the molecular-to-atomic hydrogen mass fraction is $\lesssim 50\%$.

10.3 Methods

10.3.1 Stellar Mass

We measure stellar masses using the Le Phare[4] code developed by Arnouts & Ilbert. We synthesize synthetic magnitudes using stellar population synthesis models of Bruzual & Charlot (2003) and a Chabrier (2003) IMF. The synthetic magnitudes are generated by varying stellar population parameters. The models have two metallicities and seven exponentially decreasing star formation models (SFR $\propto e^{-t/\tau}$) with τ =

[4]http://www.cfht.hawaii.edu/∼arnouts/LEPHARE/cfht_lephare/ lephare.html

$0.1, 0.3, 1, 2, 3, 5, 10, 15$ and 30 Gyrs. We apply the extinction law of Calzetti et al. (2000) allowing E(B−V) to range from 0 to 0.6. The ages of the stellar population range from 0 to 13 Gyrs. Each synthetic SED generated is normalized to solar luminosity. The stellar mass is the scaling factor between the synthetic SED and the observed photometry. There is a distribution of stellar masses derived which depend on the different stellar population parameters adopted to generate the synthetic SEDs. We adopt the median of this distribution as our stellar mass estimate. The absolute uncertainty in stellar mass is ~ 0.3 dex (Conroy 2013).

10.3.2 Gas-Phase Oxygen Abundance

Flux ratios of collisionally excited lines to recombination lines are sensitive to temperature and therefore metallicity. Various metallicity diagnostics which use ratios of strong emission lines have been empirically and/or theoretically calibrated (for a review see Kewley & Ellison 2008). Empirical diagnostics are typically calibrated to metallicities measured from temperature sensitive auroral lines (e.g., Pettini & Pagel 2004). Theoretical calibrations rely on detailed photoionization modeling to derive metallicity diagnostics (e.g., Kewley & Dopita 2002). Kewley & Ellison (2008) show that there are systematic offsets in the absolute metallicities derived using different diagnostics. However, they find that both the empirically and theoretically calibrated metallicity diagnostics are relatively accurate. Our results only depend on relative accuracy in measurements of metallicity. The metallicity diagnostics we use deliver relative accuracy at the level required for this work.

For the SDSS, SHELS and DEEP2 samples we derive metallicities using the $R23$ strong line method calibrated by Kobulnicky & Kewley (2004, hereafter KK04). A major advantage of this method is that it explicitly solves and corrects for the ionization parameter which may evolve with redshift (Kewley et al. 2013). The relevant ratios of measured emission line intensities are

$$R23 = \frac{[\mathrm{OII}]\lambda 3727 + [\mathrm{OIII}]\lambda 4959 + [\mathrm{OIII}]\lambda 5007}{\mathrm{H}\beta} \tag{10.3}$$

and

$$O32 = \frac{[\mathrm{OIII}]\lambda4959 + [\mathrm{OIII}]\lambda5007}{[\mathrm{OII}]\lambda3727}. \tag{10.4}$$

The SDSS line fluxes are corrected for dust extinction. For the SHELS and DEEP2 data we use the line equivalent widths[5]. We assume that the [OIII]λ5007 to [OIII]λ4959 intensity ratio is 3 (Osterbrock 1989) and adopt a value of 1.33 times the [OIII]λ5007 intensity when summing the [OIII]λ5007 and [OIII]λ4959 line fluxes or equivalent widths. The $R23$ method is sensitive to the ionization state of the gas and the $O32$ ratio is used to correct for variations. The $R23$ method has two metallicity branches. All galaxies in this study are sufficiently massive to be on the upper branch. The intrinsic uncertainty of an individual measurement is ~ 0.1 dex (Kobulnicky & Kewley 2004).

A disadvantage of using the $R23$ method is that the emission lines used in the diagnostic are separated by $\sim 1300\mathring{A}$. For high redshift galaxies, observing such large baselines is very time intensive and not feasible in large samples. The $N2$ method requires only the line flux ratio of the [NII]λ6584 to Hα. Because the lines are closely spaced in wavelength, an extinction correction is not required. We apply the $N2$ method calibrated by Pettini & Pagel (2004, hereafter PP04) to the summed-spectra emission line fluxes measured from the FMOS-COSMOS sample at $z \sim 1.6$. The intrinsic uncertainty of an individual measurement is 0.18 dex.

There is an absolute offset of $\sim$ 0.3 dex between the metallicities measured using empirically and theoretically calibrated diagnostics. By applying different diagnostics to the same $\sim 30,000$ galaxies in the SDSS, Kewley & Ellison (2008) derive formulae to convert metallicities from one baseline diagnostic to another. We convert metallicities measured for the FMOS-COSMOS sample using the PP04 diagnostic to the KK04 diagnostic using the conversion formulae in Kewley & Ellison (2008).

At metallicities above solar, the $N2$ diagnostic saturates (Baldwin et al. 1981; Kewley & Dopita 2002). The metallicity of the highest stellar mass bin of the FMOS-COSMOS sample

[5]Equivalent widths may be substituted for dust corrected line flux ratios when measuring metallicities (Kobulnicky & Phillips 2003; Zahid et al. 2011; Moustakas et al. 2011).

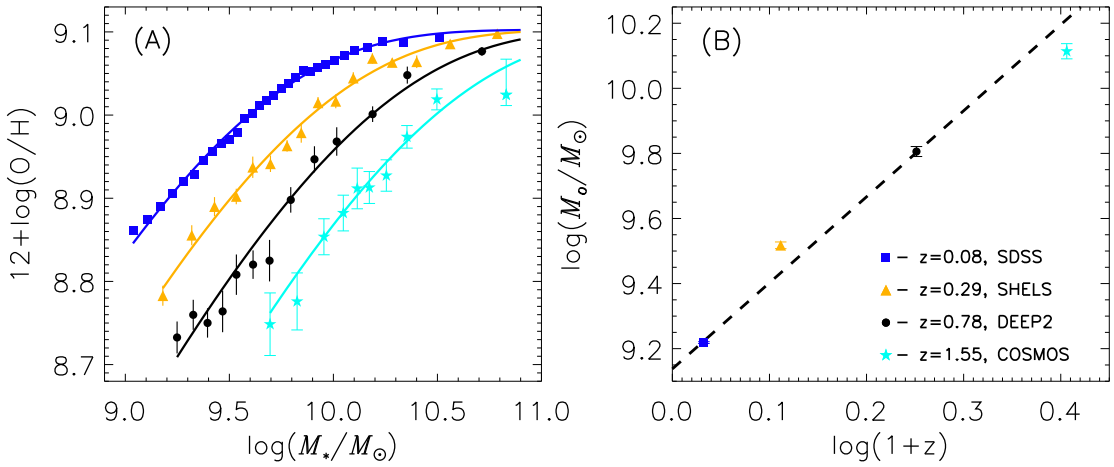

Figure 10.1 (A) The MZ relation for $z \lesssim 1.6$. The solid curves are the best single parameter model fits to the MZ relation. The model is defined in Equation 10.5. Z_o and γ fixed to the locally measured value from the SDSS data. (B) The best fit value of M_o as a function of redshift. The dashed line is a fit to M_o as a function of redshift and is given by Equation 10.8.

suffers from this saturation. Since we have a limited number of objects with individual line detections in the FMOS-COSMOS sample and we have no independent estimate of the metallicity for the galaxies affected by saturation, we are not able to quantify and correct for the systematic underestimate. From analysis of local SDSS galaxies, we estimate that the systematic effect of $N2$ saturation results in a ~ 0.03 dex underestimate of the metallicity. Rather than apply a 0.03 dex correction to the data, we take a more conservative approach and add 0.03 dex to the uncertainty of the metallicity measured in the highest stellar mass bin of the FMOS-COSMOS sample.

Throughout this work, the metallicity is given as a ratio of the number of oxygen atoms to hydrogen atoms and is quoted as 12 + log(O/H).

10.4 The Mass-Metallicity Relation

We derive the MZ relation for the SDSS, SHELS and DEEP2 samples by binning the metallicities measured in individual galaxies. We sort the SDSS, SHELS and DEEP2 data

into 30, 16 and 13 equally populated stellar mass bins, respectively. We calculate the median stellar mass and metallicity in each bin. The metallicity error associated with the median in each bin is determined from bootstrapping the data. The MZ relation we measure from the FMOS-COSMOS sample is derived from emission lines measured from summed spectra sorted into 10 bins of stellar mass. The metallicity errors are calculated from propagating the observational uncertainties.

Many mathematical models may quantitatively fit data but not all models are physically interpretable. For example, the MZ relation can be fit by a polynomial. However, the best fit parameters derived from a polynomial fit can not be straightforwardly interpreted since the model parameters are not related to physical quantities. We propose a new model for fitting the MZ relation which we can physically interpret. This model is similar in form to the model proposed by Moustakas et al. (2011) and used in Zahid et al. (2013a). We emphasize that the parameterization adopted in this work is different. Our interpretation of the fit parameters is presented in the following section (Section 10.5). We model the MZ relation as

$$12 + \log(O/H) = Z_o + \log\left[1 - \exp\left(-\left[\frac{M_*}{M_o}\right]^{\gamma}\right)\right]. \tag{10.5}$$

In this model, Z_o is the saturation metallicity. It quantifies the asymptotic upper metallicity limit (Moustakas et al. 2011; Zahid et al. 2013a). M_o is the characteristic turnover mass above which the metallicity asymptotically approaches the upper metallicity limit, Z_o. At stellar masses $< M_o$, the MZ relation reduces to a power law with an index γ.

We fit the MZ relation with the model parameterized by Equation 10.5 using the *MPFIT* package implemented in IDL (Markwardt 2009). The data are inverse variance weighted and the errors are propagated through to the fit parameters. The best fit parameters and errors are given in the top half of Table 10.1. For all four samples, the values of Z_o and γ are consistent within the errors ($\lesssim 2\sigma$). We also fit the data with a single parameter model in which we fix Z_o and γ to the SDSS values, allowing only M_o to vary. The single parameter model values are listed in the bottom half of Table 10.1.

Table 10.1. MZ Relation Fit

Sample	Redshift	Z_o	$\log(M_o/M_\odot)$	γ	χ^2_r
			BEST FIT		
SDSS	0.08	9.102±0.002	9.219±0.007	0.513±0.009	1.89
SHELS	0.29	9.102±0.004	9.52±0.02	0.52±0.02	1.68
DEEP2	0.78	9.10±0.01	9.80±0.05	0.52±0.04	1.28
COSMOS	1.55	9.08±0.07	10.06±0.20	0.61±0.15	0.47
			Z_o, γ FIXED		
SDSS	0.08	9.102	9.219±0.003	0.513	1.89
SHELS	0.29	9.102	9.52±0.01	0.513	1.46
DEEP2	0.78	9.102	9.81±0.02	0.513	1.08
COSMOS	1.55	9.102	10.11±0.02	0.513	0.52

We plot the MZ relation for $z \lesssim 1.6$ in Figure 10.1A. The data show that at a fixed stellar mass, the metallicity increases as the Universe evolves. The MZ relation flattens at high stellar masses. Massive metal-rich galaxies at high redshifts have metallicities comparable to massive local galaxies. In Zahid et al. (2013a) we show the flattening of the MZ relation results from galaxies enriching to an empirical metallicity limit. This limit is parameterized by Z_o and does not evolve significantly with redshift. The solid curves in Figure 10.1A show the single parameter model fits. The redshift evolution of the MZ relation can be parameterized solely by evolution in the characteristic turnover mass. The value of M_o derived from fitting the single parameter model is plotted in Figure 10.1B. The single parameter model fit to the data shows that the characteristic turnover mass, M_o, is an order of magnitude larger at $z \sim 1.6$. In Section 10.5 and 10.6 we elucidate the physical basis for this evolution.

We test the null hypothesis that three parameter model better reproduces the data. The reduced χ^2 values for the three and single parameter model fits are given in Table 10.1. An F-test analysis confirms that the three parameter model does not provide an statistically significant improvement to the fit.

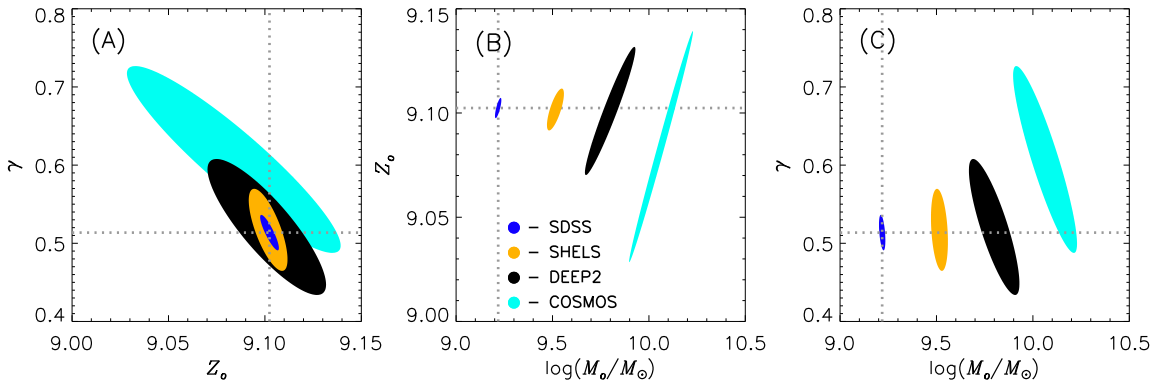

Figure 10.2 The error ellipses indicating the covariance between the fit parameters. The best-fit values of Z_o, M_o and γ and their errors are given in the top half of Table 10.1. The parameter errors are determined by propagating the observational uncertainties and the error ellipses are calculated from the covariance matrix. The dotted gray lines indicate the best fit value of Z_o and γ from the SDSS data.

The parameters of the model given by Equation 10.5 are covariant. In Figure 10.2 we examine the covariance of the best-fit parameters. We plot the 95% confidence ellipse. For clarity in the figure, the error ellipses for the FMOS-COSMOS fit are decreased by a scale factor of three. The dotted gray lines are the best-fit values of the parameters for the SDSS data. In Figure 10.2A we plot the covariance of γ and Z_o. Figure 10.2B and 10.2C show the covariance between Z_o and M_o and γ and M_o, respectively. The data show that there is clear evolution in M_o. The orientation of the error ellipse indicates that Z_o and M_o are weakly covariant in all four samples. There is little to no covariance between Z_o and γ for the SDSS and SHELS samples. There is a small degree of covariance between Z_o and γ for the DEEP2 and FMOS-COSMOS sample.

We conclude that the one parameter model is sufficient to describe the data and the best-fit value of M_o is not strongly dependent on our choice to fix Z_o and γ to the SDSS values.

The MZ relation for $z \lesssim 1.6$ is a simple function of redshift. The parameters in Equation 10.5 that fit the redshift dependent MZ relation are

$$Z_o = 9.102 \pm 0.002, \tag{10.6}$$

$$\gamma = 0.513 \pm 0.009, \tag{10.7}$$

and

$$\log(M_o/M_\odot) = (9.138 \pm 0.003) + (2.64 \pm 0.05)\log(1+z). \tag{10.8}$$

The redshift evolution of the MZ relation for $z \lesssim 1.6$ is sufficiently parameterized by evolution in the characteristic turnover mass, M_o.

The data are consistent with a single, redshift independent value for Z_o and γ. The fact that the MZ relation evolution only depends on the characteristic turnover mass, M_o, means that relation between metallicity and stellar mass scaled by M_o is independent of redshift. We plot the relation between metallicity and $\gamma\log(M_*/M_o)$ in Figure 10.3. The key to unlocking the origin of the MZ relation is our ability to explain the relation plotted in Figure 10.3. Thus we must determine physical meaning of Z_o, γ and M_o.

10.5 An Analytical Model of Chemical Evolution

We begin our exploration of the physical origin of the MZ relation by examining analytical models of chemical evolution. The equations below do not necessarily have analytical solutions. We will make several physically motivated simplifying assumptions to arrive at an analytical solution. We recommend Edmunds (1990) for a general discussion of analytical models of chemical evolution.

While metallicities are traditionally quoted as a number density of oxygen to hydrogen, in the following discussion we define the metallicity as $Z \equiv M_z/M_g$. Here M_z is the mass of oxygen in the gas-phase and M_g is the hydrogen gas mass. A constant scale factor relates metallicity defined in terms of mass density to metallicity defined in terms of number density

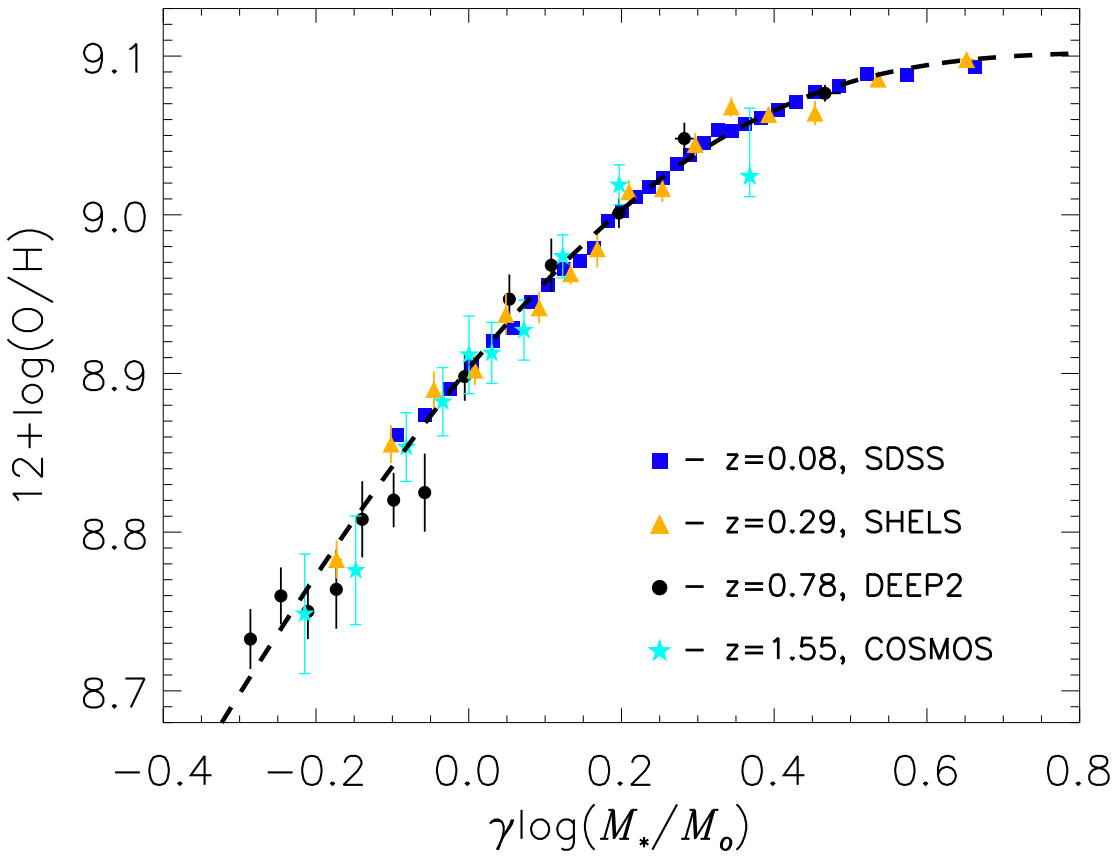

Figure 10.3 The metallicity plotted against the stellar mass normalized to the measured characteristic turnover mass, M_o of each data set. The dashed curve is given by Equation 10.5 and the parameters are given in Table 10.1 under the heading "Z_o, γ FIXED".

(Peeples & Shankar 2011). We analyze the case of a single galaxy as it evolves chemically. We can thus parameterize the problem only in terms of stellar mass. To model the chemical evolution of arbitrary galaxy populations, time must be included in the equations. In this case, partial derivatives replace all derivatives below. The analytical solution that we derive based on a single galaxy is generalizable to the case of an arbitrary galaxy population. Our interpretation is independent of whether we analyze the case of a single galaxy or a population of galaxies.

We start with the equation of chemical evolution describing the change in the metallicity with respect to stellar mass. This is given by

$$\frac{\mathrm{d}Z}{\mathrm{d}M_*} = \frac{\mathrm{d}}{\mathrm{d}M_*}\left(\frac{M_z}{M_g}\right) = \frac{1}{M_g}\left(\frac{\mathrm{d}M_z}{\mathrm{d}M_*} - Z\frac{\mathrm{d}M_g}{\mathrm{d}M_*}\right). \tag{10.9}$$

From observations we know that at low stellar masses we have an MZ relation with a positive power law index. In this case we necessarily have

$$\frac{\mathrm{d}M_z}{\mathrm{d}M_*} > Z\frac{\mathrm{d}M_g}{\mathrm{d}M_*}. \tag{10.10}$$

When the metallicity is small, the second term of Equation 10.9 ($Z\frac{\mathrm{d}M_g}{\mathrm{d}M_*}$) is negligible. From measurements of the stellar and gas content of galaxies in the local Universe, we have that $M_g \propto \sqrt{M_*}$ (Papastergis et al. 2012; Peeples et al. 2013). The change in gas mass with respect to stellar mass is then $\mathrm{d}M_g/\mathrm{d}M_* \propto 1/\sqrt{M_*}$. At higher stellar masses, the second term of the right hand side of Equation 10.9 ($Z\frac{\mathrm{d}M_g}{\mathrm{d}M_*}$) tends to zero. In this case, the change in metallicity with respect to stellar mass can be approximated by

$$\frac{\mathrm{d}Z}{\mathrm{d}M_*} \approx \frac{1}{M_g}\frac{\mathrm{d}M_z}{\mathrm{d}M_*}. \tag{10.11}$$

This equation simply states that the chemical evolution of a galaxy is dominated by the production of metals and not by a slowly changing gas reservoir.

To solve Equation 10.11 we must define the right hand side. The change in oxygen mass is given by

$$\mathrm{d}M_z = Y\mathrm{d}M_* - Z\mathrm{d}M_* + RZ\mathrm{d}M_* + Z_i\mathrm{d}M_i - Z_w\mathrm{d}M_w. \tag{10.12}$$

The first term on the right hand side is the production of newly synthesized oxygen where Y is the nucleosynthetic yield. Y is the mass of oxygen created per unit SFR. $\mathrm{d}M_*$ is the mass of newly formed stars, i.e. the SFR. Y does not depend strongly on any galaxy properties (Thomas et al. 1998; Kobayashi et al. 2006). We treat Y as a constant. The second term on the right hand side is the mass of oxygen in the ISM that forms into stars. The second

term is negative indicating that the oxygen going into stars is taken out of the ISM. The third term on the right hand side is the mass of oxygen that goes into stars but is returned back to the ISM via stellar mass loss where R is the fraction of mass returned back to the ISM. The third term represents previously synthesized oxygen returned back to the ISM by stellar winds and supernovae. The timescale for stellar mass return is short compared to the galaxy evolution timescale. We assume that stellar mass is instantaneously returned back into the ISM. The fourth and fifth terms represent the inflows and outflows (winds) of oxygen, respectively. The terms Z_i, $\mathrm{d}M_i$, Z_w and $\mathrm{d}M_w$ are the inflow metallicity, mass rate of inflow, outflow metallicity and mass rate of outflows, respectively. Dividing Equation 10.12 by $\mathrm{d}M_*$ we obtain

$$\frac{\mathrm{d}M_z}{\mathrm{d}M_*} = Y - Z(1-R) + Z_i\frac{\mathrm{d}M_i}{\mathrm{d}M_*} - Z_w\frac{\mathrm{d}M_w}{\mathrm{d}M_*}. \tag{10.13}$$

This equation is the rate of change of the oxygen mass with respect to the SFR.

We combine the effects of outflows and inflows into a single factor defined as

$$\zeta \equiv Z_w\frac{\mathrm{d}M_w}{\mathrm{d}M_*} - Z_i\frac{\mathrm{d}M_i}{\mathrm{d}M_*}. \tag{10.14}$$

ζ is the oxygen mass loss factor. Each of the terms on the right hand side of Equation 10.14 are uncertain (see Zahid et al. 2014). However, in Zahid et al. (2012b) we derive empirical constraints for the net loss of oxygen from galaxies. We show that the total mass of oxygen expelled from galaxies over their lifetime is nearly proportional to their stellar mass. This means

$$\int_0^{M_*} \zeta \mathrm{d}M'_* \propto M_*, \tag{10.15}$$

implying that ζ is constant. In a more recent empirical analysis, Peeples et al. (2013) confirm that the mass of oxygen lost relative to the mass of oxygen produced is independent of stellar mass in star-forming galaxies. They estimate that on average, galaxies lose $\sim 80\%$ of the oxygen they produce. The physical mechanism of outflows is not well understood though it

is generally considered to be driven by energy/momentum from massive stars. Perhaps it is not that surprising that the mass of oxygen expelled from a galaxy scales with stellar mass since the total energy/momentum which is responsible for driving outflows in a galaxy is directly proportional to current stellar mass. With the adoption of ζ as a constant we have

$$\frac{\mathrm{d}Z}{\mathrm{d}M_*} \approx \frac{Y_N - Z(1-R)}{M_g}. \tag{10.16}$$

Here we have combined the production and loss of oxygen, both of which are proportional to stellar mass, into a single term defined as $Y_N \equiv Y - \zeta$. We refer to this as the net yield. The net yield is the mass of oxygen produced by star formation modulo the oxygen expelled from the ISM.

The measured hydrogen gas mass of star forming galaxies is reasonably well described by a power law over ~ 4 decades in stellar mass (Papastergis et al. 2012; Peeples et al. 2013). To solve Equation 10.16 we parameterize the relation between gas mass and stellar mass by

$$M_g = G M_*^g, \tag{10.17}$$

where G is the zero point and g is the power law index of the relation. The solution to Equation 10.16 is

$$Z(M_*) = \frac{Y_N}{1-R}\left[1 - \exp\left(-\left[\frac{1-R}{1-g}\right]\frac{M_*}{M_g}\right)\right]. \tag{10.18}$$

This equation has the same form as the equation we fit to the MZ relation (Equation 10.5). By taking the logarithm of Equation 10.18, we can directly relate our fit parameters in Equation 10.5 to the physical parameters analytically describing chemical evolution. The asymptotic metallicity Z_o is

$$Z_o = \log\left(\frac{Y_N}{1-R}\right). \tag{10.19}$$

The maximum metallicity observed in galaxies is set by the net yield, Y_N. From Equation 10.16 we see that the metallicity saturates ($\mathrm{d}Z/\mathrm{d}M_* \approx 0$) when the amount of metals produced, Y_N, equals the amount of metals locked up in stars, $Z(1-R)$. The arguments

of the exponentials in Equations 10.5 and 10.18 can be equated to give

$$\frac{1-R}{1-g}\left(\frac{M_*}{M_g}\right) \approx \frac{M_*}{M_g} \approx \left(\frac{M_*}{M_o}\right)^{\gamma}. \tag{10.20}$$

The return fraction R and the power law index of the gas mass relation, g, are nearly equal ($R \sim g \sim 0.5$). Hereafter, we drop the prefactor term of the left hand side of Equation 10.20. Substituting our relation for the gas mass as a function of stellar mass from Equation 10.17 we have

$$\left(\frac{M_*}{M_o}\right)^{\gamma} \approx \frac{M_*^{1-g}}{G} \tag{10.21}$$

The low mass end slope we fit to the MZ relation, γ, is related to the power law index of the gas mass relation by $\gamma = 1 - g$. The characteristic turnover mass, M_o, is related to the zero point of the relation between gas mass and stellar mass by $M_o = G^{1/\gamma}$. M_o is the stellar mass at which the gas-to-stellar mass ratio is unity. This interpretation suggests that the redshift evolution of the MZ relation is due to the larger gas masses of galaxies at early times. From examination of Equation 10.20, we learn that universal relation plotted in Figure 10.3 is a relation between metallicity and stellar-to-gas mass ratio, M_*/M_g.

We test the consistency of our interpretation by comparing the observed gas-to-stellar mass relation in local galaxies with the SDSS MZ relation fit parameters. Peeples et al. (2013) derive the relationship between gas mass and stellar mass from ~ 260 star-forming galaxies where both the atomic and molecular gas masses are measured. The relation they derive is given by $\log(M_g/M_*) = -0.48\log(M_*/M_\odot) + 4.39$. For this relation, $g = 0.52$ and $M_g = M_*$ at $\log(M_*/M_\odot) = 9.15$. Our interpretation says that the $\gamma = 1 - g$ and M_o is the stellar mass where the gas-to-stellar mass ratio is unity. Based on the gas-to-stellar mass relation measured by Peeples et al. (2013) we would predict an MZ relation with $\gamma = 1 - g = 0.48$ and $M_o = 9.15$. We measure $\gamma = 0.51$ and $M_o = 9.2$ for the local relation. The fit parameters of the SDSS MZ relation are remarkably consistent with the measured gas-to-stellar mass relation in local galaxies.

10.6 A Numerical Model of Chemical Evolution

The simplifying assumptions made in deriving an analytical solution may obfuscate our interpretation. In this section we numerically model the chemical evolution of galaxies. The model serves as a heuristic tool to explore the validity of our interpretation of the MZ relation.

We self-consistently model the metallicity of galaxy populations as they evolve applying empirical constraints for their stellar mass growth. To derive the star formation history (SFH) of galaxies, we use the approach developed in Zahid et al. (2012b) (also see Leitner 2012). Galaxies exhibit a tight relation (~ 0.25 dex scatter) between stellar mass and SFR out to at least $z \sim 2$ (Noeske et al. 2007; Salim et al. 2007; Elbaz et al. 2007; Pannella et al. 2009; Whitaker et al. 2012; Zahid et al. 2012b; Kashino et al. 2013). Observations allow us to parameterize the SFR as a function of stellar mass and redshift. To derive the stellar mass histories of star-forming galaxies, we require that as galaxies evolve, they remain on the mean stellar mass-SFR (MS) relation at all epochs. The stellar mass history is given by

$$M_*(t) = (1 - R) \int_{t_i}^{t} \Psi(M_*, t')dt'. \tag{10.22}$$

$\Psi(M_*, t)$ is the star formation rate as a function of stellar mass and time. It is derived from observations of the MS relation at several epochs and is given by Equation 13 in Zahid et al. (2012b). The integration is carried out from some initial time, t_i to some later time, t.

The rate at which oxygen accumulates in the ISM is given by

$$\frac{\mathrm{d}M_g^o}{\mathrm{d}t} = Y_N \Psi - \frac{\mathrm{d}M_*^o}{\mathrm{d}t} \tag{10.23}$$

Here M_g^o is the mass of oxygen in the gas phase. The first term on the right hand side is the net production term where as before, Y_N, is the net yield. The first term accounts for oxygen production and loss in outflows. The second term on the right hand side is the rate

at which oxygen is locked up into stars and is given by

$$\frac{\mathrm{d}M_*^o}{\mathrm{d}t} = (1 - R)Z\Psi. \tag{10.24}$$

Here M_*^o is the mass of oxygen locked up in stars. Both Z and Ψ are explicitly dependent on time and stellar mass. We set the return fraction to $R = 0.45$ which is appropriate for a Chabrier IMF (Leitner & Kravtsov 2011).

The time rate of change of the metallicity depends on the mass of oxygen produced, the mass of oxygen locked up in stars, which is itself dependent on the metallicity of the gas at the time of star formation and the change in the gas content as the galaxy evolves. The time rate of change of metallicity is given by

$$\frac{\mathrm{d}Z}{\mathrm{d}t} = \frac{\mathrm{d}}{\mathrm{d}t}\left(\frac{M_g^o}{M_g}\right), \tag{10.25}$$

Equation 10.25 is just a restatement of Equation 10.9. We can numerically solve Equation 10.25 without the simplifying assumptions required in arriving at an analytical solution. The last quantity we need to numerically solve Equation 10.25 is the gas mass which we parameterize as a function of stellar mass and time:

$$\log(M_g/M_\odot) = G + \alpha \log(1 + z) + \beta \log(M_*/M_\odot). \tag{10.26}$$

In this parameterization G is the zero point of the gas mass at $z = 0$ and α and β parameterize the redshift and stellar mass dependence, respectively.

The solution to Equation 10.25 is the metallicity history of an individual galaxy as it evolves. Equations 10.23 - 10.25 are three coupled differential equations. We numerically solve these equations using an iterative method and a time step of 0.01 Myr. We solve Equation 10.25 for a population of galaxies which covers a wide range in stellar mass. From the metallicity history of a population of galaxies, we can calculate the MZ relation at

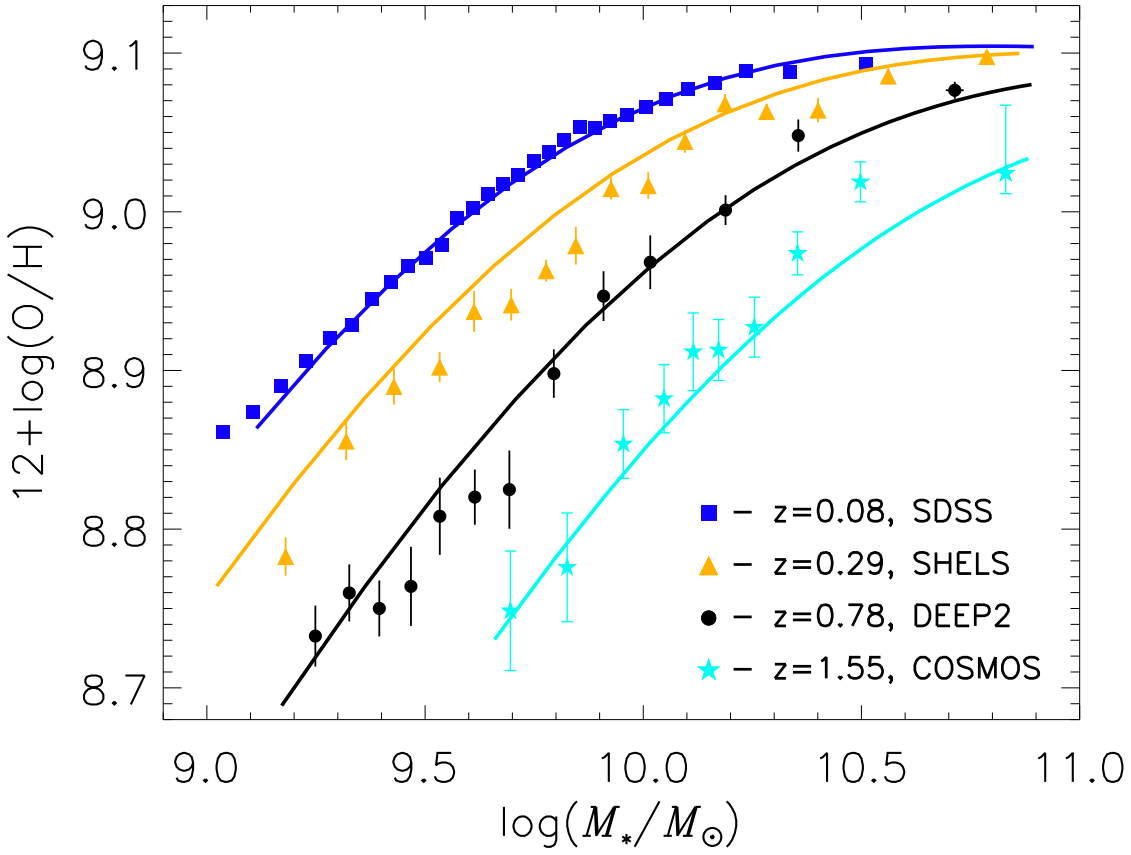

Figure 10.4 The MZ relation ranging for $z \lesssim 1.6$. The solid curves are the MZ relations determined from the numerical model by solving Equation 10.25.

each observed epoch. Y_N, G, α and β are free parameters in our model. We vary these parameters in order to reproduce the observed MZ relations.

In Figure 10.4 we show the model MZ relations plotted over the observed MZ relations. The model parameters are $Y_N = 5.7 \times 10^{-3}$, $G = 5.04$, $\alpha = 1.34$ and $\beta = 0.44$. The gas mass relation in our model that produces the model results in Figure 10.4 is given by

$$\log(M_g/M_\odot) = 5.04 + 1.34 \log(1+z) + 0.44 \log(M_*/M_\odot). \tag{10.27}$$

This implies a slope of the MZ relation $\gamma = 1 - g = 0.56$, close to our measured value of $\gamma = 0.513$. By combining Equations 10.8 and 10.20 we can derive the gas mass relation implied by observations as in Section 10.5. The gas mass relation inferred from observations is

$$\log(M_g/M_\odot) = 4.82 + 1.37\log(1+z) + 0.47\log(M_*/M_\odot). \quad (10.28)$$

The gas mass relation derived from our observations (Equation 10.28) is very similar to the relation required in our model to reproduce the MZ relation (Equation 10.27). We emphasize that our numerical model reproduces the data remarkably well considering that both the metallicities and stellar masses carry ~ 0.3 dex absolute systematic uncertainties (Kewley & Ellison 2008; Conroy 2013).

The purpose of this exercise is to test many of the assumptions made in the previous section. The model parameters for the gas mass relation are derived by fitting to the observed MZ relations using the simple equations of chemical evolution given by Equations 10.23 - 10.25. The analysis based on our models is independent of the analysis presented in Section 10.6. The fact that we are able to reproduce the evolution of the MZ relation suggests that the interpretation presented in the previous section is consistent with the observed MZ relation. In particular, the model analysis confirms that the following simplifications and interpretations are consistent with the data: 1) The build-up of metals, and not a changing gas reservoir, is the dominant process governing the evolution of the metallicity in individual galaxies. The second term on the right hand side of Equation 10.9 is negligible compared to the first term. 2) The slope of the MZ relation is related to the slope of the gas mass relation and is reasonably approximated by $\gamma \approx 1 - g$. The slope of the gas-to-stellar mass relation is not strongly dependent on redshift. 3) The evolution of the characteristic turnover mass of the MZ relation, M_o, is related to the evolution of the zero point of the gas mass relation. 4) The MZ relation saturates when the mass of oxygen produced by massive stars equals the mass of oxygen locked up by low mass stars.

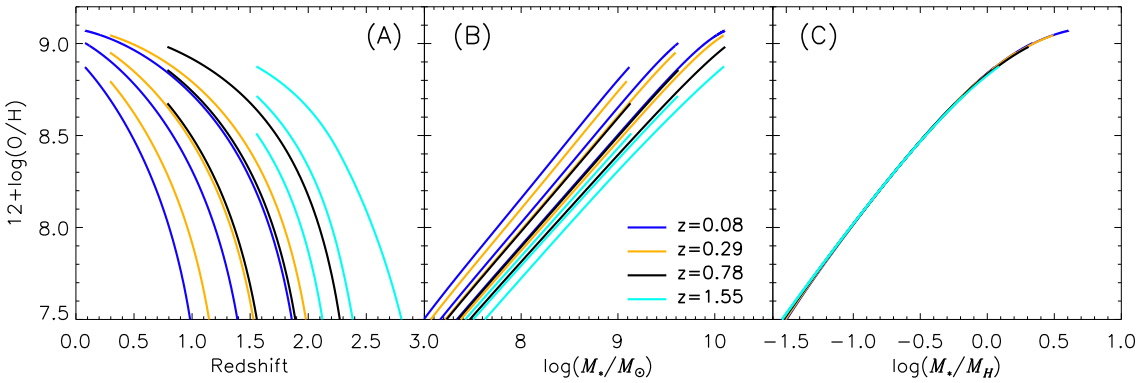

Figure 10.5 The metallicity as a function of (A) redshift, (B) stellar mass and (C) stellar-to-gas mass ratio for individual model galaxies. We plot three galaxies with final stellar mass $\log(M_*/M_\odot) \sim 9.5, 10, 10.5$ at each of the four epochs where we observe the MZ relation.

The metallicity relation plotted in Figure 10.3 is a significant observational result. In Section 10.6 we interpret the relation plotted in Figure 10.3 as a universal relation between metallicity and the stellar-to-gas mass ratio, M_*/M_g. The MZ relation is a snapshot of the chemical properties of a population of galaxies at an instant in time. If the relation between metallicity and stellar-to-gas mass ratio is indeed universal, it should apply to individual galaxies as they evolve. Our numerical model allows us to examine the chemical evolution of one galaxy over time. In Figure 10.5A, 10.5B and 10.5C we plot the chemical evolution of individual model galaxies as a function of redshift, stellar mass and stellar-to-gas mass ratio, respectively. We plot three galaxies with $\log(M_*/M_\odot) \sim 9.5, 10, 10.5$ as they evolve to each of the four epochs where we observe the MZ relation. Each galaxy in this plot finishes on the model MZ relation plotted in Figure 10.4, i.e. the end points of the evolution in Figure 10.5B are the MZ relations at the four epochs. Figure 10.5C shows galaxies evolve along a universal relation between metallicity and stellar-to-gas mass ratio. This type of evolution is not a generic result of the numerical model. It depends on the particular parameterization of the gas mass to stellar mass relation. The results of our numerical modeling support our interpretation based on analytical models.

10.7 The Observed Relation Between Metallicity and the Stellar-to-Gas Mass Ratio

We can observationally test our interpretation of the universal metallicity relation presented in Figure 10.3 with the ALFALFA sample cross-matched with SDSS (see Section 10.2.5).

We determine metallicities from strong nebular emission lines. The metallicity derived from an integrated spectrum is a global nebular luminosity-weighted measurement. Galaxies have gas disks that extend well beyond their stellar and star-forming disks (van der Kruit & Freeman 2011). The 3.5 arc-minute beam of the ALFALFA covers the outer disk of galaxies in the cross-matched sample. To make a proper apples-to-apples comparison of the gas mass and metallicity, we need to derive a gas mass that is weighted in a manner comparable to the nebular luminosity-weighting of the metallicity. The nebular luminosity is dominated by young, massive stars. The luminosity of young massive stars is proportional to the SFR. We derive the SFR-weighted hydrogen gas mass to properly compare with the luminosity-weighted metallicity we measure.

Bigiel & Blitz (2012) measure the hydrogen gas (HI + H_2) profile using resolved measurements from the HERACLES (Leroy et al. 2009) and THINGS (Walter et al. 2008) surveys. They observe a universal gas profile when the scale length is normalized to $R25$ and the surface density is normalized to the surface density at the transition radius where the HI to H_2 gas masses are equal. $R25$ is defined as the 25 mag arcsec^{-2} B-band isophote. Within $R25$ the measured gas profiles exhibits $\sim 25-40\%$ scatter. The universal gas profile Bigiel & Blitz derive is

$$\Sigma_{\rm gas} \propto e^{-1.65r/r_{25}}. \tag{10.29}$$

Here, r/r_{25} is the radius in units of $R25$. Leroy et al. (2008) combine FUV *GALEX* and 24 μm *Spitzer* imaging to measure the SFR profile. We calculate the average SFR profile in units of $R25$ from their measurements of 18 galaxies with $M_* > 10^9 M_\odot$. The average SFR profile is

$$\Sigma_{\rm SFR} \propto e^{-4.34r/r_{25}} \tag{10.30}$$

There is $\sim 30\%$ scatter in the average profile that we calculate.

We determine the SFR-weighted hydrogen gas mass from the gas and star formation rate profiles. The weighting factor is

$$W_{\rm SFR} = \frac{\int_0^\infty r\,\Sigma_{\rm gas}\,\Sigma_{\rm SFR}\,{\rm d}r}{\int_0^\infty r\,\Sigma_{\rm gas}\,{\rm d}r\int_0^\infty \Sigma_{\rm SFR}\,{\rm d}r} = 0.33. \tag{10.31}$$

On average, 1/3 of the gas in galaxies is located within their star-forming disks. The SFR-weighted hydrogen gas mass is

$$M_{\rm H} = W_{\rm SFR}\,M_{\rm H,measured}. \tag{10.32}$$

Here $M_{\rm H,measured}$ is the measurement from ALFALFA with the H_2 contribution estimated using scaling relations presented in Saintonge et al. (2011, see Section 10.2.5). The combined scatter from the gas and SFR profiles is ~ 0.3 dex. This lower limit for the uncertainty for the SFR-weighted hydrogen mass measurement does not include the observational uncertainty associated with the measurement.

In Figure 10.6 we observationally test our interpretation of the universal metallicity relation by plotting the metallicity as a function of the stellar-to-gas mass ratio observed in local galaxies. The black points are the 2633 galaxies in our cross-matched sample. The stellar masses, metallicities and hydrogen gas masses are directly measured. The blue dashed curve is the universal relation between metallicity and stellar-to-gas mass ratio plotted in Figure 10.3 using the relation given by Equation 10.20. The median metallicity in 12 equally populated bins of stellar-to-gas mass ratio is plotted by the red curve. The metallicity errors are bootstrapped. We have not required a minimum fiber covering fraction when selecting the SDSS data and the ALFALFA detection threshold likely biases the sample. Some of the deviations between the two curves may be attributed to these effects. Moreover, the stellar masses have ~ 0.1 dex observational uncertainty. This combined with the > 0.3 dex uncertainty in the hydrogen mass estimates means that the error on an individual measurement of the stellar-to-gas mass ratio is at least 0.4 dex. The blue and red curves

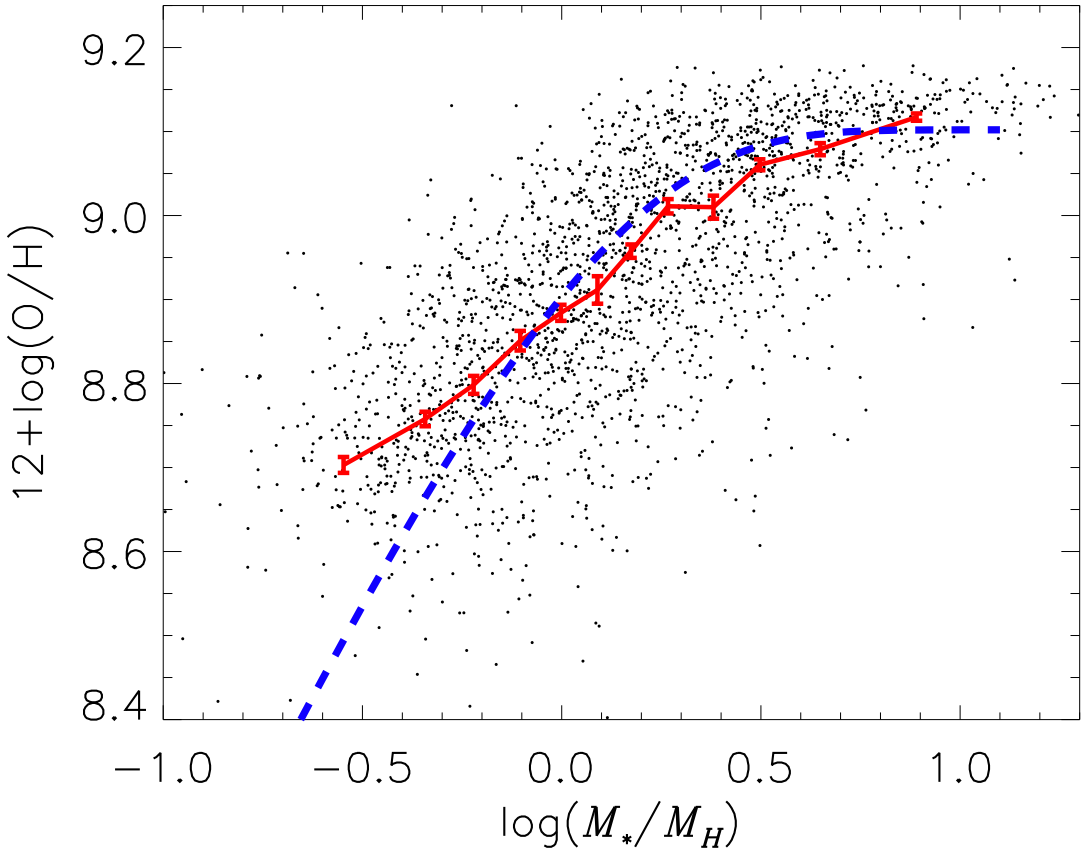

Figure 10.6 The metallicity as a function of the stellar-to-gas mass ratio. The black points are 2633 individual galaxies where we are able to estimate the metallicities, stellar and gas masses from observations. The red curve is the median metallicity in 12 equally populated bins of stellar-to-gas mass ratio. The blue curve is derived by combining Equation 10.5 and 10.20 and adopting the locally measured value of $Z_o = 9.102$.

differ by $\lesssim 0.1$ dex. This is good agreement in light of the large uncertainties involved in this measurement. We conclude that the observational data are consistent with the universal relation of chemical evolution.

10.8 Discussion

We analyze observations of the MZ relation for $z \lesssim 1.6$. The MZ relation exhibits very simple redshift evolution which we parameterize by redshift evolution in the characteristic

turnover mass where the metallicity begins to saturate. We physically interpret our fit parameters by comparing them to solutions of analytical models of chemical evolution. We test and strengthen our interpretation by numerically modeling the chemical evolution of individual galaxies. We observationally test our interpretation and show that it is consistent with the best data currently available. Our analysis provides a simple and intuitive perspective of galactic chemical evolution. *Galaxies follow a universal relation between metallicity and stellar-to-gas mass ratio as they evolve.* Metallicity is defined as the ratio of oxygen to hydrogen. The net mass of oxygen produced is directly proportional to galaxy stellar mass. Given the definition of metallicity, a universal relation between metallicity and stellar-to-gas mass ratio should be expected.

The chemical evolution of galaxies can be characterized as having three distinct regimes: gas-rich, gas-poor and gas-depleted. Figure 10.7 is a schematic which illustrates the three regimes. The gas-rich regime is plotted in blue. Galaxies are in the gas-rich regime when $M_g > M_*$. In the gas-rich regime, the metallicity is proportional to stellar-to-gas mass ratio. This can be seen by Taylor expanding Equation 10.18. The gas-poor regime is plotted in green. Galaxies cross over to the gas-poor regime when $M_g < M_*$. In the gas-poor regime the metallicity is high enough that the mass of oxygen that is being locked up in stars becomes an appreciable fraction of the mass of oxygen produced. Galaxies exponentially approach the metallicity saturation limit. The gas-depleted regime is plotted in red. Galaxies in the gas-depleted regime have $M_g/M_* \ll 1$. In this regime, the metallicity is so high that the mass of oxygen taken out of the ISM and locked up in low mass stars equals the mass of oxygen produced by massive stars. The metallicity can not increase beyond this point.

The MZ relation originates from the more fundamental universal relation between metallicity and stellar-to-gas mass ratio. At a fixed stellar mass, the metallicities of galaxies increase as the Universe evolves because of a commensurate decline in their gas content. The slope of the MZ relation at $M_* < M_o$ is set by the slope of the relation between gas mass and stellar mass. This is because the slope of the more fundamental relation between

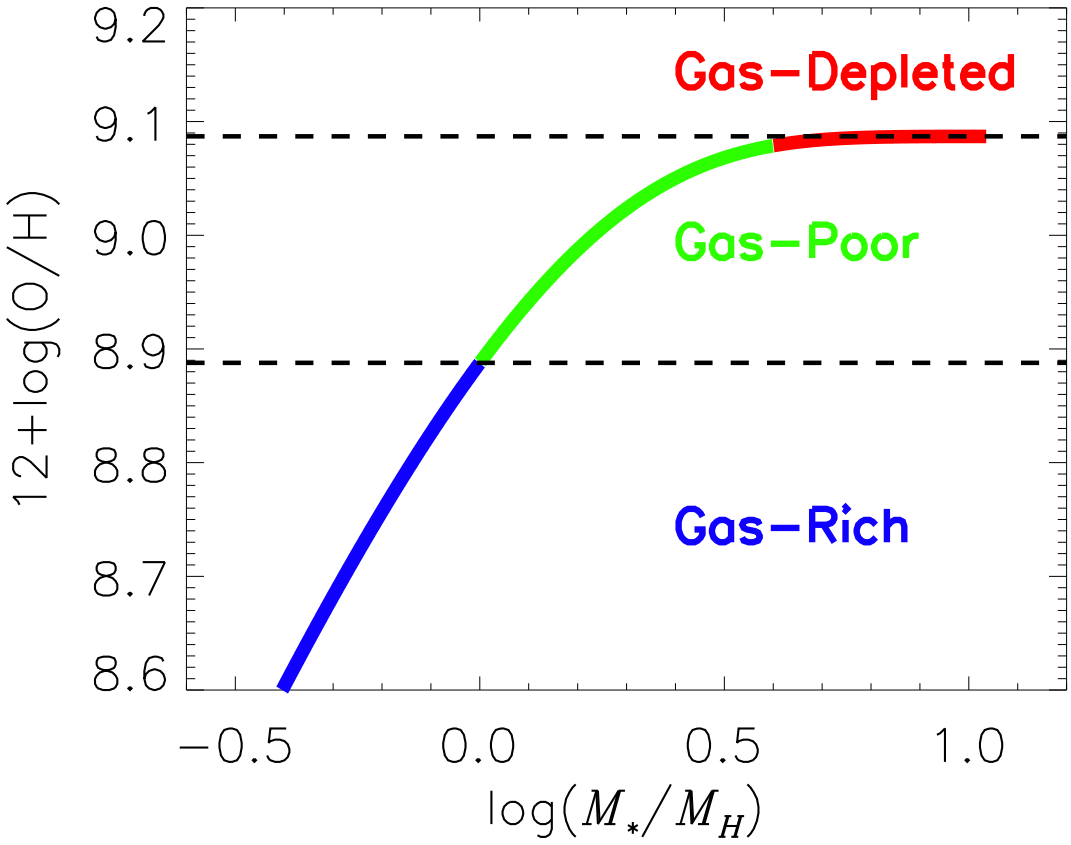

Figure 10.7 A schematic illustrating the three regimes of galactic chemical evolution.

metallicity and gas-to-stellar mass ratio is unity for galaxies with $M_* < M_o$ (see Equation 10.18). The scatter observed in the MZ relation largely reflects the scatter in gas mass at a fixed stellar mass. The relation between stellar mass, metallicity and SFR (e.g. Mannucci et al. 2010) is a natural consequence of the universal metallicity relation. At a fixed stellar mass, galaxies with larger gas reservoirs will typically exhibit elevated SFRs and diluted metallicities and vice versa. Several authors have recognized variations in the gas content of galaxies as the basis of the observed relation between stellar mass, metallicity and SFR (e.g., Davé et al. 2011; Dayal et al. 2013; Bothwell et al. 2013; Lilly et al. 2013; Davé et al. 2013).

The universal relation of chemical evolution implies that the metallicity of a galaxy is instantaneously set by its stellar-to-gas mass ratio. Gas flows and star formation move galaxies along−*not off*–the universal metallicity relation. Unlike the MZ relation in which the stellar mass is monotonically increasing, the stellar-to-gas mass ratio can increase or decrease. The response of galaxies to large gas accretion events will be to instantaneously move down the universal metallicity relation. Conversely, galaxies will move up the universal metallicity relation as they deplete their gas reservoirs by star formation and outflows.

The intrinsic scatter in the universal metallicity relation is likely to be small. At a fixed stellar mass we expect some scatter in the net yield, Y_N due to scatter in total mass of oxygen expelled from galaxies. Any scatter in the net yield would directly translate into scatter in the universal metallicity relation. Mergers and starbursts will likely also contribute to the scatter in the universal metallicity relation since these events significantly disrupt the ISM of galaxies. The observed scatter in the FMR of Mannucci et al. (2010) and HI FMR of Bothwell et al. (2013) is ~ 0.07 dex. Since the FMR is directly a result of the universal metallicity relation, the measured scatter in the FMR provides an upper limit for the scatter in the universal metallicity relation.

If our interpretation is correct, the metallicities of galaxies provide an accurate probe of their ISM gas content. We derive the relation between average gas mass and stellar mass by combining Equations 10.8 and 10.20. The average mass of hydrogen gas in the star-forming disk of galaxies as a function of redshift and stellar mass is

$$M_g(M_*, z) = 3.87 \times 10^9 \, (1+z)^{1.35} \left(\frac{M_*}{10^{10} M_\odot} \right)^{0.49} \; [M_\odot]. \tag{10.33}$$

In the absence of direct measurements, the gas mass of galaxies can be estimated from measurements of stellar mass and metallicity by combining Equation 10.5 and 10.20 and solving for M_g. The hydrogen gas mass as a function of stellar mass and metallicity is

$$M_g(M_*, Z) = \frac{-M_*}{\ln\left(1 - 10^{[Z - Z_o]}\right)} \; [M_\odot]. \tag{10.34}$$

The stellar mass is measured in units of $M_{\odot}$ and $Z_o = 9.10$. We emphasize that metallicities must be converted into the KK04 diagnostic when using Equation 10.34. Gas masses estimated using Equation 10.34 carry the uncertainties associated with stellar masses, metallicities and the intrinsic scatter in the universal metallicity relation. The relations presented by Equation 10.33 and 10.34 are valid for galaxies at $z \lesssim 1.6$. These relations are testable predictions of the gas content of galaxies based on the observed evolution of the MZ relation.

A tight relation between stellar mass and SFR (MS relation) is observed to extend out to at least $z \sim 2$ (Noeske et al. 2007; Salim et al. 2007; Elbaz et al. 2007; Pannella et al. 2009; Whitaker et al. 2012; Zahid et al. 2012b; Kashino et al. 2013). The slope of the MS relation does not evolve significantly with redshift and the zero point declines by a factor of ~ 20 since $z \sim 2$. The slope of the MZ relation is set by the slope of the relation between gas mass and stellar mass. From our observations we conclude that the slope does not evolve significantly for $z \lesssim 1.6$. The nearly constant slope of the MS relation is consistent with a constant slope that we infer for the relation between gas mass and stellar mass based on our measured MZ relations. From Equation 10.33, we estimate that the zero point of the relation between gas mass and stellar mass evolves by a factor of ~ 3 since $z \sim 1.6$. This evolution is significantly smaller than the zero point evolution of the MS relation. This implies that the star formation efficiency, the SFR relative to gas mass, increases with redshift. This increase may be the result of higher molecular-to-atomic hydrogen mass ratios in high redshift galaxies (see Dutton et al. 2010).

We have provided evidence for a universal relation between metallicity and stellar-to-gas mass ratio for galaxies at $z \lesssim 1.6$. Our observations only extend down to stellar masses of $\sim 10^9 M_{\odot}$ and gas-to-stellar mass ratios of ~ 0.5. By summing the spectra of $\sim 200,000$ galaxies in the SDSS, Andrews & Martini (2013) measure the MZ relation down to stellar masses of $\sim 10^{7.5} M_{\odot}$. They measure a continuous MZ relation which flattens at high stellar masses and scales as $O/H \propto M_*^{1/2}$ at stellar masses $< 10^9 M_{\odot}$. Our measurements are

consistent with the scaling of the MZ relation measured by Andrews & Martini (2013) suggesting that the universal metallicity relation may extend well into the dwarf regime.

Additional observational tests are needed to establish the universal metallicity relation. Measurements of stellar masses, metallicities and gas masses of dwarf galaxies will allow us to directly measure how low in stellar mass and stellar-to-gas mass ratio the universal metallicity relation extends . Metal-rich dwarf galaxies have been observed (Zahid et al. 2012a). These galaxies will provide an interesting test of the university metallicity relation. Measurements of gas masses for galaxies outside the local Universe will provide the most important test of the universal metallicity relation. The combination of *ALMA* and *SKA* will soon make this possible. Finally, we have examined the global properties of galaxies. The universal relation should be tested in galaxies where spatially resolved measurements of the metallicity and gas content are available. Several integral field surveys of nearby galaxies currently underway (e.g., SAMI, WALLABY, MANGA) should prove useful for further investigating the spatially resolved nature of the universal metallicity relation.

The physical basis of the universal metallicity relation needs to be explored in much greater detail. Several aspects of this work imply a cosmological origin for the relation. The evolution of the characteristic turnover mass, M_o, is proportional to $(1+z)^{2.6}$. This scaling with redshift is similar to the $(1+z)^{2.5}$ scaling of the growth rate of dark matter halos in simulations (Fakhouri et al. 2010). Additionally, our observations suggest that $M_g \propto \sqrt{M_*}$ for $z \lesssim 1.6$. This scaling of gas and stellar mass is similar to the scaling between stellar and halo mass, M_h, determined from abundance matching (Behroozi et al. 2013) and from galaxy-galaxy weak lensing, galaxy clustering and galaxy distribution (Leauthaud et al. 2012). This implies that M_g/M_h is nearly constant with respect to stellar mass. The slope of the relation between stellar mass and halo mass does not evolve significantly out to $z \sim 1.6$ (Leauthaud et al. 2012; Behroozi et al. 2013). An M_g/M_h ratio that is constant with stellar mass may be the physical origin for the constant slope of the relation between gas mass and stellar mass.

A detailed analysis of systematic issues related to measurements of the MZ relation should soon be possible as larger data sets become available. In particular, metallicities are derived using techniques that are calibrated using observations of local galaxies. If ISM conditions evolve with redshift, these calibrations may need to be revised. Our analysis is primarily based on the R23 diagnostic calibrated by Kobulnicky & Kewley (2004). However, long-standing discrepancies between various metallicity diagnostics remain unresolved (e.g., Kudritzki et al. 2008; Bresolin et al. 2009; Kudritzki et al. 2012; Nicholls et al. 2012; Dopita et al. 2013). Discrepancies between various metallicity diagnostics do not change the major conclusions of this work but the quantitative analysis presented is subject to these uncertainties. Additionally, larger and more complete spectroscopic samples combined with cosmological simulations should allow us to assess selection biases in our measurement of the MZ relation. The MZ relation appears to be insensitive to selection biases and we anticipate that correction for these biases will not change the major conclusions presented in this work.

10.9 Summary and Conclusions

We measure the MZ relation for $z \lesssim 1.6$ using a consistent methodology. We interpret our observations with the aid of analytical and numerical models. We propose a new paradigm for understanding the chemical evolution of galaxies. The main results of our analysis are that:

- The evolution of the MZ relation for $z \lesssim 1.6$ is very simple. The evolution can be parameterized solely by the redshift dependency of the characteristic turnover mass, M_o. M_o is the stellar mass where the MZ relation begins to flatten.The relation between metallicity and stellar mass normalized to M_o is independent of redshift for $z \lesssim 1.6$.

- We physically interpret the parameters we fit to the MZ relation using analytical and numerical models. The MZ relation saturates at a maximum metallicity, Z_o. The

saturation occurs when the gas-phase abundance is high enough that the mass of oxygen locked up in low mass stars equals the mass of oxygen produced by massive stars. Galaxies are not able to enrich beyond this metallicity. The slope of the MZ relation, γ, is set by the slope of the relation between gas mass and stellar mass. The characteristic stellar mass, M_o, is the stellar mass where the stellar-to-gas mass ratio is unity.

- We show that the redshift independent metallicity relation is a relation between metallicity and stellar-to-gas mass ratio. Numerical modeling suggests that all galaxies follow this metallicity relation as they evolve. We refer to the relation between metallicity and stellar-to-gas mass ratio as the universal metallicity relation.

- The MZ relation originates from the universal metallicity relation. The evolution of the MZ relation is due to the evolving gas content of galaxies.

- We directly measure the stellar masses, metallicities and gas masses for a sample of local galaxies. These data are consistent with the universal metallicity relation.

- We show that the chemical evolution of galaxies can be characterized by three distinct regimes of evolution. In the gas-rich regime when $M_g > M_*$ the metallicity is proportional to the stellar-to-gas mass ratio. In the gas-poor regime when $M_g < M_*$ metallicity exponentially approaches the saturation limit. In the gas-depleted regime when $M_g \ll M_*$, the metallicity is saturated and does not increase beyond this limit.

- The observed evolution of the MZ relation is due to the evolving of gas content of galaxies. We derive the average gas mass as function of stellar mass and redshift. The universal metallicity relation is a relation between stellar mass, metallicity and gas mass. We provide an equation to estimate gas mass from measurements of stellar mass and metallicity.

We outline some observational tests necessary to further validate the universal metallicity relation. *ALMA* combined with *SKA* will be transformative for our understanding of the gas

content of galaxies. These facilities should allow us to directly test the universal metallicity relation out to high redshifts.

References

Abazajian, K. N., et al. 2009, ApJS, 182, 543

Andrews, B. H., & Martini, P. 2013, ApJ, 765, 140

Baldwin, J. A., Phillips, M. M., & Terlevich, R. 1981, PASP, 93, 5

Behroozi, P. S., Wechsler, R. H., & Conroy, C. 2013, ApJ, 770, 57

Berg, D. A., et al. 2012, ApJ, 754, 98

Bigiel, F., & Blitz, L. 2012, ApJ, 756, 183

Bothwell, M. S., Maiolino, R., Kennicutt, R., Cresci, G., Mannucci, F., Marconi, A., & Cicone, C. 2013, MNRAS, 433, 1425

Bresolin, F., Gieren, W., Kudritzki, R.-P., Pietrzyński, G., Urbaneja, M. A., & Carraro, G. 2009, ApJ, 700, 309

Brooks, A. M., Governato, F., Booth, C. M., Willman, B., Gardner, J. P., Wadsley, J., Stinson, G., & Quinn, T. 2007, ApJ, 655, L17

Bruzual, G., & Charlot, S. 2003, MNRAS, 344, 1000

Bundy, K., et al. 2006, ApJ, 651, 120

Calura, F., Pipino, A., Chiappini, C., Matteucci, F., & Maiolino, R. 2009, A&A, 504, 373

Calzetti, D., Armus, L., Bohlin, R. C., Kinney, A. L., Koornneef, J., & Storchi-Bergmann, T. 2000, ApJ, 533, 682

Cardelli, J. A., Clayton, G. C., & Mathis, J. S. 1989, ApJ, 345, 245

Chabrier, G. 2003, PASP, 115, 763

Coil, A. L., Newman, J. A., Kaiser, N., Davis, M., Ma, C.-P., Kocevski, D. D., & Koo, D. C. 2004, ApJ, 617, 765

Conroy, C. 2013, ARA&A, 51, 393

Conroy, C., Graves, G., & van Dokkum, P. 2013, ArXiv e-prints

Daddi, E., Cimatti, A., Renzini, A., Fontana, A., Mignoli, M., Pozzetti, L., Tozzi, P., & Zamorani, G. 2004, ApJ, 617, 746

Dalcanton, J. J., Yoachim, P., & Bernstein, R. A. 2004, ApJ, 608, 189

Davé, R., Finlator, K., & Oppenheimer, B. D. 2011, MNRAS, 2110

Davé, R., Katz, N., Oppenheimer, B. D., Kollmeier, J. A., & Weinberg, D. H. 2013, MNRAS, 434, 2645

Davis, M., et al. 2003, in SPIE, ed. P. Guhathakurta, Vol. 4834, 161–172

Dayal, P., Ferrara, A., & Dunlop, J. S. 2013, MNRAS, 430, 2891

Dopita, M. A., Sutherland, R. S., Nicholls, D. C., Kewley, L. J., & Vogt, F. P. A. 2013, ApJS, 208, 10

Dutton, A. A., van den Bosch, F. C., & Dekel, A. 2010, MNRAS, 405, 1690

Edmunds, M. G. 1990, MNRAS, 246, 678

Elbaz, D., et al. 2007, A&A, 468, 33

Ellison, S. L., Patton, D. R., Simard, L., & McConnachie, A. W. 2008, ApJ, 672, L107

Erb, D. K., Shapley, A. E., Pettini, M., Steidel, C. C., Reddy, N. A., & Adelberger, K. L. 2006, ApJ, 644, 813

Faber, S. M., et al. 2003, in Society of Photo-Optical Instrumentation Engineers (SPIE) Conference Series, Vol. 4841, Society of Photo-Optical Instrumentation Engineers (SPIE) Conference Series, ed. M. Iye & A. F. M. Moorwood, 1657–1669

Fabricant, D., et al. 2005, PASP, 117, 1411

Fakhouri, O., Ma, C.-P., & Boylan-Kolchin, M. 2010, MNRAS, 406, 2267

Finlator, K., & Davé, R. 2008, MNRAS, 385, 2181

Foster, C., et al. 2012, A&A, 547, A79

Gallazzi, A., Charlot, S., Brinchmann, J., White, S. D. M., & Tremonti, C. A. 2005, MNRAS, 362, 41

Geller, M. J., Dell'Antonio, I. P., Kurtz, M. J., Ramella, M., Fabricant, D. G., Caldwell, N., Tyson, J. A., & Wittman, D. 2005, ApJ, 635, L125

Goulding, A. D., et al. 2012, ApJS, 202, 6

Haynes, M. P., et al. 2011, AJ, 142, 170

Hosek, Jr., M. W., et al. 2014, ArXiv e-prints

Hughes, T. M., Cortese, L., Boselli, A., Gavazzi, G., & Davies, J. I. 2012, ArXiv e-prints

Hummer, D. G., & Storey, P. J. 1987, MNRAS, 224, 801

Ilbert, O., et al. 2009, ApJ, 690, 1236

Kashino, D., et al. 2013, ApJ, 777, L8

Kewley, L. J., & Dopita, M. A. 2002, ApJS, 142, 35

Kewley, L. J., Dopita, M. A., Leitherer, C., Davé, R., Yuan, T., Allen, M., Groves, B., & Sutherland, R. 2013, ApJ, 774, 100

Kewley, L. J., & Ellison, S. L. 2008, ApJ, 681, 1183

Kewley, L. J., Groves, B., Kauffmann, G., & Heckman, T. 2006, MNRAS, 372, 961

Kewley, L. J., Jansen, R. A., & Geller, M. J. 2005, PASP, 117, 227

Kimura, M., et al. 2010, PASJ, 62, 1135

Kirby, E. N., Cohen, J. G., Guhathakurta, P., Cheng, L., Bullock, J. S., & Gallazzi, A. 2013, ApJ, 779, 102

Kobayashi, C., Umeda, H., Nomoto, K., Tominaga, N., & Ohkubo, T. 2006, ApJ, 653, 1145

Kobulnicky, H. A., & Kewley, L. J. 2004, ApJ, 617, 240

Kobulnicky, H. A., & Phillips, A. C. 2003, ApJ, 599, 1031

Köppen, J., Weidner, C., & Kroupa, P. 2007, MNRAS, 375, 673

Kudritzki, R.-P., Urbaneja, M. A., Bresolin, F., Przybilla, N., Gieren, W., & Pietrzyński, G. 2008, ApJ, 681, 269

Kudritzki, R.-P., Urbaneja, M. A., Gazak, Z., Bresolin, F., Przybilla, N., Gieren, W., & Pietrzyński, G. 2012, ApJ, 747, 15

Lara-López, M. A., et al. 2010, A&A, 521, L53+

—. 2013, MNRAS, 433, L35

Larson, R. B. 1974, MNRAS, 169, 229

Laskar, T., Berger, E., & Chary, R.-R. 2011, ApJ, 739, 1

Leauthaud, A., et al. 2012, ApJ, 744, 159

Lee, H., Skillman, E. D., Cannon, J. M., Jackson, D. C., Gehrz, R. D., Polomski, E. F., & Woodward, C. E. 2006, ApJ, 647, 970

Leitner, S. N. 2012, ApJ, 745, 149

Leitner, S. N., & Kravtsov, A. V. 2011, ApJ, 734, 48

Lequeux, J., Peimbert, M., Rayo, J. F., Serrano, A., & Torres-Peimbert, S. 1979, A&A, 80, 155

Leroy, A. K., et al. 2009, AJ, 137, 4670

Leroy, A. K., Walter, F., Brinks, E., Bigiel, F., de Blok, W. J. G., Madore, B., & Thornley, M. D. 2008, AJ, 136, 2782

Lilly, S. J., Carollo, C. M., Pipino, A., Renzini, A., & Peng, Y. 2013, ApJ, 772, 119

Ly, C., Malkan, M. A., Nagao, T., Kashikawa, N., Shimasaku, K., & Hayashi, M. 2014, ApJ, 780, 122

Maiolino, R., et al. 2008, A&A, 488, 463

Mannucci, F., Cresci, G., Maiolino, R., Marconi, A., & Gnerucci, A. 2010, MNRAS, 408, 2115

Mannucci, F., et al. 2009, MNRAS, 398, 1915

Markwardt, C. B. 2009, in Astronomical Society of the Pacific Conference Series, Vol. 411, Astronomical Data Analysis Software and Systems XVIII, ed. D. A. Bohlender, D. Durand, & P. Dowler, 251

Møller, P., Fynbo, J. P. U., Ledoux, C., & Nilsson, K. K. 2013, MNRAS, 430, 2680

Moustakas, J., et al. 2011, ArXiv e-prints

Nicholls, D. C., Dopita, M. A., & Sutherland, R. S. 2012, ApJ, 752, 148

Niino, Y. 2012, ApJ, 761, 126

Noeske, K. G., et al. 2007, ApJ, 660, L43

Osterbrock, D. E. 1989, Astrophysics of gaseous nebulae and active galactic nuclei, ed. D. E. Osterbrock

Padmanabhan, N., et al. 2008, ApJ, 674, 1217

Pannella, M., et al. 2009, ApJ, 698, L116

Papastergis, E., Cattaneo, A., Huang, S., Giovanelli, R., & Haynes, M. P. 2012, ApJ, 759, 138

Peeples, M. S., & Shankar, F. 2011, MNRAS, 417, 2962

Peeples, M. S., Werk, J. K., Tumlinson, J., Oppenheimer, B. D., Prochaska, J. X., & Katz, N. 2013, ArXiv e-prints

Pérez-Montero, E., et al. 2013, A&A, 549, A25

Pettini, M., & Pagel, B. E. J. 2004, MNRAS, 348, L59

Rosales-Ortega, F. F., Sánchez, S. F., Iglesias-Páramo, J., Díaz, A. I., Vílchez, J. M., Bland-Hawthorn, J., Husemann, B., & Mast, D. 2012, ArXiv e-prints

Saintonge, A., et al. 2011, MNRAS, 415, 32

Salim, S., et al. 2007, ApJS, 173, 267

Sánchez, S. F., et al. 2013, A&A, 554, A58

Savaglio, S., et al. 2005, ApJ, 635, 260

Scoville, N., et al. 2007, ApJS, 172, 1

Strauss, M. A., et al. 2002, AJ, 124, 1810

Thomas, D., Greggio, L., & Bender, R. 1998, MNRAS, 296, 119

Tremonti, C. A., et al. 2004, ApJ, 613, 898

Troncoso, P., et al. 2014, A&A, 563, A58

van der Kruit, P. C., & Freeman, K. C. 2011, ARA&A, 49, 301

Walter, F., Brinks, E., de Blok, W. J. G., Bigiel, F., Kennicutt, Jr., R. C., Thornley, M. D., & Leroy, A. 2008, AJ, 136, 2563

Weiner, B. J., et al. 2007, ApJ, 660, L39

Whitaker, K. E., van Dokkum, P. G., Brammer, G., & Franx, M. 2012, ApJ, 754, L29

Wittman, D. M., et al. 2002, in Society of Photo-Optical Instrumentation Engineers (SPIE) Conference Series, Vol. 4836, Society of Photo-Optical Instrumentation Engineers (SPIE) Conference Series, ed. J. A. Tyson & S. Wolff, 73–82

Yabe, K., et al. 2014, MNRAS, 437, 3647

—. 2012, PASJ, 64, 60

Yates, R. M., Kauffmann, G., & Guo, Q. 2012, MNRAS, 422, 215

Zahid, H. J., Bresolin, F., Kewley, L. J., Coil, A. L., & Davé, R. 2012a, ApJ, 750, 120

Zahid, H. J., Dima, G. I., Kewley, L. J., Erb, D. K., & Davé, R. 2012b, ApJ, 757, 54

Zahid, H. J., Geller, M. J., Kewley, L. J., Hwang, H. S., Fabricant, D. G., & Kurtz, M. J. 2013a, ApJ, 771, L19

Zahid, H. J., et al. 2013b, ArXiv e-prints

Zahid, H. J., Kewley, L. J., & Bresolin, F. 2011, ApJ, 730, 137

Zahid, H. J., Torrey, P., Vogelsberger, M., Hernquist, L., Kewley, L., & Davé, R. 2014, Ap&SS, 349, 873

Chapter 11

Conclusions and Future Directions

A coherent picture of galactic chemical evolution is emerging (see Chapters 2 - 5). This is largely a result of larger samples of galaxies observed outside the local Universe and the application of consistent methodologies for analyzing these galaxies. The chemical evolution of the star-forming population across cosmic time appears to be quite simple. At a fixed stellar mass, galaxies are more enriched at late times. The mass-metallicity (MZ) relation exhibits a power-law tail at low stellar masses and exponentially flattens to an asymptotic saturation metallicity for massive galaxies. The power-law slope and the saturation metallicity do not evolve out to $z \sim 2$. This evolution of the MZ relation can be completely characterized by evolution in the stellar mass where galaxies make the transition from the power-law tail to the asymptotic saturation. This transition or turnover mass is an order of magnitude larger at $z \sim 1.5$ compared to the local Universe.

It is crucial to assess the impact of mass loss through outflows on the chemical evolution of star-forming galaxies. I construct phenomenological models to quantify mass loss in galaxies (see Chapters 6 - 9). A fundamental conclusion of these models is that while the total mass ejected from galaxies over their lifetime remains uncertain, the total amount of oxygen expelled from galaxies scales directly with galactic stellar mass. Under the assumption that the outflowing metallicity is the same as the ISM metallicity, I argue that the hydrodynamical simulations may overestimate mass loss by two orders of magnitude

(Chapter 7). These new empirical constraints are extremely valuable for understanding the MZ relation.

Understanding the chemical evolution of star-forming galaxies requires us to explain the origin of the MZ relation. I fit the MZ relation using a parameterization that is motivated by analytical models of chemical evolution (see Chapter 10). This key step allows me to physically interpret the origin and evolution of the MZ relation. The power-law slope of the MZ relation is set by the slope of the relation between stellar mass and gas mass. The turnover mass is the stellar mass where the stellar-to-gas mass ratio is unity and the saturation metallicity is set by the net yield which is a scaler quantity. The net yield is the nucleosynthetic yield minus the constant fraction of oxygen lost in outflows. Evolution of the relation between stellar mass and gas mass drives the observed evolution of the MZ relation. The higher metallicities observed in galaxies at late time is due to a commensurate decline in the gas content of galaxies.

The relation between metallicity and stellar mass normalized to the turnover mass is redshift independent. I refer to this relation as the Universal Metallicity Relation. Based on our physical interpretation of the MZ relation, the Universal Metallicity Relation is the relation between metallicity and stellar-to-gas mass ratio. Numerical modeling suggests that Universal Metallicity Relation is a relation that is followed by all galaxies as they evolve. This relation provides a fundamentally new paradigm for understanding the chemical evolution of star-forming galaxies.

Future work will expand on many of the themes explored in this dissertation. The Universal Metallicity Relation makes very specific predictions regarding the cosmological evolution of star-forming galaxy gas content. Testing these predictions with direct observations is crucial. ALMA and SKA will be transformative for our knowledge of gas in the Universe and should allow us to directly test our model. The Universal Metallicity Relation is a relation among global properties of galaxies. However, I expect that it should have a local analog since the metallicity of galaxies is instantaneously set by the metal and gas content. Integral field spectrographic surveys such as SAMI or MANGA that are

currently underway will provide important insight into the spatially resolved nature of the Universal Metallicity Relation.

Based on empirically motivated models, I conclude that oxygen mass loss scales is proportional to stellar mass. I intend to test the impact of outflows on metallicity more directly. Outflowing material can be directly traced by observing blue shifted absorption lines in the UV spectra of star-forming galaxies. Based on these observations, the velocity and mass of the outflow can be estimated. By directly comparing the outflow properties of galaxies with observations of their metallicity, I will be able to assess what impact outflows have on metallicity.

The chemical evolution of galaxies is observed to be very simple and appears to be the result of evolution in the relation between stellar mass and gas mass. Based on the Universal Metallicity Relation, I predict that the slope of the relation between stellar mass and gas mass does not evolve with redshift for $z \lesssim 2$. One very important question to address is what is the physical basis for such simple evolution. The slope of the relation between stellar mass and dark matter halo mass is the same as the slope of the relation between stellar mass and gas mass. This may just be a coincidence; but on the other hand, it may be telling us something fundamental about galaxy evolution. If indeed the two slopes are identical, this implies that at any given redshift, the ratio of the gas-to-halo mass is independent of stellar mass. This suggests an important and currently inexplicable connection between dark matter halos and their gas content. I will be collaborating with simulators to further explore this issue.